光応答制御に基づく生命現象の解明と
がん・老化研究への応用

平成25年度～平成27年度私立大学戦略的研究基盤形成支援事業

研　究　成　果　報　告　書

平成28年5月

学校法人名：　学校法人学習院

大　学　名：　学習院大学

研究組織名：　理学部

研究代表者名：花岡　文雄

（学習院大学理学部生命科学科）

目　次

I. はじめに

太陽は、地球における生命の誕生から今日に至るその繁栄に極めて重要な役割を果たしてきた。太陽光には様々な波長の光（電磁波）が含まれており、人間の目に見える可視光は、生物に様々な情報を与え、環境への適応能力の獲得に貢献している。一方、可視光の範囲外にある光は、環境情報としての役割の他に、遺伝情報物質である DNA に損傷を与え発がんの原因になるなど、生体システムの維持にとって脅威となる一面を持っている。

本研究では、微生物から高等動植物に至る様々な生物について、分子レベルから個体レベルに至るあらゆる階層を研究対象として、様々な波長の光が生物に与える影響や情報としての光が関わる生命機能を明らかにし、さらに、それらの情報を基に生物の光情報による環境適応システムの解明と、光を利用した生命機能の解析技術や発がん制御技術の創出を目的とした。具体的には以下の三つの研究課題、すなわち「①放射線が生命に及ぼす影響と耐性機能の解明（**花岡／菱田／安達**）」、「②光の情報を受け取る分子メカニズムの解明（**岡田／岡本／清末**）」、「③光を利用した生命機能の解明と発がん制御技術の開発（**中村／小島／馬渕／西坂**）」に取り組んだ。

各研究課題には、それぞれ3ないし４名の研究者を配置し、菱田教授、清末教授、馬渕教授にそれぞれの課題の取りまとめ役を依頼し、全体を研究代表者の花岡が総括するという体制をとった。3つの研究課題は互いに密接に関係しており、すべて学習院大学生命科学科・大学院自然科学研究科の生命科学専攻に所属しているので、月に2回、定期的に開かれる専攻会議の場で議論した。本プロジェクトの途中から中村教授が東工大に異動したが、その後も本学の非常勤講師を務めており、頻繁に議論を行った。さらに中村教授以外のメンバーは地理的にも近接した二つの建物で研究を行っており、必要なときにはいつでも行き来して情報交換を行った。

各研究室には基本的に1名の助教がおり、教授とともに本プロジェクトに関与した。また、本プロジェクトで雇用したポスドクは、PD 研究員という身分でプロジェクトを推進した。さらに全体4～5名のリサーチアシスタントと各研究室数名から 10 名近くの大学院生も積極的に本プロジェクトに参加し、主にマンパワーとして貢献した。主要な装置、設備の利用・管理について、メーカーによる説明会を開催したり、研究参加者からの個別相談に対応したりといった技術的サポートをプロジェクトメンバーの研究室に所属する各助教が、また各種申請書・報告書等の作成支援および経理業務といった事務的サポートを理学部事務室が中心となってそれぞれ行ない、円滑な研究遂行のための支援体制を構築した。

共同研究機関としては、プロジェクトの途中から中村教授の異動先である東工大の資源化学研究所が主たるものであるが、それ以外にも国内外の複数の研究機関と積極的に共同研

究を進めた。これら3つの研究テーマのメンバーがグループ内及びグループ間で共同研究やセミナーなどを行い、互いに連携しながら研究を推進した。中村は、平成 25 年 9 月 1 日から東京工業大学の資源化学研究所に教授として転出したが、その後も共同研究機関の立場でプロジェクトに参加した。西坂は平成25年度まで「最先端次世代研究開発支援プログラム」に参画中のため、初年度は連携研究者として参加した。

建物としては、本プロジェクトの前身である「生体システムの環境応答に関する分子細胞生物学的研究 －老化・がん化の制御に向けて－」の予算から補助を受けた南 7 号館（自然科学研究棟：整備年度 H21）に 1,718 m^2 と、旧くから存在・使用している南 6 号館（生命分子科学研究所：整備年度 H4）に 448 m^2 が存在し、それぞれ 7 研究室（当初は 8 研究室）と 2 研究室がプロジェクトを推進した。本プロジェクトの途中から、中村教授は東工大の資源化学研究所に教授として転出し、そちらの建物でプロジェクトを推進した。

本事業で助成され購入した「アコースティックソルビライザー」および「デジタルマイクロスコープ」は、それぞれ稼働時間約 450 時間／年と 500 時間／年、また別予算で購入した「オールインワン蛍光顕微鏡システム」、「共焦点スキャナユニット」、「倒立顕微鏡 Ti-E パーフェクトフォーカスシステム」等の顕微分光関連設備については、それぞれ約 1,200 時間／年、100 時間／年、1,000 時間／年の稼働時間が実績として残された。これらの設備は、上記二つの建物に設置され、プロジェクト参加研究員 10 名（現在 9 名）、助教 10 名（現在 9 名）、PD 研究員 1 名に加え、大学院生約 15 名、学部生約 45 名が有効に利用した。

本プロジェクトの構成員の多方面の卓越した研究を基盤に、多様な生物が様々な波長の光にどのように応答し、適応しているのかを分子レベルで解析し、そのメカニズムを明らかにすることを目標とした。さらにそのメカニズムに欠陥が生じたとき、老化やがん化といったプロセスがどのように促進されるのかを明らかにすることによって、これら高次生命現象を制御する方策を探ることも目指した。

II. 研究組織

研究課題1. 放射線が生命に及ぼす影響と耐性機能の解明

研究者名	プロジェクトでの研究課題	プロジェクトでの役割
花岡　文雄	遺伝子損傷の細胞応答とがん化・老化	紫外線等による DNA 損傷が個体のがん化・老化に及ぼす影響とその防御機構の研究
菱田　卓 （取りまとめ役）	DNA 損傷ストレスに対する耐性機構の解明	電離放射線や紫外線などの微量かつ慢性的な DNA 損傷ストレスに対する生物の適応機構の解明
安達　卓	放射線に対する細胞死耐性の機構	放射線が導く細胞死応答に対して耐性をもつ細胞における分子機構の解明

研究課題2. 光の情報を受け取る分子メカニズムの解明

研究者名	プロジェクトでの研究課題	プロジェクトでの役割
岡田　哲二	受容体分子構造基盤の解明	視覚関連タンパク質の動作原理の解明
岡本　治正	眼の発生・機能関連新規遺伝子の同定	光情報の処理にかかわる新規因子の同定
清末　知宏 （取りまとめ役）	高等植物の光環境応答と花成	光周性による成長相転換制御機構の解明

研究課題3. 光を利用した生命機能の解明と発がん制御技術の開発

研究者名	プロジェクトでの研究課題	プロジェクトでの役割
中村　浩之	光を利用した生命機能解明とがん治療	光触媒による生命機能解明のための新しいケミカルプローブの開発を行うとともに、ホウ素と中性子の核反応による新しい放射線療法のためのホウ素薬剤開発を行う
小島　修一	生体防御関連タンパク質の構造および生化学的解析	タンパク質の活性制御領域の構造・機能解析と新規阻害剤の開発
馬渕　一誠 （取りまとめ役）	細胞分裂構造の制御メカニズムの解明	細胞のがん化と、がん細胞の浸潤運動のメカニズムの理解
西坂　崇之	光学顕微鏡技術を駆使した生体分子の動態の可視化	光学顕微鏡技術の開発によって生体分子やその超構造の動態を明らかにし、生命機能のより詳細な理解に貢献する

III. 研究課題1 「放射線が生命に及ぼす影響と耐性機能の解明」

本課題では、遺伝子 DNA に損傷を与える主要な環境要因である紫外線や電離放射線に着目し、これらの要因による DNA 損傷が生物にどのような影響を及ぼすか、そして生物はこれらの DNA 損傷にどのようにして耐性を獲得するのかを中心に解析した。特に紫外線への曝露によって高頻度に皮膚がんを発症するヒト遺伝病、色素性乾皮症（XP）、中でもバリアント群 XP の原因遺伝子産物である XPV タンパク質（Polη ）の構造と機能について、タンパク質レベル、細胞レベル、個体レベルなど様々な観点から研究を行った。また放射線や紫外線による細胞の耐性に DNA の相同組換え機構が働いていること、そして出芽酵母においては慢性的な紫外線ストレスが染色体の倍数化を引き起こすという興味深い結果が得られており、それらのメカニズムについて明らかにする試みがなされた。一方、ショウジョウバエのオス成虫がもつ内部生殖器官である附属腺を用いて、放射線ストレスへの細胞応答の代表である細胞死に対して耐性になる場合とそうでない場合との比較を行い、興味深い結果が得られた。以下に、これらの研究について、それぞれの研究担当者からの解説と業績リスト、そして代表的な論文 2 編ずつを掲載する。

遺伝子損傷の細胞応答とがん化・老化

教授　花岡　文雄
助教　横井　雅幸
助教　川元　洋子
（2013 年度のみ）

[目的]

遺伝子 DNA は種々の内的あるいは外的な要因によって、その複製を阻害されたり、損傷を受けたりしている。そのような状態を放置すると個体に老化やがん化をもたらす。特に日光中の紫外線には地球上の全ての生物が例外なく曝されており、DNA にシクロブタン型ピリミジン二量体（cyclobutane pyrimidine dimer: CPD）や 6-4 光産物といった損傷が生じる。生物は、こうした紫外線損傷を修復したり、DNA 合成期に乗り越えたり（translesion synthesis: TLS）する能力を備えているが、ヒトにはそうした能力に欠損を持つ遺伝的疾患が複数存在する。中でも色素性乾皮症（xeroderma pigmentosum: XP）の患者は皮膚の早期老化および高い頻度での皮膚がんの発症を特徴とする。本研究では我々のグループが発見したバリアント群 XP の責任遺伝子産物で、CPD を効率良く正確に乗り越える DNA ポリメラーゼであるポル・イータ（Pol η）[1] を中心に、ヒトおよびマウスの TLS ポリメラーゼの生理的な機能やその X 線結晶構造 [2] に基づいた変異体を解析し、TLS ポリメラーゼの欠損や変異による個体のがん化・老化の分子的な基盤を明らかにすることを目的とする。

[結果と考察]

1.　TLS ポリメラーゼの多彩な機能について

(1) Pol η が体細胞超突然変異に働く分子メカニズムの解明

B 細胞において、V(D)J 組換え後に免疫グロブリン遺伝子に起きる体細胞超突然変異（somatic hypermutation: SHM）は、免疫グロブリンに多様性をもたらすために必須のメカニズムである。これまでの研究から、RGYW と WA（R は purine; Y:は pyrimidine; W は A または T）という二つの SHM のホットスポットのうち WA に関しては Pol η がメインな役割を果たしていると考えられている。今回、我々は米国 NIH のグループなどとの共同研究により、ヒト Pol η の触媒活性を担う部分タンパク質（1-432）とプライマー末端の鋳型側の WA モチーフが TA または AA、あるいは非 WA の配列（CA または GA）との共結晶を作成し、それらの X 線結晶構造を解析した。その結果、WA モチーフの T に対して dGTP が wobble 塩基対を形成する際に Gln-38 と Arg-61 とが安定化に働いていること、プライマー末端の W（T:A または A:T）の弱い塩基対と Pol η との相互作用が WA モチーフへの G の誤塩基取り込みに導くことが明らかになった。二つの WA モチーフの中でも AA よりも TA 配列が A から G への変異をより起こし易いこと、また Pol η は T:G 誤塩基対を効率良く伸長し、突然変異を完成させることが判明した [3]。

(2) DNA の再複製における TLS ポリメラーゼの役割

DNA の再複製は、遺伝子重複などのゲノム不安定性に寄与する異常複製の主要なプロセスである。しかしどの DNA ポリメラーゼがこのプロセスに働いているかは明らかになっていない。本研究では、DNA 複製に必須の因子である Cdt1 を阻害することによって、1 細胞周期に一度しか DNA 複製が起きないようにしている重要な因子である geminin を

siRNA 処理によって DNA 再複製を誘導する系[4]を用い、Pol η、ポル・カッパ（Pol κ）、ポル・イオタ（Pol ι）、REV1 などの忠実度の低い Y ファミリー・ポリメラーゼやポル・デルタ（Pol δ）やポル・イプシロン（Pol ε）などの複製型ポリメラーゼの DNA 再複製への関与を調べた。その結果、これらの TLS 型や複製型の DNA ポリメラーゼはヒト U2OS 細胞の再複製部位へとリクルートされること、またこれらのポリメラーゼを RNAi によってノックダウンすると geminin レベルの低下によって誘導される「DNA の再複製」が抑制されることが分かった[5]。興味深いことに、Y ファミリー・ポリメラーゼは複製型ポリメラーゼとは異なる経路で再複製に働いていることが示唆された。さらに cyclin E の過剰発現による DNA の再複製にも Pol η と Pol κ が関与していること、また Pol η の触媒活性が必要なことも明らかとなった。

2. シトシンを含む CPD とそれに対する Pol η の働き

(1) CPD 中で安定なシトシンの誘導体

CPD は紫外線による DNA の損傷の中で主要なものであるが、通常、実験に使用されるのはほとんどチミン-チミン二量体である。それは DNA 中のシトシンが生理的な条件下でも不可逆的に脱アミノ化を受けてウラシルになりやすく、CPD を形成するとさらに脱アミノ化が促進されるので、実用的でないのである。先行研究で、5-メチルシトシン（mC）はシトシンよりも安定なこと、mC を含む CPD もシトシンを含む CPD よりも安定なことが示されていたので、DNA 合成機でオリゴ DNA を合成する際、さらに安定と思われる N^4-mC（mC^m）をチミンと共に CPD 形成させた T[]mC^m を有機合成し使用した。その結果、T[]mC^m を含むオリゴ DNA の寿命は生理的条件下で約 1 週間と比較的長く、ヒト Pol η を用いた *in vitro* の TLS 反応において T[]mC^m の mC^m の反対側に dGMP の取り込みだけでなく、TMP も相当な頻度（約 6/16 の割合）で取り込まれること、また TMP が取り込まれた場合、そこで DNA 合成が停止しやすいことが分かった[6]。

(2) 野生型および Pol η 欠損マウス皮膚における紫外線誘発突然変異の塩基配列特異性

λ ファージをベースに、*lacZ* 遺伝子をレポーターにしたプラスミドを持つマウスを野生型および Pol η 欠損マウスと掛け合わせ、背中の皮膚に UVB を照射して、表皮と真皮における紫外線誘発突然変異の頻度（mutant frequency: MF）とスペクトルを解析した[7]。表皮および真皮のいずれにおいても、Pol $\eta^{-/-}$ マウスは、野生型（Pol $\eta^{+/+}$）およびヘテロ（Pol $\eta^{+/-}$）マウスに比べ高い UVB 誘発 MF を示した。野生型とヘテロとでは有意な差は見られなかった。野生型と Pol $\eta^{-/-}$ マウスで UVB 誘発および未処理の条件下での変異スペクトルを比較したところ、いずれにおいても UVB 照射に特異的で dipyrimidine 部位での C から T への transition がメインであった。しかしながら変異スペクトルを詳細に検討したところ、野生型の上皮では 5'-TCG-3'配列での変異がドミナントであるのに対し、Pol $\eta^{-/-}$ マウスではそのような配列特異性が見られなかった。このことは、Pol $\eta^{-/-}$ マウスでは CPD の乗り越えに変異を起こしやすい TLS ポリメラーゼが働いており、特に 5'-TCG-3'配列がホットスポットになっていることを示唆している。

3. 複数の TLS ポリメラーゼ間での機能の連携

以前、我々は Pol η と Pol ι の単独あるいは二重欠損マウスの紫外線照射皮膚がん誘発実験により、Pol η／Pol ι 二重欠損マウスでは、Pol η 単独欠損マウスと比べ UVB 誘発皮膚

がんの頻度はあまり変わらないが、Pol η 単独欠損マウスではもっぱら上皮性のがんを生じるのに対し、Pol ι 単独欠損あるいは Pol η /Pol ι 二重欠損マウスにおいては、Pol η 単独欠損マウスでは見られない肉腫の形成を認めた [8]。これらのことは、Pol η も Pol ι もマウスの UVB による皮膚がん誘発を抑制していること、またその抑制の部位、組織等が異なることを示唆している。そこで大腸菌 *rpsL* 遺伝子を約 100 コピー、レポーターとしてゲノム中に有するマウスを上記のポリメラーゼ欠損マウスと掛け合わせキメラマウスを作成し、これらのマウス表皮を用いて、UVB 誘発 MF と変異スペクトルを解析した。予想通り、Pol η 単独欠損マウスは野生型に比べ非常に高い UVB 誘発 MF を示し、Pol ι 単独欠損では野生型とほとんど変わらなかった。興味深いことに、Pol η /Pol ι 二重欠損マウスにおいては Pol η 単独欠損マウスに比べ、UVB 誘発 MF が低かった。このことは、Pol η が欠損している状況で、Pol ι は Pol η の代わりに働くが、その際、誤塩基を対合しやすいことを示している。変異スペクトルの解析から、Pol η 単独欠損でも Pol η /Pol ι 二重欠損でも、UVB 誘発変異のほとんどはジピリミジン部位に起きていること、Pol η 単独欠損で変異は G:C と A:T の両方の塩基対で起きていることから *in vivo* で Pol η はシトシンとチミンのいずれのピリミジンを含む二量体も正しく乗り越えることが分かった。さらに Pol η /Pol ι 二重欠損では、G:C から A:T へのトランジションが Pol η 単独欠損に比べ有意に低下することから、Pol ι はシトシンを含む二量体の乗り越え時に誤対合を起こしやすいことが示唆された [9]。

[まとめ]

Pol η が体細胞超突然変異に働いていることは、様々な免疫学的な解析から分かっていたが、今回、ヒト Pol η の立体構造が安定な部分タンパク質と様々な鋳型・プライマー末端の共結晶の構造解析から、実体としてヒト Pol η が変異の誘導に機能しているメカニズムを明らかにしたことは大きな意義がある。また発がんとの関係で重要な事象である「DNA の再複製」に複製型ポリメラーゼだけでなく、TLS 活性を持つ Y ファミリーポリメラーゼも機能していることは大変興味深い。特に Pol η の触媒活性が必要である点は、がん化のメカニズムを考える上でも重要である。

これまでシトシンを含む CPD の研究は、その不安定さゆえにチミン-チミン二量体に比べて遥かに立ち後れていた。今回、N4-メチル-5-メチルシトシンとチミンの二量体が比較的安定に存在することが分かり。これまで実験的にアプローチ出来なかった点に大きく寄与することが期待される。

今回の研究で、UVB 誘発皮膚がんの突然変異頻度と変異スペクトルが色々と解析出来た。こうした研究は、皮膚がんだけでなく、一般的にがんの発生にどのような変異が重要であるかを知るための大事なステップとなるであろう。

[参考文献]

1. Masutani, C., Kusumoto, R., Yamada, A., Dohmae, N., Yokoi, M., Yuasa, M., Araki, M., Iwai, S., Takio, K., and Hanaoka, F. (1999) The *XPV* (xeroderma pigmentosum variant) gene encodes human DNA polymerase η. Nature *399,* 700-704.
2. Biertümpfel, C., Zhao, Y., Kondo, Y., Ramon-Maiques, S., Gregory, M., Lee, J. Y., Masutani, C., Lehmann, A. R., Hanaoka, F., and Yang, W. (2010) Structure and mechanism of human DNA polymerase η. Nature *465*, 1044-1049.

3. Zhao, Y., Gregory, M. T., Biertümpfel, C., Hua, Y. J., Hanaoka, F., and Yang, W. (2013) Mechanism of somatic hypermutation at the WA motif by human DNA polymerase eta. Proc. Natl. Acad. Sci. USA *110*, 8146-8151.
4. Melixetian, M., Ballabeni, A., Masiero, L., Gasparini, P., Zamponi, R., Bartek, J., Lukas, J., and Helin, K. (2004) Loss of geminin induces rereplication in the presence of functional p53. J. Cell Biol. *165*, 473-482.
5. Sekimoto, T., Oda, T., Kurashima, K., Hanaoka, F., and Yamashita, T. (2015) Both high-fidelity replicative and low-fidelity Y-family polymerases are involved in DNA rereplication. Mol. Cell. Biol. *35*, 699-715.
6. Yamamoto, J., Oyama, T., Kunishi, T., Masutani, C., Hanaoka, F., and Iwai, S. (2014) A cyclobutane thymine-N4-methylcytosine dimer is resistant to hydrolysis but strongly blocks DNA synthesis. Nucleic Acids Res. *42*, 2075-2084.
7. Ikehata, H., Chang, Y., Yokoi, M., Yamamoto, M., and Hanaoka, F. (2014) Remarkable induction of UV-signature mutations at the 3'-cytosine of dipyrimidine sites except at 5'-TCG-3' in the UVB-exposed skin epidermis of xeroderma pigmentosum variant model mice. DNA Repair *22,* 112-122.
8. Ohkumo, T., Kondo, Y., Yokoi, M., Tsukamoto, T., Yamada, A., Sugimoto, T., Kanao, R., Higashi, Y., Kondoh, H., Tatematsu, M., Masutani, C., and Hanaoka, F. (2006) UV-B radiation induces epithelial tumors in mice lacking DNA polymerase η and mesenchymal tumors in mice deficient for DNA polymerase ι. Mol. Cell. Biol. *26*, 7696-7706.
9. Kanao, R., Yokoi, M., Ohkumo, T., Sakurai, Y., Dotsu, K., Kura, S., Nakatsu, Y., Masutani, C., and Hanaoka, F. (2015) UV-induced mutations in epidermal cells of mice defective in DNA polymerase η and/or ι. DNA Repair *29*, 139-146.

［原著論文］

1. Eki, T., Murakami, Y., and Hanaoka, F. (2013) Trapping DNA replication origins from the human genome. Genes *4*, 198-225. 査読有
2. Zhao, Y., Gregory, M. T., Biertümpfel, C., Hua, Y. J., Hanaoka, F., and Yang, W. (2013) Mechanism of somatic hypermutation at the WA motif by human DNA polymerase eta. Proc. Natl. Acad. Sci. USA *110*, 8146-8151. 査読有
3. Nishi, R., Sakai, W., Tone, D., Hanaoka, F., and Sugasawa, K. (2013) Structure-function analysis of the EF-hand protein centrin-2 for its intracellular localization and nucleotide excision repair. Nucleic Acids Res. *41*, 6917-6929. 査読有
4. Yamamoto, J., Oyama, T., Kunishi, T., Masutani, C., Hanaoka, F., and Iwai, S. (2014) A cyclobutane thymine-N4-methylcytosine dimer is resistant to hydrolysis but strongly blocks DNA synthesis. Nucleic Acids Res. *42*, 2075-2084. 査読有
5. Shibutani, T., Ito, S., Toda, M., Kanao, R., Collins, L. B., Shibata, M., Urabe, M., Koseki, H., Masuda, Y., Swenberg, J. A., Masutani, C., Hanaoka, F., Iwai, S., and Kuraoka, I. (2014) Sci. Rep. Jun 9;*4*:5220. 査読有
6. Kamath-Loeb, A. S., Balakrishna, S., Whittington, D., Shen, J. C., Emond, M. J., Okabe, T., Masutani, C., Hanaoka, F., Nishimura, S., and Loeb, L. A. (2014) Sphingosine, a modulator of human translesion DNA polymerase activity. J. Biol. Chem. *289*, 21663-21672. 査読有
7. Ikehata, H., Chang, Y., Yokoi, M., Yamamoto, M., and Hanaoka, F. (2014) Remarkable induction of UV-signature mutations at the 3'-cytosine of dipyrimidine sites except at 5'-TCG-3' in the UVB-exposed skin epidermis of xeroderma pigmentosum variant model mice. DNA Repair *22*, 112-122. 査読有
8. Akimoto, Y., Yamamoto, S., Iida, S., Hirose, Y., Tanaka, A., Hanaoka, F., and Ohkuma, Y. (2014) Transcription cofactor PC4 plays essential roles in collaboration with the small subunit of general transcription factor TFIIE. Genes Cells *19*, 879-890. 査読有
9. Sekimoto, T., Oda, T., Kurashima, K., Hanaoka, F., and Yamashita, T. (2015) Both high-fidelity replicative and low-fidelity Y-family polymerases are involved in DNA rereplication. Mol. Cell. Biol. *35*, 699-715. 査読有
10. Matsumoto, S., Fisher, E. S., Yasuda, T., Dohmae, N., Iwai, S., Mori, T., Nishi, R., Yoshino, K., Sakai, W., Hanaoka, F., Thomä, N.H., and Sugasawa, K. (2015) Functional regulation of the damage-recognition factor DDB2 by ubiquitination and interaction with xeroderma pigmentosum group C protein. Nucleic Acids Res. *43*, 1700-1713. 査読有
11. Kanao, R., Masuda, Y., Deguchi, S., Yumoto-Sugimoto, M., Hanaoka, F., and Masutani, C. (2015) Relevance of simultaneous mono-ubiquitinations of multiple units of PCNA homo-trimers in DNA damage tolerance. PLoS One 2015; *10*: e0118775. 査読有
12. Tanaka, A., Akimoto, Y., Kobayashi, S., Hisatake, K., Hanaoka, F., and Ohkuma, Y. (2015) Association of the winged helix motif of the TFIIEα subunit of TFIIE with either the TFIIEβ subunit or TFIIB distinguishes its functions in transcription. Genes Cells *20*, 203-216. 査読有
13. Tsaalbi-Shtylik, A., Ferrás, C., Pauw, B., Hendriks, G., Temviriyanukul, P., Calléja, F., Van Hees, S., Akagi, J., Iwai, S., Hanaoka, F., Jansen, J. G., and de Wind, N. (2015) Excision of translesion synthesis errors orchestrates responses to helix-distorting DNA lesions. J. Cell Biol. *209*, 33-46. 査読有
14. Kanao, R., Yokoi, M., Ohkumo, T., Sakurai, Y., Dotsu, K., Kura, S., Nakatsu, Y., Masutani, C., and Hanaoka, F. (2015) UV-induced mutations in epidermal cells of mice defective in DNA polymerase η and/or ι. DNA Repair *29*, 139-146. 査読有
15. Akita, M., Tak, Y. S., Shimura, T., Matsumoto, S., Okuda-Shimizu, Y., Shimizu, Y., Nishi, R., Saitoh, H., Iwai, S., Mori, T., Ikura, T., Sakai, W., Hanaoka, F., and Sugasawa, K. (2015) SUMOylation of xeroderma pigmentosum group C protein regulates DNA damage recognition during nucleotide excision repair. Sci. Rep. 2015 Jun 4;*5*:10984. 査読有
16. Uchiyama, M., Terunuma, J., and Hanaoka, F. (2015) The protein level of Rev1, a TLS polymerase in fission yeast, is strictly regulated during the cell cycle and after DNA damage. PLoS One 2015 Jul 6;*10*:e0130000. 査読有

17. Masuda, Y., Kanao, R., Kaji, K., Ohmori, H., Hanaoka, F., and Masutani, C. (2015) Different types of interaction between PCNA and PIP boxes contribute to distinct cellular functions of Y-family DNA polymerases. Nucleic Acids Res. *43*, 7898-7910. 査読有
18. Osakabe, A., Tachiwana, H., Kagawa, W., Horikoshi, N., Matsumoto, S., Hasegawa, M., Matsumoto, N., Toga, T., Yamamoto, J., Hanaoka, F., Thomä, N. H., Sugasawa, K., Iwai, S., and Kurumizaka, H. (2015) Structural basis of pyrimidine-pyrimidone (6-4) photoproduct recognition by UV-DDB in the nucleosome. Sci. Rep. 2015 Nov 17;*5*:16330. 査読有
19. Kashiwaba, S., Kanao, R., Masuda, Y., Kusumoto-Matsuo, R., Hanaoka, F., and Masutani, C. (2015) USP7 is a suppressor of PCNA ubiquitination and oxidative-stress-induced mutagenesis in human cells. Cell Rep. 2015 Dec 15;*13*:2072-2080. 査読有

[総説等]

1. Hanaoka, F. (2013) Xeroderma Pigmentosum. In "Brenner's Encyclopedia of Genetics, 2nd Edition" Vol. 7, 359-362.
2. 花岡文雄　環境と遺伝子変化. 新訂　物質環境科学 ('14); 濱田嘉昭、花岡文雄 共編、放送大学教育振興会、pp.114-127 (2014).
3. 花岡文雄　遺伝子損傷の修復. 新訂　物質環境科学 ('14); 濱田嘉昭、花岡文雄 共編、放送大学教育振興会、pp.128-142 (2014).
4. 花岡文雄　環境と化学物質. 新訂　物質環境科学 ('14); 濱田嘉昭、花岡文雄 共編、放送大学教育振興会、pp.143-157 (2014).
5. 花岡文雄　紫外線と健康. 新訂　物質環境科学 ('14); 濱田嘉昭、花岡文雄 共編、放送大学教育振興会、pp.158-171 (2014).
6. 濱田嘉昭、花岡文雄　放射線と化学. 生活と化学 ('14); 濱田嘉昭、花岡文雄 共編、放送大学教育振興会、pp.161-178 (2014).
7. Masuda, Y., Hanaoka, F., and Masutani, C. Translesion DNA synthesis and damage tolerance pathways. In "DNA Replication, Recombination, and Repair: Molecular Mechanisms and Pathology", (eds by F. Hanaoka, and K. Sugasawa) Springer, Japan, pp. 249-304 (2016).
8. Hanaoka, F., and Sugasawa, K. Edition: DNA Replication, Recombination, and Repair: Molecular Mechanisms and Pathology (Tokyo, Springer)

［口頭発表］

1. Hanaoka, F., Structure and function of mammalian DNA polymerase eta with special reference on translesion synthesis and somatic hypermutation. 京都大学大学院医学研究科・免疫ゲノム医学特別セミナー、招待講演（2013 年 5 月 27 日、京都）
2. 川元ー尾崎洋子、水島恒裕　出芽酵母 COP9 シグナロソームの発現系構築. 第 13 回日本蛋白質科学会年会、ポスター発表（2013 年 6 月 12-14 日、鳥取）
3. 花岡文雄　がんとは何か？　―その発生のメカニズムを探る―　読売サイエンスフォーラム ―学習院大学理学部の研究力―　ここまで来た！がん研究最前線　招待講演（2013 年 7 月 27 日、東京）
4. 越坂部晃永、堀越直樹、立和名博昭、香川亘、安田武嗣、花岡文雄、菅澤薫、岩井成憲、胡桃坂仁志　紫外線損傷 DNA を含むヌクレオソームの生化学的および構造生物学的解析、第 86 回日本生化学会大会、口頭発表・ポスター発表（2013 年 9 月 11-13 日、横浜）
5. 川元ー尾崎洋子、水島恒裕　出芽酵母 COP9 シグナロソームの発現系構築、第 86 回日本生化学会大会、ポスター発表（2013 年 9 月 11-13 日、横浜）
6. 横井雅幸　ゲノム情報維持における DNA ポリメラーゼ・イオタの役割、国立遺伝学研究所研究集会「染色体 DNA の安定維持の分子メカニズム」、口頭発表（2013 年 9 月 27-28 日、三島）

7. Sekimoto, T., Oda, T., Masutani, C., Hanaoka, F., and Yamashita, T., Y-family polymerases participate in oncogene-induced DNA re-replication. 第 72 回日本癌学会学術総会、ポスター発表（2013 年 10 月 3-5 日、横浜）
8. Yokoi, M., Sakurai, Y., and Hanaoka, F., DNA polymerse ι, as a member of genome guardians. 第 72 回日本癌学会学術総会、ポスター発表（2013 年 10 月 3-5 日、横浜）
9. 越坂部晃永、立和名博昭、堀越直樹、香川亘、安田武嗣、花岡文雄、菅澤薫、岩井成憲、胡桃坂仁志　紫外線損傷 DNA を含むヌクレオソームの構造生物学・生化学的解析、第 22 回 DNA 複製・組換え・修復ワークショップ、ポスター発表（2013 年 11 月 20-22 日、仙台）
10. 倉島公憲、小田司、関本隆志、小林広美、尤礼佳、花岡文雄、山下孝之　c-Myc 発現亢進による複製ストレスにおけるポリメラーゼ η と PML の関与、第 22 回 DNA 複製・組換え・修復ワークショップ、ポスター発表（2013 年 11 月 20-22 日、仙台）
11. 小林百合香、宮澤沙絵、水野武、立澤桜子、花岡文雄、鳥越秀峰　マウステロメア結合タンパク質 Pot1a/b と DNA ポリメラーゼ α の相互作用解析、第 22 回 DNA 複製・組換え・修復ワークショップ、ポスター発表（2013 年 11 月 20-22 日、仙台）
12. 泉雅子、水野武、今本尚子、阿部知子、花岡文雄　ヒト Mcm10 と Mcm2-7 複合体の相互作用とその制御機構の解析、第 22 回 DNA 複製・組換え・修復ワークショップ、ポスター発表（2013 年 11 月 20-22 日、仙台）
13. 水野武、小林百合香、宮澤沙絵、泉雅子、花岡文雄、鳥越秀峰　DNA ポリメラーゼ α を複製フォークに呼び込む因子群 iPAOBs の提唱、第 22 回 DNA 複製・組換え・修復ワークショップ、ポスター発表（2013 年 11 月 20-22 日、仙台）
14. 櫻井靖高、横井雅幸、花岡文雄　皮膚細胞における TLS ポリメラーゼの役割分担、第 22 回 DNA 複製・組換え・修復ワークショップ、口頭発表（2013 年 11 月 20-22 日、仙台）
15. 金尾梨絵、増田雄司、花岡文雄、益谷央豪　ヒト細胞における PCNA の翻訳後修飾による複製阻害回避機構の解析、第 22 回 DNA 複製・組換え・修復ワークショップ、口頭発表（2013 年 11 月 20-22 日、仙台）
16. 安田武嗣、香川亘、斉藤健吾、荻朋男、鈴木健裕、堂前直、日野拓也、中沢由華、早乙女（中邑）愛、下等宝光、Genet, M., 花岡文雄、菅澤薫、田嶋克史、胡桃坂仁志　ヒト Rad52 タンパク質のアセチル化による DNA 二重鎖切断修復制御、第 22 回 DNA 複製・組換え・修復ワークショップ、口頭発表（2013 年 11 月 20-22 日、仙台）
17. Hanaoka, F., Role of DNA polymerase eta in somatic hypermutation. The 3rd Frence-Japanese Cancer Meeting、招待講演（2013 年 11 月 20-23 日, Toulouse, France）
18. 水野武、渋谷麻美、花岡文雄、今本尚子　哺乳類細胞核内の異常タンパク質を排除するタンパク質品質管理機構に働くタンパク質分解系の解析、第 31 回染色体ワークショップ・第 12 回核ダイナミクス研究会、口頭発表（2013 年 11 月 25-27 日、箱根）
19. 内山雅司、小田嶋嶺太、花岡文雄　分裂酵母 Rev1 の過剰発現による chk1 欠損株のシスプラチン感受性の相補は損傷乗り越え機構と細胞周期チェックポイント機構が相互に協調することを示す、第 36 回日本分子生物学会年会、ポスター発表（2013 年 12 月 3-6 日、神戸）
20. 水野武、渋谷麻美、花岡文雄、今本尚子　哺乳類細胞核内の異常タンパク質を排除す

るタンパク質品質管理機構に働くタンパク質分解系の解析、第 36 回日本分子生物学会年会、ポスター発表（2013 年 12 月 3-6 日、神戸）

21. 阿曽沙織、照沼淳子、金谷秀人、内山雅司、花岡文雄　分裂酵母 Rev3 の APMI 型 PCNA 結合領域は Rev3/Rev7 と Cdc1/Cdc2 から成る DNA Polymerase zeta;複合体形成に必須である、第 36 回日本分子生物学会年会、ポスター発表（2013 年 12 月 3-6 日、神戸）
22. 船岳朋弘、内山雅司、花岡文雄　分裂酵母 Rev1 BRCT 領域の機能解析、第 36 回日本分子生物学会年会、ポスター発表（2013 年 12 月 3-6 日、神戸）
23. 渋谷卓未、横井雅幸、Yang, W., 花岡文雄　ヒト DNA ポリメラーゼ η の W297 を中心とした疎水性ポケットとヌクレオチドの相互作用に関する研究、第 36 回日本分子生物学会年会、ポスター発表（2013 年 12 月 3-6 日、神戸）
24. 倉島公憲、小田司、関本隆志、小林広美、尤礼佳、花岡文雄、山下孝之　c-Myc による DNA 複製ストレスに DNA ポリメラーゼ η が関与する、第 36 回日本分子生物学会年会、ポスター発表（2013 年 12 月 3-6 日、神戸）
25. 栗山磯子、水野武、赤木純一、横井雅幸、花岡文雄、吉田弘美、水品善之　DNA ポリメラーゼ η を阻害するビタミン K3 誘導体と紫外線照射の併用効果の影響、第 36 回日本分子生物学会年会、ポスター発表（2013 年 12 月 3-6 日、神戸）
26. 渡部周二、堀岡敬太、吉政隆、小田島千尋、花岡文雄、浴俊彦　染色体動態制御に必須な線虫 RNA 干渉タンパク質 DRH-3 の分子機能解析、第 36 回日本分子生物学会年会、ポスター発表（2013 年 12 月 3-6 日、神戸）
27. 関本隆志、小田司、倉島公憲、花岡文雄、山下孝之　ポリメラーゼ η は、発がんシグナルが誘導する DNA 再複製に関与する、第 36 回日本分子生物学会年会、ポスター発表（2013 年 12 月 3-6 日、神戸）
28. 金尾梨絵、増田雄司、花岡文雄、益谷央豪　ヒト細胞における PCNA ホモ 3 量体の翻訳後修飾による DNA 損傷トレランス制御、第 36 回日本分子生物学会年会、ポスター発表、（2013 年 12 月 3-6 日、神戸）
29. 浴俊彦、村上康文、花岡文雄　2 種類のオリジントラップ法によるヒト複製オリジン断片の単離と配列解析、第 36 回日本分子生物学会年会、ポスター発表（2013 年 12 月 3-6 日、神戸）
30. Yokoi, M., Sakurai, Y., Hando, N., Morita, D., and Hanaoka, F., Physiological role of TLS polymerases in mouse skin upon UV irradiation. International Conference, Kyoto, 2014: Replication, Repair and Transcription; coupling mechanisms and chromatin dynamics for genome integrity. 招待講演（2014 年 2 月 4-5 日、京都）
31. Kanao, R., Masuda, Y., Hanaoka, F., and Masutani, C., Regulation of DNA damage tolerance distinct from Polη-mediated translesion synthesis. International Conference, Kyoto, 2014: Replication, Repair and Recombination; coupling mechanisms and chromatin dynamics for genome integrity. 招待講演（2014 年 2 月 4-5 日、京都）
32. Yang, W., Lee, Young-Sam, Zhao, Y., Nakamura, T., Biertümpfel, C., Yamagata, Y., Hua, Y., and Hanaoka, F., All road leads to DNA-lesion bypass: mechanisms of translesion synthesis. International Conference, Kyoto, 2014: Replication, Repair and Recombination; coupling mechanisms and chromatin dynamics for genome integrity. 招待講演（2014 年 2 月 4-5 日、京都）

33. Osakabe, A., Tachiwana, H., Horikoshi, N., Kagawa, W., Yasuda, T., Hanaoka, F., Sugasawa, K., Iwai, S., and Kurumizaka, H., Structural and biochemical analyses of the nucleosome containing UV-damaged DNA. International Conference, Kyoto, 2014: Replication, Repair and Recombination; coupling mechanisms and chromatin dynamics for genome integrity. 招待講演（2014 年 2 月 4-5 日、京都）
34. Hanaoka, F., Defective translesion DNA synthesis and links to human disease. International Symposium on Xeroderma Pigmentosum and Related Diseases: Disorders of DNA Damage Response –Bench to Bedside- 招待講演（2014 年 3 月 5-7 日、神戸）
35. Akagi, J., Hashimoto, K., Yokoi, M., Ohmori, H., Iwai, S., Moriya, M., and Hanaoka, F., Site-specific replicative analysis of 6-4 photoproduct using a series of TLS polymerases deficient mouse cells. International Symposium on Xeroderma Pigmentosum and Related Diseases: Disorders of DNA Damage Response –Bench to Bedside- ポスター発表（2014 年 3 月 5-7 日、神戸）
36. Sakurai, Y., Yokoi, M., Morita, D., and Hanaoka, F., Specific role of translesion synthesis polymerases eta and iota in UV-induced mutagenesis of skin cells and tissues. International Symposium on Xeroderma Pigmentosum and Related Diseases: Disorders of DNA Damage Response –Bench to Bedside- ポスター発表（2014 年 3 月 5-7 日、神戸）
37. Kanao, R., Masuda, Y., Hanaoka, F., and Masutani, C., Regulation of DNA damage torelance distinct from Polη-mediated translesion synthesis in human cells. International Symposium on Xeroderma Pigmentosum and Related Diseases: Disorders of DNA Damage Response –Bench to Bedside- 口頭発表（2014 年 3 月 5-7 日、神戸）
38. Ikehata, H., Yokoi, M., Yamamoto, M., and Hanaoka, F., *In vivo* UVB-induced mutation spectrum in the skin epidermis of XP variant model mice. International Symposium on Xeroderma Pigmentosum and Related Diseases: Disorders of DNA Damage Response –Bench to Bedside- 口頭発表（2014 年 3 月 5-7 日、神戸）
39. Yokoi, M., Sakurai, Y., Sugimoto, T., and Hanaoka, F., Association between global genome NER and translesion synthesis in UV sensitivity of MEFs and UV-induced tumorigenesis in mous skin. International Symposium on Xeroderma Pigmentosum and Related Diseases: Disorders of DNA Damage Response –Bench to Bedside- 口頭発表（2014 年 3 月 5-7 日、神戸）
40. Masuda, Y., Kanao, R., Hanaoka, F., and Masutani, C., Two different types of interactions between PCNA and Y-family DNA polymerases have distinct roles for translesion DNA synthesis. International Symposium on Xeroderma Pigmentosum and Related Diseases: Disorders of DNA Damage Response –Bench to Bedside- 口頭発表（2014 年 3 月 5-7 日、神戸）
41. Sekimoto, T., Oda, T., Kurashima, K., Hanaoka, F., and Yamashita, T., DNA polymerase η promotes DNA rereplication. International Symposium on Xeroderma Pigmentosum and Related Diseases: Disorders of DNA Damage Response –Bench to Bedside- 口頭発表（2014 年 3 月 5-7 日、神戸）
42. 花岡文雄　損傷トレランスと突然変異生成に働く乗り越え複製ポリメラーゼ、日本薬学会第 134 年会、特別講演（2014 年 3 月 28-30 日、熊本）

43. 金尾梨絵、増田雄司、花岡文雄、益谷央豪　ヒト細胞における PCNA ホモ三量体の翻訳後修飾による複製阻害回避機構、ポスター発表（2014 年 3 月 28-30 日、熊本）
44. Takaoka, S., Yokoi, M., Nakanishi, A., Yamamoto, M., and Hanaoka, F., Mammalian GyrI-like gene has an essential role in early mouse embryonic development. 第 47 回日本発生生物学会年会、ポスター発表（2014 年 5 月 28-30 日、名古屋）
45. 花岡文雄　損傷を乗り越える DNA ポリメラーゼについて、平成 26 年度日本生化学会関東支部例会、特別講演（2014 年 6 月 14 日、水戸）
46. Akagi, J., Hashimoto, K., Yokoi, M., Ohmori, H., Iwai, S., Moriya, M., Ogawa, K., and Hanaoka, F., Effects of sequence context on error-prone translesion synthesis past 6-4 photoproducts. Gordon Research Conferences on Mutagenesis　ポスター発表（2014 年 6 月 15 日-20 日、Girona, Spain）
47. 花岡文雄　損傷トレランス研究の 40 年：SOS 応答から損傷乗り越えポリメラーゼへ、第 36 回光医学・光生物学会、特別講演（2014 年 7 月 25 日-26 日、大阪）
48. Sakurai, Y., Yokoi, M., Murakumo, Y., and Hanaoka, F., Roles of translesion synthesis polymerases eta and iota in UV-induced mutagenesis in mice. DNA Polymerases: Biology, Diseases and Biomedical Applications. ZING Conference 2014、招待講演　（2014 年 8 月 31 日-9 月 4 日、Cambridge, UK）
49. Masuda, Y., Kanao, R., Ohmori, H., Hanaoka, F., and Masutani, C. Different types of interactions between PCNA and Y-family DNA polymerases for translesion DNA synthesis. DNA Polymerases: Biology, Diseases and Biomedical Applications. ZING Conference 2014、口頭発表（2014 年 8 月 31 日-9 月 4 日、Cambridge, UK）
50. 花岡文雄　損傷乗り越え合成ポリメラーゼと発がん、第 73 回日本癌学会学術総会、シンポジウム「クロマチン制御と発がん」（2014 年 9 月 25-27 日、横浜）
51. 倉島公憲、小田司、関本隆志、花岡文雄、山下孝之　DNA ポリメラーゼ η （Polη ）は c-myc による複製ストレスを抑制する、第 73 回日本癌学会学術総会、ポスター発表（2014 年 9 月 25-27 日、横浜）
52. 櫻井靖高、横井雅幸、塚本徹哉、小田司、魏民、山下孝之、鰐淵英機、立松正衛、村雲芳樹、花岡文雄　紫外線照射 DNA の損傷乗り越え複製において DNA ポリメラーゼイータとイオタが果たす生理的役割、第 73 回日本癌学会学術総会、ポスター発表（2014 年 9 月 25-27 日、横浜）
53. 益谷央豪、金尾梨絵、増田雄司、花岡文雄　PCNA の翻訳後修飾による損傷トレランス制御機構の解析、日本放射線影響学会 第 57 回大会 ワークショップ「紫外線誘発 DNA 損傷に対する生物の防御戦略とその分子基盤、口頭発表（2014 年 10 月 1-3 日、鹿児島）
54. 池畑広伸、横井雅幸、山本雅之、花岡文雄　色素性乾皮症バリアント群モデルマウス皮膚における UVB 誘発突然変異スペクトルの解析、日本放射線影響学会 第 57 回大会、口頭発表（2014 年 10 月 1-3 日、鹿児島）
55. Sakurai, Y., Yokoi, M., and Hanaoka, F. Roles of DNA polymerases eta and iota in UV-induced mutagenesis. The 5th US-Japan DNA Repair Meeting、口頭発表（2014 年 10 月 28-31 日、鳴門）
56. Osakabe, A., Tchiwana, H., Horikoshi, N., Kagawa, W., Yamamoto, J., Yasuda, T., Hanaoka, F., Sugasawa, K., Iwai, S., and Kurumizaka, H. Structures of nucleosomes containing UV-damaged

DNA bases and the damaged base recognition mechanism by DNA repair proteins. 5th US-Japan DNA Repair Meeting、口頭発表（2014 年 10 月 28-31 日、鳴門）

57. Yang W., Lee, Y-S., Gregory, M., Nakamura, T., Biertuempfel, C., and Hanaoka, F. Mechanisms for translesion DNA synthesis. 5th US-Japan DNA Repair Meeting、口頭発表（2014 年 10 月 28-31 日、鳴門）
58. Masutani, C., Kanao, R., Masuda, Y., and Hanaoka, F. Relevance of simultaneous mono-ubiquitination of multiple units of PCNA homo-trimers in DNA damage tolerance. 5th US-Japan DNA Repair Meeting、口頭発表（2014 年 10 月 28-31 日、鳴門）
59. Sekimoto, T., Oda, T., Kurashima, K., Hanaoka, F., and Yamashita, T. Y-family polymerases are involved in oncogene-induced aberant replication. 5th US-Japan DNA Repair Meeting、口頭発表（2014 年 10 月 28-31 日、鳴門）
60. 横井雅幸　アミノ酸置換変異体を用いたヒト Polη の機能解析、国立遺伝学研究所研究集会「染色体 DNA の安定維持の分子メカニズム」、口頭発表（2014 年 11 月 6-7 日、三島）
61. Hanaoka, F., Sakurai, Y., and Yokoi, M. Roles of mammalian DNA polymerases eta and iota in UV-induced mutagenesis. The 9th 3R Symposium、招待講演　（2014 年 11 月 17-21 日、御殿場）
62. Masutani, C., Kanao, R., Masuda, Y., and Hanaoka, F. Relevance of simultaneous mono-ubiquitinations of multiple units of PCNA homo-trimers in DNA damage tolerance. The 9th 3R Symposium、ポスター発表（2014 年 11 月 17-21 日、御殿場）
63. Masuda, Y., Kanao, R., Ohmori, H., Hanaoka, F., and Masutani, C. Interactions between PCNA and Y-family DNA polymerases. The 9th 3R Symposium、ポスター発表（2014 年 11 月 17-21 日、御殿場）
64. Hanaoka, F. Differential roles of translesion synthesis polymerases eta and iota in UV-induced mutagenesis. The 4th Japan-France Cancer Workshop、招待講演（2014 年 11 月 19-21 日、京都）
65. 大熊芳明、秋本勇亮、山本誠士、飯田智、久武幸司、花岡文雄、田中亜紀　転写初期における転写開始複合体のダイナミックな変化、第 37 回日本分子生物学会年会、口頭発表・ポスター発表　（2014 年 11 月 25-27 日、横浜）
66. 泉雅子、水野武、今本尚子、阿部知子、花岡文雄　ヒト Mcm10 と Mcm2-7 複合体の相互作用の解析、第 37 回日本分子生物学会年会、ポスター発表（2014 年 11 月 25-27 日、横浜）
67. 安田武嗣、香川亘、斎藤健吾、荻朋男、花岡文雄、菅澤薫、胡桃坂仁志、田嶋克史　ヒト RAD52 タンパク質のアセチル化制御、第 37 回日本分子生物学会年会、ポスター発表　（2014 年 11 月 25-27 日、横浜）
68. 金尾梨絵、増田雄司、花岡文雄、益谷央豪　変異体 PCNA 発現ヒト細胞を用いた DNA 損傷トレランス制御の解析、第 37 回日本分子生物学会年会、ポスター発表（2014 年 11 月 25-27 日、横浜）
69. 秋元勇亮、田中亜紀、飯田智、花岡文雄、大熊芳明　転写コファクターPC4 は基本転写因子 TFIIE と結合して転写開始から伸長への移行段階に機能する、第 37 回日本分子生物学会年会、ポスター発表（2014 年 11 月 25-27 日、横浜）

70. 内山雅司、花岡文雄　分裂酵母 TLS ポリメラーゼ Rev1 は CDK inhibitor Rum1 を通じて G1/S における細胞周期遅延を引き起こす、第 37 回日本分子生物学会年会、ポスター発表　（2014 年 11 月 25-27 日、横浜）
71. 阿曽沙織、照沼淳子、内山雅司、花岡文雄、大森治夫、分裂酵母 DNA ポリメラーゼ ζ における Rev3 と Rev3 の相互作用について、第 37 回日本分子生物学会年会、ポスター発表　（2014 年 11 月 25-27 日、横浜）
72. 越阪部晃永、立和名博昭、堀越直樹、香川亘、山元淳平、安田武嗣、花岡文雄、菅澤薫、岩井成憲、胡桃坂仁志　ヌクレオソームにおける紫外線損傷塩基の収納およびその認識機構の解析、第 37 回日本分子生物学会年会、ポスター発表（2014 年 11 月 25-27 日、横浜）
73. 渋谷卓未、横井雅幸、Wei Yang、花岡文雄　プリンアナログはヒト DNA ポリメラーゼ η の W297 を介してその活性を阻害する、第 37 回日本分子生物学会年会、ポスター発表　（2014 年 11 月 25-27 日、横浜）
74. 森田大輝、櫻井靖高、伊藤若菜、横井雅幸、花岡文雄　マウス皮膚由来細胞の紫外線感受性における不活性型 Polη の発現の影響、第 37 回日本分子生物学会年会、ポスター発表　（2014 年 11 月 25-27 日、横浜）
75. 赤木純一、豊田武士、Young-Man Cho、横井雅幸、大森治夫、花岡文雄、小川久美子　損傷乗り越え型 DNA ポリメラーゼ η・ι・κ 三重欠損細胞の変異原に対する高感受性を用いた新規遺伝子毒性検出法の検討、第 37 回日本分子生物学会年会、ポスター発表（2014 年 11 月 25-27 日、横浜）
76. 小林百合香、荘司健太、水野武、伊藤岳、花岡文雄、今本尚子、鳥越秀峰　マウステロメア結合タンパク質 Tpp1、Tin2 に依存した Pot1a/b の核局在と複合体形成解析、第 37 回日本分子生物学会年会　ポスター発表（2014 年 11 月 25-27 日、横浜）
77. 金尾梨絵、増田雄司、花岡文雄、益谷央豪　ヒト細胞における PCNA の翻訳後修飾による DNA 損傷トレランス制御機構の解析、がん支援活動シンポジウム、ポスター発表（2015 年 1 月 27-28 日、東京）
78. Hanaoka, F., Functional roles of TLS polymerases in mouse skin upon UV irradiation. Gordon Research Conferences on Mammalian DNA Repair、招待講演（2015 年 2 月 8-13 日、Ventura, USA）
79. 櫻井靖高、横井雅幸、塚本徹哉、魏　民、鰐淵英機、村雲芳樹、花岡文雄　紫外線に誘発される突然変異において DNA ポリメラーゼ・イータとイオタが皮膚細胞と組織で果たす役割、第 104 回日本病理学会総会　ポスター発表（2015 年 4 月 30-5 月 2 日、名古屋）
80. Hanaoka, F., Forty years of DNA damage tolerance. 15th International Congress of Radiation Research (ICRR 2015), 招待講演（2015 年 5 月 25-29 日、京都）
81. 水野武、石田竜次、下仲基之、花岡文雄、今本尚子　哺乳類細胞核内のタンパク質品質管理機構の解明、第 67 回日本細胞生物学会大会、口頭発表（2015 年 6 月 30 日-7 月 2 日、東京）
82. 荘司健太、小林百合香、水野武、花岡文雄、今本尚子、鳥越秀峰　マウステロメア結合タンパク質シェルタリンの複合体形成機構　−Tin2 の機能ドメインを通じて—、第 67 回日本細胞生物学会大会、ポスター発表（2015 年 6 月 30 日-7 月 2 日、東京）

83. Uchiyama, M., Terunuma, J., and Hanaoka, F., Regulation of the protein level of Rev1 in fission yeast. Genomic Integrity, ZING Conference 2015, 招待講演（2015 年 8 月 1-5 日、Cairns, Australia）
84. Osakabe, A., Tachiwana, H., Kagawa, W., Horikoshi, N., Matsumoto, S., Yamamoto, J., Hanaoka, F., Sugasawa, K., Iwai, S., and Kurumizaka, H., Structural and biochemical analyses for accommodation and recognition of UV-damaged bases within nucleosome.「クロマチン動構造」国際シンポジウム、口頭発表（2015 年 8 月 23～26 日、淡路）
85. 花岡文雄　私の DNA 修復研究：XPC から XPV へ、新学術領域研究「ゲノム普遍的制御」終了シンポジウム：ゲノム安定性の機構と生命の維持　ー進化、癌化、老化の理解のために　口頭発表（2015 年 8 月 29-30 日、京都）
86. 赤木純一、横井雅幸、Cho Young-Man、豊田武士、花岡文雄、小川久美子　Hypersensitivity of Polη, ι, and κ triple knockout cells to mutagens is a valuable indicator of genotoxicity. 第 74 回日本癌学会学術総会、ポスター発表（2015 年 10 月 8-10 日、名古屋）
87. 金尾梨絵、増田雄司、花岡文雄、益谷央豪　Regulation of DNA damage tolerance by simultaneous mono-ubiquitinations of multiple-units of PCNA in human cells. 第 74 回　日本癌学会学術総会、ポスター発表（2015 年 10 月 8-10 日、名古屋）
88. 倉島公憲、関本隆志、小田　司、花岡文雄、山下孝之　Polη, a member of Y-family DNA polymerases, prevents generation of DNA double strand breaks induced by c-myc expression. 第 74 回日本癌学会学術総会、ポスター発表（2015 年 10 月 8-10 日、名古屋）
89. 横井雅幸、花岡文雄　High concentration of dATP attenuated the catalytic rate and efficiency of translesion synthesis Polη . 第 74 回日本癌学会学術総会、ポスター発表　（2015 年 10 月 8-10 日、名古屋）
90. 金尾梨絵、柏葉脩一郎、増田雄司、松尾-楠本理加、花岡文雄、益谷央豪　酸化損傷によって誘導される PCNA のモノユビキチン化を制御する新規メカニズムの解析、第 23 回 DNA 複製・組換え・修復ワークショップ、口頭発表（2015 年 10 月 19-21 日、焼津）
91. 益谷央豪、柏葉脩一郎、金尾梨絵、松尾-楠本理加、花岡文雄、増田雄司　PCNA のユビキチン化を制御して過酸化水素誘発突然変異を抑制するヒト細胞のメカニズム、BMB2015 ワークショップ「放射線生物影響の課題に挑む分子生物学研究の力」、口頭発表（2015 年 12 月 1-4 日、神戸ポートアイランド）
92. 花岡文雄　総括、BMB2015 ワークショップ「放射線生物影響の課題に挑む分子生物学研究の力」、口頭発表（2015 年 12 月 1-4 日、神戸ポートアイランド）
93. 安田武嗣、香川　亘、荻　朋男、齊藤健吾、加藤宝光、鈴木健祐、藤堂　直、滝澤和也、早乙女（中邑）愛、中沢由華、Matthew D. Genet、宇井彩子、花岡文雄、菅澤　薫、岡安隆一、Penny A. Jeggo、胡桃坂仁志、田嶋克史　ヒト RAD52 のアセチル化を介した相同組換えにおけるアセチル化および脱アセチル化酵素の新規機能の解明、BMB2015 ワークショップ「多様な DNA 損傷応答の統合制御機構 2015～ゲノム不安定性の病態解明研究、口頭発表（2015 年 12 月 1-4 日、神戸ポートアイランド）
94. 道津貫太郎、大雲剛志、横井雅幸、花岡文雄　酸化損傷剤、臭素酸カリウムへの細胞内感受性における DNA ポリメラーゼ η、ι の働き、BMB2015 ポスター発表（2015 年 12 月 1-4 日、神戸ポートアイランド）
95. 横井雅幸、尾仲紗也加、美島一太、花岡文雄　ヒト Polη のフィンガーおよびリトルフ

ィンガードメインの変異が CPD の乗り越え合成に及ぼす影響、BMB2015 ポスター発表（2015 年 12 月 1-4 日、神戸ポートアイランド）

96. 小林百合香、荘司健太、水野　武、花岡文雄、今本尚子、鳥越秀峰　マウステロメア結合タンパク質 Tpp1、Tin2 に依存した Pot1a/b の核局在と複合体形成解析、BMB2015 ポスター発表（2015 年 12 月 1-4 日、神戸ポートアイランド）
97. 赤木純一、横井雅幸、Young-Man Cho、豊田武士、大森治夫、花岡文雄、小川久美子　損傷乗り越え型 DNA ポリメラーゼ η・ι・κ 三重欠損細胞は様々な機序の遺伝性毒性物質に感受性を示し、遺伝毒性物質のスクリーニングに有効である、BMB2015 ポスター発表（2015 年 12 月 1-4 日、神戸ポートアイランド）
98. 倉島公憲、関本隆志、小田　司、川端　剛、花岡文雄、山下孝之　Y-family 損傷乗り越え DNA ポリメラーゼ（Y-Pol）の一員 Polη は MYC がん遺伝子の誘導する複製ストレスを軽減する、BMB2015 ポスター発表（2015 年 12 月 1-4 日、神戸ポートアイランド）
99. 越阪部晃永、立和名博昭、堀越直樹、香川亘、松本翔太、山元淳平、花岡文雄、菅澤薫、岩井成憲、胡桃坂仁志　クロマチンにおける紫外線損傷 DNA 認識機構の解析、第 33 回染色体ワークショップ・第 14 回核ダイナミクス研究会、口頭発表（2016 年 1 月 12-14 日、松島）
100. 金尾梨絵、柏葉脩一郎、増田雄司、松尾（楠本）理加、花岡文雄、益谷央豪　PCNA のモノユビキチン化の制御によるヒト細胞での酸化的 DNA 損傷誘発突然変異抑制機構、日本薬学会第 136 年会、ポスター発表（2016 年 3 月 27-29 日、横浜）

Mechanism of somatic hypermutation at the WA motif by human DNA polymerase η

Ye Zhao[a,b], Mark T. Gregory[b], Christian Biertümpfel[b,1], Yue-Jin Hua[a,2], Fumio Hanaoka[c,2], and Wei Yang[b,2]

[a]Institute of Nuclear-Agricultural Sciences, Zhejiang University, Hangzhou 310029, China; [b]Laboratory of Molecular Biology, National Institute of Diabetes and Digestive and Kidney Diseases, National Institutes of Health, Bethesda, MD 20892; and [c]Faculty of Science, Gakushuin University, Tokyo 171-8588, Japan

Edited by Dinshaw J. Patel, Memorial Sloan–Kettering Cancer Center, New York, NY, and approved March 29, 2013 (received for review February 18, 2013)

Somatic hypermutation is programmed base substitutions in the variable regions of Ig genes for high-affinity antibody generation. Two motifs, RGYW and WA (R, purine; Y, pyrimidine; W, A or T), have been found to be somatic hypermutation hotspots. Overwhelming evidence suggests that DNA polymerase η (Pol η) is responsible for converting the WA motif to WG by misincorporating dGTP opposite the templating T. To elucidate the molecular mechanism, crystal structures and kinetics of human Pol η substituting dGTP for dATP in four sequence contexts, TA, AA, GA, and CA, have been determined and compared. The T:dGTP wobble base pair is stabilized by Gln-38 and Arg-61, two uniquely conserved residues among Pol η. Weak base paring of the W (T:A or A:T) at the primer end and their distinct interactions with Pol η lead to misincorporation of G in the WA motif. Between two WA motifs, our kinetic and structural data indicate that A-to-G mutation occurs more readily in the TA context than AA. Finally, Pol η can extend the T:G mispair efficiently to complete the mutagenesis.

π–cation stacking | A-to-G transition | immunoglobulin

After V(D)J recombination, nascent antibodies produced in B cells usually have low affinity for antigens. Somatic hypermutation (SHM), which generates mutations in the variable region at a frequency far beyond the rate of spontaneous mutations, potentially changes the conformation of the antigen-binding site and can increase antigen recognition by up to 1,000-fold (1, 2). Mutations have been observed at all four bases, but two sequence motifs, RGYW and WA (R, purine; Y, pyrimidine; W, A or T), have been shown to be the mutation hotspots (3). Although the mechanism of SHM and its target selection is incompletely understood, activation-induced cytidine deaminase (AID) (4, 5), which converts cytosine into uracil, for example, in the RGYW motif, initiates SHM by converting a C:G base pair to a U:G mismatch. Removal of the U by uracil–DNA glycosylase (UNG) generates an abasic site in the DNA, which may lead to a variety of base substitutions (6–8). For the WA motif, it is suggested that after AID-dependent deamination of a cytosine, recognition of the U:G mismatch by mismatch repair protein MutSα (MSH2–MSH6 heterodimer, in which MSH stands for MutS Homolog) leads to the recruitment of DNA polymerase η (Pol η), and with an incision made by UNG the ensuing short-patch repair synthesis results in mutations of A:T pairs to G:C (Fig. 1*A*) (9–11).

Pol η is one of the highly conserved translesion synthesis (TLS) DNA polymerases found in all eukaryotes and is specialized in bypassing UV-induced cyclobutane pyrimidine dimers (CPDs) in an error-free manner (12, 13). Deficiency of Pol η in humans causes a variant form of the cancer predisposition syndrome xeroderma pigmentosum (XP-V) (14). Patients are thousands of times more likely to develop skin cancer from exposure to sunlight. Like all Y-family DNA polymerases, human Pol η has no proofreading 3′–5′ exonuclease activity (15). Purified Pol η is highly mutagenic on normal DNA and prefers to misincorporate dGTP opposite dT, thereby generating A-to-G transition on a newly synthesized strand (13, 16). The base-substitution spectrum of SHM from XP-V patients is altered with severely decreased mutations at A:T pairs (11, 17, 18). Similar suppression of A:T to G:C mutations was observed in the *POLH*-deficient mice (19–21). Interestingly, the MSH2–MSH6 heterodimer interacts and stimulates Pol η activity in vitro (22), and mutations of A:T base pairs were abolished in SHM when both *POLH* and *MSH2* genes were knocked out (23).

Crystal structures of the polymerase domain of human Pol η (1–432 aa) complexed with different lesion DNA substrates were reported recently (24–27). These structures revealed a uniquely enlarged active site that can readily accommodate two normal template bases, a *cis–syn* thymine dimer (CPD), or to a certain extent intrastrand cisplatin cross-linked guanines (Pt-GG). In addition, the "molecular splint" of human Pol η stabilizes the upstream DNA duplex in a normal B-form conformation, even in the presence of cross-linked bases by forming numerous salt bridges and hydrogen bonds with the phosphate backbones, thus facilitating primer extension after CPD lesions (24–27). Misincorporation by Pol η, however, has not been investigated in a sequence-dependent manner or at atomic resolution.

To elucidate the molecular mechanism of Pol η in SHM, we set out to determine crystal structures of the polymerase domain of human Pol η (1–432 aa) (24–27) in the process of misincorporating dGTP opposite T in the WA motif (TA or AA) and non-WA sequences (CA or GA) as well as when extending the primer after a T:G mispair. In addition, steady-state kinetic parameters are measured to complement structural observations.

Results

Pol η Prefers to Mutate WA to WG. We first compare the efficiency of human Pol η incorporating dATP vs. dGTP opposite a template T following a perfectly paired T, A, G, or C at the primer 3′ end (Table S1). The four sequence contexts are labeled as TA, AA, GA, and CA, respectively, where the second nucleotide, an A, represents the correct nucleotide to be incorporated, but it may become G due to misincorporation, for example, in the TA and AA cases (WA motif). The measured K_M and k_{cat} indicate that human Pol η inserts the correct base (dATP) with a similar efficiency (less than twofold difference), regardless of the sequence context. For misincorporation, the K_M for dGTP increases by ∼10-fold compared with dATP in all four sequence variations, but the catalytic rates (k_{cat}) differ with sequence contexts (Table S1). The k_{cat} is reduced by 3.6- and 5.6-fold in the TA and AA case, respectively, and is reduced by 8.0-fold in the GA case. As for CA, dGTP misinsertion is severely inhibited, and the k_{cat} is reduced 31-fold. Thus, the relative efficiencies of misincorporation at TA, AA, GA, and CA are 1/40, 1/52, 1/106, and 1/321, respectively, of the correct incorporation, making the WA motif twofold to eightfold more susceptible to A-to-G mutation.

Author contributions: Y.Z. and W.Y. designed research; Y.Z., M.T.G., and C.B. performed research; Y.Z., Y.-J.H., F.H., and W.Y. analyzed data; and Y.Z. and W.Y. wrote the paper.

The authors declare no conflict of interest.

This article is a PNAS Direct Submission.

Data deposition: The atomic coordinates, structure factors, and diffraction data have been deposited in the Protein Data Bank, www.pdb.org (PDB ID codes 4J9K–4J9S).

[1]Present address: Max Planck Institute of Biochemistry, 82152 Martinsried, Germany.

[2]To whom correspondence should be addressed. E-mail: wei.yang@nih.gov, 20070117@gakushuin.ac.jp, or yjhua@zju.edu.cn.

This article contains supporting information online at www.pnas.org/lookup/suppl/doi:10.1073/pnas.1303126110/-/DCSupplemental.

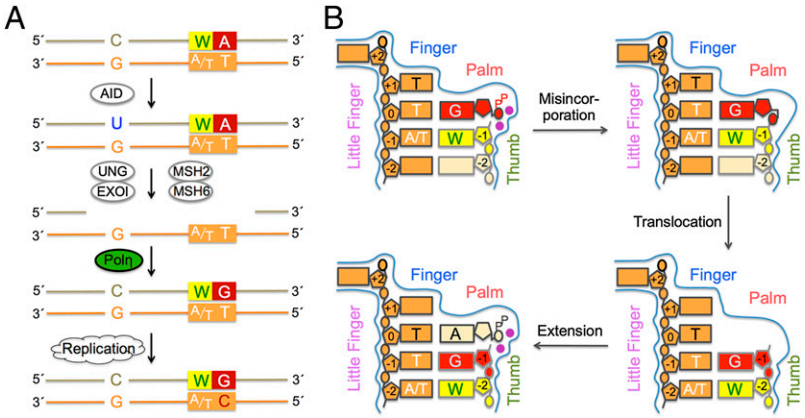

Fig. 1. SHM at the WA motif. (*A*) Model of SHM targeting the WA motif through short-patch DNA synthesis. The initial incision targeting the variable region of Ig genes depends on AID and UNG. Recruitment of Pol η is enhanced by MutSα, which recognized the U:G mismatch. The template strand is in orange, and the primer strand (subject to mutation) is shown in yellow. The WA motif is highlighted with A in red. (*B*) Structural determination of the four stages of dGTP misincorporation in this study. The W of the WA motif is highlighted in yellow and the A subject to replacement by G in red. The protein domains of Pol η in contact with DNA and dNTP are outlined and labeled. The two Mg^{2+} ions in the active site are shown as purple spheres.

Structures of dGTP Misincorporation Opposite T. Crystal structures of human Pol η incorporating dATP or its nonreactive analog 2′-deoxyadenosine-5′-[(α,β)-imido]triphosphate (dAMPNPP) opposite T template have been reported (27, 28). Here we focus on the structures of dGTP misincorporation. Human Pol η (1–432 aa) complexed with DNA and nonhydrolyzable 2′-deoxyguanosine-5′-[(α,β)-imido]triphosphate (dGMPNPP) opposite T after A, T, G, or C at the 3′ primer end were crystallized in the $P6_1$ space group. These crystals contain one complex per asymmetric unit and are isomorphous to the Pol η ternary complexes with perfectly base-paired DNA and incoming nucleotides (*Materials and Methods* and Fig. 1*B*). The structures were refined to resolutions between 1.85 and 2.25 Å (Table 1). The overall protein structures in these misincorporation complexes (AA/G, TA/G, CA/G, and GA/G) are similar to each other and to that of the correct incorporation (T:dATP) complexes, except for a slight closing of the finger and thumb domain as if to squeeze the primer strand and dGMPNPP toward each other (Fig. 2*A* and Movie S1). Among the misincorporation complexes, there are small but perceptible deviations of a loop (Gln-373–Ser-379) in the little finger (LF) domain (25). The catalytic triad Asp-13, Asp-115, and Glu-116 in the palm domain that chelate the two Mg^{2+} ions essential for catalysis overlay well with those in the ternary complex of dATP incorporation (25). The 7-bp upstream duplex is kept in the straight B form between the thumb and LF domain as observed (27, 28) (Fig. 2*A*).

A clear deviation in the four Pol η misincorporation complexes is observed at the T:dGMPNPP mispair surrounded by the finger and palm domains (Fig. 2*A*). As typically observed for a T:G wobble pair with two hydrogen bonds, the templating base T shifts toward the major groove, and the dGMPNPP shifts toward the minor groove (Fig. 2 *B*–*D*). Despite the shift of the

Table 1. Data collection and refinement statistics of Pol η ternary complex

	TA/G	CA/G	AA/G	GA/G	Extension complex
Data collection					
Space group	$P\,6_1$	$P\,6_1$	$P\,6_1$	$P\,6_1$	$P\,6_1$
Lattice constant					
a, *b*, *c*; Å	98.58	98.43	98.43	98.66	99.51
	98.58	98.43	98.43	98.66	99.51
	81.67	81.96	82.01	81.96	81.57
Wavelength, Å	1.0000	1.0000	1.0000	1.0000	1.5418
Resolution, Å	30.0–2.03	30.0–1.85	30.0–2.25	30.0–1.95	30.0–2.60
R_{sym}, %	10.2 (61.5)	8.7 (66.4)	9.8 (59.5)	9.3 (42.6)	13.0 (68.8)
$I/\sigma I$	12.2 (2.0)	14.6 (2.0)	14.5 (3.0)	19.2 (4.8)	12.4 (2.4)
Completeness, %	96.3 (97.9)	98.6 (96.8)	99.7 (99.7)	98.6 (100.0)	99.5 (95.7)
Wilson B factor, $Å^2$	23.1	18.2	25.8	18.2	34.1
Redundancy	4.5 (3.9)	3.8 (3.1)	4.4 (4.4)	6.4 (6.3)	4.8 (4.7)
Refinement					
Resolution, Å	30.0–2.03	30–1.85	30.0–2.25	30.0–1.95	30–2.60
No. of reflections	28,419	38,030	21,434	32,381	14,145
R_{work}/R_{free}	16.4/18.7	17.2/20.8	18.0/22.3	16.5/19.9	20.8/23.4
No. of atoms					
Protein/DNA	3,366/386	3,366/366	3,359/368	3,366/363	3,279/383
Ligand/ion	81	57	46	45	42
Water	261	374	188	326	98
B factors, $Å^2$					
Protein/DNA	28.0/30.2	18.7/23.6	24.1/28.6	21.4/23.9	37.4/48.5
Ligand/ion	30.9	18.6	16.4	12.7	35.6
Water	34.3	25.1	24.0	26.2	36.6
rms deviations					
Bond length, Å	0.006	0.011	0.005	0.010	0.007
Bond angle, °	0.981	1.169	0.917	1.229	1.102

Data in the highest resolution shell are shown in parentheses.

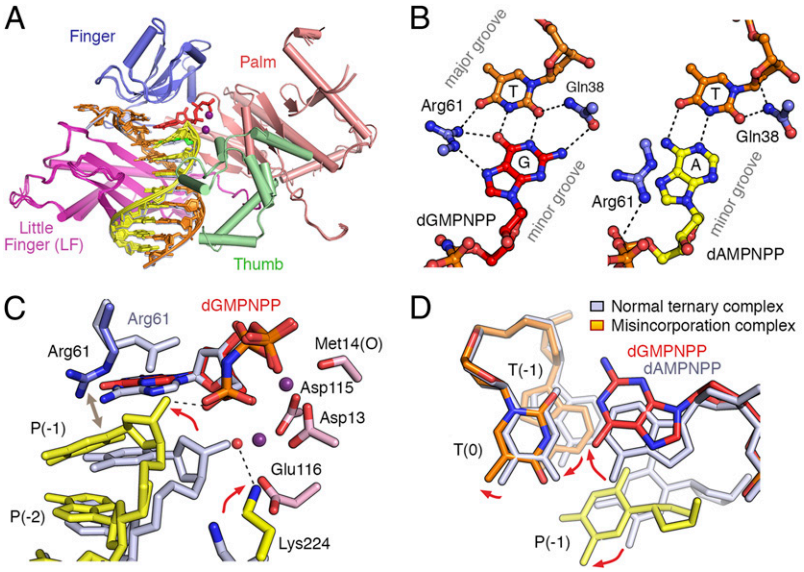

Fig. 2. Structures of dGTP misincorporation by Pol η. (*A*) Structure superposition of Pol η complexed with DNA and nonhydrolyzable dGMPNPP opposite dT in all four sequence contexts. The protein is shown in ribbon diagrams with palm domain in pink, thumb in green, finger in blue, and little finger (LF) in magenta. DNA is shown as stick-and-ladder in yellow (primer) and orange (template). Mg^{2+} ions (purple spheres) and incoming dGMPNPP (red sticks) are also shown. (*B*) Correct (T:dATP) and incorrect (T:dGMPNPP) nascent base pair in complex with Pol η. The conserved residues Gln-38 and Arg-61 are shown in blue sticks. (*C*) Superposition of the Pol η active site in dGTP misincorporation (colored) and normal ternary complexes [gray; PDB ID code 3MR2]. Alterations of primer end and Lys-224 are indicated by red arrows. The water molecule that participates in Mg^{2+} coordination is shown as a red sphere. A gray double arrow indicates the cation–π stacking. (*D*) Superposition of the nascent (0) and (−1) base pairs in normal productive (gray) and mispaired nonproductive ternary complexes (colored). The movement of each nucleotide is indicated by red arrows.

bases, the triphosphate of dGMPNPP remains coordinated by the two active site Mg^{2+} ions and situated nearly the same as that of a correctly paired dAMPNPP (Fig. 2 *A* and *C*). Two residues, Gln-38 and Arg-61, are uniquely conserved among all Pol η homologs, and both appear to contribute to the misincorporation. Gln-38 interacts with both thymine and guanine bases in the minor groove (Fig. 2*B*); Arg-61 adopts a rotamer conformation that has not been observed in Pol η–DNA complexes before and makes hydrogen bonds with O4 of dT and O6 and N7 of dGMPNPP in the major groove (Fig. 2*B*).

The largest structural change in the T:dGMPNPP complexes occurs at the 3′ primer end. Perhaps due to the molecular splint effect of Pol η on the template strand, the 0.7-Å shift of the templating base T toward the major groove leads to a shift of its immediate neighbor upstream (−1 position) in the same direction, which via base pairing induces a displacement of the 3′ primer end (Fig. 2 *C* and *D*). The last base of the primer strand is no longer stacked with the incoming dGMPNPP and instead is stacked with the guanidino group of Arg-61. As a result, the 3′-OH shifts >4 Å compared with all Pol η ternary structures solved to date and is hydrogen bonded with a nonbridging oxygen of the α-phosphate of dGMPNPP (Fig. 2*C*). Concomitantly, a water molecule replaces the 3′-OH as a ligand for the A-site Mg^{2+}, and Lys-224 also switches from interacting with the last phosphate group of the primer strand to interacting with the active-site carboxylate Glu-116 and a water molecule (Fig. 2*C*). In all four Pol η ternary complexes with the T:dGMPNPP mispair, the dominant conformation is the misaligned primer and dGMPNPP that are incompatible with the nucleophilic attack.

Unique Structural Features of the WA Motif. The four structures of Pol η misincorporating dGTP do have differences. After close inspection of the electron density maps, we found that in the TA/G and AA/G structures, which are of the WA motif, there is distinct positive electron density in the $F_o - F_c$ difference map that indicates a second conformation of the 3′ primer end with ∼30% occupancy (Fig. 3*A*). Although a minor species in the population, the second conformation of the 3′-OH is highly similar to the primer end in the normal ternary complex and is aligned with the α-phosphate of dGMPNPP for the phosphoryltransfer reaction (Fig. 3*B*). However, in the CA/G or GA/G complexes, the misaligned 3′ end is the only conformational species observed (Fig. 3*C*). By serendipity, two slightly different DNA sequences were used, one in the TA/G and GA/G and the other in the AA/G and

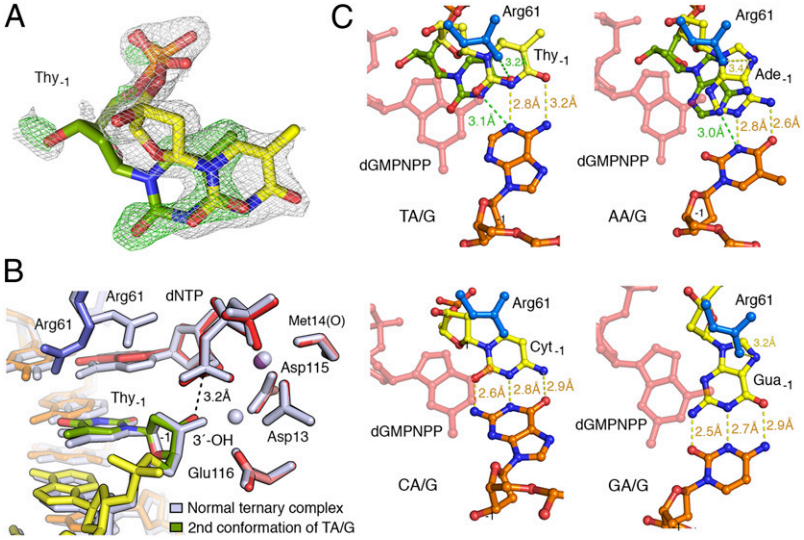

Fig. 3. The alternative DNA conformations observed in TA/G and AA/G that is compatible with dGTP incorporation. (*A*) The primer 3′ nucleotide (Thy) in the TA/G structure. The major (yellow) and the minor conformation (green) of the last nucleotide is superimposed with the $2F_o - F_c$ (silver; contoured at 1.0σ) and $F_o - F_c$ omit map (green; contoured at 2.5σ), which were calculated without the minor conformation species. (*B*) The minor conformation of TA/G is compatible with the phosphoryltransfer reaction. Superposition of the minor conformation of the TA/G structure (colored) with the normal ternary complex (gray; PDB ID code 3MR2). (*C*) Interactions between Arg-61 (blue) and the −1 base pair (yellow, green primer, and orange template) in TA/G, AA/G, CA/G, and GA/G complexes. The incoming dGMPNPP is shown as semitransparent pink sticks. Hydrogen bonds and van der Waals contacts are indicated by color-coded dashes and distances.

CA/G structures (Table S2). The structural differences observed between the WA and non-WA motif complexes are therefore independent of DNA sequence.

Several factors appear to contribute to the minor but productive conformational species found with the WA motif. The first is likely the base-pair strength at the 3′ primer end. Based on the electron density, when the 3′ primer end is aligned with the incoming nucleotide in the productive conformation, its base-pairing partner in the template strand does not appear to have a second conformation to maintain the proper Watson–Crick hydrogen bonds. Therefore, the primer end has to break the hydrogen bonds with the template to assume the minor conformational species. In the CA/G and GA/G cases, the G:C or C:G pair at the 3′ primer end shares three hydrogen bonds despite the base pair being severely buckled (Figs. 3*C* and 4*A*). The reduced number of hydrogen bonds in A:T pairs and the buckle between the base pairs (Fig. 4*B*) may facilitate formation of the second conformational species in the WA motif. Particularly in the TA/G case, the T:A base pair retains only one hydrogen bond due to base pair opening (Fig. 3*C*).

The second factor is the interaction of the base at the 3′ end (−1) with the guanidino group of Arg-61 and with the surrounding bases. It has often been observed that Arg interacts well with the major groove side O6 and N7 of guanine (Fig. S1), and such polar interactions between Arg-61 and the guanine base at the 3′ end are apparent (Fig. 3*C*). As a result, the 3′ guanine in the GA/G structure maintains its base stacking with the upstream neighbors and has the least buckle (Fig. 4*A*). When the 3′ primer end is a cytosine (CA/G), the base tilts by ∼25° to avoid electrostatic repulsion between Arg-61 and N4 of the base, thus resulting in the cytosine stacking with the guanidinium of Arg-61 instead of its neighboring bases (Fig. 3*C* and 4*A*). In both cases, the 3′ base is structurally stable and does not have an alternative conformation. When a thymine is at the primer 3′ end (TA/G), Arg-61 forms favorable polar interactions with O4 of the base, particularly when the T assumes the second conformation that is stacked with its neighboring bases (Fig. 3*C*). In contrast, the electrostatic repulsion between Arg-61 and N4 most likely prevents the cytosine adopting the second conformation. When an adenine is at the 3′ primer end, the electrostatic repulsion between its N6 and Arg-61 probably leads to the base offset in both conformations compared with guanine (Fig. 3*C*). The strong propensity of adenine to form base stacking (29) likely leads to the productive conformation in the AA/G structure, where the 3′ primer end stacks with both dGMPNPP and the upstream base (Fig. 4 *A* and *B*).

The third factor is likely the global position of the DNA substrate relative to the polymerase. Among the four misincorporation complexes, the upstream DNA in the CA/G and GA/G structures are shifted along the DNA helical axis toward the incoming nucleotide and the finger domain (Fig. 4*A*). However, in the TA/G complex, it is more similar to the normal ternary complex, and the DNA in the AA/G complex is in between. Favorable van der Waals interactions between the template strand bases and residues in the LF domain are observed in the WA cases (Fig. 4*B*), which likely stabilize the DNA in a more native-like conformation. The shift of the DNA substrate also affects the interaction between the finger domain and the downstream single-stranded DNA. In the TA case, the downstream DNA conformation is most similar to the undamaged ternary complexes (Fig. 4 *A* and *B*). In the other three cases, despite the same template length as in the undamaged ternary complexes (25, 27), the +1 nucleotide is flipped out and occupies the usual binding site of the +2 nucleotide, and the hydroxyl group of S62 turns to occupy the void (Fig. 4*C*).

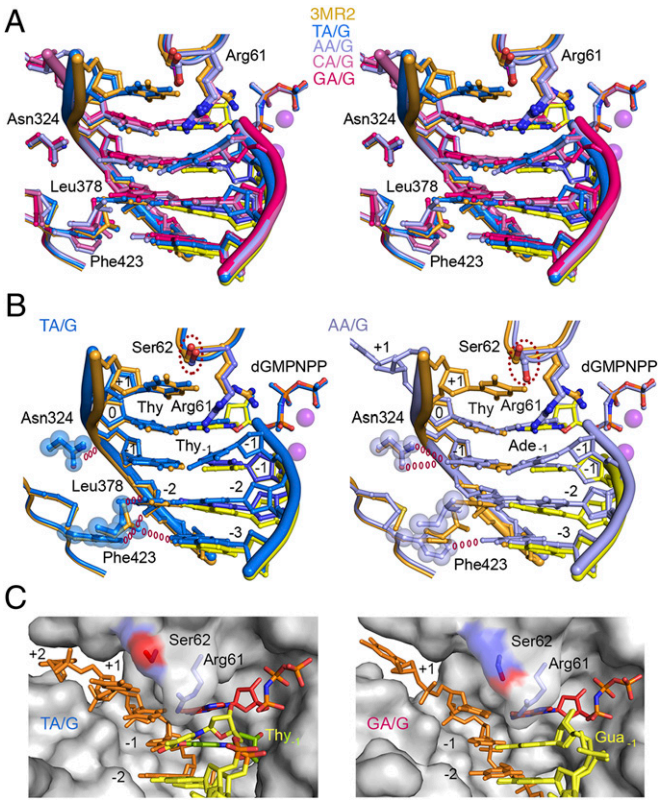

Fig. 4. Unique interactions found in TA/G and AA/G complexes. (*A*) Stereoview of the superposition of the four Pol η misincorporation and the normal ternary complexes. Each complex is color-coded as indicated. The upward shift of the DNA duplex in GA/G, CA/G, and AA/G complexes is obvious after the entire protein is superimposed. (*B*) Distinct interactions between the LF domain and the DNA found in TA/G and GA/G. The van der Waals contacts are indicated by lines formed by open circles. (*C*) Side-by-side views of TA/G and GA/G with Pol η shown as gray molecular surface and Ser-62 side chain in blue carbon and red oxygen. The shift of the DNA substrate in GA/G is accommodated by the rotamer change of Ser-62.

Arg-61 Plays a Key Role in Misincorporation. Arg-61 adopts a rotamer conformation that forms extensive hydrogen bonds with T:G mispair to favor the dGMPNPP binding. However, Arg-61 also stabilizes the displaced 3′ primer end by cation–π stacking interactions that prevent the polymerization reaction. Only when A or T is at the primer end does the 3′ primer end occasionally revert to the reactive conformation for polymerization, as is evident in the alternative conformations. The arrangement of Arg-61 stabilizing the T:G mismatch and stacking with the base preceding the G is also observed in the postreaction Pol η–product DNA binary complex when a T:G mismatch is at the DNA primer end, but not when it is T:A (Fig. 5*A* and Table S3). To delineate the hydrogen bonding vs. the base stacking roles of Arg-61 in SHM of the WA motif, we replaced Arg-61 by Lys, which has an amino group to mimic electrostatic interaction and hydrogen-bonding ability of Arg but has greatly reduced potential to stack with DNA bases (30).

K_M and k_{cat} of the R61K mutant Pol η in dATP and dGTP incorporation in the TA, AA, and CA sequence contexts were measured (Table S1). When incorporating the correct dATP, K_M of R61K is increased by twofold to threefold, and the overall efficiency is reduced by twofold to fourfold compared with wild-type (WT) Pol η in the three sequence contexts tested. This reduction is not surprising because the guanidino group of Arg-61 forms bifurcated hydrogen bonds with the α and β phosphates of the nucleotide (28), and Lys, being shorter than the Arg side chain, is a poor substitute for such interactions. Interestingly, the trend that the WA motifs are more susceptible to dGTP misincorporation is the same with R61K as WT Pol η, indicating that the positive charge of Arg-61 may be the determinant in influencing the mutability of the WA motif. Surprisingly, the R61K mutant compared with WT Pol η has a threefold to

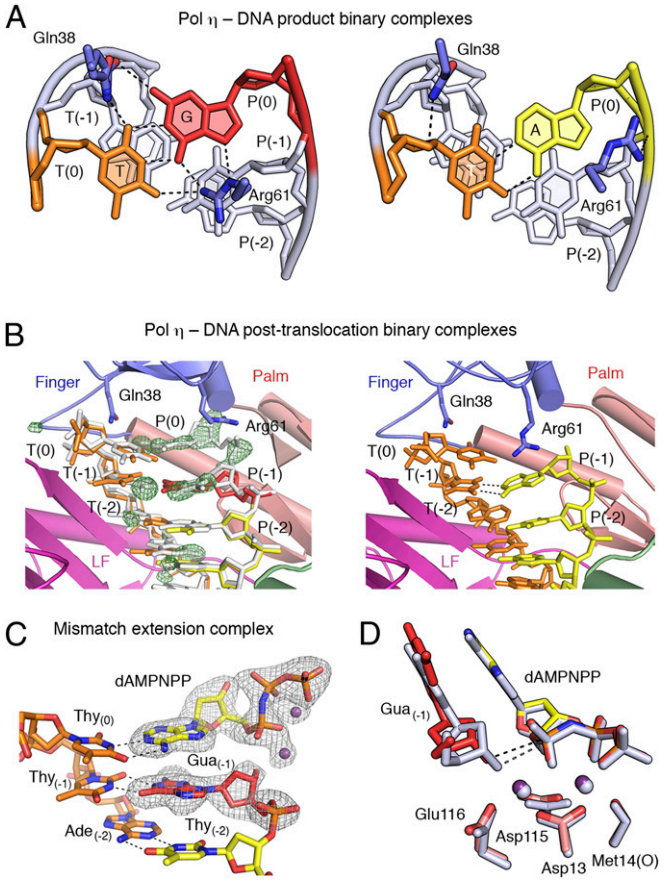

Fig. 5. Translocation and extension of T:G mispair. (*A*) Structures of post-insertion Pol η–DNA binary complexes. The wobble nascent base pair of the misincorporation is shown side by side with the normal incorporation looking down the DNA helical axis. The template base is shown in orange and the newly incorporated base in yellow (correct) or red (incorrect). Arg-61 interacts with the mispaired guanine base. (*B*) Structures of posttranslocation binary complexes. In the T:G mismatch complex (*Left*), the DNA exhibits two equal populations of translocated (multicolored) and untranslocated (gray) conformations. The $F_o - F_c$ omit map, which was calculated with 100% translocated population and contoured at 2.5σ in green, superimposes well with the untranslocated conformation. (*C*) Structure of the T:G mismatch extension complex. The $2F_o - F_c$ map (gray; contoured at 1.0σ) corresponding to the primer end and incoming nucleotide is superimposed with the refined structure. (*D*) Superposition of the T:G mismatch extension (colored) and normal ternary complex structure (gray; PDB ID code 3MR2). The 3′–OH at the primer end and the α-phosphate of dAMPNPP are aligned in the mismatch extension complex, albeit slightly shifted relative to the active site of Pol η.

sixfold higher propensity to make dGTP incorporation, suggesting that stacking of Arg-61 with the primer end actually reduces the misincoporation efficiency (Table 1). Previously, it was shown that R61A mutation reduces dGTP misinsertion opposite T (27) and increases nucleotide insertion fidelity in general at the cost of reduced catalytic efficiency (31). We deduce that the positive charge of Arg-61 (or R61K) must be required to stabilize the T:dGTP mispair (Fig. 2*B*), thus promoting misincoporation.

Extension of a T:G Mispair by Pol η. For the A-to-G mutation to persist in somatic cells, it is necessary that the DNA primer be extended after the mismatch during the short-patch DNA synthesis to prevent the misinserted G from being removed by the editing function of a replicative polymerase. Most polymerases are inefficient in mismatch extension (32). To extend a T:G mismatch, both the translocation step and the primer extension step are examined (Fig. 1*B*). Human Pol η was cocrystallized with a T:A pair or mismatched T:G at the DNA duplex end as the posttranslocation binary complexes (Fig. 1*B* and Table S3). These crystals diffracted X-rays to 1.95 Å (T:A) and 2.35 Å (T:G), respectively. In these binary complexes, however, a subpopulation of DNA duplex is observed to remain in the product state rather than fully translocated (Fig. 5*B*). We suspect that stacking of Arg-61 with the purines at the primer 3′ end may cause the sluggish translocation because with a pyrimidine at the 3′ end there is no sign of untranslocated species (26). The incomplete translocation is more severe with an T:G mismatch than T:A base pair (Fig. S2), which may contribute to the 12-fold increase in K_M when extending a T:G mismatch compared with normal extension (Table S1).

We have also obtained ternary-complex crystals of Pol η incorporating dAMPNPP after a T:G mismatch, and the structure was determined at 2.6 Å (Table 1). In the presence of an incoming dAMPNPP, the 3′ primer end resumes the near-normal position despite the wobble T:G pair. The reactants are more or less superimposable with the perfectly matched substrates (Fig. 4*C*). To validate the reaction-ready nature of this structure, we measured the extension efficiency of the T:G mispair in solution by Pol η and showed that the catalytic efficiency (k_{cat}/K_M) is reduced by 32-fold compared with normal DNA synthesis (Table S1). Pol η is thus more efficient in primer extension after a mismatched base pair than replicative and B-family TLS polymerases, whose catalytic efficiency is reduced by 10,000 and 100 folds, respectively (32).

Discussion

Pol η binds dGTP tightly during misincorporation with a K_M of ~10 μM regardless of sequence context (Table S1), indicating there is no sequence context preference in the dGTP binding step. The crystal structures of dGTP misincorporation in all four sequence contexts show the common feature that the T:G wobble pair fits well in the active site and interacts snugly with the conserved Gln-38 and Arg-61 in the major and minor groove (Fig. 2*B*). These interactions are rather different from other Y-family DNA polymerases, for example, Pol ι or Dpo4. The incoming dGTP is unable to stack with the primer 3′ end in the Dpo4 misincorporation ternary structure (33) (Fig. S3*A*). In the Pol ι case, the mismatched T and G maintains *anti–anti* conformation, but the templating base is displaced from its normal position and is not paired with the incoming dGTP (34) (Fig. S3*B*). Gln-59, which is conserved among Pol ι homologs and equivalent of Gln-38 in human Pol η, forms a hydrogen bond with only the N2 atom of the guanine base but not with the template T. Steady-state kinetic measurement indicates that replacing either Gln-38 or Arg-61 by Ala in Pol η dramatically inhibits the misincorporation as well as bypassing of CPDs (27). We find that replacing Arg-61 with Lys also greatly increases the misincorporation frequency and reduces the catalytic efficiency. The equivalent of Arg-61 in Pol ι is a Lys (35). Nature through evolution probably has selected Arg-61 and Gln-38 in Pol η to maximize the efficiency and accuracy for UV–lesion bypass. Pol η-dependent dGTP misincorporation at the WA motif in SHM is likely a byproduct that takes advantage of the conserved Arg-61 and Gln-38 late in the evolutionary history.

The k_{cat} of dGTP misincorporation is significantly reduced compared with the correct incorporation and differs according to the base-pair sequence at the primer end. The catalytic efficiencies of dGTP misincorporation in the TA and AA contexts are higher than the GA and CA, and the relative efficiency is TA > AA > GA >> CA (Table S1). These results correlate well with the published SHM spectrum, which shows that the TA mutations are strongly favored over AA mutations by Pol η (36). The reduced k_{cat} correlates with the displacement of the primer end due to cation–π interaction mediated by Arg-61. For efficient catalysis, it is essential that the 3′-OH group of the primer end and the α-phosphate of the incoming dNTP be perfectly aligned. Misalignment between primer end and incoming nucleotide, even

slightly, will inhibit the nucleotidyl-transfer reaction (25). Arg-61 also provides another barrier in misincorporation by impeding the translocation step as observed in our binary complexes after misincorporation and before the next round of incorporation. Misincorporation is much enhanced by the R61K mutant Pol η. Lys, which has a shorter side chain than Arg and reduced capability to form cation–π stacking with the primer end (Fig. 2*C*), is more prone to misincorporate dGTP than WT Pol η (Table 1). Besides the dominant misaligned conformation, the electron density in our structures revealed that there is a second population of primer end in the TA/G and AA/G, but not CA/G or GA/G, complexes that superimposes well with the normal ternary complex and supports the chemistry.

Because the R61K mutant polymerase still favors dGTP misincorporation in the WA motif, we suspect that the cation–π stacking between Arg-61 and the primer end is not the main reason for the WA motif to be an SHM hotspot. The different stability of A:T and T:A vs. G:C and C:G base pairs most likely underlies the high efficiency of dGTP misincorporation in the WA motif. In addition, the stacking propensity of the 3′ base with its neighbors and its electrostatic interactions with Arg-61 may influence whether the 3′-OH can revert to the reactive conformation and also the probability of such reversion. T and A at the primer 3′ end are thus found to be more able than G and C to align with the incoming dGTP and form a productive complex for misincorporation to take place. Together, the strong dGTP binding, even when it is a mismatch for the template T, weaker hydrogen bonding between A and T at the 3′ primer strand end, and efficient mispair extension by Pol η provide the molecular rationale for the conversion of WA motifs to WG during SHM.

Materials and Methods

Crystallization and Structure Determination. Site-directed mutagenesis, protein expression, and purification of WT or R61K human Pol η (1–432 aa) were performed as described (27). Purified Pol η was stored in 20 mM Tris·HCl, (pH 7.5), 450 mM KCl, and 3 mM DTT. After mixing Pol η and DNA at a 1:1.05 molar ratio, the complex was transferred into 20 mM Tris·HCl (pH 7.5), 150 mM KCl, 3 mM DTT, and 5 mM $MgCl_2$ and concentrated to 3 mg/mL Pol η. To make ternary complexes, an appropriate dNTP analog (purchased from Jena Bioscience) was added. Crystals were grown by the hanging-drop vapor-diffusion method with optimized reservoir buffer containing 0.1 M Mes (pH 6.0), 5 mM $MgCl_2$, 19–21% (wt/vol) MPEG2000 (polyethylene glycol monomethyl ether 2000) (27). The oligos and incoming nucleotides used in crystallization are summarized in Table S2. Crystals grew to maximal dimensions with diffraction quality in 3–7 d. Diffraction data were collected at beamline 22-BM at Advanced Photon Source, Argonne National Laboratory, processed with HKL2000 (37) or XDS (38), and converted to structure factors by using TRUNCATE (39). Refinement and structure analyses (Table 1 and Table S3) were performed by using COOT (40), PHENIX (41), and PyMOL (www.pymol.org).

Kinetic Measurements. The primer extension assay and steady-state K_M and k_{cat} measurements were carried out by using a 5′-fluorescein labeled primer and normal template oligonucleotides as described (25). The DNA sequences and nucleotides used in these assays are shown in Table S1. Quantification and curve fitting was also performed as described (32).

ACKNOWLEDGMENTS. We thank Drs. R. Craigie and D. Leahy for critical reading of the manuscript. This work was supported by the Intramural Research Program of National Institute of Diabetes and Digestive and Kidney Diseases, National Institutes of Health (Y.Z., M.T.G., C.B., and W.Y.); a Chinese Ministry of Education scholarship (Y.Z.); National Natural Science Foundation of China Grant 31210103904 (to Y.-J.H.); and Grants-in-Aid for Scientific Research from the Ministry of Education (KAKENHI) (to F.H.).

1. Rajewsky K, Förster I, Cumano A (1987) Evolutionary and somatic selection of the antibody repertoire in the mouse. *Science* 238(4830):1088–1094.
2. Kim S, Davis M, Sinn E, Patten P, Hood L (1981) Antibody diversity: Somatic hypermutation of rearranged VH genes. *Cell* 27(3 Pt 2):573–581.
3. Di Noia JM, Neuberger MS (2007) Molecular mechanisms of antibody somatic hypermutation. *Annu Rev Biochem* 76:1–22.
4. Sohail A, Klapacz J, Samaranayake M, Ullah A, Bhagwat AS (2003) Human activation-induced cytidine deaminase causes transcription-dependent, strand-biased C to U deaminations. *Nucleic Acids Res* 31(12):2990–2994.
5. Muramatsu M, Nagaoka H, Shinkura R, Begum NA, Honjo T (2007) Discovery of activation-induced cytidine deaminase, the engraver of antibody memory. *Adv Immunol* 94:1–36.
6. Rada C, Di Noia JM, Neuberger MS (2004) Mismatch recognition and uracil excision provide complementary paths to both Ig switching and the A/T-focused phase of somatic mutation. *Mol Cell* 16(2):163–171.
7. Saribasak H, et al. (2006) Uracil DNA glycosylase disruption blocks Ig gene conversion and induces transition mutations. *J Immunol* 176(1):365–371.
8. Schanz S, Castor D, Fischer F, Jiricny J (2009) Interference of mismatch and base excision repair during the processing of adjacent U/G mispairs may play a key role in somatic hypermutation. *Proc Natl Acad Sci USA* 106(14):5593–5598.
9. Jansen JG, et al. (2006) Strand-biased defect in C/G transversions in hypermutating immunoglobulin genes in Rev1-deficient mice. *J Exp Med* 203(2):319–323.
10. Masuda K, et al. (2005) DNA polymerase theta contributes to the generation of C/G mutations during somatic hypermutation of Ig genes. *Proc Natl Acad Sci USA* 102(39): 13986–13991.
11. Zeng X, et al. (2001) DNA polymerase eta is an A-T mutator in somatic hypermutation of immunoglobulin variable genes. *Nat Immunol* 2(6):537–541.
12. Masutani C, Kusumoto R, Iwai S, Hanaoka F (2000) Mechanisms of accurate translesion synthesis by human DNA polymerase eta. *EMBO J* 19(12):3100–3109.
13. Johnson RE, Washington MT, Prakash S, Prakash L (2000) Fidelity of human DNA polymerase eta. *J Biol Chem* 275(11):7447–7450.
14. Masutani C, et al. (1999) The XPV (xeroderma pigmentosum variant) gene encodes human DNA polymerase eta. *Nature* 399(6737):700–704.
15. Yang W, Woodgate R (2007) What a difference a decade makes: Insights into translesion DNA synthesis. *Proc Natl Acad Sci USA* 104(40):15591–15598.
16. Matsuda T, Bebenek K, Masutani C, Hanaoka F, Kunkel TA (2000) Low fidelity DNA synthesis by human DNA polymerase-eta. *Nature* 404(6781):1011–1013.
17. Faili A, et al. (2004) DNA polymerase eta is involved in hypermutation occurring during immunoglobulin class switch recombination. *J Exp Med* 199(2):265–270.
18. Zeng X, Negrete GA, Kasmer C, Yang WW, Gearhart PJ (2004) Absence of DNA polymerase eta reveals targeting of C mutations on the nontranscribed strand in immunoglobulin switch regions. *J Exp Med* 199(7):917–924.
19. Delbos F, et al. (2005) Contribution of DNA polymerase eta to immunoglobulin gene hypermutation in the mouse. *J Exp Med* 201(8):1191–1196.
20. Pavlov YI, et al. (2002) Correlation of somatic hypermutation specificity and A-T base pair substitution errors by DNA polymerase eta during copying of a mouse immunoglobulin kappa light chain transgene. *Proc Natl Acad Sci USA* 99(15):9954–9959.
21. Rogozin IB, Pavlov YI, Bebenek K, Matsuda T, Kunkel TA (2001) Somatic mutation hotspots correlate with DNA polymerase eta error spectrum. *Nat Immunol* 2(6): 530–536.
22. Wilson TM, et al. (2005) MSH2-MSH6 stimulates DNA polymerase eta, suggesting a role for A:T mutations in antibody genes. *J Exp Med* 201(4):637–645.
23. Delbos F, Aoufouchi S, Faili A, Weill JC, Reynaud CA (2007) DNA polymerase eta is the sole contributor of A/T modifications during immunoglobulin gene hypermutation in the mouse. *J Exp Med* 204(1):17–23.
24. Ummat A, et al. (2012) Structural basis for cisplatin DNA damage tolerance by human polymerase η during cancer chemotherapy. *Nat Struct Mol Biol* 19(6): 628–632.
25. Zhao Y, et al. (2012) Structural basis of human DNA polymerase η-mediated chemoresistance to cisplatin. *Proc Natl Acad Sci USA* 109(19):7269–7274.
26. Ummat A, et al. (2012) Human DNA polymerase η is pre-aligned for dNTP binding and catalysis. *J Mol Biol* 415(4):627–634.
27. Biertümpfel C, et al. (2010) Structure and mechanism of human DNA polymerase eta. *Nature* 465(7301):1044–1048.
28. Nakamura T, Zhao Y, Yamagata Y, Hua YJ, Yang W (2012) Watching DNA polymerase η make a phosphodiester bond. *Nature* 487(7406):196–201.
29. Kool ET (2001) Hydrogen bonding, base stacking, and steric effects in DNA replication. *Annu Rev Biophys Biomol Struct* 30:1–22.
30. Sathyapriya R, Vishveshwara S (2004) Interaction of DNA with clusters of amino acids in proteins. *Nucleic Acids Res* 32(14):4109–4118.
31. Kondo Y (2005) Studies of *in vivo* and *in vitro* function of DNA polymerase eta. PhD dissertation (Osaka Univ, Osaka).
32. Wang F, Yang W (2009) Structural insight into translesion synthesis by DNA Pol II. *Cell* 139(7):1279–1289.
33. Vaisman A, Ling H, Woodgate R, Yang W (2005) Fidelity of Dpo4: Effect of metal ions, nucleotide selection and pyrophosphorolysis. *EMBO J* 24(17):2957–2967.
34. Kirouac KN, Ling H (2009) Structural basis of error-prone replication and stalling at a thymine base by human DNA polymerase iota. *EMBO J* 28(11):1644–1654.
35. Alt A, et al. (2007) Bypass of DNA lesions generated during anticancer treatment with cisplatin by DNA polymerase eta. *Science* 318(5852):967–970.
36. Yavuz S, Yavuz AS, Kraemer KH, Lipsky PE (2002) The role of polymerase eta in somatic hypermutation determined by analysis of mutations in a patient with xeroderma pigmentosum variant. *J Immunol* 169(7):3825–3830.
37. Otwinowski Z, Minor W (1997) Processing of X-ray diffraction data collected in oscillation mode. *Methods Enzymol* 276:307–326.
38. Kabsch W (2010) XDS. *Acta Crystallogr D Biol Crystallogr* 66(Pt 2):125–132.
39. Collaborative Computational Project, Number 4 (1994) The CCP4 suite: Programs for protein crystallography. *Acta Crystallogr D Biol Crystallogr* 50(Pt 5):760–763.
40. Emsley P, Cowtan K (2004) Coot: Model-building tools for molecular graphics. *Acta Crystallogr D Biol Crystallogr* 60(Pt 12 Pt 1):2126–2132.
41. Adams PD, et al. (2010) PHENIX: A comprehensive Python-based system for macromolecular structure solution. *Acta Crystallogr D Biol Crystallogr* 66(Pt 2): 213–221.

DNA Repair 29 (2015) 139–146

Contents lists available at ScienceDirect

DNA Repair

journal homepage: www.elsevier.com/locate/dnarepair

UV-induced mutations in epidermal cells of mice defective in DNA polymerase η and/or ι

Rie Kanao[a,b,c,d], Masayuki Yokoi[a,c,e], Tsuyoshi Ohkumo[a], Yasutaka Sakurai[a,c], Kantaro Dotsu[a,c], Shinobu Kura[f], Yoshimichi Nakatsu[f], Teruhisa Tsuzuki[f], Chikahide Masutani[a,d,e], Fumio Hanaoka[a,b,c,e,*]

[a] Graduate School of Frontier Biosciences, Osaka University, 1-3 Yamada-oka, Suita, Osaka 565-0871, Japan
[b] Graduate School of Pharmaceutical Sciences, Osaka University, 1-6 Yamada-oka, Suita, Osaka 565-0871, Japan
[c] Faculty of Science, Gakushuin University, 1-5-1 Mejiro, Toshima-ku, Tokyo 171-8588, Japan
[d] Research Institute of Environmental Medicine, Nagoya University, Furo-cho, Chikusa-ku, Nagoya 464-8601, Japan
[e] Solution Oriented Research for Science and Technology, Japan Science and Technology Agency, Tokyo, Japan
[f] Faculty of Medical Sciences, Kyushu University, 3-1-1 Higashi-ku, Maidashi, Fukuoka 812-8582, Japan

ARTICLE INFO

Article history:
Received 17 November 2014
Received in revised form 2 February 2015
Accepted 3 February 2015
Available online 16 February 2015

Keywords:
DNA polymerase η
DNA polymerase ι
Translesion synthesis
UV-induced mutagenesis
Xeroderma pigmentosum variant (XP-V)

ABSTRACT

Xeroderma pigmentosum variant (XP-V) is a human rare inherited recessive disease, predisposed to sunlight-induced skin cancer, which is caused by deficiency in DNA polymerase η (Polη). Polη catalyzes accurate translesion synthesis (TLS) past pyrimidine dimers, the most prominent UV-induced lesions. DNA polymerase ι (Polι) is a paralog of Polη that has been suggested to participate in TLS past UV-induced lesions, but its function *in vivo* remains uncertain. We have previously reported that Polη-deficient and Polη/Polι double-deficient mice showed increased susceptibility to UV-induced carcinogenesis. Here, we investigated UV-induced mutation frequencies and spectra in the epidermal cells of Polη- and/or Polι-deficient mice. While Polη-deficient mice showed significantly higher UV-induced mutation frequencies than wild-type mice, Polι deficiency did not influence the frequencies in the presence of Polη. Interestingly, the frequencies in Polη/Polι double-deficient mice were statistically lower than those in Polη-deficient mice, although they were still higher than those of wild-type mice. Sequence analysis revealed that most of the UV-induced mutations in Polη-deficient and Polη/Polι double-deficient mice were base substitutions at dipyrimidine sites. An increase in UV-induced mutations at both G:C and A:T pairs associated with Polη deficiency suggests that Polη contributes to accurate TLS past both thymine- and cytosine-containing dimers *in vivo*. A significant decrease in G:C to A:T transition in Polη/Polι double-deficient mice when compared with Polη-deficient mice suggests that Polι is involved in error-prone TLS past cytosine-containing dimers when Polη is inactivated.

1. Introduction

Xeroderma pigmentosum (XP) is a genetic disorder characterized by ultraviolet light (UV) sensitivity and increased incidence of skin cancers. XP has been classified into eight genetic complementation groups, XP-A–G and XP-V [1]. Cells derived from XP-A through XP-G patients are deficient in nucleotide excision repair (NER), which repairs a variety of DNA lesions including UV-induced cyclobutane pyrimidine dimers (CPDs) and (6-4) photoproducts. The variant form (XP-V) is characterized by proficiency in NER but deficiency in translesion synthesis (TLS). TLS is a mechanism that prevents replication blockage at a DNA lesion by using specialized DNA polymerases that incorporate nucleotides opposite the lesion and continue DNA synthesis past the site of damage [1]. We have identified human DNA polymerase η (Polη) as the product of the gene associated with XP-V, *POLH*. Polη catalyzes accurate translesion synthesis (TLS) past *cis–syn* thymine–thymine dimers [2–5], an important mechanism to prevent UV-induced skin cancers in human cells.

Mammalian cells are now known to have fifteen DNA template-dependent DNA polymerases, and these are classified into five families, A, B, X, Y, and AEP (*a*rchaeo-*e*ukaryotic *p*rimase superfamily)

* Corresponding author at: Faculty of Science, Gakushuin University, 1-5-1 Mejiro, Toshima-ku, Tokyo 171-8588, Japan. Tel.: +81 3 3986 0221x6457; fax: +81 3 5992 1029.
E-mail address: fumio.hanaoka@gakushuin.ac.jp (F. Hanaoka).

http://dx.doi.org/10.1016/j.dnarep.2015.02.006
1568-7864/

according to similarities in their primary structures [6–9]. The Y-family, which was shown to carry out TLS past some lesions, consists of Polη, Polι, Polκ, and REV1 [10]. Polι, encoded by the *POLI* gene, incorporates one or two nucleotides opposite (6-4) photoproducts *in vitro* but cannot bypass these lesions by itself [11,12], although limited Polι dependent bypass of CPD lesions has been observed depending upon the local sequence context and metal ion used as a cofactor [11,13–15]. Whereas Polι is a paralog of Polη, no human disease related to Polι-deficiency has been identified so far, and its physiological relevance has not been clarified. Polκ is the eukaryotic homologue of the *Escherichia coli* DinB protein (DNA polymerase IV) and has been shown to be involved in accurate TLS past N^2-adducts of dG and also in both spontaneous and induced mutagenesis [16,17]. Although Polκ was suggested to be involved in NER of UV-induced lesions [18,19], it seems unlikely that Polκ plays an important role in TLS past UV lesions since the enzyme showed no activity to bypass past CPD and (6-4) photoproduct *in vitro* [20]. REV1 has a dCMP transferase activity, but the protein appears to exert its role in UV-induced responses, as a scaffold protein interacting with Polζ, Polη, Polι, and Polκ [10]. Polζ is a B-family polymerase containing REV3 and REV7 subunits and is believed to function as an "extender" enzyme after a TLS DNA polymerase (for example, Polι) inserting a nucleotide opposite a given DNA lesion [10].

To investigate the physiological roles of Polη and Polι, we have previously generated mice mutated in *Polh* and/or *Poli* genes [21]. Polη-deficient mice were generated by inserting a G418 resistance gene cassette into exon 8 of the *Polh* gene, resulting in production of a truncated, nonfunctional Polη protein. Using the 129 mouse derived embryonic stem (ES) cell line, which carries a spontaneous Polι nonsense mutation [22], we obtained Polη/Polι double-deficient mice as well as Polι-deficient mice. We found that the incidence of skin tumors was greatly increased in the Polη- and Polη/Polι double-deficient mice after UV irradiation, that Polη/Polι double-deficient mice started to develop skin tumors earlier than Polη-deficient mice, and that the average number of skin tumors was higher in the double-deficient mice than in the Polη-deficient mice. In addition, we found that epithelial and mesenchymal tumors were formed in Polη- and Polι-deficient mice, respectively [21]. These results suggest that, in addition to Polη, Polι also participates in suppressing skin carcinogenesis. Other groups had also shown the importance of Polη and Polι to suppress UV-induced skin tumors. Polη-deficient mice, generated by disruption of exon 4 of the *Polh* gene, are highly susceptible to UV-induced skin tumors [23]. Polη/Polι double-deficient mice, in turn, develop UV-induced skin tumors earlier than Polη-deficient mice [24].

To investigate the functions of Polη and Polι in suppressing UV-induced carcinogenesis, we examined the mutation frequencies and spectra in UV-irradiated and unirradiated epidermis in Polη-deficient, Polι-deficient, and Polη/Polι double-deficient mice, using the *rpsL* transgene as a mutation reporter sequence. Our results show that Polη plays crucial roles in suppressing any types of UV-induced base substitution at dipyrimidine sites *in vivo* and that Polι participates in error-prone TLS past UV lesions in the absence of Polη.

2. Materials and methods

2.1. Generation of transgenic mice

The *rpsL* transgenic mouse line (ssw2-14p) used in this study was derived from C57BL/6J mice, but carries approximately 100 hemizygous copies of the pSSW plasmid; it has been described previously [25]. The pSSW plasmid carries a reporter gene, *rpsL* from *E. coli*, with a dominant streptomycin-sensitive (Sm^s) phenotype in bacterial cells, and a kanamycin-resistant (Km^r) gene. Polη- and/or Polι-deficient mice were established as previously described [21]. $Polh^{+/-}$, $Poli^{+/-}$ mice were mated with the *rpsL* transgenic mice to generate $rpsL^{Tg/+}$ $Polh^{+/-}$ $Poli^{+/-}$ mice. By mating the $rpsL^{Tg/+}$ $Polh^{+/-}$ $Poli^{+/-}$ mice with $Polh^{+/-}$ $Poli^{+/-}$ mice, $rpsL^{Tg/+}$ $Polh^{-/-}$ $Poli^{+/+}$, $rpsL^{Tg/+}$ $Polh^{+/+}$ $Poli^{-/-}$, and $rpsL^{Tg/+}$ $Polh^{-/-}$ $Poli^{-/-}$ mice were generated. The handling and sacrifice of all animals were carried out in accordance with nationally prescribed guidelines, and ethical approval for the studies was granted by the Committee for Animal Experiments, Graduate School of Frontier Biosciences of Osaka University.

2.2. Preparation of UVB irradiated and unirradiated epidermal genomes

At 8 weeks of age, after shaving of dorsal hair, mice from each respective genotype were irradiated with UVB (FL20SE-E; Toshiba, Tokyo, Japan) at 400 J/m^2. One week after irradiation, these mice were sacrificed, and the irradiated dorsal and unirradiated ventral skins were collected. These skin samples were treated with 20 mM EDTA in PBS at 37 °C, and the epidermis was peeled from the dermis using a spatula. The isolated epidermal samples were frozen in liquid nitrogen and stored at −80 °C. To prepare genomic DNA, the epidermal samples were first incubated in lysis buffer (10 mM Tris–HCl (pH 8.0), 100 mM EDTA, 200 mM NaCl, 0.5% SDS, 0.1 mg/ml RNaseA) at 37 °C for 1 h, followed by 1 mg/ml Proteinase K for 3 h. After phenol/chloroform extraction, genomic DNA was obtained by ethanol precipitation.

2.3. rpsL *mutagenesis assay*

Mutation analyses were performed as described [25] with minor modifications. Briefly, 10 μg of isolated genomic DNA was digested with 35 U of *Ban*II (TaKaRa, Shiga, Japan) at 37 °C for 3 h, which incises once the pSSW plasmid, in order to excise the integrated shuttle vector at unit size. The *Ban*II digested DNA was then treated with 350 U of T4 DNA ligase (TaKaRa, Shiga, Japan) for 2 h at 16 °C for self-circularization. One microgram of the resulting DNA was introduced into *E. coli* DH10B cells by electroporation (1.8 kV/mm). Then, a portion of the cells were plated onto LB plates containing kanamycin (50 μg/ml), and the remainders were plated onto plates containing both kanamycin and streptomycin (200 μg/ml). These plates were incubated at 28 °C for 48 h. Total numbers of kanamycin-resistant colonies were calculated from the number of colonies formed and the amount of DNA used. Mutation frequency was calculated as the ratio of total colony numbers on the plate containing kanamycin and streptomycin to those on the plate containing kanamycin only. For mutation spectrum analysis, DNA fragments containing the *rpsL* gene were amplified by PCR from the kanamycin- and streptomycin-resistant colonies. The primers F (5′-CACCTGATTGCCCGACATTA-3′) and R (5′-CAGGGTCGGAACAGGAGAGC-3′) were used for the PCR. The amplified PCR products were directly sequenced with the forward primer (5′-GACGAATTCCCGGTTTGACTGGTC-3′) and the reverse primer (5′-GGATTGTCCAAAACTCTACGAG-3′). Mutations found in the *rpsL* coding region and surrounding sequences containing the promoter and ribosomal recognition regions (from position −120 to position 375) were exhibited in the mutation spectrum.

2.4. Statistical analyses

Statistical analyses for mutation frequency included the Student's *t*-test and Fisher's exact probability test. The CLUSTERM

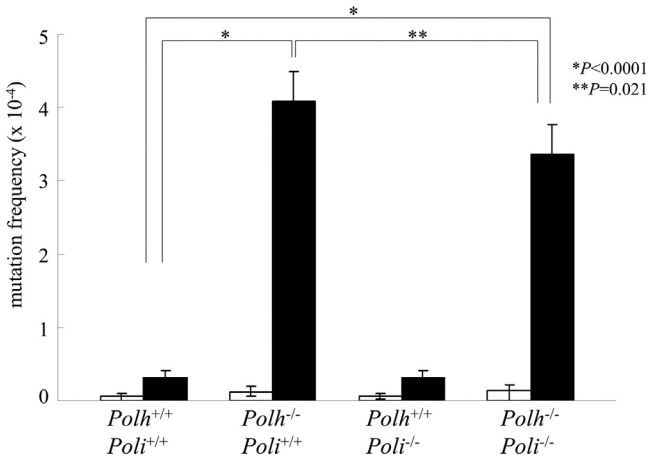

Fig. 1. Mutation frequencies of the *rpsL* transgene in UVB-irradiated and unirradiated epidermis from *Polh*$^{+/+}$ *Poli*$^{+/+}$, *Polh*$^{-/-}$ *Poli*$^{+/+}$, *Polh*$^{+/+}$ *Poli*$^{-/-}$, and *Polh*$^{-/-}$ *Poli*$^{-/-}$ mice. Mean mutation frequencies of six mice are plotted with standard deviations. Open and filled bars indicate data for unirradiated and irradiated epidermis, respectively. All differences in mean mutation frequencies between UV-irradiated and unirradiated mice are statistically significant ($P = 0.0006$ for *Polh*$^{+/+}$ *Poli*$^{+/+}$ mice, and $P < 0.0001$ for *Polh*$^{-/-}$ *Poli*$^{+/+}$, *Polh*$^{+/+}$ *Poli*$^{-/-}$ and *Polh*$^{-/-}$ *Poli*$^{-/-}$ mice). Differences between irradiated *Polh*$^{-/-}$ *Poli*$^{+/+}$ mice and irradiated *Polh*$^{+/+}$ *Poli*$^{+/+}$ mice, and between irradiated *Polh*$^{-/-}$ *Poli*$^{-/-}$ mice and irradiated *Polh*$^{+/+}$ *Poli*$^{+/+}$ mice are both statistically significant ($P < 0.0001$). The difference between irradiated *Polh*$^{-/-}$ *Poli*$^{-/-}$ mice and irradiated *Polh*$^{-/-}$ *Poli*$^{+/+}$ mice is statistically significant ($P = 0.021$).

program (http://www.itb.cnr.it/webmutation/) was employed to predict mutation hotspots [26].

3. Results

3.1. Polη but not Polι suppresses UV-induced mutations in epidermal cells

Polh$^{+/+}$ *Poli*$^{+/+}$, *Polh*$^{-/-}$ *Poli*$^{+/+}$, *Polh*$^{+/+}$ *Poli*$^{-/-}$ and *Polh*$^{-/-}$ *Poli*$^{-/-}$ mice carrying the *rpsL* transgene hemizygously were obtained by crossing of *Polh*$^{+/-}$ *Poli*$^{+/-}$ mice with *rpsL* transgenic mice. Those mice had its back shaved and irradiated with 400 J/m^2 UVB once. One week after irradiation, the mice were sacrificed, and irradiated dorsal skin samples and unirradiated ventral skin samples were collected and separated into epidermis and dermis. Genomic DNAs were extracted from the epidermis and subjected to mutation analysis as described in Section 2. Six mice from each genotype were examined. The number of screened and mutated colonies, together with mutation frequencies of each individual mouse, is shown in Table 1. The mean mutation frequencies for six mice are depicted in Fig. 1. There was no significant difference in the mutation frequency of the unirradiated epidermal cells among the four genotypes. The increases in mutation frequency following UV-irradiation were statistically significant in all genotypes. UV-induced mutation frequencies for *Polh*$^{-/-}$ *Poli*$^{+/+}$ (4.07×10^{-4}) and *Polh*$^{-/-}$ *Poli*$^{-/-}$ mice (3.36×10^{-4}) were approximately 13- and 11-fold higher, respectively, than that of *Polh*$^{+/+}$ *Poli*$^{+/+}$ mice (3.07×10^{-5}), indicating that Polη exerts a crucial role for suppressing mutations by UV-irradiation. On the other hand, the UV-induced mutation frequency in *Polh*$^{+/+}$ *Poli*$^{-/-}$ mice (3.22×10^{-5}) were not significantly different from that in wild-type mice ($P = 0.82$), suggesting that Polι does not influence UV-induced mutagenesis in the epidermis in the presence of Polη. Interestingly, however, the UV-induced mutation frequency in the genome from *Polh*$^{-/-}$ *Poli*$^{-/-}$ mice was significantly lower than that of *Polh*$^{-/-}$ *Poli*$^{+/+}$ mice ($P = 0.020$), suggesting that Polι contributes to increasing mutations in the absence of Polη.

Table 1
Mutation frequencies in UVB irradiated and unirradiated epidermal genomes from *Polh*$^{+/+}$ *Poli*$^{+/+}$, *Polh*$^{-/-}$ *Poli*$^{+/+}$, *Polh*$^{+/+}$ *Poli*$^{-/-}$, and *Polh*$^{-/-}$ *Polh*$^{-/-}$ mice.

Genotype	UV irradiation	A[a] ($\times 10^5$)	B[b]	Mutation frequency ($\times 10^{-5}$)
Polh$^{+/+}$ *Poli*$^{+/+}$	–	3.44	5	1.45
		4.81	1	0.21
		5.25	3	0.57
		9.22	3	0.33
		7.73	1	0.13
		6.56	2	0.30
	+	5.46	13	2.38
		3.99	15	3.76
		3.80	5	1.32
		7.81	24	3.07
		7.25	23	3.17
		3.37	16	4.75
Polh$^{-/-}$ *Poli*$^{+/+}$	–	3.94	9	2.28
		4.67	4	0.86
		6.45	3	0.47
		2.76	4	1.45
		3.10	6	1.94
		5.83	2	0.34
	+	3.55	158	44.5
		2.73	102	37.4
		2.96	124	41.9
		3.02	140	46.4
		3.16	127	40.2
		2.55	87	34.1
Polh$^{+/+}$ *Poli*$^{-/-}$	–	6.75	6	0.89
		3.43	1	0.29
		3.06	1	0.33
		3.15	1	0.32
		4.62	1	0.22
		3.36	4	1.19
	+	3.23	10	3.10
		4.95	20	4.04
		3.11	8	2.57
		3.36	7	2.08
		3.62	11	3.04
		3.57	16	4.48
Polh$^{-/-}$ *Poli*$^{-/-}$	–	3.65	2	0.55
		5.36	4	0.75
		3.51	2	0.57
		4.59	4	0.87
		3.91	10	2.56
		4.24	10	2.36
	+	2.16	90	41.7
		3.17	109	34.4
		2.85	92	32.3
		3.42	101	29.5
		2.20	75	34.1
		2.69	79	29.4

[a] Total number of Km^r colonies, as calculated from the number of Km^r colonies counted and the amount of DNA sample used for A and B.
[b] Total number of Km^r and Sm^r colonies counted.

3.2. Sequence analysis of mutations

To identify the types and locations of mutations, we sequenced the *rpsL* coding region and its upstream region containing the promoter and the ribosomal recognition sequences (from position −120 to position 375) in the mutants. The identified mutations are shown in Fig. 2A–D. As summarized in Table 2, base substitutions were among the most common mutations induced by UV-irradiation in all mouse genotypes. Statistical analysis revealed that *Polh*$^{-/-}$ *Poli*$^{+/+}$ and *Polh*$^{-/-}$ *Poli*$^{-/-}$ mice had significantly higher base substitutions, namely, 4.03×10^{-4} and 3.22×10^{-4},

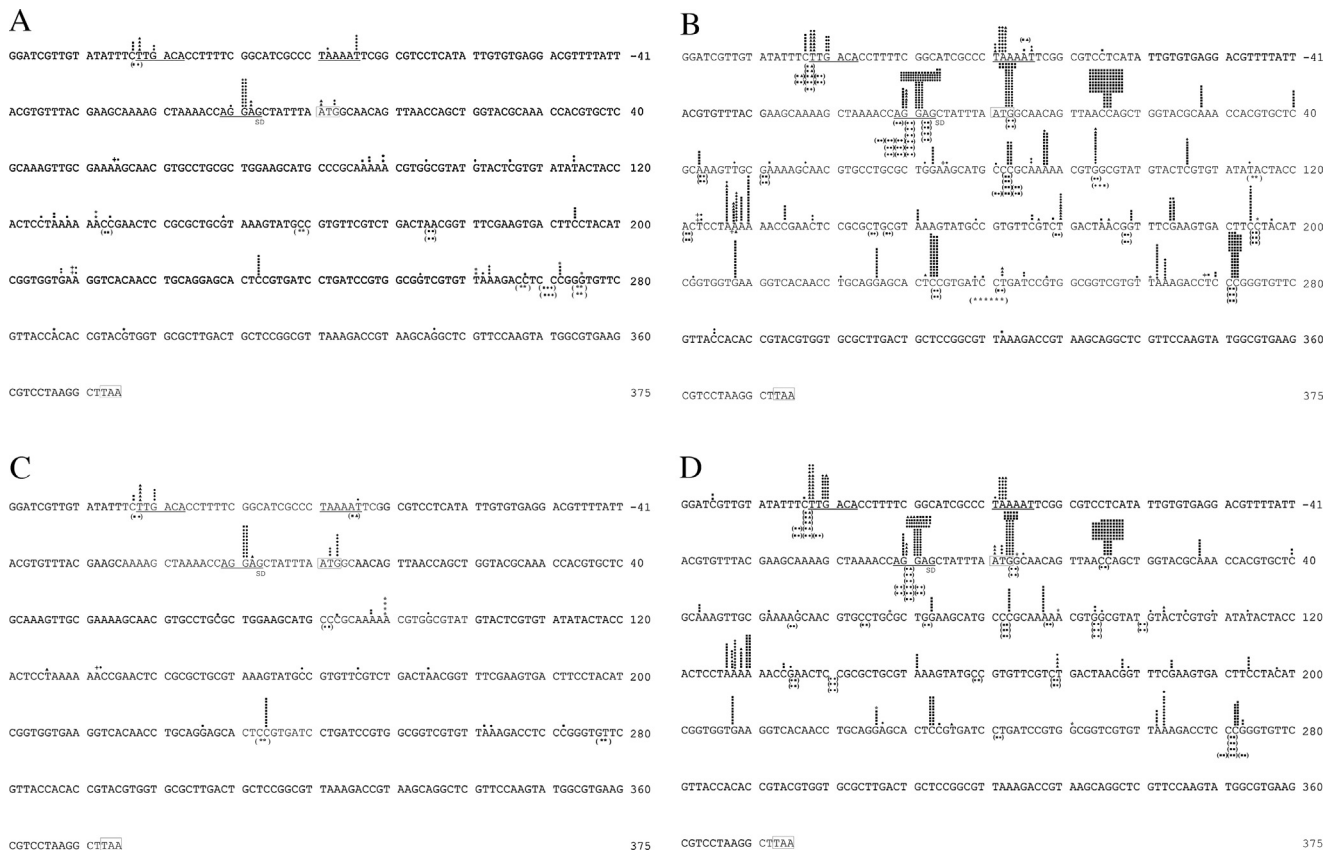

Fig. 2. Site-distribution of UV-induced mutations observed in (A) *Polh*$^{+/+}$ *Poli*$^{+/+}$, (B) *Polh*$^{-/-}$ *Poli*$^{+/+}$, (C) *Polh*$^{+/+}$ *Poli*$^{-/-}$ and (D) *Polh*$^{-/-}$ *Poli*$^{-/-}$ mice. Base substitutions are indicated above the wild-type *rpsL* sequence by the following symbols. A, T, C and G are indicated by circle, square, triangle and diamond, respectively. Deletions and additions are indicated by an asterisk (*) and plus (+), respectively. Tandem mutations are indicated below the sequence in parentheses. The nucleotide positions, starting from the first position of the initiation codon, for translation are shown at the right side of the sequence. The start codon and the termination codon are surrounded by boxes. The promoter sequence and the ribosomal recognition sequence (Shine–Dalgarno sequence; SD) are underlined.

respectively, than *Polh*$^{+/+}$ *Poli*$^{+/+}$ (2.51×10^{-5}) and *Polh*$^{+/+}$ *Poli*$^{-/-}$ (2.78×10^{-5}) mice ($P < 0.0001$) (Table 3). On the other hand, there were no statistically significant differences in the frequencies of UV-induced frameshift mutations between the four genotypes. An important point to note is that most of the UV-induced mutations were found at dipyrimidine sites (Fig. 2A–D and Table 3). The frequencies of base substitutions at dipyrimidine sites in *Polh*$^{-/-}$ *Poli*$^{+/+}$ and *Polh*$^{-/-}$ *Poli*$^{-/-}$ mice were significantly higher than those

Table 2
Class-distribution of *rpsL* mutations.

	Polh$^{+/+}$ *Poli*$^{+/+}$		*Polh*$^{-/-}$ *Poli*$^{+/+}$		*Polh*$^{+/+}$ *Poli*$^{-/-}$		*Polh*$^{-/-}$ *Poli*$^{-/-}$	
UV	–	+	–	+	–	+	–	+
Base substitutions	0.16 (6)[a]	2.62 (83)[c]	0.37 (10)[c]	43.2 (777)[c]	0.12 (3)	3.11 (68)	0.24 (6)	33.2 (547)
Transitions								
G:C→A:T	0.08 (3)	1.58 (50)[c]	0.22 (6)	23.5 (422)[c]	0.12 (3)	2.11 (46)[c]	0.16 (4)	16.4 (271)[c]
A:T→G:C	0.08 (3)	0.28 (9)	0.04 (1)[c]	3.95 (71)[c]	<0.04 (0)	0.32 (7)[c]	<0.04 (0)	4.00 (66)[c]
Transversions								
G:C→T:A	<0.03 (0)	<0.03 (0)	0.04 (1)	5.45 (98)[c]	<0.04 (0)	0.14 (3)	0.04 (1)	3.94 (65)[c]
G:C→C:G	<0.03 (0)	0.03 (1)	0.04 (1)	0.50 (9)[c]	<0.04 (0)	<0.05 (0)	<0.04 (0)	0.43 (7)
A:T→T:A	<0.03 (0)	0.41 (13)	0.04 (1)	5.95 (107)[c]	<0.04 (0)	0.32 (7)	0.04 (1)	4.73 (78)[c]
A:T→C:G	<0.03 (0)	0.13 (4)	<0.04 (0)	0.56 (10)[c]	<0.04 (0)	0.09 (2)	<0.04 (0)	0.73 (12)[c]
Tandems	<0.03 (0)	0.19 (6)	<0.04 (0)	3.34 (60)[c]	<0.04 (0)	0.14 (3)	<0.04 (0)	2.91 (48)[c]
Others	0.24 (9)	0.60 (19)[c]	0.75 (20)[c]	0.61 (11)[c]	0.45 (11)	0.41 (9)	1.03 (26)	1.33 (22)
1 bp deletions	0.14 (5)	0.32 (10)[c]	0.49 (13)[c]	0.11 (2)	0.25 (6)	0.18 (4)	0.44 (11)	0.30 (5)
1 bp insertions	<0.03 (0)	0.10 (3)[c]	<0.04 (0)	0.28 (5)[c]	0.04 (1)	0.05 (1)	<0.04 (0)	<0.06 (0)
Large deletions[b]	0.08 (3)	0.19 (6)	0.26 (7)	0.22 (4)[c]	0.16 (4)	0.14 (3)	0.55 (14)	0.97 (16)
Large insertions[b]	0.03 (1)	<0.03 (0)	<0.04 (0)	<0.11 (0)	<0.04 (0)	0.05 (1)	0.04 (1)	0.06 (1)
Total	0.41 (15)	3.22 (102)	1.22 (30)	43.9 (788)	0.58 (14)	3.53 (77)	1.27 (32)	34.5 (569)

Mutation frequencies ($\times 10^{-5}$) were determined by total number of mutations identified from six mice for each of genotypes.
[a] Numbers in parentheses are the number of independent mutations.
[b] Large deletion and large insertion include deletions and insertions of two or more base pairs.
[c] Mutants contained two or three mutations were found.

Table 3
Mutation frequencies ($\times 10^{-5}$) of UV-induced base substitutions at dipyrimidine sites and other sites, and other mutations, including deletions and insertions.

	Polh$^{+/+}$ *Poli*$^{+/+}$	*Polh*$^{-/-}$ *Poli*$^{+/+}$	*Polh*$^{+/+}$ *Poli*$^{-/-}$	*Polh*$^{-/-}$ *Poli*$^{-/-}$
Base substitutions	2.51 ± 1.06	40.3 ± 4.01[a]	2.78 ± 1.03	32.2 ± 5.85
At dipyrimidine sites	2.31 ± 0.95	40.1 ± 4.19[b]	2.62 ± 0.81	31.7 ± 5.73
At other sites	0.20 ± 0.21	0.39 ± 0.28	0.21 ± 0.23	0.67 ± 0.72
Other mutations	0.69 ± 0.33	0.68 ± 0.47	0.44 ± 0.53	1.34 ± 2.57

Mean mutation frequencies of six mice are shown, along with standard deviations.
[a] Values are significantly different from those of non-irradiated *Polh*$^{+/+}$ *Poli*$^{+/+}$ and *Polh*$^{-/-}$ *Poli*$^{-/-}$ mice ($P < 0.0001$ and $P = 0.029$, respectively).
[b] Values are significantly different from those of non-irradiated *Polh*$^{+/+}$ *Poli*$^{+/+}$ and *Polh*$^{-/-}$ *Poli*$^{-/-}$ mice ($P < 0.0001$ and $P = 0.025$, respectively).

in *Polh*$^{+/+}$ *Poli*$^{+/+}$ and *Polh*$^{+/+}$ *Poli*$^{-/-}$ mice ($P < 0.0001$). These results indicate that Polη is predominantly responsible for suppressing mutations upon UV-irradiation, by correctly bypassing UV-induced pyrimidine dimers.

Interestingly, in *Polh*$^{-/-}$ *Poli*$^{-/-}$ mice, the frequency of UV-induced total base substitutions was significantly lower than in *Polh*$^{-/-}$ *Poli*$^{+/+}$ mice ($P = 0.029$, see Table 3). Similarly, the frequency of base substitutions at dipyrimidine sites in *Polh*$^{-/-}$ *Poli*$^{-/-}$ mice was also significantly lower than in *Polh*$^{-/-}$ *Poli*$^{+/+}$ mice ($P = 0.025$, see Table 3). In addition to this, several mutational hotspots were observed at dipyrimidine sites in the UV-irradiated epidermal genomes of *Polh*$^{-/-}$ *Poli*$^{+/+}$ mice, including −104C, −103T, −104/−103CT, −101G, −79A, −11G, −10G, −11/−10GG, 3G, 16C, 28A, 40C, 73G, 83C, 82/83CC, 88A, 94G, 106C, 127–130A, 170T, 184G, 194C, 208G, 226G, 233C, 262A, 263A, and 272C (Fig. 2B). Among these, −104C, 40C, 82/83CC, 94G, 106C, 170T, 184G, 194C, 226G, and 262A were no longer mutational hotspots in the UV-irradiated *Polh*$^{-/-}$ *Poli*$^{-/-}$ mice (Fig. 2D). These results are consistent with our interpretation that Polι participates in error-prone TLS past UV-induced lesions in an error-prone manner, especially when bypassing C within pyrimidine dimers under the Polη-deficient background.

The frequencies for each type of base substitution are depicted in Fig. 3. The G:C to A:T transition was the most prominent UV-induced mutation in all genotypes. In the genomes of *Polh*$^{-/-}$ *Poli*$^{+/+}$ and *Polh*$^{-/-}$ *Poli*$^{-/-}$ mice, the UV-induced mutational frequencies of all types of base substitutions were higher than in *Polh*$^{+/+}$ *Poli*$^{+/+}$ and *Polh*$^{+/+}$ *Poli*$^{-/-}$ mice, although G:C to C:G and A:T to C:G transversions in *Polh*$^{-/-}$ *Poli*$^{+/+}$ mice were not statistically significant compared with those in *Polh*$^{+/+}$ *Poli*$^{+/+}$ mice. These observations strongly suggest that Polη suppresses UV-induced mutations at both C and T residues in the epidermis *in vivo*. Interestingly, in *Polh*$^{-/-}$ *Poli*$^{-/-}$ mice, the frequency of G:C to A:T transitions was statistically lower than that in *Polh*$^{-/-}$ *Poli*$^{+/+}$ mice ($P = 0.0013$), suggesting that Polι contributes to UV-induced G:C to A:T transitions in the absence of Polη, probably by inserting A opposite cytosine within pyrimidine dimers.

4. Discussion

4.1. Roles of Polη in suppressing UV-induced mutagenesis

In the present study, we analyzed the UVB-induced mutations occurring in the *rpsL* transgene in epidermal cells of wild type, Polη-deficient, Polι-deficient, and Polη/Polι double-deficient mice. Although several studies have investigated the effects of Polη and/or Polι deficiencies on UV-induced mutagenesis [24,27–33], these studies were done using cultured cells *in vitro*. To the best of our knowledge, this is the first report addressing the roles of Polη and Polι in UV-induced mutagenesis *in vivo*. When irradiated with UVB, Polη-deficient mice showed significantly higher mutation frequencies than control mice. Most of the UV-induced mutations in the genomes of Polη-deficient mice were base substitutions at dipyrimidine sites (both C and T residues). These findings clearly indicate that Polη is crucial for accurate TLS past UV-induced pyrimidine dimers in the epidermal cells and in the absence of Polη, other TLS polymerases carries out mutagenic bypass past the lesions. These results account for previous findings that Polη-deficient mice suffer from high incidences of UV-induced skin tumors [21,23,24].

The most prominent UV-induced mutations were G:C to A:T transitions in all genotypes. Hydrolytic deamination of the cytosine in CPDs, which produces uracil-containing CPDs, is thought to play a key role in the UV-induced mutations at G:C base pairs [34–36]. Polη preferentially incorporates dAMP opposite uracil of T-U CPDs [37], resulting in a G:C to A:T transition, if the CPD is repaired after TLS. This may account for the frequent G:C to A:T transitions observed in Polη-proficient mice. However, the large increase in the frequency of UV-induced G:C to A:T transitions in Polη-deficient mice indicates that Polη rather functions to suppress such transitions. Similar results showing that the most prominent UV-induced mutations caused by Polη deficiency are G:C to A:T transitions were observed in two previous experiments. In the first of these, the *supF* gene was introduced into XP-V cells and human kidney 293T cells in which Polη expression was suppressed by siRNA. In the second, the *LacZ'* gene was introduced into Burkitt's lymphoma BL2 cells in which the *POLH* gene was inactivated by gene targeting [28,29,33]. Abundant G:C to A:T transitions were also observed following UV-induced mutation analyses of the *HPRT* locus in XP-V cells and primary fibroblasts obtained from Polη-deficient mice, although equivalent levels of G:C to T:A transversions were also observed in these studies [24,27,31]. These observations suggest that Polη is critical for suppressing at C (some of them might be deaminated) within UV-induced pyrimidine dimers. Although we do not know which kind of nucleotides Polη incorporates opposite the cytosine in CPDs, its preference for incorporating dAMP opposite uracil suggests that Polη needs to cooperate with other TLS polymerases or unknown factors to promote accurate bypass of the lesion. Polι is a possible candidate for this role. It is capable of incorporating dGMP opposite uracil in CPDs with half the efficiency of dAMP [14]. Polη also interacts with Polι and UV-induced nuclear foci formation by Polι is largely dependent on Polη [38]. Polη interacts with REV1 [39]. Supporting this, we have shown that the accumulation of endogenous REV1 in UV-damaged sites in nuclei depends on Polη, and that Polη-REV1 interaction is required to suppress spontaneous mutations in human cells [40]. These observations suggest that coordinated TLS by multiple DNA polymerases may take place in the presence of Polη, contributing to greater suppression of base substitutions at dipyrimidine sites than by Polη alone.

UVB exposure in mice may produce reactive oxygen species that generate oxidative base damage, such as 8-oxoG [41]. Mammalian Polη is efficient at incorporating dC opposite 8-oxoG to suppress G:C to T:A transversion *in vitro* [42,43]. Furthermore, Lee and Pfeifer reported that G:C to T:A transversions were predominant in XP-V and Polη-knockdown human cells [44]. Hence, it is reasonable to suggest that some, if not all, G:C to T:A transversions in UV-exposed Polη-deficient mice are caused by UV-induced oxidative base damage. On the other hand, there were no significant differences in the spontaneous mutation frequencies in several tissues between

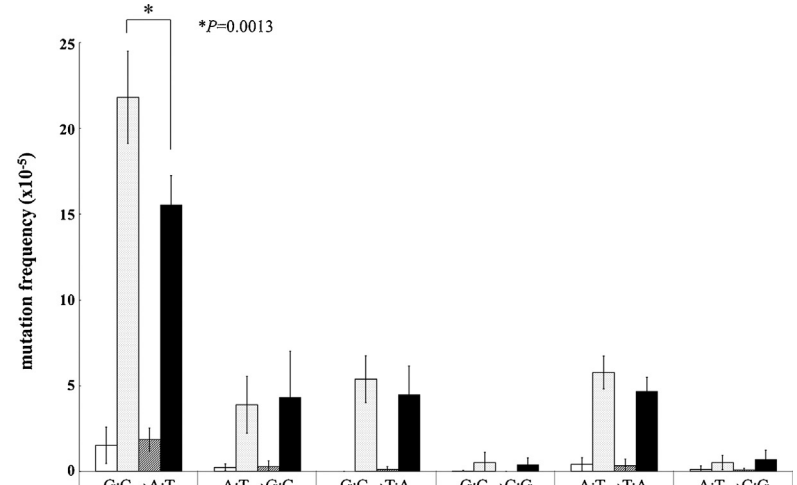

	G:C→A:T	A:T→G:C	G:C→T:A	G:C→C:G	A:T→T:A	A:T→C:G
□ *Polh*$^{+/+}$ *Poli*$^{+/+}$	1.52±1.06	0.24±0.19	<0.02	0.02±0.05	0.42±0.39	0.13±0.19
▒ *Polh*$^{-/-}$ *Poli*$^{+/+}$	21.8±2.68	3.89±1.67	5.39±1.37	0.52±0.59	5.77±0.96	0.52±0.41
▓ *Polh*$^{+/+}$ *Poli*$^{-/-}$	1.87±0.68	0.29±0.33	0.12±0.17	<0.08	0.34±0.38	0.08±0.12
■ *Polh*$^{-/-}$ *Poli*$^{-/-}$	15.6±1.70	4.33±2.69	3.94±1.77	0.40±0.39	4.69±0.81	0.71±0.53

mutation frequency (x10^{-5})

Fig. 3. UV-induced base substitutions observed in *Polh*$^{+/+}$ *Poli*$^{+/+}$, *Polh*$^{-/-}$ *Poli*$^{+/+}$, *Polh*$^{+/+}$ *Poli*$^{-/-}$ and *Polh*$^{-/-}$ *Poli*$^{-/-}$ mice. White, dotted, striped, and black bars indicate *Polh*$^{+/+}$ *Poli*$^{+/+}$, *Polh*$^{-/-}$ *Poli*$^{+/+}$, *Polh*$^{+/+}$ *Poli*$^{-/-}$ and *Polh*$^{-/-}$ *Poli*$^{-/-}$ mice, respectively. The mean mutation frequencies for the six mice are plotted along with their standard deviations. Note that these mean values differ from the total mutation frequencies listed in Table 3. Values for G:C to A:T, A:T to G:C, G:C to T:A, and A:T to T:A mutations of *Polh*$^{-/-}$ *Poli*$^{+/+}$ mice are significantly different from those of *Polh*$^{+/+}$ *Poli*$^{+/+}$ mice ($P < 0.0001$, $P = 0.0006$, $P < 0.0001$, and $P < 0.0001$, respectively). Values for G:C to A:T, A:T to G:C, G:C to T:A, A:T to T:A, and A:T to C:G mutations of *Polh*$^{-/-}$ *Poli*$^{-/-}$ mice are significantly different from those of *Polh*$^{+/+}$ *Poli*$^{+/+}$ mice ($P < 0.0001$, $P = 0.0068$, 0.0005, $P < 0.0001$, and $P = 0.042$, respectively). The value for the G:C to A:T transition of *Polh*$^{-/-}$ *Poli*$^{-/-}$ mice is significantly different from that of *Polh*$^{-/-}$ *Poli*$^{+/+}$ mice ($P = 0.0013$).

one-year-old Polη-deficient and -proficient mice [32]. It remains uncertain whether or not oxidative base damage is involved in the enhancement of mutagenesis in UV-exposed Polη-deficient mice.

4.2. Roles of Polι in UV-induced mutagenesis

UV-induced mutation frequencies in epidermal genomes from Polι-deficient mice were not significantly different from those of wild-type mice, but the mutation frequency in Polη/Polι double-deficient mice was statistically lower than in Polη-deficient mice. These results imply that Polι would not cause mutations in the UV-irradiated epidermal genome when Polη is present, but would cause UV-induced mutations in its absence. This is especially true for Polι and G:C to A:T transitions, in which the difference is statistically significant in Polη-deficient mice. This is consistent with a previous report that Polι preferentially incorporates dAMP opposite T-U CPDs *in vitro* [14], which would give rise to G:C to A:T transitions. Polι also preferentially incorporates dTMP opposite TT-CPD *in vitro* [11], which would generate A:T to T:A transversion. In the experiments described in this report, however, we have not yet observed any statistical difference in the frequency of transversion between Polη-deficient and Polη/Polι double-deficient mice.

Gueranger et al. [33] reported that Polι deficiency did not affect UV-induced mutations in a shuttle vector in the presence of Polη but did reduce some mutational hotspots observed in Polη-targeted BL2 cells. Wang et al. [31] also reported that suppression of Polι expression decreased UV-induced mutation frequencies in Polη-deficient XP-V cells. These observations are consistent with our findings that Polι acts as a mutator in the absence of Polη. However, Dumstorf et al. [24], investigating primary fibroblasts isolated from Polη- and/or Polι-deficient mice, have reported that Polι deficiency causes a decrease in UV-induced base substitutions not only in the absence of Polη but also in its presence. We cannot explain the discrepancies between these observations, but it may be possible that the difference depends on the type of cells employed, *i.e.* that there is an inherent difference between dermal fibroblasts and epithelial cells. Dumstorf et al. also reported biases for UV-induced base substitutions between nontranscribed and transcribed strands of the *Hprt* locus in wild-type and Polη- deficient cells which were lower in Polη/Polι double-deficient cells [24]. We did not, however, observe this strand bias. This is probably due to the different transcription status of the *Hprt* gene and the *rpsL* reporter gene, *i.e.* the *Hprt* gene is an actively transcribed housekeeping gene but the *rpsL* reporter gene has no eukaryotic promotor. So, UV-induced photoproducts could be selectively removed from the transcribed strand of the *Hprt* gene [45] but not of the *rpsL* gene.

The lower UV-induced mutation frequency in Polη/Polι double-deficient mice than in Polη-deficient mice was unexpected, as it is inconsistent with previous observations that Polη/Polι double-deficient mice start to develop skin tumors earlier, and go on to develop higher numbers of skin tumors than Polη-deficient mice [21,24]. It should be noted that UV-irradiation procedures used for tumor formation are different from those used for mutagenesis analyses, *i.e.* mice were irradiated every day, with 2 kJ/m^2 of UVB, for 20 weeks, in tumor formation assays, but were only irradiated once, with 0.4 kJ/m^2 of UVB, in mutagenesis assays. In addition, we have reported that Polη and Polι deficiencies induce epithelial and mesenchymal tumors, respectively, suggesting that the contributions of Polη and Polι to mutation avoidance in the epidermis are different from those in the dermis. Petta et al. demonstrated that Polι is involved in oxidative base damage tolerance independently of Polη [46]. Our present study, however, did not show a greater number of mutations in UV-irradiated epidermal cells from Polι-deficient mice. These are issues that we hope to solve in the near future.

4.3. UV-induced mutagenesis in the absence of Polη

Small numbers of UV-induced G:C to C:G and A:T to C:G transversions may suggest that cells do not have DNA polymerases

that efficiently incorporate dCMP opposite cytosine, uracil, or thymine dimers. However, a clear increase in UV-induced transitions in the Polη-deficient mice indicates that an error-prone TLS mechanism exists in the epidermis *in vivo*. We showed that Polι partially causes mutations in the UV-irradiated genome in the absence of Polη; however, the majority of these mutations could be produced by other TLS polymerases. Polζ and REV1 are likely candidates for error-prone enzymes. Previous studies using both mouse and human cells have shown that reduced expression or disruption of *REV3* or *REV7* genes, which encode Polζ, results in a decrease in UV-induced mutation frequencies [33,39,47,48]. In human cells, reduced *REV1* gene expression has been reported to decrease the frequency of UV-induced mutation [39,47,49]. Moreover, a targeted deletion of the BRCT domain in mouse cells decreased UV-induced mutation frequency [50]. In addition, Polκ-deficient and *Polk*-knockdown cells exhibit UV sensitivity [51–53], indicating that this polymerase is also involved in UV-damage tolerance mechanisms. Polκ participates in nucleotide excision repair (NER) [18,19]. However, it also appears to play a role in TLS past UV-induced lesions, as shown in *Xenopus* egg extracts and NER-deficient XP-A cells [53–55]. Finally, it should be pointed out that replicative DNA polymerase(s) may add one or more nucleotides (mostly one dAMP) to the primer terminus before dissociating from it, Polζ extending further [56]. If A is inserted opposite to C in pyrimidine dimers in such a way by a replicative DNA polymerase and extended by Polζ, it should result in a G:C-to-A:T transition. Although disruption of the *Rev3* gene results in embryonic lethality in mice [47], *Rev1, Rev7* and *Polκ* knockout and *Rev3* conditional knockout animals have been successfully generated [57–61]. To further understand the mechanisms that protect against and produce mutations and tumors after UV-irradiation, it will be necessary to perform *in vivo* UV-induced mutagenesis experiments with mice defective in multiple TLS polymerases.

4.4. Conclusions

In this study, we show that Polη is important for suppressing any types of UV-induced base substitution at dipyrimidine sites, and that Polι acts as a mutator at UV lesions in the absence of Polη in epidermal cells.

Conflict of interest statement

None declared.

Acknowledgements

We thank all of the members of the Hanaoka Laboratory at Osaka University for critical discussions and helpful comments. We are grateful to Dr. Haruo Ohmori (Gakushuin University) for his critical reading of the manuscript and valuable suggestions. This study was supported by KAKENHI (Grant-in Aid for Scientific Research) from the Ministry of Education, Culture, Sports, Science, and Technology of Japan (17013053 to F.H.) and by Solution Oriented Research for Science and Technology from the Japan Science and Technology Agency.

References

[1] E.C. Friedberg, G.C. Walker, W. Siede, R.D. Wood, R.A. Schulz, T. Ellenberger, DNA Repair and Mutagenesis, ASM Press, 2006.
[2] C. Masutani, R. Kusumoto, A. Yamada, et al., The *XPV* (xeroderma pigmentosum variant) gene encodes human DNA polymerase η, Nature 399 (1999) 700–704.
[3] C. Masutani, M. Araki, A. Yamada, et al., Xeroderma pigmentosum variant (XP-V) correcting protein from HeLa cells has a thymine dimer bypass DNA polymerase activity, EMBO J. 18 (1999) 3491–3501.
[4] C. Masutani, R. Kusumoto, S. Iwai, F. Hanaoka, Mechanisms of accurate translesion synthesis by human DNA polymerase η, EMBO J. 19 (2000) 3100–3109.
[5] R.E. Johnson, M.T. Washington, S. Prakash, L. Prakash, Fidelity of human DNA polymerase η, J. Biol. Chem. 275 (2000) 7447–7450.
[6] S.S. Lange, K. Takata, R.D. Wood, DNA polymerases and cancer, Nat. Rev. Cancer 11 (2011) 96–110.
[7] S. García-Gómez, A. Reyes, M.I. Martínez-Jiménez, E.S. Chocrón, S. Mourón, G. Terrados, C. Powell, E. Salido, J. Méndez, I.J. Holt, L. Blanco, PrimPol, an archaic primase/polymerase operating in human cells, Mol. Cell 52 (2013) 541–553.
[8] S. Mourón, S. Rodriguez-Acebes, M.I. Martínez-Jiménez, S. García-Gómez, S. Chocrón, L. Blanco, J. Méndez, Repriming of DNA synthesis at stalled replication forks by human PrimPol, Nat. Struct. Mol. Biol. 20 (2013) 1383–1389.
[9] J. Bianchi, S.G. Rudd, S.K. Jozwiakowski, L.J. Bailey, V. Soura, E. Taylor, I. Stevanovic, A.J. Green, T.H. Stracker, H.D. Lindsay, A.J. Doherty, PrimPol bypasses UV photoproducts during eukaryotic chromosomal DNA replication, Mol. Cell 52 (2013) 566–573.
[10] J.E. Sale, A.R. Lehmann, R. Woodgate, Y-family DNA polymerases and their role in tolerance of cellular DNA damage, Nat. Rev. Mol. Cell Biol. 13 (2012) 141–152.
[11] A. Tissier, E.G. Frank, J.P. McDonald, S. Iwai, F. Hanaoka, R. Woodgate, Misinsertion and bypass of thymine–thymine dimers by human DNA polymerase ι, EMBO J. 19 (2000) 5259–5266.
[12] Y. Zhang, F. Yuan, X. Wu, J.S. Taylor, Z. Wang, Response of human DNA polymerase ι to DNA lesions, Nucleic Acids Res. 29 (2001) 928–935.
[13] A. Vaisman, E.G. Frank, S. Iwai, E. Ohashi, H. Ohmori, F. Hanaoka, R. Woodgate, Sequence context-dependent replication of DNA templates containing UV-induced lesions by human DNA polymerase ι, DNA Repair (Amst.) 2 (2003) 991–1006.
[14] A. Vaisman, K. Takasawa, S. Iwai, R. Woodgate, DNA polymerase ι-dependent translesion replication of uracil containing cyclobutane pyrimidine dimer, DNA Repair (Amst.) 5 (2006) 210–218.
[15] E.G. G Frank, R. Woodgate, Increased catalytic activity and altered fidelity of human DNA polymerase iota in the presence of manganese, J. Biol. Chem. 282 (2007) 24689–24696.
[16] E. Ohashi, T. Ogi, R. Kusumoto, et al., Error-prone bypass of certain DNA lesions by the human DNA polymerase κ, Genes Dev. 14 (2000) 1589–1594.
[17] J. O-Wang, K. Kawamura, Y. Tada, et al., DNA polymerase κ, implicated in spontaneous and DNA damage-induced mutagenesis, is overexpressed in lung cancer, Cancer Res. 61 (2001) 5366–5369.
[18] T. Ogi, A.R. Lehmann, The Y-family DNA polymerase κ (pol κ) functions in mammalian nucleotide-excision repair, Nat. Cell Biol. 8 (2006) 640–642.
[19] T. Ogi, S. Limsirichaikul, R.M. Overmeer, M. Volker, K. Takenaka, R. Cloney, Y. Nakazawa, A. Niimi, Y. Miki, N.G. Jaspers, L.H. Mullenders, S. Yamashita, M.I. Fousteri, A.R. Lehmann, Three DNA polymerases, recruited by different mechanisms, carry out NER repair synthesis in human cells, Mol. Cell 37 (2010) 714–727.
[20] Y. Zhang, F. Yuan, X. Wu, M. Wang, O. Rechkoblit, J.S. Taylor, N.E. Geacintov, Z. Wang, Error-free and error-prone lesion bypass by human DNA polymerase kappa *in vitro*, Nucleic Acids Res. 28 (2000) 4138–4146.
[21] T. Ohkumo, Y. Kondo, M. Yokoi, et al., UV-B radiation induces epithelial tumors in mice lacking DNA polymerase η and mesenchymal tumors in mice deficient for DNA polymerase ι, Mol. Cell. Biol. 26 (2006) 7696–7706.
[22] J.P. McDonald, E.G. Frank, B.S. Plosky, et al., 129-derived strains of mice are deficient in DNA polymerase ι and have normal immunoglobulin hypermutation, J. Exp. Med. 198 (2003) 635–643.
[23] Q. Lin, A.B. Clark, S.D. McCulloch, et al., Increased susceptibility to UV-induced skin carcinogenesis in polymerase η-deficient mice, Cancer Res. 66 (2006) 87–94.
[24] C.A. Dumstorf, A.B. Clark, Q. Lin, et al., Participation of mouse DNA polymerase ι in strand-biased mutagenic bypass of UV photoproducts and suppression of skin cancer, Proc. Natl. Acad. Sci. U. S. A. 103 (2006) 18083–18088.
[25] A. Egashira, K. Yamauchi, K. Yoshiyama, et al., Mutational specificity of mice defective in the MTH1 and/or the MSH2 genes, DNA Repair (Amst.) 1 (2002) 881–893.
[26] I.G. Rogozin, F.A. Kondrashov, G.V. Glazko, Use of mutation spectra analysis software, Human Mut. 17 (2001) 83–102.
[27] Y.C. Wang, V.M. Maher, D.L. Mitchell, J.J. McCormick, Evidence from mutation spectra that the UV hypermutability of xeroderma pigmentosum variant cells reflects abnormal, error-prone replication on a template containing photoproducts, Mol. Cell. Biol. 13 (1993) 4276–4283.
[28] A. Stary, P. Kannouche, A.R. Lehmann, A. Sarasin, Role of DNA polymerase η in the UV mutation spectrum in human cells, J. Biol. Chem. 278 (2003) 18767–18775.
[29] J.H. Choi, G.P. Pfeifer, The role of DNA polymerase η in UV mutational spectra, DNA Repair (Amst.) 4 (2005) 211–220.
[30] J.H. Choi, A. Besaratinia, D.H. Lee, C.S. Lee, G.P. Pfeifer, The role of DNA polymerase ι in UV mutational spectra, Mutat. Res. 599 (2006) 58–65.
[31] Y. Wang, R. Woodgate, T.P. McManus, S. Mead, J.J. McCormick, V.M. Maher, Evidence that in xeroderma pigmentosum variant cells, which lack DNA polymerase η, DNA polymerase ι causes the very high frequency and unique spectrum of UV-induced mutations, Cancer Res. 67 (2007) 3018–3026.
[32] R.A. Busuttil, Q. Lin, P.J. Stambrook, R. Kucherlapati, J. Vijg, Mutation frequencies and spectra in DNA polymerase η-deficient mice, Cancer Res. 68 (2008) 2081–2084.
[33] Q. Gueranger, A. Stary, S. Aoufouchi, et al., Role of DNA polymerases η, ι and ζ in UV resistance and UV-induced mutagenesis in human cell line, DNA Repair (Amst.) 9 (2008) 1551–1562.

[34] A. Burger, D. Fix, H. Liu, J. Hays, R. Bockrath, *In vivo* deamination of cytosine-containing cyclobutane pyrimidine dimers in *E. coli*: a feasible part of UV-mutagenesis, Mutat. Res. 522 (2003) 145–156.
[35] I. Tessman, S.K. Liu, M.A. Kennedy, Mechanism of SOS mutagenesis of UV-irradiated DNA: mostly error-free processing of deaminated cytosine, Proc. Natl. Acad. Sci. U. S. A. 89 (1992) 1159–1163.
[36] N. Jiang, J.S. Taylor, *In vivo* evidence that UV-induced C→T mutations at dipyrimidine sites could result from the replicative bypass of *cis–syn* cyclobutane dimers or their deamination products, Biochemistry 32 (1993) 472–481.
[37] T. Takasawa, C. Masutani, F. Hanaoka, S. Iwai, Chemical synthesis and translesion replication of a *cis–syn* cyclobutane thymine–uracil dimer, Nucleic Acids Res. 32 (2004) 1738–1745.
[38] P. Kannouche, A.R. Fernández de Henestrosa, B. Coull, et al., Localization of DNA polymerases η and ι to the replication machinery is tightly co-ordinated in human cells, EMBO J. 22 (2003) 1223–1233.
[39] C. Guo, J.N. Kosarek-Stancel, T.-S. Tang, E.C. Friedberg, Y-family DNA polymerases in mammalian cells, Cell. Mol. Life Sci. 66 (2009) 2363–2381.
[40] J. Akagi, C. Masutani, Y. Kataoka, et al., Interaction with DNA polymerase η is required for nuclear accumulation of REV1 and suppression of spontaneous mutations in human cells, DNA Repair (Amst.) 8 (2009) 585–599.
[41] E. Pelle, X. Huang, T. Mammone, K. Marenus, D. Maes, K. Frenkel, Ultraviolet-B-induced oxidative DNA base damage in primary normal human epidermal keratinocytes and inhibition by a hydroxyl radical scavenger, J. Invest. Dermatol. 121 (2003) 177–183.
[42] L. Haracska, S.L. Yu, R.E. Johnson, L. Prakash, S. Prakash, Efficient and accurate replication in the presence of 7,8-dihydro-8-oxoguanine by DNA polymerase η, Nat. Genet. 4 (2000) 458–461.
[43] S.D. McCulloch, R.J. Kokosaka, P. Garg, P. Burgers, T. Kunkel, The efficiency and fidelity of 8-oxo-guanine bypass by DNA polymerase δ and η, Nucleic Acids Res. 37 (2009) 2830–2840.
[44] D.H. Lee, G.P. Pfeifer, Translesion synthesis of 7,8-dihydro-8-oxo-2′-deoxyguanosine by DNA polymerase eta *in vivo*, Mutat. Res. 641 (2008) 19–26.
[45] E. Sonneveld, H. Vrieling, L.H.F. Mullenders, A. van Hoffen, Mouse mismatch repair gene *Msh2* is not essential for transcription-coupled repair of UV-induced cyclobutane pyrimidine dimers, Oncogene 20 (2001) 538–541.
[46] T.B. Petta, S. Nakajima, A. Zlatanou, et al., Human DNA polymerase iota protects cells against oxidative stress, EMBO J. 27 (2008) 2883–2895.
[47] G.N. Gan, J.P. Wittschieben, B.Ø. Wittschieben, R.D. Wood, DNA polymerase zeta (pol ζ) in higher eukaryotes, Cell Res. 18 (2008) 174–183.
[48] K. Mcnally, J.A. Neal, T.P. McManus, J.J. McCormick, V.M. Maher, hRev7, putative subunit of hPolζ, plays a critical role in survival, induction of mutations, and progression through S-phase, of $UV_{(254\,nm)}$-irradiated human fibroblasts, DNA Repair (Amst.) 7 (2008) 597–604.
[49] P.E.M. Gibbs, X.D. Wand, Z. Li, et al., The function of the human homolog of *Saccharomyces cerevisiae* REV1 is required for mutagenesis induced by UV light, Proc. Natl. Acad. Sci. U. S. A. 8 (2007) 4186–4191.
[50] J.G. Jansen, A. Tsaalbi-Shtylik, P. Langerak, et al., The BRCT domain of mammalian Rev1 is involved in regulating DNA translesion synthesis, Nucleic Acids Res. 3 (2005) 356–365.
[51] T. Ogi, Y. Shinkai, K. Tanaka, H. Ohmori, Polκ protects mammalian cells against the lethal and mutagenic effects of benzo[*a*]pyrene, Proc. Natl. Acad. Sci. U. S. A. 99 (2002) 15548–15553.
[52] D. Schenten, V.L. Gerlach, C. Guo, et al., DNA polymerase κ deficiency does not affect somatic hypermutation in mice, Eur. J. Immunol. 32 (2002) 3152–3160.
[53] Y. Yagi, D. Ogawara, S. Iwai, F. Hanaoka, M. Akiyama, H. Maki, DNA polymerases η and κ are responsible for error-free translesion DNA synthesis activity over a cis–syn thymine dimer in *Xenopus laevis* oocyte extracts, DNA Repair (Amst.) 4 (2005) 1252–1269.
[54] O. Zvi, N. Geacintov, S. Nakajima, A. Yasui, Z. Livneh, DNA polymerase ζ cooperates with polymerase κ and ι in translesion DNA synthesis across pyrimidine photodimers in cells from XPV patients, Proc. Natl. Acad. Sci. U. S. A. 106 (2009) 11552–11557.
[55] J.H. Yoon, L. Prakash, S. Prakash, High error-free role of DNA polymerase η in the replicative bypass of UV-induced pyrimidine dimers in mouse and human cells, Proc. Natl. Acad. Sci. U. S. A. 106 (2009) 18219–18224.
[56] T. Narita, T. Tsurimoto, J. Yamamoto, K. Nishihara, K. Ogawa, E. Ohashi, T. Evans, S. Iwai, S. Takeda, K. Hirota, Human replicative DNA polymerase δ can bypass T–T (6-4) ultraviolet photoproducts on template strands, Genes Cells 15 (2010) 1228–1239.
[57] J.G. Jansen, P. Langerak, A. Tsaalbi-Shtylik, P. van den Berk, H. Jacobs, N. de Wind, Strand-biased defect in C/G transversions in hypermutating immunoglobulin genes in Rev1-deficient mice, J. Exp. Med. 203 (2006) 319–323.
[58] T. Shimizu, Y. Shinkai, T. Ogi, H. Ohmori, T. Azuma, The absence of DNA polymerase κ does not affect somatic hypermutation of the mouse immunoglobulin heavy chain gene, Immunol. Lett. 86 (2003) 265–270.
[59] N. Watanabe, S. Mii, N. Asai, M. Asai, K. Niimi, K. Ushida, T. Kato, A. Enomoto, H. Ishii, M. Takahashi, Y. Murakumo, The REV7 subunit of DNA polymerase ζ is essential for primordial germ cell maintenance in the mouse, J. Biol. Chem. 288 (2013) 10459–10471.
[60] J.P. Wittschieben, V. Patil, V. Glushets, L. Robinson, D. Kusewitt, R.D. Wood, Loss of DNA polymerase ζ enhances spontaneous tumorigenesis, Cancer Res. 70 (2010) 2770–2778.
[61] S.S. Lange, E. Bedford, S. Reh, J.P. Wittschieben, S. Carbajal, D.F. Kusewitt, J. DiGiovanni, R.D. Wood, Dual role for mammalian DNA polymerase ζ in maintaining genome stability and proliferative responses, Proc. Natl. Acad. Sci. U. S. A. 110 (2013) E687–E696.

DNA 損傷ストレスに対する耐性機構の解明

教授　菱田　卓
助教　毛谷村　賢司

[目的]

生物は、外的・内的要因による DNA 損傷ストレスに対して耐性を獲得することで様々な環境に適応してきた。しかしながら、微量ながらも長期に渡る DNA 損傷ストレスへの暴露は、生物の様々な機能に影響を及ぼし、ヒトにおいては発がんや老化と密接に関連している。紫外線や電離放射線は DNA 損傷を引き起こす普遍的かつ主要な環境要因であり、それらの損傷が修復されない場合は突然変異や細胞死の原因となる。近年、オゾン層破壊に伴う有害紫外線の増加や福島原発事故に起因する放射能汚染など、地球規模で起こる環境問題は生命システムの維持にとって脅威となりうるため、これらの環境問題に対する取り組みは益々重要となってきている。DNA 相同組換え修復機構は、紫外線による DNA 損傷が引き起こす DNA 複製阻害の解消や、電離放射線による DNA 二本鎖切断（DNA double-strand break: DSB）の修復において主要な役割を果たしており、その分子メカニズムは、バクテリアからヒトまで高度に保存されている。本研究では、進化的に保存された DNA 相同組換え修復機構の染色体構造の安定性維持における役割を明らかにするために、原核生物の大腸菌及び真核生物の出芽酵母をモデル生物として以下の２つの項目について詳細な解析を行った。１）DNA 二本鎖切断修復に関与する大腸菌 RecN タンパク質の機能解析。２）慢性的な紫外線損傷ストレスに対する耐性獲得の分子機構。

[結果と考察]

１）DSB 修復に関与する大腸菌 RecN タンパク質の機能解析

DNA 相同組換え機構は、DSB を正確に修復することができる唯一のメカニズムとして生物間で高度に保存されている。大腸菌の RecA リコンビナーゼは、DNA 切断末端の削り込みにより生じた一本鎖 DNA 上でヌクレオフィラメントを形成し、相同鎖検索および DNA 鎖交換反応を行う。さらに、一本鎖 DNA に結合することで活性化された RecA は、SOS 誘導と呼ばれる DNA 修復や細胞分裂の停止に関わる遺伝子群の発現を誘導する。Structural maintenance of chromosome (SMC) ファミリータンパク質は、原核及び真核生物において広く存在し、染色体構造の動態制御と維持に必須の役割を果たしており、DNA 複製や転写、染色体分離などの様々な染色体機能の制御に関与している。大腸菌 RecN タンパク質は SMC ファミリーに属しており、DNA 損傷依存的に発現し、ガンマ線やクロスリンク剤であるマイトマイシン C などによる DSB の修復に関与している。これまでの GFP-RecN を用いた蛍光顕微鏡解析から、RecN はマイトマイシン C 依存的に核様体上で GFP フォーカスを形成することを明らかにした [1)]。今回我々は、この DNA 損傷依存的な GFP-RecN フォーカス形成が DNA 相同組換え修復の組換え酵素である RecA を欠損した細胞において観察されないことを見いだした。さらに、*recA* の変異体ライブラリーを用いたスクリーニングから、GFP-RecN フォーカス形成能を失った新規の *recA* 変異（$recA^{Q300R}$）を同定した。興味深いことに、$recA^{Q300R}$ 変異株は、マイトマイシン C に対して高い感受性を示す一方で、紫外線に対する感受性及び RecA 依存的な遺伝子発現誘導（SOS 誘導）は野生型株と同程度であった。この結果は、RecA と RecN との間に機能的な相互作用が存在

することを示唆している。この結果に一致して、抗 Flag 抗体を用いた免疫沈降実験から、細胞内において Flag-RecN と RecA が複合体を形成していることが示された。さらに、精製した His-RecN と RecA を用いた生化学的解析から、これらのタンパク質は直接結合していることがわかった。これらの結果から、DSB 末端に生じる一本鎖 DNA 領域に RecA が結合後、RecN は RecA との物理的相互作用によって損傷部位へリクルートされることが明らかになった。次に、*recN* 及び *recA*^{Q300R} 変異株の核様体構造について蛍光顕微鏡を用いて観察した結果、いずれの変異株においても、マイトマイシン C の処理後に小さな核様体が多数観察された。このような小さな核様体の出現は、野生型細胞においては観察されないことや、大腸菌ゲノム上に一箇所存在する複製開始点付近を蛍光標識した場合に、小さな核様体には標識されないものが多数存在したことから、これらは DSB によって切断された核様体断片であることが示唆された。以上のことから、RecN は RecA との物理的な相互作用を介して核様体へ局在し、DSB が生じた核様体構造の維持にとって重要な役割を果たしていることが明らかになった。以上の結果から、RecN タンパク質は核様体上で DSB が生じた付近に局在し、DSB の両末端に結合した RecA と複合体を形成することによって核様体構造の安定性を保障すると共に、RecA による相同組換え反応の促進に関与していると考えられる。

２）慢性的な紫外線損傷ストレスに対する耐性獲得の分子機構

紫外線によって生じるピリミジン二量体は DNA 複製や転写を阻害するため、生物はピリミジン二量体を修復できるヌクレオチド除去修復（NER）機構のほか、DNA 複製阻害を解消する DNA 相同組換え及び損傷トレランス機構を持っている。これまでの研究から、我々は自然環境で問題となる慢性的低線量率の紫外線照射（chronic low-dose UV: CLUV）下で酵母細胞を培養可能な装置を作製し、慢性的な DNA 損傷ストレスに対する耐性機構の解明を行ってきた。本実験系を用いた研究から、従来の短時間の急性紫外線照射では最も高い致死性を示した NER 経路の欠損株が CLUV 環境では増殖阻害を引き起こさない一方で、DNA 損傷トレランス経路の欠損株が増殖阻害を引き起こすことを明らかにした [2]。さらに、NER の欠損株では CLUV 環境下（～24 時間）の細胞増殖に伴って C→T 型点突然変異の頻度が転写の鋳型鎖特異的に顕著に増大することを明らかにした [3]。今回、NER 欠損株（*rad14Δ*）を用いて、CLUV 環境下で継代培養による長時間（～６日間）に渡る突然変異頻度の測定を行ったところ、培養開始後数日は突然変異頻度の顕著な上昇が観察された一方で、培養３日目以降に突然変異頻度が急激に低下するという興味深い結果が得られた。そこで、CLUV 環境で継代培養した *rad14Δ* 細胞の染色体 DNA をパルスフィールドゲル電気泳動によって分離した。その結果、同じ細胞数のゲノム DNA をサンプルとして使用しているにもかかわらず、培養開始時に比べ、３日目以降の染色体のバンド強度が明らかに強いことがわかり、細胞あたりの DNA 含量の増加が起こっていることが示唆された。そこで継代培養時の細胞の DNA 含量を FACS 解析により調べたところ、３日目以降に二倍体化した細胞の割合が顕著に増大することを見いだした。したがって、突然変異頻度の急激な低下は、細胞の二倍体化（遺伝子を２コピー持つこと）を反映したものであると考えられた。さらに、一倍体及び二倍体 *rad14Δ* 細胞の CLUV 感受性を比較したところ、二倍体細胞が有意に CLUV に対して耐性を示すことがわかった。そこで二倍体細胞の出現と CLUV 耐性獲得の関連性を調べるために、DNA 損傷応答に関わる遺伝子を欠損した *rad14Δ* 細胞を作

製した。その結果、相同組換え修復に関わる *RAD51* を欠損した *rad14*Δ *rad51*Δ細胞は、二倍体特異的な CLUV 耐性能が失われており、CLUV ストレスによる二倍体細胞の出現も観察されなかった。以上の結果から、一倍体細胞に比べて二倍体細胞が CLUV ストレス環境に対して耐性であり、二倍体特異的な CLUV 耐性の獲得には相同組換え機構が関与していることが明らかになった。我々の以前の研究から、CLUV 環境では複製阻害が頻繁に生じていることが示されており、今回、二倍体細胞が CLUV に対して耐性を示す原因として、複製阻害の解消に相同染色体間の組換え反応が関与していることが考えられる。

[まとめ]

DNA 相同組換えは、致死的な影響を及ぼす DSB の修復や DNA 複製阻害の解消において重要な役割を果たしており、その制御機構の破綻は転座や重複、染色体再編、染色体喪失などの染色体不安定性の原因となっている。今回我々は、大腸菌及び出芽酵母を用いて DNA 相同組換えの制御メカニズムに関して詳細な解析を行い、それぞれ DSB 修復及び複製阻害の解消における DNA 相同組換えの新たな役割を明らかにした。大腸菌の研究では、SMC ファミリーに属する RecN タンパク質が RecA に依存して DSB 部位にリクルートされ、DSB 周辺の核様体（染色体）構造を安定化することで相同組換え修復の促進に関与していることを明らかにした。原核生物には真核生物のコヒーシンのような複製後の姉妹染色体間を束ねる SMC タンパク質が存在しないことから、DSB が生じた場合の DNA 末端部の空間的な制御機構については不明であった。今回の結果は、RecN が DSB 修復において特異的に機能する SMC タンパク質であり、DSB 周辺の染色体動態制御機構に重要な役割を果たしていることを明らかにした点は極めて重要な発見である。また、出芽酵母を用いた研究からは、慢性的な紫外線ストレス環境において、細胞は染色体の倍数性を変化させることでストレス耐性を獲得しているという興味深い現象を明らかにした。さらに、この耐性獲得には DNA 相同組換え機能が必須であることがわかった。倍数体化は、ヒトを含めた多くの生物において観察される普遍的な現象であり、生物種または組織の種類毎にその生理的な意義は異なっているものの、共通する概念として、倍数体化は多様性を生む原動力となっていることが考えられる。したがって、慢性的な紫外線ストレスに対する倍数体化の現象は、ストレス耐性または環境適応応答の一つと考えることができる。さらに、倍数体化を含めた染色体不安定性の増大はヒトのがん細胞において顕著に観察される特徴の一つとして知られており、進化的に保存された DNA 相同組換えの制御機構の解明は、発がん制御の分子基盤の解明につながることが期待できる。

[参考文献]

1. Nagashima, K., Kubota, Y., Shibata, T., Sakaguchi, C., Shinagawa, H., and Hishida, T. (2006) Degradation of *Escherichia coli* RecN aggregates by ClpXP protease and its implications for DNA damage tolerance. *J. Biol. Chem.* 281: 30941-30946.
2. Hishida, T., Kubota, Y., Carr, A. M., and Iwasaki, H. (2009) *RAD6-RAD18-RAD5* pathway-dependent tolerance to chronic low-dose UV light. *Nature* 457, 612-615.

3. Haruta, N., Kubota, Y., and Hishida, T. (2012) Chronic low-dose ultraviolet induced mutagenesis in nucleotide excision repair-deficient cells. *Nucleic Acids Res.* 40, 8406-8415.

[原著論文]

1. *Su'etsugu, M., *Harada, Y., *Keyamura, K., Matsunaga, C., Kasho, K., Abe, Y., Ueda, T., and Katayama, T. (2013)
   The DnaA N-terminal domain interacts with Hda to facilitate replicase clamp-mediated inactivation of DnaA.
   Environmental Microbiology 15, 3183-3195. *equal contributors
2. Keyamura, K., Sakaguchi, C., Kubota, Y., Niki, H., and Hishida, T. (2013)
   RecA protein recruits structural maintenance of chromosomes (SMC)-like RecN protein to DNA double-strand breaks.
   J. Biol. Chem. 288, 29229-29237.
3. Ozaki, S., Matsuda, Y., Keyamura, K., Kawakami, H., Noguchi, Y., Kasho, K., Nagata, K., Masuda, T., Sakiyama, Y., and Katayama, T. (2013)
   A replicase clamp-binding dynamin-like protein promotes colocalization of nascent DNA strands and equipartitioning of chromosomes in *E. coli*.
   Cell Reports 4, 985-995.

[総説等]

1. 菱田　卓 (2015) ゲノムを司るインターメア : 非コード DNA 領域の DNA 損傷応答 (化学同人、pp161-174)
2. 菱田　卓（2015）ノーベル化学賞：DNA 修復の分子メカニズムの解明（パリティ、Vol.30 No.12, pp43-45）

[口頭発表]

1. 毛谷村賢司、久保田佳乃、仁木宏典、菱田　卓　DNA 二重鎖切断修復に関与する SMC ファミリータンパク質 RecN の機能解析。第 10 回 21 世紀大腸菌研究会（2013 年 6 月 20-21 日、静岡）
2. 毛谷村賢司、新井康太、菱田　卓　相同染色体間の DNA 相同組換え制御メカニズムの解析。第 85 回日本遺伝学会 (2013 年 9 月 19-21 日、慶応義塾大学日吉キャンパス)
3. 毛谷村賢司、新井康太、菱田　卓　相同染色体間の組換えにおける出芽酵母 Srs2 ヘリカーゼの役割。第 22 回 DNA 複製・組換え・修復ワークショップ (2013 年 11 月 20-22 日、仙台)
4. 毛谷村賢司、金子佳樹、仁木宏典、菱田　卓　DNA 二本鎖切断修復に関与する RecN の DNA 相互作用メカニズムの解析。第 11 回 21 世紀大腸菌研究会（2014 年 6 月 5-6 日、盛岡）
5. 吉田麻美、毛谷村賢司、菱田　卓　DNA 損傷ストレス応答に関与するヒストン変異体

の網羅的解析。第 86 回日本遺伝学会（2014 年 9 月 17-19 日、滋賀）

6. 菱田　卓　慢性的な紫外線損傷ストレスに対する耐性獲得に関与するヌクレオソーム構造。第 57 回日本放射線影響学会（2014 年 10 月 1-3 日、鹿児島）

7. 毛谷村賢司、菱田　卓　相同染色体間の組換え制御機構における出芽酵母 Srs2 の役割。第 32 回染色体ワークショップ・第 13 回核ダイナミクス研究会（2014 年 12 月 15-17 日、広島）
8. 毛谷村賢司、戸羽あす美、仁木宏典、菱田　卓　二本鎖 DNA の切断修復に関与する RecN の機能解析。第 11 回 21 世紀大腸菌研究会（2015 年 6 月 4-5 日、滋賀）
9. 石毛大輔、毛谷村賢司、長谷川ゆき、岩﨑博史、菱田　卓　出芽酵母における複製ストレス応答に関わる新たな因子の探索。第 87 回日本遺伝学会（2015 年 9 月 24-26 日、東北大学川内北キャンパス）
10. 塩入拓馬、毛谷村賢司、田中修平、菱田　卓　慢性的な低線量率紫外線照射下における出芽酵母 NER 欠損株の動態解析。第 87 回日本遺伝学会（2015 年 9 月 24-26 日、東北大学川内北キャンパス）
11. 毛谷村賢司、菱田　卓　出芽酵母 Srs2 ヘリカーゼと Mus81-Mms4 ヌクレアーゼによる相同染色体間の組換え制御機構。第 23 回 DNA 複製・組換え・修復ワークショップ（2015 年 10 月 19-21 日、静岡）

[ポスター発表]

12. 櫻本健郎、毛谷村賢司、菱田　卓　出芽酵母を用いたジーンターゲティングに関与する新規遺伝子の探索。第 22 回 DNA 複製・組換え・修復ワークショップ（2013 年 11 月 20-22 日、仙台）
13. 櫻本健郎、毛谷村賢司、菱田　卓　出芽酵母を用いたジーンターゲティングに関与する新規因子の同定。第 36 回日本分子生物学会年会（2013 年 12 月 3-6 日、神戸）
14. 毛谷村賢司、久保田佳乃、小林万希子、金子佳樹、仁木宏典、菱田　卓　SMC ファミリータンパク質 RecN の DNA 二重鎖切断修復における役割。第 36 回日本分子生物学会年会（2013 年 12 月 3-6 日、神戸）
15. 毛谷村賢司、新井康太、菱田　卓　Roles of the *Saccharomyces cerevisiae* Srs2 helicase in inter-homologue recombination repair。第 9 回 3R シンポジウム（2014 年 11 月 17-21 日、静岡）
16. 重森　悠、毛谷村賢司、菱田　卓　出芽酵母 Mgs1 タンパク質の機能ドメインの解析。第 37 回日本分子生物学会年会（2014 年 11 月 25-27 日、横浜）
17. 吉田麻美、毛谷村賢司、菱田　卓　DNA 損傷ストレス応答に影響を及ぼすヒストン変異体の解析。第 37 回日本分子生物学会年会（2014 年 11 月 25-27 日、横浜）
18. Keyamura, K., and Hishida, T.　Regulation of inter-homologue recombination by the Srs2 helicase in *Saccharomyces cerevisiae*. ゲノムを支える非コード DNA 領域の機能（2015 年 8 月 7-8 日、淡路）
19. 石毛大輔、毛谷村賢司、長谷川ゆき、岩﨑博史、菱田　卓　出芽酵母における複製ストレス応答に関わる新たな因子の探索。第 23 回 DNA 複製・組換え・修復ワークショップ（2015 年 10 月 19-21 日、静岡）

20. 長谷川ゆき、毛谷村賢司、重森　悠、菱田　卓　複製ストレス応答における出芽酵母 Mgs1 の役割。第 23 回 DNA 複製・組換え・修復ワークショップ（2015 年 10 月 19-21 日、静岡）
21. 毛谷村賢司、菱田　卓　相同染色体間の組換え制御メカニズムの解析。第 38 回日本分子生物学会年会・第 88 回日本生化学会大会合同大会（2015 年 12 月 1-4 日、神戸）
22. Ishige, D., Keyamura, K., Hasegawa, Y., Iwasaki, H., and Hishida, T. A genetic screen for genes that suppress the temperature sensitivity of mgs1-18 rad18Δ cells in Saccharomyces cerevisiae.　第 38 回日本分子生物学会年会・第 88 回日本生化学会大会合同大会（2015 年 12 月 1-4 日、神戸）

THE JOURNAL OF BIOLOGICAL CHEMISTRY VOL. 288, NO. 41, pp. 29229–29237, October 11, 2013

RecA Protein Recruits Structural Maintenance of Chromosomes (SMC)-like RecN Protein to DNA Double-strand Breaks*[S]

Received for publication, May 14, 2013, and in revised form, August 21, 2013 Published, JBC Papers in Press, August 25, 2013, DOI 10.1074/jbc.M113.485474

Kenji Keyamura[‡1], **Chikako Sakaguchi**[§1], **Yoshino Kubota**[§], **Hironori Niki**[¶], **and Takashi Hishida**[‡§2]

From the [‡]*Department of Life Science, Graduate School of Science, Gakushuin University, Tokyo 171-8588, the* [§]*Research Institute for Microbial Diseases, Osaka University, Osaka 565-0871, and the* [¶]*Microbial Genetics Laboratory, Genetic Strains Research Center, National Institute of Genetics, 1111 Yata, Mishima, Shizuoka 411-8540, Japan*

Background: RecN is an SMC (structural maintenance of chromosomes) family protein that is required for DNA double-strand breaks (DSBs) repair.
Results: We identified a RecA mutant that is deficient in interacting with RecN.
Conclusion: A functional interaction between RecN and RecA is required for assembly of RecN at the sites of DSBs.
Significance: RecN is critical for protecting the structural integrity of chromosomes during DSBs repair.

Escherichia coli **RecN is an SMC (structural maintenance of chromosomes) family protein that is required for DNA double-strand break (DSB) repair. Previous studies show that GFP-RecN forms nucleoid-associated foci in response to DNA damage, but the mechanism by which RecN is recruited to the nucleoid is unknown. Here, we show that the assembly of GFP-RecN foci on the nucleoid in response to DNA damage involves a functional interaction between RecN and RecA. A novel RecA allele identified in this work,** ***recA*** ^{Q300R}**, is proficient in SOS induction and repair of UV-induced DNA damage, but is deficient in repair of mitomycin C (MMC)-induced DNA damage. Cells carrying** ***recA*** ^{Q300R} **fail to recruit RecN to DSBs and accumulate fragmented chromosomes after exposure to MMC. The ATPase-deficient RecN** ^{K35A} **binds and forms foci at MMC-induced DSBs, but is not released from the MMC-induced DNA lesions, resulting in a defect in homologous recombination-dependent DSB repair. These data suggest that RecN plays a crucial role in homologous recombination-dependent DSB repair and that it is required upstream of RecA-mediated strand exchange.**

DNA double-strand breaks (DSBs)[3] are serious genomic lesions that are potentially lethal at the cellular level. DSBs are caused by exogenous agents such as ionizing radiation, chemical mutagens, reactive oxygen species, and replicative stress (*i.e.* collapsed replication forks) (1, 2). In bacteria, homologous recombination (HR) plays a major role in repairing DSBs. HR enzymes and pathways have been extensively characterized in *Escherichia coli*, and *E. coli* HR is a paradigm for understanding HR-related processes in all organisms (3–5).

In *E. coli*, the repair of DSBs is initiated by RecBCD, which generates 3′ single-stranded DNA (ssDNA) tails at DSB sites via its helicase and nuclease activities; the ssDNA tails are then substrates for homologous pairing by RecA protein (4, 6). The RecF pathway is involved in the daughter strand gap repair in wild-type cells (3). RecF also provides an alternative pathway for HR-dependent DSB repair in *recBC* mutants when two additional nucleases, ExoI and SbcCD, are inactivated (7, 8). However, recent studies suggest that the RecFOR pathway may play a crucial role in DSB repair in bacterial species other than *E. coli* (9–13). In both pathways, RecA is loaded onto the ssDNA tail to form a nucleoprotein filament at the DSB sites. The RecA strand exchange activity generates recombination intermediates via its strand exchange activity (4, 14), which are then processed either by the Holliday junction resolvase, RuvABC, or by the RecG helicase to produce mature products (15–17). In addition, RecA is essential for the induction of the SOS response (18). RecA assembled on ssDNA stimulates self-cleavage of the LexA repressor, which in turn induces downstream SOS genes (19–21).

Structural maintenance of chromosomes (SMC) proteins are ubiquitous proteins that maintain and modulate chromosome structure in prokaryotic and eukaryotic cells (22, 23). *E. coli* RecN is a highly conserved, DNA damage-inducible SMC-like protein in bacteria that has two SOS boxes in its promoter region. Therefore, the expression of *recN* is tightly regulated by the LexA repressor (24–26). GFP-RecN forms nucleoid-associated foci in response to DNA damage and forms aggregates in the cytoplasm (27). RecN aggregates are then degraded by the ClpXP protease (27, 28), which is required for efficient recovery from DNA damage. *E. coli recN* mutants are highly sensitive to ionizing radiation, bleomycin, and the DNA cross-linking agent mitomycin C (MMC), but not to UV irradiation (29, 30). Mutants of *recN* are defective in conjugational recombination in *recBC sbcBC* strains (24), suggesting that RecN plays a role in the RecF pathway. However, RecN is also required for RecBCD-

* This work was supported by grants-in-aid for scientific research on priority areas from the Ministry of Education, Culture, Sports, Science and Technology of Japan (to T. H.).
[S] This article contains supplemental Figs. S1–S3.
[1] Both authors contributed equally to this work.
[2] To whom correspondence should be addressed: Dept. of Life Science, Graduate School of Science, Gakushuin University, Tokyo 171-8588, Japan. Tel.: 81-3-3986-0221; E-mail: takashi.hishida@gakushuin.ac.jp.
[3] The abbreviations used are: DSB, DNA double-strand break; HR, homologous recombination, MMC; mitomycin C, SMC, structural maintenance of chromosomes; ECFP, enhanced cyan fluorescent protein.

dependent repair of DSBs (31–33). Thus, RecN plays a specific role in the repair of DNA DSBs, and its role is not limited to a single branch or subpathway of HR.

In this study, we examine the mechanism by which RecN is recruited to the nucleoid in response to DNA damage. We show that a functional interaction between RecN and RecA is required for assembly of RecN foci at MMC-induced DSBs; conversely, conditions that abrogate or disrupt a stable RecN-RecA interaction lead to chromosome fragmentation and loss of cell viability in cells exposed to MMC. The RecN ATPase is not required for formation of RecN-DSB foci, but is required for release of RecN from DSBs and completion of RecA/HR-dependent DSB repair. These data demonstrate that the SMC-like protein RecN plays a crucial role in promoting RecA-dependent DSB repair.

EXPERIMENTAL PROCEDURES

Media and General Methods—Standard methods for *E. coli* genetics and recombinant DNA techniques were as described by Miller (34) and Sambrook *et al.* (35). Ampicillin (50 μg/ml), tetracycline (10 μg/ml), chloramphenicol (100 μg/ml), and kanamycin (30 μg/ml) were used where indicated. Mitomycin C (2.5 mg/ml) was dissolved in 10 mM Tris-HCl (pH 8.5) buffer. Sensitivity to UV damage was measured as described previously (36). To measure sensitivity to MMC, cultures were grown in LB broth to an A_{650} of ~0.4, serially diluted, spotted onto LB medium containing the indicated concentration of MMC, and incubated at 37 °C.

Bacterial Strains and Plasmids—Strains used in this study were isogenic with BW25141 (37) except for strains with P_{BAD}-I-SceI. Wild-type strains and deletion mutants were provided by the National BioResource Project (NBRP) (38). The strains carrying the P_{BAD}-I-SceI were a gift from S. M. Rosenberg (39). The strains carrying the inducible fluorescent repressor gene (*araC PBAD-lacI-ecfp*) and the *lacO* array were described previously (40). A fragment containing the SOS promoter and open reading frame of *recN* was cloned into the low copy plasmid pSCH19, generating pRecN (27). RecN was tagged with an enhanced GFP cassette at its NH_2 terminus to generate pSG101. Arabinose-inducible pBAD GFP-*recN* (pTF271) was constructed as described previously (27). $recN^{K35A}$ was generated from pUC19-*recN* by site-directed PCR mutagenesis, and it was substituted for wild-type *recN* in pSG101 to generate pSG105. The structures of recombinant plasmids were confirmed by DNA sequencing.

Isolation of recA Mutant—A library of *recA* mutants was generated by carrying out PCR-mediated random mutagenesis, as described previously (36). The resultant *recA* mutant clones were transformed into a *recA* strain. The transformants were resuspended in M9 salts, plated on LB plates containing ampicillin, and then irradiated with UV (20 J/m^2). After overnight incubation, UV-resistant colonies were replica-plated on LB plates containing MMC (1 μg/ml). Clones that grew very poorly or did not grow at all on the MMC plates were selected.

SOS Induction—SOS induction was assessed by measuring the degradation of LexA as described previously (36). Log phase cultures were treated with MMC (0.5 μg/ml), and aliquots were taken at multiple time points for immunoblot analysis with anti-LexA (BioAcademia), anti-RecA (BioAcademia), or anti-RecN (26). LexA resynthesis was inhibited by adding chloramphenicol (100 μg/ml) to the cultures 10 min before adding MMC.

Fluorescence Microscopy and Localization Analysis of GFP-RecN—Exponentially growing cultures were treated with 0.5 μg/ml MMC at 37 °C. Cells were fixed with methanol, stained with 1 μg/ml DAPI (4′, 6′-diamidino-2-phenylindole), and spread (1–2 μl) on a cover glass. GFP fluorescence was not affected by prior fixation of the sample. Fluorescence microscopy was performed on a Zeiss Axioplan2 (41). *Scale bars* of 5 or 10 μm are shown in the figures. Images of both nucleoids (*blue* as a color signal) and GFP-RecN foci (*green* as a color signal) were merged on identical cells. In the merged image, GFP-RecN foci localized on the nucleoid appeared as a *light blue color*, whereas GFP-RecN foci in the cytoplasm appeared as a *green color*. The localization of GFP-RecN foci was determined based on these visual criteria, and more than 150 individual cells were scored for each strain.

To observe the *ori1* loci (15 kbp distance from *oriC*) on chromosomes, we constructed wild-type and Δ*recN* strains carrying both a *lacO* array inserted into the *ori1* locus and an inducible fluorescent repressor gene (*araC PBAD-lacI-ecfp*) (40, 42, 43). Cells were grown at 37 °C for 90 min in LB medium containing 0.2% arabinose and 1 μg/ml MMC and then analyzed by fluorescence microscopy.

Effect of I-SceI-induced DSBs on the Localization of RecN—To detect DSB-induced RecN foci, Δ*recA* strains carrying the P_{BAD}I-SceI cassette in the chromosome and a single I-SceI recognition site at the *codA21* locus in the F′ episome (39) were transformed with pSG101 (*gfp-recN*) and with pRecA or $pRecA^{Q300R}$. When cultures had reached early log phase, I-SceI was induced by the addition of 0.2% arabinose (w/v). One hour after the addition of arabinose, aliquots were taken and examined under the microscope.

RESULTS

RecA Is Required for the Formation of Nucleoid-associated GFP-RecN Foci in MMC-treated Cells—When DNA is damaged or replication is inhibited, ssDNA-bound RecA becomes conformationally active and promotes cleavage of the LexA repressor, which results in the induction of SOS genes including *recN* (21, 44). Previously, we showed that GFP-RecN formed foci on nucleoids after DNA damage (27). This implied that RecN could be recruited to the nucleoid at a step after RecA is loaded onto damaged DNA. To specifically examine this sequence of events, we measured GFP-RecN foci in a Δ*recA* strain. Wild-type *recN* is a part of the SOS regulon, and its expression is completely dependent on activated RecA. Therefore, this experiment was performed in cells that expressed *GFP-recN* under control of the inducible *PBAD* promoter. Fig. 1*A* shows that arabinose-inducible *GFP-recN* fully complements the MMC sensitivity of Δ*recN*, when cells are grown in the presence of arabinose, but not when cells are grown in the presence of glucose. Furthermore, GFP-RecN foci form in the cytoplasm of both MMC-treated and untreated wild-type cells and Δ*recA* cells, whereas nucleoid-associated GFP-RecN foci form in wild-type MMC-treated cells but are absent in Δ*recA*

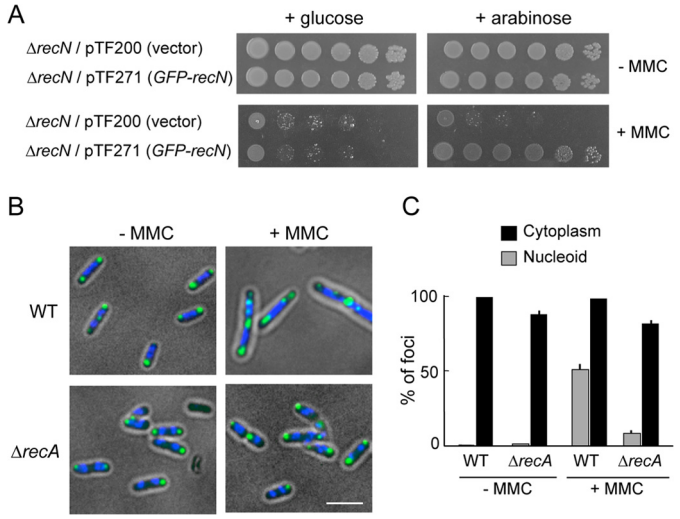

FIGURE 1. **RecN foci in wild-type and Δ*recA* cells with or without DNA damage.** *A*, Δ*recN* cells carrying either an arabinose-inducible GFP-*recN* gene (pTF271) or a pBAD vector (pTF200) were diluted and spotted onto LB plates with or without MMC (0.5 μg/ml) in the presence of either glucose or arabinose. *B*, the subcellular localization of GFP-RecN foci in response to MMC-induced damage. Wild-type or Δ*recA* cells carrying pTF271 were exposed to MMC (0.5 μg/ml) followed by the addition of arabinose (0.05%, w/v) to induce GFP-RecN. The panels show GFP/DAPI-merged images of cells 30 min after the addition of arabinose. *Scale bar* indicates 2.5 μm. *C*, quantitative analysis of GFP-RecN foci. For cells incubated with or without MMC, ~150 cells were examined. The results represent the average of at least three independent measurements. *Error bars* indicate S.D.

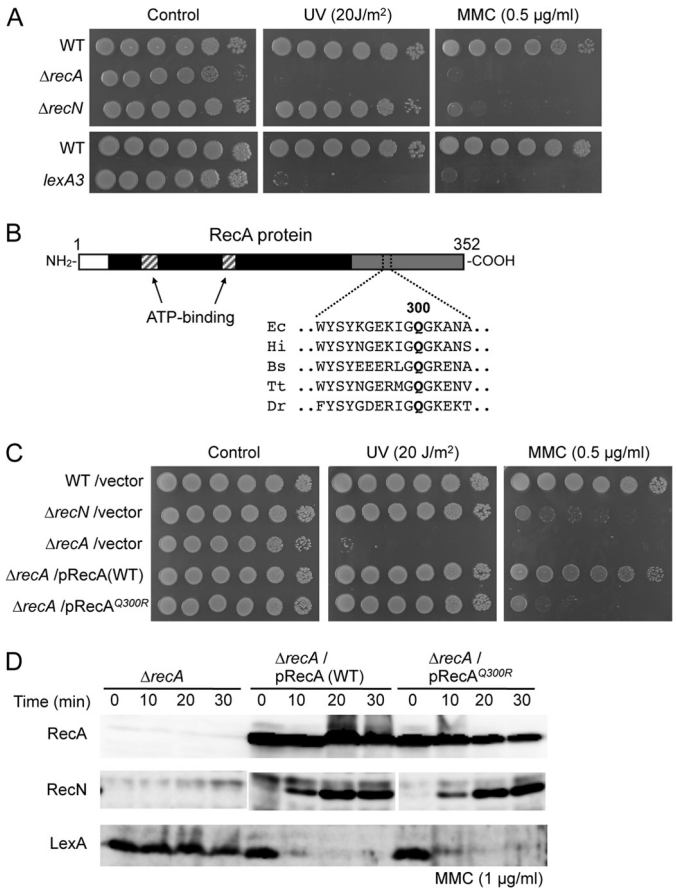

FIGURE 2. **Effect of *recA*^{Q300R} on DNA repair and SOS response.** *A*, sensitivity of cells to MMC and UV irradiation. 10-fold serial dilutions of the indicated strains were spotted on LB plates. DNA damage was induced by either MMC or UV irradiation. *B*, Q300 is conserved in bacterial RecA orthologs. A map of the *E. coli* RecA region between amino acids 290 and 305 is shown. *Ec*, *E. coli*; *Hi*, *H. influenzae*; *Bs*, *B.subtilis*; *Tt*, *Thermus thermophilus*; *Dr*, *D. radiodurans*. *C*, sensitivity of *recA*^{Q300R} cells to MMC and UV irradiation was examined as in *A*. *D*, RecA^{Q300R} is proficient in SOS induction. Protein extracts from cells treated with MMC for the indicated times were prepared and analyzed by Western blot using anti-RecA, anti-RecN, or anti-LexA antibodies. For the LexA degradation assay, chloramphenicol (100 μg/ml) was added at time 0 to inhibit resynthesis of LexA protein.

MMC-treated cells (Fig. 1, *B* and *C*). These results suggest that RecA is required to recruit GFP-RecN to DNA damage sites in MMC-treated cells.

Isolation of a recA Mutant That Mimics the Phenotype of Δ*recN*—Although RecA plays the central role in recombinational repair and is the master inducer of the SOS pathway, it is unclear what functions of RecA are required to recruit RecN to the nucleoid in MMC-treated cells. The phenotype of Δ*recA* or SOS-deficient *lexA3* cells (45) differs from the phenotype of Δ*recN* cells; the former are hypersensitive to MMC and UV, whereas the latter are hypersensitive to MMC but insensitive to UV (Fig. 2*A*). Therefore, a library of *recA* mutants was generated and screened for mutants that provide resistance to UV but confer sensitivity to MMC. Three candidate mutants were isolated from ~2,000 clones. All three mutants carry an arginine substitution at the highly conserved C-terminal Gln-300 of RecA (Fig. 2*B*). Fig. 2*C* shows that this allele, *recA*^{Q300R}, fully complements the UV sensitivity of Δ*recA* cells, but does not complement their MMC sensitivity. In the wild-type strain, MMC-induced DNA damage leads to proteolytic cleavage of LexA, the repressor of the SOS regulon, and induces the SOS response (Fig. 2*D*). Similarly, *recA*^{Q300R} is capable of inducing expression of the SOS regulon and specific proteolytic cleavage of LexA in MMC-treated cells (Fig. 2*D*). Thus, *recA*^{Q300R} is proficient in the DNA damage-induced SOS response, and its phenotype is similar to the phenotype of Δ*recN*.

Nucleoid Fragmentation in MMC-treated Δ*recN and recA*^{Q300R} *Cells*—To explore these results further, Δ*recA*, *recA*^{Q300R}, Δ*recN*, and Δ*ruvB* cells were stained with DAPI and examined by fluorescence and phase-contrast microscopy for genome integrity and cell morphology. Under conditions of exponential growth in the absence of MMC, all cells had a normal morphology, with two centrally located nucleoids per cell (Fig. 3*A*). Wild-type cells treated with MMC for 90 min became highly filamented with elongated, evenly spaced nucleoids (Fig. 3*A*). This morphology is typical of SOS-activated cells (46). By contrast, a large fraction of MMC-treated SOS-defective Δ*recA* were anucleate, and filamentous cells were hardly detected (Fig. 3*A*). RuvABC resolvasome branch-migrates and resolves Holliday junctions, and inactivation of any of the three Ruv functions blocks resolution of recombinational repair intermediates (3). Therefore, RuvB plays a role in the later steps of HR. MMC-treated *ruvB* mutants formed both filamentous and anucleate cells. As reported previously (47), the nucleoids of filamentous *ruvB* cells were centrally located and little to no DNA migrated to cell poles, which is in contrast to the morphology of filamentous wild-type cells (*i.e.* well partitioned nucleoids). This indicates that the accumulation of intermediates of HR-mediated DSB repair results in chromosome nondisjunction and the production of anucleate cells. MMC-treated Δ*recN* and *recA*^{Q300R}

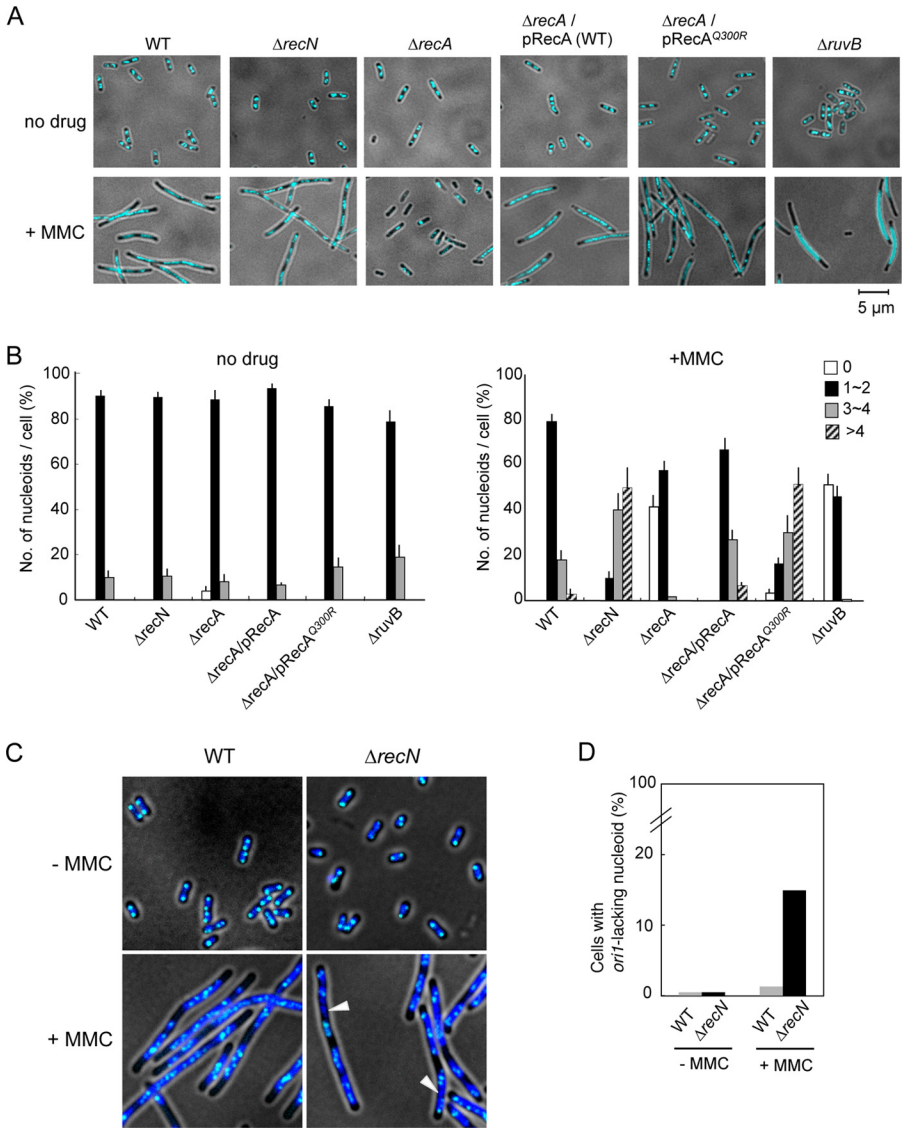

FIGURE 3. **Morphological changes in MMC-treated wild-type, Δ*recN*, and *recA* cells.** Exponentially growing cells were fixed and stained with DAPI and analyzed by fluorescence microscopy. *A*, the panels show DAPI images of cells incubated for 90 min in the presence or absence of MMC (1 μg/ml). Nucleoids are visualized as a *light blue color*. *B*, quantitative analysis of nucleoids. For cells with or without MMC-induced DNA damage, >200 cells were examined. The results represent the average of at least three independent measurements. *Error bars* indicate S.D. *C*, localization of a LacI-ECFP to the nucleoid. The wild-type and Δ*recN* strains carry an ectopic tandem array of *lacO* at *ori1* (15 kb counterclockwise of *oriC*). The panels show merged images of LacI-ECFP (*light blue*) and nucleoids (*dark blue*). *White arrows* indicate nucleoids that fail to bind LacI-ECFP, and by implication, *ori*C-lacking nucleoids. D, quantification of cells lacking *ori1* foci. Wild-type and Δ*recN* cells were treated with MMC for 90 min and examined by fluorescence microscopy. For cells with or without MMC-induced damage, >200 cells were examined.

cells were as filamentous as wild-type cells, but had an abnormal morphology characterized by multiple, short, diffuse nucleoids (Fig. 3*A*). In wild-type cells, the number of nucleoids per cell was largely unaffected by exposure to MMC, whereas the number of nucleoids per cell increased when Δ*recN* and *recA*^{Q300R} cells were exposed to MMC (Fig. 3*B*). Furthermore, abnormal nucleoid morphology was not generally observed in UV-irradiated Δ*recN* and *recA*^{Q300R} cells (supplemental Fig. S1). These results support the conclusion that *recA*^{Q300R} is a phenocopy of Δ*recN*. Our interpretation of this result is that RecN is dysfunctional in the *recA*^{Q300R} mutant.

We hypothesized that the abnormal nucleoid morphology of MMC-treated Δ*recN* cells might reflect the presence of unrepaired DSBs and chromosome fragmentation. Therefore, a fluorescence-based method was used to visualize chromosome fragments. For this purpose, *oriC* was labeled indirectly, via LacI-ECFP (enhanced cyan fluorescent protein) bound to an ectopic tandem array of Lac repressor-binding sites (240 × *lacO*) at the *ori1* locus (15 kb counterclockwise of *oriC*) (40). LacI-ECFP was expressed from the chromosomally integrated gene under the control of the *PBAD* promoter. Wild-type and Δ*recN* cells were treated or not with MMC and visualized using fluorescence microscopy. The results revealed 2–4 *ori1* foci per cell in the majority of wild-type and Δ*recN* cells in the absence of MMC. In these cells, all nucleoids contained at least one *ori1* focus (Fig. 3*C*). When treated with MMC, the number of *ori1* foci per nucleoid increased significantly in wild-type and Δ*recN* cells, and the foci were distributed throughout the elongated nucleoid (Fig. 3*C*). Notably, >15% of Δ*recN* cells carried nucleoids lacking *ori1* foci, whereas such nucleoids were infrequent

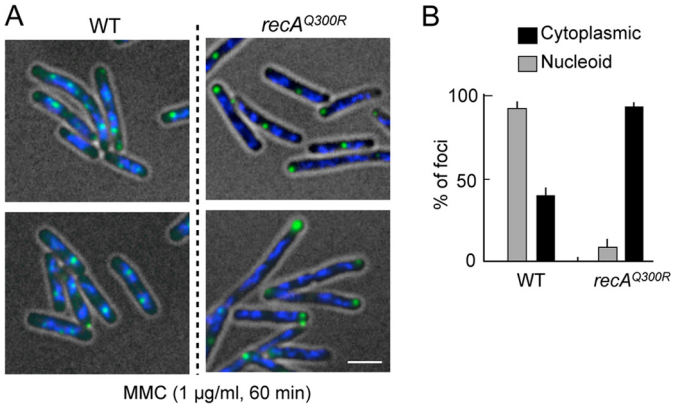

FIGURE 4. **Nucleoid-associated RecN foci in response to MMC-induced DNA damage.** *A*, MMC damage-induced RecN foci in *recA*^{Q300R} cells. Cells carrying the SOS-inducible *GFP-recN* (pSG101) were exposed to MMC for 60 min. The panels show GFP/DAPI-merged images of cells. *Scale bar* indicates 2.5 μm. *B*, quantitative analysis of GFP-RecN foci. For cells with MMC damage, >150 cells were examined. The results represent the average of at least three independent measurements. *Error bars* indicate S.D.

in wild-type cells (<1.4%) (Fig. 3*D*). These results demonstrate the presence of aberrant nucleoids lacking *oriC* in MMC-treated Δ*recN* cells, which likely represent subchromosomal fragments.

RecA^{Q300R} *Is Defective in Recruiting RecN to Nucleoids in MMC-treated Cells*—The results described above suggest that RecA^{Q300R} does not recruit RecN to the nucleoid, under conditions where wild-type RecA does so (*i.e.* in MMC-treated wild-type cells). To explore this further, GFP-RecN foci were quantified in MMC-treated Δ*recA* Δ*recN* cells expressing SOS-inducible *GFP-recN* and either wild-type *recA* or *recA*^{Q300R}. After exposure to MMC for 60 min, >90% of wild-type cells contained nucleoid-associated GFP-RecN foci (Fig. 4, *A* and *B*). By contrast, <5% of cells expressing *recA*^{Q300R} had nucleoid-associated GFP-RecN foci, whereas the number and fraction of cells with cytoplasmic GFP-RecN foci was higher in cells expressing *recA*^{Q300R} than that in cells expressing wild-type *recA* (Fig. 4, *A* and *B*). These results indicate that RecA is required for the formation of MMC-induced, nucleoid-associated RecN foci and that RecA^{Q300R} has a specific defect in this function/role.

RecA Is Required to Recruit RecN to sites of DSBs—To examine the recruitment of RecN to a unique DSB site in RecA-proficient cells, I-*Sce*I was used to introduce a site-specific DSB into a strain that carries the P_{BAD}I-*Sce*I cassette on the chromosome and a single I-*Sce*I recognition site on the F′ episome (39). Appropriately engineered cells were transformed with a plasmid expressing *GFP-recN* from its native SOS-inducible promoter, grown to early log phase and exposed to arabinose to induce I-*Sce*I. Control cells were grown in medium lacking arabinose. *Vsp*I endonuclease digestion resulted in a 1.8-kb fragment containing the I-*Sce*I cleavage site. I-*Sce*I digestion produced two fragments, one of which with a size of 1.2 kb hybridized to the site 1 probe (Fig. 5*A*). The kinetics of DSB formation was monitored by Southern blot analysis of *Vsp*I-digested DNA isolated from samples taken at different times after the addition of 0.2% arabinose or glucose to the culture. A 1.2-kb fragment was not detected when cells were maintained in glucose-containing medium, whereas it was detected within 30 min in wild-type cells proficient for RecBCD after the addition of arabinose (Fig. 5, *A* and *B*). The intensity of the 1.2-kb fragments increased with time, reaching a maximum intensity ~1 h after the addition of arabinose. Similar results were obtained when the site 2 probe was used to detect the I-*Sce*I cleavage site (Fig. 5*A* and supplemental Fig. S2). One possible explanation for the kinetics of DSB formation is that I-*Sce*I digestion is not synchronous in the entire population, and the breaks may be repaired very efficiently. Thus, the only breaks generated just before samples were taken might be detected by Southern blotting. This is consistent with previous studies using chromosomally integrated I-*Sce*I site, where DSB products are readily detected in wild-type cells even after 1 h of I-*Sce*I induction (48).

Fig. 5*C* shows that nucleoid-associated GFP-RecN foci were detected in cells that expressed I-*Sce*I and carried an F′ episome with an I-*Sce*I cleavage site. By contrast, GFP-RecN foci were not observed when the same cells were grown in glucose-containing medium (to repress I-*Sce*I) or if the cells did not carry an I-*Sce*I-sensitive F′ episome (Fig. 5*C*). Furthermore, the number of nucleoid-associated GFP-RecN foci was much lower in *recA*^{Q300R} mutant cells (<1%) than in cells expressing wild-type *recA* (18%) (Fig. 5*D*). These results indicate that, in wild-type cells, a single I-*Sce*I-induced DSB induces an SOS response and promotes the formation of nucleoid-associated GFP-RecN foci in a RecA-dependent manner.

RecN ATPase Activity Is Required for Release from Growth Arrest in Cells with DNA Damage—RecN has a typical SMC family protein domain structure, including an extensive, centrally located coiled-coil domain and globular N- and C-terminal domains with Walker A and Walker B nucleotide-binding motifs, respectively (49). A previous study showed that substitution of Lys-35 with alanine in the Walker A motif resulted in a complete loss of RecN DNA repair activity *in vivo* (50). Biochemical characterization of *Deinococcus radiodurans* RecN showed that RecN^{K67A} (an lysine-to-alanine substitution at position 67, which corresponds to *E. coli* RecN Lys-35) abolished ATPase activity, but did not impair ATP binding *in vitro* (49). Fig. 6*A* shows that expression of *recN*^{K35A} in a Δ*recN* background conferred sensitivity to MMC that was equivalent to that of Δ*recN*. The overproduction of RecN^{K35A} rendered wild-type cells sensitive to MMC (Fig. 6*A*), demonstrating that *recN*^{K35A} is a dominant-negative allele of *recN*. GFP-RecN^{K35A} formed nucleoid-associated foci in >80% of MMC-treated cells, and these foci failed to form in cells expressing *recA*^{Q300R} (Fig. 6*B*). This result indicates that the ATPase activity of RecN is not required for formation of nucleoid-associated RecN foci. However, Δ*recN* cells expressing wild-type *GFP-recN* resumed normal cell growth, and nucleoid-associated GFP-RecN foci dissociated after exposure to MMC was terminated (Fig. 6*C*). By contrast, Δ*recN* cells expressing *GFP-recN*^{K35A} became highly filamented, acquired fragmented nucleoid structures, and retained GFP-RecN^{K35A} foci for 2 h after exposure to MMC was terminated (Fig. 6*C*). These results demonstrate that ATPase-defective RecN^{K35A} is recruited to sites of DNA damage, but may not be properly released because of the defects in HR-mediated repair of MMC-induced DSBs.

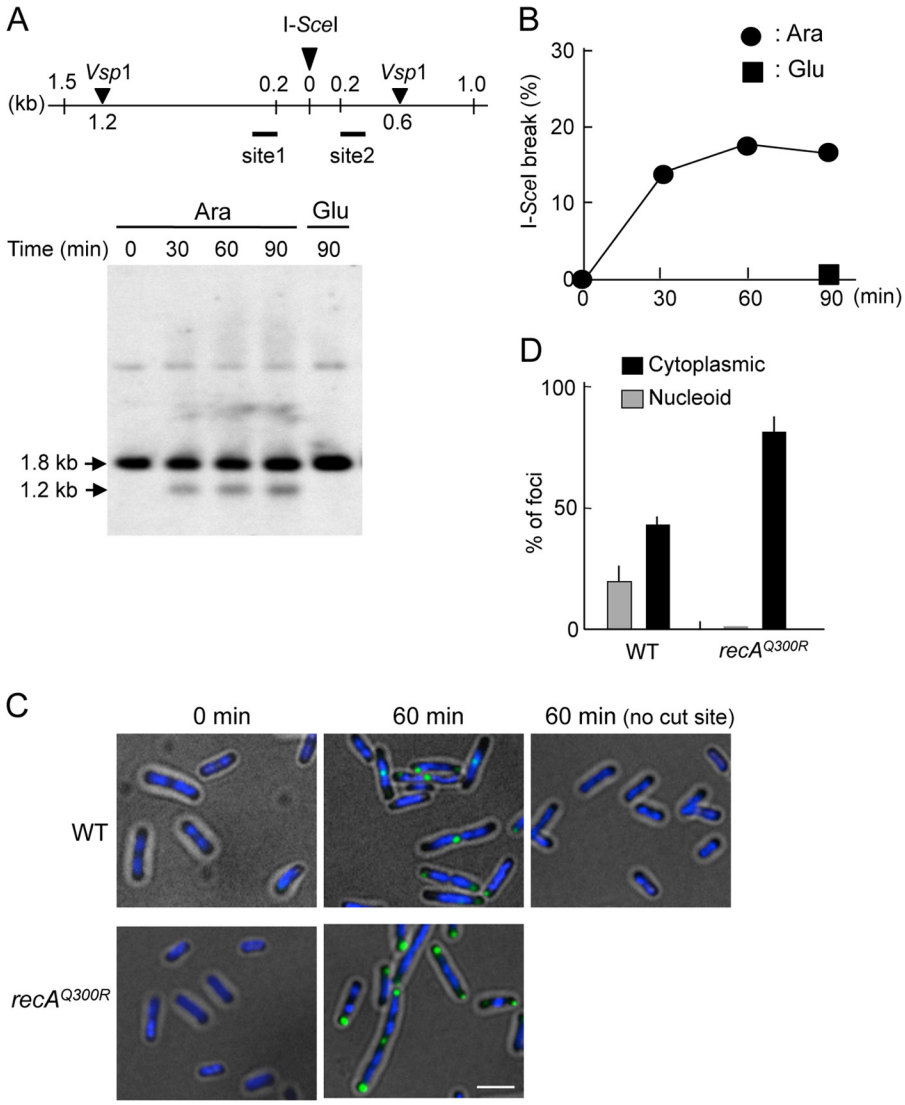

FIGURE 5. **RecA is required for the assembly of RecN at the sites of DSBs.** *A*, Southern blot of the flanking region of the I-*Sce*I site before and after induction of I-*Sce*I. Exponentially growing cells were cultured, and either arabinose (*Ara*) was added to induce I-*Sce*I or glucose (*Glu*) was added as a control. Cells were taken at the indicated times. The DNA digested with *Vsp*I was analyzed on a 1% agarose gel and detected by Southern analysis using site 1 probe. The *top panel* illustrates the DNA sequences flanking the I-*Sce*I cleavage site in the *codA21*::miniTn7Kan locus on the F′ episome. The location of *Vsp*I cut sites and the sizes of the DNA fragments after *Vsp*I digestion are shown. Site 1 and site 2 regions were used for Southern blot analysis. *B*, quantitation of Southern blot analysis. *I-SceI break* refers to the levels of the 1.2-kb fragment resulting from DSB formation. *C*, GFP-RecN foci at a unique I-*Sce*I-induced nascent DSB. The panels show GFP/DAPI-merged images of cells with or without a single I-*Sce*I recognition site. *recA*Δ cells expressing SOS-inducible *GFP-recN* and either wild-type *recA* or *recA*^{Q300R} were incubated for 1 h in the presence of arabinose to induce I-*Sce*I. *Scale bar* indicates 2.5 μm. *D*, quantitative analysis of GFP-RecN foci. The results represent the average of at least three independent measurements. *Error bars* indicate S.D.

DISCUSSION

Previous studies demonstrate that RecN protein forms both nucleoid-associated and cytoplasmic foci in cells exposed to DSB-inducing agents and that cytoplasmic RecN aggregates are degraded by the ClpXP protease (27). Here, we demonstrate that RecN is recruited to nucleoids in a RecA-dependent manner. We characterize a novel *recA* allele, *recA*^{Q300R}, which promotes expression of SOS-inducible genes but does not promote formation of nucleoid-associated RecN foci. RecN accumulates at a unique I-*Sce*I-induced DSB in wild-type *recA* cells but not in *recA*^{Q300R} cells. Thus, we conclude that RecA plays an essential role in DNA damage-induced expression of *recN* and the assembly of RecN foci at the sites of DSBs. ATPase-deficient *recN*^{K35A} mutants are proficient in forming nucleoid-associated foci at DSBs, but fail to resume growth after release from MMC-induced cell-cycle arrest. This results in highly filamented cells with nucleoid-associated GFP-RecN^{K35A} foci and fragmented nucleoid structures. One possible explanation for the presence of persistent foci associated with damaged DNA in *recN*^{K35A} cells is that RecN^{K35A} is recruited to DSBs, but is not released from DSB sites because it lacks ATPase activity; under such conditions, mutant RecN^{K35A} DNA damage foci persist and accumulate, which interferes with RecA-mediated synaptic steps in the HR pathway.

This study also reveals that Δ*recN* and *recA*^{Q300R} cells are hypersensitive to MMC but not to UV. A previous study showed that cells expressing *recA*Δ*C17* (a deletion mutant lacking residues 336–352) are hypersensitive to MMC but not to UV (51). Here, we confirm that *recA*Δ*C17* cells are sensitive to MMC, although they are less sensitive than Δ*recN* and

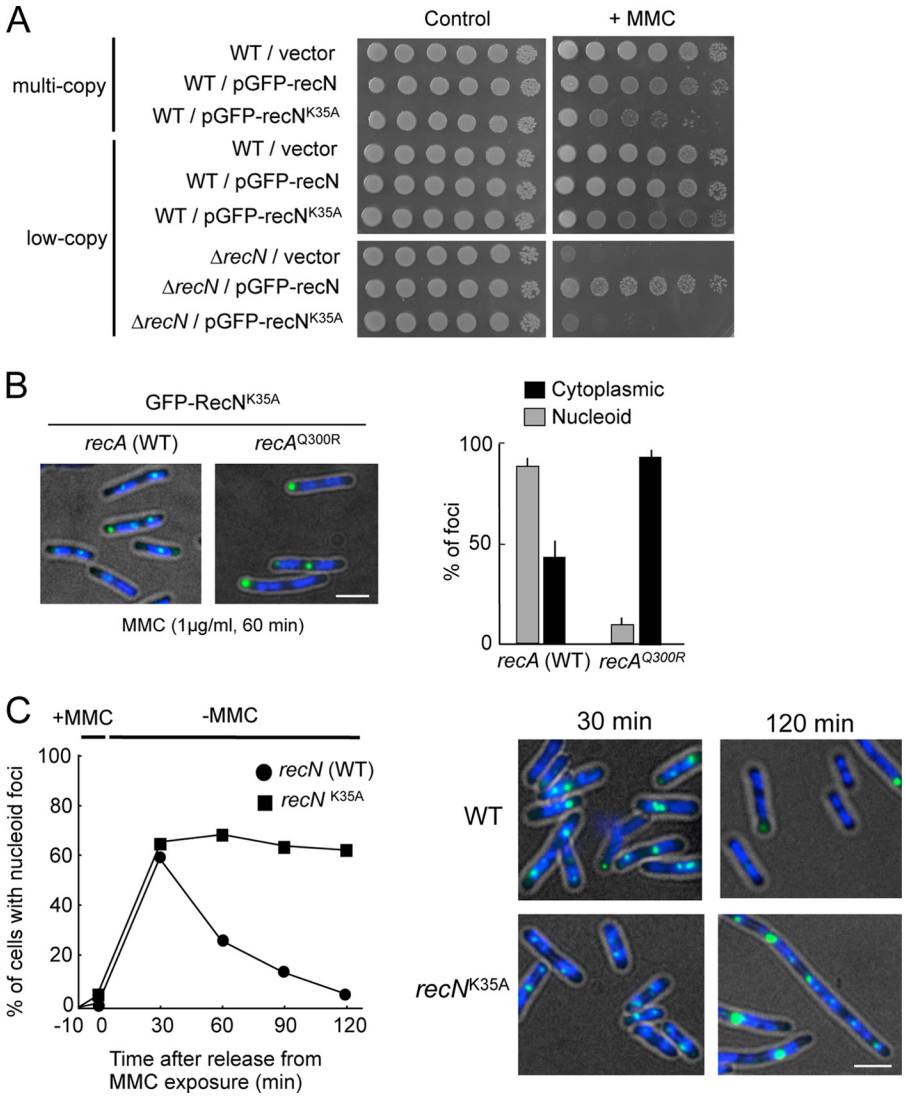

FIGURE 6. **RecN^{K35A} is deficient in HR-mediated recovery after exposure to MMC.** *A*, sensitivity of cells to MMC. The indicated strains were grown in LB. Cells were diluted and spotted onto LB with or without MMC (0.5 μg/ml). *B*, subcellular localization of GFP-RecN^{K35A}. The panels show GFP/DAPI images of Δ*recN* cells containing SOS-inducible *GFP-recN^{K35A}* after 30 min of incubation in the presence of MMC. Quantitative analysis of GFP-RecN^{K35A} foci is shown to the *right*. The results represent the average of at least three independent measurements. *C*, wild-type and *recN^{K35A}* cells were treated with MMC for 10 min and then transferred to MMC-free medium ($t = 0$). At the indicated time points, cells were analyzed for the presence of RecN foci. The *right panels* show the GFP/DAPI images of cells at the indicated time after transfer to MMC-free media. *Scale bar* indicates 2.5 μm. *Error bars* indicate S.D.

recA^{Q300R} cells (supplemental Fig. S3). We found that nucleoid-associated GFP-RecN foci form normally in MMC-treated *recAΔC17* cells (supplemental Fig. S3), indicating that the defects in the response to MMC in *recA^{Q300R}* cells are not a result of a dysfunctional RecA C-terminal domain. However, it still remains possible that the C-terminal region of RecA plays a role in modulating RecN function at a later step in the repair/response to MMC-induced DSBs.

Previous studies suggest that the SOS response plays a critical role in DSB repair in *E. coli* but not in *Bacillus subtilis* (52). Indeed, unlike in *E. coli*, the expression of *B. subtilis* RecN appears to be SOS-independent (53), and GFP-*B. subtilis* RecN foci associate with DSBs before RecA is recruited to the DNA lesion (10). By contrast, *E. coli recN* is typical of SOS-regulated genes in that its expression is tightly repressed in unstressed cells. This suggests that *E. coli* RecN participates in HR repair of DSBs after RecA senses DNA damage. Consistent with this, the present study indicates that RecA actively recruits RecN to DSBs. These results may reflect species-specific attributes of *E. coli* and *B. subtilis* HR pathways. The purified *B. subtilis* RecN (and also *D. radiodurans* RecN) binds to DNA and has DNA-stimulated ATPase activity *in vitro* (54, 55). Unfortunately, it has been difficult to purify *E. coli* RecN because it is relatively insoluble and highly susceptible to degradation (data not shown). A recent study showed that *Haemophilus influenzae* RecN can be purified to near homogeneity and is fully functional in *E. coli* (50). Purified *Haemophilus influenzae* RecN does not bind DNA, and DNA had no significant effect on *Haemophilus influenzae* RecN ATPase activity *in vitro*, which contrasts with the activity of *B. subtilis* RecN. This observation supports our conclusion that *E. coli* RecN is recruited to DSBs through its interaction with RecA. Thus, the difference in the DNA binding specificities of RecN orthologs may explain their different affinities for their respective bacterial nucleoids. How-

ever, our data do not exclude the possibility that *E. coli* RecN has DNA binding activity. It is also conceivable that RecA facilitates the binding and/or retention of RecN on damaged DNA.

SMC proteins are highly conserved ATPases whose role in higher order chromosome organization and dynamics is conserved from bacteria to humans. DSBs are one of the most cytotoxic forms of DNA damage, and therefore, the repair of DSBs is crucial for cell survival and for maintaining the integrity of the genome. In this study, we provide evidence that the recruitment of RecN to DSBs requires interaction with RecA. Any defect in the interaction results in chromosomal fragmentation, such as that observed in cells exposed to the DSB-inducing agent MMC. Based on these results and implications, we propose a mechanism by which RecN promotes RecA-dependent DSB repair. The initial presynaptic step of the DNA strand exchange reaction is formation of a RecA-ssDNA nucleoprotein filament. RecA-dependent recruitment of SMC-like RecN to DSBs follows, serving a scaffolding function to facilitate subsequent search by RecA for homologous templates in the segregated sister chromatids. Lastly, RecA mediates strand exchange. This model might be compatible with the *recN* studies in *B. subtilis*; here, we allow for the fact that RecN plays a role in an early step of DSB repair and that the mechanism by which RecN is recruited to DSBs differs.

In future studies, it will be interesting to investigate how RecN SMC complexes actually promote RecA-dependent DSB repair. Therefore, novel integrated biochemical and structural approaches to examine this and other questions concerning the roles of RecN and RecA will be required. The results of such studies should advance our understanding of the mechanism of DSB repair in prokaryotic and eukaryotic cells.

Acknowledgments—We are grateful to S. M. Rosenberg for providing the E. coli strains. We thank T. Kado for technical assistance. We thank the members of the Hishida laboratory for stimulating discussions.

REFERENCES

1. Cox, M. M., Goodman, M. F., Kreuzer, K. N., Sherratt, D. J., Sandler, S. J., and Marians, K. J. (2000) The importance of repairing stalled replication forks. *Nature* **404,** 37–41
2. Kuzminov, A. (2001) DNA replication meets genetic exchange: chromosomal damage and its repair by homologous recombination. *Proc. Natl. Acad. Sci. U.S.A.* **98,** 8461–8468
3. Kuzminov, A. (1999) Recombinational repair of DNA damage in *Escherichia coli* and bacteriophage λ. *Microbiol. Mol. Biol. Rev.* **63,** 751–813
4. Kowalczykowski, S. C. (2000) Initiation of genetic recombination and recombination-dependent replication. *Trends Biochem. Sci.* **25,** 156–165
5. Cox, M. M. (2001) Historical overview: searching for replication help in all of the rec places. *Proc. Natl. Acad. Sci. U.S.A.* **98,** 8173–8180
6. Singleton, M. R., Dillingham, M. S., Gaudier, M., Kowalczykowski, S. C., and Wigley, D. B. (2004) Crystal structure of RecBCD enzyme reveals a machine for processing DNA breaks. *Nature* **432,** 187–193
7. Lloyd, R. G., and Low, K. B. (1996) *Escherichia coli and Salmonella: Cellular and Molecular Biology*, 2nd Ed., pp. 2236–2255, American Society for Microbiology Press, Washington, D.C.
8. Amundsen, S. K., and Smith, G. R. (2003) Interchangeable parts of the *Escherichia coli* recombination machinery. *Cell* **112,** 741–744
9. Rocha, E. P., Cornet, E., and Michel, B. (2005) Comparative and evolutionary analysis of the bacterial homologous recombination systems. *PLoS Genet.* **1,** e15
10. Sanchez, H., Kidane, D., Castillo Cozar, M., Graumann, P. L., and Alonso, J. C. (2006) Recruitment of *Bacillus subtilis* RecN to DNA double-strand breaks in the absence of DNA end processing. *J. Bacteriol.* **188,** 353–360
11. Cao, Z., Mueller, C. W., and Julin, D. A. (2010) Analysis of the *recJ* gene and protein from *Deinococcus radiodurans*. *DNA Repair* **9,** 66–75
12. Bentchikou, E., Servant, P., Coste, G., and Sommer, S. (2010) A major role of the RecFOR pathway in DNA double-strand-break repair through ESDSA in *Deinococcus radiodurans*. *PLoS Genet.* **6,** e1000774
13. Cox, M. M., Keck, J. L., and Battista, J. R. (2010) Rising from the ashes: DNA repair in *Deinococcus radiodurans*. *PLoS Genet.* **6,** e1000815
14. Lusetti, S. L., and Cox, M. M. (2002) The bacterial RecA protein and the recombinational DNA repair of stalled replication forks. *Annu. Rev. Biochem.* **71,** 71–100
15. Lloyd, R. G., and Sharples, G. J. (1993) Dissociation of synthetic Holliday junctions by *E. coli* RecG protein. *EMBO J.* **12,** 17–22
16. Shinagawa, H., and Iwasaki, H. (1996) Processing the Holliday junction in homologous recombination. *Trends in biochemical sciences* **21,** 107–111
17. Sharples, G. J., Ingleston, S. M., and Lloyd, R. G. (1999) Holliday junction processing in bacteria: insights from the evolutionary conservation of RuvABC, RecG, and RusA. *J. Bacteriol.* **181,** 5543–5550
18. Little, J. W., and Mount, D. W. (1982) The SOS regulatory system of *Escherichia coli*. *Cell* **29,** 11–22
19. Little, J. W. (1991) Mechanism of specific LexA cleavage: autodigestion and the role of RecA coprotease. *Biochimie* **73,** 411–421
20. Luo, Y., Pfuetzner, R. A., Mosimann, S., Paetzel, M., Frey, E. A., Cherney, M., Kim, B., Little, J. W., and Strynadka, N. C. (2001) Crystal structure of LexA: a conformational switch for regulation of self-cleavage. *Cell* **106,** 585–594
21. Courcelle, J., Khodursky, A., Peter, B., Brown, P. O., and Hanawalt, P. C. (2001) Comparative gene expression profiles following UV exposure in wild-type and SOS-deficient *Escherichia coli*. *Genetics* **158,** 41–64
22. Graumann, P. L. (2001) SMC proteins in bacteria: condensation motors for chromosome segregation? *Biochimie* **83,** 53–59
23. Hirano, T. (2006) At the heart of the chromosome: SMC proteins in action. *Nat. Rev. Mol. Cell Biol.* **7,** 311–322
24. Lloyd, R. G., Picksley, S. M., and Prescott, C. (1983) Inducible expression of a gene specific to the RecF pathway for recombination in *Escherichia coli* K12. *Mol. Gen. Genet.* **190,** 162–167
25. Finch, P. W., Chambers, P., and Emmerson, P. T. (1985) Identification of the *Escherichia coli recN* gene product as a major SOS protein. *J. Bacteriol.* **164,** 653–658
26. Rostas, K., Morton, S. J., Picksley, S. M., and Lloyd, R. G. (1987) Nucleotide sequence and LexA regulation of the *Escherichia coli recN* gene. *Nucleic Acids Res.* **15,** 5041–5049
27. Nagashima, K., Kubota, Y., Shibata, T., Sakaguchi, C., Shinagawa, H., and Hishida, T. (2006) Degradation of *Escherichia coli* RecN aggregates by ClpXP protease and its implications for DNA damage tolerance. *J. Biol. Chem.* **281,** 30941–30946
28. Neher, S. B., Villén, J., Oakes, E. C., Bakalarski, C. E., Sauer, R. T., Gygi, S. P., and Baker, T. A. (2006) Proteomic profiling of ClpXP substrates after DNA damage reveals extensive instability within SOS regulon. *Mol. Cell* **22,** 193–204
29. Sargentini, N. J., and Smith, K. C. (1983) Characterization of an *Escherichia coli* mutant (*radB101*) sensitive to γ and UV radiation, and methyl methanesulfonate. *Radiat. Res.* **93,** 461–478
30. Kosa, J. L., Zdraveski, Z. Z., Currier, S., Marinus, M. G., and Essigmann, J. M. (2004) RecN and RecG are required for *Escherichia coli* survival of Bleomycin-induced damage. *Mutat. Res.* **554,** 149–157
31. Picksley, S. M., Attfield, P. V., and Lloyd, R. G. (1984) Repair of DNA double-strand breaks in *Escherichia coli* K12 requires a functional *recN* product. *Mol. Gen. Genet.* **195,** 267–274
32. Lloyd, R. G., Buckman, C., and Benson, F. E. (1987) Genetic analysis of conjugational recombination in *Escherichia coli* K12 strains deficient in RecBCD enzyme. *J. Gen. Microbiol.* **133,** 2531–2538
33. Wang, T. C., and Smith, K. C. (1988) Different effects of *recJ* and *recN* mutations on the postreplication repair of UV-damaged DNA in *Escherichia coli* K-12. *J. Bacteriol.* **170,** 2555–2559
34. Miller, J. H. (1992) *A Short Course in Bacterial Genetics: A Laboratory*

Manual and Handbook for Escherichia coli and Related Bacteria, Cold Spring Harbor Laboratory Press, Cold Spring Harbor, NY
35. Sambrook, J., Fritsch, E. F., and Maniatis, T. (1989) *Molecular Cloning: A Laboratory Manual*, 2nd Ed., Cold Spring Harbor Laboratory Press, Cold Spring Harbor, NY
36. Shibata, T., Hishida, T., Kubota, Y., Han, Y. W., Iwasaki, H., and Shinagawa, H. (2005) Functional overlap between RecA and MgsA (RarA) in the rescue of stalled replication forks in *Escherichia coli*. *Genes Cells* **10,** 181–191
37. Datsenko, K. A., and Wanner, B. L. (2000) One-step inactivation of chromosomal genes in *Escherichia coli* K-12 using PCR products. *Proc. Natl. Acad. Sci. U.S.A.* **97,** 6640–6645
38. Baba, T., Ara, T., Hasegawa, M., Takai, Y., Okumura, Y., Baba, M., Datsenko, K. A., Tomita, M., Wanner, B. L., and Mori, H. (2006) Construction of *Escherichia coli* K-12 in-frame, single-gene knockout mutants: the Keio collection. *Mol. Syst. Biol.* **2,** 2006.0008
39. Ponder, R. G., Fonville, N. C., and Rosenberg, S. M. (2005) A switch from high-fidelity to error-prone DNA double-strand break repair underlies stress-induced mutation. *Mol. Cell* **19,** 791–804
40. Nozaki, S., Niki, H., and Ogawa, T. (2009) Replication initiator DnaA of *Escherichia coli* changes its assembly form on the replication origin during the cell cycle. *J. Bacteriol.* **191,** 4807–4814
41. Hishida, T., Han, Y. W., Shibata, T., Kubota, Y., Ishino, Y., Iwasaki, H., and Shinagawa, H. (2004) Role of the *Escherichia coli* RecQ DNA helicase in SOS signaling and genome stabilization at stalled replication forks. *Genes Dev.* **18,** 1886–1897
42. Lau, I. F., Filipe, S. R., Søballe, B., Økstad, O. A., Barre, F. X., and Sherratt, D. J. (2003) Spatial and temporal organization of replicating *Escherichia coli* chromosomes. *Mol. Microbiol.* **49,** 731–743
43. Hatano, T., Yamaichi, Y., and Niki, H. (2007) Oscillating focus of SopA associated with filamentous structure guides partitioning of F plasmid. *Mol. Microbiol.* **64,** 1198–1213
44. Humayun, M. Z. (1998) SOS and Mayday: multiple inducible mutagenic pathways in *Escherichia coli*. *Mol. Microbiol.* **30,** 905–910
45. Little, J. W., and Harper, J. E. (1979) Identification of the lexA gene product of *Escherichia coli* K-12. *Proc. Natl. Acad. Sci. U.S.A.* **76,** 6147–6151
46. Friedberg, E. C., Aguilera, A., Gellert, M., Hanawalt, P. C., Hays, J. B., Lehmann, A. R., Lindahl, T., Lowndes, N., Sarasin, A., and Wood, R. D. (2006) DNA repair: from molecular mechanism to human disease. *DNA Repair* **5,** 986–996
47. Ishioka, K., Fukuoh, A., Iwasaki, H., Nakata, A., and Shinagawa, H. (1998) Abortive recombination in *Escherichia coli ruv* mutants blocks chromosome partitioning. *Genes Cells* **3,** 209–220
48. Meddows, T. R., Savory, A. P., and Lloyd, R. G. (2004) RecG helicase promotes DNA double-strand break repair. *Mol. Microbiol.* **52,** 119–132
49. Pellegrino, S., Radzimanowski, J., de Sanctis, D., Boeri Erba, E., McSweeney, S., and Timmins, J. (2012) Structural and functional characterization of an SMC-like protein RecN: new insights into double-strand break repair. *Structure* **20,** 2076–2089
50. Grove, J. I., Wood, S. R., Briggs, G. S., Oldham, N. J., and Lloyd, R. G. (2009) A soluble RecN homologue provides means for biochemical and genetic analysis of DNA double-strand break repair in *Escherichia coli*. *DNA Repair* **8,** 1434–1443
51. Lusetti, S. L., Wood, E. A., Fleming, C. D., Modica, M. J., Korth, J., Abbott, L., Dwyer, D. W., Roca, A. I., Inman, R. B., and Cox, M. M. (2003) C-terminal deletions of the *Escherichia coli* RecA protein. Characterization of *in vivo* and *in vitro* effects. *J. Biol. Chem.* **278,** 16372–16380
52. Simmons, L. A., Goranov, A. I., Kobayashi, H., Davies, B. W., Yuan, D. S., Grossman, A. D., and Walker, G. C. (2009) Comparison of responses to double-strand breaks between *Escherichia coli* and *Bacillus subtilis* reveals different requirements for SOS induction. *J. Bacteriol.* **191,** 1152–1161
53. Au, N., Kuester-Schoeck, E., Mandava, V., Bothwell, L. E., Canny, S. P., Chachu, K., Colavito, S. A., Fuller, S. N., Groban, E. S., Hensley, L. A., O'Brien, T. C., Shah, A., Tierney, J. T., Tomm, L. L., O'Gara, T. M., Goranov, A. I., Grossman, A. D., and Lovett, C. M. (2005) Genetic composition of the *Bacillus subtilis* SOS system. *J. Bacteriol.* **187,** 7655–7666
54. Sanchez, H., and Alonso, J. C. (2005) *Bacillus subtilis* RecN binds and protects 3′-single-stranded DNA extensions in the presence of ATP. *Nucleic Acids Res.* **33,** 2343–2350
55. Reyes, E. D., Patidar, P. L., Uranga, L. A., Bortoletto, A. S., and Lusetti, S. L. (2010) RecN is a cohesin-like protein that stimulates intermolecular DNA interactions in vitro. *J. Biol. Chem.* **285,** 16521–16529

Supplemental Data:

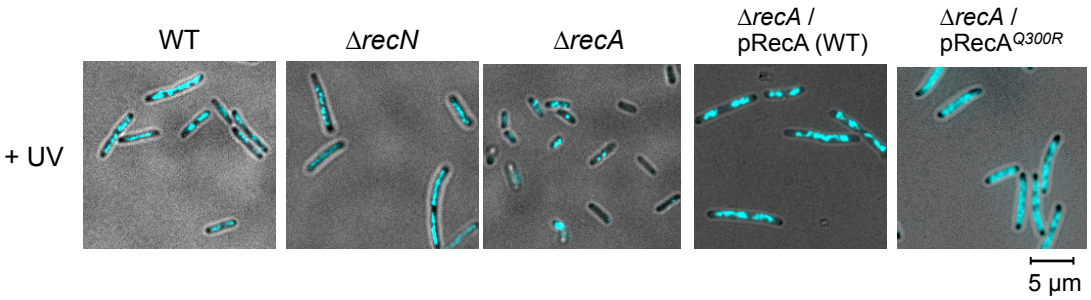

Figure S1. Morphological changes in UV-treated cells. Exponentially growing cells were irradiated with UV (20 J/m^2) and samples were taken at 90 min after UV irradiation. Cells were fixed and stained with DAPI, and analyzed by fluorescence microscopy.

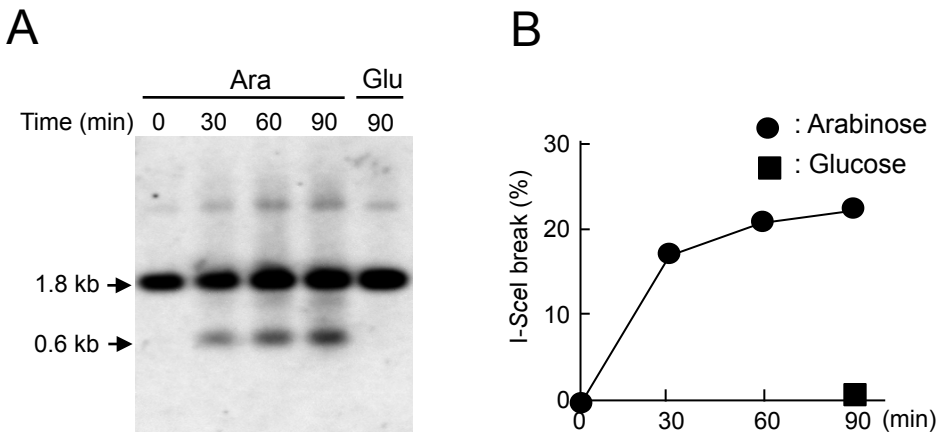

Figure S2. Southern blot analysis of DNA extracted at different times after DSB induction. (*A*) Exponentially growing cells were cultured with addition of arabinose (for induction of I-*Sce*I) or glucose (as a control). Cells were taken at the indicated times. The DNA was digested with *Vsp*I and probed with a site2 fragment. (*B*) Quantitation of Southern blot analysis. "I-*Sce*I break" refers to the levels of the 0.6-kb fragment resulting from DSB formation.

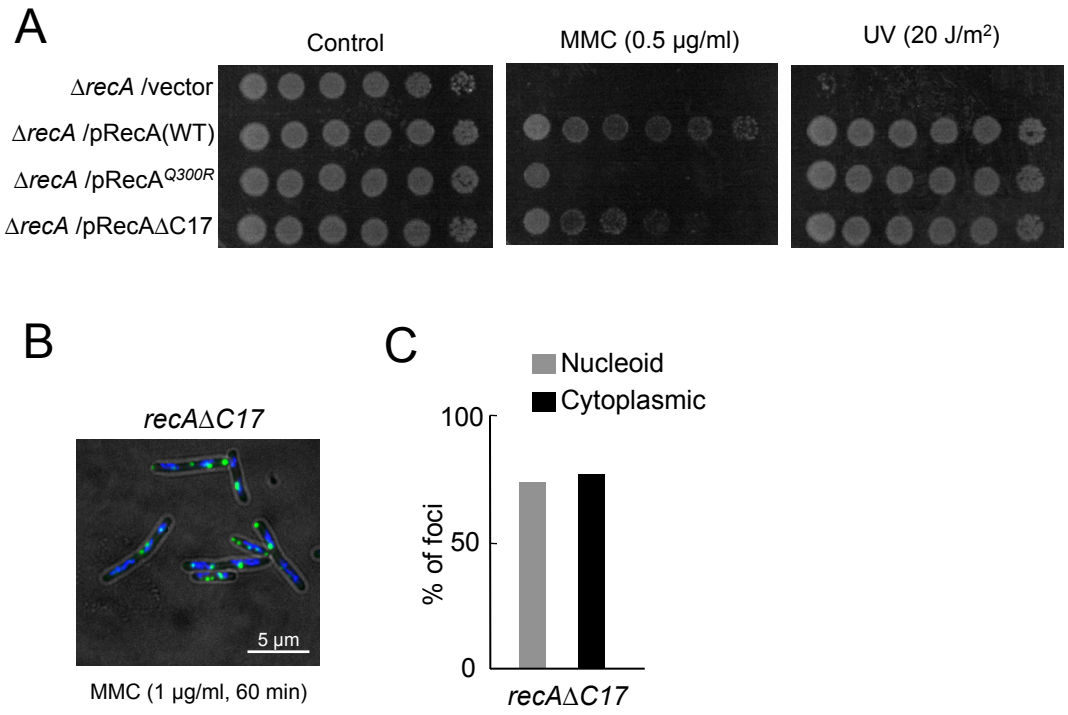

Figure S3. Assembly of RecN at the sites of DSBs in *recAΔC17* mutants. (*A*) Sensitivity of cells to MMC and UV irradiation. Ten-fold serial dilutions of the indicated strains were spotted onto LB plates containing the 0.5 μg/ml MMC. For UV irradiation, the indicated strains were spotted onto LB plates, DNA damage was induced by UV. (*B*) MMC damage-induced RecN foci in *recAΔC17* cells. Cells carrying the SOS inducible *GFP-recN* were exposed to MMC for 60 min. The panels show GFP/DAPI-merged images of cells. (*C*) Quantitative analysis of GFP-RecN foci. For cells with MMC damage, >150 cells were examined. The results represent the average of at least three independent measurements.

RecA Protein Recruits Structural Maintenance of Chromosomes (SMC)-like RecN Protein to DNA Double-strand Breaks

Kenji Keyamura, Chikako Sakaguchi, Yoshino Kubota, Hironori Niki and Takashi Hishida

J. Biol. Chem. 2013, 288:29229-29237.
doi: 10.1074/jbc.M113.485474 originally published online August 25, 2013

DOJIN BIOSCIENCE 23

ゲノムを司るインターメア

非コードDNAの新たな展開

小林武彦 編

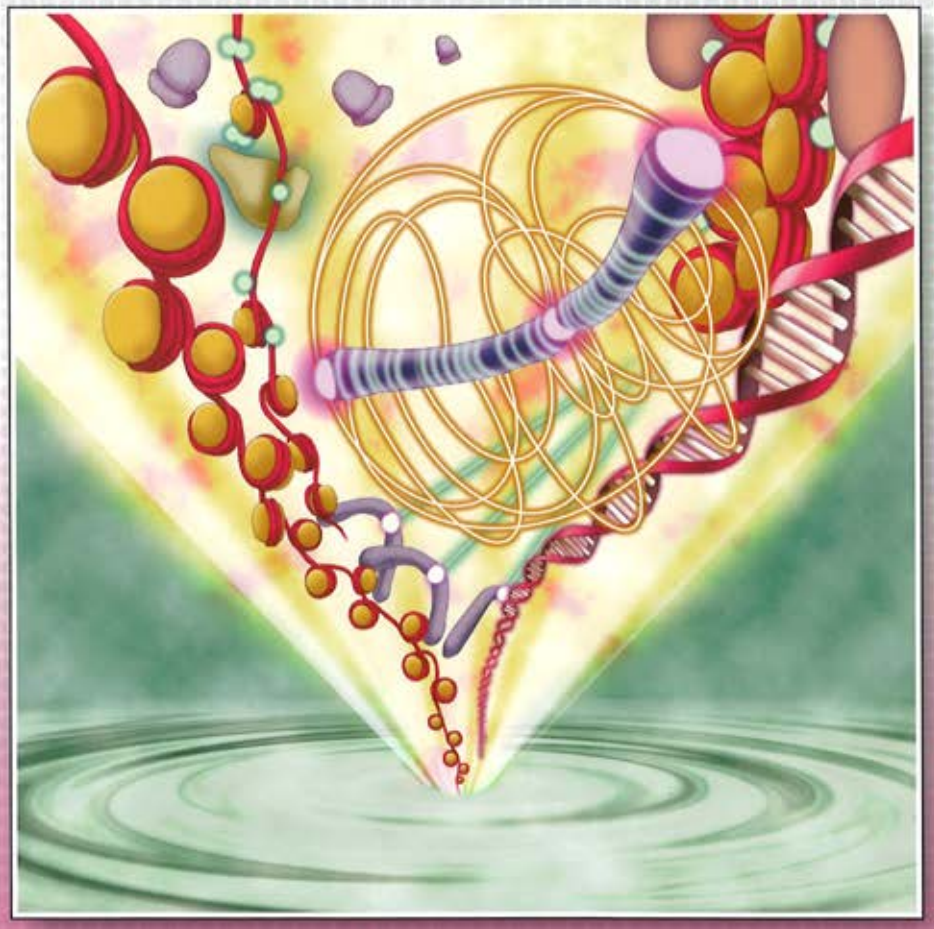

化学同人

目　次

chapter 13

非コード DNA 領域の DNA 損傷応答

Summary

ゲノムの本体である DNA では，地球環境および細胞内環境に由来するさまざまな因子によって，常に DNA 損傷が発生している．DNA 損傷によって引き起こされる DNA 複製阻害は，遺伝子（コード）領域の突然変異を誘発する主要な原因であり，ヒトにおいては発がんやさまざまな疾患と密接に関連している．したがって，コード領域上の DNA 損傷を取り除くことは生命機能の恒常性を維持するために重要である．一方，ヒトのような高等真核生物ではゲノムの大部分を非コード領域が占めているため，ゲノム安定性維持の観点からすると，非コード領域上の DNA 損傷が及ぼす影響はきわめて大きいと考えられる．本章では，DNA 損傷をはじめとするさまざまな要因によって発生する複製ストレスと非コード DNA 領域の安定性維持との関連性について触れながら，複製ストレスを解消する分子メカニズムについて概説する．

13.1 DNA 損傷応答と非コード DNA

13.1.1 DNA 損傷と非コード DNA

ゲノムは一般に“生命の設計図”と表現されることが多い．しかしながら，この設計図という言葉から連想される静的なイメージとは異なり，ゲノムの本体である DNA は極性をもった窒素やリン，酸素などを多く含む非常に反応性に富んだ化学的性質を備えており，DNA 複製や転写を行う動的な場を提供している．一方で，このような化学的性質は意図しない DNA の化学的な変化，すなわち DNA 損傷を引き起こす原因ともなっている．DNA 損傷には，さまざまな環境要因によって誘発される外因性の損傷と DNA 自身がもつ化学的性質や代謝産物などによって誘発される内因性の損傷が存在する．主要な外的要因としては，電離放射線や紫外線などの物理的変異原のほか，アルキル化剤やクロスリンク剤のような化学的変異原がある．また内的要因としては，活性酸素などの代謝産物に加えて，pH や温度の変化なども DNA 損傷を引き起こす要因となっている．これらの外的および内的要因によって生じる DNA 損傷の代表例として，脱塩基，塩基の脱アミノ化，塩基の互変異性化，アルキル化 DNA 損傷，酸化 DNA 損傷，ピリミジンダイマー，DNA 鎖間の架橋形成，DNA 鎖切断などがある．ここに述べた DNA 損傷の多くはゲノム上のランダムな場所で常に発生しており，DNA 損傷が修復されずにそのまま放置された場合は，遺伝子の突然変異を引き起こす原因となりうる．そのため生物は，これらの DNA 損傷をもとの状態に戻す多様な DNA 損傷修復機構を進化の過程で獲得している（図 13.1）．

近年，さまざまな生物種のゲノム配列を明らかにする，いわゆる“ゲノムプロジェクト”が盛んに行われている．ヒトゲノムは 2004 年までに全塩基配列の決定が終了し，約 30 億塩基対からなるヒトゲノム配列のうち，28.5 億塩基対の配列

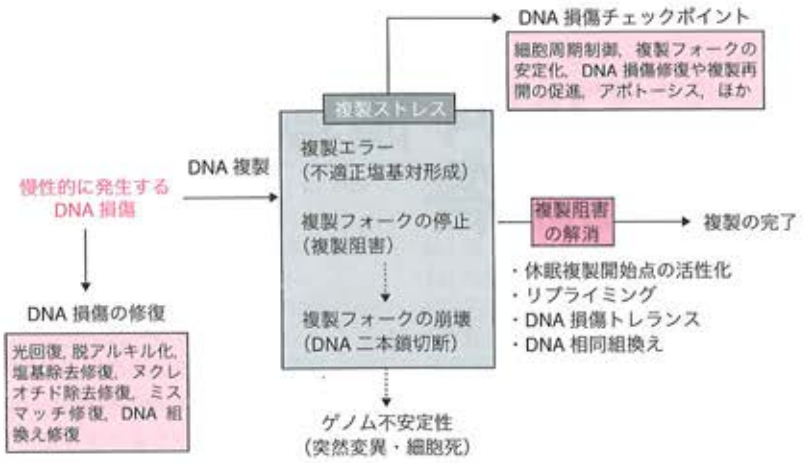

図 13.1　慢性的に発生する DNA 損傷に対処するしくみ

DNA 損傷を慢性的に受け続けるような状況においては，DNA 損傷の修復前に複製フォークが衝突する“複製ストレス”が頻繁に発生している．複製ストレスのなかでも，複製阻害は DNA 損傷チェックポイントの活性化を引き起こす．生物は，複製阻害の原因である DNA 損傷を修復することなく複製阻害を解消するいくつかの機構をもっているが，それがうまく機能しない場合は複製フォークの崩壊による DSB が生じ，ゲノム不安定性が引き起こされる．

が正確に解読されている（残りの未解読部分は短い配列が反復している構成的ヘテロクロマチン領域）[1]．ゲノム配列を解析した結果，タンパク質のアミノ酸情報をコードする領域はゲノム全体の 2%程度であり，それ以外の非コード領域は，散在反復配列（SINE，LINE，LTR など）や縦列反復配列（マイクロサテライトやミニサテライトなど）などの反復配列が全体の半数近くを占めており，その他の非コード領域は，イントロンや未だ配列上からは機能が不明な非反復配列などから構成されていることが明らかとなった．さらに，遺伝子の一部として転写されるイントロンを除く非コード領域を染色体構造の観点から分類すると，染色体の分離に必要な紡錘体が結合するキネトコア（動原体）が形成されるセントロメア，染色体末端部分の保護構造が形成されるテロメア，“残りの非コード領域”に分けることができる．われわれは，このゲノムの大部分を占める“残りの非コード領域”をインターメアと名づけて染色体の構造や機能面における役割に注目している．とくに，ゲノムのランダムな場所で発生する DNA 損傷との関連性に着目すると，ゲノムの大部分を占めるインターメア領域はゲノム安定性維持に重要な役割を果たしていることが考えられる．

ヒトを含む真核生物の DNA は，ヒストンと結合したヌクレオソームを基本単位として，クロマチンと呼ばれる高次構造を形成しており，インターメアを含む非コード領域にある反復配列の大部分は染色体が密に凝集したヘテロクロマチンを形成している．このように，非コード領域は塩基配列やクロマチン構造の両面においてコード領域とは異なった特徴をもっている．なぜこのような大量の非コード領域がヒトゲノム上に存在するか，という疑問に対してはまだ明確な解答は得られていないが，さまざまな生物種のゲノム比較から，ゲノム全長に対するコード領域の割合を示す遺伝子密度が低い（非コード領域の割合が高い）ことと，生命としての複雑さにはある一定の相関性が示されている．

非コード DNA 領域の塩基配列に関しては，反

復配列の回数の変化や塩基レベルの突然変異などが生じた場合でも，その多くが生命機能に影響を及ぼさないことが知られている．実際，哺乳類間で保存されている非コード配列はヒトゲノム全体の 3 ～ 4%程度であり，この値はコード領域の保存性と比べてきわめて低い[2]．このように，非コード領域は突然変異に対して比較的寛容な領域であり，生物種によって配列上の多様性をもつ一方で，高等真核生物の生命機能にとって何らかの利益，たとえばクロマチンを介した広範な染色体制御機能やゲノム安定性の維持などに重要な役割を果たしている可能性が考えられる．

13.1.2　ヘテロクロマチン領域における DNA 損傷応答

ヘテロクロマチンは，その凝集した染色体構造により DNA 修復酵素の損傷部位へのアクセスに対して阻害的に働くため，DNA 損傷の修復が起こりにくい領域と考えられている．実際，非コード領域の一つでありヘテロクロマチンを形成しているヒトのテロメア領域では，紫外線による DNA 損傷の大部分が修復されないまま細胞分裂が起こっていることが示されている[3]．しかしながら，近年，クロマチンモデリング因子やヒストンの翻訳後修飾などを介したクロマチン構造の変化が，染色体上で駆動する複製や転写などのマシナリーの制御に直接的に関与することが示されており，さまざまな DNA 損傷の修復においてもクロマチン構造変換を介するしくみが明らかとなってきている．とりわけ電離放射線などによって生じる DNA 二本鎖切断（DNA double-strand break：DSB）は，一つでも修復されずに残ってしまうと染色体切断による細胞死の原因となるため，ヘテロクロマチンにおいても DSB の修復は必須である．

ヘテロクロマチンで DSB が生じた場合，DSB 末端を認識する MRN 複合体（MRE11/RAD50/NBS1）とともに DNA 損傷チェックポイントキナーゼである ATM が結合する．自己リン酸化により活性化した ATM は，さまざまなタンパク質をリン酸化することで DNA 損傷応答を引き起こすが，そのなかの一つにヘテロクロマチン構成因子で転写の抑制に関与する KAP1（KRAB-associated protein 1）がある．ATM は KAP1 の Ser824 をリン酸化することで KAP1 と CHD3 との結合を阻害するため，CHD3-NuRD ヒストン脱アセチル化酵素複合体がヘテロクロマチンから解離する（図 13.2）[4]．また，DSB に応答したカゼインキナーゼ 2 による HP1β タンパク質のリン酸化は，HP1 のヒストン H3K9me3 からの一時的な解離を促進する．さらに，ヒストンアセチルトランスフェラーゼである Tip60 が H3K9me3 に結合することで ATM やヒストン H4，H2AX のアセチル化を引き起こす（図

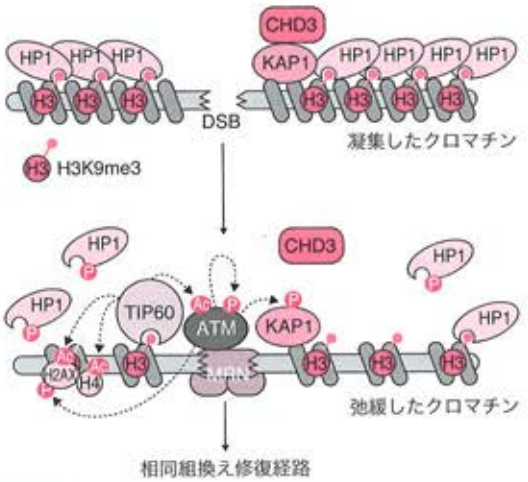

図 13.2　DSB に応答したヘテロクロマチン動態制御機構
DSB がヘテロクロマチン領域に生じた場合は，DSB 末端部周辺において局所的なクロマチンの脱凝縮が起こると考えられる．DSB 末端に結合する MRN 複合体は ATM 損傷チェックポイントキナーゼをリクルートする．そして，ATM によるヘテロクロマチン結合タンパク質である KAP1 のリン酸化や，CK2 による HP1 のリン酸化が起こり，ヘテロクロマチン構成因子が解離する．さらに，TIP60 が ATM やヒストン h4 などのアセチル化を引き起こすことで，クロマチン構造が弛緩し，DNA 組換え修復が促進する．

13.2)[5]．これらの反応はいずれも DSB 周辺のヘテロクロマチンの脱凝縮に関与していることから，DSB 修復の促進に関与していると考えられる．HP1 に関しては DSB 部位に結合するという報告もあり，おそらくいったん解離した後に DSB 部位へ結合することで，DNA 損傷応答に何らかの役割を果たしていることが考えられる．

このように，ヘテロクロマチンはこれまで DNA 損傷修復が起こらない（起こりにくい）領域と考えられてきたが，クロマチン結合因子やヒストン修飾酵素によるクロマチンの構造変換を介した修復システムが存在すると考えられる．

13.2　DNA 複製ストレス応答

13.2.1　DNA 複製ストレスと非コード DNA

DNA 損傷が複製フォークの進行を阻害したり，不適正塩基対の形成を引き起こしたりする“複製ストレス”は，ゲノム不安定性を引き起こす主要な原因である（図 13.1）．複製ストレスによって引き起こされる突然変異が遺伝子のコード領域や発現制御領域で起こった場合は，タンパク質の機能や発現量に影響を及ぼす一方で，非コード領域における突然変異は生命機能に影響を及ぼさない場合が多い．このことは，コード領域上の複製ストレスの発生を抑えることが生命機能の維持にとって重要であることを意味するが，DNA 損傷はランダムな場所で発生するため，コード領域で生じる DNA 損傷の発生のみを低く抑えることは現実的には困難である．しかしながら，一定量の化学変異原が細胞内に存在し，それによって引き起こされる DNA 損傷の数が決まっている場合を想定すると，非コード領域を多くもつゲノムのほうがコード領域に DNA 損傷が発生する確率を減らすという間接的な効果（バッファー効果）が期待できる．つまり非コード領域は，コード領域における突然変異の原因となる DNA 損傷の発生を間接的に抑えることで，ゲノム安定性維持に貢献している可能性が考えられる．

ただし，この仮説にはいくつかの問題が存在する．たとえば，非コード領域の特徴であるヘテロクロマチン構造は DNA 損傷の修復効率を低下させるため，複製ストレスが起こりやすくなることや，非コード領域に多く含まれる反復配列などは，複製ストレスを引き起こす直接的な原因となることが知られている（13.2.2 項）．このように，非コード領域の拡大は複製ストレスのさらなる増加を引き起こすことから，複製ストレスに対処するしくみがゲノム安定性を維持するためにきわめて重要な役割を果たしていると考えられる．

13.2.2　さまざまな DNA 複製ストレス要因

複製ストレスはさまざまな要因によって発生することが知られている．たとえば転写装置との衝突はコード領域における特異的な複製ストレス要因といえる．本節は，非コード領域を含むゲノム全体において，複製ストレスを引き起こす要因について紹介する[6]．

(1) DNA 損傷は複製ストレスを引き起こす主要な要因である

DNA 損傷にはさまざまな修復経路が効率的に働いているが，非コード領域の例にあるように何らかの理由で DNA 損傷修復機構がうまく働かない場合や，修復しきれない量の過剰な DNA 損傷がゲノム上に存在するような場合は，DNA 損傷がゲノム上に蓄積する結果となるため複製ストレスが発生しやすくなる（図 13.3）．さらに，生理的な条件下で生じる DNA 損傷は，微量であってもゲノム上で常に発生しているため，DNA 複製が起こるよりも前にすべての DNA 損傷をあらかじめ修復することは不可能である．したがって，DNA 損傷を慢性的に受け続けるような状況においては，複製ストレスが頻繁に起こっていると考

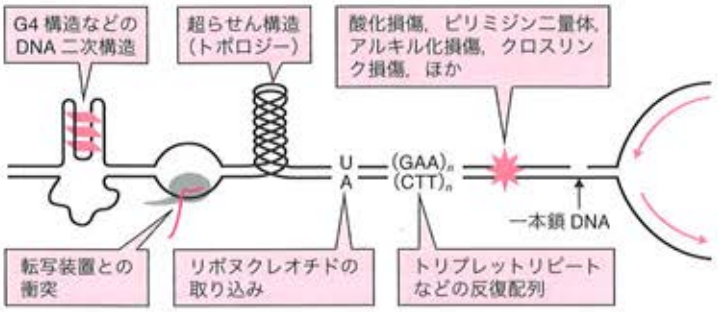

図 13.3　複製ストレスを引き起こすさまざまな要因
DNA 複製フォークの進行を阻害したり，遅めたりする要因にはさまざまなものが存在する．これらの代表例として，DNA 損傷のほか，リボヌクレオチドの取り込み，転写装置との衝突，繰り返し配列，DNA の二次構造やトポロジカルストレスなどがある．

えられる．

(2) DNA 複製に関与するさまざまな因子が複製ストレスを引き起こす原因となる場合

ヒドロキシ尿素（hydroxyurea：HU）は，リボヌクレオチド還元酵素の阻害剤であり，細胞内 dNTP 濃度を低下させるため，S 期において DNA 複製フォークの進行を停止させる作用がある．また，ゲノム複製に関与する DNA ポリメラーゼ δ（デルタ：Polδ）や ε（イプシロン：Polε）は，DNA 合成の際にリボヌクレオチドとデオキシリボヌクレオチドの区別があいまいなため，細胞内リボヌクレオチド濃度が上昇した場合は誤ってリボヌクレオチドを取り込んでしまう．取り込まれたリボヌクレオチドは RNaseH2 により取り除かれるが，取り除かれる前に複製フォークが到達すると複製阻害を引き起こす（図 13.3）．

(3) タンパク質-DNA 複合体が複製フォーク進行の物理的障害となる場合

タンパク質-DNA 複合体のなかには，特定の配列に結合して一方向からの複製フォークのみを強く阻害することで，複製の終結や染色体構造の制御などに利用されているものも存在する．たとえば，大腸菌の Tus タンパク質は，複製開始点のほぼ反対にある *ter* 領域に結合し，一方向からくる DnaB ヘリカーゼのみを阻害することで複製の終結に関与している．また，染色体 DNA と核膜や核内構造体との結合部では，DNA 複製や転写の際に生じるトポロジカルストレスが複製ストレスの原因となる場合も知られている（図 13.3）．

(4) DNA の構造または配列上の特徴が複製ストレスを誘発する原因となる場合

ラギング鎖合成における岡崎フラグメントの形成不全や，不完全な DNA 修復などによって生じる DNA ニックやギャップがゲノム上に存在すると，DNA 複製フォークが通過する際に DSB が生じる（図 13.3）．また，非コード領域において多く存在する反復配列は，DNA 二次構造を形成しやすい特徴をもっており，これらは複製阻害の原因となることが知られている．たとえば，逆方向反復配列によって形成される十字構造は DNA 複製阻害を引き起こし，染色体転座などの原因となることが報告されている．また，3 塩基単位の反復配列（トリプレットリピート）は複製フォークの進行遅延や複製阻害を引き起こし，反復配列の過伸長（expansion）や短縮（contraction）の原因となっている（図 13.3）．これらは，反復配列によってできるヘアピン構造が複製阻害を引き起こすことで，DNA 合成の際に複製スリップが起こりやすくなり，鋳型の一部が重複して合成されたり，部分的に合成されなかったりするためである．

ヒトにおいては，トリプレットリピートの過伸長が疾患の原因となることが知られている．たとえば，*FXN* 遺伝子のイントロンに存

在する GAA/TTC リピートの過伸長は，フリードライヒ運動失調症の発症に関与している．この GAA/TTC リピートを酵母ゲノムに導入した研究から，GAA/TTC リピート上では複製フォークの進行方向（ラギング鎖合成の鋳型が 5′GAA3′ リピートの場合）に依存した複製阻害が引き起こされることや，複製阻害に伴ってリピート配列上で形成されるヘアピン構造をミスマッチ修復酵素が切断することによって DSB が生じ，リピートの過伸長を引き起こすことが示されている[7]．さらに，テロメアやサテライト配列をはじめとするおもに非コード領域に散在している G リッチ配列は，グアニン四重鎖（guanine quadruplex：G4）と呼ばれる DNA 二次構造を形成するため，複製フォークの進行阻害や複製阻害に伴う DSB を引き起こす原因となっている（図 13.3）．

13.2.3　DNA 複製ストレスを解消する三つの機構

真核生物のゲノム複製を担う DNA ポリメラーゼ（Polδ/Polε）は，複製フォークの進行に必要な DNA 二本鎖を巻き戻す Mcm2-7 ヘテロ六量体ヘリカーゼや，DNA クランプの役割を果たしている増殖細胞核抗原（proliferating cell nuclear antigen：PCNA）のほか，さまざまな分子が結合した巨大な複製装置として機能している（図 13.4）．DNA 損傷による複製阻害が生じた場合，DNA ヘリカーゼの進行と DNA ポリメラーゼの停止という脱共役反応により，DNA 損傷より下流に一本鎖 DNA 領域が生じる．このような複製阻害部位において，DNA 損傷の直接的な修復は複製の再開を可能にする一つの方法であるが，巨大な複製装置が損傷部位付近に結合しているため修復酵素が働きにくく，また損傷部位周辺が一本鎖 DNA となっているため，修復酵素が DNA 損傷を認識することが困難であると考えられる（図 13.4）．

このような事態に対処するために，生物は DNA 損傷を残したまま複製阻害の解消を行うことで，複製の完了を保障する複数の機構をもっている（図 13.1）．たとえば DNA 損傷によりラギング鎖の DNA 合成が阻害された場合は，複製フォークの進行が妨げられることはないが，岡崎フラグメントの合成阻害による一本鎖 DNA ギャップが形成される（図 13.5 a）．一方，リーディング鎖の DNA 合成が阻害された場合は，複製フォークの進行阻害が起こる．このような複製阻害の解消には大きく三つの方法が存在し，それぞれが独立した方法で複製の完了を保障している．

一つ目は，真核生物では一つの染色体に複数の複製開始点が存在し，両方向性の DNA 合成を行うため，停止した複製フォークの進行方向に対し

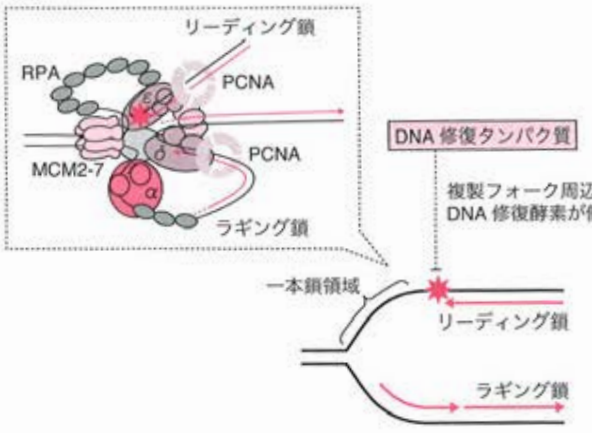

図 13.4　リーディング鎖合成阻害時のフォーク構造
DNA 損傷により複製フォークが停止した場合，DNA 損傷周辺は一本鎖領域となっているため，DNA 修復が起こらない．また，DNA 複製フォークには，複数のタンパク質からなる巨大な複製装置が結合している．そのため，停止した複製フォーク周辺では DNA 修復が起こりにくい．

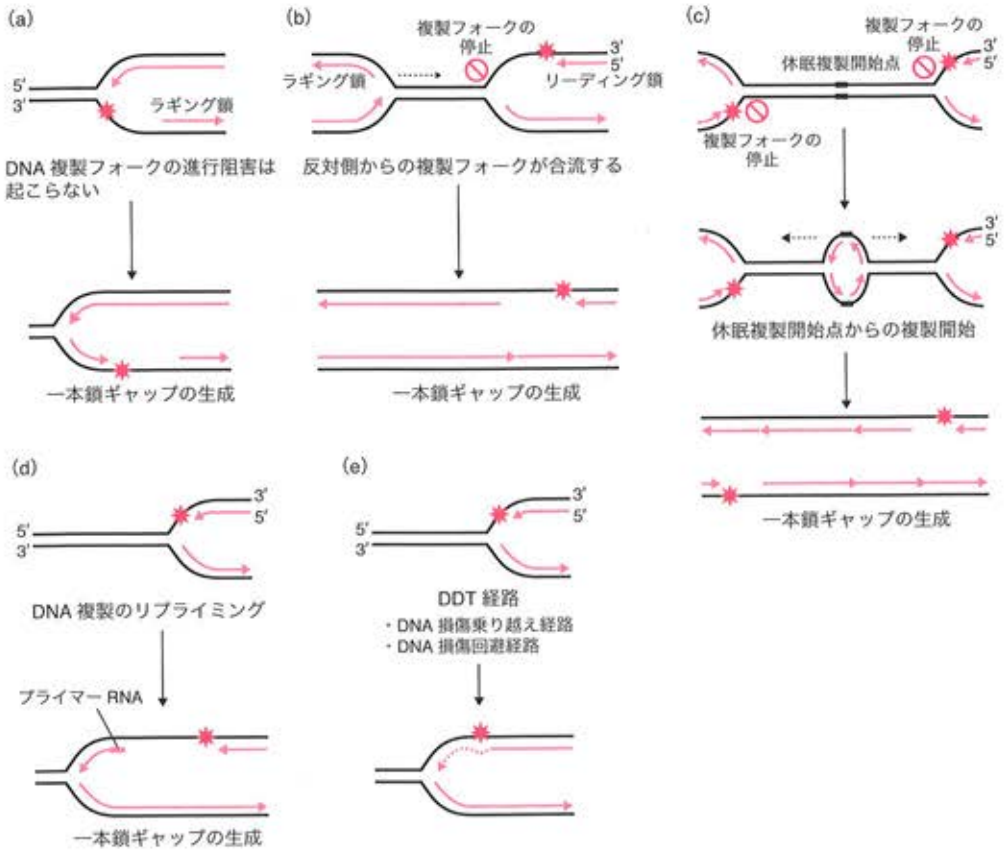

図 13.5　DNA 損傷の修復を伴わない複製ストレスの解消メカニズム

(a) ラギング鎖合成阻害時は，複製フォークの進行阻害は起こらない一方で，岡崎フラグメントの連結が起こらないため，一本鎖ギャップが形成される．(b) 反対方向からくる複製フォークが停止した複製フォークと合流すると，複製阻害が解消する．この場合，損傷部位周辺に一本鎖ギャップが形成される．(c) 休眠複製開始点の活性化による複製阻害の解消．休眠複製開始点が活性化することで未複製部分の合成と複製阻害の解消が起こる．(d) リーディング鎖合成阻害時に阻害部位よりも下流においてリプライミングが起こり，複製が再開される．その結果，不連続なリーディング鎖が合成される．(e) DDT 経路により複製阻害が解消される．ほかの複製阻害の解消とは異なり，複製後に一本鎖ギャップを生じない．

て反対側から複製フォークが到達すると複製阻害部位の解消が起こる機構である（図 13.5 b）．このとき，複製阻害により DNA 合成が停止したリーディング鎖側は，反対側からくる複製フォークのラギング鎖側に相当するため，二つの複製フォークが合流する際に複製阻害部位付近に一本鎖 DNA ギャップ領域が残される（図 13.5 b）．これまでの研究から，ヒトゲノム上で複製ストレスによる DSB が発生しやすい領域（複製脆弱領域）として，複製開始点の数が少なく一つの複製フォークによって長い距離の DNA 合成が必要な領域であることが指摘されている[8]．出芽酵母では，開始点からの複製開始頻度を低下させて一つの複製フォークが合成する距離を長くすると，S 期の遅延や一本鎖 DNA の蓄積，染色体の構造異常等が起こることが知られている．このような複製脆弱領域では，何らかの原因によって複製阻害が生じた場合に反対方向からの複製フォークによる複製ストレスの解消が困難なため，未複製の領域が残されたまま染色体の分離が起こることや，長い時間複製阻害が解消されないことによる複製フォークの崩壊，DNA エンドヌクレアーゼによ

る DSB などが起こりやすいことが考えられる．

真核生物の G1 期のゲノム上には，複製の開始が可能な状態（複製のライセンシング）の複製開始点が実際に複製を開始する数よりも多く存在しており，このような潜在的な開始点は休眠複製開始点（dormant origin）と呼ばれている．休眠複製開始点は，通常の複製開始点からの複製が停止した場合に応答して複製が開始されることが知られており，MCM2-7 の発現レベルを抑制した細胞では，休眠複製開始点からの複製がほとんど起こらないだけでなく，ゲノム不安定性が増大し，発がんとの関連性が示されている[9]．したがって，休眠複製開始点からの複製の開始は，複製開始点間の距離を縮めることで未複製領域の発生を抑えるとともに，ゲノム不安定性の原因となる複製阻害を迅速に解消する機構であると考えられる（図 13.5 c）．

二つ目は，リーディング鎖合成の阻害部位よりも下流において RNA プライマーの合成（リプライミング）が起こり，新規複製フォークの構築により複製阻害が解消される機構である（図 13.5d）．原核生物においては，リーディング鎖合成の停止が起こった場合に，DnaG プライマーゼによる RNA プライミングと複製の再開が複製阻害部位よりも下流で起こり，一本鎖ギャップ領域を残した不連続なリーディング鎖合成が起こることが生化学的に示されている[10]．真核生物においても，これまでにヒトや酵母においてリプライミングによる複製再開が起こっていることを示唆する報告がある[11]．さらに最近の研究から，高等真核生物に存在する PrimPol は紫外線損傷による複製阻害部位において，それ自身がもつプライマーゼ活性によって紫外線損傷部位よりも下流にリプライミングを行うことで損傷部位をバイパスする DNA 合成活性をもつことが明らかになっている[12]．

三つ目は，DNA 損傷トレランス（DNA damage tolerance：DDT）と呼ばれる停止した複製フォークの再開を行う機構である（図 13.5 e）．DDT 経路は大きく分けて二つのサブ経路が存在し，それぞれ損傷乗り越え型 DNA 合成（translesion DNA synthesis：TLS）経路と，DNA 損傷回避（DNA damage avoidance）またはテンプレートスイッチ（template switch）経路と呼ばれている．ここでは，13.3.3 項で述べるテンプレートスイッチと区別するため DNA 損傷回避経路と呼ぶ．TLS 経路は，生存に非必須な複数種の DNA ポリメラーゼ（TLS ポリメラーゼ）が関与している．TLS ポリメラーゼは，損傷塩基を鋳型として DNA 合成を行うことができる一方で，DNA 複製忠実度が非常に低く，校正エクソヌクレアーゼ活性をもっていない．したがって，DNA 損傷部位の乗り越えの際に誤った塩基を挿入する場合があり，突然変異を起こす原因となっている．一方 DNA 損傷回避経路は，DNA 損傷によって合成を停止した新生鎖が一時的に無傷の姉妹染色体を鋳型として DNA 合成を行う経路であり，DNA 損傷部位を直接的に乗り越えないため，誤りのない損傷バイパスが可能である．いずれの経路においても，複製阻害の解消後に一本鎖 DNA は生じない．

13.3　DDT 経路の分子メカニズム

13.3.1　DDT 経路の活性化

DDT 経路において中心的な働きをする Rad18 は，RING ドメインをもつユビキチン（ubiquitin：Ub）リガーゼ（E3）であり，Ub 結合酵素（E2）の Rad6 と安定な複合体を形成している．Rad18 は，PCNA や一本鎖結合タンパク質である RPA との相互作用のほか，DNA 結合活性をもつため，これらの結合を介して複製阻害部位へリクルートされると考えられている．Rad6-Rad18 複合体は PCNA Lys164 のモノ Ub 化修飾に関

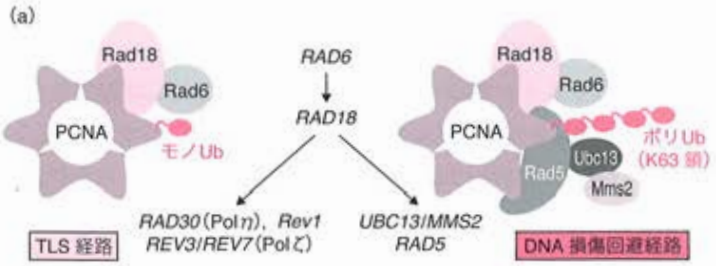

図 13.6　DDT 経路と PCNA のユビキチン化制御

Rad6-Rad18 複合体は，複製阻害に応答した PCNA のモノ Ub 化修飾に関与しており，TLS 経路の活性化を引き起こす．一方，Rad6-Rad18 に Mms2-Ubc13 と Rad5 が働くと，PCNA のポリ Ub 化修飾が起こる．ポリ Ub 化修飾が起こると DNA 損傷回避経路と呼ばれる複製阻害のバイパス経路が活性化する．

(b) DDT 経路関連タンパク質

出芽酵母	ヒト	機　能
Rad6	HHR6A, HHR6B	Ub 結合酵素 (E2)
Rad18	RAD18	Ub リガーゼ (E3)
Ubc13	UBC13	Ub 結合酵素 (E2)
Mms2	MMS2	E2 バリアント
Rad5	HLTF, SHPRH	Ub リガーゼおよび SWI/SNF2 型ヘリカーゼ
Rev1, Polζ, Polη	Rev1, Polζ, Polη, Polκ, Polι, ほか	TLS ポリメラーゼ
PCNA	PCNA	DNA クランプ，K164 が Ub 化される

与し，Rad6-Rad18 に加えて Ubc13-Mms2 (E2) と Rad5 (E3) が働くと，Ub の 63 番目のリシン残基を介した PCNA Lys164 のポリ Ub 化修飾が起こることが示されている[13] (図 13.6)．モノ Ub 化およびポリ Ub 化修飾された PCNA は，それぞれ TLS 経路と DNA 損傷回避経路の活性化に関与している．Ubc13-Mms2 複合体はともに Ub 結合酵素 (E2) に類似した構造をもつが，Ubc13 のみが E2 活性をもっている．Rad5 は Swi-Snf2 型 ATPase および RING ドメインをもつ Ub リガーゼであり，Rad18 および Ubc13 と相互作用することから，PCNA のポリ Ub 化修飾に関わる因子の複合体形成に重要な役割を果たしている (図 13.6)．ヒトにおいても PCNA の Ub 化修飾は観察されており，Rad6，Rad18 のほかに，酵母 Ubc13-Mms2 ホモログとして UBC13-MMS2，Rad5 ホモログとして HLTF と SHPRH が同定されている (図 13.6)．

13.3.2　TLS 経路

TLS 経路は DNA 損傷ストレス耐性において重要な役割を果たしている一方で，DNA 損傷時に起こる突然変異誘発の主要な原因ともなっているため，TLS 経路の制御はゲノム安定性の維持にとって重要である．TLS 経路では，ゲノム複製型 DNA ポリメラーゼに代わって TLS ポリメラーゼが損傷部位の乗り越え合成を行うことにより，複製阻害の解消が行われる (図 13.7)．出芽酵母の TLS ポリメラーゼには，Y-family に属する Polη (イータ) と Rev1，および B-family に属する Polζ (ゼータ) の 3 種類が存在する (図 13.6)．ヒトでは，さらに多くの TLS ポリメラーゼが同定されており，そのなかで Polη，Polι (イオタ)，Polκ (カッパ)，Rev1 が Y-family DNA ポリメラーゼに属している．

これまでの研究から，TLS 経路に属する Y-family DNA ポリメラーゼの複製阻害部位へのリクルートには PCNA のモノ Ub 化修飾が促進的な働きをしていることがわかっている．これらのポリメラーゼには PCNA と結合する PIP-box のほか，Ub と結合する UBZ (ubiquitin-binding zinc finger) や UBM (ubiquitin-binding motif) などのモチーフが存在し，モノ Ub 化 PCNA への結合に関与している．B-family に属する Pol

ζはUb結合モチーフをもたないが，Rev1タンパク質との相互作用によって複製阻害部位へリクルートされることがわかっている．TLSポリメラーゼは，鋳型の損傷塩基に対合する塩基を挿入後，それ自身または別のTLSポリメラーゼによってDNAの伸長合成が行われる．Polζは，末端部にミスマッチの塩基対をもつプライマーからのDNA合成を行うことができるため，ほかのTLSポリメラーゼによる損傷乗り越え合成後のDNA伸長反応を担うことが可能である．

TLSポリメラーゼが複数存在する理由としては，損傷の種類に応じてTLSポリメラーゼを使い分けていると考えられている．実際，多くのTLSポリメラーゼは，それぞれ特異的な損傷塩基に対するTLS活性をもっており，どのTLSポリメラーゼが関与するかによって損傷バイパス時の正確性の程度に影響を与えている．たとえば，劣性の遺伝病である色素性乾皮症のバリアント群（xeroderma pigmentosum variant：XPV）の責任遺伝子産物として同定されたPolηは，少なくとも紫外線によって生じるチミンダイマーのような損傷塩基に対しては，正しい塩基（二つのアデニン）を対合させることができるため，エラーフリーの働きをしている[14]．一方，Polζは誤りがちな損傷バイパス活性をもち，出芽酵母においては，紫外線やアルキル化剤などによって誘発する突然変異の大部分はPolζに依存している．

TLS経路の制御に関しては，複数のTLSポリメラーゼがモノUb化PCNAと結合できることや，ヒトの場合ではPCNAモノUb化修飾はTLS活性に重要ではあるが必須ではないといった報告もあり，生体内でこれらのTLSポリメラーゼがどのように使い分けられているかについては，まだ不明な点が多い．しかしながら，最近の研究からTLS経路の制御にかかわる新規のタンパク質がいくつか報告されている．たとえば，ヒトのUb結合タンパク質であるSprtanは，モノUb化PCNAとの相互作用により複製阻害部位にリクルートされ，PCNAのモノUb化修飾やポリメラーゼスイッチなどの促進などに働くことでTLSポリメラーゼの制御に関与することが示された[15]．また，PAF15はS期にUb化修飾されてPCNAと結合しており，複製ストレス時に起こるPAF15の脱Ub化によってPCNAから解離するとPolηによる損傷バイパスが活性化することが示されている．さらに，PCNAのUb化修飾は可逆的な反応であり，ヒトのPCNA脱Ub化酵素であるUSP1は紫外線照射後にプロテアソームにより分解されることが知られている．このように，DNA損傷に対する耐性獲得とともに突然変異の誘発に関与するTLSポリメラーゼは，さまざまな制御因子やUb化修飾の制御によって複雑かつ厳密に制御されている．

13.3.3　DNA損傷回避経路

DNA損傷回避経路は，PCNAのポリUb化修飾に依存して起こることが知られているが，現在までにポリUb化修飾の役割については明らかになっていない．一つの可能性として，PCNAのポリUb化修飾はモノUb化修飾を抑えることでTLS経路の抑制に関与していることが考えられている．一方，最近のヒト細胞を用いた研究から，SNF2ファミリーに属するZEANB3がポリUb化PCNAに結合し，停止した複製の再開に関与することが示された[16]．このように，まだ詳細なメカニズムは不明だが，ポリUb化修飾は単なるTLS経路の抑制だけではなく，ほかの因子の結合を介してDNA損傷回避経路の促進に直接的に関与していることが考えられる．

停止した複製フォークの新生鎖がどのようにして姉妹染色体を鋳型としてDNA合成を行うかについては，これまでの研究から大きく二つのモデル（テンプレートスイッチおよびフォーク退行）が示されている．前者のテンプレートスイッ

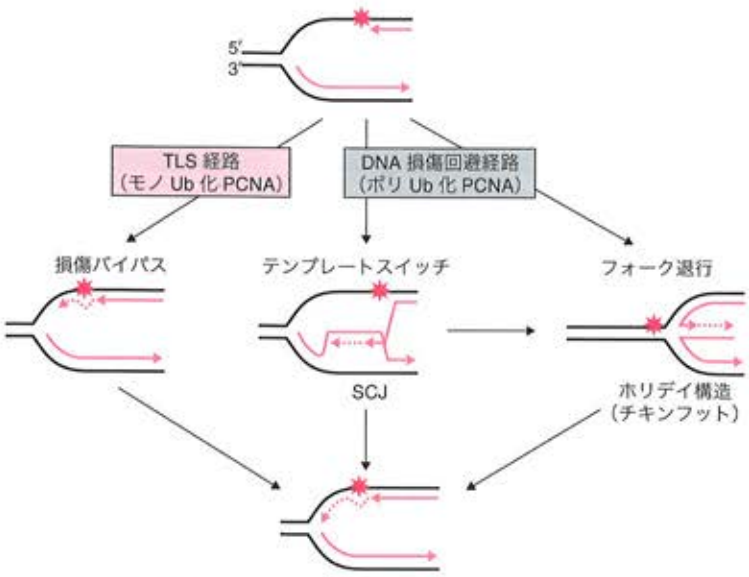

図 13.7　DDT 経路による複製阻害の解消メカニズム

TLS 経路は，TLS ポリメラーゼによる直接的な損傷部位の乗り越え合成が行われる．テンプレートスイッチとフォーク退行反応の違いは新生鎖を利用した初期反応が異なっており，新生鎖が鎖交換反応によって姉妹染色体に侵入し，SCJ 構造をつくるのがテンプレートスイッチ反応であり，新生鎖同士のアニーリングによってホリデイ構造をつくるのがフォーク退行反応である．テンプレートスイッチにおいて，姉妹染色体を鋳型とした修復合成が末端部分まで進行するとフォーク退行反応と同一のホリデイ構造が形成される．点線部分は新規の DNA 合成を示す．

チモデルでは，合成を停止している新生リーディング鎖の 3′ 末端が姉妹染色体の相同領域に侵入し，姉妹染色体を鋳型として DNA 合成が行われることで姉妹染色体間接合体（sister chromatid junction：SCJ）が形成される（図 13.7）．後者のフォーク退行モデルでは，複製フォーク付近の鋳型鎖が部分的に逆方向に巻き戻ることで新生リーディング／ラギング鎖間のアニーリングが起こり，ホリデイ構造またはチキンフット構造（鶏の足に似ている）と呼ばれる DNA 四本鎖による十字構造が形成され，そこで DNA の合成や修復が行われる（図 13.7）．いずれの場合も，その後に SCJ またはホリデイ構造が解消されることで損傷塩基箇所の乗り越えが完了する．

複製阻害に伴うホリデイ構造の形成に関しては，電子顕微鏡観察から，出芽酵母の DNA 損傷チェックポイントの欠損株やトポイソメラーゼ阻害剤の存在下のほか，ヒトの GAA リピート領域などで生じる複製阻害部位において観察されている．さらに，DNA 損傷回避経路に属する出芽酵母 Rad5 やヒト HLTF は，それらがもつ DNA ヘリカーゼおよびアニーリング活性によってフォーク退行反応を促進することが *in vitro* で示されている[17]．一方，複製阻害部位のフォーク構造を詳細に解析できる二次元電気泳動を用いた研究から，Rad18 や Rad5 依存的に SCJ 構造がつくられることが示されている[18]．このように，これまでの研究では，いずれか一方のモデルを支持するというよりは，むしろいずれの反応も複製阻害の解消に働いている可能性を示している．

13.3.4　複製後修復（一本鎖ギャップ修復）

生物は複数の複製阻害の解消方法をもっており，これらは複製の完了を保障する一方で，DDT 経

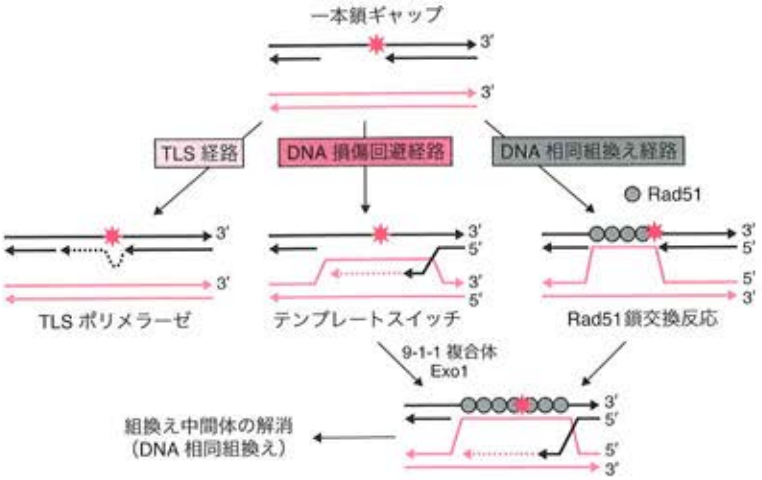

図 13.8　複製後修復(複製後に生じる一本鎖ギャップの修復機構)
一本鎖ギャップ DNA は，TLS ポリメラーゼによるギャップ領域の修復合成のほか，テンプレートスイッチまたは DNA 相同組換えによる姉妹染色体を鋳型とした修復が行われる．テンプレートスイッチおよび DNA 相同組換えによる組換え中間体形成後は，おそらく相同組換え後期過程に働く DNA ヘリカーゼやヌクレアーゼによって中間体が解消されると考えられる．

路を除くといずれも複製阻害の解消が起こった付近に一本鎖ギャップ領域が残る．複製後修復(post-replication repair：PRR) 経路という名称は，もともと DDT 経路と同義的につかわれていたが，現在では複製後にできる一本鎖ギャップの修復と定義するほうがより生理的な現象を反映している．一本鎖 DNA には RPA が全体を覆うように結合しており，これにより RPA と相互作用する相同組換えタンパク質の Rad52 が一本鎖 DNA 領域にリクルートされる．Rad52 は，DNA 鎖交換反応を触媒する Rad51 のヌクレオフィラメント形成を促進し，その結果，Rad51 に依存した姉妹染色分体間の鎖交換反応が起こる．その後，修復 DNA 合成と組換え中間体の解消によって一本鎖ギャップの修復が完了する (図 13.8)．最近の研究から，DDT 経路は停止した複製フォークの直接的な再開に加えて，PRR にも関与していることが示されている[22]．とくに，テンプレートスイッチによる一本鎖ギャップ修復では，これまで別経路で働くと考えられていた Rad51 や，DNA 損傷チェックポイントに関与する 9-1-1 (RAD9/HUS1/RAD1) 複合体と Exo1 が必要であることが示されている (図 13.8)[18,23]．この 9-1-1 複合体の働きは，DNA 損傷チェックポイントとは異なっており，おそらく一本鎖ギャップ領域の安定化や Exo1 による一本鎖領域の拡大などに関与していることが考えられている．このように PRR に複数の経路が関与する理由としては，一本鎖ギャップ領域周辺の構造または配列が複製阻害要因によって異なっているため，状況に応じて TLS やテンプレートスイッチ，相同組換えのなかから選択されていると考えられるが，詳細については現時点では不明である．

13.4　おわりに

人はさまざまなストレスに直面したとき，ストレスの原因を取り除く“厳密性”と，ストレスを受け流す“寛容性”を使い分けてストレスに対する耐性を獲得している．これをゲノムに置き換

えると，コード領域はDNA損傷ストレスに対して突然変異を許さない厳密性を要求し，非コード領域のなかでもとくにインターメアはある程度の突然変異を許す寛容性をもつ領域といえる．この寛容性を生みだすメカニズムが，今回紹介したDNA損傷トレランスをはじめとする複製阻害の解消機構である．このような機構が働くことにより，インターメア領域ではDNA損傷をすべて修復する労力(エネルギーの無駄使い)から解放されるだけでなく，複製されない部分が残ってしまうような，より重篤な染色体レベルの異常を引き起こすリスクを回避していると考えられる．つまり，ゲノムに大量のインターメア領域を保持するヒトを含めた生物にとっては，この複製の完了を保障する機構がきわめて重要な役割を果たしていると考えられる．

今後の研究で，インターメア領域を大量にもつことがコード領域の厳密性に及ぼす影響や，インターメア領域のDNA損傷に対する寛容性が染色体安定性に及ぼす影響などについて，明らかになることを期待したい．

(菱田　卓)

文　献

1) International Human Genome Sequencing Consortium, *Nature*, **431**, 931 (2004).
2) T. S. Mikkelsen et al., *Nature*, **447**, 167 (2007).
3) P. J. Rochette, D. E. Brash, *PLoS Genetics*, **6**, e1000926 (2010).
4) A. A. Goodarzi et al., *Nat. Struct. Mol. Biol.*, **18**, 831 (2011).
5) T. Ikura et al., *Mol. Cell Biol.*, **27**, 7028 (2007).
6) M. K. Zeman, K. A. Cimprich, *Nat. Cell Biol.*, **16**, 2 (2014).
7) A. A. Shishkin et al,. *Mol. Cell*, **35**, 82 (2009).
8) A. Letessier et al., *Nature*, **470**, 120 (2011).
9) J. J. Blow et al., *Trends Biochem. Sci.*, **36**, 405 (2011).
10) R. C. Heller, K. J. Marians, *Nature*, **439**, 557 (2006).
11) I. Elvers et al., *Nucleic Acids Res.*, **39**, 7049 (2011).
12) T. Helleday, *Nat. Struct. Mol. Biol.*, **20**, 1348 (2013).
13) C. Hoege et al., *Nature*, **419**, 135 (2002).
14) C. Masutani et al., *Nature*, **399**, 700 (1999).
15) R. C. Centore et al., *Mol. Cell*, **46**, 625 (2012).
16) C. Alberto et al., *Mol. Cell*, **47**, 396 (2012).
17) A. Blastyák et al., *Mol. Cell*, **28**, 167 (2007).
18) B. Dana et al., *Nature*, **456**, 915 (2008).
19) B. Pfander et al., *Nature*, **436**, 428 (2005).
20) H. Gali et al., *Nucleic Acids Res.*, **40**, 6049 (2012).
21) G. L. Moldovan et al., *Mol. Cell*, **45**, 75 (2012).
22) G. I. Karras, S. Jentsch, *Cell*, **141**, 255 (2010).
23) G. I. Karras et al., *Mol. Cell*, **49**, 536 (2013).

細胞死耐性の分子メカニズムの解析

教授　安達　卓
助教　谷口喜一郎

[目的]

一般に、アポトーシスという細胞死現象の発見は、1972 年の Kerr 夫妻（Scotland）によるものとされている。しかしながら、放射線によって導かれる細胞死は、典型的なアポトーシスでありながら、その発見は 100 年以上も前のことであり、様々な動物組織の間でその応答に差があることが研究されていた。例えば、分裂頻度が高く、分化レベルが浅く、再生能力の高い組織（即ち、現在で言う組織幹細胞をもつ再生組織）では、この細胞死は容易に誘導されるが、逆に非再生系組織の倍数化細胞やがん組織にある増殖細胞などでは誘導されなくなるという性質は、広く多細胞動物一般に認められ、Bergonie-Tribondeau の法則として 1906 年に報告されたものである。しかし、これを説明する分子メカニズムについては、現在でも十分に解明できてはいない（参考文献１、２）。この仕組みの解明は、単に放射線に対する防御能を知るのみならず、原子力発電等の放射線を利用した諸技術の発展に伴って必要となるもので、また近年展開されるガンの放射線治療を改良する際にも、重要な情報を与えると考えられ、社会的にも大きな意義をもつ研究であると推察される。本研究では、遺伝的解析に優れたモデル生物であるショウジョウバエを用い、前立腺相同の非再生系生殖器官である附属腺に焦点をあてて、そこに自然に生じている、分化細胞の細胞死耐性の分子メカニズムを明らかにすることを目的とした。

[結果と考察]

ショウジョウバエのオス成虫がもつ内部生殖器官の一つ、附属腺は、幹細胞をもたない非再生組織であり、一旦生じた分化細胞は、生涯にわたって長く維持される必要がある。そのために、これらの細胞では、各種の細胞死誘導性刺激に対し抵抗性が生じていることが期待された。そこで、エックス線照射（DNA 損傷）・パラコート投与（活性酸素上昇）・reaper 遺伝子強制発現（Initiator Caspase 活性化）・Dcp-1 遺伝子強制発現（effector Caspase 活性化）など、様々な細胞死誘導性刺激を与えて細胞死応答を調べ、再生系組織における応答との比較を行った。その結果、これらいずれの刺激を与えても、再生系組織では細胞死が誘導されたが、附属腺細胞においては、エックス線照射・パラコート投与・reaper 遺伝子強制発現では、予想どおり顕著な抵抗性を見せて細胞死が誘導されなかったものの、Dcp-1 遺伝子強制発現のみが細胞死を誘導できることが分かった。従って、細胞死抵抗性は細胞死誘導経路の中では、effector Caspase 上流で生じることが推察された（図１）。

そこで、ショウジョウバエにおける２種の effector Caspase パラログである、Dcp-1 と Drice について、内在性の遺伝子発現量を、翅原基（再生組織）におけるそれと比較した。その結果、Dcp-1 では顕著に、Drice においても一定程度の発現量の低下を観察することができ、これらの発現抑制が、この組織における細胞死耐性の一因であることが予測された。

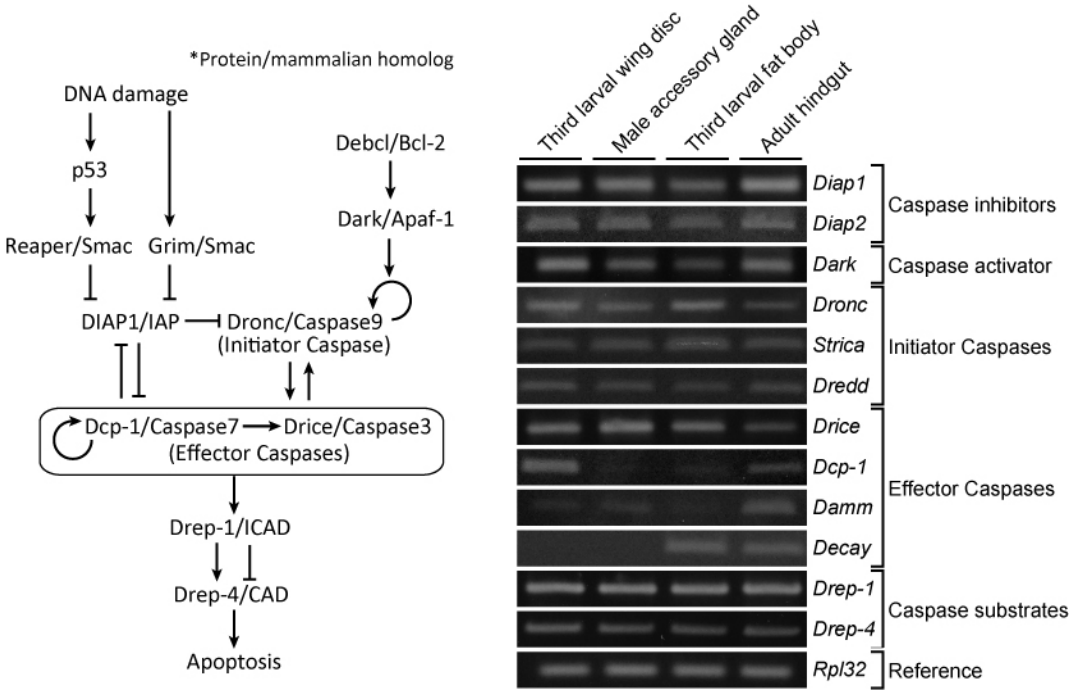

図1.　　一般に知られているアポトーシスの誘導経路（左）、および各因子の各組織における発現を RT-PCR で検出した実験結果（右）

ショウジョウバエにおいて細胞死耐性を見せる組織は、成虫にある附属腺だけではなく、幼虫における唾液腺・脂肪体・消化管や、成虫における後腸などが、その性質を見せる。これら様々な組織における細胞死耐性が共通したメカニズムによってもたらされているかどうか調べるために、まず reaper 遺伝子強制発現による細胞死誘導性を確認したところ、附属腺細胞と同様に、細胞死を誘導することはできなかった。よってその耐性の制御点も、附属腺細胞と同様に、initiator Caspase の下流である。そこで次に、Dcp-1 の強制発現による効果を検証したところ、幼虫脂肪体では附属腺細胞と同様に細胞死が誘導されたが、成虫後腸では附属腺細胞とは異なり、依然として細胞死耐性を見せ続けた。従って、この組織における細胞死耐性制御点は effector Caspase よりさらに下流にあるか、また独立の経路において存在していると予測された。実際、遺伝子発現量を調べると、幼虫脂肪体や成虫後腸においても、Dcp-1 の明瞭な発現低下が認められるのに加えて、成虫後腸ではもう一つの effector Caspase である Drice や Initiator Caspase である Dronc、また effector Caspase 下流の CAD (Caspase-Activated DNase)などの発現も低く、また幼虫脂肪体では、Apf-1（アポプトソーム構成因子）の発現量が特異的に低いなどの特徴が認められた。

これらの知見を総合すると、個体の内部で様々な組織が見せる細胞死耐性は、effector Caspase の発現量低下という共通した性質が基盤にある一方で、各組織で独自の遺伝子の発現が抑えられるという多様化した仕組みと組み合わされて成り立っていることが明らかとなった。なお、これらの遺伝子発現量調節が、ヒストンのメチル化状況や microRNA によって影響を受けている訳ではないことを、これらの各現象に関わる遺伝子である dUTX（ヒストン脱メチル化酵素）や Drosha（miRNA プロセシング RNase）のノックダウンによって検証済みである。

一方、Dcp-1 遺伝子のシス調節領域にあるエンハンサー／サイレンサーを介したシンプルな転写調節が、これらの細胞死耐性組織における Dcp-1 発現低下を招いているのかどうかを知るために、Dcp-1 遺伝子の 5'非翻訳領域にリポーター遺伝子 lacZ が挿入されたショウジョウバエ系統 P{PZ}dcp-1[02131]を用い、その lacZ 発現を調べた。その結果、オス成虫附属腺・幼虫脂肪体・成虫後腸のいずれにおいても翅原基より低い発現量が観察された。

さらに、もう一つの effector Caspase である Drice のエンハンサー／プロモーター制御下で、成虫附属腺や幼虫脂肪体において低レベルで Dcp-1 遺伝子を発現する形質転換系統、Drice-Dcp-1 を作成し、その個体において細胞死誘導が起き得るかどうかについて調べている。現在までのところ、エックス線照射による細胞死誘導は、成虫附属腺・幼虫脂肪体・成虫後腸のいずれにおいても認められなかった。しかし、これは細胞死抑制の原因が Dcp-1 にはないことを直ちに示すものではないと考えられる。なぜなら、これらの組織においては DNA 損傷と reaper 遺伝子発現誘導の間を介在する p53 遺伝子の発現が抑制されていることが知られ、このために、下流の Caspase 経路を活性化することが出来なくなっていると考えられる。そこで今後さらに、この Drice-Dcp-1 バックグラウンドにおいて、reaper 遺伝子を強制発現させて細胞死が誘導されるかどうかを確認することで、Dcp-1 発現量低下が細胞死耐性獲得の主要な原因であることを明確にしたいと考えている（谷口ら未発表）。

以上に加えて、この研究と密接に関連する３つの研究を、並行して進めている。一つは、附属腺細胞の老化細胞死に関するものである。上述のように、附属腺細胞はストレス性の刺激に対する細胞死応答を起こし難いが、老化が極度に進んだ時には、機能破綻した一部の細胞が細胞死に向かう（谷口ら未発表）。この際にどのような分子メカニズムが働くのかについて調べているが、その過程で、附属腺としてのマスターコントロール遺伝子である Paired（ホメオドメイン含有タンパク質）を初めとした様々な因子の発現量が減少する上、３種類の細胞内シグナルが同時に働くことで、細胞死耐性を解除していることが判明した（谷口ら未発表）。この研究過程では、老化した附属腺と若齢の附属腺との間に認められる遺伝子発現量の差の網羅的な解析を、次世代シーケンサーを用いた RNA-seq より行った。これにより判明した発現量が低下する数十個の遺伝子については、細胞死耐性をもたらす責任候補遺伝子として位置づけて、各遺伝子の RNAi に基づく老化細胞死検定を進めて、幾つかの重要な遺伝子が絞り込まれるに至っている。ここまでの経過においては、本助成金により購入されたキーエンス社デジタルマイクロスコープ VHX-2000 が効力を発揮し、細胞死検定を迅速に進めることができた。

他の関連する研究として、倍数化によって附属腺に類似した細胞死抑制を見せる消化管細胞において、マスターコントロール遺伝子 GATAe の発現抑制が示す表現型を調べている（参考文献３）。眼の発生におけるマスターコントロール遺伝子 Pax6 に関する初期の研究で良く知られるように、マスターコントロール遺伝子の発現消失は一般に細胞死を起こし、ホメオティック遺伝子の発現消失が、細胞分化タイプの転換を起こすのとは対照的である（参考文献４）。附属腺と消化管のどちらにおいても、マスターコントロール遺伝子の発現が失われ、器官のアイデンティティを失った際の応答には、共通の仕組みが予想される。

ショウジョウバエのオス成虫附属腺は、それを構成している上皮組織の細胞のすべてが、常に核を２つずつもつという珍しい特徴をもっている。我々は、その２核化のメカニズムについても研究を進めてきたが（参考文献５）、通常の細胞分裂時には、分裂細胞は上皮層から頂端側へ逸脱して分裂するが、附属腺において細胞質分裂を伴わない核分裂が起きる際には、核分裂細胞は上皮層から逸脱することなく、隣接した上皮細胞と細胞側面を接着させたまま、核が頂端基底方向に分かれることが分かった。この事実が意味していることは、通常の増殖組織では比較的自由に ON/OFF 制御されている細胞間接着が、附属腺では OFF することが困難な状態にあると考えられる。すると、アポトーシスの際に、周辺細胞やマクロファージが貪食するために生じるアポトーシス小体などへの細胞形態変化も、困難になっている状態が考えられる。実際、附属腺細胞が極度に老化した時に起きる老化細胞死においても、細胞はアポトーシス小体を作ることなく、そのままの形で内部の消化が進む。一方、アポトーシスの過程は、周囲の細胞が貪食しないと進行しないことが知られていて（参考文献６）、これら一連の事実により、附属腺細胞はアポトーシスを起こせないようになっているという仕組みも考えられる。

[まとめ]

以上のように、附属腺のもつ細胞死耐性がどのような仕組によるのか明らかにしてきた。その基本として、effector Caspase の発現抑制のように共通した仕組みがあるのに加えて、各耐性組織に固有の遺伝子発現抑制が組み合わされている。また、老化が進んだ状況では、マスターコントロール遺伝子ほかの遺伝子発現低下に加え、平常時には働かない３種類の細胞内シグナルが働くことにより細胞死耐性が解除され、細胞死へ向かうことが分かった。

[参考文献]

1. Mehrotra, S., Maqbool, S. B., Kolpakas, A., Murnen, K., and Calvi, B. R. .Endocycling cells do not apoptose in response to DNA rereplication genotoxic stress. Genes Dev., 22: 3158-3171 (2008).
2. Hassel, C., Zhang, B., Dixon, M., and Calvi, B. R. Induction of endocycles represses apoptosis independently of differentiation and predisposes cells to genome instability. Development 141: 112-123 (2014).
3. Okumura, T., Takeda, K., Kuchiki, M., Akaishi, M., Taniguchi, K., and Adachi-Yamada, T. GATAe regulates intestinal stem cell maintenance and differentiation in Drosophila adult midgut. Dev. Biol., 410: 24-35 (2016).
4. Takemura, M. and Adachi-Yamada, T. Repair responses to abnormalities in morphogen activity gradient. Dev. Growth Differ., 53: 161-167 (2011).
5. Taniguchi, K., Kokuryo, A., Imano, T., Minami, R., Nakagoshi H., and Adachi-Yamada, T. Isoform-specific functions of Mud/NuMA mediate binucleation of Drosophila male accessory gland cells. BMC Dev. Biol., 14: 46 (2014).
6. Li, W. and Baker, N. E. Engulfment is required for cell competition. Cell, 129: 1215-1225 (2007).

［原著論文］

1. Okumura, T., Takeda, K., Taniguchi, K. and Adachi-Yamada, T. βv integrin inhibits chronic and high level activation of JNK to repress senescence phenotypes in Drosophila adult midgut. PLoS One, 9, e89387 (2014).

2. Taniguchi, K., Kokuryo, A., Imano, T., Minami, R., Nakagoshi H., and Adachi-Yamada, T. Isoform-specific functions of Mud/NuMA mediate binucleation of Drosophila male accessory gland cells. BMC Dev. Biol., 14: 46 (2014).

3. Okumura, T., Takeda, K., Kuchiki, M., Akaishi, M., Taniguchi, K., and Adachi-Yamada, T. GATAe regulates intestinal stem cell maintenance and differentiation in Drosophila adult midgut. Dev. Biol., 410: 24-35 (2016).

[総説等]

1. Takemura, M. and Adachi-Yamada, T. “Apoptosis during cellular pattern formation” in Apoptosis, InTech (2013).

［口頭発表］

【国外学会】

1. Analysis of βv integrin mutant showing a premature aging phenotype in Drosophila adult midgut
   奥村高志, 武田晃司, 谷口喜一郎, 安達卓
   55rd Annual Drosophila Research Conference (2014.3.26-30, アメリカ, サンディエゴ)
2. Isoform-specific functions of Mud/NuMA mediate binucleation of Drosophila male accessory gland cells
   谷口喜一郎, 國領顯彦, 今野貴夫, 南竜之介, 中越英樹, 安達卓
   55rd Annual Drosophila Research Conference (2014.3.26-30, アメリカ, サンディエゴ)
3. Cytokinesis-deficient binucleation in Drosophila accessory gland for providing plasticity of organ size
   谷口喜一郎, 國領顯彦, 今野貴夫, 坂田瑠美, 南竜之介, 中越英樹, 安達卓
   BSCB/BSDB/JSDB Joint Spring Meeting 2012 (2012.4.15-18, イギリス, コヴェントリ)
4. The tissue-specific integrin, βvintegrin, is required for proper proliferation of intestinal stem cells in the Drosophila adult midgut
   奥村高志, 安達卓

BSCB/BSDB/JSDB Joint Spring Meeting 2012 (2012.4.15-18, イギリス, コヴェントリ)

5. Cytokinesis-deficient binucleation in Drosophila accessory gland for providing plasticity of organ size
   谷口喜一郎, 國領顯彦, 今野貴夫, 坂田瑠美, 南竜之介, 中越英樹, 安達卓
   53rd Annual Drosophila Research Conference (2012.3.7-11, アメリカ, シカゴ)

【国内学会】

1. ショウジョウバエ中腸から分泌されるホルモンによる寿命制御
   武田晃司, 奥村高志, 山口未音, 朽木めぐみ, 谷口喜一郎, 安達卓
   第38回日本分子生物学会年会・第88回日本生化学会大会合同大会（2015.12.1-4, 神戸）
2. ショウジョウバエ雄蛹期附属腺における二核化とcell cycle arrestの関係
   越田惠子, 谷口喜一郎, 岡田朋也, 中越英樹, 安達卓
   第38回日本分子生物学会年会・第88回日本生化学会大会合同大会（2015.12.1-4, 神戸）
3. ショウジョウバエ雄附属腺の細胞二核化におけるDppシグナルの関与
   若松憲之, 谷口喜一郎, 岡田朋也, 中越英樹, 安達卓
   第38回日本分子生物学会年会・第88回日本生化学会大会合同大会（2015.12.1-4, 神戸）
4. ショウジョウバエ組織における生理的アポトーシス耐性の解析
   谷口喜一郎, 中越英樹, 安達卓
   第38回日本分子生物学会年会・第88回日本生化学会大会合同大会（2015.12.1-4, 神戸）
5. ショウジョウバエ各種器官の近遠軸成長におけるDachsousの役割について
   岡田朋也, 坂田瑠美, 安部翔太, 谷口喜一郎, 安達卓
   第37回日本分子生物学会年会（2014.11.25-27, 横浜）
6. Isoform-specific functions of Mud/NuMA mediate binucleation of Drosophila male accessory gland cells
   谷口喜一郎, 國領顯彦, 今野貴夫, 南竜之介, 中越英樹, 安達卓
   第11回日本ショウジョウバエ研究会（2014.6.4-6, 金沢）
7. Acquisition of apoptosis-resistances in Drosophila accessory gland exocrine cells
   谷口喜一郎, 安達卓
   新学術領域研究「上皮管腔組織形成」第１回国際シンポジウム（2013.6.22-23, 札幌）
8. Mud/NuMAはショウジョウバエ雄生殖器附属腺において細胞二核化を制御する
   谷口喜一郎, 國領顯彦, 今野貴夫, 南竜之介, 中越英樹, 安達卓
   第65回日本細胞生物学会大会（2013.6.19-21, 名古屋）

Taniguchi et al. BMC Developmental Biology (2014) 14:46
DOI 10.1186/s12861-014-0046-5

BMC Developmental Biology

RESEARCH ARTICLE Open Access

Isoform-specific functions of Mud/NuMA mediate binucleation of *Drosophila* male accessory gland cells

Kiichiro Taniguchi[1], Akihiko Kokuryo[2,3], Takao Imano[2,3], Ryunosuke Minami[4], Hideki Nakagoshi[4] and Takashi Adachi-Yamada[1,2,3*]

Abstract

Background: In standard cell division, the cells undergo karyokinesis and then cytokinesis. Some cells, however, such as cardiomyocytes and hepatocytes, can produce binucleate cells by going through mitosis without cytokinesis. This cytokinesis skipping is thought to be due to the inhibition of cytokinesis machinery such as the central spindle or the contractile ring, but the mechanisms regulating it are unclear. We investigated them by characterizing the binucleation event during development of the *Drosophila* male accessory gland, in which all cells are binucleate.

Results: The accessory gland cells arrested the cell cycle at 50 hours after puparium formation (APF) and in the middle of the pupal stage stopped proliferating for 5 hours. They then restarted the cell cycle and at 55 hours APF entered the M-phase synchronously. At this stage, accessory gland cells binucleated by mitosis without cytokinesis. Binucleating cells displayed the standard karyokinesis progression but also showed unusual features such as a non-round shape, spindle orientation along the apico-basal axis, and poor assembly of the central spindle. Mud, a *Drosophila* homolog of NuMA, regulated the processes responsible for these three features, the classical isoform Mud^{PBD} and the two newly characterized isoforms Mud^{L} and Mud^{S} regulated them differently: Mud^{L} repressed cell rounding, Mud^{PBD} and Mud^{S} oriented the spindle along the apico-basal axis, and Mud^{S} and Mud^{L} repressed central spindle assembly. Importantly, overexpression of Mud^{S} induced binucleation even in standard proliferating cells such as those in imaginal discs.

Conclusions: We characterized the binucleation in the *Drosophila* male accessory gland and examined mechanisms that regulated unusual morphologies of binucleating cells. We demonstrated that Mud, a microtubule binding protein regulating spindle orientation, was involved in this binucleation. We suggest that atypical functions exerted by three structurally different isoforms of Mud regulate cell rounding, spindle orientation and central spindle assembly in binucleation. We also propose that Mud^{S} is a key regulator triggering cytokinesis skipping in binucleation processes.

Keywords: *Drosophila*, Male accessory gland, Binucleation, Cytokinesis, Central spindle, Cell rounding, Spindle orientation, Mud

* Correspondence: Takashi.Adachi-Yamada@gakushuin.ac.jp
[1]Department of Life Science, Faculty of Science, Gakushuin University, Tokyo 171-8588, Japan
[2]Institute for Biomolecular Science, Gakushuin University, Tokyo 171-8588, Japan
Full list of author information is available at the end of the article

Background

Most eukaryotic cells contain only a single nucleus because the karyokinesis in the M phase of the cell cycle is followed by cytokinesis. In certain cells, however, such as cardiomyocytes and hepatocytes, cytokinesis does not always occur, which results in cells containing two nuclei [1,2]. Sarcomere assembly is a possible factor repressing cytokinesis in cardiomyocytes [1,3], and insulin signaling plays a part in the generation of binucleate hepatocytes [2].

The production of binucleate cells is thought to result from the repression of certain phases of cytokinesis, such as formation of the contractile ring and ingression of the cleavage furrow. Cytokinesis occurs only when there is sufficient activation of Rho GTPase at the division plane. After chromosome segregation, a prominent bundle of microtubules, called the central spindle, forms between the spindle poles [4-6]. The centralspindlin complex, consisting of kinesin-6 and RhoGAP, moves toward the plus ends of the microtubules, corresponding to the cell equator, and associates with RhoGEF [7]. The RhoGEF thus specifically activates Rho GTPase at the division plane. Rho signaling activates effector proteins, such as diaphanous and Rho kinase, that in turn activate the formation of the actin contractile ring that completes cell division by pinching the daughter cells apart [8]. Loss of this cytokinesis machinery results in incomplete cytokinesis and produces binucleate cells [7,9,10]. There is, however, no solid evidence that normal binucleation events are regulated by inhibiting the functions of cytokinesis components, and little is known about the key regulators repressing the formation of cytokinesis machinery during binucleation. On the other hand, recent studies have shown a link between binucleation and inhibition of the cytokinesis machinery in cancer cells [11,12].

To investigate the mechanism by which cytokinesis is skipped during binucleation, we used as a model system the *Drosophila* male accessory gland, which produces seminal fluid proteins promoting reproductive success, such as the sex peptide Acp70A [13,14]. The exocrine epithelial cells in the male accessory gland, both the main cells and the secondary cells, are obviously binucleate (Figure 1A) [15]. We previously showed that binucleation increases the plasticity of the cell shape, thereby enabling the volume of the accessory gland cavity to change [16], but the mechanisms of binucleation have remained unclear.

In the work reported here, we investigated the binucleation event in the accessory gland primordia, which was characterized by synchronous entry into the M phase after a cell-cycle-arrested interval during the mid-pupal developmental stage following standard cell proliferation in the early stage. We found that the binucleation results not from cell fusion but from mitosis without cytokinesis. We examined the mechanisms of binucleation by focusing on various morphological features different from those of standard dividing cells. We propose that isoform-specific functions of the microtubule binding protein Mud, a *Drosophila* homolog of NuMA, are the key regulators in binucleation of the *Drosophila* male accessory gland cells.

Results

Accessory gland epithelial cells are binucleated synchronously in the mid-pupal stage by mitosis without cytokinesis

We first determined whether binucleation of the accessory gland epithelial cells is a result of skipping cytokinesis (as in cardiomyocytes). We observed the developmental stages and M-phase entry by using an antibody against phospho-histone H3 (P-H3), a marker for M-phase chromatin. Until 50 hours after puparium formation (APF), the accessory gland epithelial cells randomly entered the M phase but did not produce binucleate cells (Additional file 1: Figure S1A–E, A'–E' and J) (Figure 1D). That is, standard cell division occurred. Subsequently, the cells arrested their cell cycle and delayed their M-phase entry for about 5 hours (50-55APF) (Additional file 1: Figure S1F and F') (Figure 1D). The secondary cells then entered the M phase at 55 hours APF (Figure 1B and D) (Additional file 1: Figure S1G and G'), and the main cells entered the M phase at 60 hours APF (Figure 1C and D) (Additional file 1: Figure S1H and H'). We also found that the mitotic wave for binucleation in the main cell population initiated at the middle zone of the accessory gland lobe and propagated to the proximal and distal parts (Additional file 1: Figure S2). These results indicate a unique cell cycle regulation in this organ development. Importantly, the synchronous entries into the M phase accompanied the production of binucleate cells (Additional file 1: Figure S1K and Figure S2). No cytokinesis was evident in this M phase (Figure 2F–J and F'–J'). After binucleation, the accessory gland epithelial cells did not enter a subsequent M phase (Additional file 1: Figure S1I and I', Figure S3) but showed a single round of the S phase, indicated by PCNA-GFP labeling (Additional file 1: Figure S3), indicating that endoreplication occurred (Figure 1D). Thus the accessory gland epithelial cells, both secondary and main cells, became octaploid cells with two tetraploid nuclei. In the following section, we describe our examination of binucleation in the main cells. The secondary cells probably binucleated in the same way the main cells did.

Central spindle assembly and actin-contractile ring formation are inhibited during binucleation

We next identified the cytological differences between standard cell division and binucleation in order to obtain

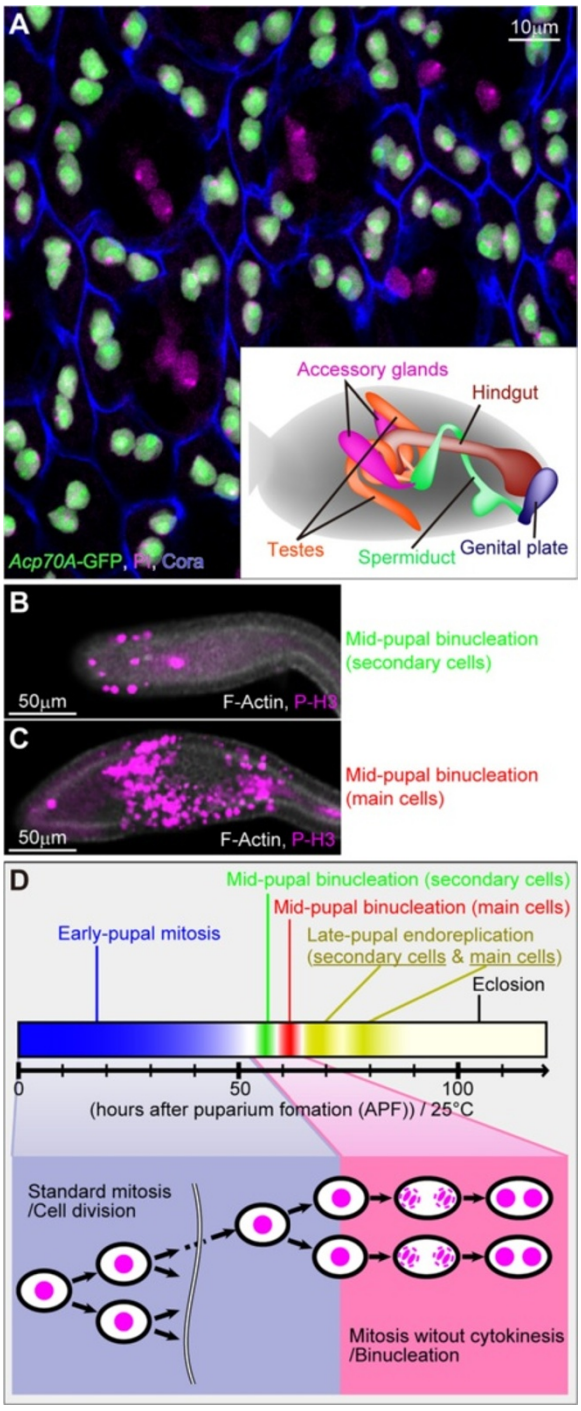

Figure 1 Synchronous binucleation of *Drosophila* male accessory gland cells occurs in the pupal stage. (A) Adult accessory gland epithelium labeled as indicated at the bottom left. Main cells (nuclei stained both green and magenta) and secondary cells (nuclei stained only magenta) are shown. The inset at the bottom right depicts an adult male abdomen (gray) and the reproductive systems around the hindgut. Posterior is to the right. Scale bar, 10 μm. **(B and C)** Synchronous entry into M phase in secondary **(B)** and main **(C)** cells in the accessory glands during mid-pupal binucleation stages. Labels as indicated at the bottom right. Scale bars, 50 μm. **(D)** Schematic diagram showing cell cycle transition of epithelial cells in accessory gland during the pupal stage.

clues to the mechanisms of cytokinesis skipping. For this purpose, we compared cell division in the early pupal accessory gland primordium and binucleation in the mid-pupal one (Figure 1D). We focused on the following three differences. First, during the standard cell division in the early stage of accessory gland development, the M-phase cells were apically extruded and rounded (Figure 2A–C and A'–C'), as is widely found in the standard epithelia [17]. During binucleation, however, cells were retained in the epithelial monolayer and did not show rounding (Figure 2F–H and F'–H' compared with A–C and A'–C'). Second, the spindle orientation in standard mitosis was parallel to the epithelial plate (Figure 2A–C and A'–C') [17]. The spindle formed during binucleation, in contrast, was always oriented perpendicular to the epithelial plate (Figure 2F–H and F'–H'). Third, in standard cell division, the central spindles between segregated chromatids arose from anaphase to telophase, and then an actin contractile ring formed at the division plane (Figure 2D,E,D' and E') [4-6,8]. During binucleation, in contrast, the central spindle was not properly assembled (Figure 2I,J,I' and J'). Consequently, the subsequent formation of the contractile ring was also incomplete at telophase (Figure 2J and J'), although the cleavage furrow was slightly formed at late anaphase (Figure 2I and I'). On the other hand, other components of the mitotic spindle of binucleating cells looked normal, including the metaphase spindle (Figure 2G and G' compared with B and B') [6] and kinetochore microtubules (Figure 3C compared with A) [6,18]. Also apparently normal in the binucleating cells was the M phase progression indicated by the relationship between chromatid segregation (Figure 2G,H,G' and H' compared with B,C,B' and C') [18] and the decay of cyclin B (Figure 3D and D' compared with B and B') [19]).

Forced activation of Rho GTPase in binucleation stage produces actin contractile ring

Looking at the above three differences for clues to the mechanism of binucleation in the experiments intended to produce artificially rounded cells, we saw that cell

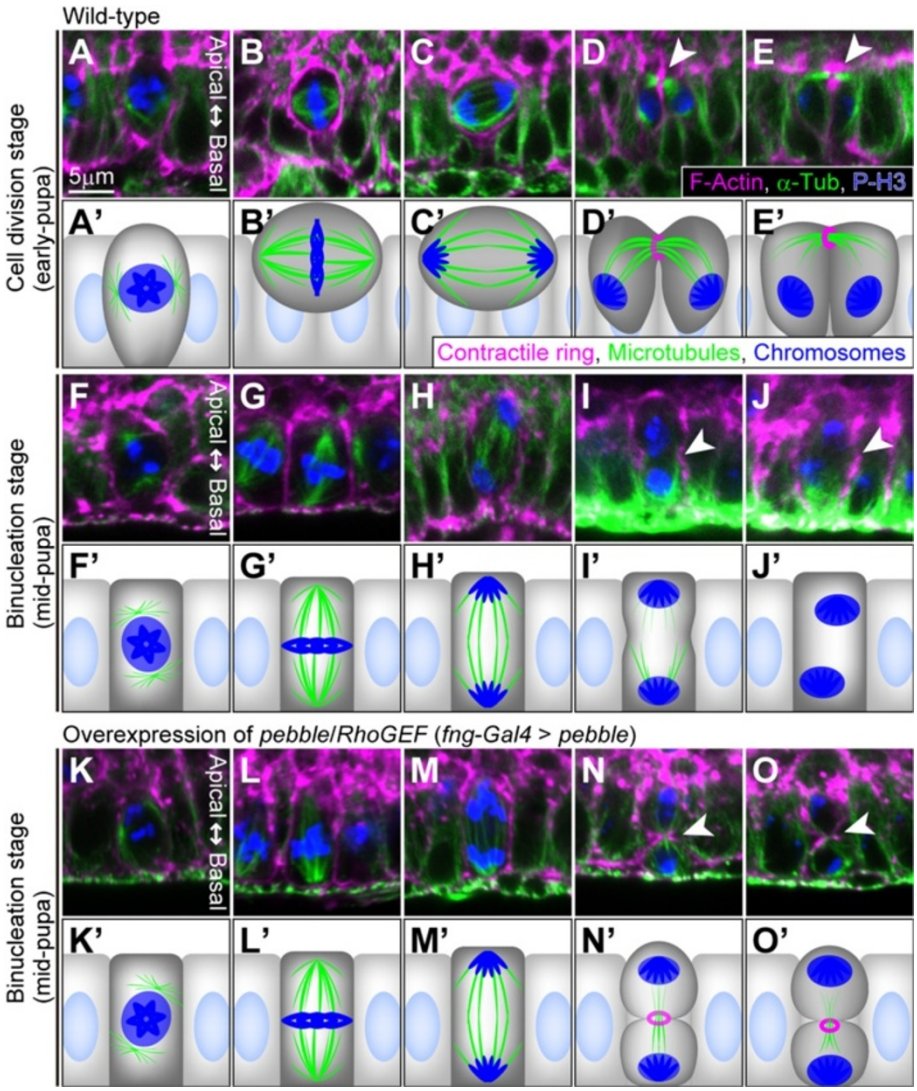

Figure 2 Central spindle and contractile ring are not formed during binucleation. Photomicrographs showing cross-sectional views of cells **(A–O)** and their schematic diagrams **(A'–O')** are arrayed from left to right according to the M phase progression. **(A–E)** Main cells during cell division stage in early pupa (30–35 hours APF). **(F–J)** Main cells during binucleation stage in mid-pupa (60–65 hours APF). **(K–O)** Binucleation-stage main cells in which *pebble* was overexpressed just before binucleation. Arrowheads in **(D, E, I, J, N and O)** indicate equatorial planes in late anaphase and telophase during cell division and binucleation. Cells are labeled as indicated at the bottom of **(E)**. Scale bar in **(A)**, 5 μm, is applicable to **(A–O)**.

extrusion and rounding did not seem to affect binucleation. In the binucleation stage neither overexpression of Sterile20-like kinase, which is related to cortical rigidity and cell rounding in standard cell division [20,21], nor knockdown of the adherens junction protein *D*E-cadherin encoded by *shotgun* [22], which maintains epithelial stability, led to cytokinesis (Additional file 1: Figure S4A–D) (Table 1). Binucleation also seemed to not be affected by the orientation of the mitotic spindle. This is because disruption of vertical spindle orientation in the binucleation stage by using a mutant for the centrosome protein Centrosomin or Sas-4 did not cause ectopic cytokinesis progression (Additional file 1: Figure S4E–H) (Table 1) [23-25]. On the other hand, in *centrosomin* and *Sas-4* mutants, weak assembly of the central spindle and an abnormal contractile ring could be observed at low frequencies (6% in $centrosomin^{HK21}$ and 9% in $Sas\text{-}4^{S2214}$). However, we found that these induction-of-cytokinesis features were observed even in the cells showing normal (vertical) spindle orientation. Thus these results mean that contribution of the centrosome to the cytokinesis skipping during binucleation may be nonessential or even trivial.

Mis-assembly of the central spindle and incomplete formation of the contractile ring strongly induced skipping of

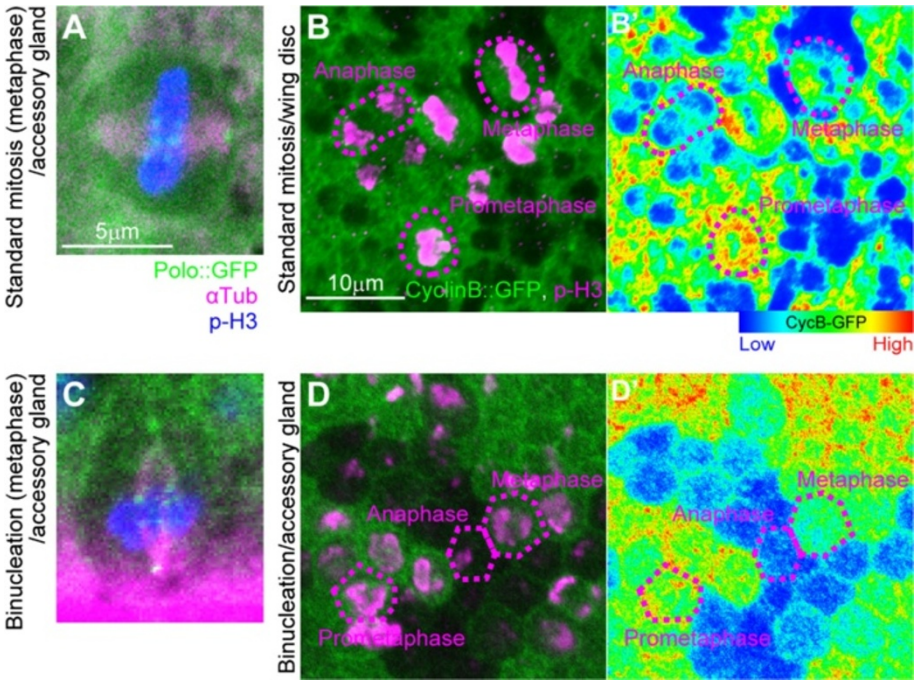

Figure 3 Metaphase spindle formation and metaphase-anaphase transition are normal during binucleation. (A and C) Localization of polo to kinetochores in main cells in metaphase during cell division in early pupa **(A)** and during binucleation in mid-pupa **(C)**. Cells are labeled as indicated at the bottom of **(A)**. *En face* views **(A)** and cross-sectional views **(C)**. Scale bar, 5 μm, is applicable to **(A and C)**. **(B, B', D and D')** Levels of cyclin B. *En face* images of the wing disc epithelium in third-instar larva as an example of proliferating tissue **(B and B')** and the accessory gland epithelium in mid-pupa as an example of binucleating tissue **(D and D')**. Cells in **(B and D)** are labeled as indicated at the bottom right of **(B)**. Intensities of cyclin B:: GFP in **(B)** and **(D)** are represented by a rainbow-color scale, with red meaning high intensity and blue meaning low intensity. Magenta dashed lines indicate outlines of mitotic cells in various M-phase subphases. Scale bar in **(B)**, 10 μm, is applicable to **(B, B', D and D')**.

cytokinesis during binucleation. The formation of the actin-contractile ring requires sufficient activation of Rho GTPase at the division plane [8]. To activate Rho GTPase encoded by Rho1, we temporarily elevated the level of the RhoGEF pebble around the binucleation stage. Pebble activates a Rho1 signaling cascade that phosphorylates MRLC (a regulatory light chain of non-muscle myosin II) encoded by *spaghetti squash* (*sqh*) to form the contractile ring [5,7,8]. Overexpression of *pebble* resulted in F-actin accumulation at the cleavage furrow, a sign of contractile ring formation, and in furrow ingression during the binucleation stage (Figure 2K–O and K'–O') (Table 1). We also found that overexpression of the activated form of *sqh* ($sqh^{D20.D21}$) induced the formation of the contractile ring (Additional file 1: Figure S4I) (Table 1). Furthermore, we tested a moderate overexpression of wild-type *sqh* or *Septin-2* to see whether cells in the binucleation stage have a latent ability to create a contractile ring. Since the septin proteins are contractile ring components that act together with actomyosin and microtubules [26], we could easily see contractile ring formation in the telophase cells (Additional file 1: Figure S4J–M) (Table 1). These results indicate that the level of central spindle assembly in accessory gland cells in telophase was too low to sufficiently activate Rho1 signaling for cytokinesis.

Mud regulates central spindle assembly, spindle orientation and cell rounding during binucleation

The insufficient activity of Rho1 signaling in binucleation is thought to be due to the insufficient assembly of the central spindle from anaphase to telophase, so we hypothesized that factors that repressed the central spindle assembly would be key regulators in skipping cytokinesis. Moreover, as stated above, the reduced central spindle assembly during binucleation should be accompanied by a non-round cell shape and orientation of the mitotic spindle along the apico-basal axis. Thus we examined candidate factors – such as mitotic kinesins (*kinesin-like protein at 10A, kinesin-like protein at 61 F, Pavarotti* and *no distributive disjunction*) [4], microtubule-associated proteins (*chromosome bows* and *Eb1*) [4], microtubule-severing proteins (*katanin 60*, *spastin*) [27], Par proteins (*bazooka*, *par-1*) [28] and spindle orientation proteins (*rapsynoid*, *G protein αi subunit* and *mushroom body defect* (*mud*)) [29-31], with regard to their effects on cellular phenotypes of accessory gland cell binucleation. We found that loss of *mud* disrupted normal binucleation phenotypes, including

Table 1 Effect of various genetic manipulations on central spindle assembly and contractile ring formation during binucleation

Manipulation	Genotype	Frequencies of phenotypes in mitotic behavior	
		Central spindle assembly	Contractile ring formation
None (wild-type)	*Canton-S*	0% (N = 42, 7)	0% (N = 42, 7)
		(5%, partial*)	(5%, partial**)
Induction of cell rounding	*fng-Gal4* (*Tub-Gal80^{TS}*) > *sterile 20-like kinase*	0% (N = 34, 7)	0% (N = 34, 7)
		(12%, partial*)	(18%, partial**)
	fng-Gal4 (*Tub-Gal80^{TS}*) > *shotgun.IR*	0% (N = 37, 6)	0% (N = 37, 6)
		(8%, partial*)	(14%, partial**)
Disruption of centrosome***	*centrosomin^{HK21}* homozygote	6% (N = 36, 6)	6% (N = 36, 6)
		(11%, partial*)	(8%, partial**)
	Sas-4^{S2214} homozygote	9% (N = 34, 7)	9% (N = 34, 7)
		(18%, partial*)	(29%, partial**)
Activation of contractile ring formation	*fng-Gal4* (*Tub-Gal80^{TS}*) > *pebble*	0% (N = 34, 6)	44% (N = 34, 6)
		(56%, partial*)	(41%, partial**)
	fng-Gal4 (*Tub-Gal80^{TS}*) > *sqh$^{D20.D21}$*	6% (N = 33, 6)	39% (N = 33, 6)
		(64%, partial*)	(48%, partial**)
	sqh-GFP	11% (N = 36, 6)	14% (N = 36, 6)
		(47%, partial*)	(53%, partial**)
	Septin-2-GFP	3% (N = 36, 7)	14% (N = 36, 7)
		(22%, partial*)	(42%, partial**)

Numbers of cells and tissues (pairs of lobes) observed are shown as (N = cells, tissues).
*A phenotype class with partial assembly of central spindle-like structure.
**A phenotype class with partial accumulation of F-actin accompanied by furrow progression.
***Very low frequency of cells shows obvious misorientation of spindle axis.

reduced central spindle assembly and other features of cell morphology during binucleation (Figure 4) (Tables 2 and 3). *mud* encodes the *Drosophila* homolog of NuMA, which is associated with microtubules and plays a role in microtubule polymerization and determination of the spindle orientation [29-31]. In *mud^{4}* hemizygotes and *mud*-knockdown cells, abnormally clear central spindle assembly and contractile ring formation were seen even in the binucleation stage (Figure 4B–E and B'–E' compared with Figure 2I, J, I' and J') (Table 2 and Table 3). Loss of *mud* was also associated with other morphological defects, such as abnormal spindle orientation and cell rounding (Figure 4H–J and H'–J' compared with Figure 2H and H') (Table 2 and Table 3). We thus confirmed that one copy of a chromosomal duplication encompassing the *mud* gene region (Figure 4A) rescued these defects (Figure 4F, G, F' and G') (Table 2). These results suggest that Mud contributes to various cell morphologies during binucleation. We considered its repression of the central spindle assembly to be a major cause of binucleation because in *mud^{4}* hemizygotes, we frequently observed cytokinesis progression even when neither horizontal spindle orientation nor cell rounding was observed (Figure 4B–E and B'–E') (Additional file 2: Table S1).

Mud represses development of central spindle during binucleation

We showed that Mud repressed central spindle assembly and led to cytokinesis skipping. We made further observations of the central spindle assembly in wild-type and *mud*-knockdown cells in the binucleation stage. In particular, we used Pav::GFP (GFP-fusion of Pavarotti, a centralspindlin component) as a marker for the plus ends of the microtubules in the mitotic spindle [32,33]. Regarding the control results, during the standard cell division at the early pupal stage, Pav::GFP was localized to the midzone of the central spindle at telophase, as reported previously (Figure 4K). During binucleation, in contrast, we never observed Pav::GFP-accumulated microtubules around the cell equator region (Figure 4L). Detailed observation of Pav::GFP accumulation revealed that the impairment of central spindle assembly during binucleation was not due to impaired initiation of microtubule assembly. That is because the Pav::GFP accumulation around cell equator at anaphase was similarly observed in the case of dividing cells, implying that the central spindle precursor could develop at early anaphase (Additional file 1: Figure S5F and F' compared with A and A'). But during binucleation, impaired

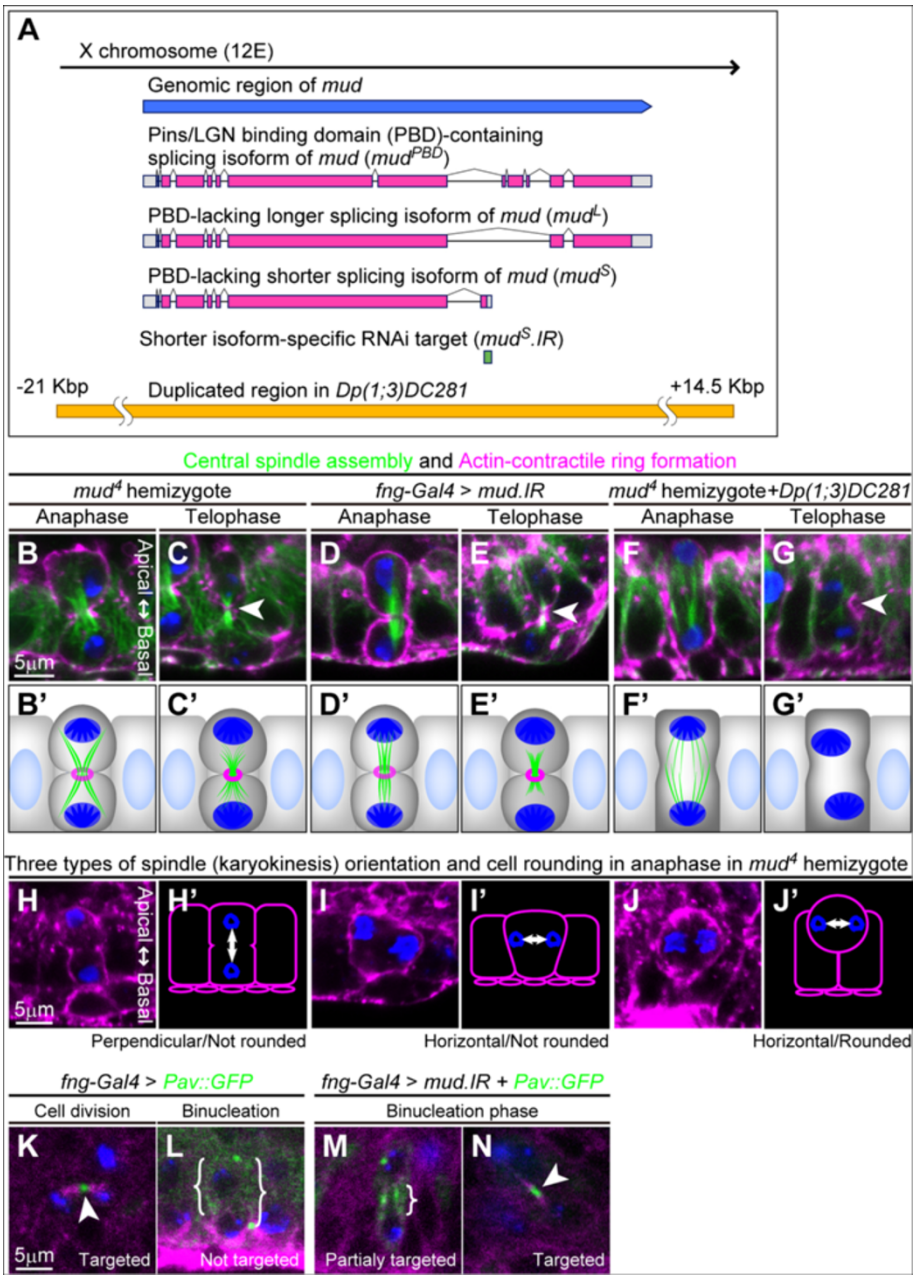

Figure 4 Loss-of-function for *mud* erases various characteristics of binucleation. (A) Schematic diagram of the *mud* transcriptional unit and three representative splicing variants of *mud* (coding regions are in magenta). Regions corresponding to mud^{S}*.IR* (green) and chromosomal duplication in *Dp(1;3)DC281* (yellow) are also shown. **(B–G)** Cross-sectional views of main cells in late anaphase **(B, D and F)** and telophase **(C, E and G)** during the binucleation stage in mutants hemizygous for mud^{4} **(B and C)**, in knockdown for *mud* **(D and E)** and in mutants hemizygous for mud^{4} rescued by one copy of *Dp(1;3)DC281* **(F and G)**. Cells are labeled with phalloidin (magenta), anti-α-Tub antibody (green), and anti-P-H3 antibody (blue). Arrowheads in **(C, E and G)** indicate equatorial planes. Scale bar in **(B)**, 5 μm, is applicable to **(B–G)**. **(B′–G′)** Schematic diagrams of **(B and G)**. **(H–J)** Three representative types of spindle orientation and cell shapes (bottom). Cross-sectional views of main cells in late anaphase during the binucleation stage in mutants hemizygous for mud^{4} are shown. Cells are labeled with phalloidin (magenta) and anti-P-H3 antibody (blue). Scale bar in **(H)**, 5 μm, is applicable to **(H–J)**. **(H′–J′)** Schematic diagrams of **(H–J)**. **(K–N)** Main cells expressing Pav::GFP plus ends marker in telophase in wild-type **(K,L)** and *mud*-knockdown **(M,N)** cells. Cell division stage in early pupa (K, *en face* view) and binucleation stage in mid-pupa (**L–N**, cross sectional views) are shown. Cells are labeled with anti-α-Tub antibody (magenta), Pav::GFP fluorescence with anti-GFP antibody (green) and anti-P-H3 antibody (blue). Arrowheads in **(K and N)** and curly brackets in **(L and M)** indicate the localization of Pav::GFP on microtubules. Scale bar in **(K)**, 5 μm, is applicable to **(K–N)**.

Table 2 Ability of Mud variants to rescue binucleation defects in *mud* mutants

Genotype		Frequencies of phenotypes in mitotic behavior during binucleation			
		Central spindle assembly	Contractile ring formation	Cell rounding	Abnormal spindle orientation***
Wild-type (control)		0% (N = 42, 7)	0% (N = 42, 7)	0% (N = 49, 5)	6% (N = 49, 5)
		(5%, partial*)	(5%, partial**)		
mud^{4} hemizygote (*mud*^{4}/*Y*) + rescue construct (RC)	No RC	82% (N = 40, 9)	87% (N = 40, 9)	30% (N = 40, 8)	40% (N = 40, 8)
		(15%, partial*)	(13%, partial**)		
	RC = *DC281*	0% (N = 30, 4)	0% (N = 30, 4)	8% (N = 38, 4)	5% (N = 38, 4)
		(40%, partial*)	(57%, partial**)		
	RC = *mud*^{PBD}	63% (N = 30, 4)	67% (N = 30, 4)	37% (N = 30, 4)	17% (N = 30, 4)
		(33%, partial*)	(33%, partial*)		
	RC = *mud*^{L}	30% (N = 43, 9)	30% (N = 43, 9)	12% (N = 41, 7)	44% (N = 41, 7)
		(51%, partial*)	(56%, partial**)		
	RC = *mud*^{S}	13% (N = 40, 8)	18% (N = 40, 8)	34% (N = 44, 7)	20% (N = 44, 7)
		(45%, partial*)	(33%, partial**)		

Numbers of cells and tissues (pairs of lobes) observed are shown as (N = cells, tissues).
*A phenotype class with partial assembly of central spindle-like structure.
**A phenotype class with partial accumulation of F-actin accompanied by furrow progression.
***Spindle orientated horizontally (0° ± 45°) rather than vertically in metaphase.
DC281: Chromosomal duplication encompassing the *mud* gene region.

microtubule bundling or destabilization of the microtubules was apparent at late anaphase (Additional file 1: Figure S5G–J and G'–J' compared with C–E and C'–E'). As a result, during binucleation the development of microtubules was insufficient for their interdigitation at the spindle midzone. We also observed that the contractile ring component Peanut (Pnut), a Septin family protein, was localized around the cleavage furrow at anaphase but diffused during telophase (Additional file 1: Figure S6D–F and D'–F' compared with A–C and A'–C'). These results imply that the contractile ring begins to form during anaphase and is degraded during telophase.

We also checked whether the loss of *mud* affected the localization of Pav::GFP during binucleation. In *mud*-knockdown cells, the localization of Pav::GFP was restricted to the midzone of the central spindle (Figure 4N). We also found that this localization was correlated with the central spindle formation. Cells with partially assembled central spindles showed a partial localization of Pav::GFP at the midzone (Figure 4M), whereas cells with strongly assembled central spindles showed a clear localization (Figure 4N). These results suggest that Mud represses microtubule polymerization so much that microtubule filaments are not targeted around the cell equator.

Isoform-specific functions of Mud regulate various traits in binucleation

Although Mud is known to promote polymerization of microtubules [34], our results showed that Mud may be a negative regulator of spindle formation during the

Table 3 Effects of knockdown for *mud* on binucleation and asymmetric cell division (asym. cell div.)

RNAi target	Frequencies of phenotypes in mitotic behaviors during				
	binucleation				asym. cell div.
	Central spindle assembly	Contractile ring formation	Cell rounding	Abnormal spindle orientation***	Multi-bristle
None (*fng-Gal4*)	0% (N = 35, 6)	0% (N = 35, 6)	5% (N = 40, 6)	8% (N = 40, 6)	0% (N^{W} = 60)
	(0%, partial*)	(3%, partial**)			
mud.IR	80% (N = 35, 7)	86% (N = 35, 7)	28% (N = 40, 5)	35% (N = 40, 5)	85% (N^{W} = 40)
	(20%, partial*)	(14%, partial**)			
mud^{S}*.IR + Dcr2*	27% (N = 37, 5)	29% (N = 37, 5)	5% (N = 42, 5)	31% (N = 42, 5)	0% (N^{W} = 40)
	(51%, partial*)	(41%, partial**)			

Numbers of cells and tissues (pairs of lobes) observed are shown as (N = cells, tissues).
Numbers of adult wings observed are shown as (N^{W} = wings).
*A phenotype class with partial assembly of central spindle-like structure.
**A phenotype class with partial accumulation of F-actin accompanied by furrow progression.
***Spindle orientated horizontally (0° ± 45°) rather than vertically in metaphase.

binucleation process. The above results also indicate that unknown functions of Mud regulate central spindle assembly, spindle orientation, and cell rounding. Interestingly, *mud* generates various splicing variants that have different C-termini (Additional file 1: Figure S3A and referred to in http://flybase.org). To understand the relationship between these unknown functions of Mud and its structural isoforms that had not fully been analyzed, we compared the functions of three different splicing variants (Figure 4A) (Additional file 1: Figure S7): a Pins binding domain (PBD)-containing isoform (Mud^{PBD}), a PBD-lacking longer isoform (Mud^{L}) and a PBD-lacking shorter isoform (Mud^{S}). Mud^{PBD} is well-known major variant that regulates spindle polarity in a Pins/LGN-dependent manner and promotes microtubule polymerization [29-31,34]. Mud^{L} and Mud^{S}, both of which lack the Pins/LGN-binding domain (Figure 4A) (Additional file 1: Figure S7), have not yet been examined and their functions are unclear. We thus expected that mud^{L} or mud^{S} would exhibit novel functions that regulate central spindle assembly and spindle orientation during binucleation.

To identify isoform-dependent functions of Mud, we tested the ability of Mud^{PBD}, Mud^{L} and Mud^{S} to rescue the various defects in binucleation in *mud* hemizygotes. Overexpression of mud^{PBD} (Additional file 1: Figure S7 and Figure S8) rescued only their abnormal spindle orientation (Figure 6A–C and A'–C'), reducing the frequency of abnormal spindle orientation from 40% in mud^{4}/Y to 17% in $mud^{4}/Y + mud^{PBD}$ (Table 2). Overexpression of mud^{S} (Additional file 1: Figure S7 and Figure S8) rescued their abnormally enhanced central spindle assembly (Figure 6H–J and H'–J'), reducing the frequency of central spindle assembly from 82% in mud^{4}/Y to 13% in $mud^{4}/Y + mud^{S}$ (Table 2). mud^{S} also partially rescued the abnormal spindle orientation (Figure 6G and G'), reducing the frequency of abnormal spindle orientation from 40% in mud^{4}/Y to 20% in $mud^{4}/Y + mud^{S}$ (Table 2). In contrast, the overexpression of mud^{L} (Additional file 1: Figure S7 and Figure S8) effectively rescued the cell rounding

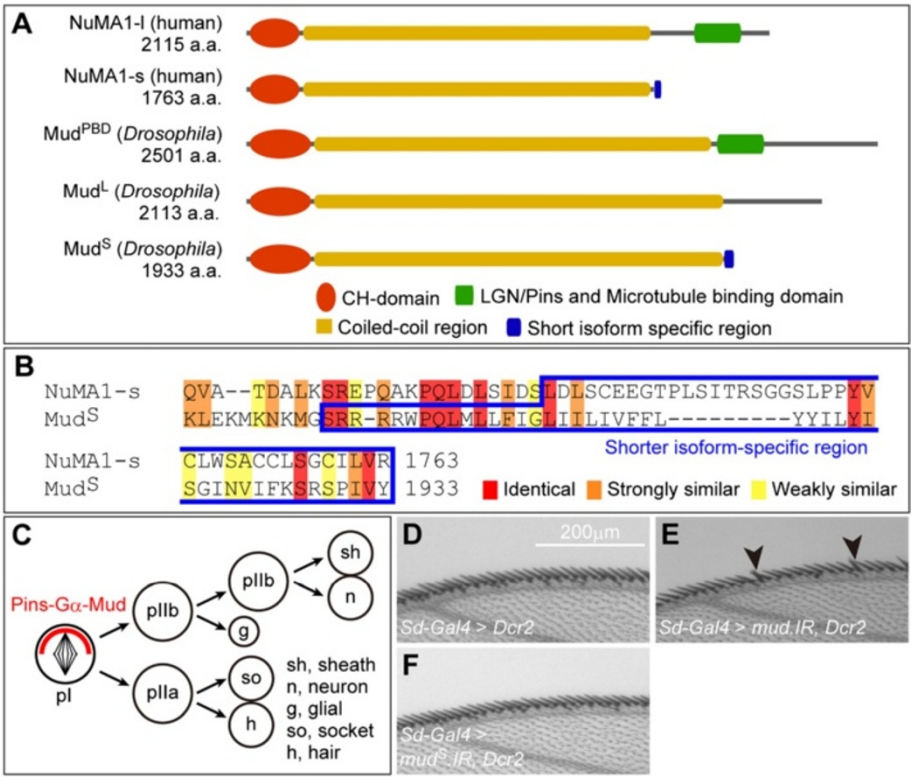

Figure 5 mud^{S} is not required for the spindle orientation during asymmetric cell division. (A) Schematic diagram of molecular structures of human NuMA1 and *Drosophila* Mud. Shared domains are as indicated at the bottom. **(B)** Amino acid sequence alignment of the C-terminal regions of NuMA1-s and Mud^{S}. The blue box indicates short isoform- specific regions in NuMA1-s (amino acids 1701–1763) and Mud^{S} (amino acids 1880–1933). Red, orange and yellow overlays indicate similarities as indicated at the bottom. **(C)** Schematic diagram of SOP lineage in *Drosophila* wing margin. Cells indicated at the bottom right are produced in this lineage. Mud forms a complex with Gα and Pins that is localized asymmetrically (red crescent). **(D–F)** Bristles on adult anterior wing margin in wild-type **(D)**, in knockdown of all *mud* isoforms **(E)**, and in knockdown specific to mud^{S} **(F)**. Arrowheads in **(E)** indicate multi-bristle phenotypes.

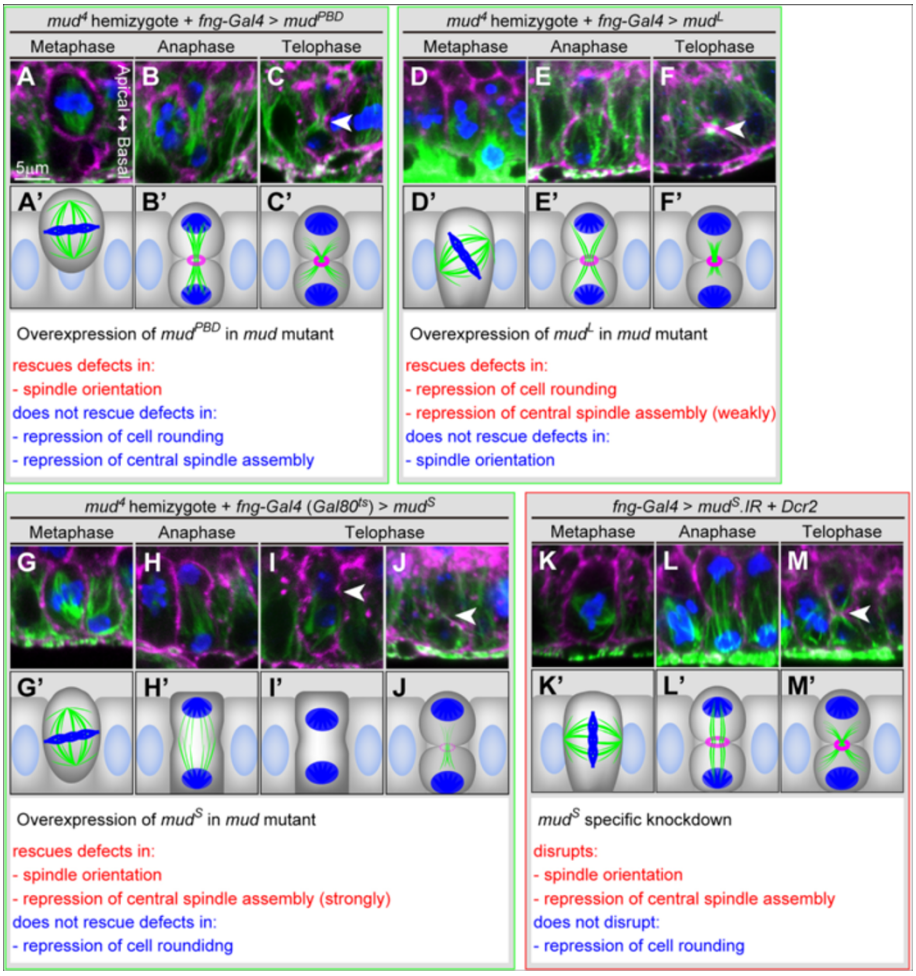

Figure 6 Three types of *mud* splicing isoforms differently regulate morphologies of binucleating cells. (A–J) Rescue of *mud* mutant phenotypes by each *mud* isoform. Cross-sectional views of main cells in metaphase **(A, D and G)**, late anaphase **(B, E and H)** and telophase **(C, F, I and J)** during the binucleation stage in mutants hemizygous for mud^4 with overexpression of *FLAG::*mud^{PBD} **(A–C)**, *FLAG::*mud^L **(D–F)** or *FLAG::*mud^S **(G–J)**. Cells are labeled with phalloidin (magenta), anti-α-Tub antibody (green) and anti-P-H3 antibody (blue). The cell in **(I)** shows neither a central spindle assembly nor furrow progression. The cell in **(J)** shows furrow progression but no central spindle assembly. Arrowheads in **(C, F, I and J)** indicate equatorial planes. Scale bar in **(A)**, 5 μm, is applicable to **(A–J)**. **(A'–J')** Schematic diagrams of **(A–J)**. Cross-sectional views of mud^S- knockdown main cells in metaphase **(K)**, late anaphase **(L)** and telophase **(M)** during the binucleation stage. Cells are labeled with phalloidin (magenta), anti-α-Tub antibody (green) and anti-P-H3 antibody (blue). Arrowhead in **(M)** indicates an equatorial plane. Scale bar in **(A)**, 5 μm, is applicable to **(K–M)**. **(K'–M')** Schematic diagrams of **(K–M)**. Effects on cell morphologies in each of the three rescued genotypes (**(A–C)**: mud^4 hemizygotes rescued by mud^{PBD}, **(D–F)**: mud^4 hemizygotes rescued by mud^L, **(G–J)**: mud^4 hemizygote rescued by mud^S) and in mud^S-knockdown cells **(K–M)** are listed under each set of diagrams.

phenotype found in *mud* hemizygotes (Figure 6D and D'), reducing the frequency of cell rounding from 30% in mud^4/Y to 12% in $mud^4/Y + mud^L$ (Table 2). mud^L also partially rescued the abnormally enhanced assembly of central spindle (Figure 6E, E', F and F'), reducing the frequency of central spindle assembly from 82% in mud^4/Y to 30% in $mud^4/Y + mud^L$ (Table 2), but its ability was obviously less than that of mud^S (compare the reduction to 30% by $mud^4/Y + mud^L$ with the reduction to 13% by $mud^4/Y + mud^S$). These results imply that Mud has the following isoform-dependent functions during binucleation: Mud^L represses cell rounding and weakly represses central spindle assembly, Mud^{PBD} and Mud^S each play a role in orienting the spindle axis along the apico-basal axis, and Mud^S also strongly represses central spindle assembly.

Mud^S orients mitotic spindle along the apico-basal polarity and inhibits cytokinesis

The above overexpression results suggest that Mud^S contributes to cytokinesis skipping during binucleation more than Mud^L does, but the functions of Mud^S during *Drosophila* development have not yet been reported. We therefore tried to determine whether endogenously

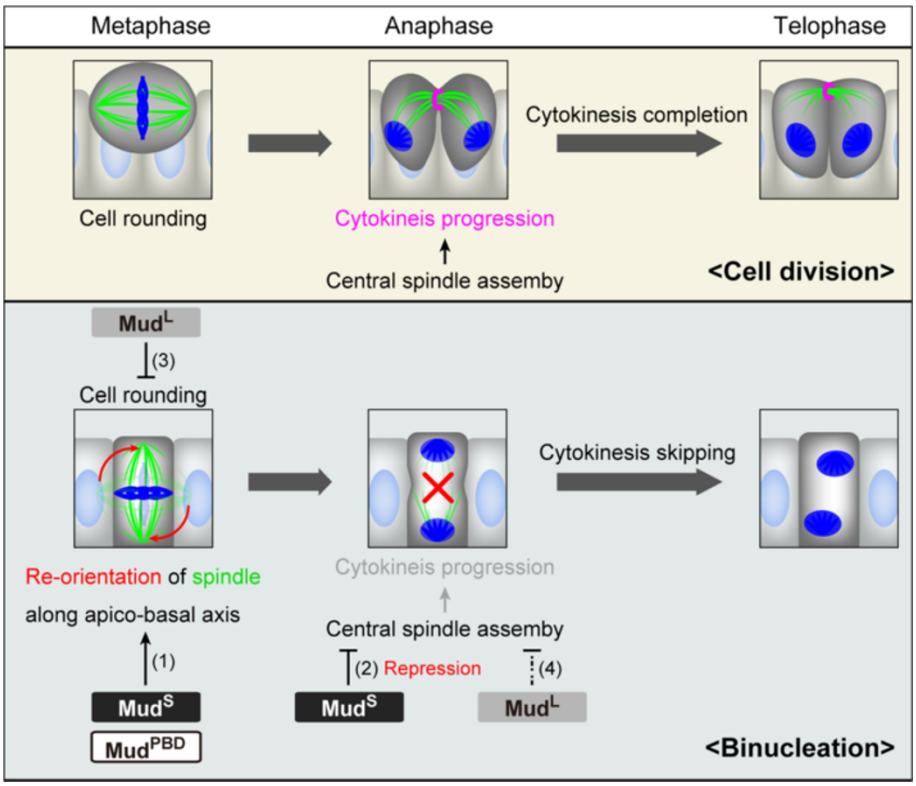

Figure 7 Model for binucleation and isoform-specific functions of Mud. Schematic diagrams of cell division and binucleation are shown. In binucleation, Mud^{S} changes mitosis from cell division to binucleation by (1) reorienting the mitotic spindle from horizontal to vertical along the apico-basal axis and (2) repressing assembly of the central spindle. Mud^{PBD} is also required at this time for orienting the spindle along the apico-basal axis. Mud^{L}, in contrast, (3) represses mitotic cell rounding and may assist in the process of cytokinesis skipping by (4) partially repressing the assembly of the central spindle.

expressed *mud*^{S} actually regulates binucleation in the accessory gland. To do so, we performed a *mud*^{S}-specific knockdown (Figure 4A and Figure 6H–K and I'–K') (Additional file 1: Figure S7 and Figure S8) and found that the *mud*^{S}-knockdown cells showed abnormally enhanced assembly of the central spindle (Figure 6L, L', M and M') and abnormal orientation of the mitotic spindle (Figure 6K and K') (Table 3). These results strongly suggest that Mud^{S} represses central spindle assembly and orients the spindle axis vertically but does not regulate cell rounding.

Mud^{PBD} is known to regulate spindle orientation during asymmetric cell division, so we tried to determine whether the spindle orientation-regulating function of Mud^{S} during binucleation is independent of that of Mud^{PBD}. We tried to do that by determining whether a knockdown of Mud^{S} affected asymmetric cell division in the sensory organ precursor cells (SOPs) on the adult wing margins (Figure 5C). The spindle orientation of this asymmetric cell division is known to be regulated by Mud^{PBD} in a Pins- and Gαi-dependent manner, and loss of this function results in a multi-bristle phenotype on the adult wing (Figure 5C). In fact, the knockdown of all Mud isoforms caused abnormal spindle orientation and the multi-bristle phenotype (arrowheads in Figure 5E compared with D) (Table 3) [29,35,36]. The knockdown of *mud*^{S} alone, in contrast, did not induce the multi-bristle phenotype (Figure 5F) (Table 3), although it effectively caused spindle orientation changes during binucleation (Figure 6I and I') (Table 3). These results suggest that even though Mud^{S} regulates spindle orientation during binucleation, it is not involved in the spindle orientation during asymmetric cell division of SOPs.

As shown above, Mud^{S} seems to convert the mitotic morphologies from the cell-division type (horizontal spindle orientation and cytokinesis progression) to the binucleation type (vertical spindle orientation and cytokinesis skipping) (Figure 6) (Table 2 and Table 3). To examine this hypothesis, we tested the ability of Mud^{S} to convert the mitotic morphologies of cells in the early pupal accessory gland primordia, in which standard cell division occurs. The results showed that the spindle orientation changed from horizontal to vertical (Figure 8E compared with Figure 2D). Furthermore, binucleate cells appeared with some frequency (arrowhead in Figure 8F). This effect of overexpression of *mud*^{S} on cell morphologies

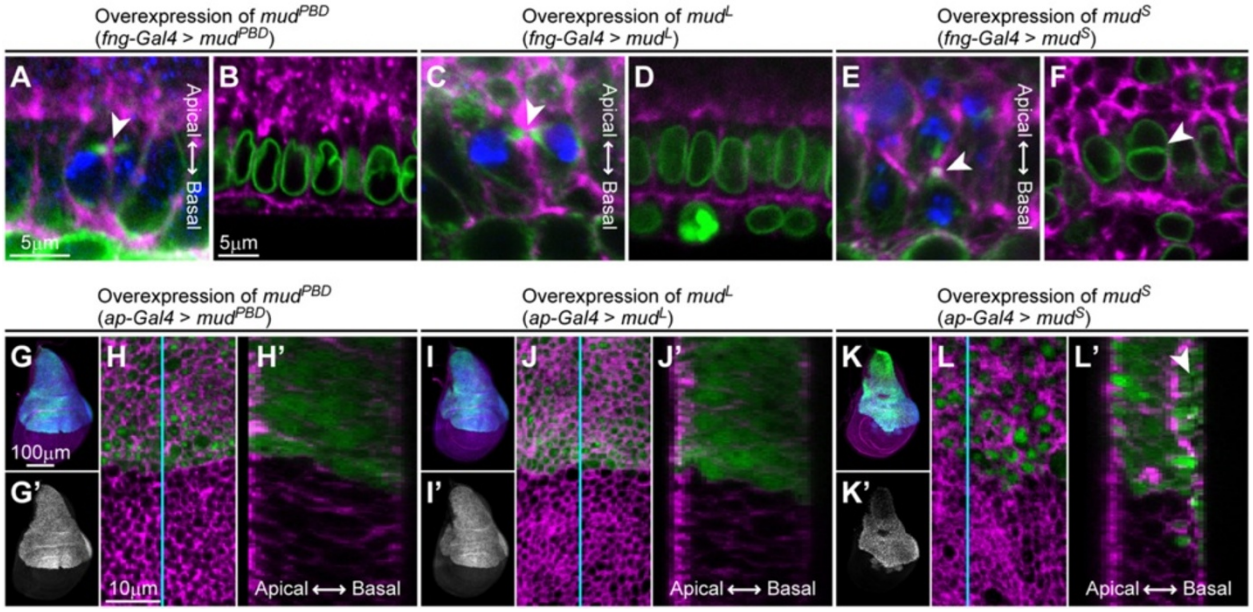

Figure 8 Overexpression of *mud*^{S} is sufficient for converting dividing cells into binucleating ones. (A–F) Cross-sectional views of main cells in early pupal proliferating stage in which *mud*^{PBD} **(A and B)**, *mud*^{L} **(C and D)** or *mud*^{S} **(E and F)** are overexpressed. Cells in telophase **(A, C and E)** or interphase **(B, D and F)** are shown. Cells are labeled with phalloidin (magenta), anti-α-Tub antibody **(green in A, C and E)**, anti-LamDm$_0$ antibody **(green in B, D and F)** and anti-P-H3 antibody (blue). Arrowheads in **(A, C and E)** indicate equatorial planes. The arrowhead in **(F)** indicates a binucleate cell. Scale bar in **(A)**, 5 μm, is applicable to **(A, C and E)**. Scale bar in **(B)**, 5 μm, is applicable to **(B, D and F)**. **(G, G', I, I', K and K')** Wing imaginal discs in which *FLAG::mud*^{PBD} **(G)**, *FLAG::mud*^{L} **(I)** or *FLAG::mud*^{S} **(K)** is induced in their dorsal compartment (labeled with GFP). Cells are labeled with phalloidin (magenta), GFP (green) and anti-FLAG antibody (blue). Gray-scale images in **(G', I' and K')** are of the blue channels in **(G, I and K)**. Scale bar in **(G)**, 100 μm, is applicable to **(G, G', I, I', K and K')**. **(H, J and L)** Magnified views of **(G, I and K)** around the dorso-ventral boundaries. Magenta and green channels are shown. Cells with expression of *mud*^{S} were enlarged in volume (L), possibly as a result of cytokinesis defects. **(H', J' and L')** Cross-sectional images reconstructed by using a stack of confocal sections at cyan lines in **(H, I and L)**. The epithelium with expression of *mud*^{S} has an abnormally folded or layered structure (**arrowhead in L'**). Scale bar in **(H)**, 10 μm, is applicable to **(H, H', J, J', L and L')**.

can be seen not only in the accessory gland but also in the wing imaginal disc (Figure 8K, K', L and L'). Overexpression of *mud*^{PBD} or *mud*^{L}, in contrast, affected neither spindle orientation nor cytokinesis (Figure 8A–D, G–J and G'–J'). These results suggest that Mud^S can convert mitotic morphologies from the cell-division type to the binucleation type.

Discussion

Regulation of M-phase entry in binucleation of *Drosophila* male accessory gland

We characterized the final M-phase entry that contributed to binucleation of cells in the *Drosophila* male accessory gland (Figure 1D) (Additional file 1: Figure S1). We showed that the entry into the binucleation stage took place with a two-step cell cycle transition: cell cycle arrest for 5 hours and subsequent synchronous entry into the M phase (Figure 1D) (Additional file 1: Figure S1). Thus, standard cell division and binucleation are separated by a 5-hour interval of cell cycle arrest (Additional file 1: Figure 1D) (Additional file 1: Figure S1). This may indicate that standard mitosis and binucleation have very different regulations of the cell cycle and cytokinesis. In fact, although in most tissues in *Drosophila* standard mitosis can occur normally without the spindle checkpoint [37], we previously demonstrated that the knockdown of *mad2*, a spindle checkpoint component, frequently causes a defect in chromosomal segregation in accessory gland cells [16]. This is consistent with our proposal that binucleation is regulated by a system different from the one regulating standard mitosis.

Morphological features of mitotic cells during binucleation

We identified three morphological features characteristic of binucleation: the non-round shape of mitotic cells, the apico-basal orientation of the mitotic spindle and the poor assembly of the central spindle (Figure 2F–J and F'–J' compared with A–E and A'–E'). The reduction of central spindle assembly could directly repress cytokinesis, but we did not find the significance of the vertical orientation of the spindle or the non-round shape of

the cell. We can explain it as follows. If most cells of the epithelium synchronously enter the M phase with the cell rounding phenotype, the stability of the monolayer epithelium may be severely disrupted. In fact, we observed a severe defect in epithelial stability after the binucleation stage in a *mud* mutant in which the cells were rounded during the binucleation stage (data not shown). In addition, if the spindles in columnar cells are horizontally oriented, they will be less stable than they would be if they were vertically oriented because a spindle is aligned more stably along a longer axis than a shorter one [38]. Vertical orientation of the spindle and lack of cell rounding may thus be appropriate for synchronous binucleation of columnar cells, but these morphological features do not directly regulate cytokinesis skipping.

Mechanisms by which Mud regulates central spindle assembly, spindle orientation, and cell rounding during binucleation

We propose that Mud is a key factor in regulating binucleation. We demonstrated that Mud functions in a way that represses central spindle assembly, orients the mitotic spindle along the apico-basal axis and inhibits mitotic cell rounding during mitosis (Figure 7). We found a clue as to how Mud represses the central spindle assembly. In standard cell division, during late anaphase the microtubules of the central spindle are polymerized in order to target their plus ends at the cell equator [32,33], and we confirmed this in our experiments in which the plus ends were labeled with Pav::GFP (Figure 4K). During binucleation, in contrast, the Pav::GFP marker did not sufficiently target the cell equator (Figure 4L). This implies that the polymerization of the microtubules of the central spindle is insufficient to target them at the cell equator, and the central spindle therefore does not develop completely. We also showed that the Mud is needed in order to repress the growth of microtubules. In fact, the knockdown of *mud* promoted the growth of microtubules that targeted their plus ends at the cell equator even in the binucleation stage (Figure 4M and N). However, the underlying molecular mechanisms of Mud in repressing polymerization of microtubules remain unclear. Moreover, the question of how Mud regulates the mitotic spindle orientation along the apico-basal axis and how it inhibits mitotic cell rounding are also unclear. The logical next step will be to relate the isoform of each Mud to various effector molecules regulating the orientation and the rounding.

Alternative splicing of *mud*/*NuMA* produces three types of structurally different proteins

We showed that the three types of alternative splicing products Mud^{PBD}, Mud^{L} and Mud^{S} have distinct functions from one another (Figure 6, Figure 5, Figure 8 and Figure 7). It is known that the *mud* gene produces four isoforms (RH, RI, RJ and RL) that contain the Pins/LGN binding domain (PBD) and three isoforms (RF, RG and RK) that do not contain it (Figure 5A) (Additional file 1: Figure S7) (http://flybase.org). Moreover, the three PBD-lacking isoforms are structurally classified into the following two types: a longer isoform (RF) that simply skips the PBD-encoding exons by alternative splicing, and two shorter isoforms (RG and RK) that contain a shorter isoform-specific exon instead of the PBD-encoding exons (Figure 5A) (Additional file 1: Figure S7).

At least one of the PBD-containing isoforms (RL) is functional and known to regulate the spindle orientation in a Pins/LGN-dependent manner in asymmetric cell division [29-31]. In contrast, although mud^{L} and mud^{S} are actually transcribed [34] there is no evidence that Mud^{L} and Mud^{S} are functional and have Pins/LGN-independent functions. As in the *Drosophila* gene *mud*, splicing variants also occur in human *NuMA1*, and these variants encode a longer isoform (NuMA1-l), a shorter isoform (NuMA1-s) and a medium isoform (NuMA1-m) [39]. Although the functions of NuMA1-m and NuMA1-s are unclear, NuMA1-l has an LGN-binding domain in the C-terminal region and determines the spindle polarity in an LGN-dependent manner, the same as in the case of *Drosophila* Mud^{PBD} (Figure 5A) [40]. NuMA1-m and NuMA1-s, in contrast, like *Drosophila* Mud^{L} and Mud^{S} do not have an LGN-binding domain in the C-terminal region (Figure 5A). Interestingly, we found sequence similarities between human NuMA1-s and *Drosophila* Mud^{S} in their C-terminal domains, including the shorter isoform-specific regions (Figure 5B). These similarities suggest that Mud^{S} in *Drosophila* functions similarly to NuMA1-s in humans.

Isoform-dependent functions of Mud mediate various morphological changes of binucleating cells

We showed that the functions of mud^{PBD}, mud^{L} and mud^{S} are independent during binucleation. The repression of mitotic cell rounding was a Mud^{L}-specific function. In contrast, changing the orientation of the mitotic spindle along the apico-basal axis was controlled by both Mud^{PBD} and Mud^{S} (Figure 6 and Figure 7) (Table 2 and Table 3). Mud^{PBD} was previously reported to be required for the spindle orientation during asymmetric cell division [29,35,36]. We showed, however, that Mud^{S} is not associated with the spindle orientation during asymmetric cell division (Figure 5F). On the other hand, the overexpression of mud^{S} but not mud^{PBD} reoriented the spindle along the apico-basal axis in dividing cells (Figure 8A and E). These results suggest that Mud^{PBD} and Mud^{S} regulate the spindle orientation independently.

The function repressing central spindle assembly during binucleation was also shared by Mud^{L} and Mud^{S}, but we showed that Mud^{S} contributed the most to repressing spindle assembly. In fact, the overexpression of mud^{S} effectively rescued the mud^{4} mutant phenotype, the abnormally enhanced assembly of the central spindle (Figure 6I and J) (Table 2). In addition, like the mud^{4} mutant, a mud^{S}-specific knockdown abnormally enhanced central spindle assembly in the binucleation stage (Figure 6L and M) (Table 3). Mud^{L}, in contrast, only partially repressed the central spindle assembly during binucleation (Figure 6F) (Table 2). Moreover, overexpression of mud^{S}, but not mud^{L}, inhibited cytokinesis to produce binucleate cells in dividing cells such as the early pupal accessory gland cells (Figure 8D and F) and the larval wing disc cells (Figure 8J and L). This also suggests that mud^{S} mainly contributes to the repression of central spindle assembly (Figure 7).

Conclusions

We described the binucleation event of the *Drosophila* male accessory gland during pupal development and analyzed the cellular mechanisms regulating this binucleation. We characterized a unique cell cycle regulation in the developing accessory gland: the M-phase entry for binucleation occurred synchronously at 55 APF after a cell cycle arrest for 5 hours. We also found that Mud, the *Drosophila* homolog of mammalian NuMA, regulated various features of the binucleating cells, such as a non-round shape, spindle orientation along the apico-basal axis, poor assembly of the central spindle and cytokinesis skipping. It is known that Mud binds Pins to determine the mitotic spindle orientation during the standard cell division or asymmetric cell division [29-31,41,42]. Interestingly, we found atypical functions of Mud that depended on three types of splicing isoforms, each differently regulating the above various features of binucleating cells. We concluded that Mud^{PBD}, which is a well-known isoform having a PBD (Figure 5A) (Additional file 1: Figure S7), oriented the spindle along the apico-basal axis. Mud^{L}, one of the newly characterized isoforms and simply lacking a PBD, inhibited the mitotic cell rounding and weakly impaired the central spindle assembly (Figure 7). Mud^{S}, another newly characterized isoform, containing a shorter isoform-specific domain instead of a PBD-containing domain (Figure 5A) (Additional file 1: Figure S7), oriented the spindle along the apico-basal axis and strongly impaired the central spindle assembly (Figure 7). Importantly, overexpression of Mud^{S} induced an ectopic binucleation even in the cell division stage, whereas overexpression of Mud^{PBD} or Mud^{L} did not (Figure 8). These results suggest that Mud^{S} is an important regulator triggering cytokinesis skipping in binucleation. Abnormal expression of NuMA is known to be correlated with the production of cancer cells in mammals [43]. Our finding of atypical functions of Mud may contribute to the understanding of the relationship between NuMA and tumor progression.

Methods

Drosophila strains

Canton-S and w^{1118} were used as wild-type strains and the following mutant alleles were used: a functional null allele $centrosomin^{HK21}$ [25], a strong loss-of-function allele $Sas\text{-}4^{S2214}$ [23], and a strong loss-of-function allele mud^{4} [34]. *Dp(1:3)DC281* is a chromosome with a duplication of the *mud* gene region [44]. fng^{NP5399} (*fng-Gal4*, Gal4 Enhancer Trap Insertion Database, http://kyotofly.kit.jp/stocks/GETDB/getdb.html) expresses *Gal4* in the pupal accessory gland epithelial cells and larval-pupal wing disc (data not shown). *AyGal4*, $apterous^{MD544}$ (*ap-Gal4*), and *Act5C-Gal4* have been described previously [45,46]. *hs-FLP* was used as the source of the FLP recombinase [47]. $Tub\text{-}Gal80^{TS}$ was used for the TARGET system [48]. *UAS-Sterile20-like kinase*, *UAS-pebble* and $UAS\text{-}sqh^{D20.D21}$ express the wild type of *Sterile20-like kinase* [49], the wild type of *pebble* [50] and a constitutively active forms of *sqh* [51]. The strains *103962* (*UAS-shotgun.IR*, VDRC), $mud^{JF02911}$ (*UAS-mud.IR*, Transgenic RNAi project) [52] and *VALIUM20-mCherry* (*UAS-mCherry.IR*, Transgenic RNAi project at Harvard Medical School) [52] express inverted repeat RNAs (which form hairpin loop double-stranded RNAs) for *shotgun*, *mud*, and *mCherry*. The strains *mus209.ΔNhe::GFP* (*PCNA-GFP*) [53], *Ubi-Cyclin B::GFP* [54], *sqh::GFP* [55] and *Septin2::GFP* [56] have been described previously. $polo^{CC01326}$ (*polo::GFP*) is a protein trap line of *polo* (FlyTrap, http://cooley.medicine.yale.edu/flytrap/index.aspx#page2) [57].

Immunostaining and microscopic analysis

The dissected accessory glands were fixed with 4% formaldehyde (Wako) and stained using standard immunostaining protocols. For the DNA staining, the fixed samples were pretreated with RNase (Wako, 0.025 mg/ml) for 15 minutes at 37°C and then stained with propidium iodide (Invitrogen, 1:500). Rhodamine-phalloidin (Invitrogen, 1:40) was used to stain the filamentous actin (F-actin). The following primary antibodies were used: rabbit anti-phospho-histone H3 (P-H3) polyclonal antibody (Millipore, 1:200), mouse anti-α-tubulin (α-Tub) monoclonal antibody (Sigma, 1:50), rat anti-α-tubulin (α-Tub) monoclonal antibody (Millipore, 1:25), rabbit anti-PKCζ (C-20) polyclonal antibody cross-reacting with *Drosophila* aPKC (Santa Cruz, 1:200), mouse anti-coracle (Cora) monoclonal antibody (Developmental Studies Hybridoma Bank, 1:20), mouse anti-lamin Dm_0

($LamDm_0$) monoclonal antibody (Developmental Studies Hybridoma Bank, 1:40), mouse anti-peanut (Pnut) monoclonal antibody (Developmental Studies Hybridoma Bank, 1:5) and mouse anti-FLAG M2 (FLAG) monoclonal antibody (Sigma, 1:200). The following secondary antibodies were used: Cy3-conjugated donkey anti-mouse IgG (Jackson ImmunoResearch, 1:200), Cy2-conjugated donkey anti-mouse IgG (Jackson ImmunoResearch, 1:200), Cy5-conjugated donkey anti-mouse IgG (Jackson ImmunoResearch, 1:200), Alexa Fluor 488-conjugated donkey anti-rat IgG (Millipore, 1:200) and Cy5-conjugated donkey anti-rabbit IgG (Jackson ImmunoResearch, 1:200). Stained samples were mounted in 50% glycerol/PBS containing 0.25% n-propyl gallate (Wako) and observed with an ECLIPSE TE2000-U with a Digital ECLIPSE C1 and C1Si confocal system (Nikon). Images were processed using EZ-C1 Gold Version 3.70 (Nikon), Adobe Photoshop CS3 Extended (Adobe Systems), and Adobe Illustrator CS3 (Adobe Systems).

Detection of formation of central spindle and contractile ring

We used microtubule bundles and actin filaments as markers for the central spindle and contractile ring, respectively. In central spindle assembly, microtubule filaments bundle together, forming a large structure that crosses the cell equator. We regarded microtubule-related structures having these features (i.e., bundling and equator-crossing) with fewer microtubule filaments as partially assembled central spindles. However, if the filaments neither associated with each other nor crossed the cell equator, we did not regard the structures as central spindles.

The accumulation of actin filaments in the equatorial region of the cell membrane is usually associated with formation of a cleavage furrow, and we considered a contractile ring to have partially formed if either of these two features was observed.

Temporal expression of genes using the TARGET system

The TARGET system [48] was used for the temporal expression of genes in the pupal accessory gland epithelium. To restrict the expression of the target genes by activation of $Gal80^{TS}$, flies were reared at a permissive temperature (19°C). To permit moderate expression of the target genes by weak activation of $Gal80^{TS}$, flies were reared at a semi-permissive temperature (26°C).

To fully express *Sterile20-like kinase*, *pebble* and $sqh^{D20.D21}$ in the accessory gland primordia just before binucleation (Figure 2K–O) (Table 1), pupae reared at 19°C for 110 hours after puparium formation (APF) were incubated at 29°C for 5 hours (genotypes: *w*/*Y*; *Tub-*$Gal80^{TS}$*/UAS-Sterile20-like kinase*; *fng-Gal4*/+, *w*/*Y*; *Tub-*$Gal80^{TS}$*/UAS-shotgun.IR*; *fng-Gal4*/+, *w*/*Y*; *Tub-*$Gal80^{TS}$*/UAS-pebble*; *fng-Gal4*/+, *w*/*Y*; *Tub-*$Gal80^{TS}$*/UAS-*$sqh^{D20.D21}$; *fng-Gal4*/+). To knockdown *shotgun* by expressing *shorgun.IR* in the accessory gland primordia just before binucleation (Additional file 1: Figure S4A and B) (Table 1), pupae reared at 19°C for 80 hours APF were incubated at 29°C for 20 hours (genotypes: *w*/*Y*; *Tub-*$Gal80^{TS}$*/UAS-shotgun.IR*; *fng-Gal4*/+). To moderately express mud^S in the accessory gland primordia just before binucleation (Figure 6D–G), pupae reared at 19°C for 110 hours APF were incubated at 26°C for 5 hours (genotype: mud^4*/Y*; *Tub-*$Gal80^{TS}$/+; *fng-Gal4*/*UAS-FLAG::*mud^S). To express mud^{PBD}, mud^L and mud^S in the accessory gland primordia in the cell-division stage (Figure 5G–J), pupae reared at 19°C for 40 hours APF were incubated at 29°C for 5 hours (genotypes: *w*/*Y*; *Tub-*$Gal80^{TS}$/+; *fng-Gal4*/*UAS-FLAG::*mud^{PBD}, *w*/*Y*; *Tub-*$Gal80^{TS}$/+; *fng-Gal4*/*UAS-FLAG::*mud^L, *w*/*Y*; *Tub-*$Gal80^{TS}$/+; *fng-Gal4*/*UAS-FLAG::*mud^S). Pupae were dissected immediately after the target gene inductions described above.

Construction of plasmids

pP-Acp70A-Stinger:

The upstream enhancer of *Acp70A* (-477 to -34) was amplified from the genome DNA of *Canton-S* with a PCR (primer set #1 in Additional file 2: TableS2) and subcloned into T vector *pMD20* (TaKaRa) by using TA cloning. The fragment for the Acp70A enhancer was digested with *Bgl*II and *Not*I and subcloned into *pH-Stinger* (Drosophila Genomics Resource Center (DGRC)) to construct *pP-Acp70A-Stinger*.

pUAS-FLAG::mud^{PBD}*-attB* (see Additional file 1: Figure S7, Figure S8 and Additional file 2: Table S1):

The genomic fragment encompassing three subisoforms of mud^{PBD} (*mud-RH*, *mud-RI*, and *mud-RL* in Additional file 1: Figure S7) (from just after the start codon to the stop codon) was amplified with a PCR (primer set #2 in Additional file 2: Table S2) from the BAC clone CH322-147E14 (P[acman] Resources) [58] and subcloned into *T vector pMD20* (TaKaRa) by using TA cloning. The forward primer also included the Kozak sequence, start codon and *FLAG* tag sequence. The seventh intron (eighth intron in the case of *mud-RI*), which included the mud^S-specific exon, was removed from the fragment with an inverse PCR (primer set #3 in Additional file 2: Table S2) and ligated to generate a *FLAG*-tagged protein-coding region including *mud-RH*, *mud-RI* and *mud-RL*. This fragment was digested with *Not*I and *Kpn*I and subcloned into *pUASattB* (FlyC31, http://www.flyc31.org/) [59] to generate *pUAS-FLAG::*mud^{PBD}*-attB*.

pUAS-FLAG::mud^L*-attB* (see Additional file 1: Figure S7, Figure S8 and Additional file 2: Table S1):

The genomic fragment encompassing a mud^{L} (*mud-RF* in Additional file 1: Figure S7) (from just after the start codon to the stop codon) was amplified with PCR (primer set #2 in Additional file 2: Table S2) from the BAC clone CH322-147E14 (P[acman] Resources) [58] and subcloned into *T vector pMD20* (TaKaRa) by using TA cloning. The forward primer also included the Kozak sequence, start codon and *FLAG* tag sequence. The seventh intron, which included the PBD-encoding exons and mud^{S}-specific exon, was removed from the fragment with an inverse PCR (primer set #4 in Additional file 2: Table S2) and ligated to generate a *FLAG*-tagged Mud-RF-coding fragment. This fragment was digested with *Not*I and *Kpn*I and subcloned into *pUASattB* (FlyC31, http://www.flyc31.org/) [59] to generate *pUAS-FLAG::*mud^{L}*-attB*.

pUAS-FLAG::mud^{S}*-attB* (see Additional file 1: Figure S7, Figure S8 and Additional file 2: Table S2):

The genomic fragment encompassing two subisoforms of mud^{S} (*mud-RG* and *mud-RK* in Additional file 1: Figure S7) (from just after the start codon to the stop codon) was amplified with a PCR (primer set #5 in Additional files 2: Table S2) from the BAC clone CH322-147E14 (P[acman] Resources) [58] and subcloned into *T vector pMD20* (TaKaRa) by using TA cloning. The forward primer also included the Kozak sequence, start codon and *FLAG* tag sequence. The *FLAG*-tagged fragment, which included both *mud-RG* and *mud-RK*, was digested with *Not*I and *Kpn*I and subcloned into *pUASattB* (FlyC31, http://www.flyc31.org/) [59] to generate *pUAS-FLAG::*mud^{S}*-attB*.

pUAS-mud^{S}*.IR-attB* (see Additional file 1: Figure S7, Figure S8 and Additional file 2: Table S2):

The genomic fragment including the mud^{S}-specific exon and upstream intron with a splice donor and acceptor (Additional file 1: Figure S7) was amplified with a PCR (primer set #6 in Additional file 2: Table S2) from the genome DNA of *Canton-S* and subcloned into *T vector pMD20* (TaKaRa) by using TA cloning (#1). The mud^{S}-specific exon without the upstream intron was also amplified with a PCR (primer set #7 in Additional file 2: Table S2) from the genome DNA of *Canton-S* and subcloned into *T vector pMD20* (TaKaRa) by using TA cloning (#2). The plasmid #1 was digested with *Not*I and *Xho*I, and the plasmid #2 was digested with *EcoR*I and *Not*I. Both of the digested fragments were combined in a single plasmid *pUASattB* (FlyC31, http://www.flyc31.org/) [59] to generate *pUAS-*mud^{S}*.IR*.

Generation of transgenic fly lines

The *pP-Acp70A-Stinger* vector was injected into *y, w* fly lines with standard protocols to generate transgenic lines. The *pUAS-FLAG::*mud^{PBD}*-attB*, *pUAS-FLAG::*mud^{L}*-attB*, *pUAS-FLAG::*mud^{S}*-attB* and *pUAS-*mud^{S}*.IR-attB* vectors were injected into y^{1}, *M{vas-int.Dm}ZH-2A, w*;; M{3xP3-RFP.attP}ZH-86Fb* or y^{1}, *M{vas-int.Dm}ZH-2A, w*; M{3xP3-RFP.attP'}ZH-51C* with ΦC31-mediated site-specific integration to generate transgenic lines.

RT-PCR to verify the expression of *UAS-mud* isoforms

Total RNA was extracted from third-instar larvae of the following four genotypes: *w/Y;;* *hs-Gal4/UAS-FLAG::*mud^{PBD}, *w/Y;;* *hs-Gal4/UAS-FLAG::*mud^{L}, *w/Y;;* *hs-Gal4/UAS-FLAG::*mud^{S}, and *w/Y;;* *hs-Gal4/+* (negative control). Before the extraction of RNA, larvae were heat-shocked twice at 37°C for 45 minutes and subsequently incubated at 25°C for 2 hours to reach the high level expression of *UAS* targeted genes. The cDNA of each genotype was synthesized using the oligo-dT primer with PrimeScript RT-PCR kit (TaKaRa). Two primer sets (#8 and #9 listed in Additional file 2: Table S2 of the supplementary material) that specifically amplify *FLAG::mud* transgenes but not endogenous *mud* genes (Additional file 1: Figure S8) were used for the PCR.

Semi-quantitative RT-PCR to verify isoform-specific knockdown by *UAS-*mud^{S}*.IR*

Total RNA was extracted from third-instar larvae of the following two genotypes: *w/Y*; *Act5C-Gal4/UAS-mCherry.IR* (control) and *w/Y*; *Act5C-Gal4/+*; *+/UAS-*mud^{S}*.IR* (knockdown for mud^{S}). The cDNA of each genotype was synthesized using the oligo-dT primer with PrimeScript RT-PCR kit (TaKaRa). Expressions of genes were normalized by using *Rpl32* as a reference gene. The three sets of primers #10, #11 and #12 listed in Additional file 2: Table S2 of the supplementary material (Additional file 1: Figure S7) were used for the PCR.

Animal ethics

All animals used in above genetic experiments were anesthetized with carbon dioxide before each mating. All procedures complied with guidelines of the Animal Ethics Committee of Gakushuin University.

Additional files

Additional file 1: Figures S1, S2, S3, S4, S5, S6, S7 and S8 are included.

Additional file 2: Tables S1 and S2 are included.

Abbreviations

APF: After puparium formation; *mud*: *mushroom body defect*; PBD: Pins binding domain; NuMA: Nuclear mitotic apparatus; RhoGAP: GTPase activating protein for Rho; RhoGEF: Guanine nucleotide exchange factor for Rho GTPase; M phase: Mitotic phase; Acp70A: Accessory gland protein 70A; P-H3: Phospho-histone H3; PCNA: Proliferating cell nuclear antigen; GFP: Green fluorescence protein; *D*E-cadherin: *Drosophila* epithelial cadherin; MRLC: Myosin regulatory light chain; *sqh*: *spaghetti squash*; Par: Partitioning-defective protein; Pav: Pavarotti; Pnut: Peanut; SOP: Sensory organ precursor cell; *fng*: *fringe*; *ap*: *apterous*; *Act5C*: *Actin 5C*; *UAS*: *Upstream activation sequence*; Tub: Tubulin; TARGET: Temporal and regional gene expression targeting; IR: Inverted repeat; aPKC: atypical protein kinase C; Cora: Coracle; $LamDm_0$: lamin Dm_0.

Competing interests
The authors declare that they have no competing interests.

Authors' contributions
KT obtained and analyzed all of the cytological data and helped in all experiments performed by other authors. AK discovered the synchronous and wavelike M-phase entry at binucleation. TI discovered the particular cell polarity during binucleation and examined PCNA::GFP expression. RM and HN analyzed the reproductive data and contributed to manuscript preparation. TAY directed the project. The manuscript was written by KT and TAY. All authors read and approved the final manuscript.

Acknowledgments
We thank S. Cohen, C. Gonzalez, K. Matsuno, J. Raff, R. Saint, A. Carpenter, the Bloomington Stock Center, Kyoto Stock Center, the National Institute of Genetics, Mitsubishi Kagaku Institute of Life Sciences and the VDRC Stock Center for supplying us with fly stocks, and we thank the Developmental Studies Hybridoma Bank at the University of Iowa for supplying us with antibodies. We also thank BestGene Inc. for generating new transgenic fly lines. We are grateful to M. Kamakura for technical advice.

Author details
[1]Department of Life Science, Faculty of Science, Gakushuin University, Tokyo 171-8588, Japan. [2]Institute for Biomolecular Science, Gakushuin University, Tokyo 171-8588, Japan. [3]Department of Biology, Graduate School of Science, Kobe University, Kobe 657-8501, Japan. [4]Graduate School of Natural Science and Technology, Okayama University, Okayama 700-8530, Japan.

Received: 13 May 2014 Accepted: 11 December 2014
Published online: 20 December 2014

References

1. Pasumarthi KB, Field LJ: **Cardiomyocyte cell cycle regulation.** *Circ Res* 2002, **90:**1044–54.
2. Celton-Morizur S, Merlen G, Couton D, Margall-Ducos G, Desdouets C: **The insulin/Akt pathway controls a specific cell division program that leads to generation of binucleated tetraploid liver cells in rodents.** *J Clin Invest* 2009, **119:**1880–7.
3. Bersell K, Arab S, Haring B, Kuhn B: **Neuregulin1/ErbB4 signaling induces cardiomyocyte proliferation and repair of heart injury.** *Cell* 2009, **138:**257–70.
4. Kwon M, Scholey JM: **Spindle mechanics and dynamics during mitosis in Drosophila.** *Trends Cell Biol* 2004, **14:**194–205.
5. D'Avino PP, Savoian MS, Glover DM: **Cleavage furrow formation and ingression during animal cytokinesis: a microtubule legacy.** *J Cell Sci* 2005, **118:**1549–58.
6. Gadde S, Heald R: **Mechanisms and molecules of the mitotic spindle.** *Curr Biol* 2004, **14:**R797–805.
7. Somers WG, Saint R: **A RhoGEF and Rho family GTPase-activating protein complex links the contractile ring to cortical microtubules at the onset of cytokinesis.** *Dev Cell* 2003, **4:**29–39.
8. Piekny A, Werner M, Glotzer M: **Cytokinesis: welcome to the Rho zone.** *Trends Cell Biol* 2005, **15:**651–8.
9. Karess RE, Chang XJ, Edwards KA, Kulkarni S, Aguilera I, Kiehart DP: **The regulatory light chain of nonmuscle myosin is encoded by spaghetti-squash, a gene required for cytokinesis in Drosophila.** *Cell* 1991, **65:**1177–89.
10. Mabuchi I, Okuno M: **The effect of myosin antibody on the division of starfish blastomeres.** *J Cell Biol* 1977, **74:**251–63.
11. Wu Q, Sahasrabudhe RM, Luo LZ, Lewis DW, Gollin SM, Saunders WS: **Deficiency in myosin light-chain phosphorylation causes cytokinesis failure and multipolarity in cancer cells.** *Oncogene* 2010, **29:**4183–93.
12. Wu Q, Xu FL, Li Y, Prochownik EV, Saunders WS: **The c-Myc target glycoprotein1balpha links cytokinesis failure to oncogenic signal transduction pathways in cultured human cells.** *PLoS One* 2010, **5:**e10819.
13. Chen PS, Stumm-Zollinger E, Aigaki T, Balmer J, Bienz M, Bohlen P: **A male accessory gland peptide that regulates reproductive behavior of female D. melanogaster.** *Cell* 1988, **54:**291–8.
14. Villella A, Peyre JB, Aigaki T, Hall JC: **Defective transfer of seminal-fluid materials during matings of semi-fertile fruitless mutants in Drosophila.** *J Comp Physiol A Neuroethol Sens Neural Behav Physiol* 2006, **192:**1253–69.
15. Bertram MJ, Akerkar GA, Ard RL, Gonzalez C, Wolfner MF: **Cell type-specific gene expression in the Drosophila melanogaster male accessory gland.** *Mech Dev* 1992, **38:**33–40.
16. Taniguchi K, Kokuryo A, Imano T, Minami R, Nakagoshi H, Adachi-Yamada T: **Binucleation of Drosophila Adult Male Accessory Gland Cells Increases Plasticity of Organ Size for Effective Reproduction.** *Biol Syst* 2012, **1:**e101.
17. Kunda P, Baum B: **The actin cytoskeleton in spindle assembly and positioning.** *Trends Cell Biol* 2009, **19:**174–9.
18. Nicklas RB: **How cells get the right chromosomes.** *Science* 1997, **275:**632–7.
19. Edgar BA, Sprenger F, Duronio RJ, Leopold P, O'Farrell PH: **Distinct molecular mechanism regulate cell cycle timing at successive stages of Drosophila embryogenesis.** *Genes Dev* 1994, **8:**440–52.
20. Kunda P, Pelling AE, Liu T, Baum B: **Moesin controls cortical rigidity, cell rounding, and spindle morphogenesis during mitosis.** *Curr Biol* 2008, **18:**91–101.
21. Kunda P, Rodrigues NT, Moeendarbary E, Liu T, Ivetic A, Charras G, Baum B: **PP1-mediated moesin dephosphorylation couples polar relaxation to mitotic exit.** *Curr Biol* 2012, **22:**231–6.
22. Tepass U, Gruszynski-DeFeo E, Haag TA, Omatyar L, Torok T, Hartenstein V: **shotgun encodes Drosophila E-cadherin and is preferentially required during cell rearrangement in the neurectoderm and other morphogenetically active epithelia.** *Genes Dev* 1996, **10:**672–85.
23. Basto R, Lau J, Vinogradova T, Gardiol A, Woods CG, Khodjakov A, Raff JW: **Flies without centrioles.** *Cell* 2006, **125:**1375–86.
24. Goshima G, Vale RD: **Cell cycle-dependent dynamics and regulation of mitotic kinesins in Drosophila S2 cells.** *Mol Biol Cell* 2005, **16:**3896–907.
25. Megraw TL, Li K, Kao LR, Kaufman TC: **The centrosomin protein is required for centrosome assembly and function during cleavage in Drosophila.** *Development* 1999, **126:**2829–39.
26. Field CM, Kellogg D: **Septins: cytoskeletal polymers or signalling GTPases?** *Trends Cell Biol* 1999, **9:**387–94.
27. Kammermeier L, Spring J, Stierwald M, Burgunder JM, Reichert H: **Identification of the Drosophila melanogaster homolog of the human spastin gene.** *Dev Genes Evol* 2003, **213:**412–5.
28. Ahringer J: **Control of cell polarity and mitotic spindle positioning in animal cells.** *Curr Opin Cell Biol* 2003, **15:**73–81.
29. Izumi Y, Ohta N, Hisata K, Raabe T, Matsuzaki F: **Drosophila Pins-binding protein Mud regulates spindle-polarity coupling and centrosome organization.** *Nat Cell Biol* 2006, **8:**586–93.
30. Siller KH, Cabernard C, Doe CQ: **The NuMA-related Mud protein binds Pins and regulates spindle orientation in Drosophila neuroblasts.** *Nat Cell Biol* 2006, **8:**594–600.
31. Bowman SK, Neumuller RA, Novatchkova M, Du Q, Knoblich JA: **The Drosophila NuMA Homolog Mud regulates spindle orientation in asymmetric cell division.** *Dev Cell* 2006, **10:**731–42.
32. Minestrini G, Mathe E, Glover DM: **Domains of the Pavarotti kinesin-like protein that direct its subcellular distribution: effects of mislocalisation on the tubulin and actin cytoskeleton during Drosophila oogenesis.** *J Cell Sci* 2002, **115:**725–36.
33. Adams RR, Tavares AA, Salzberg A, Bellen HJ, Glover DM: **pavarotti encodes a kinesin-like protein required to organize the central spindle and contractile ring for cytokinesis.** *Genes Dev* 1998, **12:**1483–94.
34. Guan Z, Prado A, Melzig J, Heisenberg M, Nash HA, Raabe T: **Mushroom body defect, a gene involved in the control of neuroblast proliferation in Drosophila, encodes a coiled-coil protein.** *Proc Natl Acad Sci U S A* 2000, **97:**8122–7.
35. Kopein D, Katanaev VL: **Drosophila GoLoco-protein Pins is a target of Galpha(o)-mediated G protein-coupled receptor signaling.** *Mol Biol Cell* 2009, **20:**3865–77.
36. Gonczy P: **Mechanisms of asymmetric cell division: flies and worms pave the way.** *Nat Rev Mol Cell Biol* 2008, **9:**355–66.
37. Buffin E, Emre D, Karess RE: **Flies without a spindle checkpoint.** *Nat Cell Biol* 2007, **9:**565–72.
38. Fink J, Carpi N, Betz T, Betard A, Chebah M, Azioune A, Bornens M, Sykes C, Fetler L, Cuvelier D, Piel M: **External forces control mitotic spindle positioning.** *Nat Cell Biol* 2011, **13:**771–8.
39. Tang TK, Tang CJ, Chao YJ, Wu CW: **Nuclear mitotic apparatus protein (NuMA): spindle association, nuclear targeting and differential subcellular localization of various NuMA isoforms.** *J Cell Sci* 1994, **107**(Pt 6):1389–402.

40. Du Q, Stukenberg PT, Macara IG: **A mammalian Partner of inscuteable binds NuMA and regulates mitotic spindle organization.** *Nat Cell Biol* 2001, **3:**1069–75.
41. Nakajima Y, Meyer EJ, Kroesen A, McKinney SA, Gibson MC: **Epithelial junctions maintain tissue architecture by directing planar spindle orientation.** *Nature* 2013, **500:**359–62.
42. Bergstralh DT, Lovegrove HE, St Johnston D: **Discs large links spindle orientation to apical-basal polarity in Drosophila epithelia.** *Curr Biol* 2013, **23:**1707–12.
43. Hasholzner U, Stieber P, Zimmermann A, Burges A, Hofmann K, Schmitt UM, Schmeller N, Schalhorn A: **Nuclear mitotic apparatus protein (NuMA) in benign and malignant diseases.** *Anticancer Res* 1999, **19:**2415–20.
44. Venken KJ, Popodi E, Holtzman SL, Schulze KL, Park S, Carlson JW, Hoskins RA, Bellen HJ, Kaufman TC: **A molecularly defined duplication set for the X chromosome of Drosophila melanogaster.** *Genetics* 2010, **186:**1111–25.
45. Ito K, Awano W, Suzuki K, Hiromi Y, Yamamoto D: **The Drosophila mushroom body is a quadruple structure of clonal units each of which contains a virtually identical set of neurones and glial cells.** *Development* 1997, **124:**761–71.
46. Milan M, Campuzano S, Garcia-Bellido A: **Developmental parameters of cell death in the wing disc of Drosophila.** *Proc Natl Acad Sci U S A* 1997, **94:**5691–6.
47. Golic KG, Lindquist S: **The FLP recombinase of yeast catalyzes site-specific recombination in the Drosophila genome.** *Cell* 1989, **59:**499–509.
48. McGuire SE, Le PT, Osborn AJ, Matsumoto K, Davis RL: **Spatiotemporal rescue of memory dysfunction in Drosophila.** *Science* 2003, **302:**1765–8.
49. Hipfner DR, Keller N, Cohen SM: **Slik Sterile-20 kinase regulates Moesin activity to promote epithelial integrity during tissue growth.** *Genes Dev* 2004, **18:**2243–8.
50. Prokopenko SN, Brumby A, O'Keefe L, Prior L, He Y, Saint R, Bellen HJ: **A putative exchange factor for Rho1 GTPase is required for initiation of cytokinesis in Drosophila.** *Genes Dev* 1999, **13:**2301–14.
51. Mitonaka T, Muramatsu Y, Sugiyama S, Mizuno T, Nishida Y: **Essential roles of myosin phosphatase in the maintenance of epithelial cell integrity of Drosophila imaginal disc cells.** *Dev Biol* 2007, **309:**78–86.
52. Ni JQ, Markstein M, Binari R, Pfeiffer B, Liu LP, Villalta C, Booker M, Perkins L, Perrimon N: **Vector and parameters for targeted transgenic RNA interference in Drosophila melanogaster.** *Nat Methods* 2008, **5:**49–51.
53. Thacker SA, Bonnette PC, Duronio RJ: **The contribution of E2F-regulated transcription to Drosophila PCNA gene function.** *Curr Biol* 2003, **13:**53–8.
54. Huang J, Raff JW: **The disappearance of cyclin B at the end of mitosis is regulated spatially in Drosophila cells.** *EMBO J* 1999, **18:**2184–95.
55. Royou A, Sullivan W, Karess R: **Cortical recruitment of nonmuscle myosin II in early syncytial Drosophila embryos: its role in nuclear axial expansion and its regulation by Cdc2 activity.** *J Cell Biol* 2002, **158:**127–37.
56. Silverman-Gavrila RV, Hales KG, Wilde A: **Anillin-mediated targeting of peanut to pseudocleavage furrows is regulated by the GTPase Ran.** *Mol Biol Cell* 2008, **19:**3735–44.
57. Morin X, Daneman R, Zavortink M, Chia W: **A protein trap strategy to detect GFP-tagged proteins expressed from their endogenous loci in Drosophila.** *Proc Natl Acad Sci U S A* 2001, **98:**15050–5.
58. Venken KJ, Carlson JW, Schulze KL, Pan H, He Y, Spokony R, Wan KH, Koriabine M, de Jong PJ, White KP, Bellen HJ, Hoskins RA: **Versatile P [acman] BAC libraries for transgenesis studies in Drosophila melanogaster.** *Nat Methods* 2009, **6:**431–4.
59. Bischof J, Maeda RK, Hediger M, Karch F, Basler K: **An optimized transgenesis system for Drosophila using germ-line-specific phiC31 integrases.** *Proc Natl Acad Sci U S A* 2007, **104:**3312–7.

Developmental Biology ■ (■■■■) ■■■–■■■

Contents lists available at ScienceDirect

Developmental Biology

journal homepage: www.elsevier.com/locate/developmentalbiology

GATAe regulates intestinal stem cell maintenance and differentiation in *Drosophila* adult midgut

Takashi Okumura [a], Koji Takeda [a,c], Megumi Kuchiki [a], Marie Akaishi [a], Kiichiro Taniguchi [a], Takashi Adachi-Yamada [a,b,*]

[a] Department of Life Science, Faculty of Science, Gakushuin University, 1-5-1 Mejiro, Toshima-ku, Tokyo 171-8588, Japan
[b] Institute for Biomolecular Science, Gakushuin University, 1-5-1 Mejiro, Toshima-ku, Tokyo 171-8588, Japan
[c] Graduate Course in Life science, Graduate school of Science, Gakushuin University, 1-5-1 Mejiro, Toshima-ku, Tokyo 171-8588, Japan

ARTICLE INFO

Article history:
Received 16 July 2015
Received in revised form
30 November 2015
Accepted 19 December 2015

Keywords:
Drosophila
Adult midgut
Intestinal stem cell
GATA transcription factor
GATAe

ABSTRACT

Adult intestinal tissues, exposed to the external environment, play important roles including barrier and nutrient-absorption functions. These functions are ensured by adequately controlled rapid-cell metabolism. GATA transcription factors play essential roles in the development and maintenance of adult intestinal tissues both in vertebrates and invertebrates. We investigated the roles of *GATAe*, the *Drosophila* intestinal GATA factor, in adult midgut homeostasis with its first-generated knock-out mutant as well as cell type-specific RNAi and overexpression experiments. Our results indicate that *GATAe* is essential for proliferation and maintenance of intestinal stem cells (ISCs). Also, *GATAe* is involved in the differentiation of enterocyte (EC) and enteroendocrine (ee) cells in both Notch (N)-dependent and -independent manner. The results also indicate that *GATAe* has pivotal roles in maintaining normal epithelial homeostasis of the *Drosophila* adult midgut through interaction of N signaling. Since recent reports showed that mammalian GATA-6 regulates normal and cancer stem cells in the adult intestinal tract, our data also provide information on the evolutionally conserved roles of GATA factors in stem-cell regulation.

1. Introduction

The adult gastrointestinal tract is continually exposed to exogenous stress and damage. Under this condition, gastrointestinal tissues have barrier, digestive, and absorptive functions, which are supported by a high cellular metabolic rate. Therefore, intestinal stem cell (ISC) maintenance is important for preserving intestinal physiological functions to constantly provide mature gastrointestinal epithelial cells including enterocytes (ECs) and enteroendocrine cells (ees) throughout an organism's life. Also, this mechanism has been reported to be conserved among mammals and *Drosophila* (Crosnier et al., 2006; Micchelli and Perrimon, 2006; Ohlstein and Spradling, 2006; Simons and Clevers, 2011; Weissman, 2000). Between both animals, similar genetic regulation of ISCs including their proliferation and differentiation has also been reported (Jiang and Edgar, 2012; Takashima and Hartenstein, 2012).

GATA transcription factors are evolutionarily conserved and play important roles in cell proliferation, differentiation, and survival of multiple developing and adult tissues/organs (Ayanbule et al., 2011; Molkentin, 2000; Murakami et al., 2005). Those in hematopoiesis and developing heart and endodermal tissues have been extensively studied and in various multicellular organisms (Ayanbule et al., 2011). In vertebrates, GATA-4, GATA-5, and GATA-6 of the six GATA factors show distinct expression patterns in adult gastrointestinal tissues (Fang et al., 2006). GATA-4 and GATA-5 tend to be highly expressed in proximal tracts, such as the stomach, jejunum and/or ileum, while GATA-6 is expressed throughout the gastrointestinal tract in mice and humans (Fang et al., 2006; Haveri et al., 2008). Consistently, GATA-4 is essential for region-specific identities (Bosse et al., 2006) and show lineage-specific expression. Briefly, GATA-4 shows high- and low-level expression in EC/proliferating crypt and Paneth cells, respectively (Bosse et al., 2006; Dusing and Wiginton, 2005). With regard to GATA-5, it is expressed in secretory lineages such as ee, Paneth, and goblet cells (Dusing and Wiginton, 2005). On the other hand, GATA-6 is mainly expressed in mature ee and immature proliferating cells in the crypt (Dusing and Wiginton, 2005). Accordingly, each of these GATA members are at least in part involved in the proliferation or differentiation of immature cells in the intestinal crypt, and gene expression in differentiated cells (Beuling et al., 2012; Beuling et al., 2011; Bosse et al., 2006; Divine et al., 2004; Haveri et al., 2008). Furthermore, GATA factors are involved in gastrointestinal diseases, including cancer, with

* Corresponding author at: Department of Life Science, Faculty of Science, Gakushuin University, 1-5-1 Mejiro, Toshima-ku, Tokyo 171-8588, Japan.
E-mail address: Takashi.Adachi-Yamada@gakushuin.ac.jp (T. Adachi-Yamada).

http://dx.doi.org/10.1016/j.ydbio.2015.12.017
0012-1606/

interaction of signal transduction such as Wnt and BMP signaling (Lin et al., 2012; Tsuji et al., 2014; Whissell et al., 2014; Zheng and Blobel, 2010). However, in invertebrates including the *Drosophila*, few studies of GATA factors have been reported regarding the maintenance of the adult digestive tract. Therefore, essential evolutionally conserved features in GATA functions in gut maintenance have remained elusive.

In *Drosophila*, five GATA transcription factor genes, *pannier* (*pnr*, also known as *GATAa*), *serpent* (*srp*, also known as *GATAb*), *grain* (*grn*, also known as *GATAc*), *GATAd*, and *GATAe*, are known (Abel et al., 1993; Lin et al., 1995; Okumura et al., 2005; Ramain et al., 1993; Rehorn et al., 1996; Winick et al., 1993). Of them, *srp*, *grn*, *GATAd*, and *GATAe* are expressed in embryonic, larval, and/or adult midguts, a counterpart of the mammalian small intestine, whose epithelium is derived from the endoderm (Murakami et al., 2005; Okumura et al., 2005; Senger et al., 2006). The *srp* and *GATAe* are required for specification and differentiation of the endoderm forming larval midgut epithelium (Okumura et al., 2005; Rehorn et al., 1996; Reuter, 1994). In addition, *srp* expression in the endoderm disappears at embryonic stages, while *GATAe* continues to be expressed from embryonic to adult stages (Okumura et al., 2005). In adult midgut homeostasis, *GATAe* has recently been reported to be required for maintenance of the EC morphological structure, digestive function, and intestinal gene expression (Buchon et al., 2013). On the other hand, the function of *grn* and *GATAd* in the midgut has remained unknown.

In this study, to determine whether GATA factors are involved in regulation of *Drosophila* adult midgut homeostasis, we conducted RNAi treatment for the five *Drosophila* GATA factor genes in ISCs and their daughter cells enteroblasts (EBs). We found that *GATAe* RNAi only induced some defective phenotypes including a decrease in ISCs/EBs. We also confirmed similar defects with the first-generated knock-out mutant of *GATAe*. Furthermore, *GATAe*-knocked out cells indicated the possibility that *GATAe* is essential for EC and ee differentiation in an N-dependent and independent manner. Based on observations of the new *GATAe* knock-out mutation, we found that *GATAe* is required for normal adult midgut development. Combined with previous reports, our results indicate that *GATAe* contributes to the development and maintenance of *Drosophila* midgut epithelia throughout life.

2. Materials and methods

2.1. Fly stocks

Canton-S and w^{1118} were used as wild-type strains. The following RNAi lines obtained from the Vienna *Drosophila* RNAi Center (VDRC) were used for knock-down of GATA family genes and *N*; *pnr* (#101522), *srp* (#112327), *grn* (#105192), *GATAd* (#50364), *GATAe* (#10420), and *N* (#100002). We also obtained the other *GATAe* RNAi lines (#33748 and #34641) from the Bloomington *Drosophila* Stock Center (BDSC). The *Df(3R)sbd45* is a deficiency line uncovering the *GATAe* locus. The reporter lines for the *Delta* (*Dl*) transcription, N-signaling activity, JAK-STAT-signaling activity, and c-Jun N-terminal kinase (JNK)-signaling activity were Dl^{05151} (*Dl-lacZ*), *Gbe+Su(H)m8-lacZ*, *10 × STAT92E-GFP*, and puc^{E69} (*puc-lacZ*), respectively (Bach et al., 2007; Biteau et al., 2008; Furriols and Bray, 2001; Martin-Blanco et al., 1998). The GAL4 lines used were *NP6267* (*esg-GAL4*) (Hayashi et al., 2002) and *Ay-GAL4* (Ito et al., 1997). The following upstream activating sequence (UAS) strains were used: *UAS-FLAG::GATAe* producing a functional tagged form of the GATAe protein (gift from Murakami), *UAS-GATAe::V5-6 × His* producing a functional fusion protein tagged with V5 epitope and 6 × His and its effect is weaker than *FLAG::GATAe* (personal communication) (gift from Murakami), $UAS\text{-}N^{ICD}$ (Go et al., 1998), *UAS-p35* (BDSC), *UAS-DIAP-myc* (gift from Hay) (Umemori et al., 2007), and *UAS-rpr* (DGRC #108447). The following UAS lines were also obtained from BDSC; *UAS-Apoliner* (Bardet et al., 2008) and $UAS\text{-}GFP^{S65T}$. The *hs-FLP* provided FLP recombinase under heat-shocked temperature, $tub\text{-}GAL80^{ts}$ ubiquitously overexpressing the temperature-sensitive GAL80 protein (McGuire et al., 2003), and *FRT82B, FRT82B,tub-GAL80*, *FRT19A*, and *tub-GAL80,hs-FLP,w*,FRT19A* used for mosaic analysis with repressible cell marker (MARCM), were also obtained from BDSC.

Flies were cultured in standard medium at appropriate temperature and females were used in all experiments in this study.

2.2. Generation of GATAe knock-out fly

Knock-out of the *GATAe* locus was conducted by ends-out gene targeting, as previously reported (Rong and Golic, 2000). To construct the pW25-*GATAe*-KO vector, the 5′ and 3′ homologous fragments were amplified by polymerase chain reaction (PCR) from w^{1118} genomic DNA with the following primers; 5′-CACCGCGGCCGCATGGTCTGCAAAACTATCTCAC-3′, 5′-CACCGGTACCTGCGTTGTCTGCTGTTCCAT-3′, 5′-CACCGGCGCGCCGGCGCTCCAAGTTTAC-3′, and 5′-CACCCGTACGCTGCAAGTGCATTAGTGTG-3′, then the amplified fragments were subcloned into the *NotI-Acc65*I and *AscI-BsiWI* sites of the pW25 vector (Drosophila Genomics Resource Center). The transgenic donor lines transformed with the pW25-*GATAe*-KO construct were generated by BestGene Inc. Male donor flies were crossed with *w;;hsp70-FLP*, *hsp70-I-SceI* females and the progeny were heat-shocked at 37 °C for an hour three times at day 2 and 3 after egg laying. The F1 females with mosaic or white eyes were collected and crossed with *w;hsp70-FLP* males, and F2 males and females with red eyes were screened and five lines, in which the pW25-*GATAe*-KO construct was replaced with *GATAe* genomic locus, were obtained. The replacement was investigated by genomic PCR with the following primers; 5R 5′-GAATTGAATTGACGCTCCGT-3′, 3R 5′-GTCCGGTTGTTTTCGTGCTC3′, 1 5′-GGTGTGGGTAGCTAATTGG-3′, 2 5′-GATCGTGATCATGATACGAC-3′, 3 5′-TCGCAGGGAGTCAACCTGA-3′, 4 5′-AGCAGCTTCAACTGCTGG-3′, and 5 5′-ATTGACTCTGTGGCGTTGAT-3′. The resulting deletion covered almost all the coding region of *GATAe*, as shown in Fig. 2A, and this line was used as a loss of the function allele of *GATAe* (termed $GATAe^{1}$) in this study.

To select the 1st instar larvae of $GATAe^{1}$ homozygotes, the green balancer *TM3,twi-GAL4,UAS-2 × GFP* was used.

2.3. Immunostaining and in situ hybridization

Larval, pupal, and adult midguts dissected at appropriate stages were fixed with 4% paraformaldehyde. After being washed with phosphate buffered saline (PBS) containing TritonX-100 (PBT), immunostaining was done with the following primary antibodies; rat anit-GFP (Nacalai Tesque, 1:200), chick anti-β-galactosidase (β-gal) (abcam, 1;200), rabbit anti-phospho histone H3 (pH3) (Upstate Biotech, 1:200), mouse anti-Prospero (Pros) (DSHB, 1:100), mouse anti-Armadillo (Arm) (DSHB, 1:50), mouse anti-Delta (Dl) (DSHB, 1:50), mouse anti-dual-phosphorylated ERK (dpERK) (Sigma-Aldrich, 1:200), and rabbit anti-Pdm1 (provided by Xiaohang, 1:200). Secondary antibodies used were Cy3- and DyLight649-conjugated anti-mouse IgG (Jackson ImmunoResearch, 1:200), Alexa Fluor® 488-conjugated anti-rat IgG (Jackson Immuno Research, 1:200), Alexa Fluor® 555-conjugated and DyLight649-conjugated anti-rabbit IgG (Jackson ImmunoResearch, 1:200), and DyLight649-conjugated anti-chick IgY (Jackson ImmunoResearch, 1:200). Rhodamine-conjugated and Alexa Fluor® 647-conjugated phalloidin (Molecular Probe, 1:100) were used to stain filamentous actin (F-actin). Nuclei were stained with DAPI (SIGMA).

For *in situ* hybridization, the adult midgut fixed with 4% paraformaldehyde was washed with PBS containing 0.1% Tween 20. After they were treated with 10 μg/ml proteinase K and refixed with 4% paraformaldehyde, hybridization with digoxygenin-labeled RNA probes was done at 60 °C overnight. After washing, they were treated with a 0.1% blocking regent (Roche) and reacted with an anti-Digoxygenin antibody labeled with alkaline-phosphatase

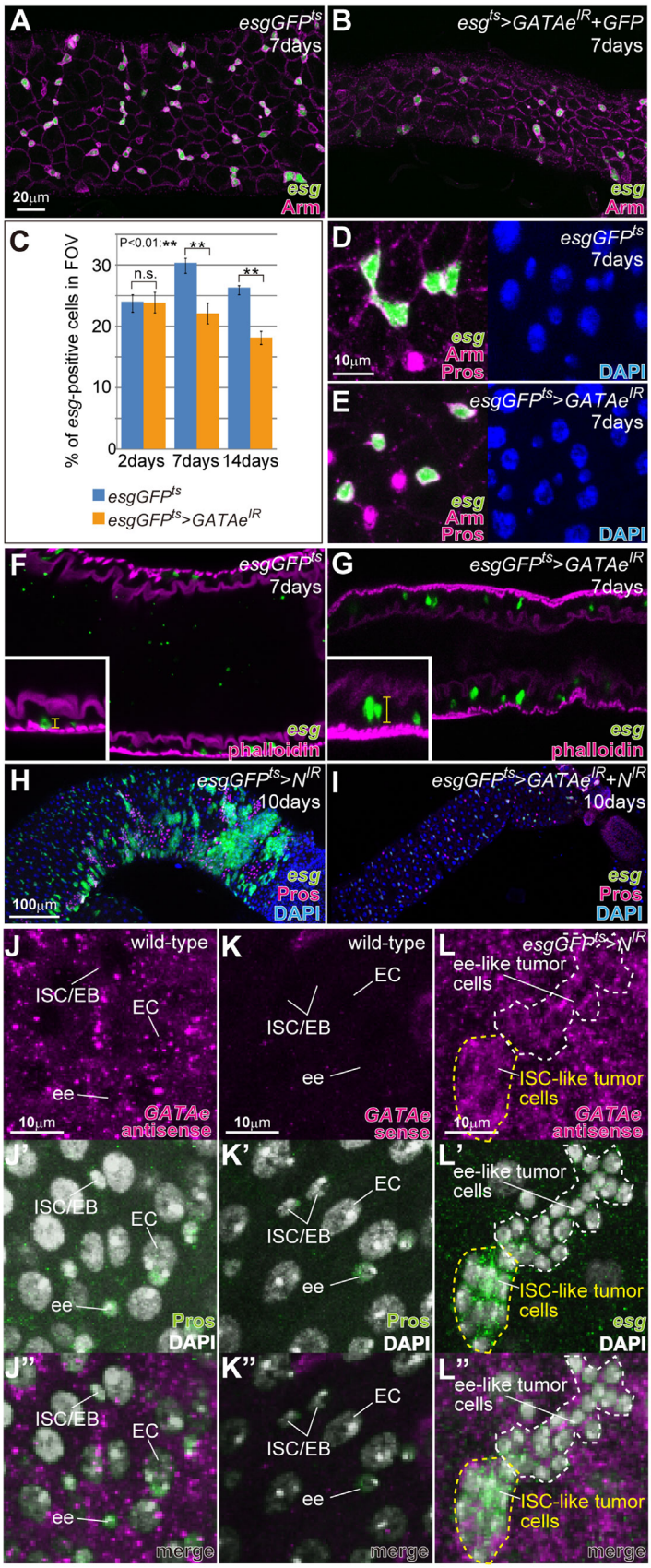

Fig. 1. *GATAe* RNAi in ISC/EBs caused a decrease of their cell number and morphological defects. (A–G) Frequency and morphology of the *esg*-positive cells in the *esgGFP*^{ts} (A, D, and F) and *esgGFP*^{ts} > *GATAe*^{IR} (B, E, and G) PMG. Green is *esg*-positive cells. Magenta in A and B, D and E, and F and G were stained with anti-Arm antibody, anti-Arm and anti-Pros antibodies, and phalloidin, respectively. Insets in F and G are magnifications. (C) Frequency of *esg*-positive cells in FOV of *esgGFP*^{ts} (24.04 ± 1.23 at 2 days old, 30.35 ± 0.77 at 7 days old, and 26.33 ± 0.39 at 14 days old) and *esgGFP*^{ts} > *GATAe*^{IR} (23.93 ± 1.73 at 2 days old, 22.17 ± 1.64 at 7 days old, and 18.16 ± 1.06 14 days old) midguts. The *esg*-positive cells in FOV of 5 or 6 midguts were counted. Error bars indicate standard error of means (S.E.M). *P*-values were calculated using Student's t test. (H and I) PMG of *esgGFP*^{ts} > *N*^{IR} (H) and *esgGFP*^{ts} > *GATAe*^{IR} + *N*^{IR} (I). Green and magenta are *esg*-positive and Pros-positive cells. (J–L) *GATAe* mRNA in the PMG of wild-type (J and K) and *esgGFP*^{ts} > *N*^{IR} (L) was detected with antisense (J and L) but not sense (K) probes (magenta). Green indicates Pros- (J', J", K' and K") and *esg*-positive (L' and L") cells. Blue and white indicate nuclei stained with DAPI.

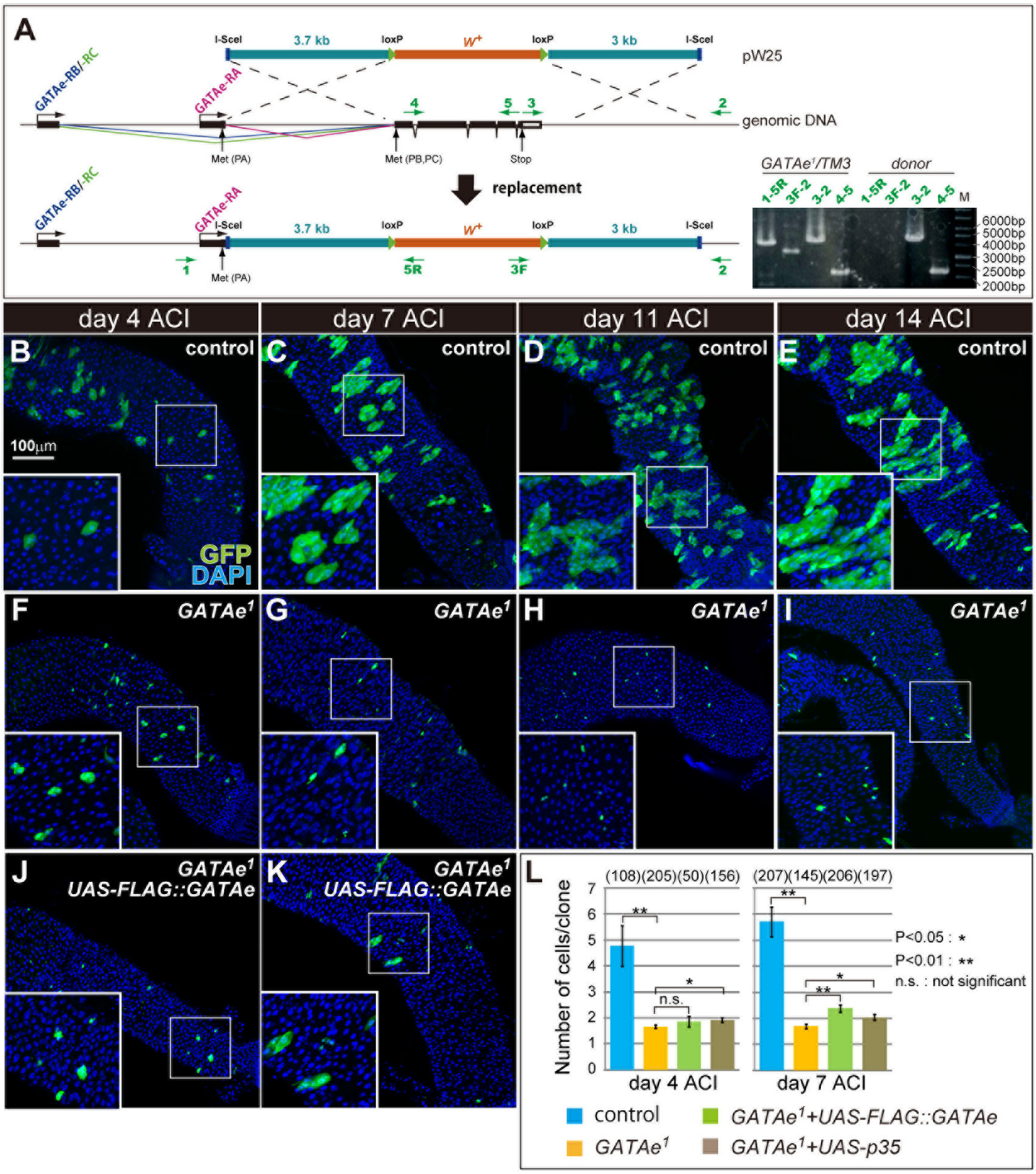

Fig. 2. Novel knock-out mutation of *GATAe* (*GATAe*^{1}) inhibited normal epithelial regeneration. (A) Replacement of *GATAe* locus induced by targeted homologous recombination. Green arrows indicate primers used in confirming the replacement. The results of genomic PCR with several pairs of primers showed precise replacement. (B–K) MARCM clones of control (B–E), *GATAe*^{1} (F–I), and *GATAe*^{1} expressing *FLAG::GATAe* (J and K) in the PMGs at 4 (B, F, and J), 7 (C, G, and K), 11 (D and H), and 14 (E and I) days after clone induction (ACI). Insets are magnification of the boxes. The MARCM clones and nuclei were marked with GFP (green) and stained with DAPI (blue). (L) Graph showing average cell number in each genotype of MARCM clones at 4 and 7 days ACI. Average cell numbers are 4.78 ± 0.78 (day 4) and 5.71 ± 0.57 (day 7) in control clones, 1.67 ± 0.07 (day 4) and 1.70 ± 0.08 (day 7) in *GATAe*^{1} clones, 1.86 ± 0.20 (day 4) and 2.39 ± 0.14 (day 7) in *GATAe*^{1} expressing *FLAG::GATAe* clones, and 1.92 ± 0.09 (day 4) and 2.05 ± 0.11 (day 7) in *GATAe*^{1} expressing *p35* clones. Error bars indicate S.E.M. *P*-values were calculated using Student's t test. The number of counted clones is in parentheses.

(Roche, 1:7000). Then, the anti-Digoxygenin antibody was detected using FastRed (Roche). The cDNAs of *GATAe* and β*int-ν* were used as templates for antisense and sense RNA probes prepared using a DIG RNA labeling kit (Roche).

The stained adult midgut was mounted in 80% glycerol and analyzed with Nikon Digital Eclipse C1 and C1Si confocal microscopes (Nikon). The images were processed with EZ-C1 3.90 Free Viewer (Nikon).

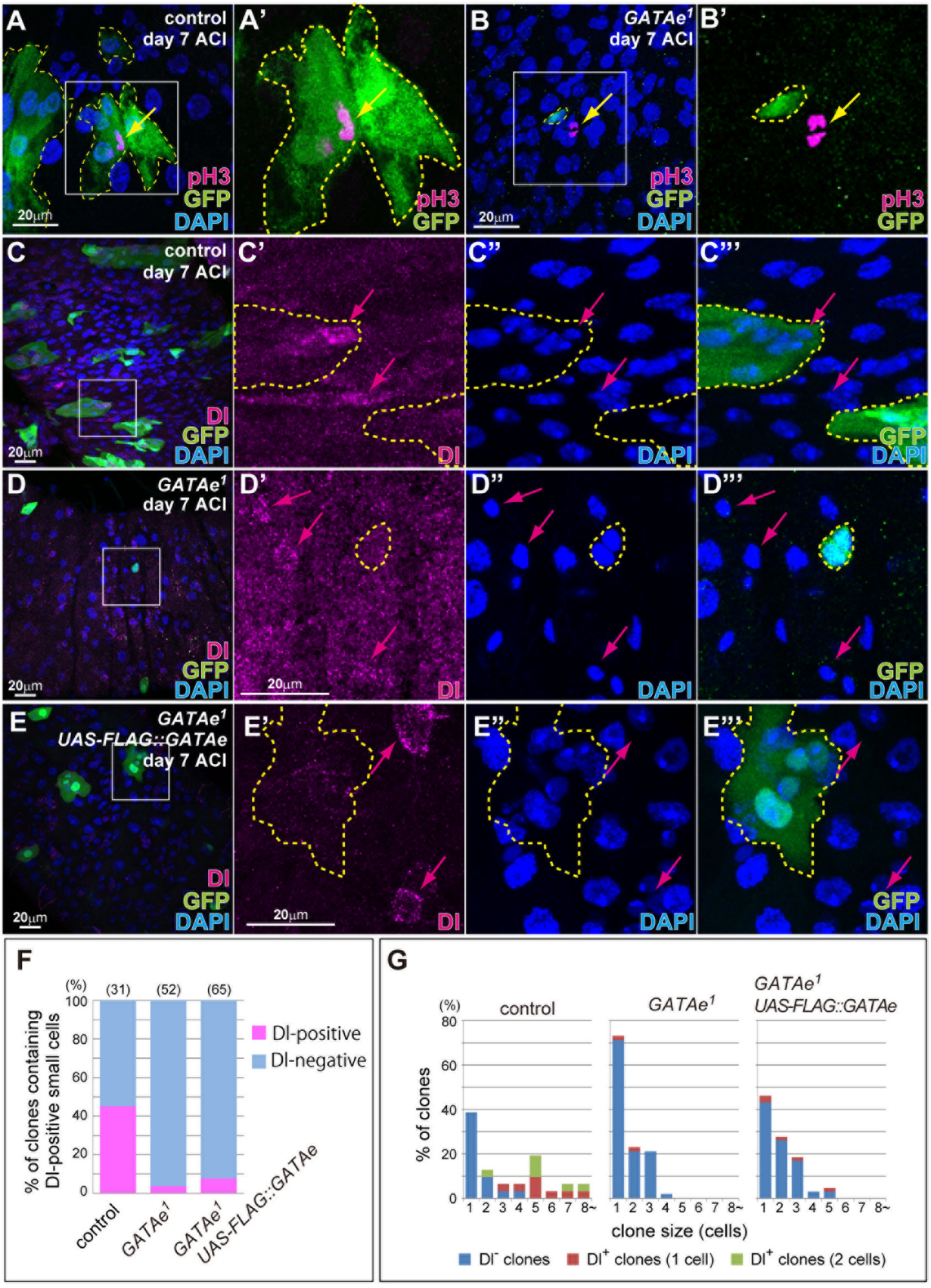

Fig. 3. *GATAe*^{1} disrupted ISC proliferation and maintenance. (A–E) MARCM clones of control (A and C), *GATAe*^{1} (B and D), and *GATAe*^{1} expressing *FLAG::GATAe* (E) immnostained with anti-pH3 (magenta in A and B) and anti-Dl (magenta in C–E) antibodies. A', B', C'-C''', D'-D''', and E'-E''' are magnifications of the boxes in A, B, C, D, and E, respectively. The yellow dotted lines indicate the outline of the MARCM clones. The yellow arrows in A and B indicate mitotic (pH3-positive) cells. The magenta arrows in C–E indicate examples of Dl-positive cells. The MARCM clones and nuclei in A–E were marked with GFP (green) and stained with DAPI (blue). (F) Frequency of MARCM clones containing Dl-positive cells in each genotype at 7 days ACI. The number of counted clones is in parentheses. (G) Clone size and ratio of clones containing no, one, and two Dl-positive cells at 7 days ACI.

2.4. TUNEL assay

The dissected adult midguts were fixed with 4% paraformaldehyde in PBS and cell death was detected with the Apoptag kit (Millipore Corporation, Billerica, MA, USA).

2.5. Temperature shift assay

In the RNAi and overexpression experiments with the TARGET system (McGuire et al., 2003), adult flies carrying *tub-GAL80^{ts}* combined with *esg-GAL4* were raised at a permissive temperature (18 °C). One-day-old flies were placed and cultured at a non-permissive temperature (29 °C) until dissection at the appropriate day old. In *GATAe* knock-down experiments by RNAi during larval and pupa stages, the given genotypes of the 1st larvae or white pupa raised at 18 °C were placed and cultured at 29 °C to the adult stages. Each genotype used in this assay is described in the Figure legends.

2.6. Mosaic analysis

To generate MARCM clones (Lee and Luo, 1999), given genotypes flies were raised and cultured at 25 °C until 7 days old, heat-shocked at 37 °C for 2 h 4 times, and additionally cultured for an appropriate number of days. The MARCM and twin-spot clones were also induced at the 3 rd instar larval stages and examined at the adult stages.

When the *GATAe* RNAi experiment with *Ay-GAL4* (Ito et al., 1997; Struhl and Basler, 1993) was conducted, adult flies were raised and cultured at 18 °C until 7 days old, heat-shocked at 37 °C for 20 min, and cultured at 25 °C for an appropriate number of days.

2.7. Quantification and statistical analysis

To examine the frequency of *esg*-positive cells in the *GATAe* RNAi experiment (Fig. 1C), the images of the posterior midgut of control (*w*;*esg-GAL4,UAS-GFP^{S65T}*/+;*tub-GAL80^{ts}*/+) and *GATAe* RNAi (*w*; *esg-GAL4,UAS-GFP^{S65T}*/*UAS-GATAe RNAi*; *tub-GAL80^{ts}*/+) flies stained with anti-GFP and anti-Pros antibodies were obtained using a confocal microscope. Then the total numbers of cells and *esg*-positive cells in the field of view (FOV) were manually counted in the posterior midgut using EZ-C1 3.90 Free Viewer (Nikon). Examples of FOV (636.5 μm × 636.5 μm) images are shown in Fig.1A and B.

To count the cell number per clone of controls (*hs-flp*/+;*Act5C-GAL4,UAS-GFP^{S65T}*/+;*FRT82B,tub-GAL80*/*FRT82B*), *GATAe^{1}* (*hs-flp*/+; *Act5C-GAL4,UAS-GFP^{S65T}*/+;*FRT82B,tub-GAL80*/*FRT82B,GATAe^{1}*), *GATAe^{1}* + *UAS-FLAG::GATAe* (*hs-flp*/+;*Act5C-GAL4,UAS-GFP^{S65T}*/*UAS-FLAG::GATAe*;*FRT82B,tub-GAL80*/*FRT82B,GATAe^{1}*), and *GATAe^{1}* + *UAS-p35* (*hs-flp*/+;*Act5C-GAL4,UAS-GFP^{S65T}*/*UAS-p35*;*FRT82B,tub-GAL80*/*FRT82B,GATAe^{1}*) generated in the posterior midgut with MARCM, we stained the adult midguts with DAPI and anti-GFP antibody, obtained images with the confocal microscope, and counted the cells in each MARCM clone (Fig. 2L and Fig. 4D). The frequencies of Dl-, Pdm1- and Pros-positive cells in each genotype clone were also counted after staining with anti-Dl, anti-Pdm1, and anti-Pros antibodies (Fig. 3F, and G, Fig. 6I, and J and Supplemental Fig. 4B).

In *FLAG::GATAe* and *GATAe::V5-6 × His* overexpression with MARCM, the frequency of each clone size was counted (Supplemental Fig. 3E). The genotypes used were *hs-flp*/+; *Act5C-GAL4,UAS-GFP^{S65T}*/*UAS-FLAG::GATAe; FRT82B,tub-GAL80*/*FRT82B,GATAe^{1}* and *tub-GAL80,hs-FLP,w^{+}, FRT19A*/*FRT19A; Act5C-GAL4,UAS-GFP^{S65T}*/+; *GATAe::V5-6 × His*/+.

The *P*-values were calculated using student's *t*-test as needed.

3. Results

3.1. GATAe-RNAi in ISCs/EBs affects midgut epithelial renewal

To determine whether the *Drosophila* GATA factors were involved in ISC regulation, we expressed each UAS-RNAi-construct against the five GATA factor genes, *pnr*, *srp*, *grn*, *GATAd*, and *GATAe*. The *escargot* (*esg*)-GAL4 driver under the control of GAL80^{ts}, a temperature-sensitive GAL80, combined with UAS-GFP (*esgGFP ^{ts}*) specifically induced strong expression of the above constructs in both ISCs and EBs at the permissive temperature of 29 °C but not at the non-permissive temperature of 19 °C (Fig. 1A) (Micchelli and Perrimon, 2006). Of the five GATA factor genes, we found that *GATAe* RNAi (*GATAe^{IR}*) caused a frequent decrease in *esg*-positive cells in the posterior midgut (PMG) when the flies were cultured at 29 °C for 7 days and 14 days but not for 2 days after eclosion (Fig. 1B and C). We also observed morphological and positional defects of *esg*-positive cells. The normal ISCs/EBs showed a pyramidal morphology and was located in an epithelial niche adjacent to the basement membrane (Fig. 1D and F). On the other hand, *GATAe^{IR}*-expressed ISCs/EBs showed a slightly larger, spherical morphology and detachment from the basal region (Fig. 1E and G compared with D and F). Similar defects were observed with the other RNAi constructs (#34641 and #33746) that direct against the different regions of *GATAe* mRNA (Supplemental Fig. 1A and B). Also, the morphological defects were not suppressed even by co-overexpression of the anti-apoptotic factors, *p35* and *Diap1* (Supplemental Fig. 1C and D).

In addition, *GATAe^{IR}* driven with *esgGFP^{ts}* resulted in a thin midgut tube (Fig. 1B and G compared with 1 A and F). This atrophy probably suggests that *GATAe^{IR}* induces an insufficient epithelial renewal. Indeed, *GATAe^{IR}* inhibited normal growth of the MARCM clones (Supplemental Fig. 1E–J) when compared with *pnr^{IR}*, *srp^{IR}*, *grn^{IR}* and *GATAd^{IR}*. *GATAe^{IR}* also inhibited ISC- and ee-like tumor formation induced by *N* RNAi (*N^{IR}*) with *esgGFP ^{ts}*, (Fig. 1H and I) (Micchelli and Perrimon, 2006). Thus, *GATAe*-knock-down in ISCs/EBs affected continuous epithelial renewal of the *Drosophila* adult midgut.

3.2. GATAe is expressed in all types of adult midgut epithelial cells

GATAe transcripts were previously detected from the adult midgut by RT-PCR and microarray analysis (Buchon et al., 2013; Okumura et al., 2005). To further examine which epithelial cell types express *GATAe* in the adult midgut, we conducted *in situ* hybridization for *GATAe* mRNA. With its antisense but not sense probe, *GATAe* mRNA was detectable at similar levels in all types of epithelial cells; ISC/EB (diploid cells), ee (Pros-positive cells) and EC (polyploid cells) (Fig. 1J–K"). Also, *GATAe* was expressed in ISC- and ee-like tumors induced by *N^{IR}* (Fig. 1L–L"). This was consistent with the tumor suppression induced by *GATAe^{IR}* (Fig. 1I). The *GATAe* expression implied that it plays important roles in all types of adult midgut epithelial cells.

3.3. Generation of novel GATAe knock-out mutant

Previously, *GATAe* functions in developmental and adult midguts were studied through RNAi experiments (Buchon et al., 2013; Okumura et al., 2005). In this study, to more directly evaluate *GATAe* roles, we generated a knock-out mutant of *GATAe* (*GATAe^{1}*) by using a homologous recombination–based gene targeting technique (Fig. 2A) (Rong and Golic, 2000). Most of the coding region of *GATAe* was replaced with the *w^{+}* gene in *GATAe^{1}*, which was verified by genomic PCR with primers corresponding to the *GATAe* locus and the knock-out construct pW25 (Fig. 2A). All individuals of *GATAe^{1}* homozygotes were died at the embryonic or the 1st instar larval stages with morphological and digestive defects in the midgut (Supplemental Fig. 6A–D). The *Df(3 R)sbd45*, a

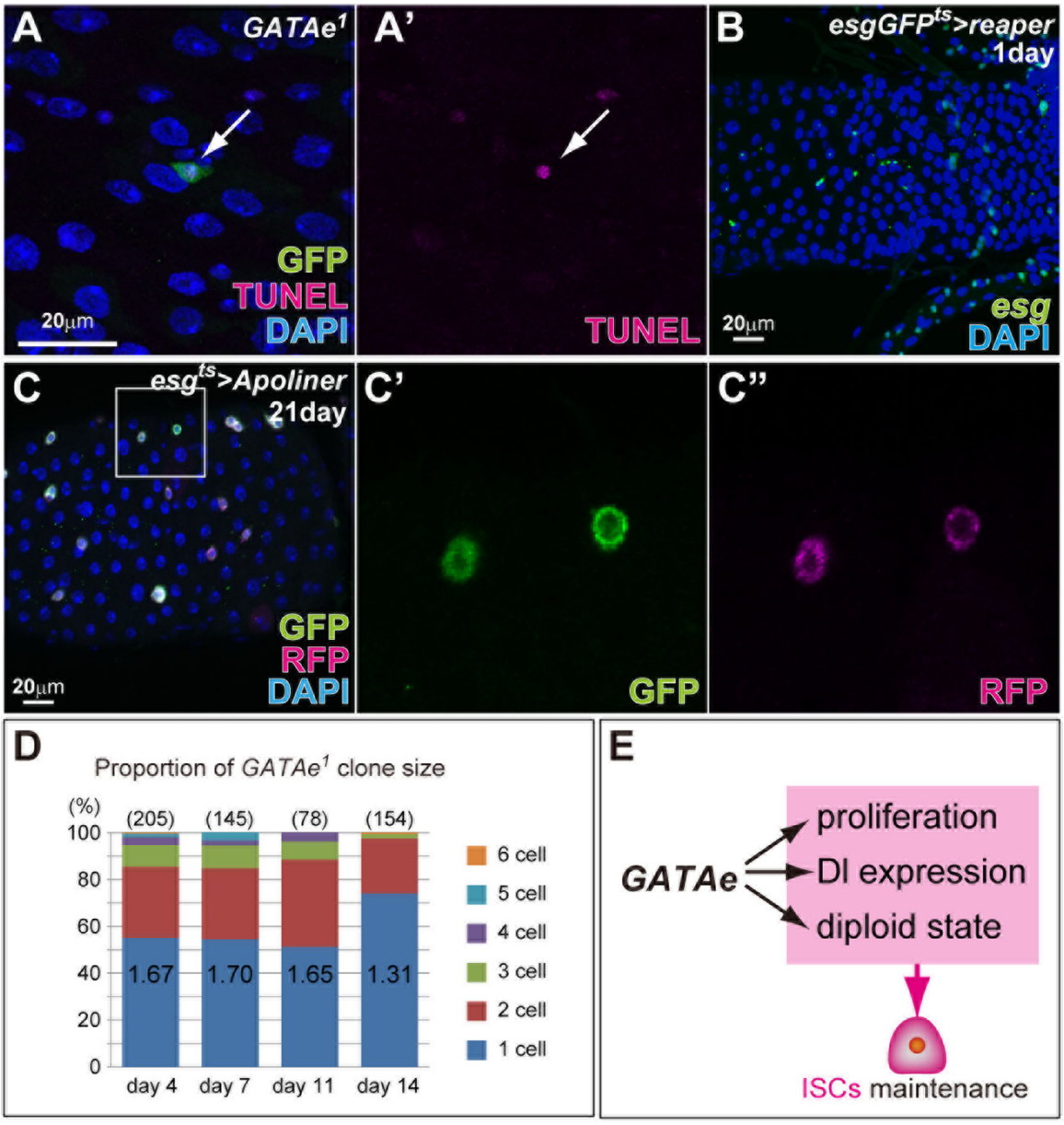

Fig. 4. *GATAe* depletion in ISC/EB-like small cells did not predominantly undergo cell death. (A) *GATAe*^{1} MARCM clone labeled with GFP (green) at 7 days ACI. TUNEL staining (magenta in A and A') was rarely detected in the *GATAe*^{1} clones (arrows in A and A'). A' is the single channel of TUNEL staining. (B) Adult PMG treated by *rpr* overexpression with *esgGFP*^{ts} for 1 day. Almost all *esg*-positive cells (green) disappeared. (C) Adult PMG expressing Apoliner and *GATAe*^{IR} that were induced by *esgGFP*^{ts} for 21days. GFP (green in C and C') and RFP (C and C") both were tethered to plasma membrane, indicating that the caspase pathway was not activated. C' and C" are single channels of GFP (green) and RFP (magenta) in the box of C, respectively. (D) Graph showing proportion of *GATAe*^{1} clone size at 4, 7, 11, and 14 days ACI. (E) Requirement of *GATAe* in ISC maintenance including its proliferation, Dl expression, diploid state, and survival.

deficiency line uncovering the *GATAe* locus failed to complement the lethality of *GATAe*^{1} (data not shown), suggesting that *GATAe* is essential for survival.

3.4. *GATAe is required for ISCs proliferation*

Next, we generated *GATAe*^{1} homozygous clones in the adult PMG with MARCM (Lee and Luo, 1999). Control clones showed normal growth at days 4, 7, 11, and 14 after clone induction (ACI) (Fig. 2B–E and L). In contrast, *GATAe*^{1} clone growth was inhibited under the same condition (Fig. 2F–I and L) and the clones largely stayed at the basal region (Fig. 6D and Supplemental Fig. 2I). In addition, at day 7 but not day 4 ACI, the *GATA*^{1} clone growth inhibition was slightly rescued by *FLAG::GATAe* overexpression (Fig. 2J–L). This slightness was probably due to the dominant effect of *GATAe* overexpression that affected ISC maintenance, as described in the discussion (Supplemental Fig. 3). Combined with the above results (Fig. 1 and Supplemental Fig. 1), we concluded that *GATAe* is required for epithelial renewal in the midgut.

We next investigated whether *GATAe* is required for ISC proliferation. To examine this, we confirmed the appearance of mitotic ISCs in *GATAe*^{1} clones with anti-phospho-Histone H3 (pH3) antibody. The result was that any mitotic ISCs were not observed in *GATAe*^{1} clones at day 7 ACI (Fig. 3A and B). Similarly, the pH3-positive cells also disappeared in the *GATAe* RNAi-treated midgut with *esgGFP*^{ts} (Supplemental Fig. 1K and L). These results suggest that *GATAe* is required for ISC proliferation.

Numerous signal transductions have been reported to be involved in promoting ISC proliferation. We asked whether the two major signaling pathways to induce ISC proliferation, Janus kinase/

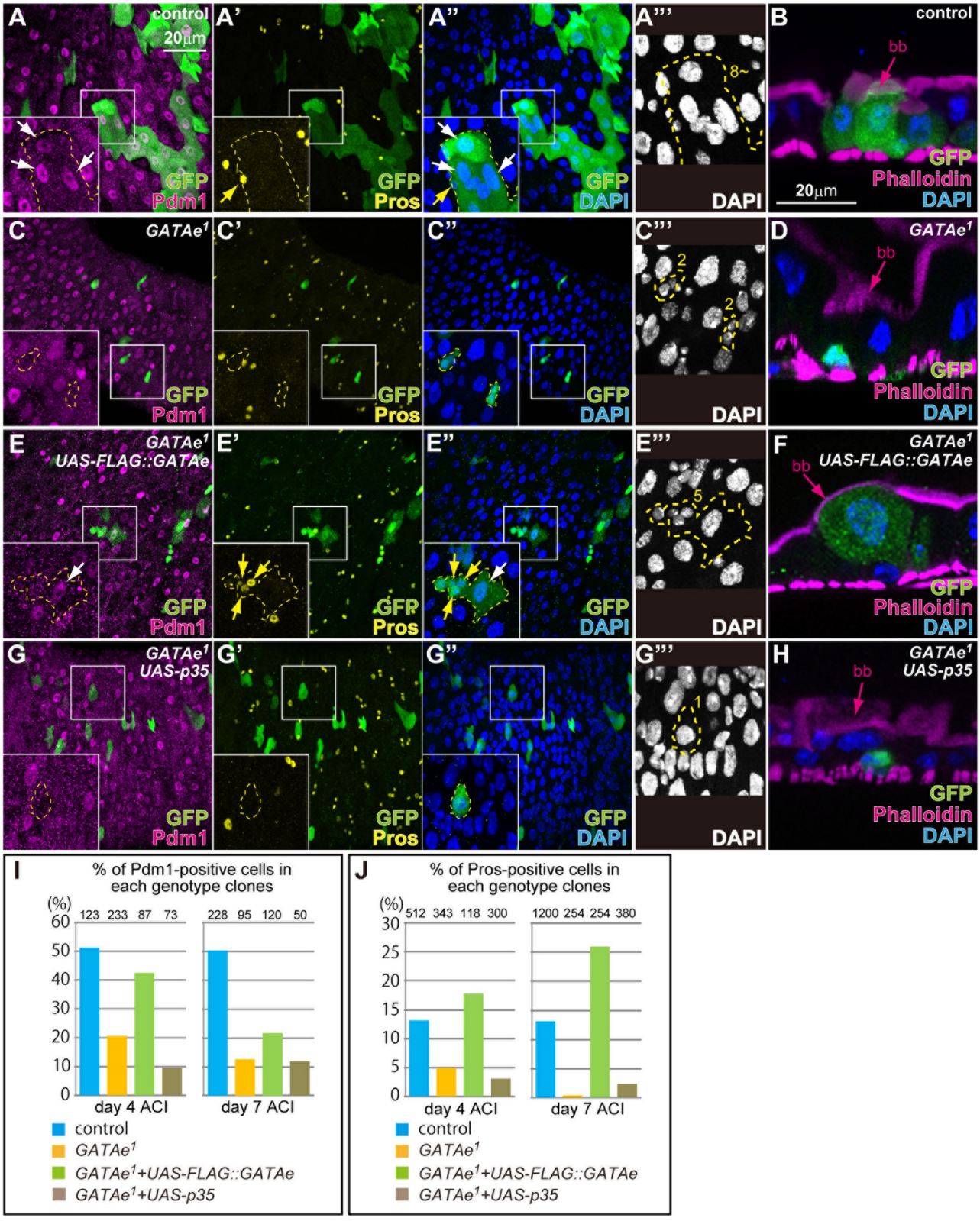

Fig. 5. *GATAe*^{1} suppressed EC and ee differentiation. (A–H) MARCM clone cells of control (A and B), *GATAe*^{1} (C and D), *GATAe*^{1} expressing *FLAG::GATAe* (E and F), and *GATAe*^{1} expressing *p35* in the PMG at day 7 ACI. The Pdm1 (magenta in A, C, E and G) and Pros (yellow in A', C', E' and G') expressions were detected with their antibodies. The cross sections of each MARCM clone in B, D F, and H were stained with phalloidin (magenta). Insets are magnifications of the boxes. White and yellow arrows indicate Pdm1- and Pros-positive cells in the clones. Magenta arrows indicate brush border (bb). MARCM clones were marked with GFP (green) and their outlines in the insets are indicated by dotted lines. Yellow numerals in A''', C''', E''' and G''' indicate cell numbers in the GFP-positive clone(s) in insets. Nuclei were stained with DAPI (blue and white). (I and J) Graphs showing frequency of Pdm1- (I) and Pros- (J) positive cells in each genotype clone. The number of counted cells is represented at the top.

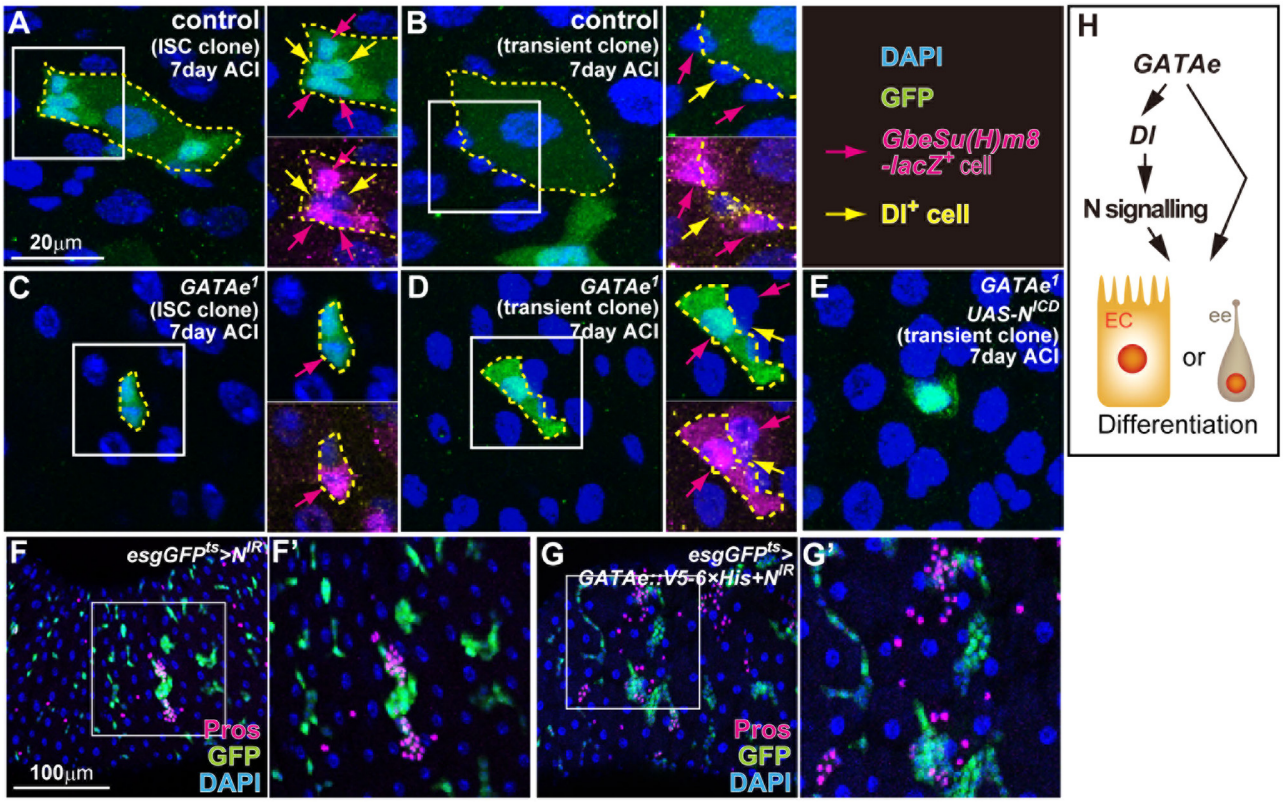

Fig. 6. *GATAe*^{1} caused cell growth inhibition without any N-signaling inactivation. (A–E) ISC (A and C) and transient (B, D, and E) MARCM clones of control (A and B), *GATAe*^{1} (C and D), and *GATAe*^{1} expressing N^{intra} (E) in the adult PMGs. The *Gbe-Su(H)m8-lacZ* (magenta) and Dl (yellow) expression were detected in A–D. The MARCM clones and nuclei were labeled with GFP (green) and DAPI (blue). Right panels are magnification of the boxes. The yellow dotted lines indicate the outline of the MARCM clones (A–D). (F and G) PMG expressing N^{IR} (F) and co-expressing *GATAe::V5-6* × *His* and N^{IR} (G) with *esgGFP*^{ts}. F' and G' are magnifications of the boxes in F and G, respectively. The *esg*-positive cells were marked with GFP (green). The Pros-positive cells (magenta) were also marked with anti-Pros antibody. Nuclei (blue) were stained with DAPI. (H) Predicted gene regulatory pathway necessary for EC and ee differentiation.

signal transducer and activator of transcription (JAK-STAT) and epidermal growth factor (EGF), are affected by *GATAe*^{IR} by using *10* × *STAT92E-GFP* and dual-phosphorylated ERK (dpERK) antibody, respectively (Jiang and Edgar, 2009; Jiang et al., 2009). However, we did not detect any obvious alteration in them in the *esgRFP*^{ts} > *GATAe*^{IR} midguts (Supplemental Fig. 1M and N). This suggested that the decrease in ISC proliferation in *GATAe*^{1} was not caused by a decrease in JAK-STAT or EGF signaling.

3.5. *GATAe is essential for maintaining stemness of ISCs*

A possible explanation for the disappearance of proliferative cells is due to ISC loss. To confirm this, we examined whether *GATAe*^{1} clones had diploid cells expressing Dl, an ISC molecular marker (Ohlstein and Spradling, 2007). In normal midguts, about half of the control MARCM clones were ISC clones that were multicellular and contained Dl^{+} cells, while the other half were transient clones that were Dl^{+} single cells at day 7 ACI (Fig. 3C, F, and G). On the other hand, the frequency of *GATAe*^{1} MARCM clones containing Dl^{+} cells drastically decreased (Fig. 3D, F, and G). Similarly, a decrease in Dl^{+} and *Dl-lacZ*$^{+}$ cells was observed in the *esgGFP*^{ts} > *GATAe*^{IR} midguts at 14 days old (Supplemental Fig. 2A–D). Under the same condition, RNAi against the other GATA factors did not abolish Dl expression both at 7 and 14 days old (Supplemental Fig. 2E–H and data not shown). Furthermore, we frequently observed the appearance of *GATAe*^{1} ISC clones without any diploid cells (Supplemental Fig. 2I and J). Instead, as observed in the *esgGFP* ^{ts} > *GATAe*^{IR} midgut, they have slightly larger nuclei when compared with the other diploid cells such as Dl^{+} ISC, mitotic ISC, and Pros^{+} ee (Fig. 3D, Supplemental Fig. 2I and J, and Supplemental Fig. 4). These results suggest that *GATAe* is required for ISC's identities and properties. On the other hand, we also found that the ISC disappearance in the *GATAe*^{1} mutant partially rescued by *FLAG::GATAe* overexpression (Fig. 3E, F, and G) as in the case of clone growth (Fig. 2).

Next, to confirm whether *GATAe*-depleted ISCs underwent apoptosis that triggered their elimination, we conducted TUNEL assay for the *GATAe*^{1} clones. However, TUNEL-positive cells were rarely observed in small *GATAe*^{1} clone cells (Fig. 4A). Consistently, *GATAe*^{1} clone size did not alter from 4 to 11 days ACI (Fig. 4D) and was not rescued enough by *p35* overexpression (Fig. 2L). Furthermore, a decrease in *esg*$^{+}$ cells by *GATAe*^{IR} (Fig. 1B, G and Supplemental Fig. 1) was not comparable to that observed in the overexpression of an apoptotic gene *reaper*, which immediately caused *esg*$^{+}$ cell disappearance (Fig. 4B). Moreover, the residual *esg*$^{+}$ cells did not show up-regulation of c-Jun N-terminal kinase (JNK) signaling monitored with *puckered* (*puc-lacZ*) (data not shown), TUNEL-positive cells (data not shown), and activation of the caspase pathway monitored with Apoliner (Fig. 4C). Apoliner indicated the translocation of EGFP but not RFP from the plasma membrane into the nuclei when apoptotic cascade was activated (Bardet et al., 2008). These results suggest that the growth inhibition of *GATAe*^{1} clones is not due to apoptosis. From the above observations, we also collectively concluded that *GATAe* is required for maintaining the stemness of ISCs (Fig. 4E).

3.6. *GATAe regulates EC and ee differentiation in an N-dependent and independent manner*

In this study, we also examined whether *GATAe* was required for EC and ee differentiation. To confirm this, we first observed their specific differentiation markers including morphological

characteristics and gene expression in *GATAe*^{1} MARCM clones (Lee et al., 2009; Micchelli and Perrimon, 2006; Ohlstein and Spradling, 2006). In control clones at 7 days ACI, differentiated ECs showed Pdm1 expression in the polyploid nucleus and an apically well-developed brush border (Fig. 5A and B). Differentiated ees had Pros expression in the diploid nucleus (Fig. 5A'). On the other hand, *GATAe*^{1} clones showed a frequent decrease in Pdm1^{+} and Pros^{+} cells at 4 and 7 days ACI (Fig. 5C–C", I, J, and Supplemental Fig. 4A and B). They also did not have any well-developed brush borders (Fig. 5D). Moreover, the decrease in ECs and ees in the *GATA*^{1} clones was partially and completely rescued by *FLAG::GATAe* overexpression (Fig. 5E–E", F, I, and J, and Supplemental Fig. 4B). Furthermore, EC disappearance was not inhibited with *p35* forced expression even in an equivalent size of EC-like cells (Fig. 5G, H and I, and Supplemental Fig. 4B). Similarly, ee loss was not rescued with *p35* forced expression (Fig. 5G' and J, and Supplemental Fig. 4B). These results indicated that *GATAe* is required for EC and ee differentiation.

Previous reports suggested that EC and ee differentiation required N signaling activation that was stimulated by Dl of ISCs (Kapuria et al., 2012; Ohlstein and Spradling, 2007). This allow us to speculate that a *GATAe* depletion influenced N signaling activation because we found that *GATAe* depletion affected Dl expression (Fig. 3D, F, G, and Supplemental Fig. 2). Therefore we examined N signaling levels with *Gbe+Su(H)m8-lacZ*, a reporter construct for N signaling activity (Furriols and Bray, 2001). In control ISC clones, some small *Gbe+Su(H)m8-lacZ*$^{+}$ cells (EBs) appeared at 7 days ACI (Fig. 6A). Under this condition, the control transient clone differentiated into a large EC in which *Gbe+Su(H)m8-lacZ* expression had already disappeared (Fig. 6B). On the other hand, *GATAe*^{1} ISC clones also contained a *Gbe+Su(H)m8-lacZ*$^{+}$ cell (Fig. 6C). Also, *GATAe*^{1} transient clone cells were small and their *Gbe+Su(H)m8-lacZ* expression still remained (Fig. 6D). These results were opposed to our expectation that *GATAe* depletion decreased *Gbe+Su(H)m8-lacZ* expression. However, it was possible that this appearance of *Gbe+Su(H)m8-lacZ*$^{+}$ cells in *GATAe*^{1} clones was due to transactivation from Dl^{+} ISCs located inside their early-stage clones and/or on the adjacent outside of them. Some Dl^{+} cells were observed around *GATAe*^{1} clones (Fig. 6A–D) and all ISCs in *GATAe*^{IR} driven with *esgGFP*^{ts} did not suppress *Gbe+Su(H)m8-lacZ* expression for 7 and 14 days (data not shown). Accordingly, we did not experimentally reveal that *GATAe* was required for N signaling activation. However, from the above results of Dl disappearance (Fig. 3D, F, G and Supplemental Fig. 2), we do not exclude the possibility that *GATAe* contributes to the N signaling activation through maintaining Dl expression.

Since excess N-signaling activation promotes EC differentiation including their growth (Kapuria et al., 2012; Micchelli and Perrimon, 2006), we tried to rescue the growth defect of *GATA*^{1} cells with forced expression of N^{ICD}, an active form of *N*. This could not, however, completely induce a large EC-like cell in *GATAe*^{1} clones (Fig. 6E). Conversely, the *GATAe* overexpression could not rescue EC differentiation defects induced by N-signaling inhibition (*esgGFP*^{ts} > N^{IR}) (Fig. 6F and G). Combined with above result of Dl disappearance, we concluded that *GATAe* is required for EC and ee differentiation in N-dependent and independent manner (Fig. 6H).

4. Discussion

It has previously been reported that *GATAe* transcripts were detected in the adult midgut (Fig.1) (Buchon et al., 2013; Okumura et al., 2005), suggesting that *GATAe* has an important role in adult midgut homeostasis. A recent report showed that *GATAe* RNAi in ECs consistently affected the adult midgut epithelial structure (Buchon et al., 2013). We further examined *GATAe* roles through *GATAe* knock-out, knock-down, and overexpression experiments, which revealed that *GATAe* has essential roles in midgut epithelial renewal where N signaling was involved.

4.1. GATAe maintains stemness of ISCs

We discuss that *GATAe* depletion abolishes ISC proliferation (Fig. 1–3 and Supplemental Fig. 1). This is the first evidence that *GATAe* is required for *Drosophila* ISC proliferation. Also, we found that *GATAe* depletion induces the disappearance of Dl^{+} ISCs without enough cell death/elimination and instead, slightly larger nuclear cells than diploid cells frequently appeared (Figs. 1 and 3 and Supplemental Figs. 2, and 4). Thus, *GATAe* depletion probably converted ISCs into non-proliferative cells. These observations suggest that *GATAe* function is required for maintaining the stemness of ISCs. In the *Drosophila* adult midgut, the epithelial basal region is a stem-cell niche where ISCs are anchored to the basement membrane (BM) with integrin. An inhibition of *myospheroid* (*mys*) encoding one of the two *Drosophila* integrin β subunits in ISCs/EBs induced ISCs differentiation (Goulas et al., 2012). In some cases, *GATAe* depletion showed the ISC's detachment (Fig. 1G), but any alteration of Mys protein levels was not observed (data not shown). Meanwhile, *GATAe* depletion decreased an expression of *βint-ν*, encoding the other integrin β subunit (Supplemental Fig. 5). However, its null homozygotes did not show ISC loss and detachment (Okumura et al., 2014). It is thought that Perlecan (Pcan), an extracellular matrix component, is the other candidate for targeting *GATAe* responsible for this phenotype. The lack of *trol* encoding Pcan autonomously caused ISC detachment from BM, proliferative cell disappearance, Dl^{+} cell loss, and inhibition of EC and ee differentiation, but not apoptosis and JAK-STAT and EGF signaling alteration (You et al., 2014). These phenotypes were very similar to those when *GATAe* was depleted. It is a possible that *GATAe* may regulate an anchor of ISCs to the BM through *trol* and maintain ISCs.

Drospohila adult midgut epithelial cells including ISCs are generated from their progenitors that express *esg* in the embryonic, larval, and pupa stages (Micchelli, 2012). Also, recent reports have indicated that *esg* regulates the stemness of ISCs in the adult midgut (Korzelius et al., 2014; Loza-Coll et al., 2014). Thus, *esg* is involved in stemness maintenance in the *Drosophila* midgut throughout life. Similarly, *GATAe* continues to be expressed from embryonic to adult midgut (Okumura et al., 2005). In addition, *GATAe* depletion caused defects in larval *esg*$^{+}$ cells and affected adult midgut development but not the other internal and external organs during the pupa stage (Supplemental Fig. 6E-N and data not shown). Furthermore, *GATAe* is required for development of the most posterior region of the adult midgut epithelium derived from the hindgut-proliferating-zone cells (Supplemental Fig. 6O, (Takashima et al., 2013). Although we did not strictly confirm if *GATAe* depletion affected *esg* expression levels in ISC, *GATAe* is required for maintaining stemness probably via the *esg* functions in *Drosophila* midgut development and maintenance throughout life.

GATAe overexpression did not largely rescue *GATAe*^{1} clone growth inhibition (Fig. 2J–L) and Dl expression disappearance (Fig. 3D, F, and G). We observed that the *FLAG::GATAe* and *GATAe::V5-6×His* overexpression with *esgGFP*^{ts} both resulted in a decrease in small *esg*$^{+}$ cells (Supplemental Fig. 3A, B compared with Fig. 1A). However, they did not affect survival, mitosis, and Dl and *Gbe+Su(H)m8-lacZ* expression of *esg*$^{+}$ cells (Supplemental Fig. 3C, D and data not shown). In addition to the decrease in small *esgGFP*$^{+}$ cells, we found that some EC-like polyploid cells showed a weak *esgGFP*$^{+}$ signal when *FLAG::GATAe* and *GATAe::V5-6×His* were overexpressed with *esgGFP*^{ts} (Supplemental Fig. 3A and B). This suggests that *GATAe* overexpression promotes EC and/or ee differentiation that inhibits ISC self-renewal. Indeed, 90%∼ of their MARCM clones were composed of single EC-like polyploid or Pros^{+} cells (Supplemental Fig. 3F-J). Also, the EC-like polyploid

cells expressed Pdm1 and a well-developed brush border (Supplemental Fig. 3G-I). This was consistent with the above results that *GATAe* overexpression could rescue EC and ee differentiation defects (Fig. 6E, F, I, and J). Thus, *GATAe* overexpression inhibited ISC self-renewal but not its differentiation.

Mouse *GATA-4* and *GATA-6* are expressed in the crypt-proliferative cells of the small intestine (Beuling et al., 2011; Bosse et al., 2006). Similarly, human *GATA-6* is expressed in the small intestine (Haveri et al., 2008). *GATA-6* conditional knock-out reduces crypt-proliferative cells that lead to a decrease in villus height and epithelial cell number in the distal ileum where *GATA-6* but not *GATA-4* is expressed (Beuling et al., 2011). Both *GATA-4* and *GATA-6* knock-out also induce similar defects in the proximal small intestine where both are expressed (Beuling et al., 2011; Walker et al., 2014). In the distal ileum, *GATA-6* knock-out also affects components and targets of Wnt- and N-signaling pathways as well as causes a decrease in crypt-cell proliferation (Beuling et al., 2011). This case might be similar to *GATAe* depletion, which decreases Dl expression and ISC proliferation (Fig. 3 and Supplemental Fig. 2). In addition, GATA-6 directly enhances expression of *LGR5* that activates Wnt signaling and represses *BMP4* expression in the stem cells of colorectal cancer (Tsuji et al., 2014; Whissell et al., 2014). Thus, GATA factors regulate signal transductions in the adult ISCs of both the *Drosophila* midgut and mammal small intestine.

4.2. GATAe regulates EC and ee differentiation in N-dependent and independent manner

The *Drosophila* adult midgut epithelium mainly consists of two types of differentiated cells, EC and ee (Marianes and Spradling, 2013; Micchelli and Perrimon, 2006; Ohlstein and Spradling, 2006). In their specification and differentiation, N signaling plays an important role (Bardin et al., 2010; Beehler-Evans and Micchelli, 2015; Kapuria et al., 2012; Ohlstein and Spradling, 2007). We showed that EC and ee differentiation were disrupted in $GATAe^{1}$ clones (Fig. 5), which were not rescued by excess N-signaling activation (Fig. 6). This suggests that *GATAe* is intrinsically required for EC and ee differentiation independently of N signaling.

A high- or low-level activation of the N-signaling pathway in EBs was stimulated from Dl expressed in neighboring ISCs (de Navascues et al., 2012). The activation subsequently regulates EC and ee differentiation (Kapuria et al., 2012; Perdigoto et al., 2011). We found that *GATAe* was required for Dl expression (Fig. 3 and Supplemental Fig. 2). These facts imply that *GATAe* also has an extrinsic role in EC and ee differentiation via Dl expression. In mouse distal ileum, *GATA-6* deletion similarly down-regulates expression of the *Delta-like 1* encoding the N ligand (Beuling et al., 2011). Conversely, N-signaling alteration did not affect *GATA-6* transcripts as in the case of *GATAe* transcripts in *N*-depleted cells (Fig. 1) (Beuling et al., 2011). A mechanism by which GATA factors regulate N-signaling ligand may be evolutionally conserved in EC and ee differentiation.

While *GATA-4* and *-5* showed regional expression patterns, *GATA-6* was constantly expressed throughout the mouse small intestine (Buchon et al., 2013; Fang et al., 2006). *GATA-6* is also expressed in the large intestine of mice and humans (Fang et al., 2006; Haveri et al., 2008). In summary, *GATA-6* is the only *GATA* factor gene expressed in the distal ileum and colon. In these regions, in addition to a decrease in crypt-cell proliferation, *GATA-6* conditional deletion decreases differentiated ee and Paneth cells, which are replaced with goblet-like cells (Beuling et al., 2011; Dusing and Wiginton, 2005). This suggests that GATA-6 plays an important role also in mammalian secreted-cell differentiation. On the other hand, the *GATA-6* role in EC differentiation has been unclear since its conditional deletion results in a dramatic decrease in ECs constructing villi, which is probably caused by the limitation of crypt-proliferative cells. Spatiotemporal studies with *Drosophila* techniques may provide insight into a detailed common function of GATA factors in EC differentiation among multicellular animals.

In $GATAe^{1}$ MARCM clone experiments, although the average size of $GATA^{1}$ clones without any dividing cells was not altered between days 4 (1.67 cell) and 7 (1.70 cell) (Fig. 2L and Fig. 4D), the frequency of $Pdm1^{+}$ and $Pros^{+}$ cells decreased during days 4–7 (EC: 20.6%→12.63%, ee: 5.67%→0.42%) (Fig. 5I and J). Some $GATA^{1}$ cells consistently showed weak Pdm1 expression (Supplemental Fig. 4A). These facts imply that, in addition to their differentiation process, *GATAe* is also required for maintenance of EC's and ee's differentiated states. In addition, to confirm the fate of undifferentiated $GATAe^{1}$ clone cells (Dl^{-}, $Pdm1^{-}$, and $Pros^{-}$ cells), we tried to observe their older clones at 21 day ACI. But, in this condition, we did not find any $GATAe^{1}$ clone cells because they were eliminated probably by cell death or apical extrusion (data not shown). A recent study suggested that *GATAe* may control the physiologically functional genes regulating digestive, metabolism, structure, and defense response in the adult midgut (Buchon et al., 2013). Also, *GATAe* regulates similar intestinal genes in the larval midgut (Okumura et al., 2007; Senger et al., 2006). In mammal intestine, GATA-4, GATA-5, and GATA-6 directly and indirectly regulate a subset of functional gene expressions (Aronson et al., 2014). Thus, in addition to ISC regulation/maintenance, GATA factors regulate differentiation and maintenance of other types of intestinal cells, which are crucial for physiological function both in mammal and *Drosophila* adult intestines.

Acknowledgments

We thank Bruce A. Hay, Ryutaro Murakami and Xiaohang Yang for providing *UAS-DIAP-myc*, *GATAe::V5-6×His* and *UAS-FLAG::GATAe* strains and anti-Pdm1 antibody. Fly stocks and antibodies were also obtained from the Bloomington *Drosophila* Stock Center (Indiana University), Drosophila Genetic Resource Center (Kyoto Institute of Technology), the Vienna *Drosophila* RNAi Center (VDRC) and Developmental Studies Hybridoma Bank (University of Iowa). We also thank BestGene Inc. for generating transgenic fly lines. We thank members of Adachi-Yamada laboratory for critical comments and discussion. This work was supported by grants from Naito Foundation and MEXT*-Supported Program for the Strategic Research Foundation at Private Universities, 2008–2012 (Grant number S0801006) (*Ministry of Education, Culture, Sports, Science and Technology)

Appendix A. Supplementary material

Supplementary data associated with this article can be found in the online version at http://dx.doi.org/10.1016/j.ydbio.2015.12.017.

References

Abel, T., Michelson, A.M., Maniatis, T., 1993. A Drosophila GATA family member that binds to Adh regulatory sequences is expressed in the developing fat body. Development 119, 623–633.

Aronson, B.E., Stapleton, K.A., Krasinski, S.D., 2014. Role of GATA factors in development, differentiation, and homeostasis of the small intestinal epithelium. Am. J. Physiol. Gastrointest. Liver Physiol. 306, G474–G490.

Ayanbule, F., Belaguli, N.S., Berger, D.H., 2011. GATA factors in gastrointestinal malignancy. World J. Surg. 35, 1757–1765.

Bach, E.A., Ekas, L.A., Ayala-Camargo, A., Flaherty, M.S., Lee, H., Perrimon, N., Baeg, G.H., 2007. GFP reporters detect the activation of the Drosophila JAK/STAT pathway in vivo. Gene Expr. Patterns 7, 323–331.

Bardet, P.L., Kolahgar, G., Mynett, A., Miguel-Aliaga, I., Briscoe, J., Meier, P., Vincent, J. P., 2008. A fluorescent reporter of caspase activity for live imaging. Proc. Natl. Acad. Sci. USA 105, 13901–13905.

Bardin, A.J., Perdigoto, C.N., Southall, T.D., Brand, A.H., Schweisguth, F., 2010. Transcriptional control of stem cell maintenance in the Drosophila intestine. Development 137, 705–714.

Beehler-Evans, R., Micchelli, C.A., 2015. Generation of enteroendocrine cell diversity in midgut stem cell lineages. Development 142, 654–664.
Beuling, E., Aronson, B.E., Tran, L.M., Stapleton, K.A., ter Horst, E.N., Vissers, L.A., Verzi, M.P., Krasinski, S.D., 2012. GATA6 is required for proliferation, migration, secretory cell maturation, and gene expression in the mature mouse colon. Mol. Cell. Biol. 32, 3392–3402.
Beuling, E., Baffour-Awuah, N.Y., Stapleton, K.A., Aronson, B.E., Noah, T.K., Shroyer, N.F., Duncan, S.A., Fleet, J.C., Krasinski, S.D., 2011. GATA factors regulate proliferation, differentiation, and gene expression in small intestine of mature mice. Gastroenterology 140 (1219-1229), e1211–e1212.
Biteau, B., Hochmuth, C.E., Jasper, H., 2008. JNK activity in somatic stem cells causes loss of tissue homeostasis in the aging Drosophila gut. Cell Stem Cell 3, 442–455.
Bosse, T., Piaseckyj, C.M., Burghard, E., Fialkovich, J.J., Rajagopal, S., Pu, W.T., Krasinski, S.D., 2006. Gata4 is essential for the maintenance of jejunal-ileal identities in the adult mouse small intestine. Mol. Cell. Biol. 26, 9060–9070.
Buchon, N., Osman, D., David, F.P., Fang, H.Y., Boquete, J.P., Deplancke, B., Lemaitre, B., 2013. Morphological and molecular characterization of adult midgut compartmentalization in Drosophila. Cell. Rep. 3, 1725–1738.
Crosnier, C., Stamataki, D., Lewis, J., 2006. Organizing cell renewal in the intestine: stem cells, signals and combinatorial control. Nat. Rev. Genet. 7, 349–359.
de Navascues, J., Perdigoto, C.N., Bian, Y., Schneider, M.H., Bardin, A.J., Martinez-Arias, A., Simons, B.D., 2012. Drosophila midgut homeostasis involves neutral competition between symmetrically dividing intestinal stem cells. EMBO J. 31, 2473–2485.
Divine, J.K., Staloch, L.J., Haveri, H., Jacobsen, C.M., Wilson, D.B., Heikinheimo, M., Simon, T.C., 2004. GATA-4, GATA-5, and GATA-6 activate the rat liver fatty acid binding protein gene in concert with HNF-1alpha. Am. J. Physiol. Gastrointest. Liver Physiol. 287, G1086–G1099.
Dusing, M.R., Wiginton, D.A., 2005. Epithelial lineages of the small intestine have unique patterns of GATA expression. J. Mol. Histol. 36, 15–24.
Fang, R., Olds, L.C., Sibley, E., 2006. Spatio-temporal patterns of intestine-specific transcription factor expression during postnatal mouse gut development. Gene Expr. Patterns 6, 426–432.
Furriols, M., Bray, S., 2001. A model Notch response element detects Suppressor of Hairless-dependent molecular switch. Curr. Biol. 11, 60–64.
Go, M.J., Eastman, D.S., Artavanis-Tsakonas, S., 1998. Cell proliferation control by Notch signaling in Drosophila development. Development 125, 2031–2040.
Goulas, S., Conder, R., Knoblich, J.A., 2012. The Par complex and integrins direct asymmetric cell division in adult intestinal stem cells. Cell Stem Cell 11, 529–540.
Haveri, H., Westerholm-Ormio, M., Lindfors, K., Maki, M., Savilahti, E., Andersson, L. C., Heikinheimo, M., 2008. Transcription factors GATA-4 and GATA-6 in normal and neoplastic human gastrointestinal mucosa. BMC Gastroenterol. 8, 9.
Hayashi, S., Ito, K., Sado, Y., Taniguchi, M., Akimoto, A., Takeuchi, H., Aigaki, T., Matsuzaki, F., Nakagoshi, H., Tanimura, T., Ueda, R., Uemura, T., Yoshihara, M., Goto, S., 2002. GETDB, a database compiling expression patterns and molecular locations of a collection of Gal4 enhancer traps. Genesis 34, 58–61.
Ito, K., Awano, W., Suzuki, K., Hiromi, Y., Yamamoto, D., 1997. The Drosophila mushroom body is a quadruple structure of clonal units each of which contains a virtually identical set of neurones and glial cells. Development 124, 761–771.
Jiang, H., Edgar, B.A., 2009. EGFR signaling regulates the proliferation of Drosophila adult midgut progenitors. Development 136, 483–493.
Jiang, H., Edgar, B.A., 2012. Intestinal stem cell function in Drosophila and mice. Curr. Opin. Genet. Dev. 22, 354–360.
Jiang, H., Patel, P.H., Kohlmaier, A., Grenley, M.O., McEwen, D.G., Edgar, B.A., 2009. Cytokine/Jak/Stat signaling mediates regeneration and homeostasis in the Drosophila midgut. Cell 137, 1343–1355.
Kapuria, S., Karpac, J., Biteau, B., Hwangbo, D., Jasper, H., 2012. Notch-mediated suppression of TSC2 expression regulates cell differentiation in the Drosophila intestinal stem cell lineage. PLoS Genet. 8, e1003045.
Korzelius, J., Naumann, S.K., Loza-Coll, M.A., Chan, J.S., Dutta, D., Oberheim, J., Glasser, C., Southall, T.D., Brand, A.H., Jones, D.L., Edgar, B.A., 2014. Escargot maintains stemness and suppresses differentiation in Drosophila intestinal stem cells. EMBO J.
Lee, T., Luo, L., 1999. Mosaic analysis with a repressible cell marker for studies of gene function in neuronal morphogenesis. Neuron 22, 451–461.
Lee, W.C., Beebe, K., Sudmeier, L., Micchelli, C.A., 2009. Adenomatous polyposis coli regulates Drosophila intestinal stem cell proliferation. Development 136, 2255–2264.
Lin, L., Bass, A.J., Lockwood, W.W., Wang, Z., Silvers, A.L., Thomas, D.G., Chang, A.C., Lin, J., Orringer, M.B., Li, W., Glover, T.W., Giordano, T.J., Lam, W.L., Meyerson, M., Beer, D.G., 2012. Activation of GATA binding protein 6 (GATA6) sustains oncogenic lineage-survival in esophageal adenocarcinoma. Proc. Natl. Acad. Sci. USA 109, 4251–4256.
Lin, W.H., Huang, L.H., Yeh, J.Y., Hoheisel, J., Lehrach, H., Sun, Y.H., Tsai, S.F., 1995. Expression of a Drosophila GATA transcription factor in multiple tissues in the developing embryos. Identification of homozygous lethal mutants with P-element insertion at the promoter region. J. Biol. Chem. 270, 25150–25158.
Loza-Coll, M.A., Southall, T.D., Sandall, S.L., Brand, A.H., Jones, D.L., 2014. Regulation of Drosophila intestinal stem cell maintenance and differentiation by the transcription factor Escargot. EMBO J.
Marianes, A., Spradling, A.C., 2013. Physiological and stem cell compartmentalization within the Drosophila midgut. eLife 2, e00886.
Martin-Blanco, E., Gampel, A., Ring, J., Virdee, K., Kirov, N., Tolkovsky, A.M., Martinez-Arias, A., 1998. puckered encodes a phosphatase that mediates a feedback loop regulating JNK activity during dorsal closure in Drosophila. Genes Dev. 12, 557–570.
McGuire, S.E., Le, P.T., Osborn, A.J., Matsumoto, K., Davis, R.L., 2003. Spatiotemporal rescue of memory dysfunction in Drosophila. Science 302, 1765–1768.
Micchelli, C.A., 2012. The origin of intestinal stem cells in Drosophila. Dev. Dyn.: Off. Publ. Am. Assoc. Anat. 241, 85–91.
Micchelli, C.A., Perrimon, N., 2006. Evidence that stem cells reside in the adult Drosophila midgut epithelium. Nature 439, 475–479.
Molkentin, J.D., 2000. The zinc finger-containing transcription factors GATA-4, -5, and -6. Ubiquitously expressed regulators of tissue-specific gene expression. J. Biol. Chem. 275, 38949–38952.
Murakami, R., Okumura, T., Uchiyama, H., 2005. GATA factors as key regulatory molecules in the development of Drosophila endoderm. Dev. Growth Differ. 47, 581–589.
Ohlstein, B., Spradling, A., 2006. The adult Drosophila posterior midgut is maintained by pluripotent stem cells. Nature 439, 470–474.
Ohlstein, B., Spradling, A., 2007. Multipotent Drosophila intestinal stem cells specify daughter cell fates by differential notch signaling. Science 315, 988–992.
Okumura, T., Matsumoto, A., Tanimura, T., Murakami, R., 2005. An endoderm-specific GATA factor gene, dGATAe, is required for the terminal differentiation of the Drosophila endoderm. Dev. Biol. 278, 576–586.
Okumura, T., Tajiri, R., Kojima, T., Saigo, K., Murakami, R., 2007. GATAe-dependent and -independent expressions of genes in the differentiated endodermal midgut of Drosophila. Gene Expr. Patterns 7, 178–186.
Okumura, T., Takeda, K., Taniguchi, K., Adachi-Yamada, T., 2014. betanu integrin inhibits chronic and high level activation of JNK to repress senescence phenotypes in Drosophila adult midgut. PLoS One 9, e89387.
Perdigoto, C.N., Schweisguth, F., Bardin, A.J., 2011. Distinct levels of Notch activity for commitment and terminal differentiation of stem cells in the adult fly intestine. Development 138, 4585–4595.
Ramain, P., Heitzler, P., Haenlin, M., Simpson, P., 1993. pannier, a negative regulator of achaete and scute in Drosophila, encodes a zinc finger protein with homology to the vertebrate transcription factor GATA-1. Development 119, 1277–1291.
Rehorn, K.P., Thelen, H., Michelson, A.M., Reuter, R., 1996. A molecular aspect of hematopoiesis and endoderm development common to vertebrates and Drosophila. Development 122, 4023–4031.
Reuter, R., 1994. The gene serpent has homeotic properties and specifies endoderm versus ectoderm within the Drosophila gut. Development 120, 1123–1135.
Rong, Y.S., Golic, K.G., 2000. Gene targeting by homologous recombination in Drosophila. Science 288, 2013–2018.
Senger, K., Harris, K., Levine, M., 2006. GATA factors participate in tissue-specific immune responses in Drosophila larvae. Proc. Natl. Acad. Sci. USA 103, 15957–15962.
Simons, B.D., Clevers, H., 2011. Strategies for homeostatic stem cell self-renewal in adult tissues. Cell 145, 851–862.
Struhl, G., Basler, K., 1993. Organizing activity of wingless protein in Drosophila. Cell 72, 527–540.
Takashima, S., Hartenstein, V., 2012. Genetic control of intestinal stem cell specification and development: a comparative view. Stem Cell Rev. 8, 597–608.
Takashima, S., Paul, M., Aghajanian, P., Younossi-Hartenstein, A., Hartenstein, V., 2013. Migration of Drosophila intestinal stem cells across organ boundaries. Development 140, 1903–1911.
Tsuji, S., Kawasaki, Y., Furukawa, S., Taniue, K., Hayashi, T., Okuno, M., Hiyoshi, M., Kitayama, J., Akiyama, T., 2014. The miR-363-GATA6-Lgr5 pathway is critical for colorectal tumourigenesis. Nat. Commun. 5, 3150.
Umemori, M., Takemura, M., Maeda, K., Ohba, K., Adachi-Yamada, T., 2007. Drosophila T-box transcription factor Optomotor-blind prevents pathological folding and local overgrowth in wing epithelium through confining Hh signal. Dev. Biol. 308, 68–81.
Walker, E.M., Thompson, C.A., Battle, M.A., 2014. GATA4 and GATA6 regulate intestinal epithelial cytodifferentiation during development. Dev. Biol. 392, 283–294.
Weissman, I.L., 2000. Stem cells: units of development, units of regeneration, and units in evolution. Cell 100, 157–168.
Whissell, G., Montagni, E., Martinelli, P., Hernando-Momblona, X., Sevillano, M., Jung, P., Cortina, C., Calon, A., Abuli, A., Castells, A., Castellvi-Bel, S., Nacht, A.S., Sancho, E., Stephan-Otto Attolini, C., Vicent, G.P., Real, F.X., Batlle, E., 2014. The transcription factor GATA6 enables self-renewal of colon adenoma stem cells by repressing BMP gene expression. Nat. Cell. Biol. 16, 695–707.
Winick, J., Abel, T., Leonard, M.W., Michelson, A.M., Chardon-Loriaux, I., Holmgren, R.A., Maniatis, T., Engel, J.D., 1993. A GATA family transcription factor is expressed along the embryonic dorsoventral axis in Drosophila melanogaster. Development 119, 1055–1065.
You, J., Zhang, Y., Li, Z., Lou, Z., Jin, L., Lin, X., 2014. Drosophila perlecan regulates intestinal stem cell activity via cell-matrix attachment. Stem Cell Rep. 2, 761–769.
Zheng, R., Blobel, G.A., 2010. GATA transcription factors and cancer. Genes Cancer 1, 1178–1188.

IV. 研究課題 2 「光の情報を受け取る分子メカニズムの解明」

本課題では、生物が光刺激をどのように受容し、その情報を細胞内へとどう伝達して最終的に個体レベルでどう応答していくのかについて、種々の実験系を用いて解析した。特にＧタンパク質共役受容体（GPCR）の原子レベルでの解析から、光受容が GPCR の構造変化によってどのように活性変化をもたらすのか、またアフリカツメガエル初期胚における眼の発生時に転写因子とシグナル伝達分子の遺伝子発現が時空間的にどのような変化を示すのかなどについて GPCR 型遺伝子の発現と併せて解析した。一方、モデル生物の一つであるシロイヌナズナの光周性花成経路で働く花成促進因子 FKF1 の機能欠損変異体（遅咲き変異体）を用いて、それを早咲きに変える変異体を単離し解析した。この現象に関与する遺伝子を同定することにより、光の受容から花成促進までの経路を明らかにすることが出来るはずである。以下、これらの研究について、それぞれの研究担当者からの解説と業績リスト、そして代表的な論文2編ずつを記載する。

受容体分子構造基盤の解明

教授　岡田　哲二
助教　高橋　清大

[目的]

生物に対する光の作用は生態系の主要な側面を左右し、かつ多岐にわたるものである。光は、高等動物での視覚のように環境情報を与える物理的なシグナルとなるが、それに対して適切な応答を示すことは生物の基本的かつ重要な機能である。分子レベルでみると、応答の第一段階を担う光受容体をはじめとして、活性調節・異常が直接的・間接的に光応答機能を左右するタンパク質に関する構造情報は、生命現象の理解に不可欠なものである。真核生物の光受容体を含む G タンパク質共役受容体や微生物のレチナールタンパク質（ロドプシン）を中心とした 7 回膜貫通タンパク質の構造解析等により活性発現・調節機構を明らかにするとともに、他分子との相互作用を介して機能発現を行う緑内障関連タンパク質の構造・機能解析を行うことを目的とする。

[結果と考察]

a. 構造未知の視覚関連タンパク質

光受容膜タンパク質として、活性化に伴う構造変化機能が損なわれるロドプシン変異体のうち、後述の網膜色素変性症との関連が最近明らかになったもの（W126L）や、GPCR と微生物ロドプシンの双方に対して部分的な配列相動性がみられるタンパク質に着目し、大量発現系の構築から結晶化を目的とする研究を継続して行っている。緑内障に関与する水溶性タンパク質 OPTN に関しては、ヒト由来の全長および N 末端側、C 末端側の約半分に相当するタンパク質を大腸菌により大量発現させ、アフィニティーカラムやゲルろ過による精製を行った。これらの精製試料から最近生成した結晶のうち、全長タンパク質については高エネルギー加速器研究機構 PF-NW12A ビームラインでの放射光共同利用実験で、3.0 Å 分解能を超える X 線回折が確認できた。この結晶生成に至る過程では、OPTN 分子の会合状態を詳細に調べ、溶液環境に依存した 2, 3, 6 量体に相当する成分間の相対量変化の様子が明らかとなった。また、緑内障との関連が強く示唆されている OPTN での変異 [1] を導入したものと結合タンパク質 TBK1 との複合体の精製および結晶化を目的とする研究も進めている。

b. 受容体活性化に伴う構造変化の配列依存性（原著論文 1）

既知の高分解能構造に関する詳細かつ系統的な解析は、受容体機能を理解するうえで極めて有効な手段と考えられる。膜貫通ヘリックス領域の構造共通性が高いことが明らかになってきた GPCR スーパーファミリーは、そのような研究の対象として前例のない適性を備えている。特に興味深い課題は、如何にして多種多様な細胞外刺激（低分子、高分子リガンド、光など）が細胞質側表面における共通性のある構造変化へと変換されるのかという点である。本研究では、近年明らかになってきた GPCR の活性型構造について、受容体サブタイプ間における共通性と特異性に関する知見を得るために、独自の手法による解析を行った。対象としたのは、ロドプシン、b2 アドレナリン受容体、A2A アデノシン受容体で、特に活性化に重要と考えられている TM3 および TM6 の変位等に着目した。TM6 の細胞質

側における変位は、いずれの受容体においても剛体運動を基本とするものであることが確認された。一方、細胞外側の変位に着目すると、TM3 および TM6 のいずれにおいても受容体特有のパターンがみられることが明らかになった。具体的には、ロドプシンにおける TM6 細胞外側での顕著な変位幅、A2A アデノシン受容体の TM3 細胞外部分における非剛体的な構造変化が特筆すべき結果として得られた。

c. 受容体活性調節と視覚疾患との関連

網膜色素変性症は主要な視覚関連疾患であり、光受容体における変異との関連を示唆する報告が数多くなされている。共同研究者により新たに見出された、日本人家族における常染色体劣性網膜色素変性症（adRP）患者でのロドプシン変異のうち、膜貫通ヘリックス 3（TM3）の W126L が生じうる影響について、分子動力学法（MD）によるシミュレーションを行った。光吸収の有無による効果の違いについても調べるため、11 シスレチナール結合の不活性型（ロドプシン）、およびレチナールを持たない活性型（オプシン）の 2 つに対応する結晶構造をモデルとして用いた。シミュレーション前後での変化が最も顕著であったのはオプシン構造における TM3 の細胞質側で、TM6 の方向への有意な変位として観察された（図 1、原著論文 2）。この結果は、光活性化において必要と考えられている TM3-TM6 間の細胞質側表面での空間形成[2]が、W126L 変異によって損なわれる可能性を示すものである。過去の変異タンパク質を用いた報告では、W126L では 11 シスレチナール結合活性を保持しているものの、光依存的な G タンパク質活性化機能が低下することが示されている[3]が、本研究結果はそれらの分子メカニズムを説明するものということができる。すなわち、W126 は膜貫通ヘリックス 4 および 5 の近傍アミノ酸と重要な疎水性相互作用に寄与しており、それらが光活性化プロセスにおいても保持されている必要があるのではないかと考えられる。W から L への置換は、これらの疎水性相互作用を弱めるため、光活性化されたタンパク質において TM6 の外向き変位が起こるとともに同じ方向への TM3 の変位が起ってしまい、空間形成が阻害されるという説明ができる。この部位における疎水性相互作用の重要性は b2 アドレナリン受容体でも指摘されている[4]ことから、ロドプシンファミリーの GPCR における機能制御の観点からも重要な知見が得られたと考えられる。

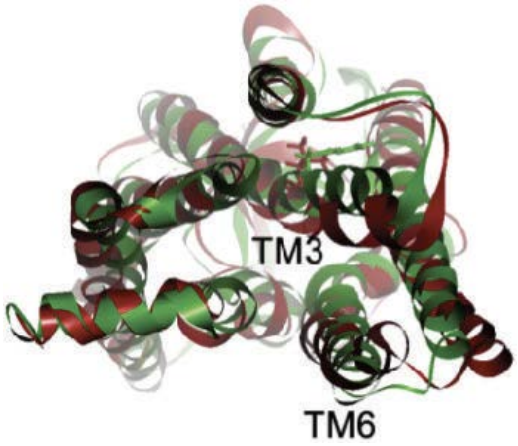

図 1：W126L オプシン表面における TM3 の変化
緑：MD 前、赤：MD 後

d. 受容体不活性状態における構造の分子進化的保存性

膜貫通型のタンパク質分子において、その折りたたまれた状態での空間的な配置の多様性と必須機能との関連は、これまで研究することが困難であった。しかし、7 回膜貫通ヘリックスという基本モチーフを共有する GPCR スーパーファミリーの高分解能構造の蓄積により、細胞内外をつなぐ情報伝達機能の中でも特に真核生物で高度に進化してきたと思われる 3 量体 G タンパク質を介した系について、その作動原理を探るための解析が可能となってきた。本研究では、分子内 C_α間距離情報の系統的な解析により、アミノ酸配列的に極め

て多様な受容体スーパーファミリーの機能発現において最も保存された空間配置を明らかにすることを試みた。空間配置の保存性評価には、単純ながらもこれまで報告例のないスコアリング法を導入し、既知のほぼ全ての不活性型結晶構造モデルを対象とした解析を行った。各ヘリックスごとの解析結果からは、スーパーファミリー全体かサブファミリーのみかによらず、TM3 の細胞質側部分での極めて高い保存性が定量的に明らかになった。予想外な結果として得られたのは、スーパーファミリー全てにおいて最も保存性が高かったヘリックス間配置は、TM1-TM3 および TM1-TM6 にみられ、特に TM1 の細胞質側部分がどちらにも寄与していることであった（図 2、原著論文 3)。上述のように、GPCR において共通すると思われる活性化機構は、TM3-TM6 間での細胞質側空間形成である。従って本研究で得られた知見は、その分子メカニズムの基盤として重要な活性化前における空間配置条件を示すものともいえる。

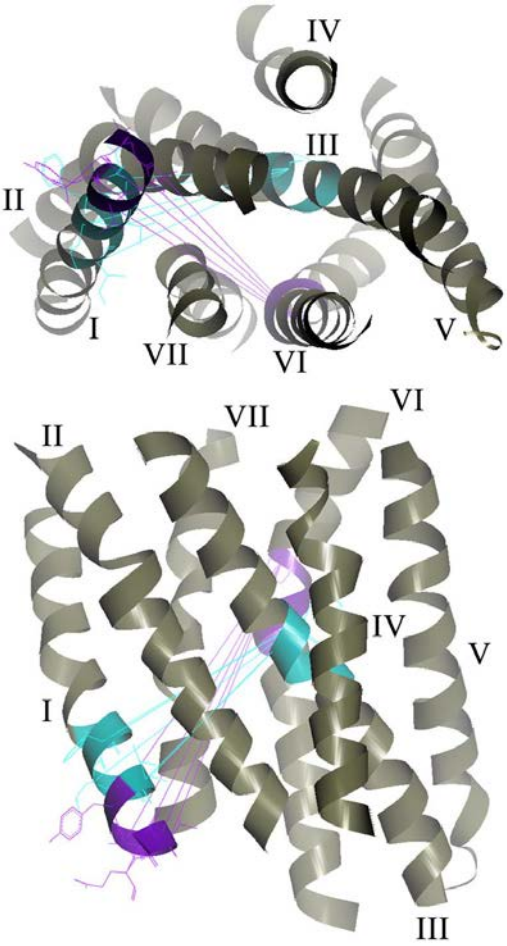

図 2 : GPCR スーパーファミリー構造における分子内ヘリックス間距離の保存性
青 : TM1-TM3、紫 : TM1-TM6

e. 微生物レチナールタンパク質をモデルとした分子内距離情報解析法の提唱

上述のように、GPCR の高分解能構造モデルの蓄積により、これまでに得ることが困難であった機能発現機構に関する情報抽出が可能となってきた。一方、その研究において採用したスコアリング法については、膨大な情報量に対して比較対象となる報告例が存在しない。従って、同様の手法を他のタンパク質あるいはタンパク質ファミリーに適用し、その結果を踏まえることによって更に有効な解析へと発展させることが重要である。本研究では、GPCR と同様の 7 回膜貫通ヘリックス構造をもつ微生物のレチナールタンパク質（ロドプシン）を対象として、DSA（distance scoring analysis）と略称を付与した解析を行った。また、その手法を簡便に適用するためのツール（score-analyzer）作成にも着手し、プロトタイプ（v01）も論文とともに公開した。微生物レチナールタンパク質の中で、最も構造研究が行われてきたのは高度好塩菌由来の光駆動性プロトンポンプとして知られるバクテリオロドプシン（bR）である。様々な変異体や光反応状態の構造も含め、数多くのモデルが PDB（Protein Data Bank）エントリーとして登録されている。これらは互いに極めて類似した構造であるが、DSA の適用によって分子内非可動部位ともいえる部分あるいはヘリックス間配置に関する情報が得られた。すなわち、bR の膜貫通ヘリックスのうち A-B, B-C, C-D という隣接するペアにおいては、特に B-C 間の保存性が高いことが明らかになった。さらに配列の異なる 13 種の微生物レチナールタンパク質を解析対象とした結果からは、いずれの場合にも機能として必須であるレチ

ナール結合に重要と考えられるヘリックス C-G 間における保存性の高さが明らかになった(図 3、原著論文 4)。特に、レチナール結合部位であるヘリックス G の Lys 側鎖の末端は、この保存されたヘリックス間部位のほぼ中間に位置しており、進化的な観点からも興味深い知見が得られたといえる。これらの解析結果は、GPCR スーパーファミリーについて行った際に得られたスコア値やそれらの距離依存性の評価においても貴重な比較対象となるものである。また、今後さらに多様なタンパク質あるいはタンパク質ファミリーへと研究を進めるための方針・計画策定等へも生かすことができる。

[まとめ]

タンパク質発現から結晶化・構造解析に関する研究は、長期計画の下での継続的な遂行が必要であるが、特に緑内障関連タンパク質については顕著な進展がみられている。既知の構造モデルからの新たな情報抽出研究は、既に立ち上げている 7 回膜貫通領域に関するデータのポータルサイト（Heptahelical Transmembrane Structure Portal, http://www.gses.jp/7tmsp/）での研究対象公開に基づいて進行してきており、今後さらに広範なタンパク質ファミリーに関する解析コンテンツ・ツール提供へと発展できる。

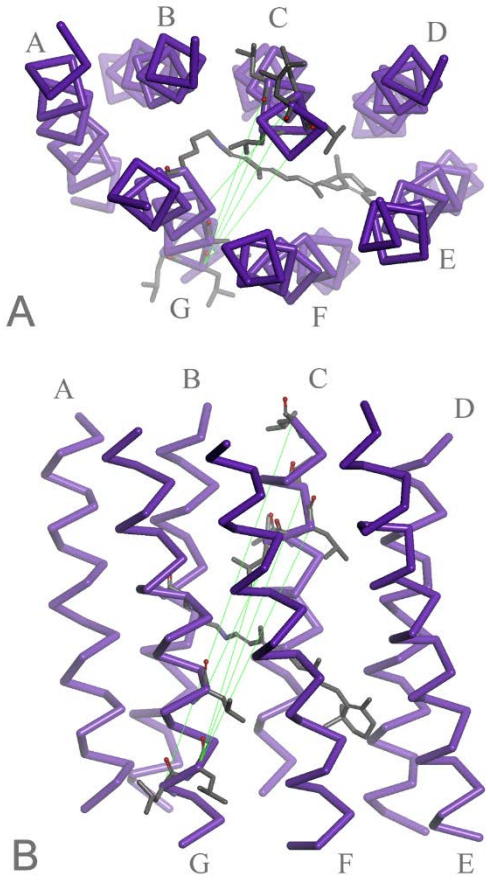

図 3：微生物レチナールタンパク質における分子内ヘリックス間距離の保存性
緑：TM3-TM7

[参考文献]

1. Rezaie T, Child A, Hitchings R, Brice G, Miller L, et al. (2002) Adult-onset primary open-angle glaucoma caused by mutations in optineurin. Science 295, 1077-1079.
2. Farrens DL, Altenbach C, Yang K, Hubbell WL, Khorana HG. (1996) Requirement of rigid-body motion of transmembrane helices for light activation of rhodopsin. Science 274, 768-770.
3. T. A. Nakayama and H. G. Khorana, “Mapping of the amino acids in membrane-embedded helices that interact with the retinal chromophore in bovine rhodopsin,” The Journal of Biological Chemistry, vol. 266, no. 7, pp. 4269–4275, 1991.
4. S. G. F. Rasmussen, H.-J. Choi, J. J. Fung et al., “Structure of a nanobody-stabilized active state of the β2 adrenoceptor,” Nature, vol. 469, no. 7329, pp. 175–180, 2011.

［原著論文］

1. Nakamura S, Itabashi T, Ogawa D, Okada T (2013) Common and distinct mechanisms of activation of rhodopsin and other G protein-coupled receptors. *Sci Rep* 3, 1844.
2. Katagiri S, Hayashi T, Akahori M, Itabashi T, Nishino J, Yoshitake K, Furuno M, Ikeo K, Okada T, Tsuneoka H, Iwata T (2014) RHO mutations (p.W126L and p.A346P) in two Japanese families with autosomal dominant retinitis pigmentosa. *J Ophthalmol* 2014, 210947.
3. Kinoshita M, Okada T (2015) Structural conservation among the rhodopsin-like and other G protein-coupled receptors. *Sci Rep* 5, 9176.
4. Asano M, Ide S, Kamata A, Takahasi K, Okada T (2016) Sequence and intramolecular distance scoring analyses of microbial rhodopsins. *F1000Res* 5, 165.

［総説等］

1. 岡田哲二、ロドプシンにみるGPCRの活性化機構－光刺激と薬剤刺激、実験医学 31(3), 375-381 (2013).

［その他］

1. Okada, T. (2013) F1000Prime Recommendation
   DOI: 10.3410/f.717991028.793473251
   http://f1000.com/prime/717991028#eval793473251
2. Okada, T. (2014) F1000Prime Recommendation
   DOI: 10.3410/f.718204478.793489214
   http://f1000.com/prime/718204478#eval793489214
3. Okada, T. (2014) F1000Prime Recommendation
   DOI: 10.3410/f.718437268.793498172
   http://f1000.com/prime/718437268#eval793498172
4. Okada, T. (2014) F1000Prime Recommendation
   DOI: 10.3410/f.718632616.793500914
   http://f1000.com/prime/718632616#eval793500914
5. Okada, T. (2015) F1000Prime Recommendation
   DOI: 10.3410/f.725624587.793508508
   http://f1000.com/prime/725624587#eval793508508
6. Okada, T. (2015) F1000Prime Recommendation
   DOI: 10.3410/f.725590722.793509916
   http://f1000.com/prime/725590722#eval793509916

SCIENTIFIC REPORTS

OPEN

SUBJECT AREAS:
BIOPHYSICS
COMPUTATIONAL BIOLOGY AND BIOINFORMATICS
X-RAY CRYSTALLOGRAPHY
STRUCTURAL BIOLOGY

Received
22 March 2013

Accepted
30 April 2013

Published
15 May 2013

Correspondence and requests for materials should be addressed to T.O. (tetsuji.okada@gakushuin.ac.jp)

Common and distinct mechanisms of activation of rhodopsin and other G protein-coupled receptors

Sumire Nakamura, Takeshi Itabashi, Daisuke Ogawa & Tetsuji Okada

Department of Life Science, Gakushuin University, 1-5-1 Mejiro, Toshima-ku, Tokyo 171-8588, Japan.

Detailed and systematic examination of high-resolution structural data is a rational strategy for understanding the function of biological macromolecules. G protein-coupled receptors (GPCRs) are an exceptionally valuable superfamily of proteins for such analysis. The most intriguing question is how a variety of extracellular stimuli evoke structural changes in the intracellular surface of the receptors. The recent active-like crystal structures of GPCRs provide information for uncovering common and distinct mechanisms of light-induced and ligand-induced activation. Based on systematic structural alignment, we have analyzed 3 receptors (rhodopsin, β_2 adrenergic receptor, adenosine A_{2A} receptor) and demonstrate that the extracellular movement of helix VI is significantly different between rhodopsin and the other 2 receptors, and that the extracellular side of helix III exhibits distinct features in the 3 receptors. These findings not only emphasize the specialization of rhodopsin as a photoreceptor but also provide insights into the mechanism leading to rearrangement of helix VI.

Most of the external stimuli for eukaryotic cells, such as chemical substances, photons, neurotransmitters, and hormones are captured by G protein-coupled receptors (GPCRs), which are defined by a heptahelical transmembrane core domain. A majority of proteins in the GPCR superfamily belong to the so-called rhodopsin family, which share several key residues in their transmembrane helices. Their activity at the intracellular surface to catalyze the GDP/GTP exchange on the α-subunit of heterotrimeric G proteins is primarily determined by the type of ligand bound to the extracellular side of the transmembrane region. Even without ligand binding, GPCRs exhibit some basal activity, which is then enhanced or attenuated by binding of an agonist or inverse-agonist, respectively[1]. Antagonists are another category of ligands that maintain GPCRs in their low activity state.

Recent crystallographic studies on GPCRs have validated previous spectroscopic studies[2], demonstrating that the key intramolecular event during activation is the displacement of transmembrane helix VI at the intracellular side[3–5]. However, the manner in which this change is regulated by various ligands acting on the extracellular side is not well understood. While there are many crystallographic models of GPCRs that describe a variety of structural states of activity in the presence of different bound ligands (agonist, antagonist, and inverse agonist), systematic comparison of data obtained for different receptors has not been reported quantitatively.

Each of the crystallographic models inevitably suffers from various sources of artifacts and/or errors, as has been documented for another class of heptahelical membrane proteins, bacteriorhodopsins, whose proton pumping movement has been extensively studied using crystallographic techniques[6]. Nonetheless, statistically significant features should become apparent by averaging as many datasets as possible.

Of the more than 15 receptors of known structure, agonist-bound forms are available only for bovine rhodopsin[7–9], β_1[10] and β_2 adrenergic receptors[4,11], the A_{2A} adenosine receptor[5,12], the NTSR1 neurotensin receptor[13], the 5-HT_{1B} and 5-HT_{2B} serotonin receptors[25,26]. Unfortunately, the agonist-bound and inactive-like states are quite similar to each other in the case of the β_1 receptor. Furthermore, the structure of the NTSR1, 5-HT_{1B} and 5-HT_{2B} receptors has not yet been obtained in the inactive-like state. As a result, detailed analysis on its activation is currently feasible only for the remaining 3 receptors.

While several previous reviews on the structure of GPCRs provide a number of insights into their mechanism of activation[14–16], systematic quantitative analysis is yet to be performed. We have recently reported a rational procedure for analyzing the experimental transmembrane structures of GPCRs, based on the defined selection and superimposition of heptahelical bundles consisting of 200 residues[17]. By extending this approach, we identify previously undiscovered structural changes accompanying the activation of these receptors. The findings and the methodology will be valuable for understanding the action of ligands on other receptors of unknown structure.

Table 1 | PDB entries used for this study

	PDB ID	
receptor	Inactive-like	Active-like
rhodopsin	1GZM-A	2X72
	1U19-A	3PQR
		3PXO
		4A4M
β_2 receptor	2RH1	3P0G
	3D4S	3SN6
	3NY8	
	3NY9	
A_{2A} receptor	3EML	2YDO
	3VG9	2YDV
	4EIY	3QAK

Results

Of all the heptahelical bundles of GPCRs archived on our website (www.gses.jp/7tmsp), we used 18 sets of coordinates in the present study (Table 1), consisting of 9 inactive (2 of rhodopsin, 4 of β_2 receptor, and 3 of A_{2A} receptor) and 9 active-like (4 of rhodopsin, 2 of β_2 receptor, and 3 of A_{2A} receptor) states. All of these structures contain the same sequence ranges of the transmembrane domains superimposed onto the same reference coordinates—the inactive state of β_2 receptor (2RH1)—by secondary structure matching[18]. The aligned structures are shown in Fig. S1. The structural differences between the inactive and active-like states were then analyzed using 8 pairs for rhodopsin, 8 pairs for β_2 receptor, and 9 pairs for A_{2A} receptor. Accordingly, we anticipated that the degree of averaging would be comparable for these 3 receptors. The details of the criteria for the selection of the coordinates are described in the Methods.

Fig. 1 shows the averaged calculated Cα displacement of 200 transmembrane residues between the inactive and active-like states of the 3 receptors. The most prominent feature commonly observed was an oscillating pattern at the cytoplasmic side of helix VI (residue no. 145 ~ 160). Although the magnitude of displacement in this region differs significantly among the receptors, which is most likely due to the current limitation of available crystallization conditions for stabilizing the fully active state for each receptor, the positions of the peaks match well with each other, indicating that similar rotational movement occurs around the axis of this helix upon activation. It is also noteworthy that, at the extracellular side of helix VI (residue no. 160 ~ 176), a significantly larger change occurs in rhodopsin than in β_2 receptor and A_{2A} receptor.

The cytoplasmic side of helix III (residue no. 75 ~ 89) is another region where these receptors exhibit substantial displacement of 1.5 ~ 2 Å, which has been attributed in part to the translational shift toward the extracellular side[5].

By averaging the values for the 3 receptors, structurally conserved residue positions were obtained, as listed in Table S1. Overall, residues around the highly conserved sequence positions (*.50 in Ballesteros-Weinstein [BW] numbering[19], where * is the serial number of helix) in helices I, II, IV, and VI appear to be fixed during activation. In particular, of the most structurally conserved 21 residues, 14 residues are in helix I (1.47, 1.48, and 1.50 ~ 1.54) and II (2.48 and 2.50 ~ 2.55). This finding is consistent with the notion that the so-called N-D pair (side chain interaction between 1.50 and 2.50) in these helices plays an important role as an intramolecular scaffold during activation.

To gain additional insight into the structural changes shown in Fig. 1, we analyzed the axis of each helix III and VI by helanal[20] (Figs S2 and S3). Examples of the inactive states are shown in Fig. 2. Each axis consists of a series of points penetrating about the center of a helix, with the number of points obtained for each axis equal to the number of residues minus 2. Thus, for convenience, we consider that both the N- and C-terminal residues lack the corresponding points (Fig. 2 and 3). As previously described, helix III of inactive rhodopsin is buried more deeply into the core of the heptahelical bundle from the center to the extracellular side than not only in the β_2 and A_{2A} receptors shown here, but also in other receptors of a known structure[17]. It is also noticeable that the extracellular part of this helix in the A_{2A} receptor is significantly distorted in the inactive-like state.

We first examined the traces of all axes and confirmed that assignment of the inactive and active-like states was reasonable for the Protein DataBank (PDB) entries shown in Table 1. The distances of the axis points were then calculated for all possible inactive/active-like pairs of a receptor. The average values are shown in Fig. 3. In the case of helix VI, the pattern of distance plots is consistent with the 3 receptors (Fig. 3, lower). Reflecting the kinked shape in the inactive state and rotational movement around an axis upon activation, a roughly linear increase of displacement occurs toward the cytoplasmic side of this helix in rhodopsin and the β_2 receptor. In contrast,

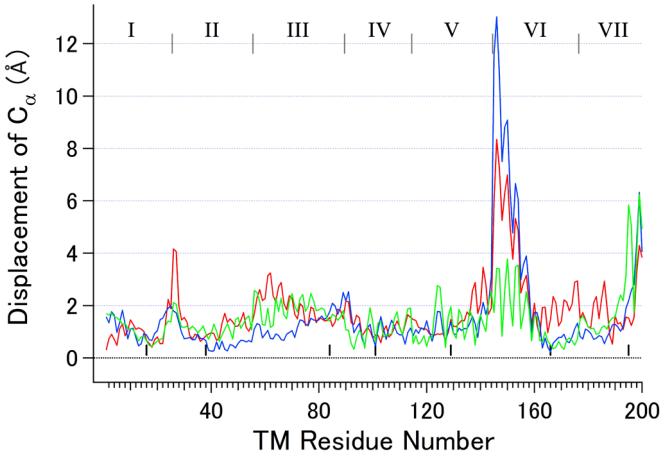

Figure 1 | Averaged displacement (Å) between the inactive and active-like states of the Cα atoms of 200 residues of the 3 receptors. Red: rhodopsin, blue: β_2 receptor, green: A_{2A} receptor. The borders between the adjacent helices are shown with gray bars at the top of the panel, while the positions of seven *.50 residues are shown with short black bars near the zero line of the graph.

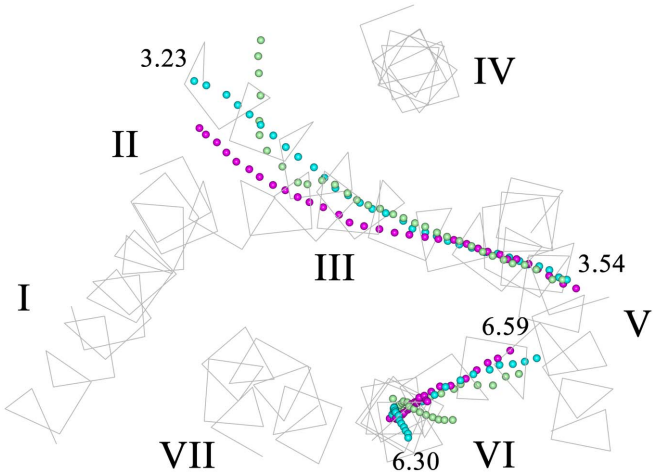

Figure 2 | Projection view of the axis points of helices III and VI in the inactive state from the cytoplasmic side. Magenta: rhodopsin (1U19-A), cyan: β_2 receptor (2RH1), light green: A_{2A} receptor (3VG9). Cα trace of β_2 receptor is also shown in gray. Ballesteros-Weinstein numbers corresponding to the endpoints of the axes are also shown.

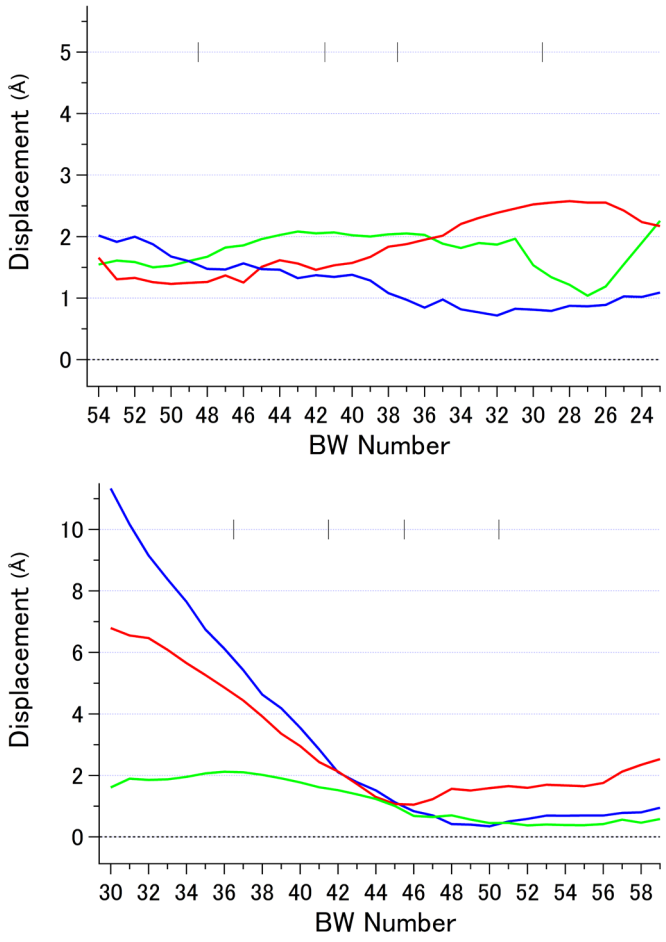

Figure 3 | Averaged difference distance (Å) plot between inactive and active-like states of 3 receptors. Upper: helix III, lower: helix VI. The horizontal axis (BW number) in the upper panel is reversed so that the cytoplasmic side is in the left side of both panels. The borders between the 5 sections stacked along the normal of the membrane plane[17] are shown with gray bars at the top of the panel.

the magnitude of displacement does not change significantly toward the extracellular side. The A_{2A} receptor exhibits a similar pattern of changes, although the increase in the cytoplasmic side is smaller and not linear. Remarkably, the change in the extracellular side of this helix is significantly larger in rhodopsin than in the other 2 receptors, and the point of minimum displacement appears to be shifted from 6.48 ~ Pro6.50 in the β_2 and A_{2A} receptors to 6.44 ~ 6.46 in rhodopsin. As shown in Fig. 2, the inactive backbone of helix III in rhodopsin deviates from the other receptors from ~ 3.40 to the remainder of the extracellular region. Importantly, 3.40 is the position directly in contact with 6.44. These observations suggest that the more buried inactive orientation of helix III and the larger movement in the extracellular side of helix VI are distinct features of rhodopsin, and that while interpreting these, the large differences of the retinal ligand shape and position before and after activation must be considered (see Discussion below).

We also found that the inactive state orientation of helix VI of β_2 receptor is much closer to the active-like helix VI of rhodopsin in the extracellular region than to that of the inactive rhodopsin. This is consistent with the finding that the degree of axis movement in the extracellular side of helix VI upon activation is larger in rhodopsin than in the β_2 receptor.

It has been noted that the activation of GPCRs involves a translational shift of helix III toward the extracellular side[5,12,14]. If the movement of this helix is only translational, the displacement of axis

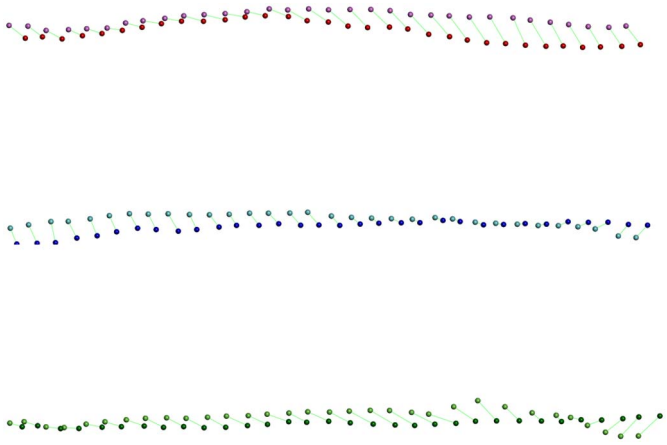

Figure 4 | Changes in the axis points of helix III during the activation of the 3 receptors. Top: rhodopsin. Magenta: inactive (1U19-A), red: active-like (3PXO). Middle: β_2 receptor. Cyan: inactive (2RH1), blue: active-like (3P0G). Bottom: A_{2A} receptor. light green: inactive (3VG9), green: active-like (3QAK). Corresponding axis points in the inactive and active-like states are connected by light green bars.

points would not exhibit a significant change depending on the position in the helix. Fig. 3 (upper panel) shows that the fairly flat pattern observed in the intracellular side is consistent with such a mechanism. However, the change in the pattern of displacement considerably differed among the 3 receptors in the extracellular side. The larger movement observed in rhodopsin is consistent with its distinct arrangement of this helix in the inactive state. On the other hand, an apparently irregular pattern was found in the extracellular side of this helix in the A_{2A} receptor, suggesting that some localized deformation occurred in this region.

To clarify the differences observed between these receptors, representative axes of inactive and active-like helix III are shown in Fig. 4. It is obvious that the translational shift of this helix toward extracellular side appears to be, at least in part, a result of twisting around the long axis. The degree of translation in the cytoplasmic side is likely to be determined by the pattern of twisting, and it varies substantially among the receptors. In the A_{2A} receptor, the pattern of twisting in the cytoplasmic side is distinct from that in the extracellular side (Fig. 4, bottom). In fact, a simple superimposition calculation fails to fit the inactive and active-like axes with each other, suggesting that helix III of the A_{2A} receptor would not behave as a rigid-body during activation.

In order to analyze the rearrangement of helix III in more detail, dihedral angles (Phi, Psi) of each residue were obtained with DSSP[21] (Fig. S4) and then averaged separately for the inactive and active-like helices (Fig. 5). In the A_{2A} receptor, significant changes in the dihedral angles occur at 3.30 ~ 3.31, depending upon the type of the bound ligand. For comparison, the results of a similar calculation for helix VI are shown in Fig. 6. As anticipated from the kinked shape, deviation from the ideal values was observed around 6.48 in the 3 receptors. The angle, however, does not change significantly, regardless of the type of the bound ligand, indicating that this helix behaves almost as a rigid-body in these receptors, as suggested previously[8].

Discussion

The present study is based on the comparison of a similar number of structures (8 ~ 9) for each of the 3 receptors. Although the quality of each structure varies substantially in terms of the claimed resolutions, from 1.8 (4EIY) to 3.5 Å (3P0G), it is unlikely that the findings reported here are affected significantly by such differences, given that we focus only on the backbone rearrangement of the receptors. The possibility that our procedure of fitting of all the inactive and

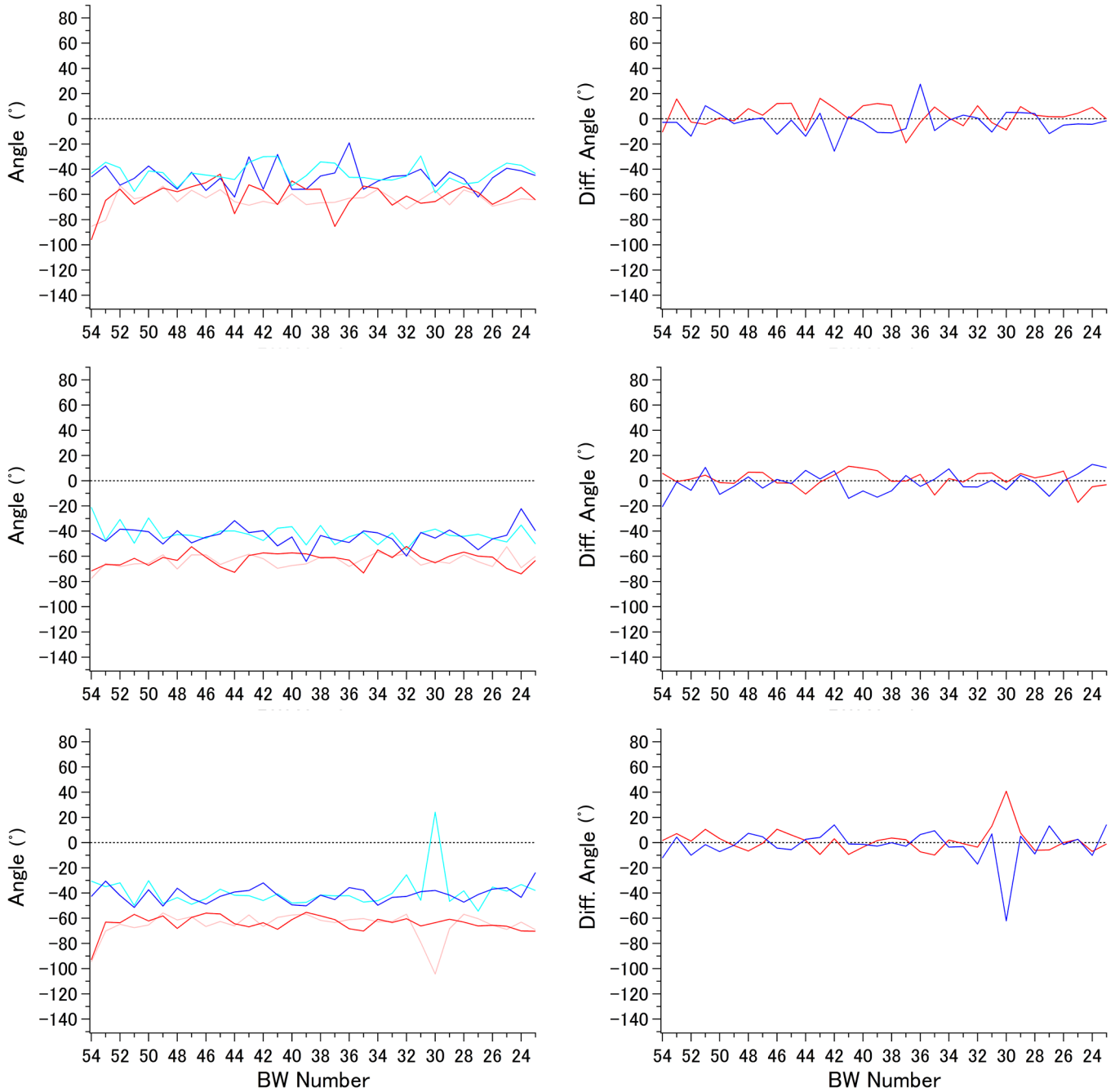

Figure 5 | Phi/Psi (°) plot of helix III. Top: rhodopsin, middle: β_2 receptor, bottom: A_{2A} receptor. Left: averaged Phi/Psi angles; pink: Phi angles of inactive-like states, red: Phi angles of active-like states, cyan: Psi angles of inactive-like states, blue: Psi angles of active-like states. Right: differences between averaged Phi (red), Psi (blue) angles of active-like and inactive-like states.

active-like structures to the inactive β_2 receptor might be inappropriate is also unlikely because we observed the same degree of movements and/or shifts of helices III and VI as those documented in previous crystallographic studies on the activation of the 3 receptors. In addition, the results of fitting independent statistics, such as Phi/Psi angle changes, further validate our procedure of model manipulation.

Given the emerging consensus view that a given GPCR can assume multiple conformational states[1,22], averaging available crystal structure models into 2 states, inactive and active-like, might be valid only for identifying substantial rearrangements of the helices. Nonetheless, our findings suggest that quantitative analyses based on such a 2 state approximation provide detailed information on not only common mechanisms but also receptor-specific mechanisms of activation.

The activity of rhodopsin changes dramatically upon photon absorption, and it is accompanied by the isomerization from 11-*cis* to all-*trans* of a covalently bound retinal ligand. 11-*cis*-retinal is known to act as a strong inverse-agonist, and the differences between the 2 forms of retinal with regard to the shape and position in the binding pocket of opsin are remarkably large compared with ligands bound to other receptors. Therefore, the magnitude of overall rearrangement of the helices in rhodopsin may be larger than the other receptors. This finding is in line with the findings that the displacement in the extracellular side of the helical bundle is larger (Fig. 1), especially in helices III and VI (Fig. 3). Although the plots in

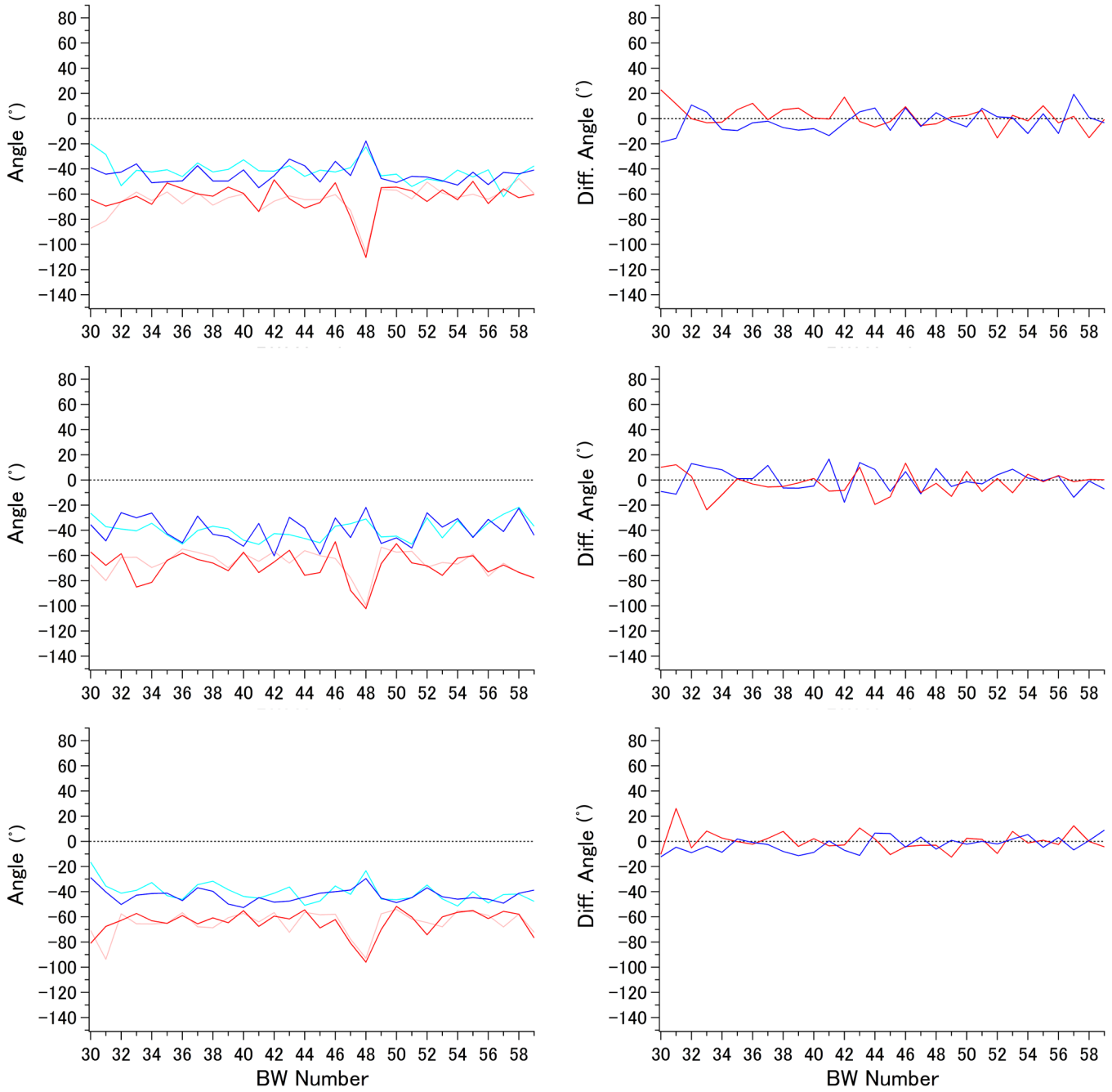

Figure 6 | Phi/Psi (°) plot of helix VI. Top: rhodopsin, middle: β_2 receptor, bottom: A_{2A} receptor. Left: averaged Phi/Psi angles; pink: Phi angles of inactive-like states, red: Phi angles of active-like states, cyan: Psi angles of inactive-like states, blue: Psi angles of active-like states. Right: differences between averaged Phi (red), Psi (blue) angles of active-like and inactive-like states.

Figures 1 and 3 may be influenced by the manner of fitting the multiple structures, the increase in the distance between the 2 helices of rhodopsin at the extracellular side was confirmed by measuring the interhelical Cα distances, which is independent of how active-like structures were fit onto the inactive ones (Fig. S5). We speculate that an extension of such an analysis would be useful for obtaining further insights into the relative positional changes among the 7 helices.

The outstanding local twist of helix III observed in the activation of the A_{2A} receptor is likely to be related to its curved shape in the inactive state, the degree of which is slightly different in the 2 states, namely, with (3VG9) or without (3EML and 4EIY) an inactivating antibody bound at the cytoplasmic side. Therefore, it is likely that the backbone rearrangement upon agonist binding at the extracellular side of this helix would directly affect the interaction with helix VI from the middle to the intracellular side of the membrane.

The Phi/Psi angles of 3.30 ~ 3.31 in the A_{2A} receptor change to a remarkable extent depending on the type of the bound ligand (Fig. 5). The side chains of these 2 residues in the 3 receptors do not point toward the interior of the helical bundle and do not appear to be directly involved in ligand binding. It should be noted that deviations in Phi/Psi angles at these residues from the canonical values are larger in the receptor with an inactivating antibody bound to an intracellular surface than that without it. This observation is in agreement with the finding that the overall twist at the extracellular side of helix III is significantly enhanced in the antibody-bound A_{2A} receptor (Fig. S2). Upon agonist binding, the overall shape of this helix

becomes more like a regular α-helical structure that exhibits little bending. It is likely that there are many other receptors of unknown structure that contain a kink at the extracellular side of helix III in the inactive structure. In such cases, a localized twisting motion would be possible depending on the type of a bound ligand, leading to rearrangement of the short segment in the helix.

In summary, the present study highlights the importance of quantitative analysis of the experimentally available structures to identify common and distinct rearrangement of transmembrane helices induced upon the activation of the 3 members of rhodopsin-like GPCRs. In particular, rearrangement of helix III was found to be a function of the type of receptor. While it has been well recognized that the interaction between this helix and helix VI is a key event in the regulation of the GPCR activity, the mechanism should be considered taking into account the non-rigid-body-like nature of the polypeptide backbone.

Methods

Selection and structural alignment of heptahelical transmembrane bundles were carried out as previously described[17]. Briefly, all the polypeptides from PDB entries were superimposed onto the inactive-like state of β_2 receptor (2RH1) by secondary structure matching[18], and 7 helices consisting of 200 residues were isolated based on unambiguous sequence alignment.

The active-like structures of rhodopsin can be classified into 2 groups, a ligand-free opsin form and an all-*trans*-retinal agonist-bound form. Because the backbone coordinates of these structures are quite similar to each other, we chose only agonist-bound structures for this study. Among the alternatives of inactive structures of the β_2 and A_{2A} receptors, the coordinates listed in Table 1 were selected by taking higher-resolution structures. Of the 3 agonist-bound structures of β_2 receptor reported to date, 3PDS was not used because of its negligible backbone deviation from the inactive-like structure.

DSSP analysis showed that all of the helices III and VI assume regular α-helical secondary structure throughout the entire lengths, with the exception of the cytoplasmic terminals of 3NY8, 3NY9, and 3.30 ~ 3.31 of 3VG9. Therefore, all helices III and VI were analyzed by helanal to determine the axes of the α-helices. Consequently, an axis point corresponding to 3.30 of 3VG9 appeared to be slightly displaced from the expected position within the helix. Although this error does not affect the findings described in this paper, we replaced the coordinate of the point by the averaged values of the preceding and the following points.

Several of the PDB entries contain 2 alternative coordinates for each of a few residues. Because deviations between the 2 Cα positions were negligibly small, we chose conformer A for all cases. Distances between the inactive and active-like axis points were obtained with Chimera[23] and CCP4MG[24] while that of entire heptahelical bundles were calculated by inserting the coordinates in a conventional equation. Phi/Psi angles were obtained by DSSP.

For interhelical Cα distance analysis, the coordinates in the inactive and active-like structures were first averaged separately for each of the 3 receptors, and the intramolecular Cα distances were calculated for all possible pairs in helices III and VI of the averaged inactive and active-like structures. The differences of the distances at each pairs of positions were then obtained between the inactive and active-like structures.

All graphs were prepared with IgorPro (WaveMetrics), and the remaining figures were prepared with CCP4MG[24] and Discovery Studio Visualizer (Accelrys).

1. Kobilka, B. K. & Deupi, X. Conformational complexity of G-protein-coupled receptors. *Trends Pharmacol. Sci.* **28**, 397–406 (2007).
2. Farrens, D. L., Altenbach, C., Yang, K., Hubbell, W. L. & Khorana, H. G. Requirement of rigid-body motion of transmembrane helices for light activation of rhodopsin. *Science* **274**, 768–770 (1996).
3. Park, J. H., Scheerer, P., Hofmann, K. P., Choe, H. W. & Ernst, O. P. Crystal structure of the ligand-free G-protein-coupled receptor opsin. *Nature* **454**, 183–187 (2008).
4. Rasmussen, S. G. *et al.* Structure of a nanobody-stabilized active state of the β(2) adrenoceptor. *Nature* **469**, 175–180 (2011).
5. Xu, F. *et al.* Structure of an agonist-bound human A_{2A} adenosine receptor. *Science* **332**, 322–327 (2011).
6. Hirai, T., Subramaniam, S. & Lanyi, J. K. Structural snapshots of conformational changes in a seven-helix membrane protein: lessons from bacteriorhodopsin. *Curr Opin Struct Biol.* **19**, 433–439 (2009).
7. Choe, H.-W. *et al.* Crystal structure of metarhodopsin II. *Nature* **471**, 651–655 (2011).
8. Standfuss, J. *et al.* The structural basis of agonist-induced activation in constitutively active rhodopsin. *Nature* **471**, 656–660 (2011).
9. Deupi, X. *et al.* Stabilized G protein binding site in the structure of constitutively active metarhodopsin-II. *Proc Natl Acad Sci USA* **109**, 119–124 (2012).
10. Warne, T. *et al.* The structural basis for agonist and partial agonist action on a β(1)-adrenergic receptor. *Nature* **469**, 241–244 (2011).
11. Søren, G. F. *et al.* Crystal structure of the β_2 adrenergic receptor–Gs protein complex. *Nature* **477**, 549–555 (2011).
12. Lebon, G. *et al.* Agonist-bound adenosine A_{2A} receptor structures reveal common features of GPCR activation. *Nature* **474**, 521–525 (2011).
13. White, J. F. *et al.* Structure of the agonist-bound neurotensin receptor. *Nature* **490**, 508–513 (2012).
14. Hulme, E. C. GPCR activation: a mutagenic spotlight on crystal structures. *Trends Pharmacol Sci.* **34**, 67–84 (2013).
15. Lebon, G., Warne, T. & Tate, C. G. Agonist-bound structures of G protein-coupled receptors. *Curr Opin Struct Biol.* **22**, 482–490 (2012).
16. Unal, H. & Karnik, S. S. Domain coupling in GPCRs: the engine for induced conformational changes. *Trends Pharmacol Sci.* **33**, 79–88 (2012).
17. Okada, T. Comparative analysis of the heptahelical transmembrane bundles of G protein-coupled receptors. *PLoS One* **7**, e35802 (2012).
18. Krissinel, E. & Henrick, K. Secondary-structure matching (SSM), a new tool for fast protein structure alignment in three dimensions. *Acta Crystallogr* **D60**, 2256–2268 (2004).
19. Ballesteros, J. A. & Weinstein, H. Integrated methods for the construction of three-dimensional models and computational probing of structure-function relations in G protein-coupled receptors. *Methods Neurosci* **25**, 366–428 (1995).
20. Bansal, M., Kumar, S. & Velavan, R. HELANAL: a program to characterize helix geometry in proteins. *J Biomol Struct Dyn* **17**, 811–819 (2000).
21. Kabsch, W. & Sander, C. Dictionary of protein secondary structure: pattern recognition of hydrogen-bonded and geometrical features. *Biopolymers* **22**, 2577–2637 (1983).
22. Kenakin, T. Ligand-selective receptor conformations revisited: the promise and the problem. *Trends Pharmacol Sci.* **24**, 346–54 (2003).
23. Pettersen, E. F. *et al.* UCSF Chimera--a visualization system for exploratory research and analysis. *J Comput Chem* **25**, 1605–1612 (2004).
24. McNicholas, S., Potterton, E., Wilson, K. S. & Noble, M. E. M. Presenting your structures: the CCP4mg molecular-graphics software. *Acta Cryst* **D67**, 386–394 (2011).
25. Wang, C. *et al.* Structural basis for molecular recognition at serotonin receptors. *Science* **340**, 610–614 (2013).
26. Wacker, D. *et al.* Structural Features for Functional Selectivity at Serotonin Receptors. *Science* **340**, 615–619 (2013).

Acknowledgments

Supported by the Ministry of Education, Culture, Sports, Science and Technology of Japan.

Author contributions

S.N., T.I., D.O. performed analysis, T.O. designed research, performed analysis, and wrote the manuscript.

Additional information

Supplementary information accompanies this paper at http://www.nature.com/scientificreports

Competing financial interests: The authors declare no competing financial interests.

How to cite this article: Nakamura, S., Itabashi, T., Ogawa, D. & Okada, T. Common and distinct mechanisms of activation of rhodopsin and other G protein-coupled receptors. *Sci. Rep.* **3**, 1844; DOI:10.1038/srep01844 (2013).

SCIENTIFIC REPORTS

OPEN

SUBJECT AREAS:
MEMBRANE BIOPHYSICS
STRUCTURAL BIOLOGY

Received
27 November 2014

Accepted
24 February 2015

Published
17 March 2015

Correspondence and requests for materials should be addressed to T.O. (tetsuji.okada@gakushuin.ac.jp)

Structural conservation among the rhodopsin-like and other G protein-coupled receptors

Mikitaka Kinoshita & Tetsuji Okada

Department of Life Science, Gakushuin University, 1-5-1 Mejiro, Toshima-ku, Tokyo 171-8588, Japan.

Intramolecular remote coupling within the polypeptide backbones of membrane proteins is difficult to analyze owing to the limited structural information available at the atomic level. Nonetheless, recent progress in the crystallographic study of G protein-coupled receptors (GPCRs) has provided an unprecedented opportunity for understanding the sophisticated architecture of heptahelical transmembrane (7TM) bundles. These 7TM bundles can respond to a wide range of extracellular stimuli while retaining the common function of binding trimeric G proteins. Here we have systematically analyzed select sets of inactive-like 7TM bundles to highlight the structural conservation of the receptors, in terms of intramolecular C_α-C_α distances. Distances with the highest scores were found to be dominated by the intrahelical distances of helix III, regardless of the choice of bundles in the set, indicating that the intracellular half of this helix is highly conserved. Unexpectedly, the distances between the cytoplasmic side of helix I and the extracellular region of helix VI provided the largest contribution to the high score populations among the interhelical pairs in most of the selected sets, including class B, C and frizzled receptors. These findings are expected to be valuable in further studies of GPCRs with unknown structure and of other protein families.

Almost all eukaryotic organisms utilize G protein-coupled receptors (GPCRs) for sensing both external and internal signals, such as those from chemical substances, hormones, and photons[1,2]. Recent advances in the structural study on the receptors of this superfamily have provided a wealth of information, promoting a wide range of researches, including for example, the rational design of drugs with improved efficacy and specificity[3,4]. However, a substantial number of unexplored targets found from unicellular eukaryotes to humans remain to be investigated in atomic detail.

A set of coordinates for a given family of proteins can be utilized to develop reliable methods for predicting the structure of related proteins, and to gain insights into the mechanisms underlying molecular evolution. There are few membrane protein families suitable for conducting detailed analysis using a wealth of data with preferable variations in both the structure and the sequence. The transmembrane domains of GPCRs, accommodating both the functionally common and the variable parts within a bundle of seven helical segments confined in the lipid bilayer, offer an excellent template model in terms of the biological significance of their structure/activity relationship and the moderate structural and sequence variations.

Previous studies on the arrangement of the seven transmembrane (7TM) helices of the inactive-like crystal structures of GPCRs have confirmed that the positions near to the highly conserved residues in the rhodopsin family, designated as *.50 (asterisk indicates helix number) with Ballesteros & Weinstein (BW) numbering[5], exhibit relatively small positional deviations among receptors[6]. However, the degree of conservation in terms of the intramolecular distances has not yet been quantitatively examined. RMSD values, often used for evaluating similarity between a pair of receptors, are not suitable for determining whether any common features are conserved among a set of receptors. Furthermore, recently determined structures of non-rhodopsin family GPCRs have demonstrated that the apparently important helix VI of the 7TM bundles deviates significantly from that of the rhodopsin family receptors[7–9]. This finding has led to questions regarding the types of structural conditions that are essential to maintaining a common function.

To address these issues, we performed an extensive distance analysis that included calculation of all the pairwise intramolecular distances between the C_α atoms within 200 residue 7TM bundles. Conservation was scored according to the coefficient of variation calculated for the receptors selected in a given set. By testing

various sets of receptor combinations, we found that this simple method of analysis provided valuable insights into the architecture of the GPCR superfamily.

Results

Receptor selection. The 7TM bundles, each containing 200 residues, were defined as previously reported for rhodopsin family receptors[6]. Thus, 200 × 199/2 = 19,900 values were examined for each of the bundles. Initially we analyzed 59 inactive bundles that were available until July 2013 (set 0) that had a crystallographic resolution higher than 3.6 Å (supporting table S1). The results obtained from this set led us to perform a further detailed study, and the list of the structures examined is summarized in supporting table S2. For instance, set 1 was composed of the structures of the rhodopsin family that were available until January 2014, and that had a resolution higher than 3.3 Å. Thus, set 1 contained 6 rhodopsin (4 bovine, 2 squid), 10 adrenergic (5 each for β_1 and β_2), 5 A_{2A} adenosine, 7 chemokine (5 CXCR4, 2 CCR5), 4 other amine (2 dopamine, 1 histamine, 1 muscarinic), 6 opioid (2 kappa, 2 N/OFQ, 1 delta, 1 mu), 1 sphingosine and 1 thrombin receptor bundles. In this set, the total number of bundles was decreased to 40, reducing possible bias toward the adrenergic receptors for which the greatest number of crystal structures is available. To evaluate the findings obtained for the rhodopsin family receptors, set 2 was defined as set 1 with the addition of three non-rhodopsin family bundles, one class B CRF_1 receptor and two chains of smoothened receptor. From set 2, the five subfamilies- rhodopsin, adrenergic, adenosine, chemokine, and opioid receptors were removed to form set 3, 4, 5, 6, and 7, respectively, to see whether any subfamily specific features exist. In sets 8 and 9, a maximum of three bundles or one bundle, respectively, for each of the receptors was included, to reduce any possible bias from larger contribution from rhodopsin family receptors. Thus, set 9 contained 18 unique receptor bundles; however this set was still biased toward the rhodopsin family, as it contained 16 rhodopsin family members and 2 non-rhodopsin family members. This was simply due to the current limited number of available structures for non-rhodopsin family receptors. Recently reported class C receptor[10] was also taken into account in set 10, which contained set 9 and mGluR1 receptor.

Since our current analysis focused only on extracting information on structural features that are relatively invariable among subfamilies of receptors that vary from each other by at least more than 1.5 Å in the overall RMSD for the TM region, any possible effects of various modifications (that mostly result in changes of < 1 Å in overall RMSD) applied to each receptor (Table S2) did not appear to affect the results significantly. As shown below, this is confirmed by the fact that we could detect a subtype–specific feature in adrenergic receptors for which both modified and unmodified structures were included in the analysis.

Ranking procedure. For each of the C_α-C_α pair distances in the sets, the average, maximum, minimum, and standard deviations were calculated. As a simple and rational measure (score) of the conservation among the bundles, we chose the inverse of coefficient of variation, wherein this coefficient is the average divided by the standard deviation. The scores obtained in the current study varied from ~ 1.5 to ~ 250. With this scoring, the higher numbers (ranks with a smaller number) were dominated by C_α pairs of adjacent amino acid positions, and these were omitted from the ranking because they do not appear to provide much information on structural conservation.

Figure 1 shows the distribution of 19,900 C_α pairs in set 1 over the whole scoring range with or without the contribution of 193 adjacent C_α pairs. The cumulative count plot (Fig. 1B) indicates that C_α pairs found in the top 1,000 ranks have scores greater than approximately 50, which corresponds to a 0.4 Å standard deviation for the average

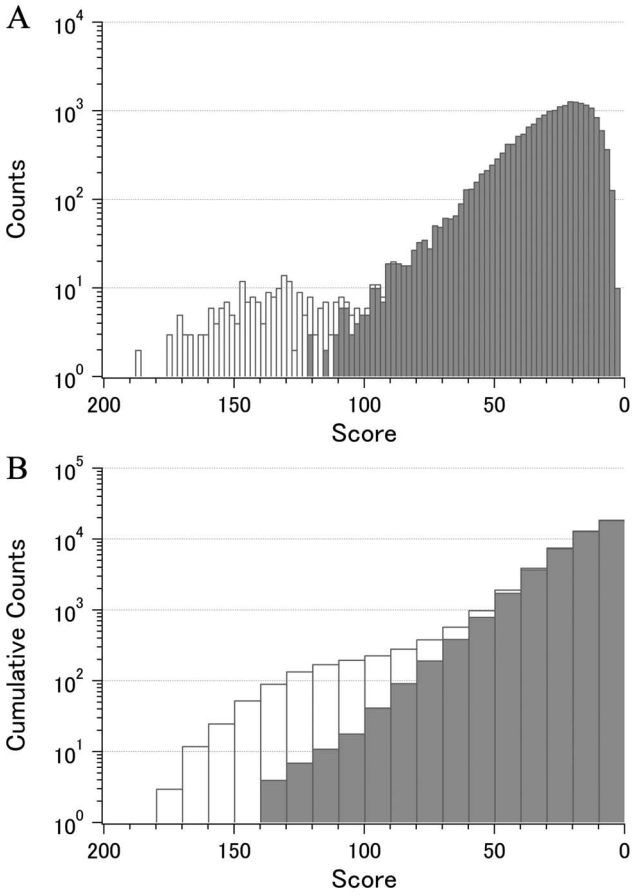

Figure 1 | Score distribution of 19,900 C_α- C_α pairs. Calculated for set 1 containing forty 7TM bundles of rhodopsin family receptors with (blank bars) or without (filled bars) the contribution of 193 adjacent pairs. A. Counts in each score range. B. Cumulative counts.

distance of 20 Å, and is fairly higher than the average score of 29.4 obtained for all 19,900 pairs. Since the top 1,000 pairs amounted to only 5% of the total, detailed analysis of this population is a reasonable approach for examining the intramolecular distance conservation among the receptors in a given set.

Data statistics. We next investigated whether the population of higher scoring C_α pairs was biased toward either long or short distances. Figure 2a shows the distribution of the average distances for the 19,900 C_α pairs in set 1. The maximum value of around 21 Å includes, for example, intrahelical distances separated by four pitches. Comparison of the average distance distribution for the C_α pairs ranked within the top 1,000 score with this distribution showed that both were similar (Fig. 2B), indicating that the current scoring was not biased toward short or large distance populations.

The relationship between the distance and the score was further examined using a scatter plot of the 19,900 C_α pairs (Fig. 3) of set 1. As described earlier, the population with scores ranging from 90 to 200 at the distance of approximately 3.8 Å originates from adjacent pairs of amino acids. The remainder of the distribution appeared uniform across the whole range of distances. While the lower limit of the scores tended to increase slightly at longer distances, our detailed analysis focused only the scores higher than approximately 50. Therefore, these statistics support the assumption that the present simple scoring system would be useful in extracting the conserved arrangement of backbone among the receptors.

Evaluation of high rank pairs. We classified the top 1,000 ranking C_α pairs into 28 helix pairs (7 intrahelical and 21 interhelical) based

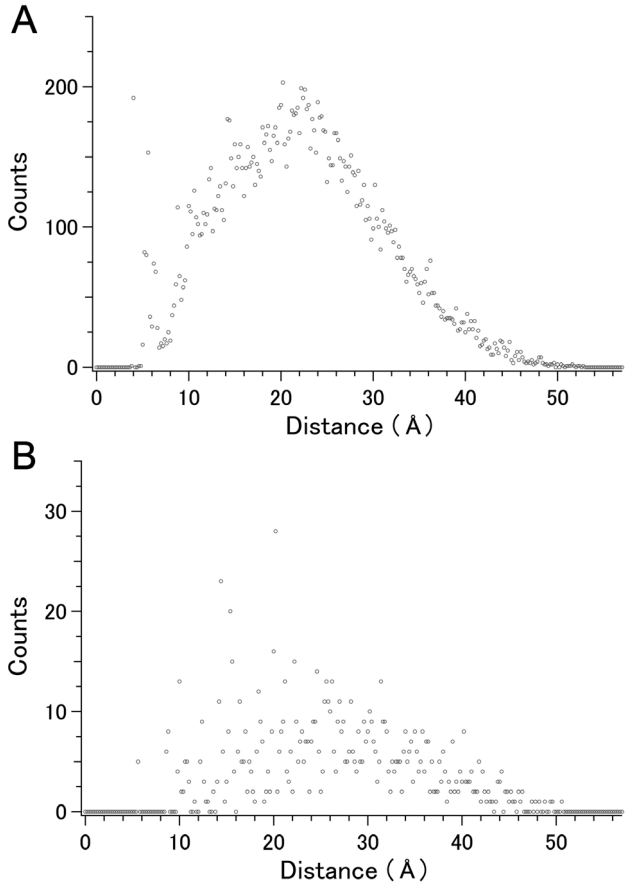

Figure 2 | Average distance distribution of C_α- C_α pairs in set 1. A. 19,900 pairs including the contribution of 193 adjacent pairs. B. The top-ranked 1,000 pairs without the contribution of 193 adjacent pairs. The point for 1000th rank included in panel B corresponds to rank 1193 in panel A, and a point corresponding to 193 adjacent pairs at a distance of ~ 3.8 Å, identical to that shown in panel A, has been omitted from panel B to make its vertical scale appropriate.

on the helices to which the C_α belonged. Because the total number of C_α pairs differs among the 28 helix pairs depending on the length (number of amino acids) of each helix, the C_α-C_α counts in the top 1,000 were compared among the 28 helix pairs after normalization. For instance, the total number of intrahelical C_α-C_α distances of helix III was 581 since we had selected its TM region from 3.22 to 3.55 (34 residues). Therefore, the 220 C_α-C_α distances found in the top 1,000 ranked pairs of set 1 corresponded to 37.9% of the total (see below and Fig. 4B). In the same way, we obtained the patterns of contribution from each of the 28 helix pairs to the top 1,000 ranked pairs for the 11 sets (from set 0 to set 10).

Figure 4 shows the cumulative numbers (ratios to the total) of the C_α pairs found in the top 1,000 ranks for 28 helix pairs for sets 0 and 1, both of which contain only rhodopsin family bundles. The corresponding data containing non-rhodopsin receptors are shown in figure 5 (sets 2, 8, 9, and 10, the latter of which had a smaller proportion of rhodopsin family members) and in supporting figure S1 (sets 3 to 7, for each of which a specific receptor subfamily was omitted from set 2).

The higher ranked C_α-C_α distances in all the sets were mainly from the intrahelical part of helix III, regardless of the inclusion of non-rhodopsin family receptors (Fig. 4, 5, Fig. S1). In the extreme cases of set 5 (with no adenosine receptors), set 9 (bundles representing 18 unique receptors), and set 10 (set 9 plus class C receptor), nearly 60% (approximately 335 of 561) of the possible C_α pairs in this helix were ranked in the top 1,000. These observations quantitatively demonstrate that the overall arrangement of this helix is much more conserved than that of the other helices among all the GPCRs whose structure is known. A slight increase in the higher ranked C_α pairs from helix III in set 5 is likely due to the uniquely distorted character of this helix in the adenosine A_{2A} receptor, as has been documented previously[11].

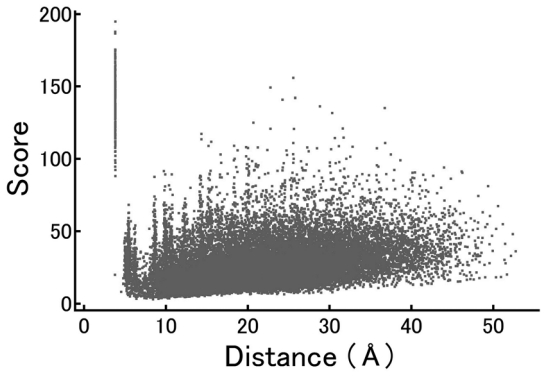

Figure 3 | Correlation between score and the average distance of the 19,900 C_α- C_α pairs in set 1.

Next we examined the conservation pattern in more details, according to the previously described horizontal sectioning of the 7TM bundle of 200 residues[6] (Table 1). As shown in Fig. S2, we defined five sections to each of the helices. Thus, the possible number of intersection pairs is 630 (105 intrahelical and 525 interhelical), for the 7TM bundle. For each of these pairs, the total number of possible C_α-C_α combination varied from 9 (section 1 of helix I and section 5 of helix 7, each of which contains only three residues) to 90 (section 1 of helices VI and VII, each of which contains 10 and 9 residues, respectively). Therefore, we evaluated the distance conservation for each of the intersection pairs by calculating the ratio of the number of C_α pairs found in the top ranked 1,000 to the total number of possible pairs (ratio column in Table 1).

Within helix III, our data show that the intracellular side appears to be more structurally conserved than the intracellular side. Direct evidence for this can be seen when comparison of the values in Table 1 is made between section pairs 2–3 and 3–4. A higher number of pairs from the 3–4 section are ranked in the top 1000, indicating that conservation of the distance from the center of helix III is more pronounced on the intracellular side. Importantly, the results of this comparison would not be affected by how the residue range for this helix was chosen; for example, a shorter length of this helix, excluding a few residues from both the intracellular and extracellular termini, should provide the same result.

Figure 4 also demonstrates that helices IV and VII are the most variable in the rhodopsin family; this is even more apparent when the non-rhodopsin family receptors are included (Fig 5 and Fig S1). Furthermore, the results of our analysis suggest that helical segments judged as regular α-helices by DSSP[12] in many of the receptors (helices I, III, and VI) tend to exhibit high intrahelical distance conservation.

Interhelical distance conservation. With regard to the interhelical components, a significant number of C_α-C_α distances of the I–VI helix pair were found in the higher ranked population of sets 0 and 1 (Fig. 4). This finding was rather unexpected because no direct contact could be found between any parts of these two helices. The positions on helix I in the higher ranked I–VI pairs were found mostly in sections 4 and 5, a region that spans from around the conserved asparagine (BW no. 1.50) to the cytoplasmic end. On the other hand, positions on helix VI involved in the higher ranked I–VI pairs were found in sections 1 and 2, extending from the extracellular end towards the region near the conserved proline (BW no. 6.50).

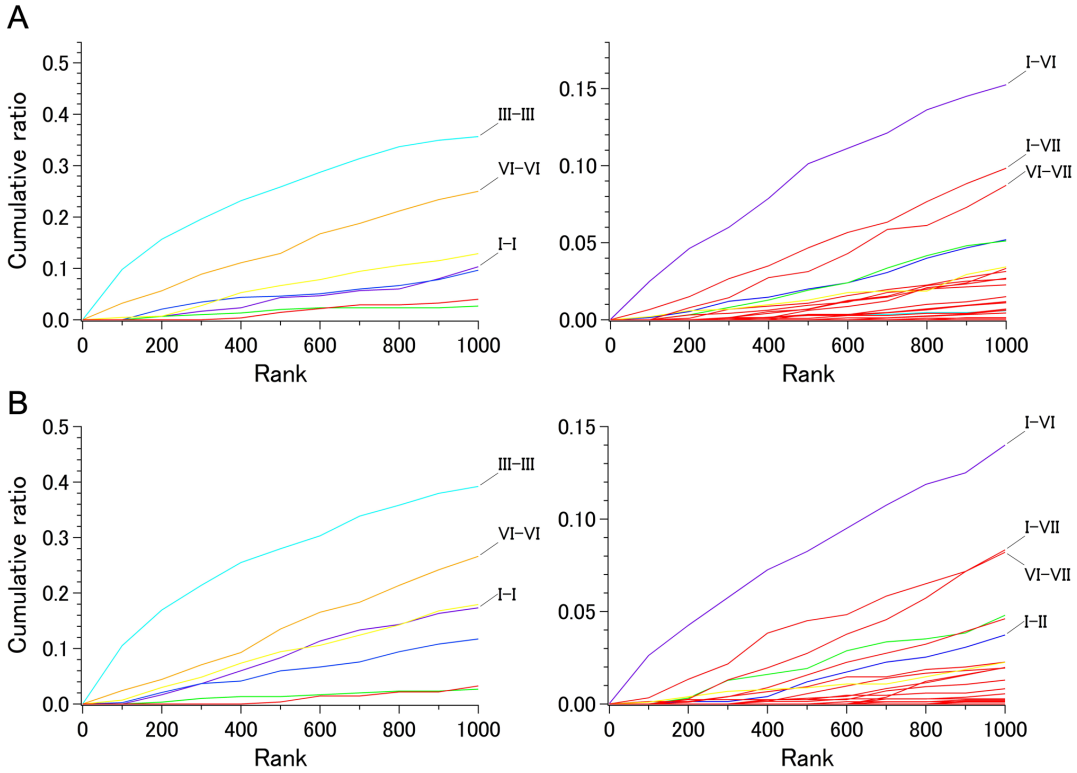

Figure 4 | Cumulative ratio of the number of C_α- C_α pairs in the top-ranked 1,000. A. Set 0 containing 59 rhodopsin family 7TM bundles. B. Set 1 containing 40 rhodopsin family 7TM bundles. Left: intrahelical pairs, Right: interhelical pairs. Intrahelical pairs are colored as follows; purple, helix I; blue, helix II; cyan, helix III; green, helix IV; yellow, helix V; orange, helix VI; red, helix VII. Interhelical pairs are colored as follows; blue, I–II; cyan, I–III; green, I–IV; purple, I–VI; yellow, III–V; red, other pairs.

Importantly, the conservation of distances between the cytoplasmic side of helix I and the extracellular side of helix VI was also apparent in all of the sets containing non-rhodopsin family receptors (Fig. 5 and Fig. S1). This finding was surprising as the superimposition of either the class B CRF_1 receptor or smoothened receptor with the rhodopsin family receptors indicated a significant displacement of the extracellular side of helix VI, while the cytoplasmic side of helix I matched rather well. These observations might indicate that the deviation at the extracellular side of helix VI between the rhodopsin family and other receptor families reflects the presence of some directional restraint within a 7TM bundle, resulting in a relatively conserved distance from the cytoplasmic part of helix I.

Another interesting observation was the outstanding conservation of the distances between helices III and V in some of the sets containing non-rhodopsin family receptors (Fig. 5 and Fig. S1). Although this feature was not evident in set 10 where class C receptor was included (Fig. 5D), detailed examination indicated that there were still some high score pairs between the cytoplasmic side of helix III and the extracellular part of helix V.

We also noticed that a significant increase in population in the higher-ranked interhelical distances of the non-rhodopsin family-containing sets was attributable to the pairs between helices I and IV (Fig. 5). Furthermore, I–III and I–II helix pairs contributed significantly to the higher-ranked interhelical distances in the case of set 10. These observations and the intrahelical distance conservation data shown above suggest that positioning of helix I within the 7TM bundle is substantially conserved among all GPCRs.

The distance conservation results are summarized graphically in Figure 6, which includes lines connecting the 5 higher-ranked C_α-C_αs in each of the major interhelical section pairs in set 10. All of these C_α pairs had scores higher than 50. Figure 7 shows the positions of residues conserved among the receptors in set 10. In summary, the present results are consistent with the previous observation that positional deviations among rhodopsin-family receptors are small on the intracellular side of helices I, II, III, and in the middle of helix VI,[6] and suggest that interhelical distance conservation correlate well with the presence of conserved amino acid type at some specific positions in the GPCRs with known structure. While no single position in the TM bundle is 100% identical among the receptors examined (Fig. S3), our analysis suggests that four of the five conserved residues, all of which are in section 4 (the middle–to–intracellular region), contribute to determining the basic arrangement of the bundle, at least from helices I to III, mostly by hydrophobic interactions. This interpretation explains why the relative contribution of the I–II and I–III pairs to the high score population increases as the ratio of the non-rhodopsin-family chains increases in a set (Fig. 5).

Discussion

Statistical and quantitative analysis of the sequences and the three-dimensional structures of a protein family provide insights into functionally relevant and evolutionary significant regions. In the case of GPCRs, one of the most intriguing questions is how the common 7TM bundle core works for diverse members that convert a variety of signals, mostly captured at the middle to the extracellular part of the bundle, to the degree of coupling with the cognate heterotrimeric G proteins at the cytoplasmic surface. Although the basic folding pattern is similar for the seven helices in all the receptors of known structure, it is now increasingly evident that there are significant variations in spacing and shape of the helices depending on the subfamilies they belong.

Structural conservation and deviation in the 7TM region of GPCRs has been examined mostly based on superimposition and RMSD examination, and has shown little ambiguity as long as the receptors belonged to the rhodopsin family. The C_α positions at or near to the conserved residues (*.50 in BW numbering) exhibited relatively small deviations among the receptors[6]. However, recent

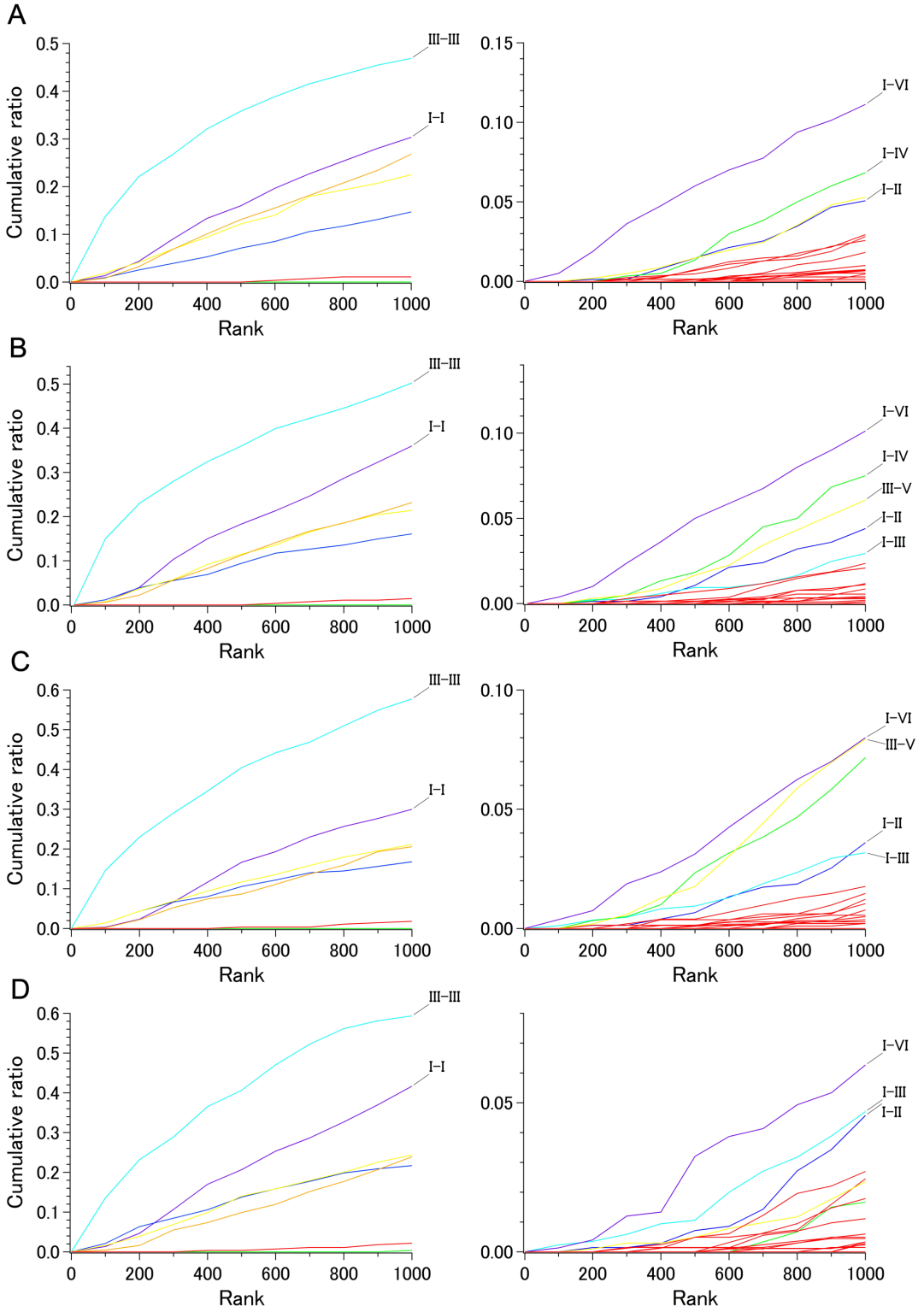

Figure 5 | Cumulative ratio of the number of C_α- C_α pairs in the top-ranked 1,000. A. Set 2 containing 40 rhodopsin family 7TM bundles and three non-rhodopsin family bundles. B. Set 8 containing 31 rhodopsin family 7TM bundles and three non-rhodopsin family bundles. C. Set 9 containing 16 rhodopsin family 7TM bundles and two non-rhodopsin family bundles. D. Set 10 containing 16 rhodopsin family 7TM bundles and three non-rhodopsin family bundles. Left: intrahelical pairs, Right: interhelical pairs. Coloring of the plots is the same as in figure 4.

determination of non-rhodopsin family receptor structures presents challenges concerning the reliable comparison and quantitation of differences among the 7TM regions. In fact, superimposition could vary, depending on how it was performed, and RMSD analysis does not appear to provide any quantitative results, as the present study does, such as the remarkable conservation of the structure of helix III and the I–VI, I–III distances.

Furthermore, rational interpretation of the increasing data on the relation between the type of bound ligand and the degree of conformational change requires understanding of common structural fea-

Table 1 | Conserved pairs within helix III and between helices I and VI

$C_\alpha 1$		$C_\alpha 2$	Set 1			Set 2		
Helix III		Helix I	Number of pairs			Number of pairs		
section		section	top1000	all	ratio	top1000	all	ratio
1		2	4	64	0.06	8	64	0.13
1		3	10	32	0.31	13	32	0.41
1		4	34	56	0.61	37	56	0.66
1		5	36	56	0.64	44	56	0.79
2		3	3	32	0.09	7	32	0.22
2		4	42	56	0.75	44	56	0.79
2		5	41	56	0.73	46	56	0.82
3		4	14	28	0.50	17	28	0.61
3		5	21	28	0.75	22	28	0.79
4		4	3	21	0.14	7	21	0.33
4		5	12	49	0.24	16	49	0.33
	others		0	83	0.00	2	83	0.02
	total		220	561	0.39	263	561	0.47
Helix I		Helix VI	Number of pairs			Number of pairs		
section		section	top1000	all	ratio	top1000	all	ratio
3		1	6	50	0.12	12	50	0.24
3		2	3	25	0.12	4	25	0.16
4		1	31	60	0.52	28	60	0.47
4		2	25	30	0.83	14	30	0.47
5		1	25	50	0.50	16	50	0.32
5		2	20	25	0.80	14	25	0.56
5		3	2	20	0.10	1	20	0.05
	others		0	540	0.00	0	540	0.00
	total		112	800	0.14	89	800	0.11

tures that define the functional basis of this large family of membrane proteins. Here, we demonstrate that intramolecular distance conservation scoring provides a reasonable measure of evolutionary conserved basic architecture of GPCRs. The present results on distance conservation are consistent with a separate examination of the backbone torsion angles (phi, psi) of set 10: the lowest deviations are found in the sections I–4 (5.2° and 6.9° for phi and psi, respectively), III–4 (5.4° and 8.2°), and VI–2 (5.1° and 7.8°).

Although the amount of available structural data is limited, our results clearly show which part of the seven helices is the most or the least conserved in terms of the intra and interhelical distances (Fig. 5). Practically, such information should be useful in screening from a set of automatically constructed model for a receptor of unknown structure. Additionally, identification of conservation patterns will further evoke studies from evolutionary point of view. For instance, it would be interesting to analyze microbial 7TM retinal proteins with the current scoring method (see below).

The most conserved intrahelical distances are assigned at the spacing containing five turns approximately from 3.32 to 3.50. In fact, close examination of this part shows no significant distortion for all the receptors of known structure. Therefore, our result suggests that the regular and conserved shape of this helical segment is a key to the common functionality of GPCRs. Interestingly, the distances between the extracellular part of this segment and the cytoplasmic part of helix I is also conserved (Fig. 6). These findings, in conjunction with the intrahelical conservation of helix I and inter-helical conservation between the cytoplasmic part of helix I and the part around 6.50 of helix VI, highlight previously unidentified intramolecular spacing that might form the critical conditions for the functionality of GPCRs. Since the two regions described for helices III and VI affect the level of activity, it is conceivable that their relative position to a distant point (e.g., the cytoplasmic part of helix I) appears to be conserved.

Distance matrix analysis has been used for detecting the conformational transitions between two states within a protein[13]. The recent high-resolution structural models of GPCRs are valuable sources of data for extracting structural information regarding the conservation and variation among the evolutionally remote members of protein families, by systematically analyzing the intramolecular distances. To our knowledge, the variety or the quantity of structural data required for this sort of analysis are not available for other membrane protein families. The structures of a related family of 7TM proteins, the microbial retinal proteins, have been extensively investigated[14]. While the sequence variation of these proteins is limited, application of the current approach to this family of proteins appears to demonstrate distinct features from GPCRs in the intramolecular conservation patterns (unpublished data).

The statistical analysis presented makes use of only one snapshot of these inherently dynamic and fluctuating molecules[15]. Therefore, the quantity and the quality of available structural data would be expected to significantly affect the reliability of the inferred results. Indeed, the present scoring and ranking were reasonably sensitive to the choice of structures in a given set, especially with regard to interhelical pairs. It is possible that further structural data would improve the characterization of each of the families within the whole GPCR superfamily.

Changes in the intramolecular interatomic distance of specific pairs of amino acids have been frequently examined when estimating the trajectories for molecular dynamics simulations[16,17]. As a reference, our 50 ns simulation of the delta opioid receptor indicated that the scores calculated for the trajectory of the distances between the C_αs of BW numbers 1.59 and 6.50, one of the highest-ranked-pair in the present study (score approximately 87 in set 10), was 51. On the other hand, the corresponding score between 3.50 and 6.30, which was expected to be sensitive to the state of receptor activity, was 12, which was comparable to that obtained in set 10 (score 5.6).

The present study focused only on the inactive-like structures that were obtained in the presence of antagonists, inverse-agonists or negative allosteric modulator. However, the degree of conformational "inactiveness" might differ among the structures in a given

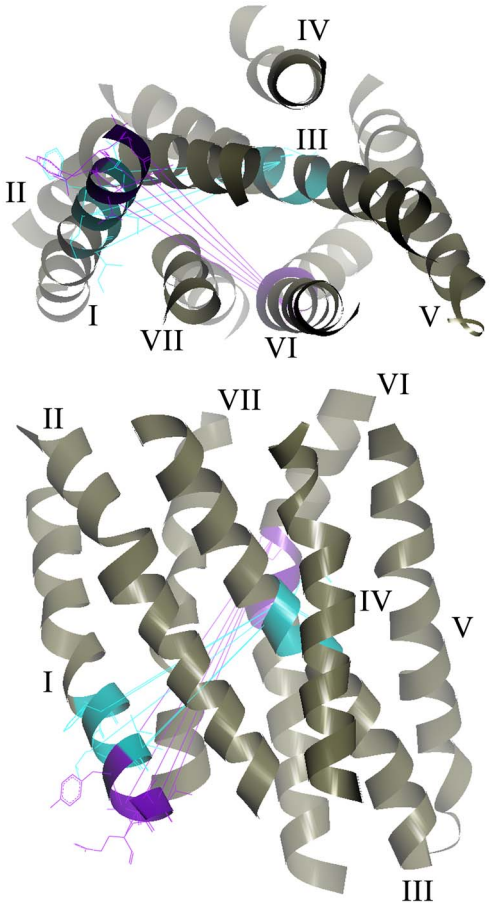

Figure 6 | Graphical representation of conserved interhelical distances in set 10 including 19 unique bundles from all GPCRs with known structure. Upper: top view from the cytoplasmic side. Lower: side view from helices II and IV. Interhelical section pairs of conserved distance are colored on the 200 residue 7TM backbone of bovine rhodopsin template (1U19-A) as follows; purple, I–VI; cyan, I–III. All of the lines shown between the pairs have scores of more than 50. For clarity, the pairs involving the residues of BW no. 3.37 and 6.50 are shown by these lines.

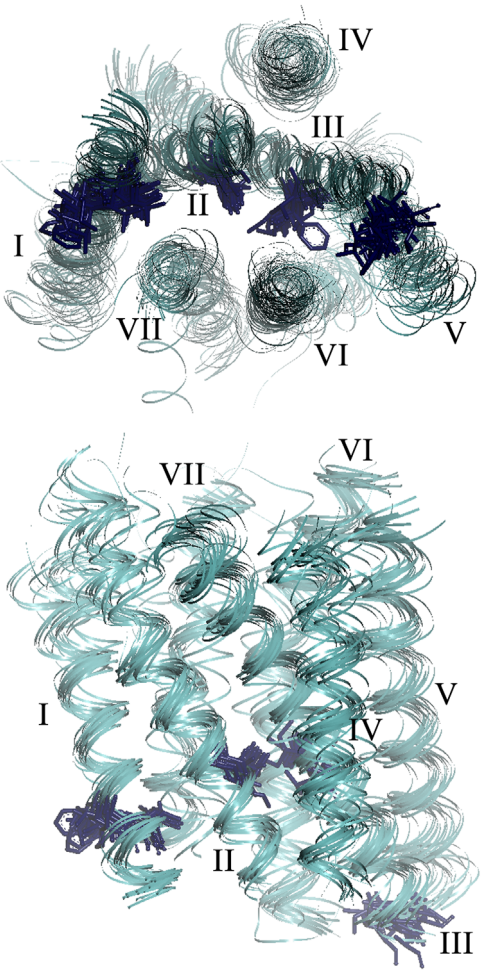

Figure 7 | Graphical representation of conserved residues among 19 receptors in set 10. Upper: top view from the cytoplasmic side. Lower: side view from helices II and IV. Five conserved positions in helices I, II, and III (Fig. S3) are shown as sticks on each of the 7TM backbone ribbons. These residues correspond to BW no. of 1.52, 1.53, 2.46, 3.43, and 3.54.

set depending on the type of ligand bound to each of the receptors. Therefore, the higher-ranked section pairs described may also be structurally conserved in the active-like states. While a direct comparison between the results obtained from inactive-like and active-like sets would be difficult due to the limited variety of receptors in the active-like set, further analysis of the active-like set is likely to provide valuable insights into the activation mechanism of the rhodopsin family receptors.

Analysis of the conserved interhelical pairs in each set appears to provide subfamily-specific information. In the case of set 4, where adrenergic receptors were omitted, we observe an increase in high score contribution from the III–V pairs. This result is consistent with the fact that superimposition of the bundles clearly showed that helix V of the β_1 and β_2 adrenergic receptors was shifted slightly upward (toward the extracellular side) from the other receptors while helix III did not exhibit any features among them.

On the other hand, deviations can also be accommodated without changing the interhelical distances. Previously reported significant deviations of bovine rhodopsin from other receptors with respect to the positioning of the extracellular part of helix III[6] did not appear to affect its distance to the cytoplasmic end of helix V. Similarly, considerable deviation of class B and smoothened receptors from rhodopsin family at the extracellular part of helix VI did not cause major distance changes from this region to the cytoplasmic end of helix I. These observations suggest that our analysis also provides information on allowable directions along which some helices can deviate without affecting the receptor's functionality. Further accumulation of high-resolution structures could confirm whether the highly diverse backbone organization in the extracellular regions of GPCRs might still be limited by directional restrains that are required to ensure the correct positioning of the cytoplasmic parts of the 7TM bundle.

The most intriguing structural feature of GPCR activation is that a variety of stimuli likely evoke large movement of helix VI while the remaining 6 helices exhibit smaller degree of rearrangement[11,18]. For such a mechanism to operate in diverse receptors, we suspect that some common and key intramolecular restraints have been conserved during evolution. In this respect, conservation of the distances from the intracellular side of helix I to the middle/extracellular part of helices III and VI might be an essential requirement.

Methods

The data processing from the original PDB entries was as follows. Each of the polypeptides in an entry was used to extract the heptahelical bundle, consisting of 200 residues, as described previously[6]. For each polypeptide, C_α coordinates were extracted by pdbset in ccp4i[19]. Temperature factor analysis was also performed using these C_α files.

In total, 19,900 interatomic distances were calculated and tabulated, using the coordinates of the 200 C_α atoms in each bundle for all the chains archived on our web

site (www.gses.jp). In cases where two conformers were provided for a residue, frequently W(4.50) in the rhodopsin family receptors, only conformer A was considered because the differences of the C_α coordinates between A and B were mostly negligible. Alignment of CRF_1 receptor in class B, mGluRs in class C, and smoothened receptor was identical to that reported previously[7–10] at the most conserved position in each helix. The 7TM bundle of the smoothened receptor (PDB ID: 4JKV) aligned to rhodopsin-like receptors was assumed to lack a residue at the amino terminal of helix IV (4.39). Therefore, in the sets containing the smoothened receptor, the total number of C_α pairs was 19,701. Similarly, the 7TM bundle of the class C mGluR1 receptor was assumed to lack two residues at the carboxyl termini of helix II (2.66 and 2.67) and VI (6.59 and 6.60), giving the total number of 18,915 for C_α pairs in set 10. Even among the receptors of the rhodopsin family, the possible sequence gaps supposed to occur in a few regions (e.g. the extracellular side of helices II and IV) in some receptors[20,21] were not taken into account, and the BW numbering was serially made in both directions from the *.50 position.

In addition to the criteria for bundle selection for each of the sets, we selected bundles for the minimal sets 9 and 10 as the ones with the highest resolution and lower overall average temperature factor. For instance, chain B of 4AMJ was chosen for the β_1 adrenergic receptor because 4AMJ has the highest resolution for this receptor and the chain B has lower overall temperature factor for C_αs than chain A.

In each of the sets, the average, standard deviation, maximum, minimum, and the inverse of coefficient of variation (score) were calculated for the 19,900 or 19,701/18,915 C_α pairs. Then sorting was made according to the score. The distribution of the average distances were examined for all 19,900 and the top ranked 1,000 C_α pairs of set 1. Two-dimensional plots showing the correlation between the score and the distance were also prepared for set 1.

Molecular dynamics (MD) simulation runs were performed on the delta opioid receptor, having complete inter-helical loops (PDB ID: 4N6H), in a lipid bilayer of 80 × 80 POPC molecules, with NAMD[22] running on a GPU accelerated PC, using particle-mesh Ewald electrostatics, 10 Å nonbond cut-off, switching function at 9 Å, 12 Å pair list cut-off and 1 fs time step. Briefly, the delta receptor polypeptide (from G36 to G338) having a complete loop connection was inserted into the POPC bilayer, hydrated, neutralized with 0.15 M NaCl by VMD[23]. The whole system was energy minimized for 50 ps and the lipid and the solvent were equilibrated by MD for 0.5 ns under NVT condition (310 K). Then, a 50 ns MD run was performed with no restraints under NPT at 1.0 bar and 310 K and the C_α-C_α distances in the trajectory were analyzed with MD tools implemented in Chimera[24]. All the graphs and the graphics were drawn with Igor Pro (WaveMetrix) and DS visualizer (Accelrys), respectively.

Backbone torsion angles were obtained by DSSP[12] and the deviations of phi and psi angles among the receptor structures were calculated for each C_α position. Then, the values were averaged for each of the 35 sections (5 sections per helix).

1. Kroeze, W. K., Sheffler, D. J. & Roth, B. L. G-protein-coupled receptors at a glance. *J. Cell Sci.* **116**, 4867–4869 (2003).
2. Fredriksson, R. & Schiöth, H. B. The repertoire of G-protein-coupled receptors in fully sequenced genomes. *Mol. Pharmacol.* **67**, 1414–1125 (2005).
3. Kolb, P. *et al.* Structure-based discovery of beta2-adrenergic receptor ligands. *Proc. Natl. Acad. Sci. U.S.A.* **106**, 6843–6848 (2009).
4. Beuming, T. & Sherman, W. Current assessment of docking into GPCR crystal structures and homology models: successes, challenges, and guidelines. *J. Chem. Inf. Model.* **52**, 3263–3277 (2012).
5. Ballesteros, J. A. & Weinstein, H. Integrated methods for the construction of three-dimensional models and computational probing of structure-function relations in G protein-coupled receptors. *Methods Neurosci.* **25**, 366–428 (1995).
6. Okada, T. Comparative analysis of the heptahelical transmembrane bundles of G protein-coupled receptors. *PLoS One* **7**, e35802 (2012).
7. Wang, C. *et al.* Structure of the human smoothened receptor bound to an antitumour agent. *Nature* **497**, 338–343 (2013).
8. Hollenstein, K. *et al.* Structure of class B GPCR corticotropin-releasing factor receptor 1. *Nature* **497**, 438–443 (2013).
9. Siu, F. Y. *et al.* Structure of the human glucagon class B G-protein-coupled receptor. *Nature* **497**, 444–449 (2013).
10. Wu, H. *et al.* Structure of a class C GPCR metabotropic glutamate receptor 1 bound to an allosteric modulator. *Science* **344**, 58–64 (2014).
11. Nakamura, S., Itabashi, T., Ogawa, D. & Okada, T. Common and distinct mechanisms of activation of rhodopsin and other G protein-coupled receptors. *Sci. Rep.* **3**, 1844 (2013).
12. Kabsch, W. & Sander, C. Dictionary of protein secondary structure: pattern recognition of hydrogen-bonded and geometrical features. *Biopolymers* **22**, 2577–2637 (1983).
13. Edman, K. *et al.* Deformation of helix C in the low temperature L-intermediate of bacteriorhodopsin. *J. Biol. Chem.* **279**, 2147–2158 (2004).
14. Gushchin, I. *et al.* Structural insights into the proton pumping by unusual proteorhodopsin from nonmarine bacteria. *Proc. Natl. Acad. Sci. U.S.A.* **110**, 12631–12636 (2013).
15. Nygaard, R. *et al.* The dynamic process of β(2)-adrenergic receptor activation. *Cell* **152**, 532–542 (2013).
16. Spijker, P., Vaidehi, N., Freddolino, P. L., Hilbers, P. A. & Goddard 3rd, W. A. Dynamic behavior of fully solvated beta2-adrenergic receptor, embedded in the membrane with bound agonist or antagonist. *Proc. Natl. Acad. Sci. U.S.A.* **103**, 4882–4887 (2006).
17. Shan, J., Khelashvili, G., Mondal, S., Mehler, E. L. & Weinstein, H. Ligand-dependent conformations and dynamics of the serotonin 5-HT(2A) receptor determine its activation and membrane-driven oligomerization properties. *PLoS Comput. Biol.* **8**, e1002473 (2012).
18. Kruse, A. C. *et al.* Activation and allosteric modulation of a muscarinic acetylcholine receptor. *Nature* **504**, 101–106 (2013).
19. Winn, M. D. *et al.* Overview of the CCP4 suite and current developments. *Acta Crystallogr.* D**67**, 235–242 (2011).
20. Gonzalez, A., Cordomí, A., Caltabiano, G. & Pardo, L. Impact of helix irregularities on sequence alignment and homology modeling of G protein-coupled receptors. *Chembiochem* **13**, 1393–1399 (2012).
21. Katritch, V., Cherezov, V. & Stevens, R. C. Diversity and modularity of G protein-coupled receptor structures. *Trends Pharmacol. Sci.* **33**, 17–27 (2012).
22. Phillips, J. C. *et al.* Scalable molecular dynamics with NAMD. *J. Comput. Chem.* **26**, 1781–1802 (2005).
23. Humphrey, W., Dalke, A. & Schulten, K. VMD - Visual Molecular Dynamics. *J. Molec. Graphics* **14**, 33–38 (1996).
24. Pettersen, E. F. *et al.* UCSF Chimera-a visualization system for exploratory research and analysis. *J. Comput. Chem.* **25**, 1605–1612 (2004).

Acknowledgments

Supported by the Ministry of Education, Culture, Sports, Science and Technology of Japan.

Author contributions

M.K. performed analysis, T.O. designed research, performed analysis, and wrote the manuscript.

Additional information

Supplementary information accompanies this paper at http://www.nature.com/scientificreports

Competing financial interests: The authors declare no competing financial interests.

How to cite this article: Kinoshita, M. & Okada, T. Structural conservation among the rhodopsin-like and other G protein-coupled receptors. *Sci. Rep.* **5**, 9176; DOI:10.1038/srep09176 (2015).

光の情報を受け取る分子メカニズムの解明

教授　岡本　治正
助教　本郷　育子

[目的]

光情報を受け取る主要組織は眼である。その複雑な多層構造の発生過程、また機能発現の分子メカニズムについてはいまだ未知な部分も多いが、近年眼について多くの発生、機能関連遺伝子が FGF シグナルの制御下にあることが明らかにされつつある。他方、当研究室ではこれまで FGF シグナルの下流にある神経系関連遺伝子を網羅的にスクリーニングする系をアフリカツメガエル初期嚢胚の未分化な外胚葉細胞を用いて確立してきた。これまでにこの外胚葉細胞を低濃度の FGF で処理して得られるトランスクリプトームに、眼を含む前脳で発現する遺伝子産物が相対的に多く存在することが明らかになっている。そこで当該研究では眼の発生、機能に関連することが期待される遺伝子に焦点を絞り、上記トランスクリプトームからのスクリーニングを行った。発生関連では、1) 転写因子型、あるいは 2) シグナル伝達関連型の、また機能関連では 3) GPCR 型の遺伝子を選抜し *in situ* hybridization により眼における発現の確認を目指した。

[結果と考察]

当該研究で解析した以下 6 種の遺伝子はいずれも、アフリカツメガエル初期胚における時間的・空間的発現パターンについて、これまで詳細な報告の乏しいものである。

1) 転写因子型

a) ***elf1* (*E74-like factor 1*)**: FGF/MAPK シグナル経路の下流で働く Ets 転写因子ファミリーのメンバー。ツメガエル初期胚での役割は不明。

神経管形成期（受精 20 時間後）に前脳領域を中心に発現が始まり、尾芽胚期（受精 32 時間後）に眼胞（眼のもとになる原基構造)、特にその周縁部に発現が確認された（**Fig.1a**)。

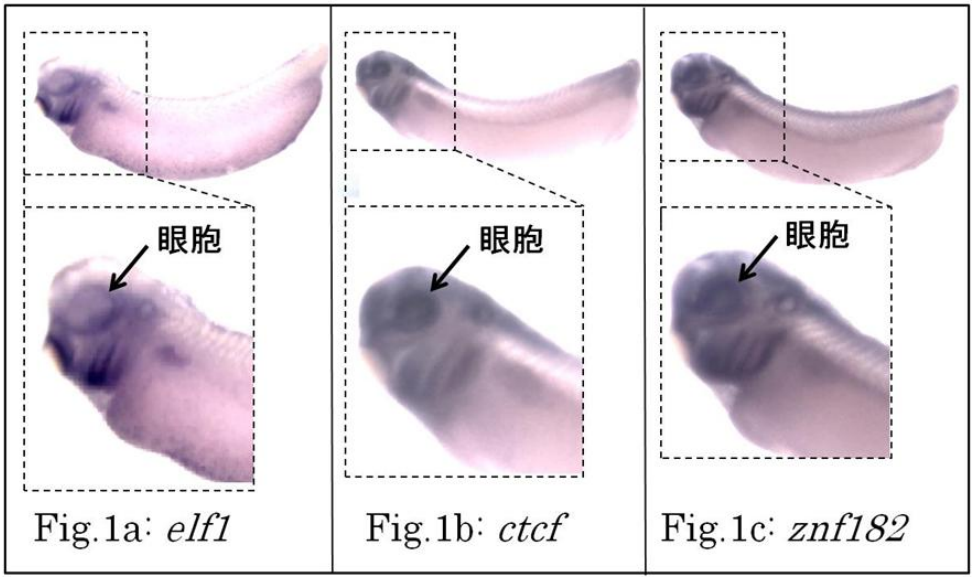

Fig.1a: *elf1*　Fig.1b: *ctcf*　Fig.1c: *znf182*

b) ***ctcf*** **(*CCCTC-binding factor*)**: Zinc-finger モチーフを DNA 結合モチーフとして持つ転写因子ファミリーのメンバー。ツメガエル初期胚での役割は不明。
神経板誘導期（受精 16 時間後）に前脳領域を中心に発現が始まり、尾芽胚期（受精 32 時間後）に眼胞での発現が確認された（**Fig.1b**）。

c) ***znf182*** **(*Zinc-finger protein 182*)**: Zinc-finger モチーフを DNA 結合モチーフとして持つ転写因子ファミリーのメンバー。ツメガエル初期胚での役割は不明。
神経板誘導期（受精 16 時間後）に前脳領域を中心に発現が始まり、尾芽胚期（受精 32 時間後）に眼胞での発現が確認された（**Fig.1c**）。

2) シグナル伝達関連型

a) ***birc2*** **(*baculoviral IAP repeat containing 2*)**: 免疫系細胞内のシグナル伝達分子とされているが、ツメガエル初期胚での役割は不明。
神経管形成期（受精 20 時間後）に前脳領域を中心に発現が始まり、尾芽胚期（受精 32 時間後）に眼胞での発現が確認された（**Fig.2a**）

b) ***frs2*** **(*FGF receptor substrate 2*)**: receptor docking protein ファミリーのメンバー。ツメガエル初期胚での役割は不明。
神経管形成期（受精 20 時間後）に前脳領域を中心に発現が始まり、尾芽胚期（受精 32 時間後）に眼胞での発現が確認された（**Fig.2b**）

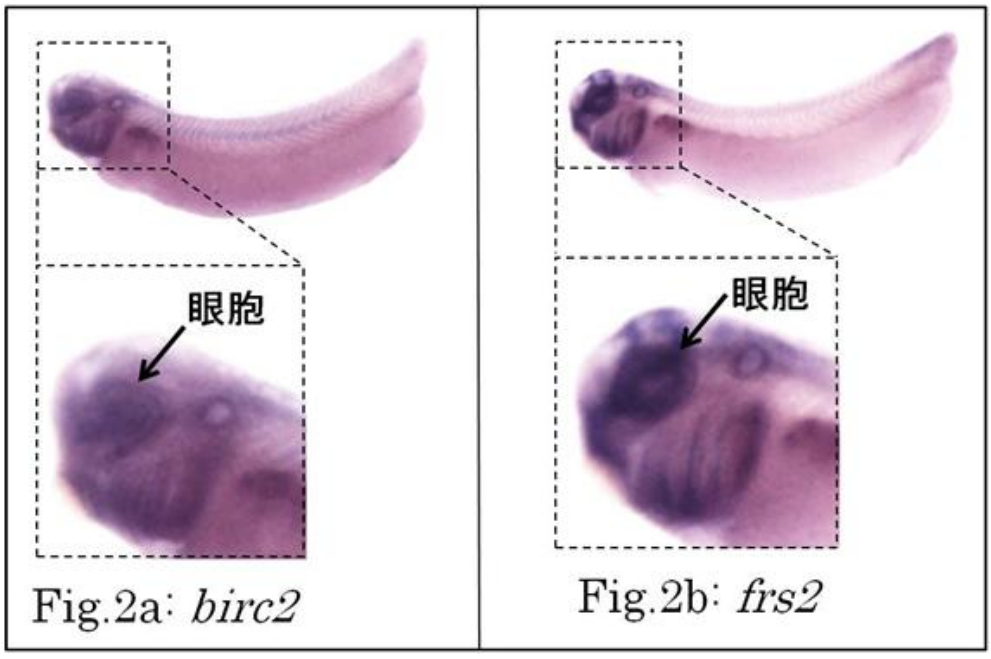

Fig.2a: *birc2*　　Fig.2b: *frs2*

3) GPCR 型

gpc160 **(*G protein-coupled receptor 160*)**: G タンパク質共役型受容体ファミリーのメンバー。ツメガエル初期胚での役割は不明。
神経管形成期（受精 20 時間後）に前脳領域を中心に発現が始まり、尾芽胚期（受精 32 時間後）に眼胞での発現が確認された（**Fig.3**）

当該研究で解析された六つの遺伝子は、いずれも尾芽胚の眼胞（眼の原基）での発現が確認された。また発現の開始は、神経板誘導期ないし神経管形成期にまでさかのぼることも示された。今後は各遺伝子について、mRNA 過剰発現による gain of function 解析、またアンチセンスRNAによる loss of function 解析を行い、各遺伝子の眼の発生、また機能発現における働きを明らかにする必要がある。

Fig.3: *gpc160*

青色光受容体（FKF1)欠損変異体を利用した花成時期制御機構の解明

教授　清末　知宏
助教　高瀬　智敬

[目的]

固着生活を営む植物にとって栄養成長から生殖成長への転換である花成を適切な時期に行うことは、繁殖戦略上極めて重要である。花成時期制御に関わる遺伝子の多くはモデル植物シロイヌナズナを用いて明らかにされてきているが、花成が光・温度・養分などの外的要因と齢・植物ホルモンなどの内的要因とによって影響を及ぼされる複雑な制御を受けているため、未だ同定されていない花成時期制御遺伝子の存在が予想されている。本研究では、シロイヌナズナの光周性花成経路ではたらく花成促進因子の一つである青色光受容体 FKF1 の機能欠損変異体（遅咲き変異体）を変異原処理することで早咲きとなる新規変異体を単離し、その原因遺伝子の同定と早咲きとなる仕組みとを解析することで、植物の栄養成長から生殖成長への転換機構の分子的な基盤を明らかにすることを目的とする。

[結果と考察]

fkf1 変異体をメタンスルホン酸エチル（EMS）処理し、M2 世代の植物を長日条件で育成して早咲き個体を得るというサプレッサースクリーニングによって 32 個体の早咲き変異体を得た。本研究ではこのうち２つの変異体 F0501、F4501 の解析を中心に行った。

[1] F0501 と F4501 の花成時期

F0501 と F4501 は早咲きの変異と *fkf1* 変異の両方を有している。そこで、早咲きの表現型が *fkf1* 変異に依存するか否かを明らかにするために、交配によって *fkf1* 変異を野生型に置き換えた植物体 F0501mono と F4501mono を作出し、Col、*fkf1*、F0501、F0501mono、F4501、F4501mono の花成時期を測定した。その結果、長日条件（16L8D、22℃）と短日条件（8L16D、22℃）のどちらでも、F0501、F0501mono、F4501、F4501mono は同時期に抽苔し、その時の葉の枚数も同程度であり、Col に比べて早咲きであった（図 1、2）。従って、F0501 と F4501 の早咲き変異は *fkf1* 変異と独立していることが明らかとなった。

[2] 早咲き原因遺伝子の同定

染色体歩行を行い、F0501 と F4501 の早咲きの原因遺伝子がそれぞれ第 2 染色体の下腕の 14.2 kbp と 260 kbp の領域内に座乗していることを明らかにした（図３）。次世代シーケンサーを用いて F0501 と F4501 の核全ゲノム DNA 塩基配列を調べた結果、染色体歩行で絞り込んだ領域内に F0501 では１つ、F4501 では４つの１塩基置換があることがわかった。更に、F0501 と F4501 は共にファミリーB に属する DNA ポリメラーゼの１つである DNA ポリメラーゼδを構成するアクセサリーサブユニットである POLD2 に変異が生じており、F0501 では POLD2 の翻訳開始点から数えて 1286 番目の塩基が G から A に、F4501 では POLD2 の翻訳開始点から数えて 323 番目の塩基が G から A に置換していることが明

らかとなった。このことから、F0501 と F4501 の早咲きは POLD2 の変異が原因であることが示唆された。以降、F0501 を *fkf1 pold2-1*、F0501mono を *pold2-1*、F4501 を *fkf1 pold2-2*、F4501mono を *pold2-2* と表記する。

[3] 早咲き変異体の POLD2 cDNA の塩基配列とコードされているアミノ酸配列

pold2-1 と *pold2-2* の葉から RNA を単離し、RT-PCR により POLD2 の cDNA を合成した後、その塩基配列を決定した。その結果、*pold2-1* では第 6 イントロンがスプライシングされず、通常より 71 bp、cDNA が長くなり、POLD2 タンパク質の 440 個のアミノ酸残基のうち 220 番目に終始コドンが生じて、219 番目で終わることがわかった。*pold2-2* では第 2 エクソンの途中でスプライシングが起こり、cDNA が通常より 93 bp 短くなることがわかった。しかし、リーディングフレームのずれは生じないため、32 から 62 番目までの 31 アミノ酸残基は欠損するものの、32 番目以降の領域の POLD2 は正常に作られることがわかった。このことから、*pold2-1* と *pold2-2* では一部が欠損した POLD2 タンパク質が作られることが示唆された。

[4] POLD2 T-DNA 挿入変異体（GK762B02、GK820B06）の表現型

POLD2 の変異が原因で *pold2-1* と *pold2-2* とが早咲きになるのであれば、T-DNA 挿入によって POLD2 の機能が失われた植物体も早咲きになると考えられる。そこで、POLD2 に T-DNA が挿入されている 2 つのライン GK762B02 と GK820B06 をストックセンター（ABRC）から入手し、その表現型を観察した。入手した種子から育てた植物体から DNA を抽出し、PCR によって遺伝子型を確認した結果、GK762B02 と GK820B06 のどちらのラインからも T-DNA 挿入ホモ接合体は得られなかった。T-DNA 挿入ヘテロ接合体の自家受粉によって得られた種子をまき、育った植物体の遺伝子型を調べたが、やはり T-DNA 挿入ホモ接合体は得られなかった。このことは、*POLD2* の T-DNA 挿入ホモ接合体が致死となることを示唆している。この点を明らかにするために、 T-DNA 挿入ヘテロ接合体の莢を剥き、中の種子を観察した。その結果、野生型ではほとんどが緑色の正常な種子であったのに対し、T-DNA 挿入ヘテロ接合体では緑色の正常な種子と茶色く小さい異常な種子とが観察された。カイ二乗検定を行ったところ、正常な種子：異常な種子の割合が 3：1 であることが確かめられたので、T-DNA 挿入ホモ接合体は種子形成の段階で致死になることが示された。

次に、T-DNA 挿入ヘテロ接合体の雄蕊と *pold2-1* の雌蕊を用いて交配を行った。交配によって得られた植物体のうち T-DNA を保有せず、*pold2-1* 変異をヘテロで有する植物体は野生型と同じ植物体の大きさを示したが、T-DNA 挿入と *pold2-1* 変異の両方をヘテロに有する植物体はとても小型になり、早咲きであった。

以上のことから、*pold2-1* と *pold2-2* では POLD2 タンパク質の一部が欠損しているものの、POLD2 の機能が部分的に残っているために致死とならずに早咲きとなったと考えられ、T-DNA 挿入と *pold2-1* 変異の両方をヘテロに持つ植物体では、部分的に機能が残っている POLD2 を 1 コピーしか有していないため、非常に小型で早咲きになったと考えられる。

[5] *fkf1 pold2-1* と *fkf1 pold2-2* との交配で得られた F_1 個体の花成時期

POLD2 が早咲きの原因遺伝子か否かを更に検証するために、*fkf1 pold2-1* の雄蕊と *fkf1*

pold2-2 の雌蕊を用いて交配を行った。得られた F_1 個体が自家受粉によるものではなく、交配によって得られたものであるか否かを調べるため、F_1 個体の *POLD2* の DNA 塩基配列を決定した。その結果、*POLD2* の翻訳開始点から数えて 1286 番目の塩基には *pold2-1* の置換した塩基（A）と正常な塩基（G）の 2 つが検出され、323 番目の塩基には *pold2-2* の置換した塩基（A）と正常な塩基（G）の 2 つが検出されたため、交配は成功していたことがわかった。長日条件で花成時期を測定したところ、F_1 個体は *fkf1* と比べて早咲きであった。F_1 個体の抽苔日と抽苔時の葉の枚数は、*fkf1 pold2-1* と *fkf1 pold2-2* のそれらと同程度であった。この遺伝的相補性は、*POLD2* が *pold2-1* と *pold2-2* の早咲きの原因遺伝子であることを支持する結果の 1 つである。

[6] FT の経時的発現解析

シロイヌナズナでは、光周性経路、自律的経路、春化経路、ジベレリン経路の 4 つの花成経路が存在し、前者の三つの経路の統合因子として花成ホルモン FT が知られている。そこで、*FT* の発現を経時的に調べたところ、Col の *FT* の発現量は ZT（Zeitgeber Time）4 と ZT16 にピークを持ち、ZT16 で最大となった。*fkf1* では Col と比べてどの時間帯でも *FT* の発現量は低くかった。*pold2-1* と *pold2-2* では、*FT* の発現量はどの時間帯でも Col より高いことがわかった。*fkf1 pold2-1* と *fkf1 pold2-2* では、*FT* の発現量はどの時間帯でも *fkf1* より高かった。更に、*fkf1 pold2-1* と *fkf1 pold2-2* では ZT8 など一部の時間帯で Col に比べて *FT* の発現量が増加するが、1 日を通しての発現量は *pold2-1* や *pold2-2* のようには大きく変わらなかった。これらのことから、*FT* の発現上昇と *FT* 以外の花成遺伝子の活性化によって *pold2-1* と *pold2-2* とが早咲きとなるのではないかと考えられた。

[7] DNA マイクロアレイ

野生型と *pold2* 変異体との間で発現が変化している遺伝子を網羅的に調べるため、DNA マイクロアレイ解析を行った。マイクロアレイに用いた RNA は、長日条件で 10 日間育てた Col、*pold2-1*、*fkf1*、*fkf1 pold2-2* の植物体全体から抽出し、サンプリングは ZT4 に行った。*pold2-1* での発現が Col と比べて 2 倍以上であり、かつ *fkf1 pold2-2* での発現が *fkf1* と比べて 2 倍以上だった遺伝子は 307 個あった（図 4）。それらを DAVID で機能分類した結果、17 個のクラスターに分類された。そのうち統計的に有意とされる Enrichment Score が 1.3 以上（Huang *et al.*, 2009）のクラスターは 4 個であり、クラスター2 には花成に関わる遺伝子群が含まれていた。その中でも reproductive developmental process に関わる遺伝子数が 22 個と最も多く、*APETALA1*（*AP1*）、*SEPALLATA3*（*SEP3*）、*FRUITFULL*（*FUL*）、*AGAMOUS-LIKE24*（*AGL24*）などが含まれていた。*AP1* や *SEP3*、*FUL* は *FT* の下流にあり、花の器官形成に関わる遺伝子である（Smaczniak *et al.*, 2012）。*AGL24* も *FT* の下流にあり、*AGL24* と *SOC1* は相互作用することで花成促進にはたらき、*AGL24* を過剰発現させたシロイヌナズナは早咲きになることが知られている（Liu *et al.*, 2008）。*AGL24* の発現は、*pold2-1* では Col 比べて 3.31 倍、*fkf1 pold2-2* では *fkf1* に比べて 6.82 倍に増加していたことから、*AGL24* が *pold2-1* と *pold2-2* の早咲きに関わる候補遺伝子の 1 つであると考えられる。

[まとめ]

本研究により、POLD2 がシロイヌナズナの新規花成抑制因子であることが示され、*FT* の発現上昇が *pold2* 変異体の早咲きの一因になりうること、*FT* 以外の遺伝子（*AGL24* が候補）も早咲きに関わっていることが示唆された。

ポリメラーゼδと同じファミリーB に属する DNA ポリメラーゼは、シロイヌナズナではδの他に、α、ε、ζがある（Garcia-Diaz et al. 2007）。DNA ポリメラーゼαの触媒サブユニットをコードする *INCURAVATA2*（*ICU2*）の変異体と DNA ポリメラーゼεの触媒サブユニットをコードする *EARLY IN SHORT DAYS 7*（*ESD7*）の変異体でも野生型に比べ早咲きになり、T-DNA が挿入されると種子形成の段階で致死になることが報告されている（Barrero et al., 2007, del Olmo et al., 2010）。ESD7 と ICU2 は *FT* の発現を抑制する LIKE HETEROCHROMATIN PROTEIN 1（LHP1）/ TERMINAL FLOWER2（TFL2）と相互作用することが知られている（del Olmo et al., 2010, Hyun et al., 2013）。LHP1/TFL2 は H3K9me2 もしくは H3K9me3 と結合し、花成制御因子遺伝子である *FT* や *FLC*、花芽器官形成遺伝子である *AGAMOUS* や *APETALA*3 などを含む多くの遺伝子の転写を抑制する（Turck et al., 2007）。今後、POLD2 による花成抑制機構の解析を進め、ICU2、ESD7 による花成抑制機構との相違点・一致点を明らかにすることで、DNA ポリメラーゼによる植物の栄養成長から生殖成長への転換機構の全貌に迫ることができると考えている。

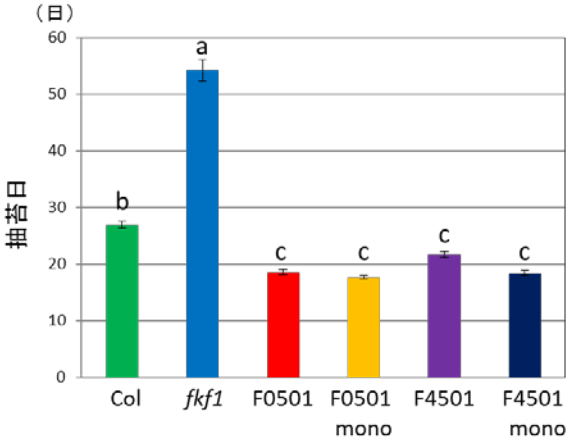

長日条件での花成時期（図１）

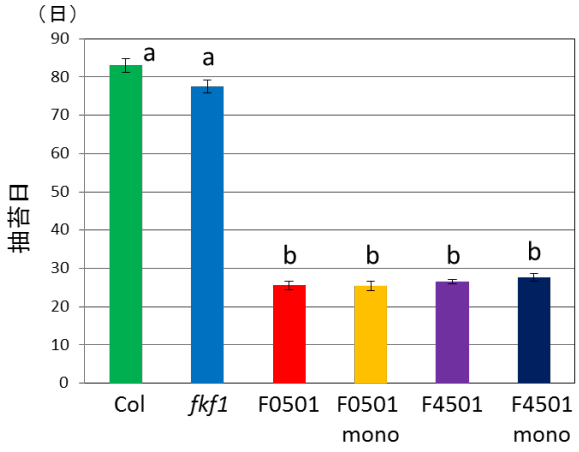

短日条件での花成時期（図２）

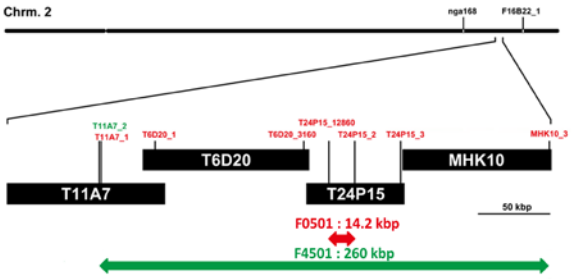

染色体歩行による早咲き原因遺伝子の同定（図３）

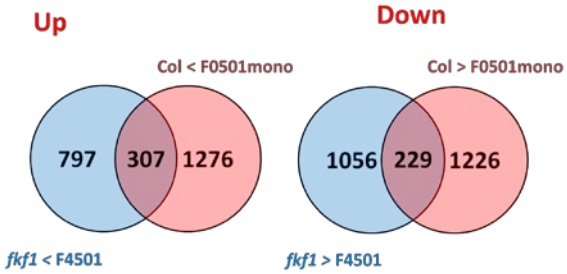

DNAマイクロアレイ（図４）

［原著論文］

1. Miyazaki, Y., Abe, H., Takase, T., Kobayashi, M., and Kiyosue, T. (2015) Overexpression of *LOV KELCH PROTEIN2* confers dehydration tolerance and is associated with enhanced expression of dehydration-inducible genes in *Arabidopsis thaliana.* Plant Cell Rep. *34*, 843-852.
2. Miyazaki, Y., Takase, T., and Kiyosue, T. (2015) ZEITLUPE positively regulates hypocotyl elongation at warm temperature under light in *Arabidopsis thaliana*. Plant Signal. Behav. *10*, e998540.
3. Saitoh, A., Takase, T., Kitaki, H., and Kiyosue, T. (2015) Gene expression profile of *Arabidopsis* plants that overexpress *ZEITLUPE/ LOV KELCH PROTEIN1*: up-regulation of auxin-inducible genes in hypocotyls. Plant Biotech. *32*, 257-261.
4. Saitoh, A., Takase, T., Kitaki, H., Miyazaki, Y., and Kiyosue, T. (2015) Gene expression profile of *zeitlupe/lov kelch protein1* T-DNA insertion mutants in *Arabidopsis thaliana*: downregulation of auxin-inducible genes in hypocotyls. Plant Signal. Behav. *10*, e1071752.
5. Takase, T., Miyazaki, T., Yasuhara, M., Mitsui, S., and Kiyosue, T. (2015) Pleiotropic phenotype of transgenic *Arabidopsis* plants that produce the LOV domain of LOV KELCH PROTEIN2 (LKP2). Plant Biotech. *32*, 273-280.
6. Miyazaki, Y., Jikumaru, Y., Takase, T., Saitoh, A., Sugitani, A., Kamiya, Y., and Kiyosue, T. (2016) Enhancement of hypocotyl elongation by LOV KELCH PROTEIN2 production is mediated by auxin and phytochrome-interacting factors in *Arabidopsis thaliana*. Plant Cell Rep. *35*, 455-467.

［著書］

1. 清末知宏 (2016) ZTL/LKP2/FKF1 光受容体「光と植物の事典」（分担著）朝倉書店。

［口頭発表、ポスター発表］

1. 矢作道枝、高瀬智敬、清末知宏：「シロイヌナズナ *fkf1* サプレッサースクリーニングによる花成時期変異体の単離と解析」、第 55 回日本植物生理学会年会、富山、2014 年 3 月 20 日。
2. 齋藤彩、宮崎裕士、木下久樹、木滝博之、高瀬智敬、清末知宏：「青色光受容体の過剰発現がシロイヌナズナの胚軸伸長に及ぼす影響」、第 37 回日本分子生物学会年会、横浜、2014 年 11 月 27 日。
3. 矢作道枝、高瀬智敬、清末知宏：「シロイヌナズナ *fkf1* サプレッサー変異体（*ef1*）の原因遺伝子の特定と特徴づけ」、第 37 回日本分子生物学会年会、横浜、2014 年 11 月 27 日。
4. 齋藤彩、宮崎裕士、高瀬智敬、清末知宏：「青色光受容体 ZTL がシロイヌナズナの胚軸伸長に及ぼす影響」、第 56 回日本植物生理学会年会、東京、2015 年 3 月 20 日。
5. 矢作道枝、高瀬智敬、清末知宏：「２つのシロイヌナズナ *fkf1* サプレッサー変異体について」、第 56 回日本植物生理学会年会、 東京、2015 年 3 月 20 日。

Plant Biotechnology 32, 273–280 (2015)
DOI: 10.5511/plantbiotechnology.15.0808b

Original Paper

Pleiotropic phenotype of transgenic *Arabidopsis* plants that produce the LOV domain of LOV KELCH PROTEIN2 (LKP2)

Tomoyuki Takase[1,2], Yuji Miyazaki[1,2], Masahiro Yasuhara[2], Shunya Mitsui[2], Tomohiro Kiyosue[1,2,*]

[1]Department of Life Science, Faculty of Science, Gakushuin University, Toshima-ku, Tokyo 171-8588, Japan; [2]Gene Research Center, Kagawa University, Kita-gun, Kagawa 761-0795, Japan
*E-mail: tomohiro.kiyosue@gakushuin.ac.jp Tel: +81-3-3986-0221 ext. 3602 Fax: +81-3-5992-1029

Received July 8, 2015; accepted August 8, 2015 (Edited by M. Sekine)

Abstract LOV KELCH PROTEIN2 (LKP2) is a blue-light receptor protein composed of three functional domains: a light, oxygen, or voltage (LOV) domain, an F-box motif (F), and Kelch repeats. LKP2 is postulated to be a component of an SCF complex and function in ubiquitination of proteins that control the circadian clock and photoperiodic flowering. Transgenic *Arabidopsis* plants that produce LOV, F, or a combination of LOV and F fused to green fluorescent protein (named GL, GF, and GLF, respectively) were produced using constructs containing the *Cauliflower mosaic virus 35S* promoter. Under continuous white light, the circadian rhythms of control and GF plants were similar, whereas those of GL and GLF plants were shorter. Under continuous red light, the hypocotyl lengths of control and GF seedlings were similar, whereas that of GL seedlings was longer. Late flowering and down-regulation of *CONSTANS* and *FLOWERING LOCUS T* were observed in GL and GLF plants compared to GF and control plants under long-day conditions. These results suggest that the previously reported pleiotropic phenotype of LKP2-overproducing plants, which show altered circadian rhythm, hypocotyl elongation, and photoperiodic flowering, is not only due to the promotion of ubiquitination and subsequent degradation of substrate proteins of the SCF^{LKP2} complex but may also be due to the functional disruption of regulatory proteins that interact with LKP2 LOV.

Key words: *Arabidopsis*, circadian rhythm, flowering time, hypocotyl elongation, LOV KELCH PROTEIN2 (LKP2).

Plants perceive light not only as the energy source for photosynthesis but also as an environmental stimulus that controls plant growth and development. Multiple photoreceptors including phytochromes, cryptochromes, and phototropins perceive environmental light signals in *Arabidopsis* (Kendrick and Kronenberg 1994; Nagatani 2010). In addition to these photoreceptors, members of the FLAVIN-BINDING KELCH REPEAT F-BOX1 (FKF1)/LOV KELCH PROTEIN2 (LKP2)/ZEITLUPE (ZTL) family are blue-light photoreceptors and are involved in regulation of the circadian clock, hypocotyl elongation, and flowering time (Jarillo et al. 2001; Kiyosue and Wada 2000; Miyazaki et al. 2011; Nelson et al. 2000; Schultz et al. 2001; Somers et al. 2000; Takase et al. 2011). *Arabidopsis* FKF1/LKP2/ZTL family proteins have three functional domains—the light, oxygen, or voltage (LOV) domain, F-box motif, and Kelch repeat—and function in ubiquitination of target proteins as components of the SKP1-Cullin-Rbx1-F-box protein (SCF) E3 ligase complex (Demarsy and Fankhauser 2009). The SCF^{ZTL} complex regulates the circadian clock by ubiquitin-dependent degradation of two circadian clock regulators, TIMING OF CAB EXPRESSION1 (TOC1) and PSEUDO-RESPONSE REGULATOR5 (PRR5) (Kiba et al. 2007; Kim et al. 2007). The SCF^{FKF1} complex regulates flowering time under long-day (LD) conditions by ubiquitin-dependent degradation of CYCLING DOF FACTOR (CDF) proteins, which are repressors of *CONSTANS* (*CO*) expression (Imaizumi et al. 2003, 2005; Sawa et al. 2007).

The LOV domains of FKF1/LKP2/ZTL family members are involved in blue-light perception by binding flavin mononucleotide, which functions as a chromophore, and by interaction with several regulatory proteins. The FKF1 LOV domain forms homodimers (Zikihara et al. 2006) and functions in the regulation of blue-light-dependent ubiquitination of CDF1 (Imaizumi et al. 2005). The degradation of ubiquitinated CDFs by

Abbreviations: ACT2, ACTIN2; 3AT, 3-amino-1*H*-1,2,4-triazole; CDF, CYCLING DOF FACTOR; CO, CONSTANS; FKF1, FLAVIN-BINDING KELCH REPEAT F-BOX1; FT, FLOWERING LOCUS T; GFP, green fluorescent protein; GI, GIGANTEA; LD, long-day; LKP2, LOV KELCH PROTEIN2; LOV, light, oxygen, or voltage; PRR5, PSEUDO-RESPONSE REGULATOR5; SCF, SKP1-Cullin-Rbx1-F-box protein; T-DNA, transfer DNA; TOC1, TIMING OF CAB EXPRESSION1; ZT, Zeitgeber time; ZTL, ZEITLUPE.

This article can be found at http://www.jspcmb.jp/
Published online September 26, 2015

26S proteasomes leads to the activation of *CO* expression, which triggers the expression of *FLOWERING LOCUS T* (*FT*), a florigen gene (Imaizumi et al. 2005). The interaction of FKF1 with GIGANTEA (GI) through FKF1 LOV is required for this activation of *CO* expression (Sawa et al. 2007). FKF1 also interacts with CO through its LOV domain in a blue-light-enhanced manner; this interaction stabilizes CO in the LD afternoon (Song et al. 2014).

ZTL interacts with TOC1 and PRR5 through its LOV domain (Kiba et al. 2007; Más et al. 2003). The ZTL LOV domain also interacts with GI. This interaction is blue-light dependent and stabilizes ZTL protein (Kim et al. 2007). Production of ZTL LOV in transgenic *Arabidopsis* causes period lengthening under red- or blue-light conditions, similar to *ztl* loss-of-function mutations, and a decreased level of endogenous ZTL protein compared to that in the control (Kim et al. 2013; Somers et al. 2000). These results suggest that production of ZTL LOV reduces endogenous ZTL protein stability by interfering with the interaction between endogenous ZTL and GI, and that the reduction in ZTL levels leads to period lengthening. Furthermore, production of ZTL LOV results in elongated hypocotyls under red- or blue-light conditions and in delayed flowering under LD conditions, similar to overproduction of ZTL (Kiyosue and Wada 2000; Somers et al. 2004). These phenotypes are postulated to be caused by the inhibition of GI functions in nuclei due to enhancement of cytosolic GI distribution caused by the ZTL LOV–GI complex (Kim et al. 2013).

LKP2 shows high amino acid sequence similarity to ZTL, and the tissue-specific expression pattern of *LKP2* overlaps largely with that of *ZTL* (Kiyosue and Wada 2000; Yasuhara et al. 2004). *LKP2*-overexpressing transgenic plants phenocopy *ZTL*-overexpressing transgenic plants: both exhibit circadian rhythm defects under continuous light or in the dark, elongated hypocotyls under continuous white or red light, and delayed flowering under LD conditions compared to control plants (Nelson et al. 2000; Schultz et al. 2001). Transfer DNA (T-DNA) insertion mutants of *lkp2* are phenotypically similar to wild-type plants (Baudry et al. 2010; Takase et al. 2011), while *ztl* T-DNA insertion mutants show slower circadian rhythms under continuous red or blue light or in the dark, shorter hypocotyls under continuous red light, and earlier flowering under non-inductive photoperiodic conditions compared to control plants (Somers et al. 2004; Takase et al. 2011). The phenotypic similarity of *lkp2* plants with wild-type plants is postulated to be due to the very low expression of *LKP2* relative to that of *ZTL* (Baudry et al. 2010; Michael et al. 2008; Mockler et al. 2007). Introduction of *LKP2* cDNA controlled by the *ZTL* promoter complemented the long-period phenotype of a *ztl* mutant (Baudry et al. 2010). These results suggest that LKP2 possesses ZTL-like functions with respect to regulation of the circadian clock, hypocotyl elongation and flowering time in *Arabidopsis*.

Similar to the overexpression of *LKP2*, production of green fluorescent protein (GFP)-LKP2 in *Arabidopsis* also causes arrhythmicity of the circadian clock, lengthens hypocotyls in continuous white light, and delays flowering under LD conditions (Miyazaki et al. 2011). In this study, we analyzed the effects of production of the GFP-tagged LOV and F-box of LKP2 on the circadian clock, hypocotyl elongation, and flowering time regulation in *Arabidopsis*, and discussed a LOV-mediated function of LKP2.

Materials and methods

Plant materials and growth conditions

All plant material was generated using the Columbia accession of *Arabidopsis thaliana*. Hypocotyl length was measured as described previously (Takase et al. 2004). *Arabidopsis* seeds were surface sterilized and placed on GM medium (Valvekens et al. 1988) supplemented with 0.8% agar. Plates were kept at 4°C for 7 days and then transferred to continuous white light at 22°C for 8 h to induce germination. After induction of germination, the plates were transferred to monochromatic light or to darkness. Blue, red, or far-red light was generated by light-emitting diodes at 450, 660, or 750 nm, respectively (NK Systems, Tokyo, Japan). Fluence rates were measured with a radiometer (model LI-189; LI-COR, Inc., Lincoln, NE, USA). Hypocotyl length was measured with Scion Image software (Scion Corp., Frederick, MD, USA). To determine the flowering time, *Arabidopsis* seeds were sown on vermiculite in pots. Pots were cold-treated at 4°C for 3 days and then transferred to LD conditions (16-h light/8-h dark) at 22°C. All statistical analyses were performed using IBM SPSS Statistics for Windows, version 20.0 (IBM Corp., Armonk, NY, USA).

Vector construction and production of transgenic plants

Three constructs encoding the LKP2 LOV domain, F-box motif, and a region that includes both the LOV domain and F-box motif were generated. PCR primers are listed in Table S1. The PCR template was cDNA from *A. thaliana* accession Columbia. Each PCR fragment was subcloned into pCR4-TOPO (Invitrogen, Carlsbad, CA, USA). After the entire inserts were sequenced, they were excised with *Bgl*II and *Bam*HI and subcloned into the *Bgl*II site of pCR4-TOPO containing the S65T GFP coding sequence (Niwa et al. 1999). The resulting vectors were then digested with *Bam*HI, and all fragments (encoding S65T GFP and LKP2 domains) were subcloned into the *Bam*HI site of the pBE2113 binary vector (Mitsuhara et al. 1996). The resulting vectors were introduced into *Agrobacterium tumefaciens* LBA4404 by triparental mating (Figurski and Helinski 1979) and subsequently into *Arabidopsis*

by the floral-dip method (Clough and Bent 1998). Homogygous T_4 progeny lines were obtained and used for the experiments.

Immunoblot analysis

Protein extraction from rosette leaves and immunoblot analysis were performed as described previously (Takase et al. 2011). Immunodetection was performed using an anti-GFP antibody (Nakalai Tesque Inc., Kyoto, Japan) and an ECL Advance system (GE Healthcare Bio-Sciences, Pittsburgh, PA, USA). Chemiluminescence signals were captured using a light-capture system (model AE-6792; ATTO, Tokyo, Japan).

Fluorescence microscopy

GFP signals from stomatal guard cells in leaf epidermal peels were observed using an IX71 microscope with a standard GFP filter (Olympus, Tokyo, Japan). The images were captured using MetaMorph imaging software (Universal Imaging Corporation, West Chester, PA, USA). A transgenic *Arabidopsis* plant expressing GFP with a nuclear localization signal of SV40 at the N-terminus (NLS-GFP) (Chiu et al. 1996; van der Krol and Chua 1991) was used as a control for nuclear localization.

Bioluminescence analysis

To measure circadian rhythms, plants from homozygous lines of *CAB2:LUC* and *CCR2:LUC* (seeds provided by Dr. S.A. Kay, University of California, San Diego) were crossed to plants from homozygous lines of GL, GF, GLF and GFP-producing plants. The resulting F_1 seedlings were grown on GM agar plates at 22°C under 12-h light/12-h dark cycles for 4 days and then transferred to continuous white light. An automated luminometer was used to monitor luciferase activity (Okamoto et al. 2005a), and circadian period length in the individual transgenic plants was estimated by visual identification of peaks and troughs followed by analysis with a rhythm-analysis program (Okamoto et al. 2005b).

Quantitative RT-PCR

Plates were incubated at 22°C under 16-h light/8-h dark for 10 days, and then seedlings were harvested every 4 h over a 24-h period. Total RNA from the whole seedlings was extracted and 500 ng was used to synthesize cDNA with a High-Capacity cDNA Reverse Transcription Kit (Applied Biosystems, Foster City, CA, USA) as previously described by Takase et al. (2011). Quantitative RT-PCR was performed using Power SYBR Green PCR Master Mix (Applied Biosystems) and an ABI PRISM 7000 sequence detection system (Applied Biosystems). The expression levels of *ACTIN2* (*ACT2*) were used to normalize expression of the target genes between samples. The primer pairs used in the PCR analysis are listed in Table S1.

Yeast two-hybrid assay

Yeast two-hybrid assays were performed as reported previously (Yasuhara et al. 2004). The Columbia version of full-length cDNA for *GI* was obtained by RT-PCR with ReverTra Dash (Toyobo, Osaka, Japan) and *GI* primers listed in Table S1,

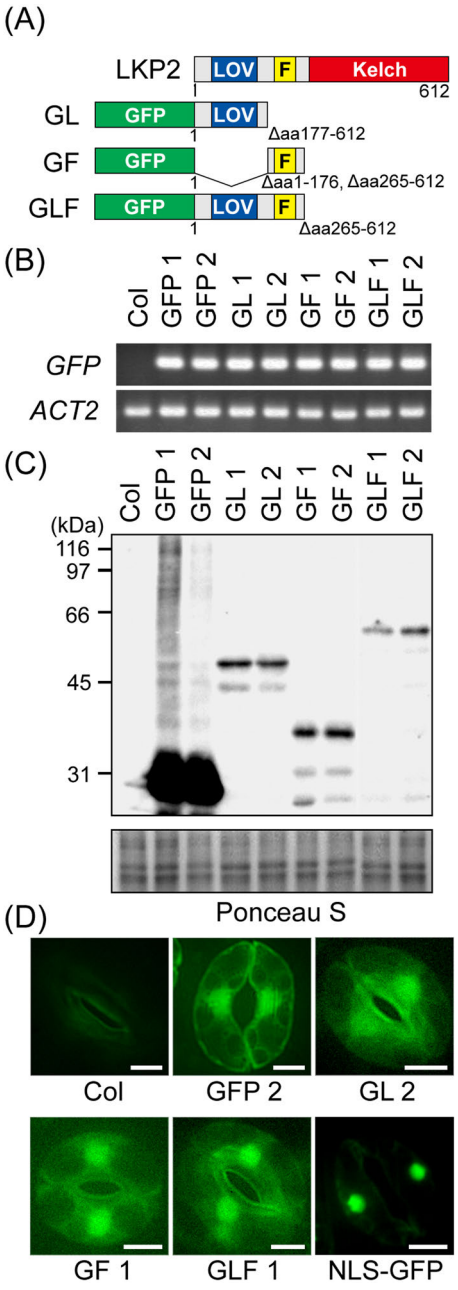

Figure 1. Structure of the GL, GF, and GLF proteins and their production in transgenic plants. (A) Schematic diagram of the GL (containing the LKP2 LOV domain), GF (containing the LKP2 F-box motif), and GLF (containing the LKP2 LOV and F-box) proteins used in this study. All of the domains were produced as C-terminal fusions to S65T green fluorescent protein (GFP). Amino acid positions correspond to those in the native LKP2 protein sequence. (B) Transgene expression in *Arabidopsis thaliana*. *GFP* primers were used to detect transgene expression by RT-PCR. Actin (*ACT2*) primers were used as the control. (C) Accumulation of GFP, GL, GF, and GLF proteins in transgenic plants. These proteins were detected by immunoblotting (top panel) using an anti-GFP antibody. Ponceau S staining of the membrane (bottom panel) was used as the loading control. (D) Subcellular localization of GFP, GL, GF, and GLF proteins in stomatal guard cells of the transgenic plants. Each panel shows a representative GFP image from the transgenic plants and non-transgenic Columbia (Col) plants. An NLS-GFP plant (containing a nuclear localization signal fused to GFP) was used as a control for the nuclear localization. Scale bars=20 μm.

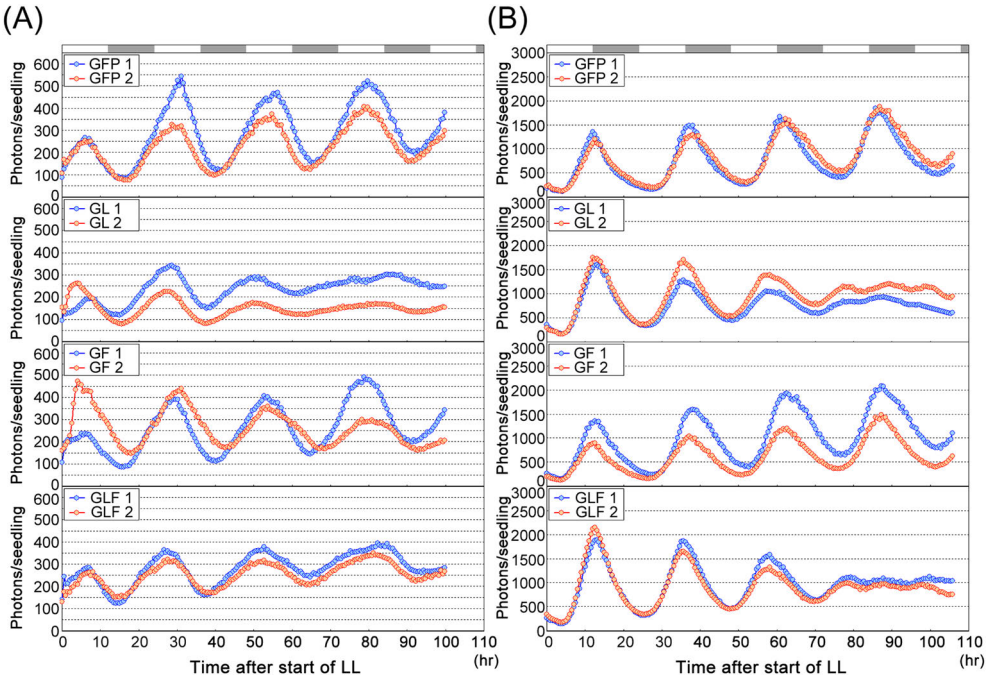

Figure 2. Circadian rhythms of GFP, GL, GF, and GLF transgenic plants under continuous white-light conditions. Graphs show luciferase activity driven by the *CAB2* (A) or *CCR2* (B) promoter under continuous white light (LL) conditions. All transgenic plants were entrained in 12-h light/12-h dark for 4 days and then transferred to LL conditions. White and gray boxes indicate subjective day and subjective night, respectively.

sequenced for verification, and then cloned into the *Bam*HI site of pGBKT7 (Clontech, Palo Alto, CA, USA), which encodes the GAL4 DNA-binding domain (bait). Fragments encoding the LOV, F-box, and Kelch repeat of LKP2 were cloned individually into pGADT7 (Clontech), which encodes the GAL4 activation domain (prey). AH109 yeast cells (Clontech) were used for the assay. Yeast transformants were grown on synthetic complete (SD) medium that lacked leucine (L) and tryptophan (W). Transformants were assayed on SD medium that lacked adenine (A), histidine (H), L, and W but was supplemented with 3-amino-1*H*-1,2,4-triazole (3AT) at 15 mM to repress the basal activity of the HIS3 reporter gene. Yeast containing two plasmids from Clontech, one plasmid encoding amino acids 72–390 of murine p53 protein (GenBank accession K01700) and the GAL4 DNA-binding domain and the other plasmid encoding the SV40 large T antigen (GenBank locus SV4CG) and the GAL4 activation domain, was used as the positive control. Interaction between GI and the LKP2 domain encoded by the prey vector was indicated by colony growth on the SD-AHLW + 3AT medium.

Results

Construction of GL, GF, and GLF transgenic plants

Three fusion genes that encode the LKP2 LOV domain (GL), the F-box motif (GF), or a combination of the LOV domain and F-box motif (GLF) attached to the C-terminus of GFP were constructed (Figure 1A) and expressed in transgenic *Arabidopsis* plants under the control of the *Cauliflower mosaic virus 35S* promoter. Two homozygous lines were examined for each construct (e.g., for GL, the lines are designated GL 1 and GL 2). The expression of each transgene was confirmed by RT-PCR (Figure 1B), and the accumulation of GL, GF, and GLF proteins of the predicted sizes was detected by immunoblotting (Figure 1C). The subcellular localization of these proteins in the transgenic plants was analyzed microscopically (Figure 1D). Fluorescence signals for GL, GF, and GLF were detected in the nucleus and cytoplasm of stomatal guard cells, while those for GFP fused with a nuclear localization signal at the N-terminus (NLS-GFP) were detected only in the nucleus.

Circadian rhythm phenotypes of transgenic plants

CAB2:LUC and *CCR2:LUC* reporters were used to measure the circadian rhythms of the transgenic plants (Figure 2 and Table S2). Both GL and GLF plants had shorter circadian rhythms (e.g., GL 1: 21.3 h, GL 2: 22.9 h; GLF 1: 23.3 h, and GLF 2: 22.7 h for *CAB2:LUC*) than control plants (e.g., GFP 1: 24.2 h and GFP 2: 24.3 h for *CAB2:LUC*) under continuous white light conditions, while the period lengths of GF plants were similar to those of control plants (e.g., GF 1: 24.5 h and GF 2: 24.5 h for *CAB2:LUC*). A decrease in amplitude over time was obvious in GL plants for both reporters and in GLF plants for the *CCR2:LUC* reporter.

Hypocotyl elongation of transgenic plants

Hypocotyl lengths were measured under continuous red (cR), blue (cB), and far-red (cFR) light and in darkness

(Figure 3 and Table S3). GFP fused to LKP2 (GLFK; Miyazaki et al. 2011) was used as a positive control. The GL, GF, and GLF seedlings and one GLFK seedling did not show significant differences in hypocotyl length in darkness compared to control (GFP) seedlings. Both GLFK lines showed longer hypocotyls under cR (0.052–1.005 W m^{-2}), cB (0.052–0.225 W m^{-2}) and cFR (0.103 W m^{-2}) than control seedlings; in particular, the GLFK hypocotyls were longer than those of any other lines under cR at 0.052 and 0.204 W m^{-2}. Both GL lines showed longer hypocotyls under cR at 0.099 and 1.005 W m^{-2} than did control seedlings. By contrast, the hypocotyl lengths of GF or GLF seedlings (at least one line per light treatment) were not significantly different from those of control seedlings under any continuous light condition examined.

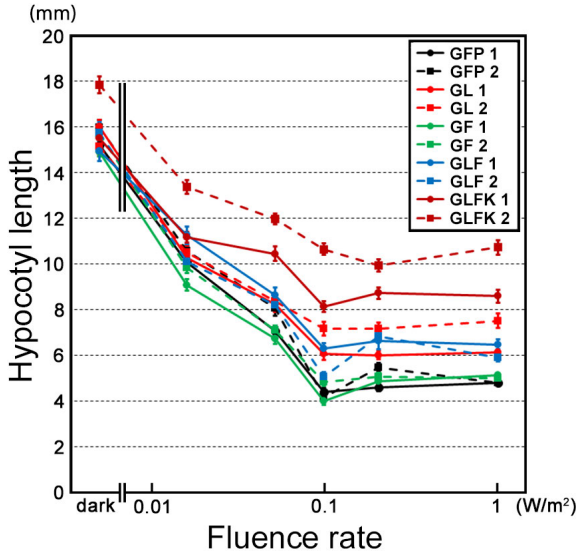

Figure 3. Hypocotyl length of GFP, GL, GF, GLF, and GFP-LKP2 (GLFK) transgenic plants under continuous red (cR) light. Seedlings were grown for 5 days under cR with various fluence rates (W m^{-2}). Each point represents the mean hypocotyl length of approximately 40 seedlings. Error bars represent standard error of the mean.

Flowering phenotypes of transgenic plants under LD conditions

Flowering times were measured under LD conditions (Figure 4). GF plants bolted after 1 month and did not show significant differences in bolting time compared with control plants. The rosette leaf numbers at bolting of GF and control plants were also not significantly different. By contrast, GL and GLF plants bolted later and had more rosette leaves at bolting than the control plants.

The expression levels of four flowering-time genes that function in the photoperiodic pathway (*FT*, *CO*, *CDF1*, and *GI*) were examined in the transgenic plants grown under LD conditions (Figure 5). Both *FT* and *CO* expression patterns in GF and control plants were similar, while those in GL and GLF plants were different. Specifically, the peak of *CO* expression at Zeitgeber time (ZT)12 and the peak of *FT* expression at ZT16, both of which were observed in GF and control plants, were absent in GL and GLF plants. By contrast, the gene expression patterns of *CDF1* and *GI* were similar among the four genotypes. These results suggest that the late flowering of GL and GLF plants is due to the down-regulation of *CO* at dusk and subsequent down-regulation of *FT*.

Interaction of LKP2 LOV with GI

Interaction of ZTL LOV with GI is postulated as a reason for the pleiotropic phenotype of ZTL LOV-producing plants (Kim et al. 2013). Though interaction between LKP2 and GI has been demonstrated *in vitro* and in yeast (Kim et al. 2007), the binding site in LKP2 has not previously been reported. Therefore, two-hybrid

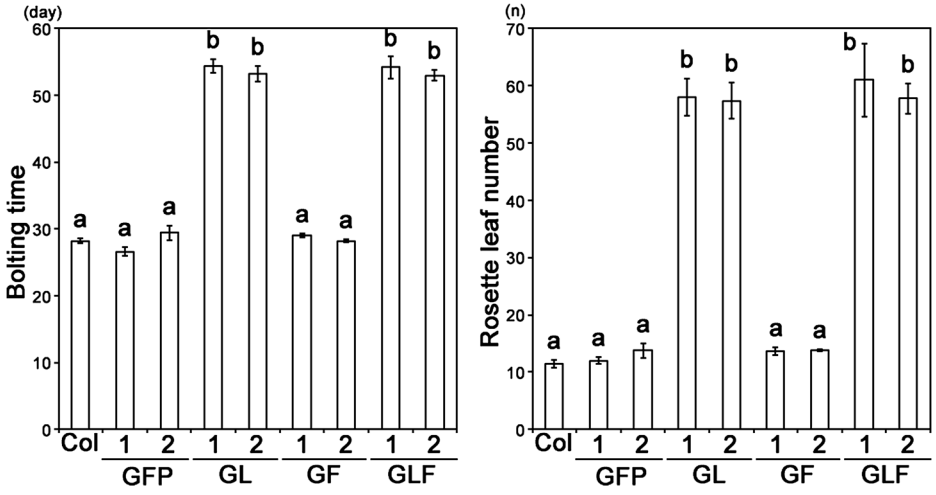

Figure 4. Flowering time of GFP, GL, GF, and GLF transgenic plants under LD conditions. Graphs show bolting time (left panel) and rosette leaf number at bolting (right panel) in transgenic plants under 16-h light/8-h dark conditions. Values are means and standard errors (n=5). Different letters indicate statistical differences detected by one-way analysis of variance (ANOVA) and Tukey–Kramer test (p<0.05).

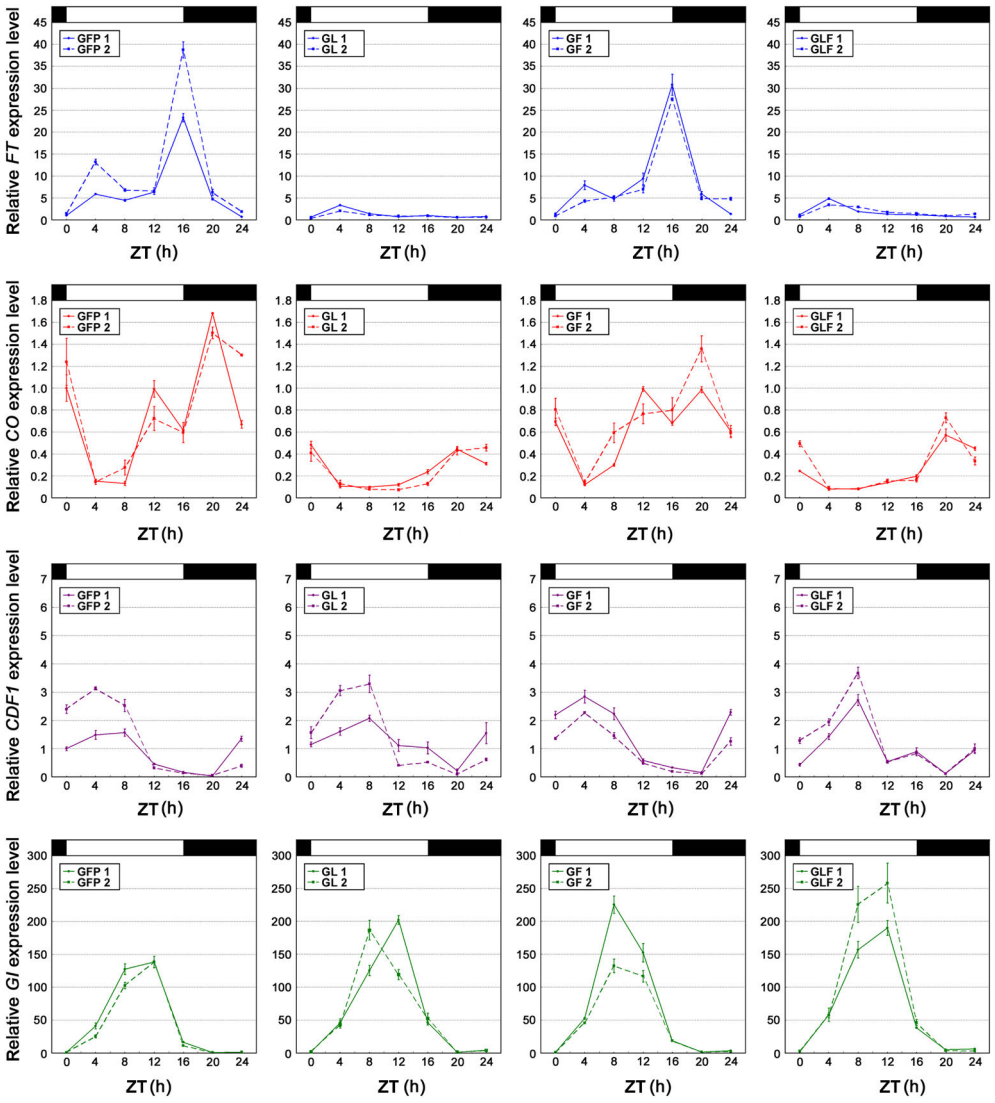

Figure 5. Expression of flowering-time genes in GFP, GL, GF, and GLF transgenic plants under 16-h light/8-h dark conditions. Relative expression levels of the flowering-time genes *FT*, *CO*, *CDF1* and *GI* were normalized to *ACT2* expression. Light and dark periods are indicated by white and black boxes, respectively. Values are means and standard error (n=3).

interaction of LKP2 LOV with GI was examined in yeast (Figure 6). GI interacted with LKP2 LOV, but not with the LKP2 F-box or Kelch repeat region.

Discussion

A fusion protein consisting of GFP and LKP2 was previously shown to be localized in the nucleus and cytoplasm of *Arabidopsis* cells (Takase et al. 2011). Consistently, the GL, GF, and GLF proteins were also localized in the nucleus and cytoplasm (Figure 1D), suggesting that the differences in phenotype among GL, GF, and GLF plants were not due to the subcellular localization of these three proteins.

Kim et al. (2013) showed that production of LOV or LOV-F of ZTL caused circadian rhythm lengthening under red- or blue light. This long-period phenotype is postulated to be due to instability of ZTL caused by interaction between ZTL LOV and GI. In contrast to ZTL LOV-producing plants, both GL and GLF plants showed short-period phenotypes under continuous white light compared to the control (Figure 2 and Table S2). The contrasting effects of ZTL LOV and LKP2 LOV in clock regulation could be due to differences between some of their interacting proteins and/or due differing affinities to interacting proteins, even though ZTL LOV and LKP2 LOV interact with overlapping sets of proteins. Both ZTL and LKP2 bind to GI (Kim et al. 2007), and both ZTL LOV and LKP2 LOV interact with two core clock proteins, TOC1 and PRR5 (Baudry et al. 2010; Yasuhara et al. 2004). The short-period phenotypes in both GL and GLF plants are phenocopies of *gi*, *toc1*, and *prr5* mutants (Mizoguchi et al. 2005; Nakamichi et al. 2005; Somers et al. 1998). Therefore, production of LKP2 LOV

might disrupt the function of clock components that can interact with LKP2 LOV and subsequently result in short circadian rhythm.

The elongated hypocotyl of GL plants is a phenocopy of that seen in LKP2 overproducers (Miyazaki et al. 2011). Hypocotyl elongation is enhanced under cR and cB by ZTL LOV production (Kim et al. 2013). As for LKP2 LOV, enhancement was obvious under cR but not under cB (Figure 3 and Table S3), though one GL line showed a significant difference from control seedlings under cB (0.102 W m^{-2} [GL 2] and 0.225 W m^{-2} [GL 1]; Table S3). Therefore, the effect of LKP2 LOV or ZTL LOV production on hypocotyl length seems to be fundamentally similar. The lower level of GLF protein accumulation in GLF seedlings compared with that of GL protein in GL seedlings might be a reason for the absence of obvious enhancement of hypocotyl elongation in GLF seedlings (Figure 1C).

Under LD conditions, production of LKP2 LOV delayed flowering and down-regulated *CO* and *FT* expression compared to control plants (Figures 4 and 5). Overproduction of LKP2 or production of LKP2 Kelch also delayed flowering and down-regulated *CO* and *FT* expression (Takase et al. 2011). LKP2 and LKP2 Kelch are postulated to capture FKF1 in the cytosol, which probably disturbs the ubiquitination and subsequent degradation of CDFs, which are repressors of *CO* and *FT* expression (Takase et al. 2011). Because LKP2 LOV cannot capture FKF1 in the cytosol (Takase et al. 2011), the mechanism for late flowering by LKP2 LOV production seems to be different from that by LKP2 Kelch. Thus, the late flowering caused by LKP2 overproduction is probably caused not only by capture of FKF1 in the cytosol but also by a LOV-mediated mechanism.

ZTL LOV facilitates cytosolic retention of GI protein by interacting with it (Kim et al. 2013). GI binds to FKF1 in the nucleus in a blue-light-dependent manner, and the GI–FKF1 complex induces expression of *CO* through ubiquitination of CDF1 (Sawa et al. 2007). Both LKP2 and LKP2 LOV can interact with GI (Figure 6; Kim et al. 2007). Given the effects of ZTL LOV production on cytosolic retention of GI (Kim et al. 2013), it is possible that the interaction between LKP2 LOV and GI enhances cytosolic GI distribution, which interferes with the formation of the GI–FKF1 complex in the nucleus and results in delayed flowering under LD conditions. This hypothesis is consistent with down-regulation of *CO* expression in both GL and GLF plants (Figure 4). GI and FKF1/LKP2/ZTL family proteins are postulated to form interrelated complexes that regulate CO stability for photoperiodic flowering (Song et al. 2014). Instability of CO could be another reason for late flowering of GL and GLF plants, in addition to the down-regulation of *CO*.

In this paper, we have shown that production of LKP2 LOV in transgenic *Arabidopsis* results in short circadian rhythm, elongated hypocotyl, and late flowering. This result provides additional evidence for the LOV-mediated functions of FKF1/LKP2/ZTL family proteins in plant growth and development.

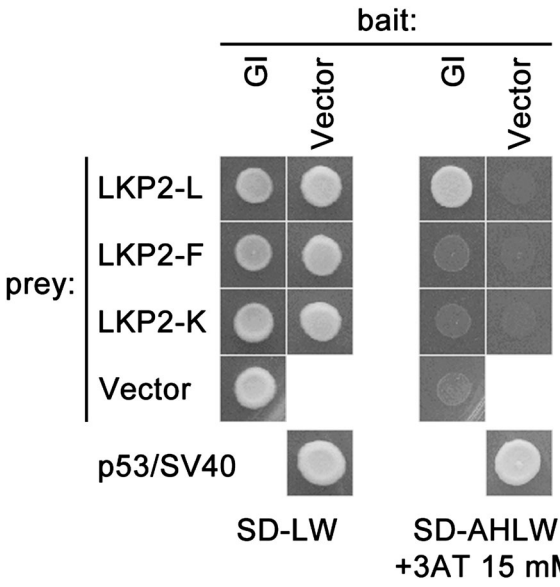

Figure 6. Yeast two-hybrid interactions between GI and three LKP2 fragments: LOV (LKP2-L), F-box (LKP2-F), and Kelch repeat (LKP2-K). Each panel in the "GI" columns shows yeast AH109 cells containing a GAL4 DNA-binding domain fusion of GI and either a GAL4 activation domain fusion of the indicated LKP2 fragment or the empty GAL4 activation domain expression vector, pGADT7 ("Vector"). The bait vector was a GAL4 DNA-binding domain expression vector, pGBKT7. Colonies were grown on SD agar medium lacking leucine and tryptophan (SD-LW; left) or lacking adenine, histidine, leucine, and tryptophan (SD-AHLW; right). The positive control (p53/SV40) contained one plasmid encoding amino acids 72–390 of murine p53 protein and the GAL4 DNA-binding domain and another plasmid encoding the SV40 large T antigen and the GAL4 activation domain.

Acknowledgements

This work was partially supported by a Grant-in-Aid for Scientific Research from the Ministry of Education, Culture, Sports, Science and Technology of Japan. We thank Dr. S.A. Kay (University of California, San Diego) for providing *CAB2:LUC and CCR2:LUC* seeds. We send our special thanks to the previous members of our former laboratory at Kagawa University.

References

Baudry A, Ito S, Song YH, Strait AA, Kiba T, Lu S, Henriques R, Pruneda-Paz JL, Chua N-H, Tobin EM, et al. (2010) F-box proteins FKF1 and LKP2 act in concert with ZEITLUPE to control *Arabidopsis* clock progression. *Plant Cell* 22: 606–622

Chiu W, Niwa Y, Zeng W, Hirano T, Kobayashi H, Sheen J (1996) Engineered GFP as a vital reporter in plants. *Curr Biol* 6: 325–330

Clough SJ, Bent AF (1998) Floral dip: A simplified method for *Agrobacterium*-mediated transformation of *Arabidopsis thaliana*. *Plant J* 16: 735–743

Demarsy E, Fankhauser C (2009) Higher Plants use LOV to

perceive blue light. *Curr Opin Plant Biol* 12: 69–74
Figurski DH, Helinski DR (1979) Replication of an origin-containing derivative of plasmid RK2 dependent on a plasmid function produced in *trans*. *Proc Natl Acad Sci USA* 76: 1648–1652
Imaizumi T, Schultz TF, Harmon FG, Ho LA, Kay SA (2005) FKF1 F-box protein mediates cyclic degradation of a repressor of CONSTANS in *Arabidopsis*. *Science* 309: 293–297
Imaizumi T, Tran HG, Swartz TE, Briggs WR, Kay SA (2003) FKF1 is essential for photoperiodic-specific light signalling in *Arabidopsis*. *Nature* 426: 302–306
Jarillo JA, Capel J, Tang RH, Yang HQ, Alonso JM, Ecker JR, Cashmore AR (2001) An *Arabidopsis* circadian clock component interacts with both CRY1 and phyB. *Nature* 410: 487–490
Kendrick RE, Kronenberg GHM (1994) *Photomorphogenesis in Plants*. Kluwer Academic Publishers, Dordrecht-Boston-London
Kiba T, Henriques R, Sakakibara H, Chua NH (2007) Targeted degradation of PSEUDO-RESPONSE REGULATOR5 by SCF^{ZTL} complex regulates clock function and photomorphogenesis in *Arabidopsis thaliana*. *Plant Cell* 19: 2516–2530
Kim WY, Fujiwara S, Suh SS, Kim J, Kim Y, Han L, David K, Putterill J, Nam HG, Somers DE (2007) ZEITLUPE is a circadian photoreceptor stabilized by GIGANTEA in blue light. *Nature* 449: 356–360
Kim J, Geng R, Gallenstein RE, Somers DE (2013) The F-box protein ZEITLUPE controls stability and nucleocytoplasmic partitioning of GIGANTEA. *Development* 140: 4060–4069
Kiyosue T, Wada M (2000) LKP1 (LOV Kelch protein 1): A factor involved in the regulation of flowering time in *Arabidopsis*. *Plant J* 23: 807–815
Más P, Kim WY, Somers DE, Kay SA (2003) Targeted degradation of TOC1 by ZTL modulates circadian function in *Arabidopsis thaliana*. *Nature* 426: 567–570
Michael TP, Breton G, Hazen SP, Priest H, Mockler TC, Kay SA, Chory J (2008) A morning-specific phytohormone gene expression program underlying rhythmic plant growth. *PLoS Biol* 6: e225
Mitsuhara I, Ugaki M, Hirochika H, Ohshima M, Murakami T, Gotoh T, Katayose Y, Nakamura S, Honkura R, Nishimiya S, et al. (1996) Efficient promoter cassettes for enhanced expression of foreign genes in dicotyledonous and monocotyledonous plants. *Plant Cell Physiol* 37: 49–59
Miyazaki Y, Yoshizumi T, Takase T, Matsui M, Kiyosue T (2011) Overexpression of *LOV KELCH PROTEIN2* enhances cell elongation and increases cell number and ploidy in the hypocotyl of *Arabidopsis thaliana*. *Plant Biotechnol* 28: 267–272
Mizoguchi T, Wright L, Fujiwara S, Cremer F, Lee K, Onouchi H, Mouradov A, Fowler S, Kamada H, Putterill J, et al. (2005) Distinct roles of GIGANTEA in promoting flowering and regulating circadian rhythms in *Arabidopsis*. *Plant Cell* 17: 2255–2270
Mockler TC, Michael TP, Priest HD, Shen R, Sullivan CM, Givan SA, McEntee C, Kay SA, Chory J (2007) The DIURNAL project: DIURNAL and circadian expression profiling, model-based pattern matching, and promoter analysis. *Cold Spring Harb Symp Quant Biol* 72: 353–363
Nagatani A (2010) Phytochrome: structural basis for its functions. *Curr Opin Plant Biol* 13: 565–570
Nakamichi N, Kita M, Ito S, Yamashino T, Mizuno T (2005) PSEUDO-RESPONSE REGULATORS, PRR9, PRR7 and PRR5, together play essential roles close to the circadian clock of *Arabidopsis thaliana*. *Plant Cell Physiol* 46: 686–698
Nelson DC, Lasswell J, Rogg LE, Cohen MA, Bartel B (2000) *FKF1*, a clock-controlled gene that regulates the transition to flowering in *Arabidopsis*. *Cell* 101: 331–340
Niwa Y, Hirano T, Yoshimoto K, Shimizu M, Kobayashi H (1999) Non-invasive quantitative detection and applications of non-toxic, S65T-type green fluorescent protein in living plants. *Plant J* 18: 455–463
Okamoto K, Onai K, Ezaki N, Ofuchi T, Ishiura M (2005a) An automated apparatus for the real-time monitoring of bioluminescence in plants. *Anal Biochem* 340: 187–192
Okamoto K, Onai K, Ishiura M (2005b) RAP, an integrated program for monitoring bioluminescence and analyzing circadian rhythms in real time. *Anal Biochem* 340: 193–200
Sawa M, Nusinow DA, Kay SA, Imaizumi T (2007) FKF1 and GIGANTEA complex formation is required for day-length measurement in *Arabidopsis*. *Science* 318: 261–265
Schultz TF, Kiyosue T, Yanovsky M, Wada M, Kay SA (2001) A role for LKP2 in the circadian clock of *Arabidopsis*. *Plant Cell* 13: 2659–2670
Somers DE, Kim WY, Geng R (2004) The F-box protein ZEITLUPE confers dosage-dependent control on the circadian clock, photomorphogenesis, and flowering time. *Plant Cell* 16: 769–782
Somers DE, Schultz TF, Milnamow M, Kay SA (2000) *ZEITLUPE* encodes a novel clock-associated PAS protein from *Arabidopsis*. *Cell* 101: 319–329
Somers DE, Webb AA, Pearson M, Kay SA (1998) The short-period mutant, *toc1-1*, alters circadian clock regulation of multiple outputs throughout development in *Arabidopsis thaliana*. *Development* 125: 485–494
Song YH, Estrada DA, Johnson RS, Kim SK, Lee SY, MacCoss MJ, Imaizumi T (2014) Distinct roles of FKF1, GIGANTEA, and ZEITLUPE proteins in the regulation of CONSTANS stability in *Arabidopsis* photoperiodic flowering. *Proc Natl Acad Sci USA* 111: 17672–17677
Takase T, Nakazawa M, Ishikawa A, Kawashima M, Ichikawa T, Takahashi N, Shimada H, Manabe K, Matui M (2004) *ydk1-D*, an auxin-responsive *GH3* mutant that is involved in hypocotyl and root elongation. *Plant J* 37: 471–483
Takase T, Nishiyama Y, Tanihibashi H, Ogura Y, Miyazaki Y, Yamada Y, Kiyosue T (2011) *LOV KELCH PROTEIN2* and *ZEITLUPE* repress *Arabidopsis* photoperiodic flowering under non-inductive conditions, dependent on *FLAVIN-BINDING KELCH REPEAT F-BOX1*. *Plant J* 67: 608–621
Valvekens D, Van Montagu M, Van Lijsebettens M (1988) *Agrobacterium tumefaciens*-mediated transformation of *Arabidopsis thaliana* root explants by using kanamycin selection. *Proc Natl Acad Sci USA* 85: 5536–5540
van der Krol AR, Chua NH (1991) The basic domain of plant B-ZIP proteins facilitates import of a reporter protein into plant nuclei. *Plant Cell* 3: 667–675
Yasuhara M, Mitsui S, Hirano H, Takanabe R, Tokioka Y, Ihara N, Komatsu A, Seki M, Shinozaki K, Kiyosue T (2004) Identification of ASK and clock-associated proteins as molecular partners of LKP2 (LOV Kelch protein2) in *Arabidopsis*. *J Exp Bot* 55: 2015–2027
Zikihara K, Iwata T, Matsuoka D, Kandori H, Todo T, Tokutomi S (2006) Photoreaction cycle of the light, oxygen, and voltage domain in FKF1 determined by low-temperature absorption spectroscopy. *Biochemistry* 45: 10828–10837

Plant Cell Rep
DOI 10.1007/s00299-015-1896-4

ORIGINAL ARTICLE

Enhancement of hypocotyl elongation by LOV KELCH PROTEIN2 production is mediated by auxin and phytochrome-interacting factors in *Arabidopsis thaliana*

Yuji Miyazaki[1] · Yusuke Jikumaru[2] · Tomoyuki Takase[1] · Aya Saitoh[1] · Asuka Sugitani[1] · Yuji Kamiya[2] · Tomohiro Kiyosue[1]

Received: 14 August 2015 / Revised: 12 October 2015 / Accepted: 3 November 2015

Abstract

Key message **Auxin and two phytochrome-interacting factors, PHYTOCHROME-INTERACTING FACTOR4 (PIF4) and PIF5, play crucial roles in the enhancement of hypocotyl elongation in transgenic *Arabidopsis thaliana* plants that overproduce LOV KELCH PROTEIN2 (LKP2).**

Abstract LOV KELCH PROTEIN2 (LKP2) is a positive regulator of hypocotyl elongation under white light in *Arabidopsis thaliana*. In this study, using microarray analysis, we compared the gene expression profiles of hypocotyls of wild-type *Arabidopsis* (Columbia accession), a transgenic line that produces green fluorescent protein (GFP), and two lines that produce GFP-tagged LKP2 (GFP-LKP2). We found that, in GFP-LKP2 hypocotyls, 775 genes were up-regulated, including 36 auxin-responsive genes, such as 27 *SMALL AUXIN UP RNA* (*SAUR*) and 6 *AUXIN/INDOLE-3-ACETIC ACID* (*AUX/IAA*) genes, and 21 genes involved in responses to red or far-red light, including *PHYTOCHROME-INTERACTING FACTOR4* (*PIF4*) and *PIF5*; and 725 genes were down-regulated, including 15 flavonoid biosynthesis genes. Hypocotyls of GFP-LKP2 seedlings, but not cotyledons or roots, contained a higher level of indole-3-acetic acid (IAA) than those of control seedlings. Auxin inhibitors reduced the enhancement of hypocotyl elongation in GFP-LKP2 seedlings by inhibiting the increase in cortical cell number and elongation of the epidermal and cortical cells. The enhancement of hypocotyl elongation was completely suppressed in progeny of the crosses between GFP-LKP2 lines and dominant gain-of-function auxin-resistant mutants (*axr2-1* and *axr3-1*) or loss-of-function mutants *pif4*, *pif5*, and *pif4 pif5*. Our results suggest that the enhancement of hypocotyl elongation in GFP-LKP2 seedlings is due to the elevated level of IAA and to the up-regulated expression of *PIF4* and *PIF5* in hypocotyls.

Keywords Hypocotyl elongation · IAA · LKP2 · Microarray · PIF · SAUR

Introduction

In plants, light regulates many aspects of development and physiological processes such as germination, de-etiolation, leaf and stem growth, flowering, entrainment of circadian rhythms, stomatal opening, chloroplast movement, and anthocyanin synthesis (Jiao et al. 2007; Kendrick and Kronenberg 1994; Mancinelli 1990; Millar 2004). Hypocotyl elongation is used as a model system to elucidate how light affects organ growth via cell expansion and division (Boron and Vissenberg 2014). In seedlings, an absence of light induces hypocotyl elongation, whereas blue, red, or far-red light inhibits it (Lau and Deng 2010). Numerous genes and proteins, including photoreceptors, induce or inhibit hypocotyl growth (Nozue and Maloof 2006).

Communicated by P. P. Kumar.

Electronic supplementary material The online version of this article (doi:10.1007/s00299-015-1896-4) contains supplementary material, which is available to authorized users.

✉ Tomohiro Kiyosue
tomohiro.kiyosue@gakushuin.ac.jp

[1] Department of Life Science, Faculty of Science, Gakushuin University, 1-5-1 Mejiro, Toshima-Ku, Tokyo 171-8588, Japan

[2] Growth Regulation Research Group, RIKEN Plant Science Center, 1-7-22 Suehiro-cho, Tsurumi, Yokohama, Kanagawa 230-0045, Japan

Published online: 25 November 2015

The direct interaction of the red/far-red light receptors, phytochromes, with transcription factors (TFs) in the nucleus is an important step in phytochrome-dependent regulation of hypocotyl elongation (Bauer et al. 2004; Nozue and Maloof 2006). Red light activates phytochrome B (phyB) and induces its translocation from the cytoplasm to the nucleus, where it regulates gene transcription via interaction with several TFs, including phytochrome-interacting factors (PIFs) and PIF-like proteins (PILs) (Bae and Choi 2008; Castillon et al. 2007). Light-activated phyB induces proteasome-mediated degradation of two homologous basic helix–loop–helix TFs, PHYTOCHROME-INTERACTING FACTOR4 (PIF4) and PIF5, which redundantly promote hypocotyl elongation; the degradation of these proteins results in the short hypocotyl under red or white light (Duek and Fankhauser 2005; Nozue and Maloof 2006; Vandenbussche et al. 2005). Phytochromes also regulate hypocotyl elongation by controlling the proteasomal degradation of photomorphogenesis-promoting TFs; this degradation is mediated by the CONSTITUTIVE PHOTOMORPHOGENIC1 (COP1)-SUPPRESSOR OF PHYA-105 (SPA) E3 ubiquitin ligase complex, and also by controlling the alternative splicing of transcripts for certain regulatory genes (Lau and Deng 2012; Shikata et al. 2014).

The FKF1/LKP2/ZTL protein family is a group of blue light receptors, which consists of FLAVIN-BINDING KELCH REPEAT F-BOX 1 (FKF1), LOV KELCH PROTEIN1 (LKP1)/ZEITLUPE (ZTL), and LOV KELCH PROTEIN2 (LKP2). Proteins of this family are highly similar to each other and possess three functional domains, i.e., the light, oxygen, or voltage (LOV) domain, F-box motif, and Kelch repeat region (Zoltowski and Imaizumi 2014). They function in polyubiquitination of target proteins as the components of the SKP1-Cullin-Rbx1-F-box protein (SCF) E3 ligase complex, and their E3 ligase activities are regulated by blue light perceived by the LOV domains (Demarsy and Fankhauser 2009). The FKF1/LKP2/ZTL family proteins regulate circadian expression of genes and photoperiodic flowering, as well as hypocotyl elongation under light (Baudry et al. 2010; Zoltowski and Imaizumi 2014). Hypocotyls of *fkf1* mutants are short under continuous blue or red light (Nelson et al. 2000). Both *LKP2*-overexpressing seedlings and *ZTL*-overexpressing seedlings produce long hypocotyls under continuous blue, red, or white light (Kiyosue and Wada 2000; Nelson et al. 2000; Schultz et al. 2001). Hypocotyls of *ztl* mutants are short under continuous red light but are indistinguishable from those of wild-type plants under blue light (Somers et al. 2000). These results suggest that proteins of this family do not function as blue light receptors in the context of the red light-induced inhibition of hypocotyl growth. ZTL interacts with phyB apoprotein; therefore, FKF1/LKP2/ZTL may affect phytochrome-mediated signaling (Jarillo et al. 2001).

The circadian clock is another factor that affects hypocotyl growth in *Arabidopsis* immediately upon germination (Dowson-Day and Millar 1999). Under constant dim light, hypocotyl elongation is fastest at subjective dusk, and stops close to subjective dawn (Dowson-Day and Millar 1999). Studies using clock mutants revealed the importance of the circadian clock in hypocotyl growth; there is a strong correlation between circadian and hypocotyl mutant phenotypes. Arrhythmic mutants tend to lack the daily arrest in hypocotyl growth in continuous light, whereas shorter- or longer-period mutants tend to have alterations in either the duration or the amplitude of the growth phase (Nozue and Maloof 2006). Since FKF1/LKP2/ZTL family proteins are involved in circadian clock regulation, they may contribute to hypocotyl growth regulation via their circadian clock function.

To clarify the molecular mechanisms of the regulation of hypocotyl elongation in *Arabidopsis* by FKF1/LKP2/ZTL family proteins, we analyzed hypocotyl elongation caused by LKP2 production. Production of green fluorescent protein (GFP)-tagged LKP2 (GFP-LKP2) caused hypocotyl elongation; hypocotyls had elongated epidermal and cortical cells and an increased number of cortical cells in comparison with controls (Miyazaki et al. 2011). The cells in GFP-LKP2 hypocotyls had larger nuclei with increased DNA content (Miyazaki et al. 2011). Production of the LOV domain of LKP2, which interacts with GIGANTEA (GI), enhances hypocotyl elongation under continuous red light and delays flowering under long-day conditions, suggesting the involvement of GI in LKP2-mediated hypocotyl elongation (Takase et al. 2015). However, the molecular mechanisms of the enhancement of hypocotyl elongation caused by LKP2 are largely unknown.

In this study, we compared the gene expression profiles of hypocotyls of wild-type *Arabidopsis* Columbia accession (Col), a transgenic line that produces GFP, and two GFP-LKP2 lines (Miyazaki et al. 2011). Using microarray analysis, we found that 775 genes were up-regulated, including 36 auxin-responsive genes, such as 27 *SMALL AUXIN UP RNA* (*SAUR*) and 6 *AUXIN/INDOLE-3-ACETIC ACID* (*AUX/IAA*) genes, and 21 genes involved in responses to red or far-red light, including *PIF4* and *PIF5*; and 725 genes were down-regulated, including 15 flavonoid biosynthesis genes. Next, we measured indole-3-acetic acid (IAA) levels in these seedlings and examined the effects of three auxin inhibitors—the polar auxin transport inhibitor *N*-1-naphthylphthalamic acid (NPA), the putative anti-auxin *p*-chlorophenoxyisobutyric acid (PCIB), and the auxin antagonist α-(phenylethyl-2-one)-indole-3-acetic acid (PEO-IAA)—on hypocotyl elongation. Finally, we examined the effects of two dominant gain-of-function auxin-resistant mutations (*axr2-1* and *axr3-1*) and

three loss-of-function mutations (*pif4*, *pif5*, and *pif4 pif5*) on hypocotyl elongation.

Materials and methods

Plant materials and growth conditions

All plant materials had the *Arabidopsis thaliana* Columbia (Col) background. Transgenic plants *35S:GFP-LKP2* (GFP-LKP2) and *35S:GFP* (GFP) were described previously (Miyazaki et al. 2011). Seeds were surface-sterilized and placed on plates with GM medium (Valvekens et al. 1988) supplemented with 0.8 % agar. Plates were kept at 4 °C for 3–7 days in the dark and then transferred to continuous white light at 22 °C (80 μmol m^{-2} s^{-1}). Seeds of *axr2-1* and *axr3-1* mutants were obtained from the ABRC stock center, and those of *pif4-101* and *pif5* (*pil6-1*) came from Dr. J. N. Maloof at the University of California, Davis (Nozue et al. 2011). The *axr* mutants were crossed with the GFP- or GFP-LKP2 plants to produce F_1 plants. Plants homozygous for GFP or GFP-LKP2 and carrying *pif* mutations were generated by crossing and self-pollination.

Microarray analysis

Hypocotyls of 5-day-old GFP-LKP2 (two lines), GFP (one line), and wild-type (Col) seedlings were used for analysis. RNA was prepared using the RNeasy Plant Mini Kit (Qiagen, Valencia, CA, USA). The microarray experiment was conducted by Miltenyi Biotec K.K. (Tokyo, Japan). RNA samples (100 ng) were used for the linear T7-based amplification step. To produce Cy3-labeled cRNA, RNA was amplified and labeled using the Agilent Low Input Quick Amp Labeling Kit (Agilent Technologies, Böblingen, Germany) following the manufacturer's protocol. The yields of cRNA and the dye incorporation rate were measured using a ND-1000 spectrophotometer (NanoDrop Technologies, Wilmington, DE, USA). Hybridization was performed according to the Agilent 60-mer oligo microarray processing protocol using the Agilent Gene Expression Hybridization Kit (Agilent Technologies). Cy3-labeled fragmented cRNA (1.65 μg) in hybridization buffer was hybridized overnight (17 h, 65 °C) with Agilent Whole *Arabidopsis* Genome Oligo Microarrays 4 × 44 K V4 (G2519F) in the hybridization chamber and oven recommended by Agilent. The microarray slides were washed with Agilent Gene Expression Wash Buffer 1 (1 × 1 min at room temperature), then with preheated Agilent Gene Expression Wash Buffer 2 (1 × 1 min at 37 °C), and finally with acetonitrile. Fluorescence signals were detected using an Agilent Microarray Scanner System (Agilent Technologies), and the Agilent Feature Extraction Software (FES) was used to read out and process the microarray image files. Microarray data are accessible through GEO series accession number GSE37197 (http://www.ncbi.nlm.nih.gov/geo/query/acc.cgi?acc=GSE37197). Putative candidate genes with a fold change of >2 or <−2 with $P < 0.01$ were used for pathway analysis in DAVID 6.7 (http://david.abcc.ncifcrf.gov/home.jsp) (Huang et al. 2009a, b). Gene annotations were retrieved from TAIR (http://www.arabidopsis.org/).

Semi-quantitative RT-PCR analysis

RNA for RT-PCR was isolated independently from that used for microarray analysis. Total RNA (1 μg) from hypocotyls of 5-day-old seedlings was primed with an oligo(dT) primer and reverse-transcribed using a High-Capacity cDNA Reverse Transcription Kit (Applied Biosystems, Foster City, CA, USA). PCR amplification was performed with AmpliTaq Gold (Applied Biosystems) and gene-specific primer sets are listed in Table S1. PCRs were carried out in a thermal cycler (GeneAmp PCR System 2700, Applied Biosystems) with denaturation at 94 °C for 5 min, followed by a variable number of cycles (Table S1) at 94 °C for 30 s, 50 °C for 20 s, and 72 °C for 1 min. PCR products were separated on a 2.0 % (w/v) agarose gel, stained with ethidium bromide, and visualized under UV light. Gel images were captured with a Printgraph video capture device (AE-6911FX; Atto, Tokyo, Japan). Each PCR fragment was sequenced directly to confirm its identity.

IAA measurements

Cotyledons, hypocotyls, and roots from 80 to 100 five-day-old seedlings were cut with a surgical knife, weighed, and frozen in liquid N_2. IAA was extracted, purified, and quantified using a liquid chromatography–electrospray ionization tandem mass spectrometry (LC–ESI–MS/MS) system as described previously (Yoshimoto et al. 2009). Six or 7 biological replicates were performed.

Measurement of hypocotyl length

Images of the hypocotyls of 5-day-old seedlings grown on agar plates (plates were kept vertically for auxin inhibitor experiments and horizontally for other experiments) were taken on a BX51 microscope (Olympus, Tokyo, Japan), and the cell length and cell number were determined with Scion Image software (Scion Corp., Frederick, MD, USA). In experiments with auxin inhibitors, agar contained 1 % DMSO (v/v, final concentration; mock), NPA (1 or 5 μM; Wako Pure Chemical Industries, Ltd., Osaka, Japan), PCIB (50 or 100 μM; MP Biomedicals, Santa Ana, CA, USA), or PEO-IAA (50 or 100 μM; provided by Dr. K. Hayashi,

Okayama University of Science). The top, middle, and bottom parts of hypocotyls were defined as reported previously (Miyazaki et al. 2011). In the case of embryonic hypocotyls, seeds were soaked in water for 6 h, the embryos were surgically excised and stained with 0.1 % (w/v) Toluidine blue (Wako Pure Chemical Industries, Ltd.). Images were taken on a BX51 microscope, and epidermal cells on a 250-μm line along the long axis of the hypocotyl at its thickest part were counted. Five independent embryos were used per line.

Results

Hypocotyl growth kinetics

GFP-LKP2 seedlings have elongated hypocotyls with longer epidermal cells in comparison with controls (Miyazaki et al. 2011; Yasuhara et al. 2004). This difference in hypocotyl cell length appeared only after germination and was not observed in embryos (Figs. S1A, B). To examine the growth kinetics of hypocotyls of GFP-LKP2 seedlings, we monitored the germination and growth of two GFP-LKP2 lines and two controls (Col and GFP) for a week (Fig. S2). All seeds germinated 2 days after incubation (DAI) under light. GFP-LKP2 hypocotyls became longer than controls at 3 DAI and the difference in the hypocotyl length was almost maximum at 5 DAI. At that time, all seedlings had two expanded green cotyledons and a small true leaf, as reported previously (Miyazaki et al. 2011), suggesting that 5-day-old seedlings of GFP-LKP2 and controls were at the same growth stage, even though their hypocotyl length was different. After 5 DAI, all hypocotyls still continued to grow for two more days without considerable elongation.

Gene expression profile of hypocotyls of GFP-LKP2 seedlings

We performed microarray analysis to compare the gene expression profiles of hypocotyls of two GFP-LKP2 lines and controls. In GFP-LKP2, a total of 775 genes were up-regulated (average fold change >2.0; $P < 0.01$; Table S2) and 725 genes were down-regulated (average fold change <−2.0; $P < 0.01$; Table S3); the functional groups of the up-regulated genes are shown in Table S4 and those of down-regulated genes in Table S5. The fact that *LKP2* (AT2G18915; average fold change 68.864) was the most up-regulated gene validated this analysis. The up- or down-regulation of the following clock genes was observed in GFP-LKP2 hypocotyls: *PSEUDO RESPONSE REGULATOR7* (*PRR7*) (AT5G02810; 8.189), *GIGANTEA* (AT1G22770; 4.343 and 3.831 by two probes), *PRR5* (AT5G24470; 2.081), and *EARLY FLOWERING4* (*ELF4*) (AT2G40080; −3.055 and −2.895). These observations are consistent with the involvement of LKP2 in circadian clock regulation. In the GFP-LKP2 hypocotyls, genes involved in responses to hormone stimuli, responses to abiotic stimuli, responses to blue light, external encapsulating structure organization, regulation of transcription, and red or far-red light signaling pathways were up-regulated, whereas those involved in secondary metabolism, responses to organic substances, flavonoid biosynthesis, and post-embryonic development were down-regulated. Among the up-regulated genes, 36 genes involved in the response to auxin had the smallest *P* value (9.28E−15; Table S4). This group included 27 *SMALL AUXIN UP RNA* (*SAUR*) (*SAUR1*, *7*, *9*, *12*, *15*, *16*, *19*, *20*, *22–29*, *50*, *52*, *61–66*, *68*, *73*, and *75*) genes, 6 *AUXIN/INDOLE-3-ACETIC ACID* (*AUX/IAA*) (*IAA1*, 2, *6*, *14*, *19*, and *29*) genes, a gene for putative *GH3* indole-3-acetic acid-amido synthetase (*DWARF IN LIGHT2*: *DFL2*), 1-aminocyclopropane-1-carboxylic acid synthase 4 (*ACS4*), and *AUXIN-REGULATED GENE INVOLVED IN ORGAN SIZE* (*ARGOS*). Based on this grouping and the result from the key word search for *IAA*, *SAUR*, *GH3*, and auxin, we constructed Table 1A. Twenty-one genes involved in responses to red or far-red light had the second smallest *P* value (2.44E−10; Table S4). This group included *PIF4*, *PIF5*, *PRR5*, *PRR7*, and *PRR9* (Table 1B). The increased expression of auxin-inducible genes suggested the elevation of IAA levels or sensitivity to IAA in hypocotyl cells of GFP-LKP2 seedlings.

We also observed up-regulation of genes involved in gibberellin biosynthesis and brassinosteroid signaling: gibberellin 20-oxidase (*GA5*) (AT4G25420; average fold change of 6.883), *BRASSINOSTEROID INSENSITIVE1* (*BRI1*) (AT4G39400; 2.999, 2.393, and 2.268 by three probes), and *BR ENHANCED EXPRESSION1* (*BEE1*) (AT1G18400; 2.008). The expression of the genes involved in cell wall loosening and expansion was also increased in GFP-LKP2 hypocotyls: *EXPANSIN3* (*EXPA3*) (AT2G37640; average fold change 6.750 and 2.015 by two probes), *EXPANSIN11* (*EXPA11*) (AT1G20190; 5.021), *XYLOGLUCAN:XYLOGLUCOSYL TRANSFERASE33* (*XTH33*) (AT1G10550; 4.688), *XTH8* (AT1G11545; 3.662), *EXPA8* (AT2G40610; 4.333, 3.533, and 3.118), *EXPANSIN-LIKE B1* (*EXLB1*) (AT4G17030; 2.568 and 2.179), *EXPA5* (AT3G29030; 2.558, 2.423 and 2.203), *EXLA1* (AT3G45970; 2.422), *EXPA12* (AT3G15370; 2.312), *EXLA3* (AT3G45960; 2.101), and *EXPA1* (AT1G69530; 2.108) (Table S2).

Semi-quantitative RT-PCR confirmed some of the microarray results, i.e., the expression of three auxin-inducible genes (*IAA6*, *SAUR25*, and *ACS4)*, two PIF genes (*PIF4* and *PIF5)*, and one gene for a cell wall-modifying enzyme (*EXPA11*) was higher in the hypocotyls of 5-day-

Table 1 Genes up-regulated in GFP-LKP2 hypocotyls under white light in comparison with those of controls (Col and GFP)

Array element	Gene locus	Gene name	Fold change	*P* value
(A) Up-regulated genes involved in the response to auxin stimulus in GFP-LKP2 hypocotyls				
A_84_P10124	AT4G14560	*IAA1*	8.516	4.98.E−07
A_84_P734158	AT3G23030	*IAA2*	2.031	1.50.E−04
A_84_P13379	AT1G52830	*IAA6*	6.303	2.56.E−14
A_84_P826648	AT4G14550	*IAA14*	2.395	4.10.E−17
A_84_P23363			2.079	5.71.E−13
A_84_P14556	AT3G15540	*IAA19*	2.805	4.19.E−14
A_84_P55550	AT4G32280	*IAA29*	2.349	8.00.E−05
A_84_P21449	AT4G34770	*SAUR1*	2.814	2.46.E−17
A_84_P21078	AT2G21200	*SAUR7*	4.076	1.00.E−25
A_84_P797355	AT4G36110	*SAUR9*	3.579	3.02.E−20
A_84_P12944			3.342	1.74.E−07
A_84_P23871	AT2G21220	*SAUR12*	3.509	6.20.E-12
A_84_P16734	AT4G38850	*SAUR15*	6.861	0.00.E+00
A_84_P17680	AT4G38860	*SAUR16*	5.534	1.05.E−27
A_84_P196504	AT5G18010	*SAUR19*	7.093	9.52.E−23
A_84_P147028	AT5G18020	*SAUR20*	5.068	3.04.E−31
A_84_P152798	AT5G18030	*SAUR21*	5.592	2.89.E−29
	AT5G18080	*SAUR24*		
A_84_P141269	AT5G18050	*SAUR22*	5.563	4.83.E−35
A_84_P94979	AT5G18060	*SAUR23*	5.332	1.00.E−26
A_84_P272980	AT5G18080	*SAUR24*	4.895	1.59.E−27
A_84_P21376	AT4G13790	*SAUR25*	9.767	4.62.E−12
A_84_P792091			8.781	3.61.E−20
A_84_P554482	AT3G03850	*SAUR26*	3.445	4.11.E−18
A_84_P18297	AT3G03840	*SAUR27*	2.747	2.47.E−18
A_84_P20189	AT3G03830	*SAUR28*	3.083	7.35.E−21
A_84_P21135	AT3G03820	*SAUR29*	2.672	4.62.E−19
A_84_P20503	AT4G34760	*SAUR50*	2.956	8.71.E−11
A_84_P832877	AT1G75590	*SAUR52*	3.091	1.69.E−18
A_84_P17068			2.905	3.00.E−05
A_84_P537376	AT1G29420	*SAUR61*	5.674	0.00.E+00
A_84_P10257	AT1G29430	*SAUR62*	3.989	3.05.E−21
A_84_P279980	AT1G29440	*SAUR63*	3.485	1.12.E−35
A_84_P846978	AT1G29450	*SAUR64*	4.002	5.37.E−13
A_84_P19713			3.425	1.96.E−25
A_84_P15930	AT1G29460	*SAUR65*	4.298	4.30.E−27
A_84_P11207	AT1G29500	*SAUR66*	3.055	2.00.E−25
A_84_P843096	AT1G29490	*SAUR68*	10.956	6.25.E−11
A_84_P169803	AT3G03847	*SAUR73*	3.541	6.06.E−12
A_84_P563710	AT5G27780	*SAUR75*	3.772	3.63.E−18
A_84_P826972	AT2G47750	*GH3.9*	3.087	1.20.E−04
A_84_P20399	AT4G03400	*DFL2*	2.954	6.03.E−18
A_84_P17344	AT2G22810	*ACS4*	13.586	9.85.E−12
A_84_P524502	AT3G59900	*ARGOS*	3.297	7.33.E−29
A_84_P179084	AT5G35735	*Auxin-responsive family protein*	2.124	3.33.E−07
A_84_P751876	AT1G11803	*Pseudogene, auxin responsive protein*	4.810	2.96.E−28
A_84_P769426	AT5G27771	*Pseudogene of auxin-responsive family protein*	3.311	6.89.E−07

Table 1 continued

Array element	Gene locus	Gene name	Fold change	*P* value
(B) Up-regulated genes involved in the response to red or far-red light in GFP-LKP2 hypocotyls				
A_84_P21376	AT4G13790	*SAUR25*	9.767	4.62.E−12
A_84_P162983	AT2G43010	*PIF4*	9.301	1.24.E−12
A_84_P23852	AT2G42540	*COR15A*	8.899	5.47.E−08
A_84_P13379	AT1G52830	*IAA6*	6.303	2.56.E−14
A_84_P21494	AT5G02810	*PRR7*	5.330	4.93.E−15
A_84_P126821	AT2G46790	*PRR9*	5.101	4.90.E−04
A_84_P240805	AT2G05100	*LHCB2.1*	4.454	1.36.E−06
A_84_P14690	AT3G59060	*PIF5*	4.170	2.25.E−14
A_84_P18969	AT1G22770	*GI*	3.831	1.86.E−10
A_84_P521683	AT2G46970	*PIL1*	3.298	2.82.E−16
A_84_P14733	AT1G06040	*STO*	3.197	1.29.E−22
A_84_P19825	AT5G04190	*PKS4*	3.074	1.08.E−10
A_84_P17015	AT1G02340	*HFR1*	2.528	3.01.E−08
A_84_P21407	AT4G25260	*Plant invertase/pectin methylesterase inhibitor superfamily protein*	2.482	4.51.E−16
A_84_P23021	AT2G29090	*CYP707A2*	2.438	2.61.E−08
A_84_P55550	AT4G32280	*IAA29*	2.349	8.00.E−05
A_84_P137439	AT3G58850	*PAR2*	2.296	6.05.E−20
A_84_P13983	AT5G24120	*SIG5*	2.294	1.19.E−07
A_84_P10576	AT1G14290	*SBH2*	2.120	1.42.E−16
A_84_P16821	AT5G24470	*PRR5*	2.081	8.52.E−10
A_84_P10694	AT2G37640	*EXPA3*	2.015	3.70.E−04

Genes involved in (A) the response to auxin or (B) red or far-red light signaling were identified by the Gene Functional Classification Tool within DAVID Bioinformatics Resources 6.7

old GFP-LKP2-1 and GFP-LKP2-2 seedlings than in control hypocotyls (Fig. 1).

IAA level is increased in GFP-LKP2 hypocotyls

In cotyledons or roots, the IAA levels were not significantly different between GFP-LKP2 and control seedlings (Fig. 2). In hypocotyls, the IAA levels were higher in GFP-LKP2 seedlings than in control seedlings (Fig. 2), which suggested that the enhancement of hypocotyl elongation in GFP-LKP2 seedlings is due to the elevated IAA levels in their hypocotyls.

Hypocotyl elongation in GFP-LKP2 seedlings is inhibited by exogenous auxin inhibitors

To evaluate the contribution of IAA to hypocotyl elongation in GFP-LKP2 seedlings, we used NPA (a polar auxin transport inhibitor; Bernasconi et al. 1996), PCIB (a putative anti-auxin; Oono et al. 2003), and PEO-IAA (an auxin antagonist that binds to TIR1/AFBs auxin receptors; Hayashi et al. 2012) (Fig. S3). Exogenous application of PCIB (25 μM) or PEO-IAA (50 μM) partially inhibited hypocotyl growth in GFP-LKP2 seedlings, but the difference between GFP-LKP2 and control seedlings was still significant (Fig. S4). By contrast, NPA (1 or 5 μM) or higher concentrations of PCIB or PEO-IAA (100 μM each) strongly inhibited the enhancement of GFP-LKP2 hypocotyl elongation, and there was no significant difference between the control(s) and at least one GFP-LKP2 line (Figs. 3, S4).

Previously, we reported that enhanced hypocotyl elongation in GFP-LKP2 seedlings is caused by the expansion of cortical and epidermal cells, and the increased number of cortical cells (Miyazaki et al. 2011). Therefore, we examined the effects of auxin inhibitors on these parameters. Epidermal cell numbers in GFP-LKP2 hypocotyls were not significantly different from those in controls either in the absence (in line with our previous report; Miyazaki et al. 2011) or in the presence of 5 μM NPA, 100 μM PCIB, or 100 μM PEO-IAA (Fig. 4a). By contrast, cortical cell numbers in GFP-LKP2 hypocotyls were 1.7–1.9 times those in controls, and this difference was strongly reduced or abolished by 5 μM NPA, 100 μM PCIB, or 100 μM PEO-IAA (Fig. 4b). The epidermal and cortical cells were significantly longer in GFP-LKP2

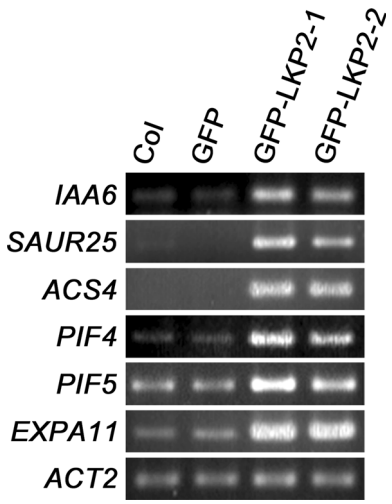

Fig. 1 Semi-quantitative RT-PCR analysis of *IAA6*, *SAUR25*, *ACS4*, *PIF4*, *PIF5*, and *EXPA11*. Hypocotyls of 5-day-old control (Col and GFP) and GFP-LKP2 seedlings (lines GFP-LKP2-1 and GFP-LKP2-2) were used. RT-PCR products were separated on a 2.0 % (w/v) agarose gel and stained with ethidium bromide. *ACTIN2* (*ACT2*) was used as a control

hypocotyls than in controls in the bottom, middle, and top hypocotyl areas, whereas the application of 5 μM NPA, 100 μM PCIB, or 100 μM PEO-IAA diminished these differences (Fig. 5). These results support the idea that high levels of IAA promote hypocotyl elongation in GFP-LKP2 seedlings.

Hypocotyl elongation is suppressed in progeny of the cross between GFP-LKP2 lines and dominant gain-of-function auxin-resistant mutants

Dominant gain-of-function mutants *axr2-1* and *axr3-1* show agravitropic root and shoot growth, short hypocotyls and stems, and auxin-resistant root growth (Nagpal et al. 2000). Because the *35S:GFP-LKP2* transgene, and the *axr2-1* and *axr3-1* genes are dominant, we crossed these *axr* mutants with GFP-LKP2 or control plants and assessed the hypocotyl length of F_1 seedlings that had one copy of *axr2-1* or *axr3-1* and *35S:GFP-LKP2* (Fig. 6). The enhancement of hypocotyl elongation in GFP-LKP2 seedlings was completely suppressed in the F_1 seedlings. These results support the involvement of IAA in the enhancement of hypocotyl elongation in GFP-LKP2 seedlings.

Hypocotyl elongation is suppressed in progeny of the cross between GFP-LKP2 lines and loss-of-function *pif* mutants

PIF4 and PIF5 redundantly promote hypocotyl elongation by directly activating the expression of genes that are involved in cell wall loosening and expansion, and *pif4*, *pif5*, and *pif4 pif5* mutants show short hypocotyls when grown under light (Hornitschek et al. 2012; de Lucas and Prat 2014). To assess the contribution of PIF4 and PIF5 to hypocotyl elongation in GFP-LKP2 seedlings, we measured the hypocotyl length in progeny derived from crosses between GFP-LKP2 seedlings and *pif4*, *pif5*, or *pif4 pif5* mutants. The enhancement of hypocotyl elongation was suppressed in all three groups, most strongly in the progeny of GFP-LKP2 and *pif4 pif5* mutant (Fig. 6). Therefore, *PIF4* and *PIF5* are critical for the enhancement of hypocotyl elongation in GFP-LKP2 seedlings.

Discussion

In this study, we found that the early or primary auxin-inducible genes from the *AUX/IAA*, *GH3*, and *SAUR* families (Hagen and Guilfoyle 2002; Woodward and Bartel 2005) were up-regulated in GFP-LKP2 hypocotyls (Table 1A). Proteins of both AUX/IAAs and GH3 families attenuate auxin responses (Staswick et al. 2005; Tiwari et al. 2001). The expression of *SAUR*s is usually associated

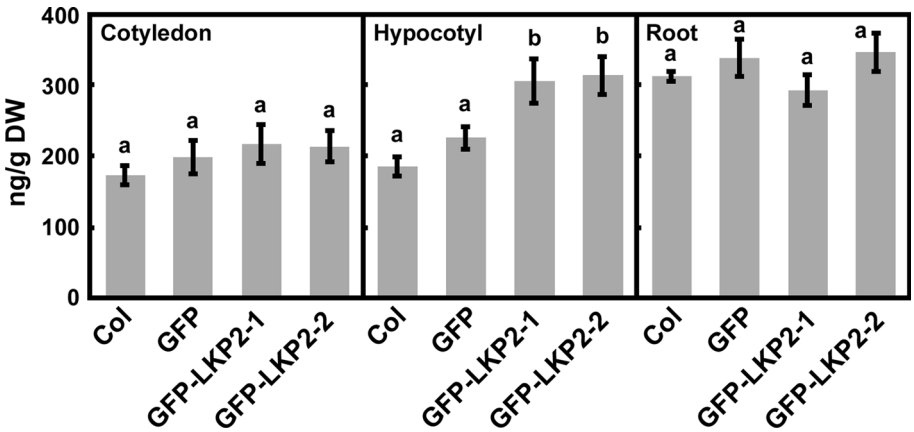

Fig. 2 IAA contents in cotyledons, hypocotyls, and roots of 5-day-old control (Col and GFP) and GFP-LKP2 seedlings (lines GFP-LKP2-1 and GFP-LKP2-2) quantified using LC–ESI-MS/MS. *Error bars* represent standard error of the mean ($n = 6$ or 7 biological replicates); *different letters* indicate statistically significant differences ($P < 0.05$, Tukey's test)

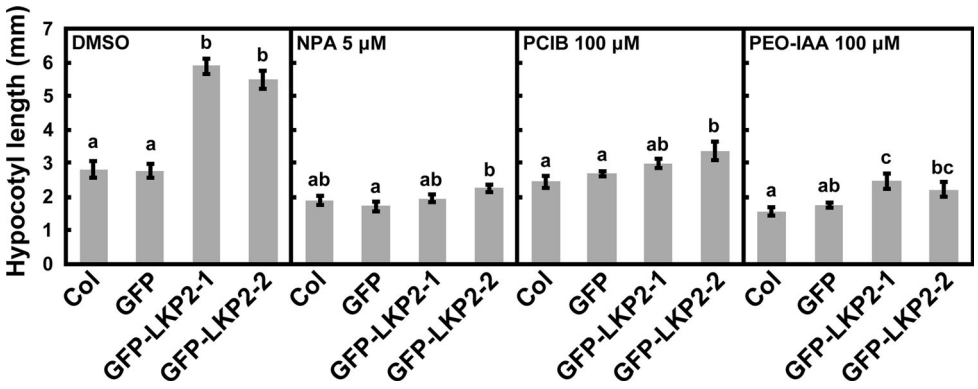

Fig. 3 Inhibition of hypocotyl elongation by auxin inhibitors. Hypocotyl length of 5-day-old control (Col and GFP) and GFP-LKP2 seedlings (lines GFP-LKP2-1 and GFP-LKP2-2) was measured in the absence or presence of the indicated concentrations of *N*-1-naphthylphthalamic acid (NPA), *p*-chlorophenoxyisobutyric acid (PCIB), or α-(phenylethyl-2-one)-indole-3-acetic acid (PEO-IAA). *Error bars* represent standard error of the mean ($n = 7$–15); *different letters* indicate statistically significant differences ($P < 0.05$, Tukey's test)

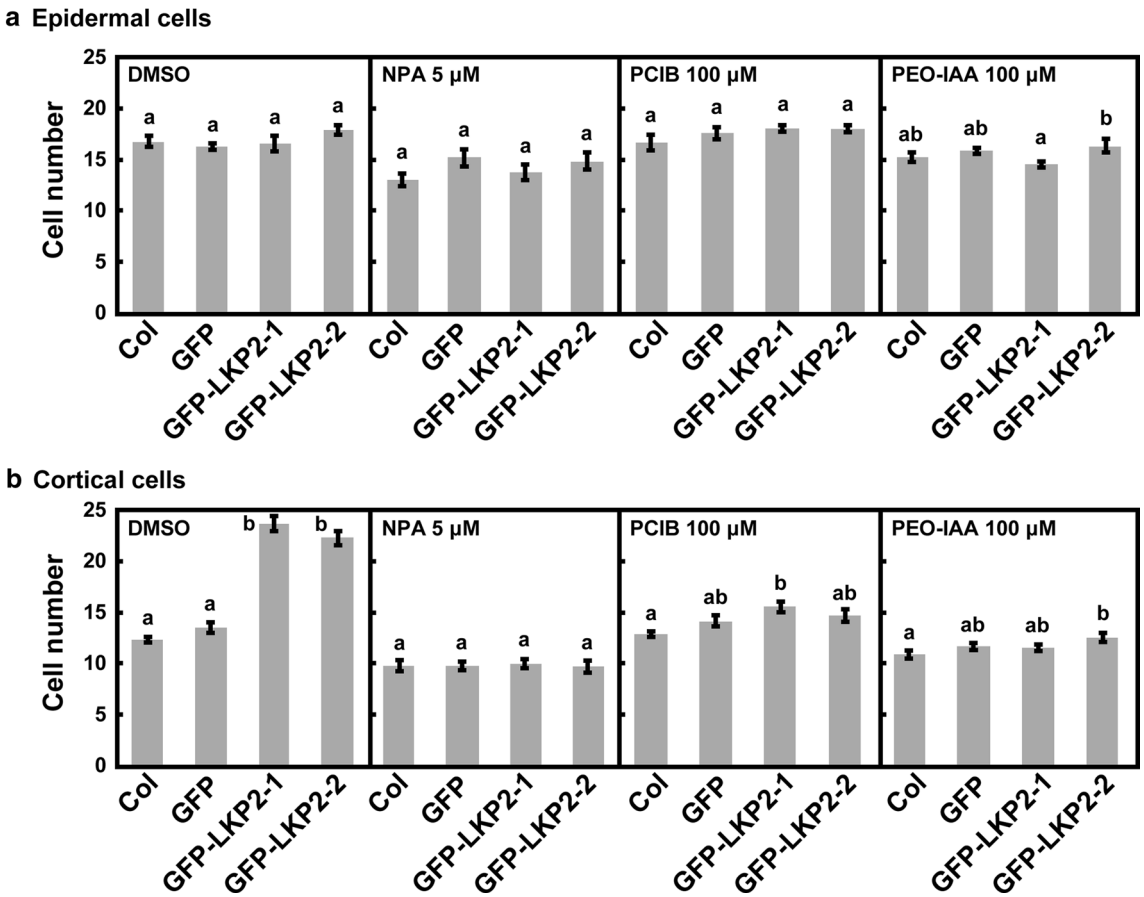

Fig. 4 Inhibition of the increase in hypocotyl cell number by auxin inhibitors. Total numbers of (**a**) epidermal and (**b**) cortical cells in 5-day-old control (Col and GFP) and GFP-LKP2 seedlings (lines GFP-LKP2-1 and GFP-LKP2-2) in the absence or presence of the indicated concentrations of *N*-1-naphthylphthalamic acid (NPA), *p*-chlorophenoxyisobutyric acid (PCIB), or α-(phenylethyl-2-one)-indole-3-acetic acid (PEO-IAA). *Error bars* represent standard error of the mean ($n = 10$); *different letters* indicate statistically significant differences ($P < 0.05$, Tukey's test)

with tissue elongation (Franklin et al. 2011; Roig-Villanova et al. 2007). Among *SAUR*s, members of two subfamilies, *SAUR19–24* and *SAUR61–68*, are considered to be positive effectors of cell expansion (Chae et al. 2012; Spartz et al. 2012, 2014). The sequences of *SAUR19–24* are highly similar to each other, and these six genes form a

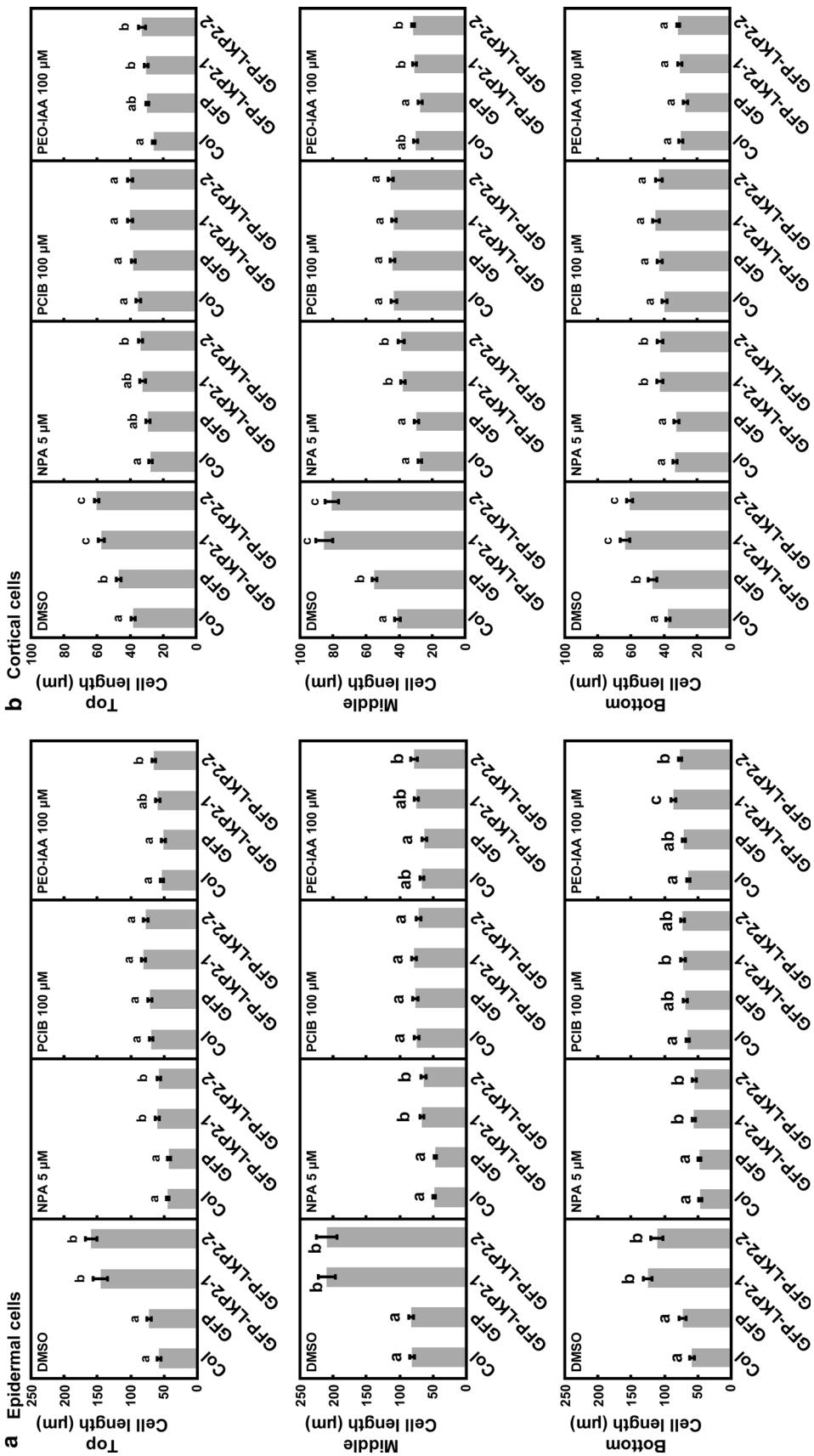

Fig. 5 Inhibition of hypocotyl cell elongation by auxin inhibitors. **a** Epidermal and **b** cortical cell length in the *top*, *middle*, and *bottom* parts of the hypocotyls of 5-day-old control (Col and GFP) and GFP-LKP2 seedlings (lines GFP-LKP2-1 and GFP-LKP2-2) in the absence or presence of indicated concentrations of *N*-1-naphthylphthalamic acid (NPA), *p*-chlorophenoxyisobutyric acid (PCIB), or α-(phenylethyl-2-one)-indole-3-acetic acid (PEO-IAA). *Error bars* represent standard error of the mean ($n = 20$); *different letters* indicate statistically significant differences ($P < 0.05$, Tukey's test)

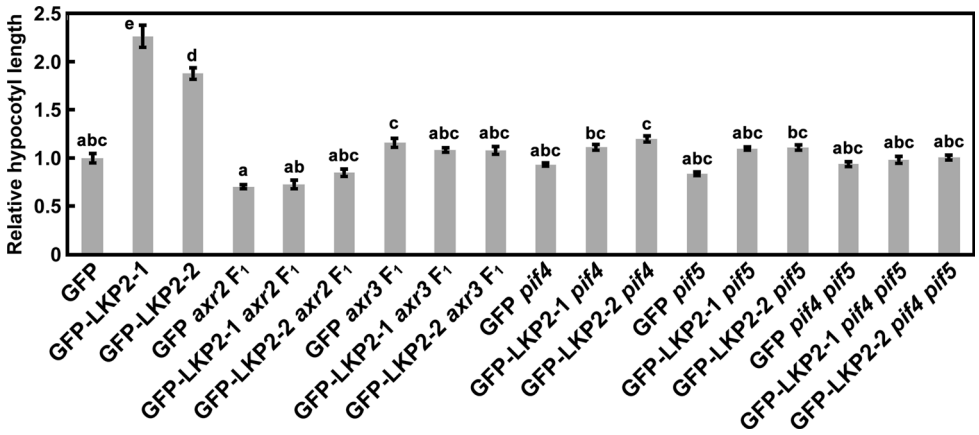

Fig. 6 Suppression of enhanced hypocotyl elongation in progeny of the crosses between GFP-LKP2 lines and dominant gain-of-function auxin-resistant mutants (*axr2-1* and *axr3-1*) or loss-of-function mutants (*pif4*, *pif5*, and *pif4 pif5*). The following seedlings were used: GFP, GFP-LKP2 (lines GFP-LKP2-1 and GFP-LKP2-2), F_1 progeny of the cross between GFP or GFP-LKP2 and *axr2* or *axr3*, and GFP and GFP-LKP2 carrying the indicated *pif* mutations. Hypocotyl length is expressed relative to that of GFP seedlings. All seedlings were 5 days old. *Error bars* represent standard error of the mean ($n = 5$–29); *different letters* indicate statistically significant differences ($P < 0.05$, Tukey's test)

cluster on chromosome 5, which suggests their functional redundancy (Franklin et al. 2011; Hagen and Guilfoyle 2002). Plants overexpressing *SAUR19* have longer hypocotyls than wild-type plants under continuous light, and plants producing GFP-SAUR19, 21, 23, or 24 fusion proteins have elongated hypocotyls under long-day conditions (Spartz et al. 2012). SAUR19 stimulates plasma membrane H^+-ATPase by inhibiting the activity of type 2C protein phosphatases, which leads to cell expansion via an acid-growth mechanism (Spartz et al. 2014). Therefore, auxin-mediated induction of *SAUR* expression is a possible mechanism for the enhancement of hypocotyl elongation in GFP-LKP2 seedlings.

Gibberellins stimulate cell elongation in *Arabidopsis* hypocotyls (Cowling and Harberd 2007), and brassinosteroids enhance light-grown hypocotyl elongation independent of, but co-operatively with, gibberellins and auxin(s) (Tanaka et al. 2003). Although genes for gibberellin biosynthesis and brassinosteroid signaling were up-regulated in GFP-LKP2 hypocotyls, further studies are needed to ascertain the contribution of these hormones to the effect of LKP2 on hypocotyl elongation.

Expression of *PIF4* and *PIF5* was up-regulated in GFP-LKP2 seedlings (Tables 1B, S2). PIF4 and PIF5 regulate auxin sensitivity to control hypocotyl growth (Chapman et al. 2012; Nozue et al. 2011). Their expression is regulated by the circadian clock (*Arabidopsis* eFP Browser: http://bar.utoronto.ca/efp/cgi-bin/efpWeb.cgi). Therefore, the up-regulation of *PIF4* and *PIF5* may be due to circadian clock defects in GFP-LKP2 plants (Miyazaki et al. 2011). PIF4 and PIF5 accumulation is regulated by light (Nozue et al. 2007). Although PIF4 and PIF5 are stable in the dark but are degraded under light, our data indicate their importance in hypocotyl elongation in GFP-LKP2 seedlings grown under continuous light. This is consistent with the up-regulation of PIF4 target genes *LONG HYPOCOTYL IN FAR-RED* (*HFR1*) and *IAA29* (Koini et al. 2009; Lorrain et al. 2008) in GFP-LKP2 hypocotyls (Table 1).

The circadian clock regulates the expression and formation of the evening complex (EC), which consists of ELF3, ELF4, and LUX ARRHYTHMO (LUX)/PHYTOCLOCK1 (PCL1) (Nusinow et al. 2011). The EC binds to the *PIF4* and *PIF5* promoters to repress *PIF4* and *PIF5* transcription (Nusinow et al. 2011). *ELF4* was down-regulated in GFP-LKP2 hypocotyls (Table S3). Thus, the up-regulation of *PIF4* and *PIF5* may be due to the down-regulation of *ELF4* (fold change of ~ -3) in GFP-LKP2 hypocotyls.

TOC1 binds to the promoters and represses the expression of *CCA1*, *LHY*, *PRR9*, *PRR7*, *TOC1*, *GI*, *LUX*, and *ELF4* (Huang et al. 2012). PRR5 also binds to the promoters and represses the expression of *CCA1*, *LHY*, and *PRR5* (Nakamichi et al. 2010). LKP2 and ZTL bind to TOC1 and PRR5 and are involved in ubiquitination and subsequent 26S proteasome-dependent degradation of TOC1 and PRR5 (Kiba et al. 2007; Más et al. 2003; Yasuhara et al. 2004). Thus, the down-regulation of TOC1 and PRR5 proteins by LKP2 overproduction may explain the up-regulation of *PRR7* ($\sim$8-fold), *GI* ($\sim$4-fold), and *PRR5* ($\sim$2-fold) expression in GFP-LKP2 hypocotyls. However, degradation of TOC1 and PRR5 proteins by LKP2 does not provide a persuasive explanation for *PIF4* and *PIF5* up-regulation in GFP-LKP2 hypocotyls, because, unlike the expression of *PRR5*, *PRR7*, and *GI*, that of *ELF4* is down-regulated.

LKP2 shows high amino acid sequence similarity to ZTL (75 % identity), and the tissue-specific expression pattern of *LKP2* largely overlaps with that of *ZTL* (Kiyosue and Wada 2000; Yasuhara et al. 2004). *LKP2*-overexpressing transgenic plants phenocopy *ZTL*-overexpressing transgenic plants: both exhibit circadian rhythm defects under continuous light or in the dark, elongated hypocotyls under continuous white or red light, and delayed flowering under long-day conditions compared with control plants (Nelson et al. 2000; Schultz et al. 2001). Transfer DNA (T-DNA) insertion mutants of *LKP2* are phenotypically similar to wild-type plants (Baudry et al. 2010; Takase et al. 2011), whereas T-DNA insertion mutants of *ZTL* show slower circadian rhythms under continuous red or blue light or in the dark, shorter hypocotyls under continuous red light, and earlier flowering under non-inductive photoperiod conditions than control plants (Somers et al. 2004; Takase et al. 2011). The phenotypic similarity of *lkp2* plants to wild-type plants is considered to be due to the very low expression of *LKP2* in wild-type plants relative to that of *ZTL* (Baudry et al. 2010; Michael et al. 2008; Mockler et al. 2007). Introduction of *LKP2* cDNA controlled by the *ZTL* promoter complemented the long-period phenotype of a *ztl* mutant (Baudry et al. 2010). These results suggest that LKP2 has ZTL-like functions with respect to the regulation of the circadian clock, hypocotyl elongation, and flowering time in *Arabidopsis*. Therefore, it is possible that ZTL also regulates hypocotyl elongation via auxin and PIF4, PIF5, or both. Indeed, transgenic *Arabidopsis* seedlings that overexpress *ZTL* accumulate higher levels of mRNAs for auxin-inducible genes and PIF target genes, and loss-of-function *ztl* mutants have lower levels of these mRNAs than wild-type seedlings (Saitoh et al. 2015a, b). Enhancement of hypocotyl elongation in *ZTL*-overexpressing seedlings was abolished by NPA, PEO-IAA, or yucasin (5-(4-chlorophenyl)-4*H*-1,2,4-triazole-3-thiol, an auxin biosynthesis inhibitor) (Saitoh et al. 2015a). A loss-of-function *fkf1 lkp2 ztl* triple mutant has shorter hypocotyls and a lower level of *PIF4* mRNA than wild-type seedlings (Fornara et al. 2015).

One major function of the FKF1/LKP2/ZTL protein family is to regulate target protein stability via ubiquitination. Thus, our microarray analysis using stable transgenic lines with ectopic expression of LKP2 does not reveal its direct targets, but downstream effects of LKP2 function. In spite of this limitation, our study suggests that LKP2-mediated hypocotyl growth is regulated at a transcriptional level mainly through auxin signaling (Fig. S5). Investigations of the functional relationships between FKF1/LKP2/ZTL family proteins and auxin, PIF transcription factors, or the EC complex would improve our understanding of diurnal plant growth.

Author contribution statement Conceived and designed the experiments: YM, YJ, YK, TK. Performed the experiments: YM, YJ, AS, AS. Analyzed the data: YM, YJ, TT. Contributed reagents, materials, and analysis tools: YM, YJ, AS, AS. Wrote the paper: YM, TK.

Acknowledgments This research was partially supported by a grant from the Ministry of Education, Culture, Sports, Science and Technology of Japan. We thank Dr. K. Hayashi (Okayama University of Science, Okayama, Japan) for kindly providing PEO-IAA, Dr. J. N. Maloof (University of California, Davis, CA, USA) for kindly providing *pif4* and *pif5* seeds, and ABRC for providing *axr2-1* and *axr3-1* seeds.

Compliance with ethical standards

Conflict of interest The authors declare no conflict of interest.

References

Bae G, Choi G (2008) Decoding of light signals by plant phytochromes and their interacting proteins. Annu Rev Plant Biol 59:281–311

Baudry A, Ito S, Song YH, Strait AA, Kiba T, Lu S, Henriques R, Pruneda-Paz JL, Chua N-H, Tobin EM, Kay SA, Imaizumi T (2010) F-box proteins FKF1 and LKP2 act in concert with ZEITLUPE to control *Arabidopsis* clock progression. Plant Cell 22:606–622

Bauer D, Viczián A, Kircher S, Nobis T, Nitschke R, Kunkel T, Panigrahi KC, Adám E, Fejes E, Schäfer E, Nagy F (2004) Constitutive photomorphogenesis 1 and multiple photoreceptors control degradation of phytochrome interacting factor 3, a transcription factor required for light signaling in *Arabidopsis*. Plant Cell 16:1433–1445

Bernasconi P, Patel BC, Reagan JD, Subramanian MV (1996) The N-1-naphthylphthalamic acid-binding protein is an integral membrane protein. Plant Physiol 111:427–432

Boron AK, Vissenberg K (2014) The *Arabidopsis thaliana* hypocotyl, a model to identify and study control mechanisms of cellular expansion. Plant Cell Rep 33:697–706

Castillon A, Shen H, Huq E (2007) Phytochrome interacting factors: central players in phytochrome-mediated light signaling networks. Trends Plant Sci 12:514–521

Chae K, Isaacs CG, Reeves PH, Maloney GS, Muday GK, Nagpal P, Reed JW (2012) *Arabidopsis* SMALL AUXIN UP RNA63 promotes hypocotyl and stamen filament elongation. Plant J 71:684–697

Chapman EJ, Greenham K, Castillejo C, Sartor R, Bialy A, Sun TP, Estelle M (2012) Hypocotyl transcriptome reveals auxin regulation of growth-promoting genes through GA-dependent and -independent pathways. PLoS One 7:e36210

Cowling RJ, Harberd NP (2007) Gibberellins control *Arabidopsis* hypocotyl growth via regulation of cellular elongation. J Exp Bot 58:4269–4281

de Lucas M, Prat S (2014) PIFs get BRright: PHYTOCHROME INTERACTING FACTORs as integrators of light and hormonal signals. New Phytol 202:1126–1141

Demarsy E, Fankhauser C (2009) Higher plants use LOV to perceive blue light. Curr Opin Plant Biol 12:69–74

Dowson-Day MJ, Millar AJ (1999) Circadian dysfunction causes aberrant hypocotyl elongation patterns in *Arabidopsis*. Plant J 17:63–71

Duek PD, Fankhauser C (2005) bHLH class transcription factors take centre stage in phytochrome signalling. Trends Plant Sci 10:51–54

Fornara F, de Montaigu A, Sánchez-Villarreal A, Takahashi Y, Loren Ver, van Themaat E, Huettel B, Davis SJ, Coupland G (2015) The GI-CDF module of *Arabidopsis* affects freezing tolerance and growth as well as flowering. Plant J 81:695–706

Franklin KA, Lee SH, Patel D, Kumar SV, Spartz AK, Gu C, Ye S, Yu P, Breen G, Cohen JD, Wigge PA, Gray WM (2011) Phytochrome-interacting factor 4 (PIF4) regulates auxin biosynthesis at high temperature. Proc Natl Acad Sci USA 108:20231–20235

Hagen G, Guilfoyle T (2002) Auxin-responsive gene expression: genes, promoters and regulatory factors. Plant Mol Biol 49:373–385

Hayashi K, Neve J, Hirose M, Kuboki A, Shimada Y, Kepinski S, Nozaki H (2012) Rational design of an auxin antagonist of the SCF(TIR1) auxin receptor complex. ACS Chem Biol 7:590–598

Hornitschek P, Kohnen MV, Lorrain S, Rougemont J, Ljung K, López-Vidriero I, Franco-Zorrilla JM, Solano R, Trevisan M, Pradervand S, Xenarios I, Fankhauser C (2012) Phytochrome interacting factors 4 and 5 control seedling growth in changing light conditions by directly controlling auxin signaling. Plant J 71:699–711

Huang DW, Sherman BT, Lempicki RA (2009a) Systematic and integrative analysis of large gene lists using DAVID bioinformatics resources. Nature Protoc 4:44–57

Huang DW, Sherman BT, Lempicki RA (2009b) Bioinformatics enrichment tools: paths toward the comprehensive functional analysis of large gene lists. Nucleic Acids Res 37:1–13

Huang W, Pérez-García P, Pokhilko A, Millar AJ, Antoshechkin I, Riechmann JL, Más P (2012) Mapping the core of the *Arabidopsis* circadian clock defines the network structure of the oscillator. Science 336:75–79

Jarillo JA, Capel J, Tang RH, Yang HQ, Alonso JM, Ecker JR, Cashmore AR (2001) An *Arabidopsis* circadian clock component interacts with both CRY1 and phyB. Nature 410:487–490

Jiao Y, Lau OS, Deng XW (2007) Light-regulated transcriptional networks in higher plants. Nat Rev Genet 8:217–230

Kendrick RE, Kronenberg GHM (1994) Photomorphogenesis in plants. Kluwer Academic Publishers, Dordrecht, Boston, London

Kiba T, Henriques R, Sakakibara H, Chua N-H (2007) Targeted degradation of PSEUDO-RESPONSE REGULATOR5 by SCF^{ZTL} complex regulates clock function and photomorphogenesis in *Arabidopsis thaliana*. Plant Cell 19:2516–2530

Kiyosue T, Wada M (2000) LKP1 (LOV Kelch protein1): a factor involved in the regulation of flowering time in *Arabidopsis*. Plant J 23:807–815

Koini MA, Alvey L, Allen T, Tilley CA, Harberd NP, Whitelam GC, Franklin KA (2009) High temperature-mediated adaptations in plant architecture require the bHLH transcription factor PIF4. Curr Biol 19:408–413

Lau OS, Deng XW (2010) Plant hormone signaling lightens up: integrators of light and hormones. Curr Opin Plant Biol 13:571–577

Lau OS, Deng XW (2012) The photomorphogenic repressors COP1 and DET1: 20 years later. Trends Plant Sci 17:584–593

Lorrain S, Allen T, Duek PD, Whitelam GC, Fankhauser C (2008) Phytochrome-mediated inhibition of shade avoidance involves degradation of growth-promoting bHLH transcription factors. Plant J 53:312–323

Mancinelli AL (1990) Interaction between light quality and light quantity in the photoregulation of anthocyanin production. Plant Physiol 92:1191–1195

Más P, Kim WY, Somers DE, Kay SA (2003) Targeted degradation of TOC1 by ZTL modulates circadian function in *Arabidopsis thaliana*. Nature 426:567–570

Michael TP, Breton G, Hazen SP, Priest H, Mockler TC, Kay SA, Chory J (2008) A morning-specific phytohormone gene expression program underlying rhythmic plant growth. PLoS Biol 6:e225

Millar AJ (2004) Input signals to the plant circadian clock. J Exp Bot 55:277–283

Miyazaki Y, Yoshizumi T, Takase T, Matsui M, Kiyosue T (2011) Overexpression of *LOV KELCH PROTEIN2* enhances cell elongation and increases cell number and ploidy in the hypocotyl of *Arabidopsis thaliana*. Plant Biotechnol 28:267–272

Mockler TC, Michael TP, Priest HD, Shen R, Sullivan CM, Givan SA, McEntee C, Kay SA, Chory J (2007) The DIURNAL project: DIURNAL and circadian expression profiling, model-based pattern matching, and promoter analysis. Cold Spring Harb Symp Quant Biol 72:353–363

Nagpal P, Walker LM, Young JC, Sonawala A, Timpte C, Estelle M, Reed JW (2000) *AXR2* encodes a member of the Aux/IAA protein family. Plant Physiol 123:563–574

Nakamichi N, Kiba T, Henriques R, Mizuno T, Chua N-H, Sakakibara H (2010) PSEUDO-RESPONSE REGULATORS 9, 7, and 5 are transcriptional repressors in the *Arabidopsis* circadian clock. Plant Cell 22:594–605

Nelson DC, Lasswell J, Rogg LE, Cohen MA, Bartel B (2000) FKF1, a clock-controlled gene that regulates the transition to flowering in *Arabidopsis*. Cell 101:331–340

Nozue K, Maloof JN (2006) Diurnal regulation of plant growth. Plant Cell Environ 29:396–408

Nozue K, Covington MF, Duek PD, Lorrain S, Fankhauser C, Harmer SL, Maloof JN (2007) Rhythmic growth explained by coincidence between internal and external cues. Nature 448:358–361

Nozue K, Harmer SL, Maloof JN (2011) Genomic analysis of circadian clock-, light-, and growth-correlated genes reveals PHYTOCHROME-INTERACTING FACTOR5 as a modulator of auxin signaling in *Arabidopsis*. Plant Physiol 156:357–372

Nusinow DA, Helfer A, Hamilton EE, King JJ, Imaizumi T, Schultz TF, Farré EM, Kay SA (2011) The ELF4-ELF3-LUX complex links the circadian clock to diurnal control of hypocotyl growth. Nature 475:398–402

Oono Y, Oura C, Rahman A, Aspuria ET, Hayashi K, Tanaka A, Uchimiya H (2003) *p*-Chlorophenoxyisobutyric acid impairs auxin response in *Arabidopsis* root. Plant Physiol 133:1135–1147

Roig-Villanova I, Bou-Torrent J, Galstyan A, Carretero-Paulet L, Portolés S, Rodríguez-Concepción M, Martínez-García JF (2007) Interaction of shade avoidance and auxin responses: a role for two novel atypical bHLH proteins. EMBO J 26:4756–4767

Saitoh A, Takase T, Kitaki H, Kiyosue T (2015a) Gene expression profile of *Arabidopsis* plants that overexpress *ZEITLUPE/LOV KELCH PROTEIN1*: up-regulation of auxin-inducible genes in hypocotyls. Plant Biotechnol. doi:10.5511/plantbiotechnology.15.0615b

Saitoh A, Takase T, Kitaki H, Miyazaki Y, Kiyosue T (2015b) Gene expression profile of *zeitlupe/lov kelch protein1* T-DNA insertion mutants in *Arabidopsis thaliana*: downregulation of auxin-inducible genes in hypocotyls. Plant Signal Behav 10:e1071752

Schultz TF, Kiyosue T, Yanovsky M, Wada M, Kay SA (2001) A role for LKP2 in the circadian clock of *Arabidopsis*. Plant Cell 13:2659–2670

Shikata H, Hanada K, Ushijima T, Nakashima M, Suzuki Y, Matsushita T (2014) Phytochrome controls alternative splicing to mediate light responses in *Arabidopsis*. Proc Natl Acad Sci USA 111:18781–18786

Somers DE, Schultz TF, Milnamow M, Kay SA (2000) *ZEITLUPE* encodes a novel clock-associated PAS protein from *Arabidopsis*. Cell 101:319–329

Somers DE, Kim WY, Geng R (2004) The F-box protein ZEITLUPE confers dosage-dependent control on the circadian clock, photomorphogenesis, and flowering time. Plant Cell 16:769–782

Spartz AK, Lee SH, Wenger JP, Gonzalez N, Itoh H, Inzé D, Peer WA, Murphy AS, Overvoorde PJ, Gray WM (2012) The *SAUR19* subfamily of *SMALL AUXIN UP RNA* genes promote cell expansion. Plant J 70:978–990

Spartz AK, Ren H, Park MY, Grandt KN, Lee SH, Murphy AS, Sussman MR, Overvoorde PJ, Gray WM (2014) SAUR inhibition of PP2C-D phosphatases activates plasma membrane H^+-ATPases to promote cell expansion in *Arabidopsis*. Plant Cell 26:2129–2142

Staswick PE, Serban B, Rowe M, Tiryaki I, Maldonado MT, Maldonado MC, Suza W (2005) Characterization of an *Arabidopsis* enzyme family that conjugates amino acids to indole-3-acetic acid. Plant Cell 17:616–627

Takase T, Nishiyama Y, Tanihibashi H, Ogura Y, Miyazaki Y, Yamada Y, Kiyosue T (2011) LOV KELCH PROTEIN2 and ZEITLUPE repress *Arabidopsis* photoperiodic flowering under non-inductive conditions, dependent on FLAVIN-BINDING KELCH REPEAT F-BOX1. Plant J 67:608–621

Takase T, Miyazaki Y, Yasuhara M, Mitsui S, Kiyosue T (2015) Pleiotropic phenotype of transgenic *Arabidopsis* plants that produce the LOV domain of LOV KELCH PROTEIN2 (LKP2). Plant Biotechnol doi:10.5511/plantbiotechnology.15.0808b

Tanaka K, Nakamura Y, Asami T, Yoshida S, Matsuo T, Okamoto S (2003) Physiological roles of brassinosteroids in early growth of *Arabidopsis*: brassinosteroids have a synergistic relationship with gibberellin as well as auxin in light-grown hypocotyl elongation. J Plant Growth Regul 22:259–271

Tiwari SB, Wang XJ, Hagen G, Guilfoyle TJ (2001) AUX/IAA proteins are active repressors, and their stability and activity are modulated by auxin. Plant Cell 13:2809–2822

Valvekens D, Van Montagu M, Van Lijsebettens M (1988) *Agrobacterium tumefaciens*-mediated transformation of *Arabidopsis thaliana* root explants by using kanamycin selection. Proc Natl Acad Sci USA 85:5536–5540

Vandenbussche F, Verbelen JP, van der Straeten D (2005) Of light and length: regulation of hypocotyl growth in *Arabidopsis*. BioEssays 27:275–284

Woodward AW, Bartel B (2005) Auxin: regulation, action, and interaction. Ann Bot 95:707–735

Yasuhara M, Mitsui S, Hirano H, Takanabe R, Tokioka Y, Ihara N, Komatsu A, Seki M, Shinozaki K, Kiyosue T (2004) Identification of ASK and clock-associated proteins as molecular partners of LKP2 (LOV kelch protein 2) in *Arabidopsis*. J Exp Bot 55:2015–2027

Yoshimoto K, Jikumaru Y, Kamiya Y, Kusano M, Consonni C, Panstruga R, Ohsumi Y, Shirasu K (2009) Autophagy negatively regulates cell death by controlling NPR1-dependent salicylic acid signaling during senescence and the innate immune response in *Arabidopsis*. Plant Cell 21:2914–2927

Zoltowski BD, Imaizumi T (2014) Structure and function of the ZTL/FKF1/LKP2 group proteins in *Arabidopsis*. Enzymes 35:213–239

V. 研究課題 3 「光を利用した生命機能の解明と発がん制御技術の開発」

本課題では、光を様々な形で利用して、生命現象の解明やがんの治療に役立てようとして研究を進めた。具体的には、がん治療法の一つである中性子照射の効率を高めるために「ホウ素脂質」を開発し、それを組み込んだナノカプセルをがん移植マウスに投与して、腫瘍の消失がみられた。また先進的な光学顕微鏡を独自に開発し、マイコプラズマの滑走運動を 3 次元的に観測する手法を開発したり、最小の回転モーターである F_1-ATPase のサブユニットの構造変化を明らかにした。一方、分裂酵母を用いて、細胞質分裂の *in vitro* 系を開発し、収縮環の働きを詳細に調べ、さらに超解像顕微鏡の利用によって収縮環の形成過程におけるミオシンとアクチン繊維の位置関係を明らかにする可能性を示した。さらにタンパク質分解酵素であるズブチリシンを阻害しうる 12 残基のペプチドを既にファージディスプレイ法で選別していたが、そのペプチドのアミノ酸を置換することにより、より強く結合するペプチドを探索し、ズブチリシンとの複合体の結晶構造を解こうとした。以下、これらの研究について、それぞれの研究担当者からの解説と業績リスト、そして代表的な論文2編ずつを記載する。

光を利用した生命機能解明とがん治療

教授　中村　浩之
助教　佐藤　伸一

[目的]

生きた細胞内で標的タンパク質を化学修飾することは、生体機能の解明だけでなく、新しい機能を付加できることから、最近盛んに研究されている。これまでは、遺伝子工学的に標的タンパク質遺伝子に蛍光タンパク質の遺伝子を導入し、細胞内で発現させる方法が一般的であったが、この手法では時間がかかるだけでなく、この導入する蛍光タンパク質が立体的に大きく、標的タンパク質が本来の機能を果たさないなどの問題点があった。それに対して、化学的分子修飾（ケミカルラベリング）によるタンパク質への機能付加は細胞内に既に存在するタンパク質を標的とし、遺伝子導入により強制的にタンパク質を発現させる分子生物学的手法とは一線を画す手法であり、ケミカルラベリングにしか成し得ないメリットがある。タンパク質中のアミノ酸残基への分子修飾法の開発は、生物学、生化学、ケミカルバイオロジーといった幅広い研究分野で有用な新たな実験手法の提供を目的とするものである。これまで用いられてきたタンパク質化学修飾法のほとんどは求電子的試薬を使って、主に Cys, Lys といった求核的アミノ酸残基との間に共有結合を形成するものであった。標的タンパク質選択的な分子修飾という点に着目すれば、求電子剤の反応性の高さゆえの非特異的結合が問題となることも多い。近年、光の特性を利用した生命機能の制御技術が精力的に研究され、飛躍的な進展を遂げている。本研究では、光を利用した生命機能解明を１つの研究課題とし、光応答性一電子酸化触媒による新規タンパク質修飾法を開発し、標的タンパク質選択的ケミカルラベリング法へと発展させることを目的とする。

また、光を用いたがん治療研究として、中性子捕捉療法のための新しいホウ素薬剤開発を目的として研究を進めた。中性子捕捉療法は、低エネルギーである熱・熱外中性子がホウ素との核反応により生ずる強力な粒子線を用いてがん細胞を殺傷する治療法である。がん部位へホウ素デリバリーと中性子線のダブルターゲティングが可能であることから、正常組織へのダメージもきわめて低く、治療後の患者への負担が極めて小さい特徴をもつ。我が国では、世界で初めて BNCT 用小型加速器の開発に成功し、2012 年からホウ素薬剤 BPA と加速器を用いた脳腫瘍ならびに頭頚部がんを対象とした第１相臨床試験が始められ、2016 年からは第２相臨床試験が計画されている。一方で、BPA 非感受性がん患者も多いことから、こういった患者への適応拡大を目的に、次世代ホウ素デリバリーシステムの構築を目的とする。

[結果と考察]

１．光を利用した生命機能解明

本研究では、標的のタンパ光触媒としてルテニウムービピリジル錯体に着目した。$Ru(bpy)_3$ 錯体は光照射刺激依存的に一電子酸化反応を触媒し、チロシルラジカルを生成することが知られている。そこで、光増感触媒に $Ru(bpy)_3$ 錯体を用いることとし、標的タンパク質に選択的に結合するリガンドにこの光増感触媒を導入すれば、この光増感触媒（local

environmental single electron transfer catalyst (LESC)と名付けた）によって標的タンパク質の Tyr 残基上に選択的にラジカルを発生させることができる。そのチロシルラジカルと選択的に反応する分子（演者らは tyrosyl radical trapper (TRT)と名付けた）を設計することで、標的タンパク質を化学修飾することができる。種々の TRT 構造をスクリーニングした結果、*N*,*N*-dimethyl amino-*N*'-acyl phenylenediamine 構造（図 1）が Tyr 残基と光触媒の活性化条件において効率的に縮合反応を起こすこと見い出した。本ラベル化反応は精製タンパク質のラベル化にも適用できることが分かったので、次に標的タンパク質の選択的ラベル化反応について検討した。リガンド連結型の Ru 錯体を用いて一電子酸化触媒となる Ru 錯体をリガンド親和性標的タンパク質に近接させることで、短寿命のチロシルラジカル生成 - トラップ反応を標的近傍で選択的に触媒することができると考えた。炭酸脱水酵素（CA）のリガンドであるスルホン酸アミドを光増感触媒 $Ru(bpy)_3$ 錯体に結合した LESC およびビオチンを結合させた TRT を用いて、マウス赤血球中のタンパク質混在系の中で CA を選択的にラベル化することに成功した（図 2）[1]。

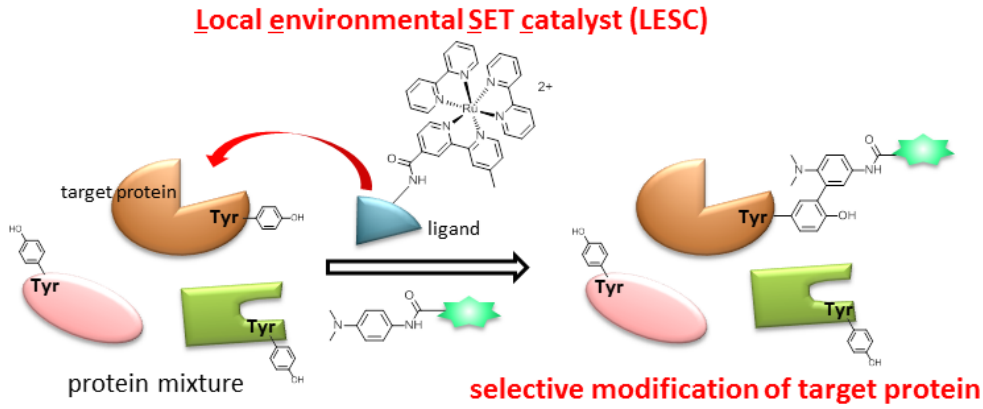

図 1. 光増感触媒の設計と生細胞内標的タンパク質修飾の戦略

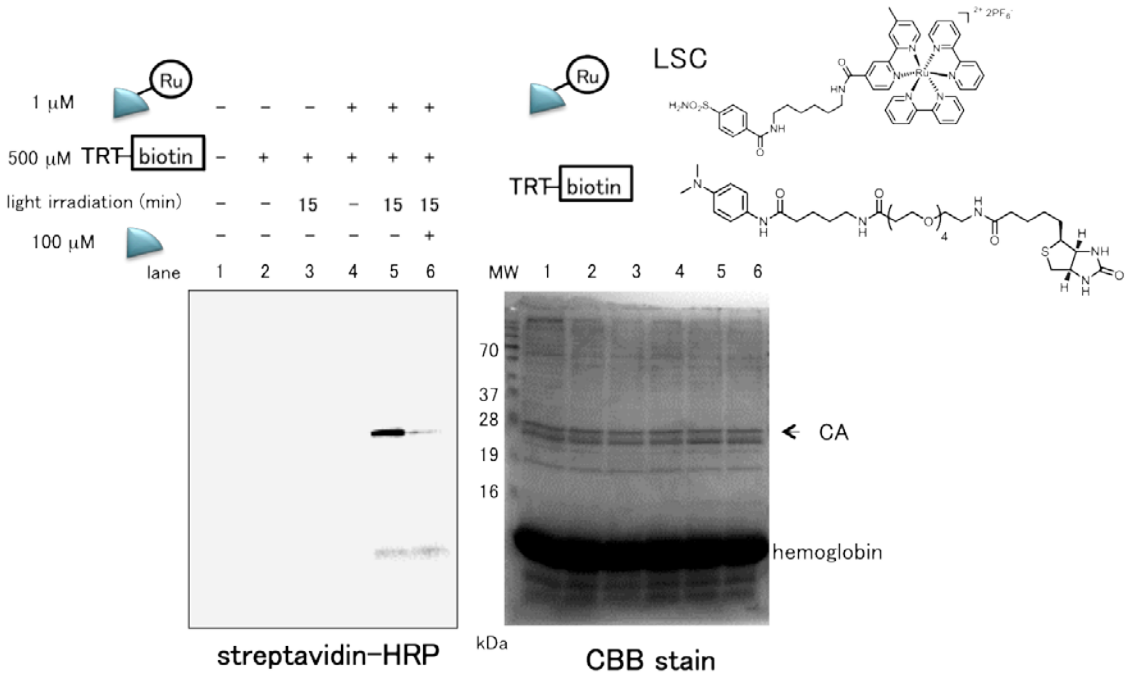

図 2. マウス赤血球中における炭酸脱水酵素（CA）の選択的ラベル化

また、LESC を用いることにより、標的タンパク質を選択的に酸化させて不活性化させる「タンパク質ノックダウン法」の開発にも成功した[2)]。

２．放射光を利用したがん治療：中性子捕捉療法

中性子捕捉療法への有効なホウ素デリバリーシステムとして、本研究ではリポソームを用いる戦略に着目した[3)]。リポソームとは，細胞などの生体膜を構成している成分であるリン脂質から形成された脂質二分子膜の人工ナノカプセルである。がん組織にある新生血管は、正常組織の血管に比べて物質透過性が高いため、200 nm より小さい粒子はより多くがん組織に透過・移行し、さらに、がん組織ではリンパ管による薬剤の回収機構が不完全なため、高分子化合物はがん組織内に滞留する。この現象は“Enhanced permeation and retention effect (EPR 効果)”と呼ばれ、1986 年に松村・前田（熊本大学）によって発見された[4)]。現在のナノ粒子を用いたドラッグデリバリーシステム（DDS）の根幹となっている多面体構造のホウ素イオンクラスター内封リポソーム製剤を用いると、高い治療効果を得られる可能性が示されてきた。その一方で、リポソームに内封されるホウ素薬剤濃度は、浸透圧の問題から限界があると同時に、リポソーム膜安定性の問題が生じた。我々は、これらの問題点に対し、２つの戦略により克服を試みた。１つは、ホウ素脂質リポソームの開発である。リポソームの脂質二分子膜は、分子間相互作用により自己集合化しているため密度が高いため、この二分子膜へホウ素分子を導入できれば、非常に高濃度でホウ素をデリバリーできると考えられる。そこで、生体膜を構成しているリン脂質の構造を基に二本鎖ホウ素イオンクラスター脂質を分子設計・合成し（図３）、世界初のホウ素脂質リポソームの開発に成功している[5)]。本研究では、さらにリポソーム膜内にもホウ素化合物を導入させることで、ホウ素高集積化に成功し、大腸がん細胞移植マウスを用いた実験では、リポソーム投与量を BSH 内封リポソームの５分の１においても、高い BNCT 抗腫瘍効果が得られ
た[6)]。

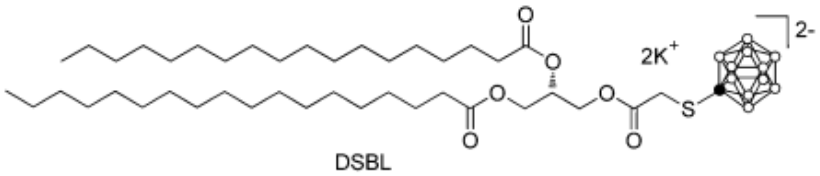

図 3. ホウ素脂質の化学構造

もう１つの戦略は、BSH をより高濃度で内封する技術の開発である。筆者らは、BSH が負電荷をもつイオンクラスターであるため、リポソームの構成成分であるリン脂質の正電荷をもつコリン部位と相互作用し、このことによってリポソーム膜が不安定化され、内封効率を下げていると考えた。そこで、BSH のカウンターカチオンを種々検討したところ、ナトリウムからスペルミジニウムカチオンに置き換えたときに、非常に効率よく BSH が内封されることを見出した（図 4)。大腸がん細胞移植マウスを用いた実験では、リポソーム投与量を BSH 内封リポソームの７分の１においても、高い BNCT 抗腫瘍効果を得ることに成功した[7)]。現在、これらのホウ素高集積化リポソームを用いて、実用化に向けた研究を進めている。

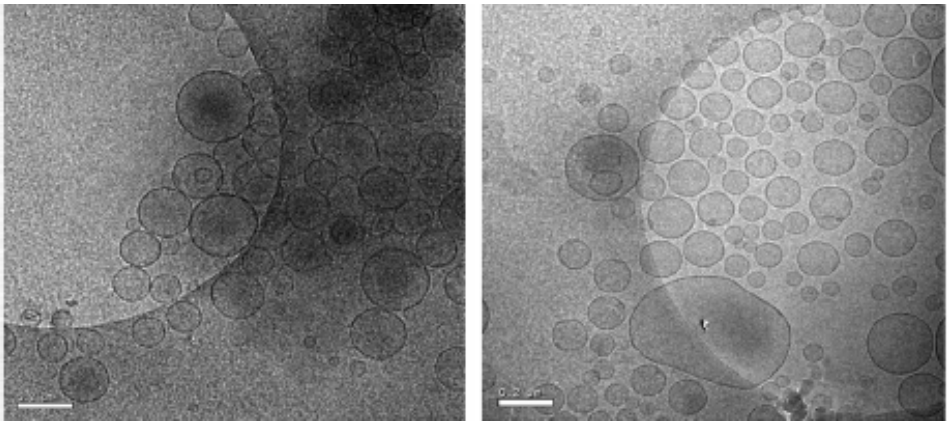

図４. ナトリウムカチオン（左）およびスペルミジウムカチオン（右）
ホウ素クラスター内封リポソームの電子顕微鏡写真

[まとめ]

光触媒による生命機能解明のための新しいケミカルプローブの開発研究では、標的タンパク質内のチロシンへの新たなラベル化法の開発ならびに局所環境での活性酸素誘導によるタンパク質ノック段法へ展開できる成果を得た。また、ホウ素高集積化ナノカプセルを用いることで、中性子捕捉治療によりがん移植マウスのがん増殖を完全に抑制する成果を得た。今後、ホウ素高集積化ナノカプセルの中性子捕捉療法への実用化に向けた研究開発を医療機関と連携して引き続き進める。

[参考文献]

1. Sato, S.; Nakamura, H. Ligand-directed Selective Protein Modification Based on Local Single Electron Transfer Catalysis *Angew. Chem. Int. Ed.* ***52***, 8681-8684 (2013).
2. S. Sato, K. Morita, Nakamura, H., , Regulation of target protein knockdown and labeling using ligand-directed Ru(bpy)3 photocatalyst *Bioconjugate Chem.* ***26***, 250-256 (2015).
3. Nakamura, H. Boron lipid-based liposomal boron delivery system for neutron capture therapy: recent development and future perspective, *Future Med. Chem*, ***5***, 715-730 (2013).
4. Matsumura, Y., and Maeda, H. A new concept for macromolecular therapeutics in cancer chemotherapy: mechanism of tumoritropic accumulation of proteins and the antitumor agent smancs, *Cancer Res*, ***46***, 6387-92 (1986).
5. Nakamura, H., Miyajima, Y., Takei, T., Kasaoka, S., and Maruyama, K., Synthesis and vesicle formation of a nido-carborane cluster lipid for boron neutron capture therapy, *Chem. Commun.*, 1910-1 (2004).
6. Koganei, H., Ueno, M., Tachikawa, S., Tasaki, L., Ban, H. S., Suzuki, M., Shiraishi, K., Kawano, K., Yokoyama, M., Maitani, Y., Ono, K., and Nakamura, H., Development of High Boron Content Liposomes and Their Promising Antitumor Effect for Neutron Capture Therapy of Cancers, *Bioconjug. Chem*, ***24***, 124-132(2013).
7. Tachikawa, S., Miyoshi, T., Koganei, H., El-Zaria, M. E., Viñas, C., Suzuki, M., Ono, K., Nakamura, H., Spermidinium closo-dodecaborate-encapsulating liposomes as efficient boron delivery vehicles for neutron capture therapy, *Chem. Commum.* ***50***, 12325-12328 (2014).

［原著論文］

1) Li,G., and Nakamura, H. Synthesis of 2-Indolyltetrahydroquinolines via Zinc(II)-Catalyzed Intramolecular Hydroarylation-Redox Cross-Dehydrogenative Coupling of *N*-Propargylanilines with Indoles **Angew. Chem. Int. Ed.** *54*, In press.
2) M, Yamauchi., Honda, N., Hazama, H., Tachikawa, S., Nakamura, H., Kaneda, Y., and Awazu, K. Effective Photodynamic Therapy in Drug-Resistant Prostate Cancer Cells Utilizing a Non-Viral Antitumor Vector **Laser Ther**. In press.
3) Sasai, M., Nakamura, H., Sougawa, N., Sakurai, Y., Suzuki, M., Matsuyama, A., and Lee, C. M. (2016) Novel hyaluronan formulation enhances the efficacy of boron neutron capture therapy for murine mesothelioma **Anticancer Res.** *36(3),* 907-911.
4) Ban, H.S., Uto, Y., Won, M., and Nakamura, H. (2016) Hypoxia-inducible factor (HIF) inhibitors: a patent survey (2011-2015) **Exp. Opin. Ther. Pat.** *26(3),* 309–322.
5) Ina, M., Yamauchi, M., Honda, N., Hazama, H., Tachikawa, S., Nakamura, H., Nishida, T., Yasuda, H., Kaneda Y., and Awazu, K. (March 2, 2015) Photodynamic therapy using hemagglutinating virus of Japan envelope (HVJ-E): a novel therapeutic approach for the treatment of hormone antagonistic prostate cancer, **Proc. SPIE 9308**, *Optical Methods for Tumor Treatment and Detection: Mechanisms and Techniques in Photodynamic Therapy XXIV*, 930814doi:10.1117/12.2080692
6) Tachikawa, S., Sato, S., Hazawa, H., Kaneda, Y., Awazu, K., and Nakamura, H. (2015) Localization-Dependent Cell-Killing Effects of Protoporphyrin (PPIX)-Lipid Micelles and Liposomes in Photodynamic Therapy **Bioorg. Med. Chem.** *23(24),* 7578-7584.
7) Sato, S., Nakamura, K., and Nakamura, H. (2015) Tyrosine-Specific Chemical Modification with *in situ* Hemin-Activated Luminol Derivatives **ACS Chem. Biol.** *10* (11), pp 2633–2640.
8) Sato, A., Itoh, T., Imamichi, S., Kikuhara, S., Fujimori, H., Hirai, T., Saito S., Sakurai, Y., Tanaka, H., Nakamura, H., Suzuki, M., Murakami, D., Baiseitov, K. Berikkhanova, Z. Zhumadilov, Imahori, Y., Itami, J., Ono, K., Masunaga, S., and Masutani, M. (2015) Proteomic analysis of cellular response induced by boron neutron capture reaction in human squamous cell carcinoma SAS cells, **Appl. Radiat. Isotope**, *106,* 213-219
9) Koganei, H., Tachikawa, S., M. E. El-Zaria., Nakamura, H., Synthesis of Oligo-*closo*-dodecaborates by Hüisgen Click Reaction as Encapsulated Agents for Preparation of High-Boron-Content Liposomes for Neutron Capture Therapy **New J. Chem**. *39*, 6388 – 6394.
10) Li, G., Azuma, S., Minegishi., and H. Nakamura, H. (2015) Synthesis and Biological Evaluation of *meta*-Carborane-Containing phenoxyacetanilides as Inhibitors of Hypoxia-Inducible Factor (HIF)-1 Transcriptional Activity
J. Organomet. Chem. *798*, 189–195 (2015). DOI:10.1016/j.jorganchem.2015.05.029
11) Minegishi, H., Futamura,Y., Fukashiro, S., Muroi, M., Kawatani, M., Osada,H., and Nakamura, H. (2015) Methyl 3-((6-methoxy-1,4-dihydroindeno[1,2-c]pyrazol-3-yl)amino) benzoate (GN39482) as a Tubulin Polymerization Inhibitor Identified by MorphoBase and ChemProteoBase Profiling Methods, **J. Med. Chem**. 58, 4230-4241.
12) Li, G., Azuma,S., Sato,S., Minegishi,H., and Nakamura, H. (2015) ortho-Carboranylphenoxyacetanilides as Inhibitors of Hypoxia-Inducible Factor (HIF)-1Transcriptional Activity and Heat Shock Protein (HSP) 60 Chaperon Activity **Bioorg. Med. Chem. Lett**. *25,* 2524-2628.
15) 山内将哉、本多典広、間久直、立川将士、中村浩之、金田安史(2015) 粟津邦男抗腫瘍効果を持つ非ウイルスベクター用いた薬剤耐性前立腺がん細胞に対する高効率な光線力学療法 **日本レーザー医学会誌**、*36(1),* 18-24.
16) Sato,S., Morita,K., and Nakamura, H. (2015) Regulation of target protein knockdown and labeling using ligand-directed Ru(bpy)3 photocatalyst **Bioconjugate Chem.** *26(2),* 250-256.
17) 中村浩之、ホウ素化合物・薬剤の歴史と現状
RADIOISOTOPES, *64(1)* 47-58 (2015) (平成 27 年 1 月 15 日発行)
DOI.org/10.3769/radioisotopes.64.47
18) Nakamura, H., Koganei, H., Miyoshi,T., Sakurai,Y., Ono,K., and Suzuki, M. (2015) Antitumor Effect of Boron Nitride Nanotubes in Combination with Thermal Neutron Irradiation on BNCT **Bioorg. Med. Chem. Lett**. *25(2),* 172-174.
19) Nakamura, H., Tazaki, L., Kanoh, D., and Sato, S. (2015) Diaryl-substituted carboranes as inhibitors of hypoxia inducible factor-1 transcriptional activity,

Pure Appl. Chem. *87(2),*145-154DOI: 10.1515/pac-2014-0911

20) 粟津邦男、金田安史、山内将哉、中村浩之 (2014)薬剤耐性前立腺がん細胞への PDT の検討 ＝非ウィルスベクターと PpIX 脂質を用いた新規光感受性薬剤の開発＝
月刊 光アライアンス　特集号「がんを抑え込む光線治療」 *25(9), 17-22.*

21) 立川将士、中村浩之 (2014)がん光線力学療法のための DDS 薬剤の開発　＝ポルフィリン脂質の開発とナノキャリアへの応用＝
月刊 光アライアンス　特集号「がんを抑え込む光線治療」 *25(9), 12-16.*

22) Tachikawa, S., Miyoshi, T., Koganei, H., M. E. El-Zaria, C. Viñas, Suzuki, M., Ono, K., and Nakamura, H. (2014) Spermidinium *closo*-dodecaborate-encapsulating liposomes as efficient boron delivery vehicles for neutron capture therapy
Chem. Commun. *50(82)* 12325 - 12328. DOI:10.1039/c4cc04344h

23) Tachikawa,S., M. E. El-Zaria, Inomata, R., Sato,S., and Nakamura, H. (2014) Synthesis of protoporphyrin–lipids and biological evaluation of micelles and liposomes
Bioorg. Med. Chem. *22(17)* 4745–4751.

24) Nakamura, H., H. S. Ban, Shimizu, K., Minegishi, H., and Sato, S., (2014) Design of Photoaffinity Probe Molecules for Identification and Modification of Target Proteins
J. Photopolym. Sci. Technol. *27(4),* 453-458.

25) Matsushima, S., Ohtsuka, K., Ohnishi, H., Fujiwara, M., Nakamura, H., Morii, T., Goto, H., and Watanabe, T. (2014) V843I, a lung cancer predisposing *EGFR* mutation, is responsible for resistance to EGFR tyrosine kinase inhibitors
J. Thor. Oncol. *9(9),* 1377-1384.

26) Sugiishi, T., Nakamura, H. (2014) Reactivity of Propargylic Amines in the Presence of Transition Metals **J. Syn. Org. Chem. Jpn**. *72(6),* 654-665.

27) C. Verdiá-Báguena, A. Alcaraz, V. M. Aguilella, A. M. Cioran, Tachikawa, S., Nakamura, H., F. Teixidor, and Clara Viñas (2014) Amphiphilic COSAN and I2-COSAN crossing synthetic lipid membranes: planar bilayers and liposomes
Chem. Commun. *50,* 6700-6703. DOI:10.1039/c4cc01283f

28) Nakamura, H., Tazaki, L., Kanoh, D., Sato, S., and H. H. Ban (2014) Diaryl-substituted ortho-carboranes as a new class of hypoxia inducible factor-1α inhibitors
J. Chem. Soc., Dalton Trans. *43(13),* 4941-4944.

29) Yamauchi, M., Honda, N., Hazama, H., Tachikawa, S., Nakamura, H., Kaneda,Y., and Awazu, K. (2014) A novel photodynamic therapy for drug resistant prostate cancer cells using porphyrus Envelope as a novel photosensitizer **Photodiagnosis and Photodynamic Therapy** *11(1),* 48-54.

31) Sato, S., and Nakamura, H. (2013) Ligand-directed Selective Protein Modification Based on Local Single Electron Transfer Catalysis
Angew. Chem. Int. Ed. *52,* 8681-8684.

32) Nakamura, H., Yasui,Y., and H. S. Ban (2013) Synthesis and Biological Evaluation of ortho-Carborane Containing Benzoxazole as an Inhibitor of Hypoxia Inducible Factor (HIF)-1Transcriptional Activity
J. Organomet. Chem. (*special issue*) *747*, 189-194.

34) Minegishi, H., Fukashiro, S., H. S. Ban., and Nakamura, H. (2013) Discovery of Indenopyrazoles as a New Class of Hypoxia Inducible Factor (HIF)-1 Inhibitors.
ACS Med. Chem. Lett. *4,* 297-301.

35) M. Bialek-Pietras, A. B. Olejniczak, Tachikawa, S., Nakamura, H., and Z. J. Lesnikowski. (2013) Towards new boron carriers for boron neutron capture therapy: metallacarboranes and their cholesterol conjugates. **Bioorg. Med. Chem.** *21,* 1136-1142.

36) Minegishi, H., Matsukawa,T., and Nakamura, H. (2013) Synthesis and Biological Evaluation of Diaryl-Substituted Carboranes as Inhibitors of Hypoxia Inducible Factor (HIF)-1 Transcriptional Activity **ChemMedChem**, *8,* 265-271.

37) Nakamura, H., Yasui, Y., Maruyama, M., Minegishi, H., H. S. Ban, and Sato, S. (2013) Development of Hypoxia-Inducible Factor (HIF)-1α Inhibitors: Effect of ortho-Carborane Substituents on HIF Transcriptional Activity under Hypoxia **Bioorg. Med. Chem. Lett.** *23,* 1455-1461.

38) Koganei, H., Ueno, M., Tachikawa, S., Tasaki, L., H. S. Ban., Suzuki, M., Shiraishi, K., Kawano, K., Yokoyama, M., Maitani,Y., Ono, K., and Nakamura, H. (2013) Development of High Boron Content Liposomes and Their Promising Antitumor Effect for Neutron Capture Therapy of Cancers **Bioconjugate Chem.** *24*, 124-132.

[総説等]

1. Nakamura, H. (2015) C(sp3)–H versus C(sp3)–C(sp) in Activation of Propargylic Amines under Transition-Metal Catalysis **Synlett**, 26(12), 1649-1664.
2. H. S. Ban and Nakamura, H. (2015) Boron-Based Drug Design Chem. Rec. 15, 616-635.
3. 中村浩之（監訳兼)、岩本武明、斎藤雅一、柴田高範、田中健、長澤和夫、西林仁昭、共訳(2015) ウェイド「有機化学」ソリューションマニュアル、丸善出版
4. 中村浩之（監訳兼)、岩本武明、斎藤雅一、柴田高範、田中健、長澤和夫、西林仁昭、共訳(2014) ウェイド「有機化学」上下巻、丸善出版
5. 中村浩之、柳衛宏宣 (2013) 第 7 章 7.1 中性子捕捉療法にける薬剤送達システム医学物理の理工学（下巻）上坂充、中川恵一、金井達明、西尾禎治、共編養賢堂 153-164 .
6. Nakamura, H. (2013) Boron Cluster Lipid Liposomes as New Vehicles for Boron Delivery System of Neutron Capture Therapy Future Med. Chem. *5(6),* 715-730.
7. Nakamura, H. (2013) Development of High Boron Content Liposomes and Their Promising Antitumor Effect for Neutron Capture Therapy **Yakugaku Zasshi**, *133(12)* 1297-1306.
8. Nakamura, H., and H. Minegishi. (2013) HSP60 as a drug target, **Curr. Pharm. Des.** *19,* 441-451.

［口頭発表］

1. 北村　捷、京極　信輔、Manjusha　Joshi、中村　浩之、岩田　耕一　ピコ秒時間分解けい光分光法で観測された単一成分脂質二重膜における不均一構造（学習院大理・東工大資源研）　日本化学会第 96 回年会（2016 年 3 月 24 日−27 日、同志社大学）
2. 佐藤　伸一、中村　公亮、中村　浩之　ルミノール誘導体を用いたチロシン残基選択的な化学修飾法開発　日本化学会第 96 回年会（2016 年 3 月 24 日−27 日、同志社大学）
3. 羽田野　兼資、佐藤　伸一、中村　浩之　光触媒を用いた Tyr 残基修飾反応における一電子移動範囲の解明　日本化学会第 96 回年会（2016 年 3 月 24 日−27 日、同志社大学）
4. 御舩　悠人、田中　浩士、中村　浩之、布施　新一郎 マイクロフローアミド結合形成法を基盤とするフェグリマイシンの全合成（東工大資源研・東工大院理工）　日本化学会第 96 回年会（2016 年 3 月 24 日−27 日、同志社大学）
5. 佐藤　伸一、中村　公亮、中野　洋文、中村　浩之　チロシン残基選択的化学修飾法を用いたチロシンホスファターゼ活性スクリーニング法の開発 日本化学会第 96 回年会（2016 年 3 月 24 日−27 日、同志社大学）
6. 中村浩之　外部エネルギーと局所増感型ナノデバイスによる低侵襲がん治療　LSC 研究発表会、**特別講演**（2016 年 3 月 18 日、神戸学院大学）
7. Nakamura, H., Development of Efficient Boron Delivery Nano Carriers for Neutron Capture Therapy , IAEA−Southern Tohoku Hospital Group Joint Workshop on BNCT, **Invited Lecture**（2016 年 3 月 7 日、郡山）
8. 中村浩之　ホウ素を使ってがんに挑む ～ホウ素創薬の最前線～　第８回「国際的キャリア展望に向けた生命化学研究者による講演会」**招待講演**（2016 年 1 月 27 日、岡山大学）
9. 佐藤伸一、中村公亮、中村浩之　ヘムを触媒とする酸化的チロシン修飾法開発とその応用 新学術領域「酸素生物学」＆「ダイイングコード」合同若手会議（2016 年 1 月 26−28 日、千葉）
10. Sato, S., Nakamura, K., and Nakamura, H., Heme−Catalyzed Tyrosine Click Reaction The 8th Takeda Science Foundation Symposium on PharmaSciences（2016 年 1 月 20−22 日、大阪）
11. Kikuchi, S., Kanoh, D., Sato, S., and Nakamura, H. Use of serum albumin as an efficient boron

delivery carrier for neutron capture therapy, The International Chemical Congress of Pacific Basin Societies 2015 (Pacifichem 2015), (2015 年 12 月 15–20 日、Honolulu, Hawaii)

12. Nakamura, H., Discovery of carboranylphenoxyacetanilides as inhibitors of heat shock protein (HSP) 60 chaperone activity, The International Chemical Congress of Pacific Basin Societies 2015,**Invited Lecture**, (Pacifichem 2015), (2015 年 12 月 15–20 日、Honolulu, Hawaii)
13. Nakamura, H. Development of boronated liposomes as efficient boron delivery vehicles for neutron capture therapy, The International Chemical Congress of Pacific Basin Societies 2015 (Pacifichem 2015), (2015 年 12 月 15–20 日、Honolulu, Hawaii)
14. Sato, S., Nakamura, K., and Nakamura, H. Tyrosine–selective chemical modification using single–electron–transfer catalyst The International Chemical Congress of Pacific Basin Societies 2015 (Pacifichem 2015), (2015 年 12 月 15–20 日、Honolulu, Hawaii)
15. Fuse, S., Mifune, Y., Tanabe, N., H. Nakamura., and Takahashi, T. Utilization of microflow technology for the site–selective modification of multifunctionalized molecules, The International Chemical Congress of Pacific Basin Societies 2015 (Pacifichem 2015), (2015 年 12 月 15–20 日、Honolulu, Hawaii)
16. Morita, T., Fuse, S., Matsumura, K., Sugiyama, H., Kobayashi, D., Tanaka, H., Nakamura, H., and Takahashi, T. Rapid synthesis of tri/tetraaryl–substituted pyrazoles via [3+2] cycloadditon and C–H direct arylation approaches, The International Chemical Congress of Pacific Basin Societies 2015 (Pacifichem 2015), (2015 年 12 月 15–20 日、Honolulu, Hawaii)
17. Nakamura, H., Overview and Prospect of Boron Agents for Neutron Capture Therapy, 1st Academic meeting for Taiwan’s Society of Neutron Capture Therapy, **Invited Lecture**,(2015 年 12 月 5 日、Taipei)
18. 小竹佑磨、布施新一郎、御舩悠人、中村浩之、田中浩士　マイクロフローリアクター内での四連続反応によるαアリールカルボニル化合物合成法の開発、第 70 回記念有機合成化学協会関東支部シンポジウム–新潟（長岡）シンポジウム（2015 年 11 月 21 日–22 日、長岡工業高等専門学校）
19. Nakamura, H., Anticancer Drug Design Using the Element Boron, Hankuk University of Foreign Studies, **Invited Seminar**, (2016 年 11 月 19 日、Korea)
20. Nakamura,H., Sato, S., and Morita., K. Target Protein–Selective Labeling and Inactivation Using Ligand–Directed Ru(bpy)3 Photocatalysts, 1st Asian Conference on Chemosensors &; Imaging Probes (2015 年 11 月 16 日–18 日、Korea)
21. Sato,S., Nakamura, K., and Nakamura, H., Heme–Catalyzed Tyrosine Click Reaction with Luminol Derivatives, 1st Asian Conference on Chemosensors & Imaging Probes, **Invited Lecture** ,(2015 年 11 月 16 日–18 日、Korea)
22. 盛田大輝、田中浩士、中村浩之、布施新一郎　４連続の直接アリール化による４置換ピラゾールの合成とその発光特性　第 108 回有機合成シンポジウム（2015 年 11 月 5 日–6 日、早稲田大学）
23. Nakamura, H., Highly Boronated Liposomes as Efficient Boron Delivery Vehicles for Neutron Capture Therapy　ZING Conferences, **Invited Lecture**,(2015 年 10 月 4 日–7 日、Spain)
24. 御舩悠人、布施新一郎、田中浩士、中村浩之、高橋孝志 カルボン酸の迅速かつ強力な活性化を基盤とするマイクロフローペプチド合成法の開発とフェグリマイシンの合成研究　第 32 回有機合成化学セミナー（ 2015 年 9 月 15 日–17 日、湯河原）
25. 中村浩之 ホウ素をつかってがんに挑む ～ホウ素創薬の最前線～　工学院大学　化学応用学特論 A、(集中講義)（2015 年 9 月 8 日、東京）
26. 盛田大輝、田中浩士、中村浩之、布施新一郎　連続的 C–H 結合直接アリール化による４置換ピラゾールの合成　第 62 回有機金属化学討論会（2015 年 9 月 7 日–9 日、関西大学、吹田）
27. 中村浩之　何故新しいホウ素薬剤は開発されないのか？　―これからの Boron Delivery System を考える―　第 12 回日本中性子捕捉療法学会学術大会(招待講演)（ 2015 年 9 月 4 日–5 日神戸学院大学、神戸）
28. 菊地　俊介、佐藤　伸一、中村　浩之　血清アルブミンを用いた新しいホウ素送達法の開

発　第 12 回日本中性子捕捉療法学会学術大会（2015 年 9 月 4 日−5 日、神戸学院大学、神戸）

29. 立川将士、佐藤伸一、間久直、金田安史、粟津邦男、 中村浩之　ポルフィリン脂質リポソームの細胞内局在と PDT 効果　第 25 回日本光線力学学会　学術講演会（2015 年 7 月 10 日−11 日、新宿）
30. 中村浩之、Clara Vinas、鈴木実、小野公二、立川将士　ホウ素高集積化リポソームを指向した内封ホウ素薬剤開発　第 31 回日本 DDS 学会学術集会（2015 年 7 月 2 日−3 日、新宿）
31. 中村浩之　光を使って生命機能を探る・操る　有機合成化学協会関東支部ミニシンポジウム（招待講演）（2015 年 6 月 27 日−28 日、神奈川）
32. 中村浩之　インデノピラゾール骨格を基軸とした創薬研究　平成 27 年度 環境調和材料・デバイスプロジェクトグループ(G4)分科会（2015 年 6 月 19−20 日、千歳）
33. 李 廣哲、峯岸 秀充、佐藤 伸一、中村 浩之　カルボラン骨格を有する新規 Hsp60 阻害剤の開発　第 19 回日本がん分子標的治療学会学術集会（2015 年 6 月 10 日−12 日、松山）
34. 佐藤伸一、中村公亮、中村浩之　ルミノール誘導体を用いたチロシン残基に選択的な共有結合形成反応の開発　日本ケミカルバイオロジー学会第 10 回年会（2015 年 6 月 10 日−12 日、東北大学、仙台）
35. 中村浩之、峯岸秀光、室井誠、二村友史、川谷誠、長田裕之　高い細胞増殖阻害を有するインデノピラゾールの発見とプロファイリング法による阻害機構の解明　新学術領域研究「天然物ケミカルバイオロジー」第 8 回公開シンポジウム（2015 年 6 月 8 日−9 日、東北大学、仙台）
36. Nakamura, H., Development of Liposomes for Efficient Boron Neutron Capture Therapy, 15th International Congress of Radiation Research (ICRR2015), **Invited Lecture**, (2015 年 5 月 25−29 日、Kyoto)
37. 中村公亮、佐藤伸一、中村浩之　Luminol 誘導体を用いた鉄触媒存在下での Tyr 残基高選択的ラベル化反応 第 69 回有機合成化学協会関東支部会シンポジウム（2015 年 5 月 16 日、横浜）
38. 中村浩之　高い細胞増殖阻害を有するインデノピラゾール化合物の発見とその作用機序解明 平成 26 年度アライアンス成果報告会（2015 年 4 月 21 日、九州大学、福岡）
39. 峯岸秀充、中村浩之　ベンゾフロピラゾール化合物の合成と HIF-1 転写活性への影響 日本化学会第 95 回年会（2015 年 3 月 26 日−29 日、船橋）
40. 大内俊明、峯岸秀充、中村浩之　イミダゾピリジン骨格を有する新規 HIF-1α阻害剤の開発 日本化学会第 95 回年会（2015 年 3 月 26 日−29 日、船橋）
41. 菊地俊介、加納大輔、佐藤伸一、中村浩之　中性子補足療法のための血清アルブミンを用いた新しいホウ素送達法の開発 日本化学会第 95 回年会（2015 年 3 月 26 日−29 日、船橋）
42. 中村公亮、佐藤伸一、中村浩之　ルミノール誘導体を用いた鉄触媒存在下での Tyr 残基特異的タンパク質ラベル化反応　日本化学会第 95 回年会（2015 年 3 月 26 日−29 日、船橋）
43. Nakamura, H., Development of Liposomes for Efficient Boron Neutron Capture Therapy **Invited Lecture** 15th International Congress of Radiation Research (ICRR2015), （2015 年 3 月 25 日−29 日、Kyoto）
44. 佐藤伸一、森田耕平、中村浩之　リガンド連結型 Ru 光触媒を用いたタンパク質ノックダウンとラベル化の制御　日本薬学会第 135 回年会（2015 年 3 月 25 日−28 日、神戸）
45. Nakamura, H., Development of Chemical Tools for Target Protein-Selective Identification and Selective Modification **Invited Lecture** at Indian Institute of Science, Bangalore, Bangalore (2015 年 3 月 10 日、India)
46. Nakamura, H., Development of Chemical Tools for Target Protein-Selective Identification and Selective Modification **Invited Lecture** at Jawaharl Nehru Centre for Advanced Scientific Research(JNCASR) Bangalore (2015 年 3 月 9 日、India)
47. Sato, S., Morita, K., and Nakamura, H., Development of Ligand-directed Ru(bpy)3 Photocatalysts for Target Protein Knockdown and Labeling　An International Symposium on Recent Advances in Chemistry (REACH-2015), **Plenary Lecture**, Shillong (2015 年 3 月 3−5 日、India)
48. Nakamura, H., Development of Chemical Tools for Target Protein-Selective Identification and

Modification **Invited Lecture** at Indian Institute of Technology, Guwahati (2015 年 3 月 2 日、India)

49. 中村浩之　DDS によるがん治療の最前線　川崎医科大学川崎医学会セミナー、**招待講演**（2015 年 2 月 26 日、倉敷）
50. 中村浩之　ホウ素でがんに挑む　第一三共株式会社品川研究開発センターセミナー、**招待講演**（2015 年 2 月 20 日、東京）
51. Inai, M., Yamauchi, M., Honda, N., Hazama, H., Tachikawa, T., Nakamura, H., Kaneda,Y., and Awazu, K., Therapeutic effect of porphyrus envelope-mediated photodynamic therapy: a novel therapeutic approach for the treatment of hormone antagonistic prostate cancer SPIE Photonics West BiOS (2015 年 2 月 7-12 日、San Francisco)
52. 中村浩之　がん細胞内部で放射線を発生させる次世代治療法ホウ素中性子捕捉療法　第３回次世代がん治療推進専門家養成プランシンポジウム（2015 年 1 月 25 日、東京）
53. Nakamura, H., Albumin-bound closo-Dodecaborate as a Promising Boron Carrier to Tumor The 2nd International Workshop on BNCT, **Invited Lecture** (2014 年 12 月 9―10 日、京 都)
54. 中村浩之　外部エネルギーによる生体内局所増感型ナノデバイスの開発? QOL の高い低侵襲がん治療を目指して　第 14 回東北大学多元物質科学研究所研究発表会、**招待講演**（2014 年 12 月 5 日、仙台）
55. 中村浩之　標的タンパク質のラベル化を指向した一電子酸化的チロシン残基修飾反応の開発佐藤伸一、第 68 回有機合成化学協会関東支部シンポジウム（新潟シンポジウム）（2014 年 11 月 29-30 日、新潟）
56. 山内 将哉、稲井 瑞穂、本多 典広、間 久直、立川 将士、中村 浩之、金田 安史、粟津 邦男　非ウイルスベクターを用いた薬剤耐性前立腺がんへの PDT における最適な薬剤調製条件の検討第 35 回　日本レー ザー医学会総会　（2014 年 11 月 29 日）
57. 山内将哉、稲井瑞穂、 本多典広、 間久直、 立川将士、 中村浩之、 金田安史、粟津邦男ホルモン拮抗ヒト前立腺がん細胞株(PC-3)における新規光感受性物質 porphyrus envelope 細胞内局在の検討　第 35 回　日本レーザー医学会総会　（2014 年 11 月 29 日）
58. 峯岸秀充、中村浩之　ベンゾフロピラゾール化合物による HIF-1 転写活性への影響　第 12 回がんとハイポキシア研究会（2014 年 11 月 21-22 日、佐賀）
59. Nakamura, H., Photoaffinity Labeling Molecules as Tools for Identification and Modification of Target Proteins Vietnam Malaysian International Chemical Congress (VMICC)2014, **Invited Lecture**, Hanoi (2014 年 11 月 7-9 日、Vietnam)
60. Sato, S., and Nakamaura, H., Target-selective Protein Modification Based on Local Environmental Single Electron Transfer Catalysis 18th Malaysian International Chemical Congress (18MICC), **Invited Lecture**, Kuala Lumpur(2014 年 11 月 3-5 日、Malaysia)
61. Nakamura, H., Development of liposomes for efficient boron neutron capture therapy International Symposium on Integrated Molecular/Materials Science and Engineering (IMSE2014), **Invited Lecture**, 南京（2014 年 11 月 1-3 日、中国）
62. 中村浩之　Target-selective Protein Modification Based on Local Environmental Single Electron Transfer Catalysis　新学術領域第 3 回国際シンポジウム（**招待講演**）（2014 年 10 月 28-29 日、大阪）
63. 中村浩之　効率的ホウ素デリバリーシステムの構築を目指して　平成 26 年度京都大学原子炉実験所専門研究会「BNCT の新展開-特殊な療法から一般的な療法への移行を目指して-」（2014 年 9 月 29-30 日、大阪）
64. Yamauchi, M., Honda, N., Hazama, H., Tachikawa, S., Nakamura, H., Kaneda, Y., and Awazu, K., A Photodynamic Therapy for Hormone Antagonistic Human Prostate Cancer Cells Utilizing Protoporphyrin IX Lipid Delivered by Hemagglutinating Virus of Japan Envelope (HVJ-E) as a Non-Viral Vector 16th International Congress on Photobiology (2014 年 9 月 8-12 日、Argentina)
65. Nakamura, H., Tazaki, L., Kanoh, D., Sato, S., and H. S. Ban., Diaryl-substituted carboranes as inhibitors of hypoxia inducible factor-1 transcriptional activity XV Internationl Meeting of Boron Chemistry, **Key Note Lecture** (2014 年 8 月 24-28 日、Prague, Zech)
66. Nakamaura, H., and Sato, S., Target-selective Protein Modification Using Ligand-conjugated Ru(bpy)3 Catalyst XXVI International Congress of Organometallic Chemistry (ICOMC-XXVI)

（2014 年 7 月 13-18 日、札幌）

67. 立川将士、佐藤伸一、間久直、粟津邦男、金田安史、中村浩之 がん光線力学的治療のためのポルフィリン脂質の開発とナノキャリアへの応用 創薬懇親会 2014 （2014 年 7 月 10-11 日、岐阜）
68. 東礎代子、李廣哲、佐藤伸一、中村浩之 カルボラン骨格を有する新規 Hsp60 阻害剤の開発 創薬懇親会 2014 （2014 年 7 月 10～11 日、岐阜）
69. Nakamura, H., H. S. Ban, Shimizu, K., Minegishi, H., and Sato, S., Design of Photoaffinity Proble Molecules for Identification and Modification of Target Proteins The 31st International Conference of Photopolymer Science and Technology Materials & Processes for Advanced Microlithography, Nanotechnology and Phototechnology (ICPST-31) **招待講演**（2014 年 7 月 8-11 日、千葉）
70. 加納大輔、立川将士、佐藤伸一、近藤夏子、鈴木実、桜井良憲、小野公二、中村浩之 生体高分子をキャリアとしたホウ素デリバリーシステム：マレイミドドデカボレート（MID）の開発と生物活性評価 第 11 回日本中性子捕捉療法学会学術大会（2014 年 7 月 5-6 日、大阪）
71. 立川将士、小金井逸人、菊池俊介、加納大輔、鈴木実、小野公二、中村浩之 リポソーム内へのホウ素高集積化を可能とするデンドリマー型新規リポソーム薬剤の開発 第 11 回日本中性子捕捉療法学会学術大会 （2014 年 7 月 5～6 日、大阪）
72. 野々口直助、宮武伸一、古瀬元雅、頼経英倫那、宮田とも、東保太一郎、藤田貢、中村浩之、川端信司、 梶本宜永、田村陽史、辻求、鳴海善文、黒岩敏彦 脳放射線壊死の病態解析と、治療実験（前臨床試験）を実施するためのラット脳放射線壊死も出るの開発 第 11 回日本中性子捕捉療法学会学術大会（2014 年 7 月 5-6 日、大阪）
73. 中村浩之 光増感分子を設計しタンパク質を探る・操る、そして創薬へ挑む 第 49 回天然物化学談話会 **招待講演**（2014 年 7 月 2-4 日、岡山）
74. 中村浩之 脱 SUMO 化酵素 SENP1 阻害剤 第 18 回日本がん分子標的治療学会学術集会（2014 年 6 月 26 日、仙台）
75. 山内将哉、本多典広、間久直、立川将士、中村浩之、金田安史、粟津邦男 非ウイルスベクターとプロトポルフィリン IX 脂質を用いた薬剤耐性前立腺がん細胞への新規光線力学療法の検討 第 24 回日本光線力学学会 学術講演会（2014 年 6 月 28 日～29 日、浜松）
76. Kanoh, Daisuke., Tachikawa, Shoji., Sato, Shinich., and H, Nakamura., Development of Albumin-bound closo-Dodecaborate and its Promising Boron Delivery Efficacy to Tumor 16th International Congress on Neutron Capture Therapy（2014 年 6 月 14 日-19 日、Finland）
77. 佐藤伸一、森田耕平、中村浩之リガンド連結型 Ru(bpy)3 触媒を用いた標的選択的タンパク質光分解とラベル化反応の制御日本ケミカルバイオロジー学会 第 9 回年会（2014 年 6 月 11 日、-13 日、大阪）
78. 中村公亮、佐藤伸一、中村浩之 Luminol 誘導体を用いた鉄触媒存在下での Tyr 残基高選択的ラベル化反応日本ケミカルバイオロジー学会 第 9 回年会（2014 年 6 月 11 日-13 日、大阪）
79. 中村浩之 光を用いて生命機能を探り操る 平成２６年度 アライアンス G4 分科会（2014 年 5 月 29 日、大阪）
80. 佐藤伸一、中村浩之 光触媒を利用した生体内標的タンパク質ラベル化法の開発 新学術領域研究「天然物ケミカルバイオロジー～分子標的と活性制御～」 第６回公開シンポジウム（2014 年 5 月 28-29 日、名古屋）
81. 峯岸秀充、深代真司、佐藤伸一、中村浩之 インデノピラゾール化合物による低酸素応答および細胞増殖に対する効果 文科省新学術領域研究・がん支援「化学療法基盤支援活動」第 3 回シンポジウム （2014 年 5 月 12 日、沖縄）
82. 佐藤伸一、安井友香、丸山美菜子、潘鉉承、中村浩之 カルボラン骨格を基盤とした新規 Hsp60 阻害剤の開発東礎代子、文科省新学術領域研究・がん支援「化学療法基盤支援活動」第 3 回シンポジウム （2014 年 5 月 12 日、沖縄）
83. 峯岸秀充、深代真司、潘鉉承、佐藤伸一、中村浩之 インデノピラゾール化合物による HIF-1 阻害活性および細胞増殖抑制作用機序の解明 日本薬学会第 134 年会（2014 年 3 月 27-30

日、熊本）

84. 立川将士、佐藤伸一、山内将哉、間久直、 栗津邦男、金田安史、 中村浩之　がん光線力学的療法のための PpIX 脂質導入ナノキャリアの開発とその効果　日本薬学会第 134 年会（2014 年 3 月 27-30 日、熊本）
85. 佐藤 伸一、中村 浩之　一電子酸化反応に基づくチロシン残基修飾法の開発と標的タンパク質選択的ラベル化法への応用　日本薬学会第 134 年会（2014 年 3 月 27-30 日、熊本）
86. 中村浩之　次世代低侵襲放射線治療：中性子捕捉療法用ホウ素デリバリーシステム開発 川崎スマートライフケア COI 拠点キックオフシンポジウム、**招待スピーチ** 、（2014 年 3 月 19 日、東京）
87. 峯岸秀充、深代真司、潘鉉承、中村浩之　インデノピラゾール化合物による HIF 阻害活性および細胞増殖抑制作用機序の解明　第 11 回がんとハイポキシア研究会　（2013 年 12 月 13-14 日、仙台）
88. Nakamura, H., Design of Photoaffinity Labeling Molecules: Tools for Identification and Modification of Target Proteins　International Conference on Emerging Trends in Chemical Sciences (IETC 2013)　**Plenary Lecture**　（ 2013 年 12 月 5 日-7 日、India）
89. 松川卓也、佐藤伸一、山乙教之、広野修一、中村浩之　ジフェニルウレア骨格を有する SENP1 阻害剤の開発　第 66 回有機合成化学協会関東支部シンポジウム（2013 年 11 月 30 日、東京）
90. 山内将哉、本田典広、間久直、立川将士、中村浩之、金田安史、栗津邦男　非ウィルスベクターとプロトポルフィリン IX 脂質を用いた薬剤耐性前立腺がん細胞への新規光線力学療法の検討　34 回日本レーザー医 学会総会（2013 年 11 月 9-10 日、東京）
91. 中村浩之　１人のがん患者を目の前にして有機化学者ができることとは何か？を考えたとき…　早稲田大学先進理工学部「実践的化学知セミナー」**招待講演**　（2013 年 11 月 8 日、東 京）
92. 中村 浩之　ホウ素創薬の最前線　CBI 学会 2013 年大会、**基調講演**（2013 年 10 月 31 日、東京）
93. Sato, S., and Nakamura, H., Target-selective Protein Labeling Based on Local Single Electron Transfer Catalysis　The 2nd International Symposium on Chemical Biology of Natural Products: Target ID and Regulation of Bioactivity　（2013 年 10 月 28-29、横浜）
94. 峯岸秀充、深代真司、潘鉉承、中村浩之　インデノピラゾール骨格を有する新規 HIF-1 阻害剤の開発と作用機序　第 57 回日本薬学会関東支部大会（2013 年 10 月 26 日、東京）
95. Sato, S., and Nakamura, H., Ligand-directed Selective Protein Modification Based on Local Environmental Single Electron Transfer Catalysis　International Chemical Biology Society 2nd Annual Conference ICBS2013 (2013 年 10 月 7-9 日、京都)
96. Koganei, H., Tachikawa, S., Suzuki, M., Ono, K., and Nakamura, H., Development of high boron content molecules and their liposome encapsulation for neutron capture therapy. 7th Young Researchers In Boron Neutron Capture Therapy Meeting. Granada　（2013 年 9 月 23－26 日、スペイン）
97. 佐藤 伸一、中村 浩之　標的指向性 Ru(bpy)3 錯体をもちいた局所環境での一電子酸化反応の制御と標的タンパク質選択ラベル化法への応用　第 60 回有機金属討論会（2013 年 9 月 12-14 日、東京）
98. 佐藤 聡、伊藤 祐、齋藤総一郎、藤森浩彰、平井崇久、今堀良夫、伊丹 純、村上康文、中村 浩之、鈴木 実、小野公二、増永慎一、 益谷美都子　ホウ素中性子線捕捉反応に対するがん細胞の応答機構のプロテオーム解析　第10回日本中性子捕捉学会（2013年9月7-8日、岡山）
99. 伊藤祐、佐藤　聡、齋藤総一郎、藤森浩彰、平井崇久、新井康仁、今堀良夫、伊丹純、村上康文、中村　浩之、鈴木　実、小野　公二 、増永慎一郎、益谷美都子　口腔がん細胞株 SAS におけるホウ素中性子線捕捉反応後の遺伝子発現解析　第 10 回日本中性子捕捉学会（2013 年 9 月 7-8 日、岡山）
100. 小金井　逸人、三好　達郎、鈴木 実、小野公二、中村 浩之　ホウ素ナノチューブ（BNNT）の中性子捕捉治療用薬剤としての可能性　第10回日本中性子捕捉学会（2013年9月7-8日、岡山）

101. 加納大輔、立川将士、佐藤伸一、中村　浩之　生体高分子への簡便なホウ素導入法の開発と DDS への展開　第 10 回日本中性子捕捉学会（2013 年 9 月 7-8 日、岡山）
102. 中村 浩之　がんを治す薬　―人々の夢実現に向けて―　読売サイエンスフォーラム ―学習院大学理学部の研究力―　ここまで来た！がん研究最前線　**招待講演**（2013 年 7 月 27 日、東 京）
103. 森田耕平、峯岸秀充、佐藤伸一、中村浩之　小分子化合物標的タンパク同定のための温和な条件下で切断可能なリンカー開発とその応用　日本ケミカルバイオロジー学会第 8 回年会（2013 年 6 月 19-21 日、東京）
104. 佐藤伸一、中村浩之　局所環境での一電子酸化反応を利用した標的タンパク質選択的ラベル化法の開発　日本ケミカルバイオロジー学会第 8 回年会（2013 年 6 月 19-21 日、東京）
105. 松川卓也、峯岸秀充、中村浩之　ジアリールカルボラン骨格を有する HIF-1 阻害剤の開発　第 17 回日本がん分子標的治療学会学術集会（2013 年 6 月 12-14 日、京都）
106. 立川将士、佐藤伸一、中村浩之　がん光線力学的治療のためのポルフィリン脂質の開発とナノキャリアーへの応用　第 23 回日本光線力学学会学術講演会 （2013 年 6 月 7-8 日、旭川）
107. Yamauchi, M., Honda, N., Hazama, H., Tachikawa, S., Nakamura, H., Kaneda, Y., and Awazu, K., Evaluation of protoporphyrin IX combined with lipid chains as a novel photosensitizer　The 14th World Congress of the International Photodynamic Association (2013 年 5 月 28 日−6 月 1 日、韓国)
108. 中村 浩之、松川卓也、佐藤 伸一　Manassantin 骨格を模倣したカルボラン含有低酸素誘導因子阻害剤の開発新学術領域「天然物ケミカルバイオロジー～分子標的と活性制御～」第 4 回公開シンポジウム（2013 年 5 月 28-29 日、つくば ）
109. 森田耕平、峯岸秀充、佐藤伸一、中村浩之　小分子化合物標的タンパク同定のための温和な条件下で切断可能なリンカー開発とその応用　新学術領域「天然物ケミカルバイオロジー～分子標的と活性制御～」第 4 回公開シンポジウム（2013 年 5 月 28-29 日、つくば）
110. Nakamura, H., Boron-Based Drug Design: Discovery of HIF-1 α Degradation Pathway Induced by Inhibiting HSP60 under Hypoxia　XVth Conference on Heterocycles in Bio-organic Chemistry (**Invited Lecture**) (2013 年 5 月 27－30 日、ラトビア)

Protein Modification

DOI: 10.1002/anie.201303831

Ligand-Directed Selective Protein Modification Based on Local Single-Electron-Transfer Catalysis**

*Shinichi Sato and Hiroyuki Nakamura**

Techniques for the visualization of target proteins in living systems are highly important to investigate the function, dynamics, localization, and crosstalk of individual proteins.[1] For this purpose, GFP fusion tags and monoclonal antibodies[2] are widely used for conventional protein labeling in molecular biology. Although these are useful methods for the real-time monitoring of target proteins in living systems, genetic manipulation is often necessary, and the conjugation of these proteins with relatively large labeling groups sometimes results in improper biophysical functions owing to undesirable interactions with other molecules.

The chemical modification of proteins with small-molecule probes has received much interest as an alternative powerful method for the study of individual proteins in their native environments. The key to this chemical modification is a bioorthogonal chemical reaction that enables the rapid and selective bioconjugation of proteins with nonnatural functional groups under physiological conditions. The most widely utilized bioorthogonal chemical reactions rely on electrophilic reagents that target nucleophilic amino acids, such as lysine and cysteine. In addition, the lysine-specific reductive alkylation using an iridium catalyst,[3] the conversion of cysteine into dehydroalanine,[4] and the radical addition reaction of cysteine with an alkene[5] were recently developed. Furthermore, remarkable attention has been paid to the modification of aromatic amino acids, such as tyrosine and tryptophan, by transition-metal-mediated processes,[6–8] the three-component Mannich reaction,[9] the click-like ene-type reaction,[10] the oxidative modification using cerium(IV) ammonium nitrate,[11] and the use of formylbenzene diazonium reagents.[12]

Although various bioorthogonal chemical reactions have been reported, there are still few reports regarding selective chemical modifications of native target proteins. Popp and Ball recently reported the site-specific protein modification of aromatic side chains with dirhodium metallopeptide catalysts.[13,14] Hamachi and co-workers pioneered a ligand-directed protein labeling method in which an electrophilic phenylsulfonate ester[15] or imidazole[16] group conjugated with ligand molecules specifically reacted with the nucleophilic amino acid side chains on the surfaces of target proteins through an S_N2-type reaction with the concomitant release of the ligand molecules. Furthermore, they were the first to demonstrate the catalytic target-selective modification using ligand-tethered *N*,*N*-dimethylaminopyridine (DMAP) catalysts (Figure 1 A), which allowed highly efficient transfer of acyl donor probes to the nucleophilic regions of the targeted protein through an S_N2-type reaction.[17,18] Herein, we report the development of a ligand-directed selective protein modification method based on local single-electron transfer catalysis (Figure 1 B). In this method, a single-electron transfer (SET) with a photocatalyst,[19,20] such as the ruthenium tris(2,2′-bipyridyl) complex ($[Ru(bpy)_3]^{2+}$), is essential for the generation of tyrosyl radicals[21,22] that react with tyrosyl radical trapping agents (TRTs) containing an *N*′-acyl-*N*,*N*-dimethyl-1,4-phenylenediamine through a catalytic oxidative radical addition reaction.

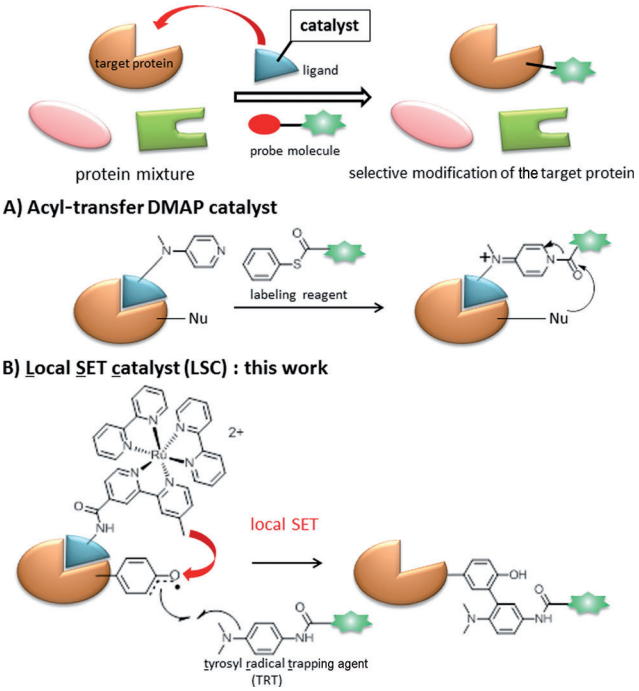

Figure 1. Ligand-directed selective protein modification. A) Acyl-transfer DMAP catalyst promotes the acylation of the nucleophilic regions of the target protein through an S_N2-type reaction. B) Local SET catalyst (LSC; this work) promotes the generation of tyrosyl radicals that react with tyrosyl radical trapping agents (TRTs) in the local environment of the probe on the target protein in the presence of visible light.

[*] Dr. S. Sato, Prof. H. Nakamura
Department of Chemistry, Faculty of Science, Gakushuin University
Mejiro, Tokyo 171-8588 (Japan)
E-mail: hiroyuki.nakamura@gakushuin.ac.jp

[**] This work was partially supported by a Grant-in-Aid for Scientific Research on Innovative Areas "Chemical Biology of Natural Products" from The Ministry of Education, Culture, Sports, Science and Technology (Japan).

Supporting information for this article is available on the WWW under http://dx.doi.org/10.1002/anie.201303831.

We first examined TRTs suitable for the SET-based addition reaction using angiotensin II as the model peptide. Among the compounds examined, *N'*-acetyl-*N*,*N*-dimethyl-1,4-phenylenediamine (**1**; Table 1) was found to be the most suitable TRT for this reaction, and the monoadduct to angiotensin II was obtained in 50% yield in the presence of the $[Ru(bpy)_3]Cl_2$ complex in Tris buffer (10 mM, pH 4.2) and

Table 1: Optimization of the addition reaction of angiotensin II with *N'*-acetyl-*N*,*N*-dimethyl-1,4-phenylenediamine (**1**).[a]

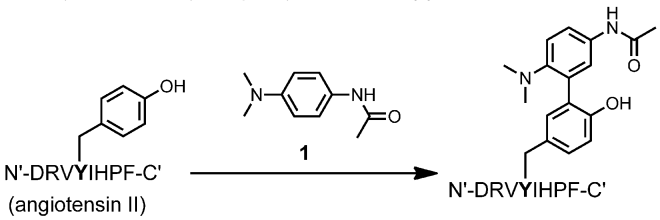

Entry	$[Ru(bpy)_3]Cl_2$	Buffer pH	Irradiation time [min]	Additive	Yield [%] (mono-/ bisadduct)
1	1 mM	6.0	15	–	55 (1:0)
2	10 μM	7.4	5	1 mM APS	70 (9:1)
3	1 mM	7.4	1	1 mM APS	95 (3:2)
4	1 mM	7.4	1	1 mM APS 10 mM DTT	0
5	1 mM	7.4	–[b]	1 mM APS	10 (1:0)
6	–	7.4	–[b]	1 mM APS	10 (1:0)
7	1 mM	7.4	–[b]	–	0

[a] Reaction conditions: angiotensin II (100 μM) and **1** (500 μM) in MES (10 mM) buffer. All reactions were quenched with DTT (10 mM) and analyzed by using MALDI-TOF MS. Each reaction was repeated several times and the average ratios of the mono- and bisadducts are indicated. [b] Incubated for 5 min without irradiation.

under irradiation with light (Table S1 in the Supporting Information). Then, we tested different buffers and additives for the addition reaction with TRT **1** under mild conditions (pH 6.0–7.4) to prevent proteins from denaturation (Table 1 and Table S2 in the Supporting Information). The addition reaction proceeded preferentially in 2-morpholinoethanesulfonic acid (10 mM, MES) buffer under irradiation with visible light for 15 min (Table 1, entry 1). It was reported that SET of the excited state $*Ru^{II}$ to Ru^{III} was accelerated in the presence of oxidants, such as ammonium persulfate (APS).[21] Therefore, we examined the effects of APS on the addition reaction of angiotensin II (100 μM) with **1** (500 μM). The reaction proceeded smoothly at pH 7.4 in the presence of APS (1 mM) and a catalytic amount of $[Ru(bpy)_3]Cl_2$ (10 μM) under irradiation with visible light for 5 min, giving the monoadduct and the bisadduct (9:1 ratio) in 70% yield (Table 1, entry 2). The use of 1 mM of $[Ru(bpy)_3]Cl_2$ accelerated the reaction rate and both mono- and bisadducts were obtained in 95% yield in a 3:2 ratio even under irradiation with visible light for 1 min (Table 1, entry 3). The reaction was abolished by addition of dithiothreitol (DTT), a radical scavenger (Table 1, entry 4). Both irradiation with visible light and the $[Ru(bpy)_3]Cl_2$ complex were essential for the addition reaction (Table 1, entries 5–7),[23] thus suggesting that the reactions proceeded through the photoinduced oxidative SET radical mechanism proposed in Scheme S1 in the Supporting Information. MS/MS analysis of the mono- and bisadducts of **1** to angiotensin II indicated that all modifications were implemented on tyrosine residues (Figures S1 and S2 in the Supporting Information). To understand the binding mode between **1** and tyrosine residues, the addition reaction of **1** with ethyl-*N*-acetyl-tyrosine amide, a model substrate, was investigated. Structural analysis revealed that a carbon–carbon bond was formed between the *ortho*-carbon atom of the phenolic oxygen of ethyl-*N*-acetyl-tyrosine amide and the *ortho*-carbon atom of the dimethylamino group of **1** (Figures S3 and S4 in the Supporting Information). We also examined the reactivity of **1** to the tryptophan residue by using the model peptide melittin. The observed oxidation of the tryptophan residue with oxygen proceeded prior to the addition with **1**.[24–26] These results suggest that this method can be used for the specific modification of tyrosine residues in the target protein.

With the suitable conditions established, we applied this tyrosine-residue-specific addition reaction to the modification of a purified protein. We designed and synthesized fluorescent TRT **2** (Scheme S3 in the Supporting Information). Bovine serum albumin (BSA), the model protein, was treated with **2** under several conditions (Figure 2). Whereas BSA was not modified in the presence of $[Ru(bpy)_3]Cl_2$ without **2** or APS (lanes 1 and 2), successful modification was observed in the presence of $[Ru(bpy)_3]Cl_2$ (10 μM), **2** (500 μM), and APS (1 mM) under irradiation with visible light for 5 min (lane 3). A slight modification of BSA with **2** was observed without irradiation and $[Ru(bpy)_3]Cl_2$ (lanes 4 and 5), thereby revealing that APS caused a photocatalyst-independent modification reaction, which was considered to be one of the undesired background reactions. This modification proceeded without APS, although an excess amount of [Ru-

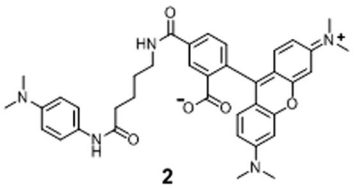

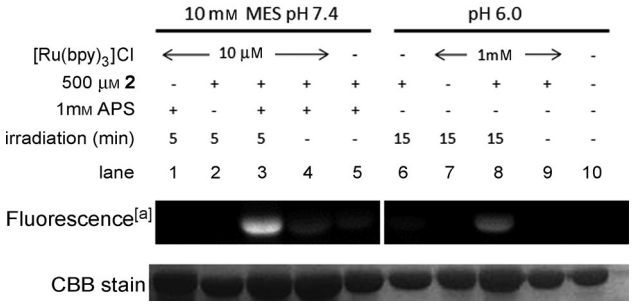

Figure 2. Modification of BSA with fluorescent TRT **2** under various conditions. Fluorescence images and coomassie brilliant blue (CBB)-stained images of SDS-PAGE gels, with the conditions for each lane given above. [a] The exposure time for fluorescence detection in lanes 6–10 was longer (3.0 s) than that in lanes 1–5 (0.3 s; also see Figure S7 in the Supporting Information).

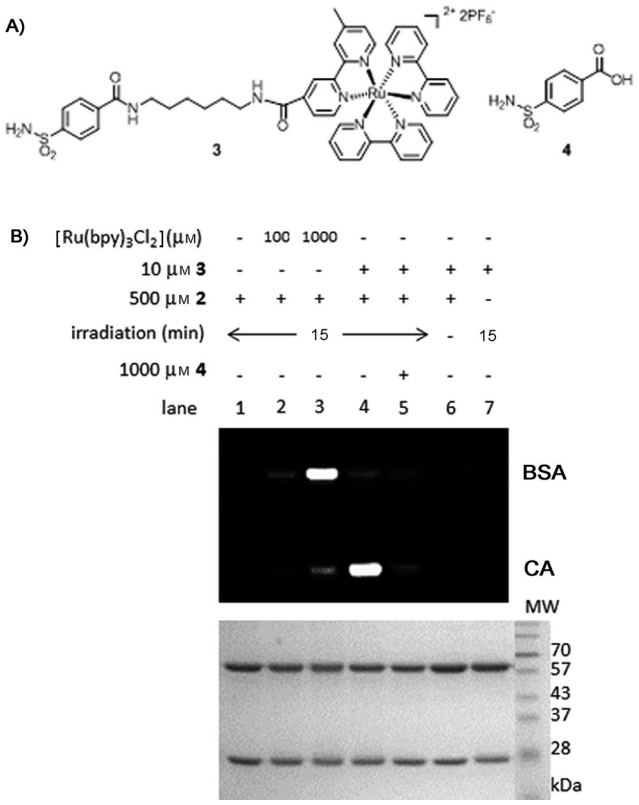

Figure 3. Selective modification of carbonic anhydrase (CA) promoted by the CA-ligand-conjugated ruthenium complex **3** as LSC in a mixture of BSA and bovine CA. A) Structures of **3** and CA-binding competitor **4**. B) Protein modification reactions were performed in a mixture of BSA (5 μM) and CA (5 μM) in MES buffer (10 mM; pH 6.0) without APS. Fluorescence images of modified proteins (upper) and whole proteins with CBB stain (lower) are shown.

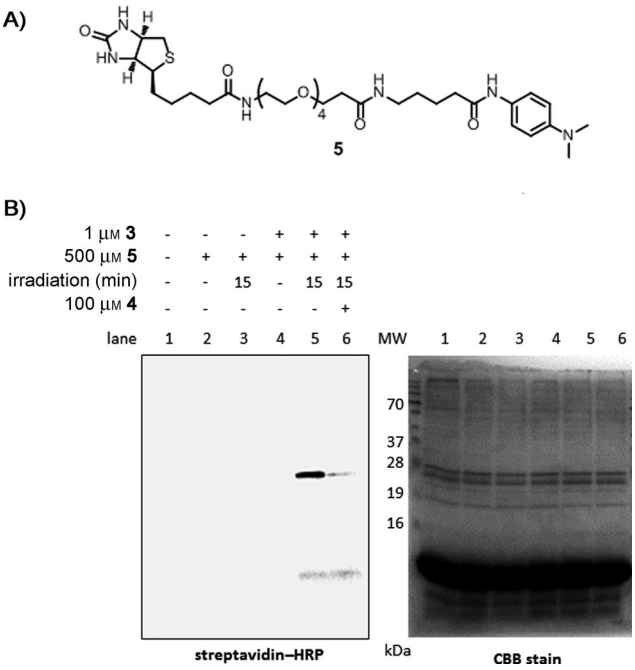

Figure 4. Selective modification of CA in mouse erythrocyte lysates. A) Structure of biotin-conjugated TRT **5**. B) The reaction for the selective modification of CA was performed in MES (10 mM, pH 6.0) using erythrocyte lysates from 6-week-old female mice. The left image shows visualization of biotinylated proteins with a streptavidin–HRP conjugate. The right image shows CBB staining of proteins in mouse erythrocyte lysates.

$(bpy)_3]Cl_2$ (1 mM) was needed. $[Ru(bpy)_3]Cl_2$ and irradiation with light were indispensable in this case (lanes 6–10). To evaluate the biocompatibility of this reaction, double modification experiments of BSA and streptavidin were carried out using PEG-conjugated TRT and tetramethylrhodamine-conjugated maleimide or *N*-hydroxysuccinimide (NHS). The electrophilic modifications proceeded even after the PEG modification, thus suggesting that this SET-based tyrosine-targeting method is compatible with the electrophilic methods targeting cysteine and lysine residues (see Figure S8 in the Supporting Information).

To clarify whether this addition reaction based on local SET is applicable to selective protein modification, we designed and synthesized a ligand-conjugated ruthenium complex as an LSC. Carbonic anhydrase (CA) and benzenesulfonamide were chosen as the model of the target protein and its ligand, respectively.[27] When the SET-based radical modification reaction was carried out in the presence of $[Ru(bpy)_3]Cl_2$ using a mixture of BSA and CA, the extent of modification of BSA was higher than of CA, because it had a larger number of accessible tyrosine residues (Figure 3, lanes 2 and 3). Meanwhile, benzenesulfonamide-conjugated ruthenium complex **3**, which was designed as a CA-targeting LSC, promoted the selective modification of CA (lane 4) with more than 100 times higher efficiency than BSA modification (lane 3; 1 mM $[Ru(bpy)_3]Cl_2$ versus lane 4; 10 μM **3**).[28] The selective modification of CA was inhibited by the CA-binding competitor **4**, which was present in an amount that was 100 times that of LSC **3** (lane 5), thereby revealing that this reaction was accelerated by the target protein–ligand interaction between CA and **3**.[29] No protein modification of both BSA and CA was observed in the absence of irradiation with visible light or **2** (lanes 6 and 7).

Finally, we applied this target-selective protein modification to native CA proteins in cell lysate using **3**. CA modification was performed in mouse erythrocytes that originally expressed CAs. However, the lysates of erythrocytes contained a large amount of hemoglobin (14 kDa) and the fluorescence of hemoglobin interfered with the fluorescence detection of CA modified with **2**. Therefore, we developed biotin-conjugated *N*,*N*-dimethyl-1,4-phenylenediamine **5** as a TRT (Figure 4A) to detect the target protein by using a streptavidin–horseradish peroxidase(HRP) conjugate. No biotinylated proteins were detected with streptavidin–HRP in the absence of **3**, biotin-conjugated TRT **5**, or irradiation (Figure 4B, lanes 1–4). Those proteins, however, were observed at 29 kDa, which corresponded to CA from the cell lysate, in the presence of **3** and **5** under irradiation with light for 15 min (lane 5), and this modification was inhibited by the addition of **4** (lane 6).[30] These results clearly indicated that SET-based protein modification using **3** and **5** specifically occurred on the target protein CA despite the coexistence of various kinds of proteins in the cell lysate. We also performed

this modification reaction in intact erythrocytes in MES-buffered saline (10 mM MES (pH 6.0), 150 mM NaCl) and again obtained similar results to those from the cell lysate (Figure S11 in the Supporting Information), thus suggesting that **5** and **3** could permeate the erythrocyte cell membrane.[31] Therefore, this target-selective protein modification based on local SET catalysis is applicable to the modification of native proteins in an intracellular environment.

In conclusion, we have developed a target-selective protein modification strategy based on local SET catalysis. In cell lysates, tyrosyl radicals were selectively generated on the target protein by SET from the photocatalyst in the local environment of the ligand, and the radicals were trapped by TRTs through the specific radical addition to tyrosine residues. Although target-selective protein modifications in cell lysates were achieved before with electrophilic reagents using ligand-tethered DMAP catalysts, those methods were limited to modifying the nucleophilic residues of the targeted proteins, such as lysine and cysteine. The current method is not only an alternative to the strategy using electrophilic agents but can also be utilized for the identification of proteins interacting with the target protein through a tyrosine–tyrosine SET addition reaction between the target protein and its interaction partners induced by the LSC-based generation of tyrosyl radicals. Studies with respect to further applications are in progress.

Received: May 4, 2013
Published online: July 3, 2013

Keywords: photocatalysts · protein modifications · radical reactions · single-electron transfer · tyrosine

[1] T. Hayashi, I. Hamachi, *Acc. Chem. Res.* **2012**, *45*, 1460 – 1469.
[2] A. M. Wu, P. D. Senter, *Nat. Biotechnol.* **2005**, *23*, 1137 – 1146.
[3] J. M. McFarland, M. B. Francis, *J. Am. Chem. Soc.* **2005**, *127*, 13490 – 13491.
[4] G. J. L. Bernardes, J. M. Chalker, J. C. Errey, B. G. Davis, *J. Am. Chem. Soc.* **2008**, *130*, 5052 – 5053.
[5] A. Dondoni, *Angew. Chem.* **2008**, *120*, 9133 – 9135; *Angew. Chem. Int. Ed.* **2008**, *47*, 8995 – 8997.
[6] J. M. Antos, M. B. Francis, *J. Am. Chem. Soc.* **2004**, *126*, 10256 – 10257.
[7] S. D. Tilley, M. B. Francis, *J. Am. Chem. Soc.* **2006**, *128*, 1080 – 1081.
[8] J. M. Antos, J. M. McFarland, A. T. Iavarone, M. B. Francis, *J. Am. Chem. Soc.* **2009**, *131*, 6301 – 6308.
[9] N. S. Joshi, L. R. Whitaker, M. B. Francis, *J. Am. Chem. Soc.* **2004**, *126*, 15942 – 15943.
[10] H. Ban, J. Gavrilyuk, C. F. Barbas, *J. Am. Chem. Soc.* **2010**, *132*, 1523 – 1525.
[11] K. L. Seim, A. C. Obermeyer, M. B. Francis, *J. Am. Chem. Soc.* **2011**, *133*, 16970 – 16976.
[12] J. Gavrilyuk, H. Ban, M. Nagano, W. Hakamata, C. F. Barbas, *Bioconjugate Chem.* **2012**, *23*, 2321 – 2328.
[13] B. V. Popp, Z. T. Ball, *J. Am. Chem. Soc.* **2010**, *132*, 6660 – 6662.
[14] Z. Chen, B. V. Popp, C. L. Bovet, Z. T. Ball, *ACS Chem. Biol.* **2011**, *6*, 920 – 925.
[15] S. Tsukiji, M. Miyagawa, Y. Takaoka, T. Tamura, I. Hamachi, *Nat. Chem. Biol.* **2009**, *5*, 341 – 343.
[16] S.-h. Fujishima, R. Yasui, T. Miki, A. Ojida, I. Hamachi, *J. Am. Chem. Soc.* **2012**, *134*, 3961 – 3964.
[17] Y. Koshi, E. Nakata, M. Miyagawa, S. Tsukiji, T. Ogawa, I. Hamachi, *J. Am. Chem. Soc.* **2008**, *130*, 245 – 251.
[18] H. Wang, Y. Koshi, D. Minato, H. Nonaka, S. Kiyonaka, Y. Mori, S. Tsukiji, I. Hamachi, *J. Am. Chem. Soc.* **2011**, *133*, 12220 – 12228.
[19] N. Hoffmann, *Chem. Rev.* **2008**, *108*, 1052 – 1103.
[20] K. Zeitler, *Angew. Chem.* **2009**, *121*, 9969 – 9974; *Angew. Chem. Int. Ed.* **2009**, *48*, 9785 – 9789.
[21] D. A. Fancy, T. Kodadek, *Proc. Natl. Acad. Sci. USA* **1999**, *96*, 6020 – 6024.
[22] K. Kim, D. A. Fancy, D. Carney, T. Kodadek, *J. Am. Chem. Soc.* **1999**, *121*, 11896 – 11897.
[23] The modifications induced by APS were observed in 10% conversion yield without irradiation with light and/or $[Ru(bpy)_3]Cl_2$ in entries 5 and 6, respectively.
[24] R. T. Dean, S. Fu, R. Stocker, M. J. Davies, *Biochem. J.* **1997**, *324 (Pt 1)*, 1 – 18.
[25] M. J. Davies, *Biochim. Biophys. Acta Proteins Proteomics* **2005**, *1703*, 93 – 109.
[26] M. J. Davies, *Biochem. Biophys. Res. Commun.* **2003**, *305*, 761 – 770.
[27] V. M. Krishnamurthy, G. K. Kaufman, A. R. Urbach, I. Gitlin, K. L. Gudiksen, D. B. Weibel, G. M. Whitesides, *Chem. Rev.* **2008**, *108*, 946 – 1051.
[28] The use of lower amounts of compound **3** resulted in lower labeling efficiency owing to the tight binding of compound **3** to CA.
[29] We examined the CA inhibitory activity of compounds **3**, **4** and $[Ru(bpy)_3]Cl_2$ according to the literature protocol reported by J. A. Verpoorte, S. Mehta, J. T. Edsall, *J. Biol. Chem.* **1967**, *242*, 4221 – 4229. Compound **3** showed higher CA inhibitory activity (IC_{50}: 0.50 μM) than compound **4** (IC_{50}: 1.6 μM). $[Ru(bpy)_3]Cl_2$ did not show a significant inhibition at 10 μM. See Figure S9 in the Supporting Information.
[30] We examined the selective modification of CA in mouse erythrocyte lysates at various concentrations of LSC **3** and found that the selectivity of the modification at 1 μM was higher than that at 10 μM, although the modification efficiency dropped. Therefore, we carried out the further CA-selective modification experiments in mouse erythrocyte lysates at 1 μM of **3**.
[31] Q. Shao, B. Xing, *Chem. Commun.* **2012**, *48*, 1739 – 1741.

ChemComm

COMMUNICATION

View Article Online
View Journal

Cite this: DOI: 10.1039/c4cc04344h

Received 9th June 2014,
Accepted 21st August 2014

DOI: 10.1039/c4cc04344h

www.rsc.org/chemcomm

Spermidinium *closo*-dodecaborate-encapsulating liposomes as efficient boron delivery vehicles for neutron capture therapy†

Shoji Tachikawa,[ab] Tatsuro Miyoshi,[b] Hayato Koganei,[b] Mohamed E. El-Zaria,[bc] Clara Viñas,[d] Minoru Suzuki,[e] Koji Ono[e] and Hiroyuki Nakamura*[ab]

***closo*-Dodecaborate-encapsulating liposomes were developed as boron delivery vehicles for neutron capture therapy. The use of spermidinium as a counter cation of *closo*-dodecaborates was essential not only for the preparation of high boron content liposome solutions but also for efficient boron delivery to tumors.**

Boron neutron capture therapy (BNCT) has been attracting growing interest as one of the minimally invasive cancer therapies.[1] Mercaptoundecahydrododecaborate ($Na_2[B_{12}H_{11}SH]$; Na_2BSH) and L-*p*-boronophenylalanine (L-BPA) have been used in BNCT for many years. L-BPA, in particular, has been widely used for the treatment of not only melanoma but also brain tumor[2] and head and neck cancer[3] because it can be taken up selectively by tumor cells through an amino acid transporter.[4] The accelerator-based BNCT is now undergoing phase I clinical study for the treatment of brain tumor and head and neck cancer patients in Japan.[5,6]

In recent years, liposomal ^{10}B carriers have attracted attention as some of the efficient boron delivery systems in BNCT.[7–10] Several efficient *in vivo* BNCTs have been reported. Yanagië and coworkers demonstrated the first antitumor effect of Na_2BSH-encapsulating liposomes conjugated with a monoclonal antibody specific for the carcinoembryonic antigen.[9a,b] Maruyama and co-workers developed transferrin-conjugating Na_2BSH-encapsulating liposomes.[9d,10] Although they succeeded in completely suppressing tumor growth in mice after neutron irradiation, the concentration of inner ^{10}B of liposomes was limited in preparation due to osmotic reasons. For this reason, boron lipids embedded within the liposome bilayer have been studied.[10–12] Hawthorne and coworkers developed liposomes incorporating $Na_3[1\text{-}(2\text{-}B_{10}H_9)\text{-}2\text{-}NH_3B_{10}H_8]$ into the internal aqueous core and K[*nido*-7-$CH_3(CH_2)_{15}$-7,8-$C_2B_9H_{11}$] into the bilayer membrane to increase the boron content in liposomes.[8b,13]

We previously developed Na_2BSH-encapsulating 10% distearoyl boron lipid (DSBL)[11b] liposomes that have high boron content with excellent boron delivery efficacy to tumors.[14] In this communication, we studied the effects of the counter cations of boron clusters on liposome formation to develop high boron content liposomes for BNCT by overcoming osmotic pressure limitations.

We selected three *closo*-dodecaborates, $Na_2[B_{12}H_{12}]$, $Na_2[B_{12}H_{11}OH]$[15] and $Na[B_{12}H_{11}NH_3]$[16] in addition to Na_2BSH (Fig. 1). We first tested the cytotoxicity of the *closo*-dodecaborates toward colon 26 cells. The *closo*-dodecaborates are relatively non-toxic and the GI_{50} values of $Na_2[B_{12}H_{12}]$, Na_2BSH, $Na[B_{12}H_{11}NH_3]$, and $Na_2[B_{12}H_{11}OH]$ are 5.1, 2.1, 32.9, and 7.7 mM, respectively (Table S1 in the ESI†). Liposomes containing the *closo*-dodecaborates were prepared from DSPC, cholesterol, and DSPE-PEG2000 by the reverse phase evaporation method with sizes of approximately 100 nm in diameter. The results are summarized in Table 1. The final boron and phosphorus concentrations of liposome solution containing $Na_2[B_{12}H_{12}]$ were 3438 ± 2.0 and 2864 ± 18.3 ppm, respectively, and the B/P ratio was 1.2 (entry 1). The higher B/P ratio indicates the higher boron content in liposomes. The liposome yield was 58% based on the total phospholipids used in the preparation. The B/P ratio of the liposome containing $Na[B_{12}H_{11}NH_3]$ was 2.2 (entry 2), which was slightly higher than those of liposomes containing Na_2BSH, $Na_2[B_{12}H_{11}OH]$, and $Na_2[B_{12}H_{12}]$ (1.2–1.6, entries 1, 3, and 4). In the case of $Na[B_{12}H_{11}NH_3]$, an ammonium ion group served as one of the two counter cations of the *closo*-dodecaborate

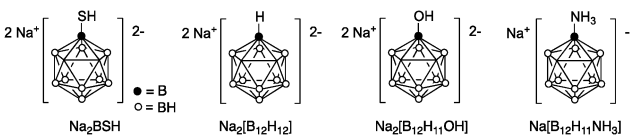

Fig. 1 Structures of *closo*-dodecaborates used for encapsulation in liposomes.

[a] *Chemical Resources Laboratory, Tokyo Institute of Technology, 4259 Nagatsuta-cho, Midori-ku, Yokohama 226-8503, Japan. E-mail: hiro@res.titech.ac.jp; Fax: +81 45 924 5244*
[b] *Department of Chemistry, Faculty of Science, Gakushuin University, Mejiro, Toshima-ku, Tokyo 171-8588, Japan*
[c] *Department of Chemistry, Faculty of Science, Tanta University, 31527-Tanta, Egypt*
[d] *Institut de Ciència de Materials de Barcelona (ICMAB-CSIC), Campus U.A.B., 08193 Bellaterra, Barcelona, Spain*
[e] *Particle Radiation Oncology Research Center, Kyoto University Research Reactor Institute, Asashiro-nishi, Kumatori-cho, Sennan-gun, Osaka 590-0494, Japan*

† Electronic supplementary information (ESI) available: Experimental details and data. See DOI: 10.1039/c4cc04344h

Table 1 Physical characteristics of liposomes containing *closo*-dodecaborates associated with sodium and various ammonium cations[a]

Entry	Boron cluster	B conc.[b,c] (ppm)	P conc. (ppm)	B/P[b,c]	Yield[d] (%)
1	Na_2BSH	3438 ± 2.0	2864 ± 18.3	1.2	58
2	$Na[B_{12}H_{11}NH_3]$	4072 ± 22.8	1835 ± 38.5	2.2	44
3	$Na_2[B_{12}H_{11}OH]$	2635 ± 184.2	1600 ± 99.0	1.5	39
4	$Na_2[B_{12}H_{12}]$	3133 ± 10.3	1932 ± 13.3	1.6	47
5	$(n\text{-}C_3H_7NH_3)_2BSH$	2874 ± 47.7	2225 ± 15.8	1.3	54
6	$(H_3NC_4H_8NH_3)BSH$	4711 ± 17.4	1833 ± 43.4	2.6	44
7	spd-BSH	13 867 ± 185.8	4046 ± 18.3	3.4	98
8	(Sperminium)BSH	9759 ± 139.6	3559 ± 44.5	2.7	87
9	spd-$[B_{12}H_{11}NH_3]$	13 970 ± 216.5	3943 ± 43.4	3.5	95

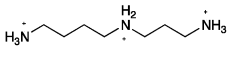
spermidinium (spd)

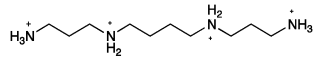
sperminium

[a] In all cases, liposomes were prepared from DSPC, cholesterol, and DSPE-PEG2000 (1 : 1 : 0.11, molar ratio) by the REV method. [b] Data are expressed as means ± standard deviation (SD). [c] Boron and phosphorus concentrations of liposome solution were determined by ICP-AES. [d] Liposome yields were calculated from the phosphorus concentration of liposome solution based on the total phospholipids used in preparation.

dianion. We speculated that ammonium counter cations would affect the encapsulation of *closo*-dodecaborates in liposomes. Recently, Gabel and coworkers reported that Na_2BSH induces aggregation and membrane rupture, increasing wall thickness of the liposome and triggering the release of liposome contents.[17] Indeed, it is known that tetramethylammonium (TMA) salts of *closo*-dodecaborates are insoluble in water, and the ion-exchange from Na_2BSH to $(TMA)_2BSH$ proceeds readily, whereas the ion-exchange from $(TMA)_2BSH$ to Na_2BSH is not easy. We predicted that encapsulation as well as liposome yield would be increased if we could reduce this interaction in the preparation of *closo*-dodecaborate-encapsulating liposomes. Thus we prepared various ammonium salts of BSH and examined their encapsulation into liposomes (entries 5–9 in Table 1). The B/P ratio of the liposome containing the $n\text{-}C_3H_7NH_3^+$ salt of BSH was similar to that of the liposome containing Na_2BSH (entries 1 *vs.* 5). The $H_3N^+C_4H_8NH_3^+$ cation increased the B/P ratio (2.6) and boron concentration (4711 ppm). Interestingly, the B/P ratio dramatically increased to 3.4 when the spermidinium (spd) cation was employed (entry 7). In addition, the liposome yield was markedly increased to 98% and the final boron concentration of the liposome solution reached 13 867 ppm. In contrast, the B/P ratio of liposome containing (sperminium) BSH dropped to 2.7, although the liposome yield was still high (87% yield) and the final boron concentration of the liposome solution was high at 9759 ppm (entry 8). Liposome containing spd-$[B_{12}H_{11}NH_3]$ showed the highest B/P ratio (3.5); the boron concentration of the liposome solution reached 13 790 ppm and the liposome yield was 95% (entry 9).

We examined whether the formation of high boron content liposomes is affected by the viscosity of the *closo*-dodecaborate solutions. However, the spd cation of $[B_{12}H_{12}]^{2-}$ does not affect the viscosity of internal aqueous solution of liposomes (Table S3, ESI†). We measured liposome yields and B/P ratios under the condition of various ratios of BSH to spd cations (Na_2BSH: [spermidine + HCl] = 1: *X*, *X* = 0, 0.25, 0.5, 1, and 2). As shown in Fig. 2, the B/P ratio

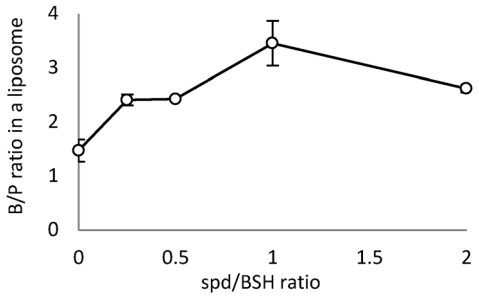

Fig. 2 Effect of the amount of spd cation on spd-BSH encapsulation in liposomes. Boron/phosphorus (B/P) ratios of $(spd)_x$-*closo*-dodecaborate-encapsulating liposomes are shown in the vertical axis.

reached a maximum of 3.4 when the BSH : spd ratio was 1 : 1. Liposome yields showed a similar tendency to B/P ratios. The highest liposome yield was observed at the BSH to spd cation ratio of 1 : 1. Transmission electron microscopy (TEM) analysis of spd-BSH-encapsulating liposomes and Na_2BSH-encapsulating liposomes was also carried out using Cryo-TEM (Fig. 3). It is notable that the liposomes interacted with each other in the case of Na_2BSH-encapsulating liposomes, whereas the liposomes dispersed in solution without interacting with each other in the case of spd-BSH-encapsulating liposomes.

We next examined boron distribution of the spd-*closo*-dodecaborate-encapsulating liposomes in colon 26 tumor-bearing mice.[18] The liposomes were injected at doses of 15, 30, and 100 mg [B] kg^{-1} body weight *via* the tail veins. Na_2BSH- and $Na_2[B_{12}H_{11}NH_3]$-encapsulating liposomes were also injected at a dose of 30 mg [B] kg^{-1} as control experiments. The time courses of boron distribution in each organ are shown in Fig. 4. Blood boron concentrations of 460.7, 104.0, and 33.2 ppm were detected 24 h after injection of spd-BSH-encapsulating liposomes (100, 30, and 15 mg [B] kg^{-1}), respectively (Fig. 4a). Blood boron concentration in mice injected with 100 mg [B] kg^{-1} of spd-BSH-encapsulating liposomes did not decrease notably during the 48 h period, whereas those in mice injected with 30 and 15 mg [B] kg^{-1} of spd-BSH-encapsulating liposomes gradually decreased in a time-dependent manner. The time courses of boron concentrations in liver, kidneys, and spleen are shown in Fig. 4b–d, respectively. Boron concentrations of 528.5, 144.2, and 74.4 ppm in liver were observed 48 h after the injection of 100, 30, and 15 mg [B] kg^{-1} of spd-BSH-encapsulating liposomes, respectively. In the meantime, maximum

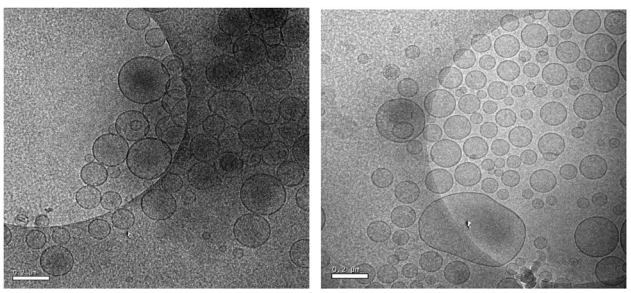

Fig. 3 TEM images of Na_2BSH-encapsulating liposomes (left) and spd-BSH-encapsulating liposomes (right). Scale bar represents 200 nm.

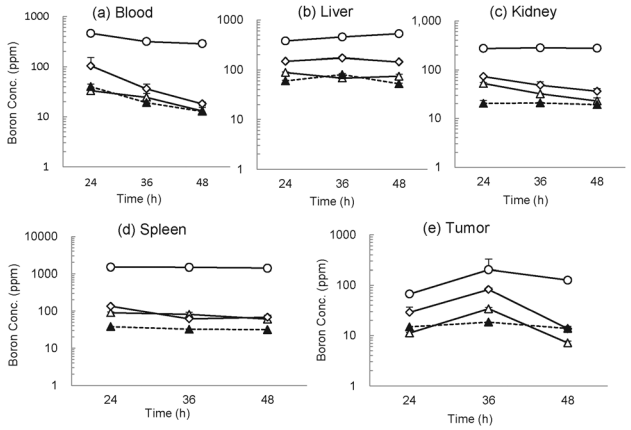

Fig. 4 Time courses of distribution of spd-BSH- and Na_2BSH-encapsulating liposomes (△, spd-BSH: 15 mg [B] kg^{-1}; ◇, spd-BSH: 30 mg [B] kg^{-1}; ○, spd-BSH: 100 mg [B] kg^{-1}; ▲, Na_2BSH: 15 mg [B] kg^{-1}). Each liposome was injected into tumor-bearing mice *via* the tail vein. Data are expressed as means ± SD (n = 5).

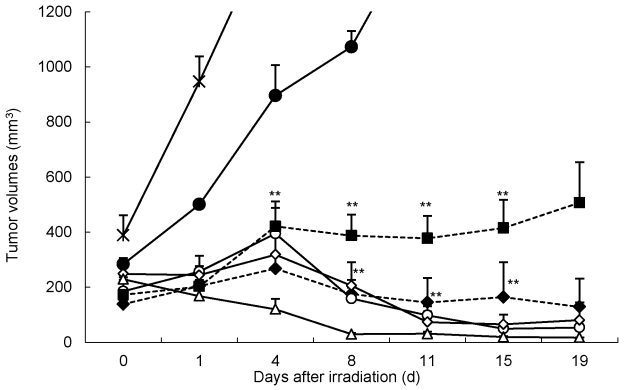

Fig. 5 Tumor volumes in mice (Balb/c, female, six weeks old, 14–20 g) bearing colon 26 solid tumor, exposed to thermal neutron irradiation (hot) for 50 min (1.3–2.2 × 10^{12} neutrons per cm^2) or not exposed to thermal neutron irradiation (cold). Irradiation was performed 36 h after injection of liposomes containing spd-[^{10}BSH] (△, 15; ◇, 30; ○, 100 mg [^{10}B] kg^{-1}) and Na_2[^{10}BSH] (◆, 30 mg [^{10}B] kg^{-1}), or 1 h after injection of Na_2[^{10}BSH] solution (■, 100 mg [^{10}B] kg^{-1}). ●, hot control; ×, cold control. **$P < 0.01$, compared with hot control.

tumor boron concentrations of 202.7 and 82.4 ppm were achieved 36 h after injection at doses of 100 and 30 mg [B] kg^{-1}, respectively. Even at the low boron dose of 15 mg [B] kg^{-1}, the tumor boron concentration was 34.0 ppm at 36 h after injection (Fig. 4e). We also demonstrated the boron distribution of Na_2BSH-encapsulating liposomes in tumor-bearing mice for comparison. Although blood and liver boron concentrations after injection of Na_2BSH-encapsulating liposomes at a dose of 30 mg [B] kg^{-1} were similar to those after injection of spd-BSH-encapsulating liposomes at a dose of 30 mg [B] kg^{-1}, kidney and spleen boron concentrations after injection of Na_2BSH-encapsulating liposomes were lower than those after injection of spd-BSH-encapsulating liposomes up to 48 h. The tumor boron concentration at 36 h after injecting Na_2BSH-encapsulating liposomes was 31.9 ppm, although the clearance of Na_2BSH-encapsulating liposomes was slow (Fig. 4e).

A similar tendency was observed in spd-[$B_{12}H_{11}NH_3$]-encapsulating liposomes (Fig. S1, ESI†). Blood, kidney, and spleen boron concentrations gradually decreased after injection. Maximum tumor boron concentrations of 242.2, 88.7, and 35.4 ppm were achieved 6 h after injection at doses of 100, 30, and 15 mg [B] kg^{-1}, respectively. Interestingly, significant tumor boron accumulation was also observed in the case of Na[$B_{12}H_{11}NH_3$]-encapsulating liposomes.

Finally, we examined the antitumor effect of liposomes containing spd *closo*-dodecaborates in colon 26 tumor bearing mice exposed to thermal neutron irradiation. Thermal neutron irradiation of the tumor-transplanted left thighs of mice was carried out 36 h after injection. The tumor growth curves of mice are shown in Fig. 5 (and in Fig. S2, ESI†). "Hot control (–●–)" and "Cold control (–×–)" represent tumor volumes of mice injected with saline with and without thermal neutron irradiation, respectively. Tumor growth was significantly suppressed in mice treated with spd-[^{10}BSH]- and spd-[$^{10}B_{12}H_{11}NH_3$]-encapsulating liposomes at doses of 15, 30, and 100 mg [^{10}B] kg^{-1} and exposed to thermal neutron irradiation. The tumor completely disappeared within three weeks even when a dose of 15 mg [^{10}B] kg^{-1} was employed. Liposomes containing Na_2[^{10}BSH] and Na[$^{10}B_{12}H_{11}NH_3$] also inhibited tumor growth at a dose of 30 mg [^{10}B] kg^{-1}, and the tumor was completely controlled three weeks after thermal neutron irradiation. Tumor growth was suppressed in mice treated with Na_2[^{10}BSH] solution (100 mg [^{10}B] kg^{-1}) during the two weeks after thermal neutron irradiation. However, the tumor started to grow thereafter (Fig. 5). In contrast, tumor growth was not suppressed in mice treated with Na[$^{10}B_{12}H_{11}NH_3$] solution (100 mg [^{10}B] kg^{-1}) even after thermal neutron irradiation (Fig. S2, ESI†).

Fig. 6 shows the survival curve of tumor-bearing mice after thermal neutron irradiation. All untreated mice without thermal neutron irradiation died within two weeks. Thermal neutron irradiation enhanced mouse survival and all mice exposed to thermal neutron irradiation died within 78 days. Prolonged survival was observed in mice injected with spd-[^{10}BSH]- and spd-[$^{10}B_{12}H_{11}NH_3$]-encapsulating liposomes; 72% of the mice that received a dose of 15 mg [^{10}B] kg^{-1} survived up to 100 days after the thermal neutron irradiation. Furthermore, a remarkable antitumor effect

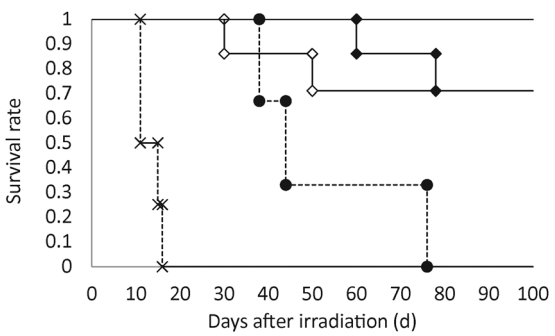

Fig. 6 Survival curve of tumor-bearing mice after thermal neutron irradiation. The irradiation was performed 36 h after injection of *closo*-dodecaborates (—, spd-BSH: 30 mg [^{10}B] kg^{-1}; ◆, spd-BSH: 15 mg [^{10}B] kg^{-1}; ◇, spd-$^{10}B_{12}H_{11}NH_3$: 15 mg [^{10}B] kg^{-1}) for 50 min (1.3–2.2 × 10^{12} neutrons per cm^2). ×, cold control; ●, hot control. Mice were sacrificed when their tumor volumes reached ~3000 mm^3.

was observed in the mice treated with spd-[^{10}BSH]-encapsulating liposomes at a dose of 30 mg [^{10}B] kg^{-1}; 100% of the mice survived up to 100 days after the thermal neutron irradiation.

We succeeded in the preparation of high boron content liposomes. The use of spd as a counter cation of *closo*-dodecaborates was essential to obtain the liposomes with high yields and high B/P ratios. All of the mice injected with 30 mg [^{10}B] kg^{-1} of spd-[^{10}BSH]-encapsulating liposomes were completely cured while five of seven mice injected with 15 mg [^{10}B] kg^{-1} of spd-[^{10}BSH]- and spd-[$^{10}B_{12}H_{11}NH_3$]-encapsulating liposomes were cured 100 days after thermal neutron irradiation. The results indicate that the total amount of phospholipids could be reduced to less than one-seventh of those used to prepare Na_2[^{10}BSH]-encapsulating liposomes.[19] We believe that the spd-*closo*-dodecaborate-encapsulating liposomes are promising candidates for clinical use in BNCT.

We thank Dr S. Kondoh (Teijin Pharm. Co. Ltd) for the measurement of osmotic pressures and Professor K. Iwata (Gakushuin University) for the measurement of the viscosity. This work was supported by Health and Labor Sciences Research Grants for research on Nanotechnical Medical from the Ministry of Health, Labor and Welfare (20100201) and the Ministry of Education, Science, Sports, Culture and Technology, Grant-in-Aid for Scientific Research (B) (No. 23390018) from Japan.

Notes and references

1 (*a*) R. F. Barth, J. A. Coderre, M. G. Vicente and T. E. Blue, *Clin. Cancer Res.*, 2005, **11**, 3987; (*b*) T. Yamamoto, K. Nakai and A. Matsumura, *Cancer Lett.*, 2008, **262**, 143; (*c*) H. Hatanaka, *J. Neurol.*, 1975, **209**, 81.
2 S.-I. Miyatake, Y. Tamura, S. Kawabata, K. Iida, T. Kuroiwa and K. Ono, *Neurosurgery*, 2007, **61**, 82.
3 (*a*) I. Kato, K. Ono, Y. Sakurai, M. Ohmae, A. Maruhashi, Y. Imahori, M. Kirihata, M. Nakazawa and Y. Yura, *Appl. Radiat. Isot.*, 2004, **61**, 1069; (*b*) T. Aihara, J. Hiratsuka, N. Morita, M. Uno, Y. Sakurai, A. Maruhashi, K. Ono and T. Harada, *Head Neck*, 2006, **28**, 850; (*c*) L. Kankaanranta, T. Seppälä, H. Koivunoro, K. Saarilahti, T. Atula, J. Collan, E. Salli, M. Kortesniemi, J. Uusi-Simola, A. Mäkitie, M. Seppänen, H. Minn, P. Kotiluoto, I. Auterinen, S. Savolainen, M. Kouri and H. Joensuu, *Int. J. Radiat. Oncol., Biol., Phys.*, 2007, **69**, 475.
4 (*a*) Y. Takahashi, Y. Imahori and K. Mineura, *Clin. Cancer Res.*, 2003, **9**, 5888; (*b*) A. Wittig, W. A. Sauerwein and J. A. Coderre, *Radiat. Res.*, 2000, **153**, 173; (*c*) G. W. Kabalka and M. L. Yao, *Anticancer Agents Med. Chem.*, 2006, **6**, 111; (*d*) Y. Imahori, Y. Ohmori, R. Fujii, K. Matsumoto and S. Ueda, *Cancer Res.*, 1995, **55**, 4225.
5 M. Suzuki, H. Tanaka, Y. Sakurai, G. Kashino, L. Yong, S. Masunaga, Y. Kinashi, T. Mitsumoto, S. Yajima, H. Tsutsui, T. Sato, A. Maruhashi and K. Ono, *Radiother. Oncol.*, 2009, **92**, 89.
6 H. Tanaka, Y. Sakurai, M. Suzuki, T. Takata, S. Masunaga, Y. Kinashi, G. Kashino, Y. Liu, T. Mitsumoto, S. Yajima, H. Tsutsui, M. Takada, A. Maruhashi and K. Ono, *Appl. Radiat. Isot.*, 2009, **67**, S258.
7 H. Nakamura, *Future Med. Chem.*, 2013, **5**, 715.
8 For passive targeting, see: (*a*) K. Shelly, D. A. Feakes, M. F. Hawthorne, P. G. Schmidt, T. A. Krisch and W. F. Bauer, *Proc. Natl. Acad. Sci. U. S. A.*, 1992, **89**, 9039; (*b*) D. A. Feakes, K. Shelly and M. F. Hawthorne, *Proc. Natl. Acad. Sci. U. S. A.*, 1995, **92**, 1367.
9 For active targeting, see: (*a*) H. Yanagië, T. Tomita, H. Kobayashi, Y. Fujii, T. Takahashi, K. Hasumi, H. Nariuchi and M. Sekiguchi, *Br. J. Cancer*, 1991, **63**, 522; (*b*) H. Yanagië, T. Tomita, H. Kobayashi, Y. Fujii, Y. Nonaka, Y. Saegusa, K. Hasumi, M. Eriguchi, T. Kobayashi and K. Ono, *Br. J. Cancer*, 1997, **75**, 660; (*c*) X. Q. Pan, H. Wang, S. Shukla, M. Sekido, D. M. Adams, W. Tjarks, R. F. Barth and R. J. Lee, *Bioconjugate Chem.*, 2002, **13**, 435; (*d*) K. Maruyama, O. Ishida, S. Kasaoka, T. Takizawa, N. Utoguchi, A. Shinohara, M. Chiba, H. Kobayashi, M. Eriguchi and H. Yanagie, *J. Controlled Release*, 2004, **98**, 195.
10 Y. Miyajima, H. Nakamura, Y. Kuwata, J.-D. Lee, S. Masunaga, K. Ono and K. Maruyama, *Bioconjugate Chem.*, 2006, **17**, 1314.
11 (*a*) H. Nakamura, Y. Miyajima, T. Takei, S. Kasaoka and K. Maruyama, *Chem. Commun.*, 2004, 1910; (*b*) J.-D. Lee, M. Ueno, Y. Miyajima and H. Nakamura, *Org. Lett.*, 2007, **9**, 323; (*c*) M. Ueno, H. S. Ban, K. Nakai, R. Inomata, Y. Kaneda, A. Matsumura and H. Nakamura, *Bioorg. Med. Chem.*, 2010, **18**, 3059.
12 (*a*) T. Li, J. Hamdi and M. F. Hawthorne, *Bioconjugate Chem.*, 2006, **17**, 15; (*b*) E. Justus, D. Awad, M. Hohnholt, T. Schaffran, K. Edwards, G. Karlsson, L. Damian and D. Gabel, *Bioconjugate Chem.*, 2007, **18**, 1287; (*c*) X. Pan, G. Wu, W. Yang, R. F. Barth, W. Tjarks and R. J. Lee, *Bioconjugate Chem.*, 2007, **18**, 101.
13 P. J. Kueffer, C. A. Maitz, A. A. Khan, S. A. Schuster, N. I. Shlyakhtina, S. S. Jalisatgi, J. D. Brockman, D. W. Nigg and M. F. Hawthorne, *Proc. Natl. Acad. Sci. U. S. A.*, 2013, **110**, 6512.
14 H. Koganei, M. Ueno, S. Tachikawa, L. Tasaki, H. S. Ban, M. Suzuki, K. Shiraishi, K. Kawano, M. Yokoyama, Y. Maitani, K. Ono and H. Nakamura, *Bioconjugate Chem.*, 2013, **24**, 124.
15 T. Peymann, C. B. Knobler and M. F. Hawthorne, *Inorg. Chem.*, 2000, **39**, 1163.
16 W. R. Hertler and M. S. Raasch, *J. Am. Chem. Soc.*, 1964, **86**, 3661.
17 (*a*) D. Gabel, D. Awad, T. Schaffran, D. Radovan, D. Daraban, L. Damian, M. Winterhalter, G. Karlsson and K. Edwards, *ChemMedChem*, 2007, **2**, 51; (*b*) D. Awad, L. Damian, M. Winterhalter, G. Karlsson, K. Edwards and D. Gabel, *Chem. Phys. Lipids*, 2009, **157**, 78.
18 All protocols were approved by the Institutional Animal Care and Use Committee of Gakushuin University.
19 Conventionally, a preinjection of liposome at a high dose was given for an achievement of targeting through saturation of liver's scavenging capacity (see; Y. Y. Kao and R. L. Juliano, *Biochim. Biophys. Acta*, 1981, **677**, 453). Such a high liposome dose may cause possible liver toxicity, since the liver's normal scavenging function is impaired. Indeed, an important character of an approved liposomal formulation (doxil) encapsulating an anticancer drug doxorubicin is the very high concentration of the encapsulated drug (also see; P. G. Tardi, N. L. Boman and P. R. Cullis, *J. Drug Targeting*, 1996, **4**, 129).

生体防御タンパク質の構造及び機能解析

教授　小島　修一
助教　津田　岳夫

[目的]

プロテアーゼやキナーゼはシグナル伝達や細胞周期制御などの様々な生命現象に関与しており、これらの異常はヒトの発がんと深く関係しており、またこれらのタンパク質の活性は、タンパク質やペプチド、さらに低分子化合物等によって巧みに調整されている。本研究では、それらのタンパク質の活性を制御しうる化合物を創製すべく、それらに対して特異的に結合するタンパク質やペプチド、そして阻害剤との相互作用を中心に生化学及び構造生物学的解析を行なうことにする。具体的にはプロテアーゼ（タンパク質分解酵素）であるズブチリシンを対象として用い、ファージディスプレイ法によってこの酵素に特異的に結合して阻害する 12 残基のペプチドを出発物質とした。そのペプチドに変異を導入して、阻害活性の増強を試みることにした。一方、ペプチドに 20 種類以外のアミノ酸を導入することによって新機能を有するペプチドの創製を目指して研究を進めている枯草菌由来の L-アミノ酸リガーゼについては、明らかにした立体構造に基づいて、この酵素への変異導入によって、基質であるアミノ酸の特異性の改変の可能性を検討した。

[結果と考察]

１．ファージディスプレイ法によって得られた 12 残基のズブチリシン阻害ペプチドへの変異導入による阻害活性の増強

ファージディスプレイ法は、バクテリオファージの表面に異種タンパク質やペプチドを提示させる研究手法であり、提示された様々なアミノ酸配列を持つタンパク質やペプチドの中から、ある機能を持った新規なタンパク質あるいはペプチドを選別することができる。この手法を用いてタンパク質間相互作用を調節する新規ペプチドを創製する研究の一環として、12 残基のペプチドをコードするライブラリーから、ズブチリシンというセリンプロテアーゼに親和性を示す SerAspPheSerCysLeuSerGluGlyCysArgThr というアミノ酸配列を持つ新規なペプチドを見出した。その後、阻害の中心が Leu6-Ser7 であると予想されること、そしてジスルフィド結合の形成に必要な Cys5、Cys10 および Gly9 を除く各アミノ酸を 1 個ずつ Ala に置換した変異ペプチドの中では、C 末端の Thr12 あるいは Ser7 を Ala に置換したペプチドが野生型より阻害活性が上昇することを明らかにした。このことは、ファージディスプレイ法によって選別されたペプチドへの変異導入により、さらに効果的な阻害剤が創製できることの可能性を示している。

そこで本研究では、12 残基のペプチドの Ser7 および Thr12 を性質の異なる他の数種類のアミノ酸に置換して、ズブチリシンに対する阻害活性の増強を試みた。具体的には大きさの異なる疎水的なアミノ酸や、正あるいは負の電荷を持つアミノ酸などへ置換した。合

わせて、阻害活性を上昇させることが明らかになったSer7 あるいは Thr12 へのアミノ酸置換を共に持つような二重変異体についても検討を行なった。これらの変異合成ペプチドのズブチリシンに対する阻害活性を図1にまとめた。

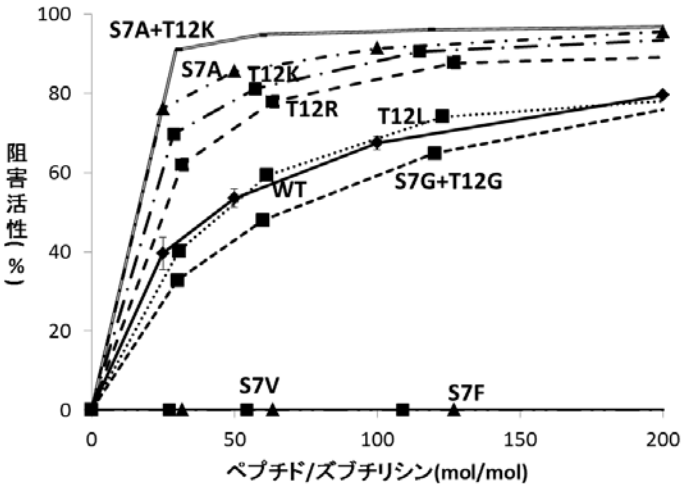

図 1

この図より、Ser7 については、Ala への置換は阻害活を上昇させたが、Lys や Val、Phe に置換すると阻害活性が極端に低下することから、7 番目でのある程度の疎水性はズブチリシンとの相互作用に好ましいものの、それ以上の大きな側鎖は荷電基同様、ズブチリシンとの相互作用を弱めることがわかった。一方、Thr12 については、Leu への置換は野生型と変わらないものの、Lys や Arg への置換は阻害活性を上昇させることがわかり、12 番目については正電荷の存在がズブチリシンとの強い相互作用に有効であることが明らかとなった。そこで、Ser7 を Ala、Thr12 を Lys に置換した二重変異体（S7A＋T12K）を合成し、ズブチリシンに対する阻害活性を測定したところ、図1に示すように、これまで合成された変異ペプチドの中で最も強い阻害活性を示すことがわかった。

この二重変異体（S7A＋T12K）とズブチリシンの相互作用を分子レベルで明らかにするために、X 線結晶構造解析によって両者の複合体の立体構造を決定しようとした。ズブチリシンに対して過剰量の二重変異体（S7A＋T12K）を加え、ゲルろ過によって複合体を精製し、様々な溶液条件にて結晶化を試みた。しかしながら現時点では、構造解析ができるだけの結晶の生成には至っていない。

２．L-アミノ酸リガーゼの結晶構造解析ならびに特異性の改変の試み

遺伝暗号に基づいてリボソーム上で生合成されたタンパク質に対して翻訳後修飾によって側鎖の構造が変わったり、アミノ酸あるいはその誘導体がアミノ酸リガーゼによって連結されることによって、20 種類以外のアミノ酸がタンパク質あるいはペプチドに導入され、新機能を発揮している例が多く報告されている。タンパク質あるいはペプチドに 20 種類以外のアミノ酸を取り込ませて新機能を持たせるため、枯草菌由来の L-アミノ酸リガーゼである YwfE タンパク質に注目し、立体構造解析およびそれに基づく変異導入による基質特異性の改変を試みている。YwfE タンパク質は非天然アミノ酸であるアンチカプシンと Ala を ATP を用いて連結する反応を触媒する。このタンパク質と GST との融合タンパク質を大腸菌を用いて大量発現させ、アフィニティークロマトグラフィーで精製後、プロテアーゼで切断して得られた YwfE タンパク質を用いて結晶化を試みた。その結果、ADP と、リン酸あるいは L-Ala 存在下、PEG3350 を含む溶液条件で結晶が得られた。

そこで本研究では、結晶化条件の最適化によって高分解能での X 線結晶構造解析を行ない、それによって得られた立体構造に基づいて YwfE タンパク質に変異を導入し、触媒反応に関わるアミノ酸残基の同定や、基質特異性の改変を試みた。

結晶化条件の最適化の結果、ADP とリン酸、ADP と L-Ala 存在下での立体構造を、それぞれ 1.9Åおよび 2.0Åで決定することができた。図 2 には ADP とリン酸を結合した YwfE タンパク質の全体の立体構造を示す。この立体構造から YwfE タンパク質は A、B および C の 3 個のドメインから構成されており、ADP は B および C ドメイン間に位置し、ATP－grasp superfamily で保存されているアミノ酸残基の側鎖によって認識されていることがわかった。

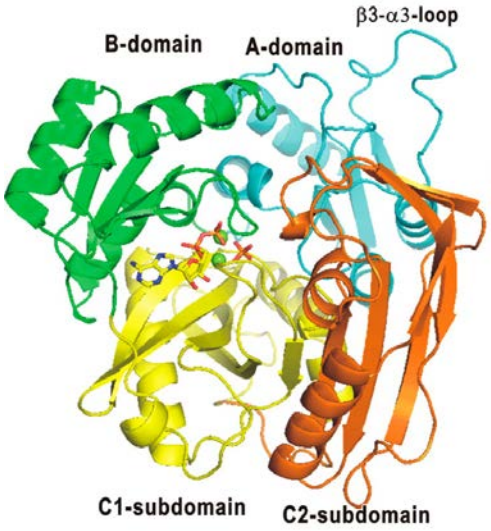

図 2

また図 3 は、ADP と、リン酸あるいは L-Ala を結合している状態の基質結合部位近傍の構造を表している。これらの構造から、Arg328 が基質である L-Ala のカルボキシル基の認識や、触媒反応に強く関与していることが示唆された。そこで、この Arg328 を他のアミノ酸に置換したところ、酵素活性は消失することがわかり、Arg328 の重要性が示された。

一方、この YwfE タンパク質がジペプチドを合成する際の N 末端側のアミノ酸として L-Ala を認識するのは、図 3 の基質結合部位の構造から、Trp332 という側鎖の大きいアミノ酸が存在しているためであると考えられた。そこで Trp322 を側鎖の小さい Ala に置換し、様々なアミノ

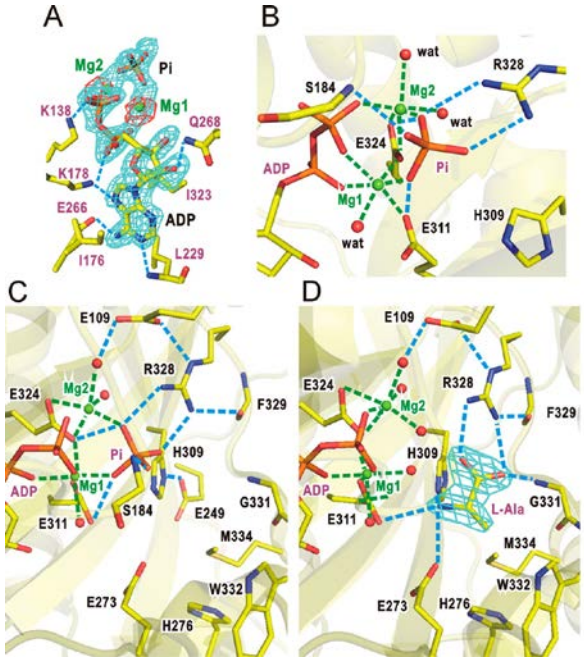

図 3

酸を用いた時の酵素活性を測定した。その結果、図 4 において△で示されたように、L-Ala が存在していなくても、L-Phe が存在しているだけで酵素活性が検出された。このことは、N 末端側のアミノ酸として L-Phe が認識されたことを示している。実際に L-Phe-L-Phe のジペプチドが合成されることも確認した。

図 4

そこでTrp332→Ala変異体についても結晶化を行い、立体構造を決定した。得られた立体構造の基質結合部位近傍の構造を図5に示す。その結果、N末端側の基質としてL-Pheを収容できるだけの大きな空隙が存在することがわかり、この空隙の出現によって、Trp332→Ala変異体において基質特異性が変化したものと考えられた。

さらにTrp332をAla以外のアミノ酸に置換したところ、L-Pheのみが存在している時の酵素活性は、Ala以外ではSerに置換した変異体のみに検出され、それ以上の大きさの側鎖のアミノ酸への置換では、Pheを基質として結合できないことがわかった。

以上のように、L-アミノ酸リガーゼであるYwfEタンパク質について、ADP、L-Alaなどの基質存在下での立体構造を決定した。それに基づいて、基質のN末端側の特異性をL-Alaに限定していると考えられるTrp332をAlaに置換することにより、L-Alaだけでなくより大きなL-Pheを認識できるよう、基質特異性の改変に成功した。このことは、この酵素がさまざまなアミノ酸の連結反応に利用できうる可能性を示している。

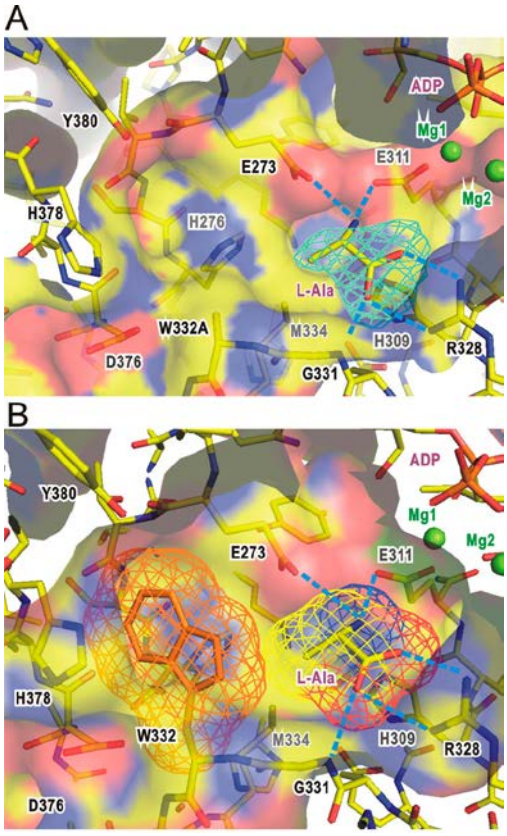

図5

[まとめ]

生体防御に関わるプロテアーゼに結合して活性を調整しうるペプチドを創製する方法としてのファージディスプレイ法によって得られた、ズブチリシンを阻害する12残基のペプチドについて、さらなる変異導入によって、より結合の強いペプチドの合成に至った。また、ペプチドに20種類以外のアミノ酸を導入しうるL-アミノ酸リガーゼであるYwfEタンパク質については、決定した立体構造に基づいて、L-Alaの認識に関わるTrp332をAlaに置換することによって、より大きなアミノ酸を認識できるよう、基質特異性の改変に成功した。これらの方法を組み合わせることによって、新機能を有するペプチドの創製の可能性が広げられると考えられる。

[参考文献]

Tsuda, T., Suzuki, T. and Kojima, S. Crystallization and preliminary X-ray diffraction analysis of *Bacillus subtilis* YwfE, an L-amino-acid ligase. Acta Crystal. F68, 203-206 (2012).

［原著論文］

1. Takei, T., Hasegawa, K., Imada, K., Namba, K., Tsumoto, K., Kuriki, Y., Yoshino, M., Yazaki, K., Kojima, S., Takei, T., Ueda, T. and Miura, K. Effects of chain length of an amphipathic polypeptide carrying the repeated amino acid sequence $(LETLAKA)_n$ on α-helix and fibrous assembly formation. Biochemistry, 52, 2810-2820 (2013)

2. Tsuda, T., Asami, M., Koguchi, Y. and Kojima, S. A single mutation alters the substrate specificity of L-amino acid ligase. Biochemistry, 53, 2650-2660 (2014)

3. Takei, T., Tsumoto, K, Yoshino, M., Kojima, S., Yazaki, K., Ueda, T., Takei, T., Arisaka, F. and Miura, K. Role of positions e and g in the fibrous assembly formation of an amphipathic α-helix-forming polypeptide. Biopolymers (Peptide Science), 102, 260-272 (2014)

4. Takei, T., Tsumoto, K., Okonogi, A., Kimura, A., Kojima, S., Yazaki, K., Takei, T., Ueda, T. and Miura, K. pH responsiveness of fibrous assemblies of repeat-sequence amphipathic α-helix polypeptides. Protein Science, 24, 883-894 (2015)

［口頭発表］

1. 津田岳夫、浅見真奈、小口孔明、小島修一、L-アミノ酸リガーゼ YwfE のアミノ酸置換による基質特異性の改変、第 66 回生物工学会大会、（2014 年 9 月 9－11 日、札幌）
2. 津田岳夫、浅見真奈、小口孔明、小島修一、変異導入による L-アミノ酸リガーゼの基質特異性の改変、BMB2015、（2015 年 12 月 1－4 日、神戸）
3. 林佳恵子、津田岳夫、小島修一、枯草菌ホスホエノールピルビン酸ムターゼ RhiH の結晶構造、BMB2015、（2015 年 12 月 1－4 日、神戸）

BIOCHEMISTRY
including biophysical chemistry & molecular biology

Article

pubs.acs.org/biochemistry

Single Mutation Alters the Substrate Specificity of L-Amino Acid Ligase

Takeo Tsuda,* Mana Asami, Yoshiaki Koguchi, and Shuichi Kojima

Department of Life Science, Faculty of Science, Gakushuin University, 1-5-1 Mejiro, Toshima-ku, Tokyo 171-8588, Japan

Supporting Information

ABSTRACT: L-Amino acid ligase (Lal) catalyzes the formation of a dipeptide from two L-amino acids in an ATP-dependent manner and belongs to the ATP-grasp superfamily. *Bacillus subtilis* YwfE, the first identified Lal, produces the dipeptide antibiotic bacilysin, which consists of L-Ala and L-anticapsin. Its substrate specificity is restricted to smaller amino acids such as L-Ala for the N-terminal end of the dipeptide, whereas a wide range of hydrophobic amino acids including L-Phe and L-Met are recognized for the C-terminal end *in vitro*. We determined the crystal structures of YwfE with bound ADP-Mg^{2+}-Pi and ADP-Mg^{2+}-L-Ala at 1.9 and 2.0 Å resolutions, respectively. On the basis of these structures, we generated point mutants of residues that are considered to participate in the recognition of L-Ala and measured their ATPase activity. The conserved Arg328 is suggested to be a crucial residue for L-Ala recognition and catalysis. The mutation of Trp332 to Ala caused the enzyme to hydrolyze ATP, even in the absence of L-Ala, and the structure of this mutant protein appeared to show a cavity in the N-terminal substrate-binding pocket. These results suggest that Trp332 plays a key role in restricting the substrate specificity to smaller amino acids such as L-Ala. Moreover, Trp332 mutants can alter the substrate specificity and activity depending on the size and shape of substituted amino acids. These observations provide sufficient scope for the rational design of Lal to produce desirable dipeptides. We propose that the positioning of the conserved Arg residue in Lal is important for enantioselective recognition of L-amino acids.

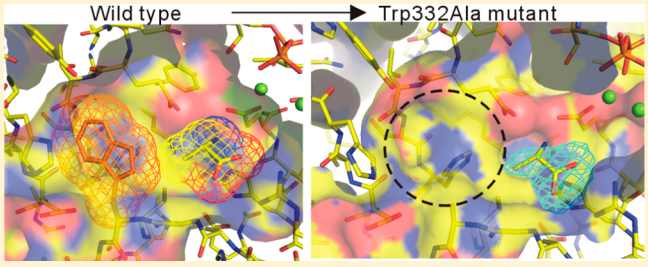

Microorganisms produce a wide range of biologically active peptide compounds such as antibiotics, antitumors, and siderophores.[1] Most of these compounds are produced via two distinct biosynthetic strategies. The first strategy uses ribosomal synthesis of linear precursor peptides that undergo posttranslational modification and proteolysis.[2] The second strategy uses nonribosomal peptide synthetase (NRPS), a large enzyme composed of multiple modules.[3,4] Independent of these two pathways, several L-amino acid ligases (Lals), which are enzymes catalyzing the ATP-dependent formation of an α-peptide bond between two L-amino acids, have been identified in certain microorganisms.[5−8] For example, *Bacillus subtilis* YwfE (also referred to as BacD), the first identified and well-studied Lal,[5] produces a dipeptide antibiotic called bacilysin that consists of L-Ala at the N-terminus and the nonproteogenic amino acid, L-anticapsin, at the C-terminus[9] (Scheme 1). The substrate specificity of YwfE is restricted to smaller amino acids such as L-Ala, for the N-terminal end of the dipeptide, whereas a wide range of hydrophobic amino acids, such as L-Phe and L-Met, are recognized for the C-terminal end. Despite the recognition of a nonproteogenic L-amino acid as a substrate by YwfE, this enzyme is not able to synthesize D-amino acid-containing dipeptides (Scheme 1).

Lal belongs to the ATP-grasp superfamily of enzymes, which catalyze the formation of an amide bond between a carboxylate compound and an amine compound in an ATP-dependent manner.[10,11] ATP-grasp enzymes share a similar overall fold composed of three domains (A, B, and C) and similar binding modes for nucleotides. However, they accept a wide range of carboxylate and amine substrates, and the sequence and structural conservation of the binding sites for these substrates is much lower. The catalytic mechanism of the enzymes in this superfamily is considered to involve the initial activation of the carboxyl group of a substrate by ATP-phosphorylation to form an acylphosphate intermediate. This is followed by a nucleophilic attack by the amine group of a second substrate on the acylphosphate to yield a tetrahedral transition state and the release of phosphate by the tetrahedral intermediate to yield a product.

Scheme 1

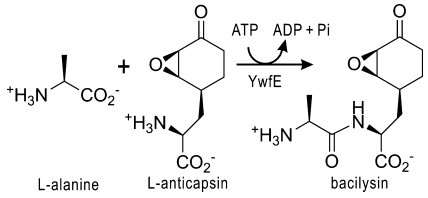

Received: January 22, 2014
Revised: April 4, 2014
Published: April 4, 2014

Some of the ATP-grasp enzymes are considered to be important targets for the development of new antibacterial drugs because of the critical nature of these enzymes and lack of human orthologues. Although Lal is not a clinical target, it has the potential to become an interesting target for the industrial production of useful dipeptides. Dipeptides have unique physicochemical properties and physiological functions. For example, the artificial sweetener aspartame is L-aspartyl-L-phenylalanine methyl ester (L-Asp-L-Phe-OMe). L-Ala-L-Gln is used as a component of patient infusions because of its higher solubility than L-Gln. L-Asp-L-Phe, a precursor of aspartame, was biosynthesized by hybrid NRPS; however, the turnover rate was extremely low (0.7 min^{-1}).[12] Compared with the NRPS system, Lal is a smaller soluble enzyme and participates in a simpler reaction to combine two amino acids. An L-Ala-L-Gln has reportedly been produced via fermentative processes using YwfE-transformed bacteria.[13] However, biochemical and structural studies of Lal are extremely limited compared with those of other members of the ATP-grasp superfamily.

The crystal structures of two Lals have recently been reported. The first determined structure was that of YwfE with bound ADP and phosphinophosphate analogue (P-analogue), which was believed to mimic the tetrahedral transition state.[14] The structure showed that YwfE binds the dipeptide in the reverse orientation to that observed in Ddl, suggesting that the substrate entry mode differs between them. The other structure was BL00235 from *Bacillus licheniformis*, which was bound to ADP and Ca^{2+} ions.[15]

Here, we describe new YwfE crystal structures with bound ADP-Mg^{2+}-Pi and ADP-Mg^{2+}-L-Ala that are refined to 1.9 and 2.0 Å resolutions, respectively. The results suggest that Trp332 plays a key role in N-terminal substrate specificity for smaller amino acids such as L-Ala. Substitution with other residues at position 332 altered the substrate specificity depending on the size and shape of the incorporated residues. These observations afford the possibility of a rational design of YwfE for the production of desirable dipeptides. Furthermore, we propose that based on a structural comparison between Lal and Ddl, the positioning of Arg328 is important for enantioselective recognition of L-amino acids.

EXPERIMENTAL PROCEDURES

Protein Preparation. Cloning, expression, and purification of *Bacillus subtilis* YwfE were performed as previously described,[16] with slight modifications. The gene encoding the full-length protein (Met1−Val472) and deletion mutant (Lys4−Tyr468) of YwfE were amplified using PCR from *B. subtilis* genomic DNA. The amplified PCR products were cloned into the pGEX-6P-1 expression vector (GE Healthcare) with *Bam*HI and *Xho*I sites to produce the fusion protein with N-terminal GST. Mutations were introduced according to the QuikChange site-directed mutagenesis procedure using oligonucleotide primers, except that KODplus (TOYOBO) polymerase was used for PCR. The DNA sequence of the expression plasmid was confirmed by automated DNA sequencing.

The *Escherichia coli* strain ArcticExpress RIL cells (DE3) (Stratagene), containing the expression plasmid, were grown at 37 °C in a Luria−Bertani medium containing 50 μg/mL ampicillin. When the optical density at 600 nm of the culture reached approximately 0.8, expression was induced by the addition of isopropyl β-D-thiogalactopyranoside to a final concentration of 0.3 mM. After an 18-h cultivation at 25 °C, the cells were harvested by centrifugation and suspended in phosphate-buffered saline (PBS) containing 1 mM dithiothreitol (DTT) and lysed by sonication. The lysate was centrifuged at 10,000*g* for 20 min, and the supernatant was loaded onto a Glutathione Sepharose FF column (GE Healthcare) preequilibrated with PBS containing 1 mM DTT. The GST-fused YwfE was eluted with 50 mM Tris-HCl (pH 8.0), 50 mM NaCl, 1 mM DTT, and 15 mM reduced glutathione. The GST tag was cleaved using PreScission protease (GE Healthcare), and the reduced glutathione was removed by extensive dialysis against 50 mM Tris-HCl (pH 8.0), 50 mM NaCl, 1 mM EDTA, and 1 mM DTT. Furthermore, the cleaved GST tag was subsequently removed by chromatography on a Glutathione Sepharose FF column (GE Healthcare). After concentration by ultrafiltration using a Vivaspin-20 10,000 MWCO (Sartorius), the flow-through fraction was loaded onto a HiLoad 16/60 Superdex 75 pg column (GE Healthcare) preequilibrated with 50 mM Tris-HCl (pH 8.0) and 100 mM NaCl. Fractions containing pure YwfE were pooled and dialyzed against 10 mM Tris-HCl (pH 8.0) containing 1 mM DTT and concentrated to approximately 20 mg/mL by ultrafiltration using a Vivaspin-20 10,000 MWCO (Sartorius). The protein concentration was determined by the BCA method (Pierce) using bovine serum albumin as a standard.

Crystallization and Data Collection. Crystallization screening was performed by the hanging-drop vapor-diffusion method at 20 °C.[16] Drops were prepared by manually mixing 2 μL of deletion mutant (Lys4−Tyr468) of YwfE protein solution (8 mg/mL) containing 10 mM ADP, 10 mM $MgCl_2$ (or 5 mM $MnCl_2$), and 10 mM sodium phosphate (pH 7.4) and 2 μL of reservoir solution containing 16%−18% (w/v) PEG 3350, 0.3 M NaCl, 0.1 M HEPES-NaOH (pH 7.0−7.25), 5% (v/v) ethylene glycol, and 1 mM DTT and were equilibrated against 500 μL of reservoir solution. Crystals of the complex with ADP-Mg^{2+}-L-Ala were grown using the same method except that 100 mM L-Ala was added instead of sodium phosphate. The crystallization conditions of the W332A mutant (Lys4−Tyr468) were the same as those for the wild type.

Diffraction data were collected at the BL5A, AR-NE3A, and AR-NW12A beamlines at the Photon Factory (PF; Tsukuba, Japan). Ethylene glycol (20%, v/v) was used as a cryoprotectant for data collection under cryogenic conditions. The crystals were soaked in cryoprotectant-containing mother liquor and flash-cooled in nitrogen stream at 100 K. Mn^{2+}-anomalous data of the Mn^{2+}-derivative crystals were collected at a wavelength of 1.2 Å. The diffraction data sets were processed using the HKL2000 program.[17] All of the crystals belonged to the space group $P6_522$, with one molecule in the asymmetric unit.

Structure Determination and Refinement. Preparation of the SeMet-labeled crystals and data collection using a single-wavelength anomalous dispersion (SAD) method were previously described.[16] To determine the structure of YwfE, SAD phasing, density modification, and automatic model building were performed at 2.8 Å using the CRANK program[18] from CCP4.[19] All of the eight selenomethionine sites in the asymmetric unit were identified with sufficient quality. An initial solvent-flattened electron density map for the polyalanine chains was modeled with the automated model building program ARP/wARP,[20] followed by manual fitting using Coot.[21] Refinement was performed by alternating cycles of manual rebuilding using Coot and refinement using CNS[22] and Refmac5 including TLS refinement.[23] All crystal structures were determined starting from the atomic model obtained

Table 1. Diffraction Data and Refinement Statistics of YwfE Crystals[a]

crystal	wild-type ADP-Mg^{2+}-Pi	wild-type ADP-Mg^{2+}-L-Ala	W332A mutant ADP-Mg^{2+}-L-Ala
wavelength (Å)	1.000	1.000	1.000
beamline	PF BL-5A	PF AR-NW12A	PF AR-NW12A
space group	$P6_522$	$P6_522$	$P6_522$
cell $a = b$ (Å)	90.58	90.02	91.13
c (Å)	252.65	249.80	258.76
resolution (Å)	20−1.9 (1.95−1.90)	20−2.0 (2.05−2.00)	20−2.30 (2.35−2.30)
completeness (%)	88.9 (96.5)	98.3 (99.4)	98.1 (100.0)
redundancy	10.6 (11.1)	9.0 (9.3)	7.6 (7.7)
I/σ (I)	53.5 (9.9)	53.5 (8.3)	55.6 (7.6)
R_{merge} (%)	0.069 (0.312)	0.068 (0.350)	0.038 (0.322)
resolution (Å)	20−1.9	20−2.0	20−2.3
number of reflections	41 606	38 656	24 089
R_{work}/R_{free} (%)	19.90/24.30	19.74/23.59	22.36/26.14
number of atoms	4056	3872	3745
protein	3626	3626	3623
ligands	34	35	35
water	396	211	87
overall B-factor (Å^2)	49.6	47.0	73.9
protein	49.7	47.4	74.3
ligands	43.1	42.2	93.6
water	49.2	40.7	51.3
rmsd			
bond lengths (Å)	0.012	0.011	0.011
bond angles (deg)	1.3	1.3	1.3
Ramachandran[b] (%)	90.1/9.7/0.2/0	89.4/10.4/0.2/0	88.0/12.0/0/0
PDB code	3WNZ	3WO0	3WO1

[a]Values in parentheses are for the highest-resolution shells. [b]Fractions of residues in most favored/additionally allowed/generously allowed/outliners of the Ramachandran plot according to Procheck[24] in the CCP4 suite.[19]

using the SAD data set. Procheck[24] was used for Ramachandran analysis. Statistics of the diffraction data and refinement are listed in Table 1 and Supporting Information, Table S1. All protein structure figures were prepared using PyMol.[25]

Measurement of ATPase Activity. ATPase activities of wild-type and mutated YwfE were measured using the Fiske−Subbarow method[26] to colorimetrically quantify the liberated Pi. Standard ATPase assays were performed at 37 °C in 100 μL of the assay buffer containing 10 mM L-Ala; 30 mM L-Phe (or 50 mM L-Met); 100 mM Bicine-NaOH (pH 9.0); 10 mM $MgCl_2$; 10 mM ATP; and 2.5, 5.0, 7.25, 10, or 15 μg/mL purified full-length YwfE in a 96-well assay plate. Reaction times (between 10 and 45 min) and concentrations of protein (between 2.5 μg/mL and 15 μg/mL) used in the assay were varied depending on the degree of activity. Reactions were started by the addition of 10 μL of 100 mM ATP and stopped by the addition of 50 μL of stop solution containing 10% TCA and 0.1% SDS. Furthermore, 100 μL of the molybdate solution (0.75% ammonium molybdate in 0.675 M H_2SO_4) followed by 10 μL of reducing solution (0.1% 1-amino-2-naphthol-4-sulfonic acid, 1.2% $NaHSO_3$, and 1.2% Na_2SO_3) were added and incubated at 37 °C for 10 min. The amount of released Pi was determined by measuring absorbance at 665 nm using a BiotracII plate reader (GE Healthcare) in a 96-well format. The absorbance of a blank, measured in the condition without protein, was subtracted. Each ATPase activity of the wild-type protein in the presence of 10 mM L-Ala or 30 mM L-Phe alone exhibited activity similar to the background. Pi standards were prepared by dissolving KH_2PO_4 in the buffer. To determine the kinetic parameters, the velocity versus substrate concentration data were subjected to nonlinear least-squares analysis using the Michaelis−Menten equation, $v = V_{max}[S]/([S] + K_m)$, using the SigmaPlot software. All data are presented as the mean ± standard deviation of at least three independent experiments.

Analysis of Dipeptide by HPLC. The reactions were performed at 37 °C in 500 μL of the assay buffer containing 50 mM L-Phe; 100 mM Bicine-NaOH (pH 9.0); 10 mM $MgCl_2$; 10 mM ATP; and 10 μg of purified full-length W332A mutant. After an 18-h incubation, the reactions were stopped by the addition of 0.1% trifluoroacetic acid, and 250 μL of the reaction mixtures were subjected to a reverse-phase HPLC (C_{18} column: 250 mm × 4.6 mm; Kaseisorb LC ODS-120−5, Tokyo Chemical Industry, Japan) with a gradient of acetonitrile in 0.1% trifluoroacetic acid at a flow rate of 0.8 mL/min (elution program: 0 to 15 min, 0% of CH_3CN; 15 to 39 min, a linear increase in CH_3CN from 0% to 32%; 39 to 40 min, a linear increase in CH_3CN from 32% to 80%). Absorbance was monitored at 230 nm. An authentic sample of L-Phe-L-Phe (Sigma-Aldrich) was used as a standard.

RESULTS AND DISCUSSION

Crystal Structures of YwfE in Complex with ADP-Mg^{2+}-Pi and ADP-Mg^{2+}-L-Ala. To elucidate the substrate binding mode and reaction mechanism of L-amino acid ligase (Lal), we prepared native and Se-Met derivative crystals of *B. subtilis* YwfE in the presence of ADP, Mg^{2+}, and L-Ala-L-Gln dipeptide.[16] Although no electron density corresponding to the dipeptide was observed, an unexplained tetrahedral-shaped piece of weak electron density appeared over the β-phosphate group of bound ADP. We assumed this to be an inorganic

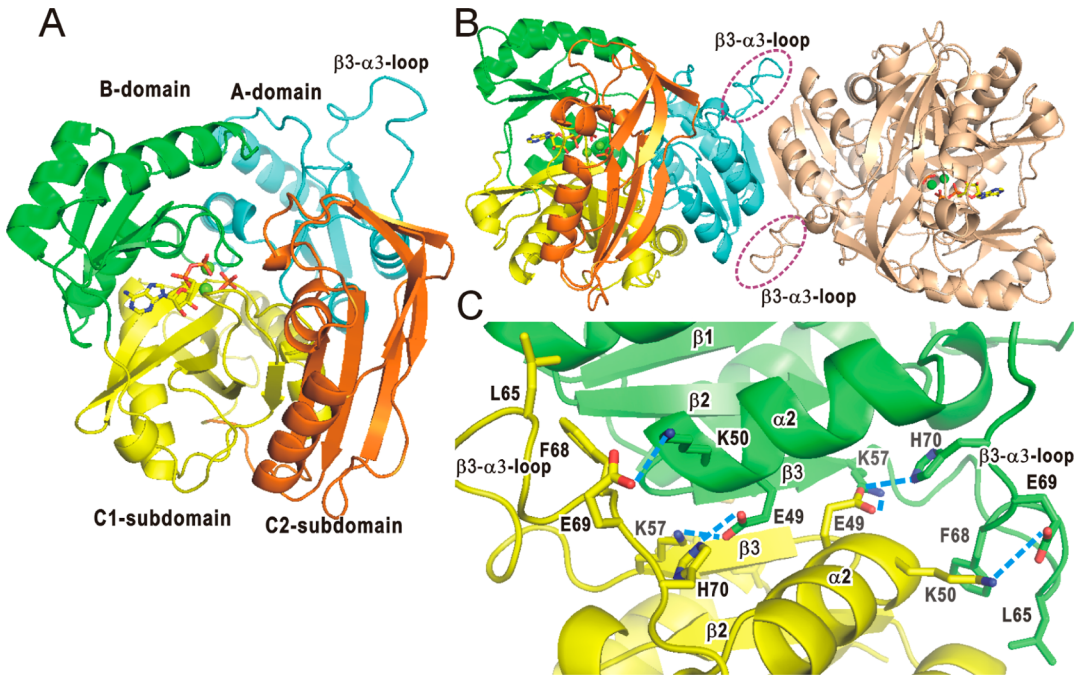

Figure 1. Crystal structure of YwfE from *Bacillus subtilis*. (A) Overall structure of YwfE with bound ADP-Mg^{2+}-Pi. ADP and Pi molecules are presented as a stick model. Two Mg^{2+} ions are presented as green spheres. (B) Oligomeric state of YwfE with bound ADP-Mg^{2+}-Pi. The purple broken circles represent the extended loop region in the A-domain. (C) Close up view of the dimer interface. Two protomers are colored yellow and green. Side chains involved in important interactions in the dimer interface are presented as stick models. The blue broken lines represent the electrostatic interactions between protomers. The figure was prepared using PyMol.[25]

phosphate ion (Pi), which may possibly be derived from the purification procedure. To obtain clear electron density, we attempted to crystallize YwfE in the presence of ADP, Mg^{2+}, and Pi instead of L-Ala-L-Gln. The structure of YwfE with bound ADP, Mg^{2+}, and Pi was determined and refined to 1.9 Å resolution (Table 1). In addition, we determined the structure of YwfE with bound ADP, Mg^{2+}, and L-Ala at 2.0 Å resolution. However, we have not yet determined the crystal structure with bound L-Ala-L-Gln. The YwfE protein used in this study consists of residues Lys4−Tyr468, which lack the N- and C-terminal short regions, so as to improve the quality of crystals, as previously reported.[16] The overall structure consists of three large A-, B-, and C-domains from the N terminus, and the C-domain is further divided into C1- and C2-subdomains flanked by a large antiparallel β-sheet (Figure 1A). The two structures with ADP, Mg^{2+}, and Pi or L-Ala were extremely similar, with a root-mean-square deviation (rmsd) of 0.23 Å for all Cα atoms. These structures were similar to those of the earlier full-length YwfE (Glu2−Val472) with bound ADP and phosphorylated phosphinate L-Ala-L-Phe analogue (P-analogue)[14] with an rmsd of 0.48 Å for 464 Cα atoms, indicating that the deletion of short peptides at both termini exerts little influence on the overall fold. Moreover, the present structures were similar to another available structure of Lal, BL00235, from *B. licheniformis*[15] with an rmsd of 2.75 Å for 365 structurally equivalent Cα atoms.

Size exclusion gel filtration analysis under low ionic strength conditions has shown dimer formation of YwfE in a solution,[16] and two protomers in the crystals formed a dimer through a crystallographic 2-fold axis (Figure 1B). Because the buried surface area of the dimer interface was calculated to cover only 6% of the total surface of the protomers, either protomer was tightly connected by extension of the central β-sheet over the adjacent protomer in the A-domain (Figure 1C). In addition, the interface was stabilized by electrostatic and hydrophobic interactions of several residues in the α2-helix, the β3-strand, and the extended loop between the β3-strand and α3-helix. This type of β-strand-mediated dimer interaction was observed in the human, yeast, and *Trypansoma brucei* glutathione synthetase (GS) structures, which belong to the ATP-grasp superfamily.[27−29] The dimer interface of *T. brucei* GS was calculated to cover 7.5% of the total surface area of a protomer.[29]

Active Site Structures of YwfE. A Fourier difference ($|F_{obs}| - |F_{calc}|$) map before the introduction of ADP, Mg^{2+}, and Pi into the atomic model clearly showed the bound nucleotide in the cleft between the B-domain and C1-subdomain (Figure 2A). ADP is recognized by conserved residues in a manner similar to that observed in other ATP-grasp enzymes. To confirm the location and number of bound Mg^{2+} ion(s), an Mn^{2+} derivative was prepared by cocrystallization with $MnCl_2$ instead of $MgCl_2$ (Table S1, Supporting Information). An anomalous Fourier map clearly showed the location of two Mn^{2+} beside the β-phosphate group of ADP. Therefore, we modeled two Mg^{2+} ions in the ADP-Mg^{2+}-Pi-bound structure. One of the Mg^{2+} ions labeled "Mg1" in Figure 2 is coordinated by oxygen atoms of the α- and β-phosphate groups of ADP, Glu311, Glu324, Pi, and one water molecule (Figure 2B and C). The other Mg^{2+} labeled "Mg2" in Figure 2 is coordinated by oxygen atoms of the β-phosphate group of ADP, Glu324, Pi, and two water molecules. The bidentate carboxyl group of Glu324, which is the highly conserved residue in ATP-grasp enzymes, bridges two Mg^{2+} ions, suggesting that it plays a crucial role in catalysis. For both Mg^{2+} ions, the metal−ligand distances range from 1.8 and 2.4 Å. In the ADP-Mg^{2+}-L-Ala-bound structure, the location and number of bound Mg^{2+} ions were also confirmed by the Mn^{2+} derivative. Two Mg^{2+} ions are octahedrally coordinated by the same ligands as observed in the

dx.doi.org/10.1021/bi500292b | *Biochemistry* 2014, 53, 2650−2660

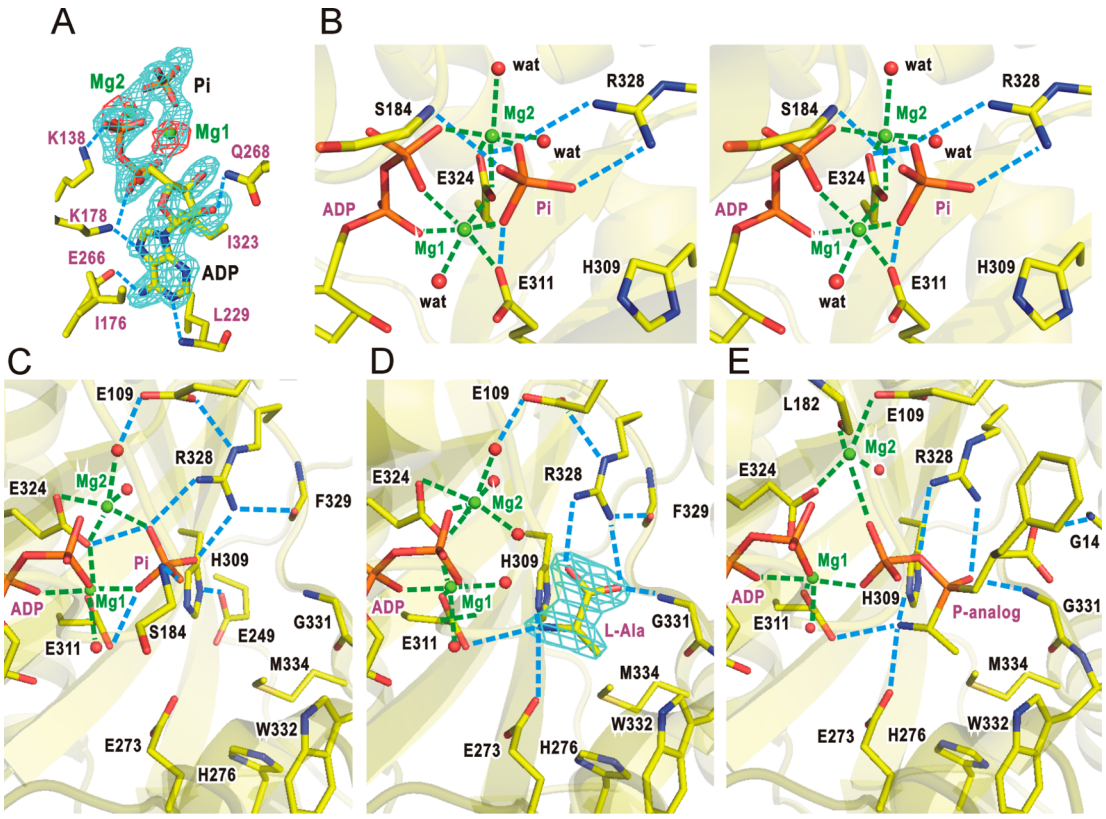

Figure 2. Details of the ligand-binding sites of YwfE. (A) Side chains important for ligand binding are presented as stick models. The cyan net represents a simulated omit map contoured at 2.5σ of ADP-Mg^{2+}-Pi. The red net represents an anomalous Fourier difference map for Mn^{2+} of ADP-Mn^{2+}-Pi-bound form contoured at 10σ. Two Mg^{2+} ions are labeled with Mg1 and Mg2. The blue broken lines represent hydrogen bonds. (B) Stereo view of the Mg^{2+}-Pi-binding site. The red spheres represent Mg^{2+}-coordinating water molecules. The green broken lines represent the coordination of Mg^{2+} ions. The close-up views of (C) ADP-Mg^{2+}-Pi-; (D) ADP-Mg^{2+}-Ala-; and (E) ADP-Mg^{2+}-P-analogue (PDB entry 3VMM)-bound structures are shown in the same view. The cyan net in D represents a simulated omit map contoured at 5σ of L-Ala.

ADP-Mg^{2+}-Pi-bound structure except for substitution of oxygen atoms from a water molecule with those from Pi (Figure 2C). In contrast, in the earlier P-analogue-bound YwfE structure, Mg2 was located at a different position and coordinated by the main-chain carbonyl group of Leu182 and the side chain of Glu109[14] (Figure 2E). A water molecule occupied the same position in our structure (Figure 2C and D). In addition, it should be noted that the present structure showed the side chain of Tyr75 pointed on the opposite side into the active site, although the earlier study suggested that Tyr75 may function as a catalytic base for the deprotonation of the amino group of L-anticapsin, which is a physiological C-terminal end substrate of YwfE[14] (Figure S1, Supporting Information).

The bound Pi is stabilized by hydrogen bonds with the main-chain amide group of Ser184 in the B-domain and the side chains of Glu311, Glu324, and Arg328 in the C1-subdomain (Figure 2B); therefore, Pi bridges these domains. In the ADP-Mg^{2+}-L-Ala-bound structure, the omit map clearly showed that the bound L-Ala was extensively recognized by the YwfE protein (Figure 2D). Both the oxygen atoms of the bound L-Ala are involved in bidentate electrostatic interactions with the guanidinium group of the side chain of Arg328, and one of the oxygen atoms is hydrogen bonded with the main-chain amide group of Gly331. The nitrogen atom of L-Ala has electrostatic interactions with the side chains of Glu273, His309, and Glu311. In addition, His309 makes van der Waals contacts with carbon and oxygen atoms of L-Ala. These residues are highly conserved among Lal, suggesting an important role in catalysis. The Cβ atom of L-Ala makes van der Waals contacts with Glu273, Trp332, and Met324. It is likely that these three residues determine the substrate specificity of YwfE for amino acid with the small side chain in the N-terminal substrate-binding pocket.

Functional Analysis by Site-Directed Mutations. It has been reported that YwfE prefers L-Ala for the N-terminal end and hydrophobic L-Phe or L-Met for the C-terminal end.[5,14] In the functional assay, we used the full-length YwfE (Met1−Val472) protein, and ATPase activity was measured in the combination of L-Ala and L-Phe or L-Met. For the wild-type enzyme, the ATPase activities increased with increasing concentrations of each amino acid, and the obtained curves were well fitted with the Michaelis−Menten equation (Figure S2, Supporting Information). The apparent K_m and k_{cat} values for Ala (1.64 ± 0.45 mM and 9.32 ± 0.89 s^{-1}), Phe (5.23 ± 1.59 mM and 10.4 ± 1.19 s^{-1}), and Met (11.3 ± 2.69 mM and 8.77 ± 0.96 s^{-1}) are similar to those previously reported.[14] The presence of either L-Ala or L-Phe did not show any activity. The affinity for L-Ser was 15-fold lower compared with that of L-Ala, and total activity was decreased to approximately half, which confirms that L-Ala is a suitable substrate for the N-terminal end.

Furthermore, on the basis of the present crystal structure, mutational analysis was performed to elucidate the contribution of each amino acid residue to substrate recognition and catalysis. ATPase assays were performed using the full-length mutants YwfE (Met1−Val472), and the obtained kinetic

dx.doi.org/10.1021/bi500292b | *Biochemistry* 2014, 53, 2650−2660

Table 2. Effect of Mutations on ATPase Activity[a]

YwfE	k_{cat} (s^{-1}) for Ala	K_m (mM) for Ala	k_{cat}/K_m ($mM^{-1}s^{-1}$) for Ala	k_{cat} (s^{-1}) for Phe	K_m (mM) for Phe	k_{cat}/K_m ($mM^{-1}s^{-1}$) for Phe
wild-type	9.32 ± 0.89	1.64 ± 0.45	6.07 ± 1.80	10.4 ± 1.19	5.23 ± 1.59	2.13 ± 0.58
E109A	<0.01			<0.01		
E109D	3.19 ± 1.43	7.12 ± 3.19	0.48 ± 0.14	1.83 ± 0.20	2.28 ± 0.96	0.91 ± 0.39
E273A	ND[b]			ND		
E273D	0.52 ± 0.26	17.06 ± 9.37	0.03 ± 0.00	0.49 ± 0.11	7.71 ± 2.58	0.08 ± 0.05
H276A	6.63 ± 1.34	7.72 ± 1.87	0.90 ± 0.26	4.36 ± 0.66	8.50 ± 0.70	0.51 ± 0.05
H309A	ND			ND		
H309R	ND			ND		
E311A	ND			ND		
E311D	<0.01			<0.01		
R328A	ND			ND		
R328 K	ND			ND		
W332A	4.32 ± 0.39	2.12 ± 0.31	2.07 ± 0.26	4.83 ± 0.55	15.9 ± 2.35	0.31 ± 0.08
M334A	2.62 ± 1.16	2.96 ± 1.82	0.95 ± 0.17	2.33 ± 0.41	3.70 ± 1.12	0.65 ± 0.08

[a]Reactions were performed as described in the Experimental Procedures section. The kinetic parameters were determined by the varying concentrations of either L-Ala or L-Phe. All k_{cat} and K_m values are shown as the mean ± standard deviation of at least three independent experiments. [b]ND means not detectable.

parameters are listed in Table 2. The mutation of each Glu273, His309, Glu311, and Arg328 residue to Ala almost completely diminished the activity, which is consistent with the structure-based predictions. An E273D mutation partially restored the activity, whereas H309R, E311D, and R328K enzymes remained inactive despite the similar charge-conserved mutations. These findings indicate that His309, Glu311, and Arg328 are the crucial residues for catalysis. It appears that the side chains of His309 and Arg328 along with the main-chain amide group of Gly331 form an oxyanion hole to stabilize the phosphorylated intermediate during the reaction cycle. The enzyme with substitution of Glu109 by Ala showed no activity, whereas that with substitution by Asp reduced the activity by approximately 30% compared with that of the wild type. The carboxyl group of Glu109 forms a hydrogen bond with the Nε atom of Arg328 (Figure 2C and D). In addition, at the opposite side, the main-chain carbonyl group of Phe329 forms a hydrogen bond with Arg328. These observations suggest that each residue plays an important role in fixing the side chain of Arg328 in the optimal conformation for L-Ala binding and catalytic reaction. An H276A mutation largely decreased the apparent K_m value for L-Ala approximately 5-fold but exerted little influence on the apparent K_m value for L-Phe, suggesting that His276 can contribute to L-Ala recognition, although it does not directly contact L-Ala. Mutation of Trp332 to Ala caused a decrease in catalytic efficiency (k_{cat}/K_m) for both L-Ala and L-Phe compared with that by the wild type. In addition, M334A mutation decreased the activity approximately 3-fold but did not strongly affect the apparent K_m value for each amino acid. Although Met334 is located in contact with the side chain of bound L-Ala, it is unlikely that this residue is essential for L-Ala binding.

L-Ala-Independent ATPase Activity of Trp332 Mutants. The W332A mutant appeared to retain considerable ATPase activity even in the absence of L-Ala (Figure 3A). In contrast, the addition of L-Ala alone to the reaction mixture showed no activity. It suggests that the mutant could accept L-Phe as an N-terminal end and may produce an L-Phe-L-Phe dipeptide, albeit at an extremely low turnover rate. To investigate the details of the L-Ala-independent ATPase activity observed in this W332A mutant, we measured ATPase activity at varying concentrations of L-Phe or L-Met in the absence of L-Ala. The activity at 50 mM L-Phe alone increased to approximately 20% of that in the presence of both L-Ala and L-Phe (Figure 3B). This L-Ala-independent activity was reduced at lower concentrations of L-Phe. Surprisingly, the ATPase activity increased with increasing concentrations of L-Met to almost the same levels regardless of L-Ala. The activity curve did not fit the Michaelis–Menten equation in the absence of L-Ala but did so in the presence of L-Ala. This observation suggests that L-Met is bound within two distinct binding pockets with different affinities in the absence of L-Ala. It was difficult to determine the apparent K_m value of each affinity.

To confirm the formation of an L-Phe-L-Phe product catalyzed by the YwfE W332A mutant, we performed reverse-phase HPLC analysis on a C_{18} column. The W332A mutant (10 μg) was incubated with 50 mM L-Phe in the presence of 10 mM ATP and 10 mM $MgCl_2$, and the reaction product in 250 μL was identified using a reference standard of an authentic L-Phe-L-Phe (2.5 μmol). The HPLC analysis showed that the W332A mutant enzyme produced about 1.4 μmol of the L-Phe-L-Phe dipeptide (Figure 4A and B). If all of the ATP molecules in the reaction mixture were consumed in order to produce the dipeptide, 2.5 μmol of the dipeptide would be detected by the HPLC analysis. The peaks that appeared before elution by acetonitrile corresponded to ATP (or ADP) and L-Phe (Figure S3A and B, Supporting Information). When the reaction was performed in the absence of ATP, the dipeptide was not observed (Figure S3C, Supporting Information). Thus, substitution of Trp332 with Ala will alter the substrate specificity of YwfE to allow the binding of larger amino acids, such as L-Phe, in the N-terminal substrate-binding pocket, and catalyzes the formation of the L-Phe-L-Phe dipeptide.

Crystal Structure of the W332A Mutant. To elucidate the role of Trp332 and the effects of its mutation on the structure of the substrate-binding pocket, we determined the crystal structure of the YwfE mutant W332A (Lys4–Tyr468) with bound ADP, Mg^{2+}, and L-Ala at 2.3 Å resolution (Table 1). The overall structure of the mutant was similar to that of the wild type with an rmsd of 1.2 Å for all Cα atoms. In addition, the mutant binds ADP and two Mg^{2+} in the same mode as that observed in the wild type. These findings indicate that mutation does not influence the overall fold or the nucleotide binding property. However, a large cavity seems to appear in the

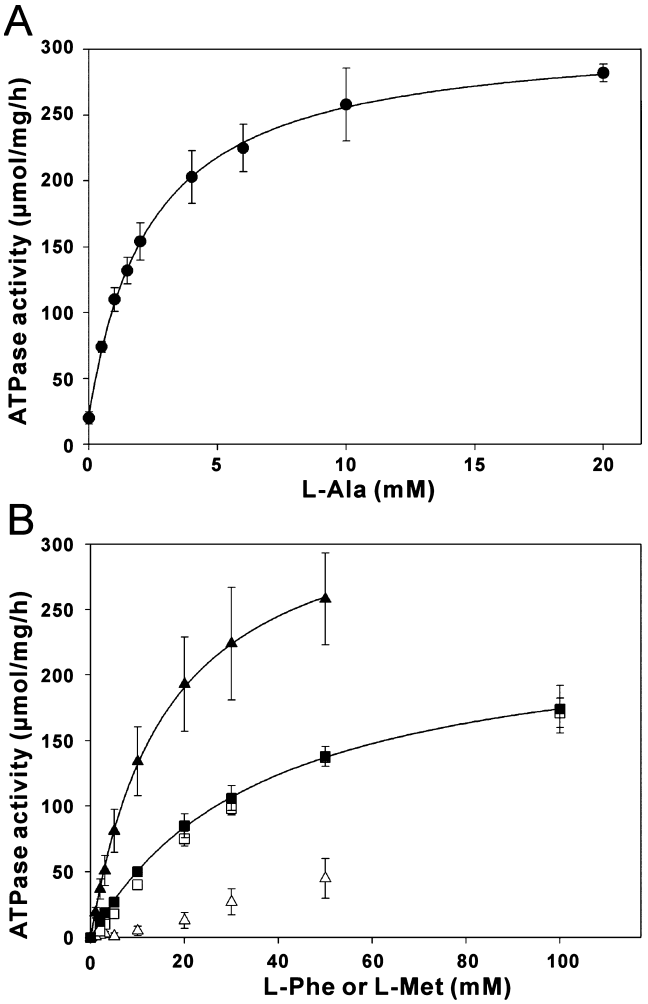

Figure 3. ATPase activity of W332A mutant. (A) The L-Ala concentration dependency of the ATPase activity of the W332A mutant was measured in the presence of 30 mM L-Phe (●). The curve was fitted to the Michaelis–Menten equation using the SigmaPlot software. The errors correspond to the standard deviation of at least three independent experiments. (B) The L-Phe (▲, △) or L-Met (■, □) concentration dependency of the ATPase activity was measured in the presence (closed symbols) or absence (open symbols) of 10 mM L-Ala. The curves could be fitted to a Michaelis–Menten equation when the measurements were performed in the presence of both L-Ala and L-Phe or L-Met.

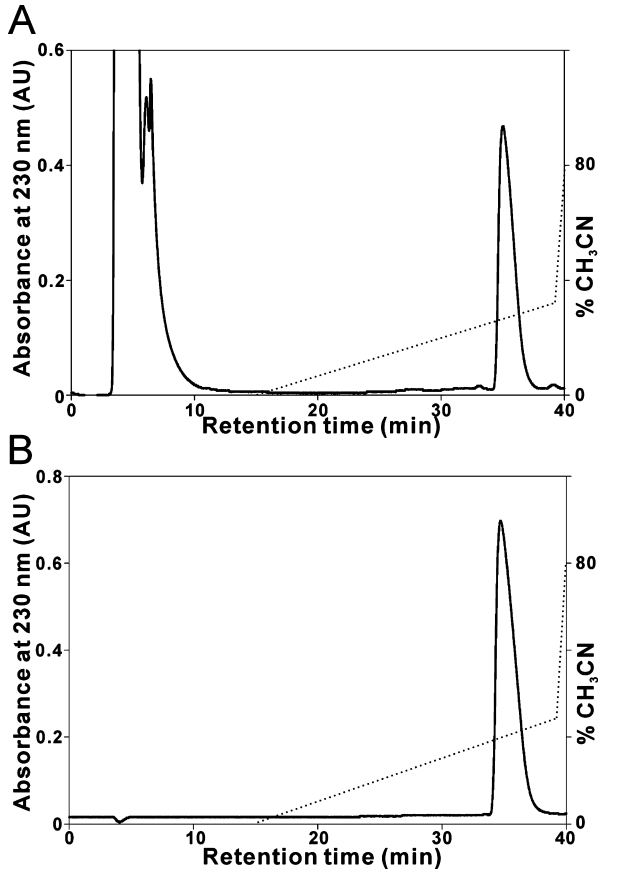

Figure 4. HPLC chromatograms. (A) 250 μL of the reaction products of the W332A mutant were separated by HPLC. The absorbance was monitored at 230 nm (left axis). The dotted lines indicate a linear gradient of acetonitrile (right axis). (B) An L-Phe-L-Phe standard (2.5 μmol) was separated by HPLC under the same conditions. The peak area values of the enzymatic reaction (A) and the standard (B) were estimated to be 38.23 AU × s and 66.56 AU × s, respectively, by using Clarify Lite software (DataApex).

mutant, due to the absence of the large indole ring of Trp332 (Figure 5A). This cavity is formed by the side chains of amino acid residues not only on the C1-subdomain (His276, Ala332, and Met334) but also on the C2-subdomain (Asp376, His378, and Tyr380). A Fourier difference ($|F_{obs}| - |F_{calc}|$) map before the introduction of L-Ala into the atomic model showed that the L-Ala bound in the same mode as that observed in the wild type. The model shows a large space over the Cβ atom of bound L-Ala, suggesting that this space is large enough to accommodate a larger amino acid such as L-Met. Thus, the large and rigid indole ring of Trp332 appears to restrict the substrate specificity for smaller amino acids such as L-Ala in the N-terminal substrate-binding pocket. The orientation of His378 was rotated by approximately 90° compared with that of the wild-type structure. This is because the planar surface of Trp332 is almost parallel to the imidazole ring of His378 via stacking interactions in the wild type (Figure 5B).

The structural and functional properties of W332A mutant YwfE remind us of those of BL00235. The crystal structure of BL00235 with bound ADP-Ca^{2+} showed a large hydrophobic cavity within a putative N-terminal substrate-binding pocket that is formed by the side chains on both C1- and C2-subdomains[15] (Figure 5C). The substrate specificity of BL00235 is entirely different from that of YwfE. It prefers L-Met and L-Leu for the N-terminal end and small substrates such as L-Ala, L-Ser, L-Thr, and L-Cys for the C-terminal end. It can be assumed that introduction of a large residue, such as Trp, into the entrance of the cavity of BL00235 would alter the substrate specificity for small amino acids, as is the case for YwfE. We have not yet obtained the crystal structure of the L-Met-bound form of the W332A mutant, although crystals were obtained in the presence of 10 mM ADP, 10 mM Mg^{2+}, and 100 mM L-Met. In the mutant crystal, the electron density corresponding to the expected side chain portion of L-Met was extremely weak, suggesting that the side chain of L-Met was disordered and did not interact strongly with the enzyme. This result is probably because of the lower affinity of the mutated enzyme for L-Met than for L-Ala, as expected from the functional assay.

Effect on the Substrate Specificity of Mutations at Position 332. To determine whether the size and shape of

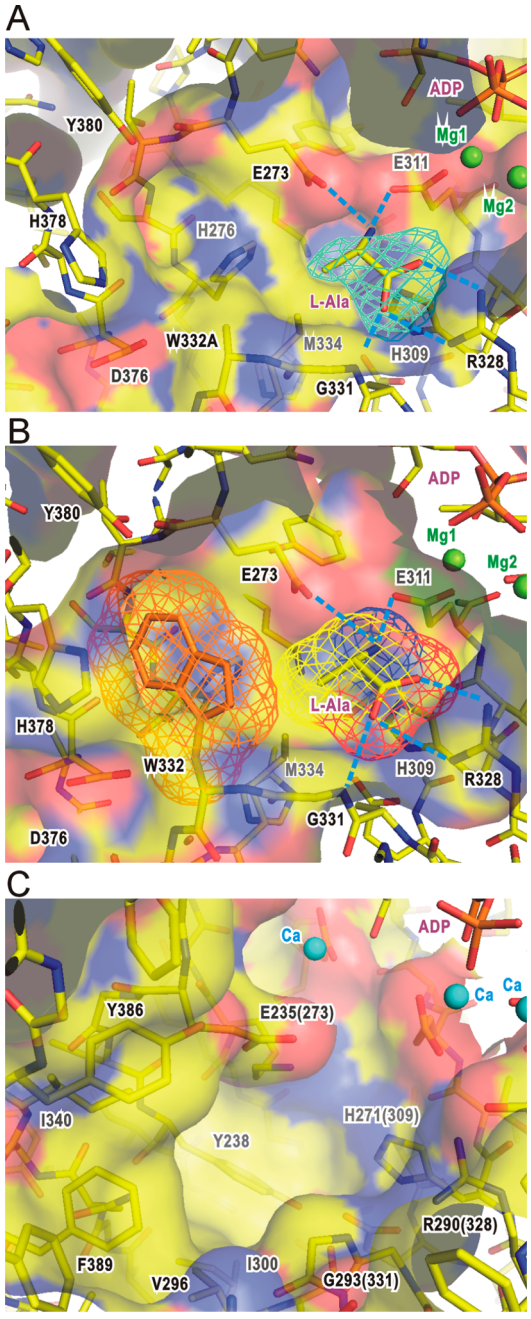

Figure 5. Molecular surface representation of the N-terminal substrate-binding site. (A) Structure of the W332A mutant of YwfE with bound ADP-Mg^{2+}-L-Ala. The cyan net represents a simulated omit map contoured at 3σ of L-Ala. (B) Structure of the wild-type YwfE with bound ADP-Mg^{2+}-Ala. The atom-type and orange nets represent van der Waals surfaces of bound L-Ala and the side chain of Trp332, respectively, in the wild-type ADP-Mg^{2+}-L-Ala-bound structure. (C) The structure of the expected N-terminal substrate-binding region of BL00235 with bound ADP-Ca^{2+} (PDB entry 3VOT). The numbers in parentheses represent the corresponding residues in YwfE.

amino acid residues at position 332 influence the L-Ala-independent ATPase activity, we prepared five additional Trp332 mutants, replacing Trp332 with Ser, Val, Leu, His, or Phe. First, we compared the effect of mutations on the ATPase activity under standard conditions (the presence of L-Ala and L-Phe). Substitutions of Trp332 with Ala, Ser, Val, Leu, or His decreased the activity approximately 70% to 40% compared with that of the wild type (black bars, Figure 6A). However,

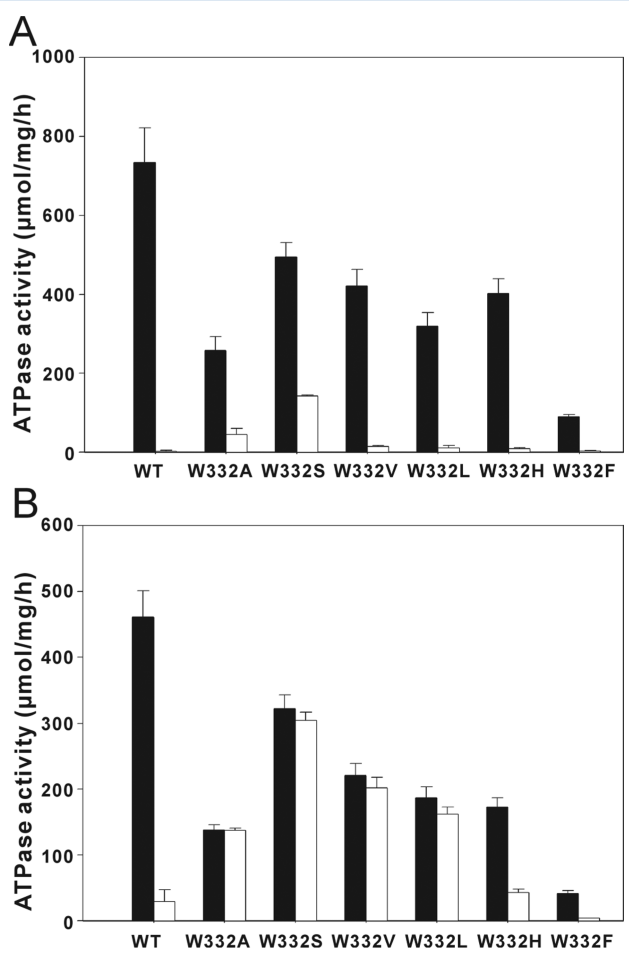

Figure 6. Effect of mutations at Trp332 on the L-Ala-independent ATPase activities. (A) The black and white bars represent 50 mM L-Phe-induced ATPase activities in the presence and absence of 10 mM L-Ala, respectively. The errors correspond to the standard deviations of at least three independent experiments. (B) The same measurements were performed except that 50 mM L-Met was used instead of L-Phe.

mutation of Trp332 to an aromatic Phe largely reduced the activity to >10% compared with that observed in the wild type. It is likely that a 6-member phenyl ring introduced at position 322 collides with the surrounding residues, such as Glu273 and His276, and influences the local structure within the substrate-binding pocket. When the same measurements were performed in the presence of L-Met instead of L-Phe, the results obtained were similar (black bars, Figure 6B). These findings indicate that the Trp residue at position 332 is not directly essential for the catalytic reaction.

Furthermore, to test each mutation on L-Ala-independent ATPase activity, the measurements were performed in the presence of 50 mM L-Phe or L-Met alone. Although the wild-type enzyme hardly showed any activity in the presence of 50 mM L-Phe alone, W332A and W332S retained activities of approximately 20% and 30%, respectively, compared with those in the presence of both L-Ala and L-Phe (white bars, Figure 6A). In contrast to these mutants, each mutant with substitution by Val, Leu, His, or Phe did not show any L-Ala-independent activity. When L-Met was used instead of L-Phe, even the wild-type enzyme retained approximately 6% of the L-Ala-dependent

dx.doi.org/10.1021/bi500292b | *Biochemistry* 2014, 53, 2650−2660

activity (white bars, Figure 6B). This result is consistent with the finding that YwfE has the ability to produce the L-Met-L-Met dipeptide.[5] In addition to W332A and W332S mutants, both W332V and W332L mutants also retained activities at almost the same levels, independent of the presence or absence of L-Ala. Furthermore, the enzyme with a mutation of Trp332 to His retained approximately 25% of the L-Ala-independent activity. These results indicate that each mutant prefers L-Met to the bulky and rigid L-Phe as a substrate. These functional and structural studies of Trp332 mutants allow us to propose that the size and shape of residues at position 332 of YwfE greatly influence substrate specificity in the N-terminal substrate-binding pocket.

Proposed Catalytic Mechanism. The reaction scheme of the ATP-grasp family is believed to proceed through the formation of an acylphosphate intermediate, which is attacked by a nucleophile, leading to a tetrahedral intermediate that ultimately collapses to form the product.[10,11] The superposition of the wild-type YwfE structure of ADP-Mg^{2+}-Pi and ADP-Mg^{2+}-L-Ala-bound forms demonstrated that one of the oxygen atoms from Pi was located very close to the position of the carboxyl oxygen from L-Ala (Figure 7). Thus, this model

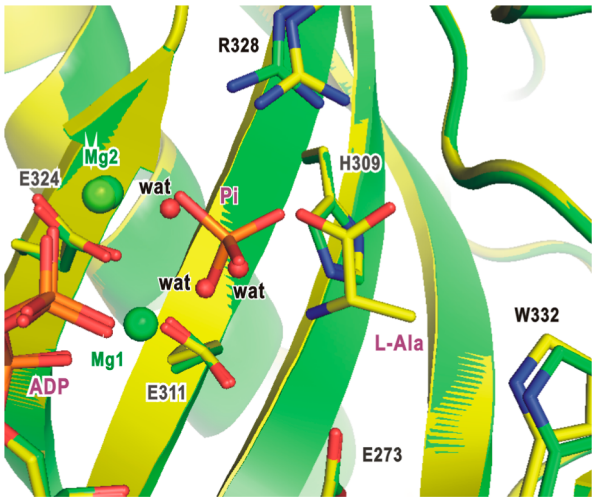

Figure 7. Model of an acylphosphate intermediate. Superimposition of models for the ADP-Mg^{2+}-L-Ala-bound form (atom color) and ADP-Mg^{2+}-Pi-bound form (green) of wild-type YwfE are shown. Side chains involved in important roles in the active site are presented as stick models. Three water molecules of the ADP-Mg^{2+}-L-Ala-bound structure are shown in red spheres.

appears to mimic the acylphosphate intermediate. In comparison with a P-analogue-bound model of YwfE, the acylphosphate portion in each model occupies a nearly identical position, suggesting that binding of phosphorylated L-Ala is firmly stabilized in the enzyme during the reaction cycle.

These considerations lead us to propose a scenario for the catalytic mechanism of YwfE enzyme. First, an ATP molecule is bound within the highly conserved nucleotide-binding cleft, and an L-Ala is recognized within the N-terminal substrate-binding pocket. Furthermore, Arg328 fixes the position of the carbonyl group of L-Ala to orient the positioning of one of the oxygen atoms and polarize a C−O bond suitable for the oxygen atom to attack the γ-phosphate group of ATP to produce an acylphosphate intermediate. An L-Phe (L-anticapsin *in vivo*) is subsequently bound within the C-terminal substrate-binding pocket, and its amino group makes a nucleophilic attack on the carbonyl carbon of the acylphosphate intermediate to form a tetrahedral transition state intermediate, which is stabilized by the positive charge environment formed with His309, Arg328, and the main-chain amide group of Gly331. Arg328 and the two Mg^{2+} ions assist the phosphate transfer and compensate the resulting negative charge in each intermediate. The phosphate is finally released from the acylphosphate to yield the L-Ala-L-Phe dipeptide (bacilysin *in vivo*), and ADP is also released from the nucleotide-binding site.

Role of Conserved Arg. In the catalysis and L-Ala recognition, the crucial residue appears to be Arg328. This Arg is conserved among the other members of the ATP-grasp enzymes. For example, the crystal structure of *E. coli* biotin-dependent carboxylase (BC) shows that bound bicarbonate is recognized by bidentate interactions with the side chain of Arg292.[30] The structure of *E. coli* PurK, one of the purine biosynthesis enzymes, in complex with ADP-Mg^{2+}-Pi, shows that conserved Arg242 recognizes the Pi molecule.[31] In the *E. coli* PurT structure, which is an enzyme participating in the purine biosynthetic pathway, Arg283 is located in the equivalent position to Arg242 in PurK.[32] In addition, the present study reveals that Arg328 plays an important role in the binding of L-Ala and Pi molecules. Amino acid sequence alignment with these enzymes indicates that the Mg1-coordinating Glu residue, which is also highly conserved in this family, is located four residues upstream from these Arg residues (Figure 8A). Although Ddl contains an Arg residue, which is crucial for D-Ala recognition and catalysis, this residue lies at a different position compared with those in other ATP-grasp enzymes. In *E. coli* DdlB,[33] Arg255 lies two residues downstream of another conserved Asp or Glu residue that coordinates Mg2. This Arg position is highly conserved among Ddl family members. YwfE and BL00235 contain important His residues, although the other members of the ATP-grasp superfamily carry uncharged residues at this position.

To compare the locations of the conserved Arg residues between Lal and Ddl, we superimposed the crystal structures of ADP-Mg^{2+}-L-Ala-bound YwfE and ADP-Mg^{2+}-D-Ala-bound Ddl from *Thermus thermophilus* HB8.[34] The structures were similar to an rmsd of 2.70 Å for structurally equivalent 255 Cα atoms. The model also showed that ADP and two Mg^{2+} occupy similar positions in each structure. As expected from the sequence alignment, the model clearly indicates that each Arg residue lies in a different position (Figure 8B). Both side chains of Arg328 in YwfE and Arg268 in TtDdl recognize each carboxyl group of bound L-Ala or D-Ala from the opposite side. As a result, the Ala molecules are bound by the enzyme in nearly reverse orientations. The different positioning of conserved Arg residues between Lal and Ddl will consequently cause the diverse orientation of the N- and C-terminal substrate-binding pockets in each enzyme. Despite the difference in the orientation of bound Ala, the two oxygen atoms of the carboxyl group of each Ala molecule exist in extremely similar positions. Superimposition of the structures of ADP-Mg^{2+}-Pi-bound YwfE and ADP-Mg^{2+}-phosphorylated phosphinate-bound *E. coli* DdlB[33] showed that the ADP, Mg^{2+}, and phosphate moieties in each structure occupied considerably similar positions (not shown). These observations suggest that the formation of an acylphosphate intermediate will occur in the same place independent of the different orientations of bound substrate amino acid. As mentioned above, L-Ala is strictly recognized by multiple electrostatic interactions with the side chains of Glu273, His309, Glu311, Arg328, and the

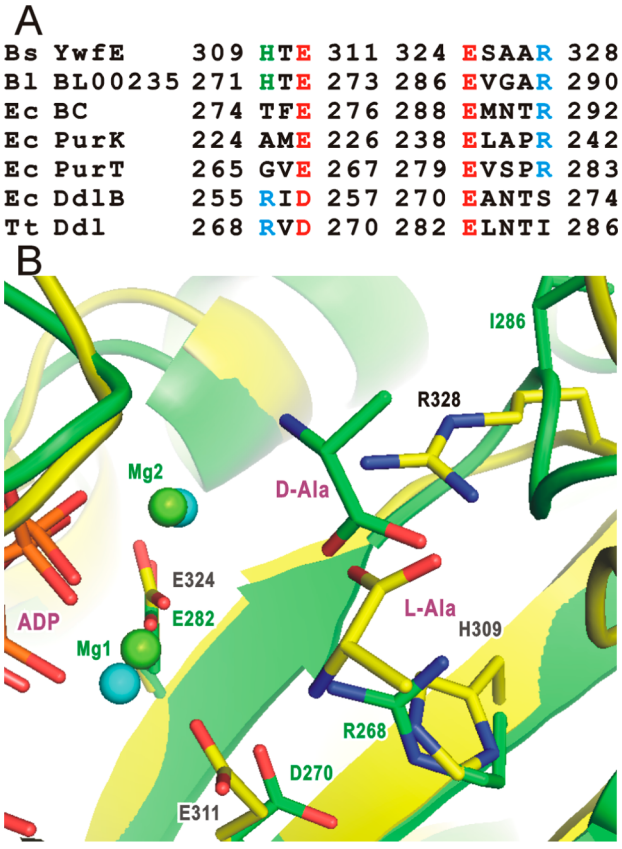

Figure 8. Conserved Arg residue in the ATP-grasp superfamily. (A) Bs, *Bacillus subtilis*; Bl, *Bacillus licheniformis*; Ec, *Esherichia coli*; Tt, *Thermus thermophilus* HB8. A structure-based sequence alignment of residues of conserved Arg (cyan), Mg^{2+}-coordinating Glu or Asp (red), and conserved His among only Lal (green) is shown. All residue numberings are shown on both sides of each line. (B) Superimposition of models for YwfE (atom color) and Ddl from *Thermus thermophilus* HB8 (green) with bound ADP-Mg^{2+}-L-Ala and ADP-Mg^{2+}-D-Ala, respectively. Mg^{2+} ions are represented by green (YwfE) and cyan (Ddl) spheres.

main-chain amide group of Gly321. Among these amino acids, the bidentate binding of the carboxyl group of L-Ala by Arg328 is important for the proper orientation of L-Ala. In addition, we propose that the different positioning of conserved Arg residues in Lal and Ddl is crucial for distinguishing the enantioselectivity in recognition of L- and D-amino acids.

Toward Rational Design of Lal. It has been proposed that Lals are potentially desirable tools for the enzymatic production of dipeptides composed of L-amino acids.[6] In the case of YwfE, an artificial sweetener aspartame (L-Asp-L-Phe-OMe) is likely to be a suitable and attractive candidate for a dipeptide that is produced by an engineered enzyme because L-Phe presents the highest affinity for the C-terminal substrate among the 20 proteogenic L-amino acids. However, restricted substrate specificity for smaller amino acids such as L-Ala at the N-terminus is one of the important issues that should be resolved for aspartame production. At present, the Trp332 mutant YwfE is a promising candidate for resolving this issue. We accordingly measured the ATPase activity of W332A mutant in the presence of L-Asp and L-Phe but observed that the activity was similar to that of the background, although L-Asp is smaller than L-Met or L-Phe. This result may be because of the negative charge of the side chain of L-Asp. To increase affinity and specificity for L-Asp, the introduction of a positively charged residue within the substrate-binding pocket of YwfE may be an effective strategy. One example of a successful change of substrate specificity was reported for subtilisin, a serine protease, in which electrostatic interactions between charged substrates and complementary charged amino acid residues in the substrate-binding pocket were engineered.[35] We are currently attempting to create a mutant YwfE with improved properties of substrate specificity and activity for L-Asp with the aim of engineering protein for the production of aspartame. Most recently, enzymatic production of L-Asp-L-Phe, a precursor of aspartame, by a two-step synthesis with a combination of Lal and yeast N-terminal amidase, given that no Lal has been identified that can produce a dipeptide carrying an acidic residue at the N terminus, has been reported.[36] In the first step, Lal catalyzed the formation of L-Asn-L-Phe from L-Asn and L-Phe, and subsequently, N-terminal amidase deamidated Asn to Asp to produce L-Asp-L-Phe. Several Lal's were identified in bacterial genomes by *in silico* screening, and each recombinant protein showed different substrate specificity. Detailed structural and functional studies of several other Lal's with bound amino acid substrates are desirable for elucidating the relationship between the substrate-binding pockets and amino acid substrate specificity. On the basis of this structural information, systematical introduction of point mutations, insertion, or deletion of amino acids in or near the substrate-binding pocket of Lal will allow the synthesis of modified Lal's with novel substrate-binding properties.

In conclusion, in this study, we determined new crystal structures of YwfE and performed mutagenesis studies. The results demonstrate that Trp332 plays a crucial role in restricting the substrate specificity for smaller amino acids such as L-Ala at the N-terminus and that a single mutation of YwfE can alter substrate specificity. To the best of our knowledge, this is the first demonstration of changing the substrate specificity of Lal by site-directed mutagenesis. These observations raise the possibility of engineering a suitable enzyme for the biosynthesis of dipeptides useful for industrial production. Taken together, our results provide useful guidelines for the rational design of Lal.

■ ASSOCIATED CONTENT

Supporting Information

Diffraction data statistics of Mn^{2+}-derivative crystals; orientation of Tyr75; ATPase activity of wild-type YwfE; and HPLC analysis. This material is available free of charge via the Internet at http://pubs.acs.org.

Accession Codes

The atomic coordinates and structure factors (codes 3WNZ, 3WO0, and 3WO1) have been deposited in the Protein Data Bank, Research Collaboratory for Structural Bioinformatics, Rutgers University, New Brunswick, NJ (http://wwwrscb.org/).

■ AUTHOR INFORMATION

Corresponding Author

*Tel: 83-3-3986-0221. Fax: 83-3-5992-1029. E-mail: takeo.tsuda@gakushuin.ac.jp.

Funding

This work was supported in part by a grant from JGC-S Scholarship Foundation to T.T.

Notes

The authors declare no competing financial interest.

■ ACKNOWLEDGMENTS

We would like to thank the beamline scientists at the Photon Factory for assistance with data collection. We thank Enago (www.enago.jp) for English language review.

■ ABBREVIATIONS

BC, biotin-dependent carboxylase; BSA, bovine serum albumin; Ddl, D-alanyl-D-alanine ligase; DTT, dithiothreitol; HPLC, high performance liquid chromatography; Lal, L-amino acid ligase; NRPS, nonribosomal peptide synthetase; PCR, polymerase chain reaction; PDB, protein data bank; PEG, poly(ethylene glycol); Pi, inorganic phosphate

■ REFERENCES

(1) Nolan, E. M., and Walsh, C. T. (2009) How nature morphs peptide scaffolds into antibiotics. *ChemBioChem. 10*, 34−53.
(2) Velasquez, J. E., and van der Donk, W. A. (2011) Genome mining for ribosomally synthesized natural products. *Curr. Opin. Chem. Biol. 15*, 11−21.
(3) Koglin, A., and Walsh, C. T. (2009) Structural insights into nonribosomal peptide enzymatic assembly lines. *Nat. Prod. Rep. 26*, 987−1000.
(4) Sieber, S. A., and Marahiel, M. A. (2005) Molecular mechanisms underlying nonribosomal peptide synthesis: approaches to new antibiotics. *Chem. Rev. 105*, 715−738.
(5) Tabata, K., Ikeda, H., and Hashimoto, S. (2005) *ywfE* in *Bacillus subtilis* codes for a novel enzyme, L-amino acid ligase. *J. Bacteriol. 187*, 5195−5202.
(6) Kino, K., Kotanaka, Y., Arai, T., and Yagasaki, M. (2009) A novel L-amino acid ligase from *Bacillus subtilis* NBRC3134, a microorganism producing peptide-antibiotic rhizocticin. *Biosci. Biotechnol. Biochem. 73*, 901−907.
(7) Kino, K., Arai, T., and Tateiwa, D. (2010) A novel L-amino acid ligase from *Bacillus subtilis* NBRC3134 catalyzed oligopeptide synthesis. *Biosci. Biotechnol. Biochem. 74*, 129−134.
(8) Senoo, A., Tabata, K., Yonetani, Y., and Yagasaki, M. (2010) Identification of novel L-amino acid α-ligases through Hidden Markov Model-based profile analysis. *Biosci. Biotechnol. Biochem. 74*, 415−418.
(9) Steinborn, G., Hajirezaei, M. R., and Hofemeister, J. (2005) *bac* genes for recombinant bacilysin and anticapsin production in *Bacillus* host strains. *Arch. Microbiol. 183*, 71−79.
(10) Galperin, M. Y., and Koonin, E. V. (1997) A diverse superfamily of enzymes with ATP-dependent carboxylate-amine/thiol ligase activity. *Protein Sci. 6*, 2639−2643.
(11) Fawaz, M. V., Topper, M. E., and Firestine, S. M. (2011) The ATP-grasp enzymes. *Bioorg. Chem. 39*, 185−191.
(12) Duerfahrt, T., Doekel, S., Sonke, T., Quaedflieg, P. J., and Marahiel, M. A. (2003) Construction of hybrid peptide synthetases for the production of α-L-aspartyl-L-phenylalanine, a precursor for the high-intensity sweetener aspartame. *Eur. J. Biochem. 270*, 4555−4563.
(13) Tabata, K., and Hashimoto, S. (2007) Fermentative production of L-alanyl-L-glutamine by a metabolically engineered *Escherichia coli* strain expressing L-amino acid α-ligase. *Appl. Environ. Microbiol. 73*, 6378−6385.
(14) Shomura, Y., Hinokuchi, E., Ikeda, H., Senoo, A., Takahashi, Y., Saito, J., Komori, H., Shibata, N., Yonetani, Y., and Higuchi, Y. (2012) Structural and enzymatic characterization of BacD, an L-amino acid dipeptide ligase from *Bacillus subtilis*. *Protein Sci. 21*, 707−716.
(15) Suzuki, M., Takahashi, Y., Noguchi, A., Arai, T., Yagasaki, M., Kino, K., and Saito, J. (2012) The structure of L-amino-acid ligase from *Bacillus licheniformis*. *Acta. Crystallogr., Sect. D 68*, 1535−1540.
(16) Tsuda, T., Suzuki, T., and Kojima, S. (2012) Crystallization and preliminary X-ray diffraction analysis of *Bacillus subtilis* YwfE, an L-amino-acid ligase. *Acta Crystallogr., Sect. F 68*, 203−206.
(17) Otwinowski, Z., and Minor, W. (1997) Processing of X-ray diffraction data collected in oscillation mode. *Methods Enzymol. 276*, 307−325.
(18) Ness, S. R., de Graaff, R. A., Abrahams, J. P., and Pannu, N. S. (2004) CRANK: new methods for automated macromolecular crystal structure solution. *Structure 12*, 1753−1761.
(19) Collaborative Computational Project, N (1994) The CCP4 suite: programs for protein crystallography. *Acta Crystallogr., Sect. D 50*, 760−763.
(20) Lamzin, V. S., and Wilson, K. S. (1993) Automated refinement of protein models. *Acta Crystallogr., Sect. D 49*, 129−147.
(21) Emsley, P., and Cowtan, K. (2004) Coot: model-building tools for molecular graphics. *Acta Crystallogr., Sect. D 60*, 2126−2132.
(22) Brünger, A. T., Adams, P. D., Clore, G. M., DeLano, W. L., Gros, P., Grosse-Kunstleve, R. W., Jiang, J. S., Kuszewski, J., Nilges, M., Pannu, N. S., Read, R. J., Rice, L. M., Simonson, T., and Warren, G. L. (1998) Crystallography & NMR system: A new software suite for macromolecular structure determination. *Acta Crystallogr., Sect. D 54*, 905−921.
(23) Winn, M. D., Murshudov, G. N., and Papiz, M. Z. (2003) Macromolecular TLS refinement in REFMAC at moderate resolutions. *Methods Enzymol. 374*, 300−321.
(24) Laskowski, R. A., MacArthur, M. W., Moss, D. S., and Thornton, J. M. (1993) PROCHECK: a program to check the stereochemical quality of protein structures. *J. Appl. Crystallogr. 26*, 283−291.
(25) DeLano, W. (2002) *The PyMOL Molecular Graphics System*; DeLano Scientific: Palo Alto, CA..
(26) Fiske, C. H., and Subbarow, Y. (1925) The colorimetric determination of phosphorus. *J. Biol. Chem. 66*, 375−400.
(27) Polekhina, G., Board, P. G., Gali, R. R., Rossjohn, J., and Parker, M. W. (1999) Molecular basis of glutathione synthetase deficiency and a rare gene permutation event. *EMBO J. 18*, 3204−3213.
(28) Gogos, A., and Shapiro, L. (2002) Large conformational changes in the catalytic cycle of glutathione synthase. *Structure 10*, 1669−1676.
(29) Fyfe, P. K., Alphey, M. S., and Hunter, W. N. (2010) Structure of *Trypanosoma brucei* glutathione synthetase: domain and loop alterations in the catalytic cycle of a highly conserved enzyme. *Mol. Biochem. Parasitol. 170*, 93−99.
(30) Chou, C. Y., Yu, L. P., and Tong, L. (2009) Crystal structure of biotin carboxylase in complex with substrates and implications for its catalytic mechanism. *J. Biol. Chem. 284*, 11690−11697.
(31) Thoden, J. B., Holden, H. M., and Firestine, S. M. (2008) Structural analysis of the active site geometry of N^5-Carboxyaminoimidazole ribonucleotide synthetase from *Escherichia coli*. *Biochemistry 47*, 13346−13353.
(32) Thoden, J. B., Firestine, S., Nixon, A., Benkovic, S. J., and Holden, H. M. (2000) Molecular structure of *Escherichia coli* PurT-encoded glycinamide ribonucleotide transformylase. *Biochemistry 39*, 8791−8802.
(33) Fan, C., Moews, P. C., Walsh, C. T., and Knox, J. R. (1994) Vancomycin resistance: structure of D-alanine: D-alanine ligase at 2.3 Å resolution. *Science 266*, 439−443.
(34) Kitamura, Y., Ebihara, A., Agari, Y., Shinkai, A., Hirotsu, K., and Kuramitsu, S. (2009) Structure of D-alanine-D-alanine ligase from *Thermus thermophilus* HB8: cumulative conformational change and enzyme-ligand interactions. *Acta Crystallogr., Sect. D 65*, 1098−1106.
(35) Wells, J. A., Powers, D. B., Bott, R. R., Graycar, T. P., and Estell, D. A. (1987) Designing substrate specificity by protein engineering of electrostatic interactions. *Proc. Natl. Acad. Sci. U S A 84*, 1219−1223.
(36) Arai, T., Noguchi, A., Takano, E., and Kino, K. (2013) Application of protein N-terminal amidase in enzymatic synthesis of dipeptides containing acidic amino acids specifically at the N-terminus. *J. Biosci. Bioeng. 115*, 382−387.

細胞分裂構造の制御メカニズムの解明

教授　馬渕　一誠
助教　柏崎　隼

[目的]

細胞の分裂は細胞の増殖や生物体の成長にとって必須の過程である。全ての細胞において細胞分裂は細胞の外部環境や細胞周期によって制御されており，制御システムに異常が生じると細胞は無限に増殖し、これが多細胞生物において起こると癌となる。したがって細胞の分裂がどのように制御されているのかを知ることは重要である。細胞分裂は染色体DNAが複製された後に２極に分離する核分裂と細胞自体が２分する細胞質分裂が連続的に起こることによって完了する。動物細胞の細胞質分裂においては分裂位置が染色体分離を担った分裂装置によって決定され、分裂位置の細胞表層に収縮環と呼ばれる構造が形成される。収縮環は細胞骨格タンパク質アクチンの繊維によって構成され，モータータンパク質ミオシン II をも含んでいる。私たちのこれまでの研究により収縮環はミオシンとアクチン繊維の相互作用によって収縮して細胞を２分すると考えられている(1)。同じ様式の分裂は原始的な真核細胞であるモデル生物としても研究されている菌類（酵母など）でも行われていることが分かってきた。本研究は分裂酵母，ウニ卵、カエル卵をもちいて、収縮環の形成と収縮がどのような分子機構により制御されているかを明らかにすることを目的とする。

[結果と考察]

1. 分裂酵母の細胞質分裂の *in vitro* 研究系の開発と成果

分裂酵母 *Schizosaccharomyces pombe* は単細胞かつ半数体で栄養増殖する子嚢菌の一種であり、細胞周期や細胞分裂の研究のモデル生物として用いられている。分裂期にはいると細胞の中央部にFアクチンリングと呼ばれる環状構造を形成し、リングの径が減少すると同時に隔壁が形成され、侵入してきて分裂する。このリングにはミオシンをはじめ(2)、動物細胞の収縮環の成分と共通のいくつかのタンパク質成分が含まれていることが分かっているが、このリングが自力で収縮するかどうかは分かっていなかった。本研究ではFアクチンリングが動物細胞の収縮環に相当する構造であると考え、分裂酵母細胞を透過性にして F アクチンリングの収縮を研究できる実験系を開発することにした。

多数のFアクチンリングを観察する必要があるので細胞周期を同調するために *cdc25* 分裂変異株を用いた。さらにリングを蛍光可視化するために、*cdc25* 株にミオシン調節軽鎖−GFP 融合タンパク質を染色体から発現させた。細胞壁を lysing enzyme 処理によって除いた。細胞を制限温度処理によって同調させ，F-アクチンリング（観察しているのはミオシンリング）が形成された事を確認して、界面活性剤により細胞膜を破壊した。こうして得られた「細胞ゴースト」にはミオシンリングは残っていたが、細胞質は消失していた。

細胞ゴースト中のミオシンリングは ATP を与えることによって速やかに収縮した。各種ヌクレオチドの中でATPが最も良い収縮を起こし、ATPの非水解性アナログでは

収縮が起こらなかった。ATP による収縮速度は動物細胞の収縮環の収縮速度に匹敵し、それは生細胞のミオシンリングの収縮速度の 20-30 倍であった。この実験結果は、ミオシンリング（F-アクチンリング）がまさに収縮環であることを初めて証明したのみならず，生細胞ではその収縮を制御するシステムが存在することを示唆した。細胞ゴーストの収縮環の収縮はミオシン ATPase 活性の阻害剤によって阻害された。またミオシンの温度感受性変異株を用いて作製したゴーストは制限温度下では収縮しなかった。従って，動物細胞同様、ミオシン II が収縮に働いていることが分かった。一方、動物細胞、分裂酵母の収縮環は収縮しながらアクチンを失って行き(3), 収縮後にはアクチン繊維が分裂位置から消失している。一方、アクチン繊維安定化剤を加えると収縮は停止する(4)。これらの研究から、アクチンの脱重合が収縮環の収縮には必須なのではないかと考えられてきた。しかしこの *in vitro* 収縮系での実験から、収縮中にアクチンは脱重合するが、それは収縮そのものには必須ではないことが証明された。また、収縮環には IQGAP, α-actinin(5), fimbrin(6)などのアクチン繊維架橋タンパク質が存在して収縮環構造を安定化していると考えられている。本研究では細胞ゴーストにこれらの精製タンパク質を加えたところ、加える量を増やすに伴って収縮は阻害された。このことから，収縮には適正量のアクチン繊維架橋タンパク質が必要であることが分かった。以上の研究は論文公表した。

2. 収縮環の形成とアクチン調節タンパク質、ミオシン

収縮環はアクチンが分裂位置で再編成される、あるいは重合することによって形成されると考えられている。そしてこれらの過程には様々なアクチン調節タンパク質が働いていると考えられている。本研究ではまず分裂酵母のアクチン脱重合因子 Adf1 の働きを調べた。そのため我々が単離した *adf1* の温度感受性変異株 *adf1-1* (7)を用いた。*adf1-1* 変異を起こすには制限温度下で数分を要した。この性質をもちい、細胞周期の様々な段階で Adf1 を失活させて分裂に対する影響を調べた。その結果、G2 期の終わりから、分裂後期 B の初めまでに Adf1 を失活させると、収縮環の形成が妨げられるか，異常になることが分かった。この結果から、収縮環の形成には Adf1 によるアクチンの再編成が必要であることが分かった。この研究は論文を執筆中である。

一方，収縮環アクチンを重合させると考えられている formin の一種 Diaphanous の局在をウニ卵を用いて調べた。ウニ Diaphanous（uDia）の抗体をモルモットで作製し、間接蛍光抗体法でその局在を調べた結果，分裂溝に点状に分布し、収縮環アクチン繊維とほぼ同レベルに存在していた。この研究は超解像顕微鏡を用いて継続中である。

また、ウニ卵を超解像蛍光顕微鏡で観察することにより，アクチン繊維とミオシンの位置関係を解析した。超解像蛍光顕微鏡の一つ SIM で観察すると、収縮環アクチン繊維の 1 本 1 本が確認でき、その間にミオシンがおそらく繊維状に存在していることがわかった。この系を用いてアクチン繊維とミオシン繊維の位置関係，収縮環形成過程での位置関係の変化を研究継続中である。

3. 収縮環の *in vitro* 形成系の開発

収縮環を *in vitro* で形成させることができれば，形成過程を簡単に人為的に制御することができるため、細胞分裂の理解は著しく進展すると思われる。このような系を開発

する目的で、アフリカツメガエルの卵母細胞の細胞質を人工脂質膜に封入する研究を行った。リポソームに細胞質を封入することも可能だが，リポソームの安定性が悪いので、オイル中で細胞質を含む脂質膜小胞を作製した。すると細胞質中に X-body と命名した小塊が形成され、脂質膜から X-body に向かってアクチンの流れが起こった。この流れは脂質膜でのアクチンの重合と X-body での脱重合がカップルして起こることで維持されていることがわかった。また流れにはミオシンの ATPase 活性が必要だった。さらに，アクチンの流れは脂質膜小胞そのものの運動を誘発した。これらの現象は生きた卵母細胞中では観察されていないが、魚の鱗のケラトサイトや培養繊維芽細胞の葉状仮足で見られる有名な現象で，運動性が見られていない卵母細胞の抽出液で観察されたことは大変興味深い。ここまでの研究成果の論文を執筆中である。今後は脂質膜小胞中に人工的に収縮環を形成させる方向で研究を発展させる。

[まとめ]

１．分裂酵母の細胞質分裂の *in vitro* 研究系の開発と成果

分裂酵母の細胞から、収縮環の *in vitro* 収縮系の開発に成功し，分裂酵母の収縮環が動物細胞のそれと同等であること、収縮にミオシンが必須であること、細胞内には収縮を制御するシステムがあること，アクチン脱重合は収縮とともに起こるが収縮には必須でないこと、収縮には適正量のアクチン繊維架橋タンパク質が必要であること、などを明らかにした。

2. 収縮環形成過程の研究

アクチン脱重合因子 ADF が収縮環形成におけるアクチンの再編成に働いていることを解明できた。また、収縮環の形成過程におけるミオシンとアクチン繊維の位置関係を分子レベルで構造の上から解明できる糸口をつかんだ。

3. 収縮環の *in vitro* 形成系の開発

本研究はまた始まった段階だが、カエル卵母細胞の抽出液にアクチン重合によって駆動される新しい運動能力があることを発見するという，大きな成果が得られている。

[参考文献]

1. Mabuchi, I., and Okuno, M. (1977). The effect of myosin antibody on the division of starfish blastomeres. J. Cell Biol. *74*, 251-263.
2. Motegi, F, Nakano, K., and Mabuchi, I. (2000). Molecular mechanism of myosin-II assembly at the division site in *Schizosaccharomyces pombe*. J. Cell Sci. *113*, 1813-1825.
3. Kamasaki, T., Osumi, M., and Mabuchi, I. (2007). Three-dimensional arrangement of F-actin in the contractile ring of fission yeast. J. Cell Biol. *178*, 765-771.
4. Hamaguchi, Y. and Mabuchi, I. (1982). Effects of phalloidin microinjection and localization of fluorescein-labeled phalloidin in living sand dollar eggs. Cell Motility *2*, 103-113.
5. Mabuchi, I., Hamaguchi, Y., Kobayashi, T., Hosoya, H., Tsukita. S. and Tsukita, S. (1985). Alpha-actinin from sea urchin eggs: biochemical properties, interaction with actin, and distribution in the cell during fertilization and cleavage. J. Cell Biol. *100*, 375-383.
6. Nakano, K., Sato, K., Morimatsu, A., Ohnuma, M., and Mabuchi, I. (2001). Interactions among a fimbrin, a capping protein, and an actin-depolymerizing factor in organization of the fission yeast actin cytoskeleton. Mol. Biol. Cell *12*, 3515-3526.

7. Nakano, K., and Mabuchi, I. (2006). Actin-depolymerizing protein Adf1 is required for formation and maintenance of the contractile ring during cytokinesis in fission yeast. Mol. Biol. Cell *17*, 1933-1945.

［原著論文］

1. Yano, K., Uesono, Y., Yoshida, S., Kikuchi, A., Kashiwazaki, J., Mabuchi, I., and Kikuchi, Y. (2013). Mih1/Cdc25 is negatively regulated by Pkc1 in *Saccharomyces cerevisiae.* Genes Cells *18*, 425-441.

2. Mishra, M., Kashiwazaki, J., Takagi, T., Srinivasan, R., Huang, Y., Balasubramanian, M. K., and Mabuchi, I. (2013). *In vitro* contraction of cytokinetic ring depends on myosin II but not on actin dynamics. Nat. Cell Biol. *15*, 853-859.

3. Nakase, Y., Nakase, M., Kashiwazaki, J., Murai, T., Otsubo, Y., Mabuchi, I., Yamamoto, M., Takegawa K., and Matsumoto, T. (2013). Fission yeast Any1, a β-arrestin-like protein, is involved in TSC-Rheb signaling and regulates amino acid transporters. J. Cell Sci. *126*, 3972-3981.

[総説等]

1. 柏崎隼、高木智子、馬渕一誠. (2013). *In vitro* における収縮環の収縮はミオシン II に依存するがアクチンのダイナミクスには依存しない。ライフサイエンス新着論文レビュー 7443.
2. 馬渕一誠. (2013). 顕微鏡でものを見ることの新しい動き−特集によせて。 生体の科学 *64*, 524-525 .
3. 馬渕一誠. (2014). 細胞はどのようにして分裂を繰り返すか。2001 年ノーベル生理学・医学賞受賞 Paul Nurse 博士。学習院大学講演録。 細胞工学 *33*, 182.
4. 柏崎隼、馬渕一誠. (2014). 収縮環の*in vitro* 収縮系の開発。生物物理 *54*, 201-205.
5. 馬渕一誠、柏崎隼. (2014). 細胞質分裂における収縮環の収縮：*in vitro*系の開発。細胞工学 *33*, 660-665.
6. Mabuchi, I., Kashiwazaki, J., and Mishra, M. (2016). *In vitro* reactivation of the cytokinetic contractile ring of fission yeast cells. Methods in Cell Biol. (Elsevier), *in press.*

［口頭発表］

1. 柏崎隼、Mishra, M., Balasubramanian, M., 馬渕一誠： 分裂酵母ゴーストを用いた収縮環の *in vitro* 再活性化。第 65 回日本細胞生物学会大会シンポジウム（2013.6.19-21, 名古屋）招待講演。

2. Mishra, M., Kashiwazaki, J., Takagi, T., Srinivasan, R., Huang, Y., Balasubramanian, M., and Mabuchi, I. 2013.: In vitro contraction of cytokinetic ring depends on myosin II but not on actin dynamics. EMBO Conference on Fission Yeast: Pombe 2013 (24-29 June 2013, London). 招待講演。

3. Balasubramanian, M., Tao, E. Y., Mishra, M., Kashiwazaki, J., Huang, Y., Huang, J. J., Takagi, T., Subramanian, D., Xie, T., and Mabuchi, I.： Cytokinesis *in vitro* and *in vivo*. EMBO Conference in Fission Yeast (24-29 June 2013, London). 招待講演。

4. Balasubramanian, M., Mishra, M., Kashiwazaki, J., Tao, E. Y., Huang, Y., Huang, J. J., Takagi, T., Subramanian, D., Xie, T., Padmanabhan, A., Haochen, J., Wedlich-Soldner, R. and Mabuchi, I.: Cytokinesis *in vitro* and *in vivo*. Cell Biology of Yeasts, (Cold Spring Harbor, NY, 2013.11.5-9). 招待講演。

5. Kashiwazaki, J., and Mabuchi, I. Actin cable motility during interphase in fission yeast. Cell Biology of Yeasts, (Cold Spring Harbor, NY, 2013.11.5-9)

6. 馬渕一誠: *In vitro* 実験系の開発による細胞質分裂の研究。NAIST シンポジウム「細胞を創る操る」(奈良、2013.11.28)、 招待講演。

7. 馬渕一誠、柏崎隼、Mishra,M., 高木智子、Srinivasan, R., Huang, Y., and Balasubramanian, M. 収縮環の *in vitro* 実験系の開発による収縮機構の研究。第 36 回日本分子生物学会年会 (神戸、2013.12.3-6)、 招待講演。

8. 柏崎隼、Mishra, M., 高木智子、Balasubramanian, M., and 馬渕一誠：分裂酵母収縮環の *in vitro* 再活性化。第 36 回日本分子生物学会年会 (神戸、2013.12.3-6)

9. Kashiwazaki. J., Mishra, M., Balasubramanian, M., and Mabuchi, I. *In vitro* contraction system of the fission yeast contractile ring. 2013 ASCB Annual Meeting. (New Orleans, 2013.12.14-18)

10. Mishra, M., Kashiwazaki, J., Takagi, T., Srinivasan, R., Huang, Y., Balasubramanian, M. K., and Mabuchi, I.: *In vitro* contraction of cytokinetic ring depends on myosin II but not on actin dynamics. 58th Annual Meeting of the Biophysical Society (15-19 Feb. 2014, San Francisco). 招待講演。

11. Mabuchi, I.: *In vitro* reactivation of contractile ring in fission yeast cell ghost. 7th APOCB Congress and ASCB Workshop (24-27 Feb. 2014, Singapore). 招待講演。

12. Mabuchi, I.: Contraction of the contractile ring as studied by using an *in vitro* system. International Symposium on the Diversity of Cell Division System in Eukaryotes. (24-25 March 2014, Tokyo). 招待講演。

13. 植田英一、柏崎隼、馬渕一誠：分裂酵母の収縮環形成における ADF/cofilin とフィンブリンの機能。 第 66 回日本細胞生物学会大会（2014.6.11-13, 奈良）

14. 野田直紀、馬渕一誠：Actin dynamics in *Xenopus* egg extract encapsulated in a lipid membrane. *Xenopus* 卵抽出液を封入した脂質膜小胞中でのアクチンのダイナミクス。日本生物物理学会第 52 回年会（2014.10.25-27 札幌）

15. 野田直紀、馬渕一誠：*Xenopus* 卵抽出液を封入した脂質膜人工小胞中でのアクチン動態。第 37 回日本分子生物学会年会（2014.11.25-27, 横浜）、招待講演。

16. Mabuchi, I. Novel approaches to study mechanism of cytokinesis in animal cells. OIST Seminar (2015.4.22 沖縄科学技術大学院大学)、招待講演。

17. Kashiwazaki, J., Mishra, M., and Mabuchi, I. Behavior of proteins during the contractile ring contraction in the *S. pombe* cell-ghost. The 18th International Fission Yeast Meeting (2015.6.21-26, 三宮)

18. 野田直紀、馬渕一誠：*Xenopus* 卵抽出液を封入した脂質膜小胞はアクチンの動態と共役して運動する。第 67 回日本細胞生物学会大会 (2015.6.30-7.2 船堀)

19. 関根彩子、小林礼、柏崎隼、植田英一、馬渕一誠： 分裂酵母 Cyclase-associated protein (CAP) の低グルコース環境への適応における役割。第 67 回日本細胞生物学会大会 (2015.6.30-7.2 船堀)

20. Noda, N., Mabuchi, I. Actin flows in *Xenopus* egg extract confined in oil and generates a force for migration of the extract. 第 53 回生物物理学会年会シンポジウム (2015. 9. 13-15, Kanazawa) 招待講演。

21. 細谷夏実、馬渕一誠： ウニ卵 formin/Diaphanous の細胞質分裂における局在。日本動物学会第 86 回大会 (2015.9.17-19, 新潟)

nature cell biology

In vitro contraction of cytokinetic ring depends on myosin II but not on actin dynamics

Mithilesh Mishra[1,5], Jun Kashiwazaki[2,5], Tomoko Takagi[2], Ramanujam Srinivasan[3], Yinyi Huang[3], Mohan K. Balasubramanian[1,3,4,6] and Issei Mabuchi[2,6]

Cytokinesis in many eukaryotes involves the contraction of an actomyosin-based contractile ring[1,2]. However, the detailed mechanism of contractile ring contraction is not fully understood. Here, we establish an experimental system to study contraction of the ring to completion *in vitro*. We show that the contractile ring of permeabilized fission yeast cells undergoes rapid contraction in an ATP- and myosin-II-dependent manner in the absence of other cytoplasmic constituents. Surprisingly, neither actin polymerization nor its disassembly is required for contraction of the contractile ring, although addition of exogenous actin-crosslinking proteins blocks ring contraction. Using contractile rings generated from fission yeast cytokinesis mutants, we show that not all proteins required for assembly of the ring are required for its contraction *in vitro*. Our work provides the beginnings of the definition of a minimal contraction-competent cytokinetic ring apparatus.

The understanding of biological processes benefits from the combined use of genetic analyses and *in vitro* reconstitution. Early studies in metazoan cells and embryos have established that an actomyosin-based contractile ring drives cytokinesis[3,4]. Isolation of the cleavage furrow containing the contractile ring has provided some structural information for the mechanism of cytokinesis[5], but the molecular components responsible for the supramolecular organization and function are not fully understood. Genetic analysis in various model organisms has succeeded in the identification of mutants defective in contractile ring assembly, characterization of which in turn has led to the identification of components of the contractile ring[1,2,6]. However, mutants defective specifically in ring contraction have not been identified, possibly because proteins involved in ring assembly might contribute to its contraction. As a result, the mechanism for ring contraction and disassembly is poorly understood. To circumvent the gaps in genetic analysis and to generate a thorough understanding of ring contraction we have sought to establish an *in vitro* system.

The fission yeast *Schizosaccharomyces pombe* divides by the use of a contractile ring and an invaginating septum[7,8]. Given the wealth of cytokinesis-defective mutants and the ease of using live-cell microscopy, we chose to establish the *in vitro* ring contraction system in this organism (Fig. 1a and Methods). We first removed the cell wall by enzymic digestion to obtain spheroplasts. Time-lapse imaging of mCherry–tubulin- and Rlc1p–3xGFP (myosin-II regulatory light chain)-expressing spheroplasts revealed that, like intact cells, spheroplasts assembled normal-appearing contractile rings[9] (Supplementary Fig. S1a,b). Then spheroplasts were permeabilized with 0.5% NP-40. The resultant cell ghosts retained a contractile ring (Fig. 1b) surrounded by plasma membrane full of holes as seen by FM4-64 staining and by thin-sectioning electron microscopy, but were devoid of any cytoplasmic structures (Fig. 1b,c). Most proteins necessary for contractile ring formation were contained in the contractile ring in cell ghosts (Fig. 1d–g and Supplementary Fig. S2a and Table S1) but other cytoplasmic components were not (Supplementary Fig. S2b and Table S1). Biochemical analysis showed that the ring components myosin-II, actin and tropomyosin Cdc8p were enriched in the ghost preparations, whereas tubulin was not (Fig. 1h and also Supplementary Fig. S2b).

To determine whether these rings were contractile, we treated cell ghosts with 0.5 mM ATP. Rings underwent rapid contraction on ATP addition (Fig. 2a,b and Supplementary Video S1). It has been reported that contractile rings isolated from spheroplasts of budding yeast disappeared on ATP addition, although the mechanisms were not explored[10]. As for the intact cells[11–13], the rate of contraction of rings from fission yeast cell ghosts was almost constant from initiation to completion, and was $0.22 \pm 0.09\ \mu m\ s^{-1}$ ($n = 37$; Fig. 2b). Contraction with a slightly reduced rate was observed even when the ATP concentration was as low as 0.01 mM (Fig. 2c and Supplementary Video S2), but not in the presence of the non-hydrolysable ATP analogue

[1]Temasek Life Sciences Laboratory, The National University of Singapore, 1 Research Link, Singapore 117604, Singapore. [2]Department of Life Sciences, Faculty of Science, Gakushuin University, 1-5-1 Mejiro, Toshima-ku, Tokyo, 171-8588, Japan. [3]Mechanobiology Institute, The National University of Singapore, 117543, Singapore. [4]Department of Biological Sciences, The National University of Singapore, 117411, Singapore. [5]These authors contributed equally to this work. [6]Correspondence should be addressed to M.K.B. or I.M. (e-mail: mohan@tll.org.sg or issei.mabuchi@gakushuin.ac.jp)

Received 13 August 2012; accepted 9 May 2013; published online 16 June 2013; DOI: 10.1038/ncb2781

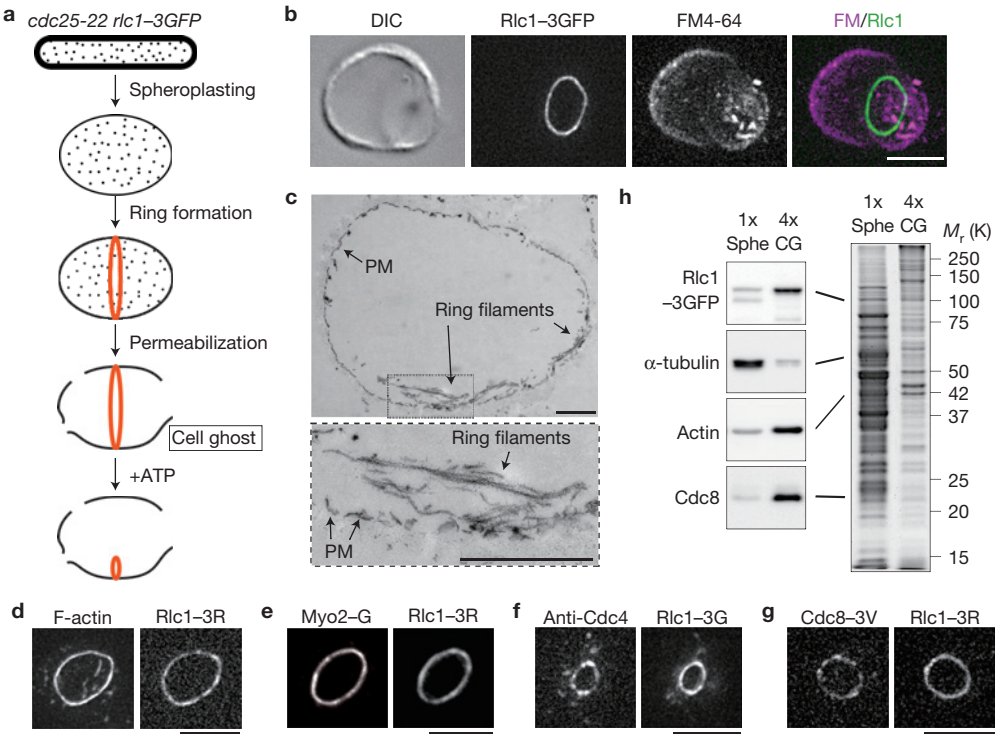

Figure 1 Contractile rings in cell ghosts. (**a**) Schematic illustration of procedure to obtain cell ghosts. (**b**) Maximum projection image of deconvolved sections of Rlc1–3xGFP and the plasma membrane stained with FM4-64 in a cell ghost. (**c**) A thin-section electron micrograph of the mid region of a cell ghost that is not parallel to the ring plane. Actin filaments in the ring were decorated with skeletal heavy meromyosin. The plasma membrane (PM) showed numerous gaps as a result of the detergent treatment. The area surrounded by a dotted rectangle is magnified below. (**d**) Maximum projection images of deconvolved sections of Rlc1–3xmDsRed and F-actin stained with BODIPY-FL–phallacidin in the cell ghosts. (**e**) Maximum projection images of deconvolved sections of Myo2–GFP and Rlc1–3xmDsRed. (**f**) Maximum projection images of deconvolved sections of Cdc4 stained with anti-Cdc4 antibody and anti-rabbit IgG labelled with tetramethylrhodamine after permeabilization and Rlc1–3xGFP. (**g**) Maximum projection images of deconvolved sections of Cdc8–3xVenus and Rlc1–3xmDsRed. (**h**) Western blot analysis of several proteins in the whole-cell lysate of spheroplasts (Sphe) or cell ghosts (CG). The density of cell ghosts was fourfold higher than that of spheroplasts. The right panel shows Coomassie-stained gels of total protein in spheroplasts and cell ghosts. Scale bars, 5 μm (**b**,**d**–**g**) and 1 μm (**c**).

AMP-PNP (Fig. 2d and Supplementary Video S3). The rate of ring contraction in cell ghosts in the presence of 0.5 mM ATP was more than 20 times faster than that in wild-type cells (Fig. 2e). The measurement of fluorescence of ring components over time revealed that whereas the total amount of most contractile ring proteins reduced only marginally, Cdc8p was rapidly depleted from the constricting ring (Fig. 2f and Supplementary Table S2). The fast rate of ring contraction *in vitro* may be a result of delinking of ring contraction from membrane and division septum assembly in cell ghosts as the associated membranes did not invaginate as the ring contracted (Fig. 2g and Supplementary Video S4). Although slow contraction was observed in the presence of other nucleoside triphosphates, the lowest K_m and highest V_m were observed for ATP (Fig. 2h,i). Thus, ring contraction in fission yeast requires ATP hydrolysis. Maximal ring contraction was observed at pH 8.0–8.5 with contraction being slower below pH 7 (Supplementary Fig. S3a). The optimal calcium concentration for ring contraction was pCa 8–9 and free Ca^{2+} lowered the contraction rate (Supplementary Fig. S3b), suggesting a Ca-sensitive step in ring contraction in fission yeast.

In time-lapse imaging of spheroplasts, contractile rings were routinely observed to initiate from a single location and occurred through what appeared as a bi-directionally growing leading cable[14] (Supplementary Fig. S1b). We established that this mode of bi-directional cable assembly was not a peculiarity of spheroplasts, because fission yeast cells rendered spherical also exhibited a similar ring assembly process (Supplementary Fig. S1c). Whereas fully formed rings underwent rapid ATP-dependent contraction, incomplete actomyosin arcs were unable to contract (Fig. 2j and Supplementary Video S5) although the fluorescence decayed significantly in the presence of ATP, which is probably due to disassembly (Supplementary Fig. S3c). This result is consistent with the observation that the forming ring consists of two semicircles of predominantly parallel F-actin filaments[15], which would not support ring contraction.

As the motor protein myosin-II hydrolyses ATP during its walking along an actin filament, we examined whether myosin-II activity was essential for ring contraction. Although myosin-II–actin interaction has been shown to be essential for cytokinesis[16], its molecular function in cytokinesis is not fully understood. We incubated cell ghosts in the presence of ATP and the myosin-II ATPase inhibitor blebbistatin (0.1 mM; ref. 17). Whereas rings underwent rapid contraction in the absence of blebbistatin, ring contraction was abolished in the presence of blebbistatin (Fig. 3a, $n=8$). We also found that incubation of cell ghosts with dehydroxestoquinone (DXQ; 2.5 mM), an inhibitor of skeletal muscle myosin II (ref. 18), and kinesin and dynein ATPases blocked ring contraction (Supplementary Fig. S3d,e). Treatment of cell ghosts with 0.1 mM sodium vanadate (an inhibitor of dynein and kinesin ATPases, but not myosin II ATPase) or microtubule-depolymerizing

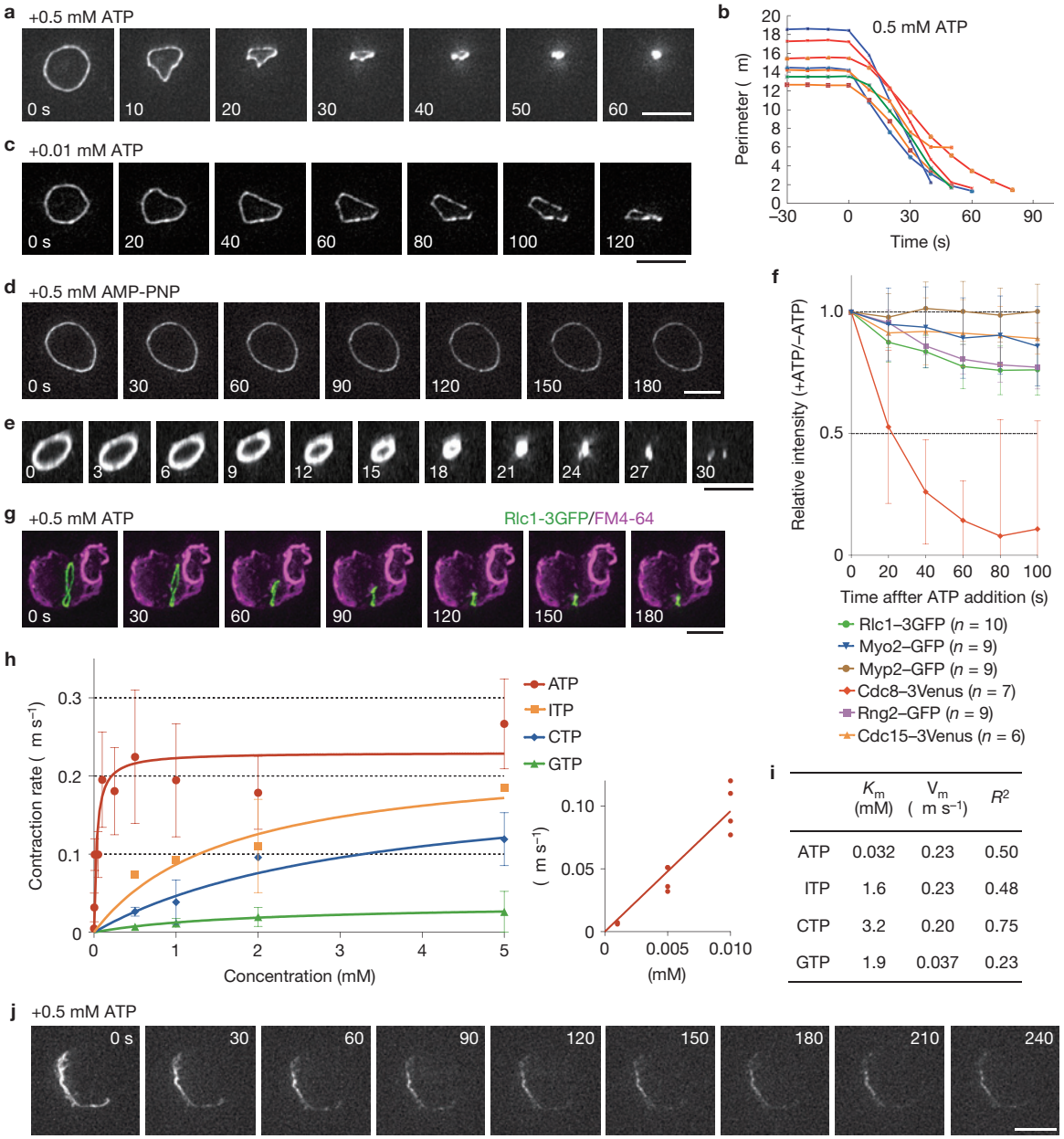

Figure 2 ATP stimulates rapid ring contraction *in vitro*. Experiments were done at 25 °C. Fluorescence micrographs of Rlc1–3xGFP are shown as maximum projections of *Z*-stacks. (**a**,**b**) Ring contraction is stimulated on ATP addition *in vitro*. 0 s indicates time of ATP addition. Typical examples of time course of ring contraction are shown. Perimeters were measured after three-dimensional rotation (Methods). Each measured value is represented. (**c**) Ring contraction is slower in the presence of 0.01 mM ATP. (**d**) The ring does not contract in the presence of 0.5 mM AMP-PNP. (**e**) Ring contraction in a cylindrical wild-type fission yeast cell. Fluorescence micrographs of Rlc1–3xGFP are shown as 30°-tilted maximum projections of *Z*-stacks. (**f**) Disassembly of each ring component after 0.5 mM ATP addition. Fluorescence intensity is shown as the relative value to that in the absence of ATP to eliminate the effect of photobleaching. Each mean value is represented. For the values at 100 s, unpaired two-tailed *t*-tests were done. Each *P* value is shown in Supplementary Table S2. (**g**) The plasma membrane of Rlc1–3xGFP-expressing cell ghosts stained with FM4-64 during contraction *in vitro* in the presence of 0.5 mM ATP. (**h**,**i**) Nucleotide specificity for ring contraction *in vitro*. Actual values are shown in Supplementary Table S3. Each curve was fitted to the Michaelis–Menten equation. The small graph shows the rates at low concentrations of ATP. K_m and V_m were estimated using Prism-5. R^2 should be close to 1.0 if the curve is well fitted. Statistics source data for Fig. 2h can be found in Supplementary Table S6. (**j**) Incomplete contractile ring does not undergo ATP-driven contraction *in vitro*. ATP (0.5 mM) was added at 0 s. See Supplementary Videos S1–S5. Time is indicated in seconds (**a**,**c**,**d**,**g**,**j**) or minutes (**e**). Scale bars, 5 μm (**a**,**c**–**e**,**g**,**j**). Error bars represent s.d. (**f**,**h**).

drugs (methyl benzimidazol-2-yl-carbamate (MBC) and thiabendazole (TBZ)) did not affect ring contraction (Supplementary Fig. S4a). The inhibition of ring contraction by DXQ, but not by vanadate, MBC or TBZ, taken together with our results with blebbistatin strongly suggested that the ATPase activity of myosin II was essential for ring contraction.

We independently confirmed the role of myosin-II in ring contraction by preparing cell ghosts from myosin-II-mutant strains.

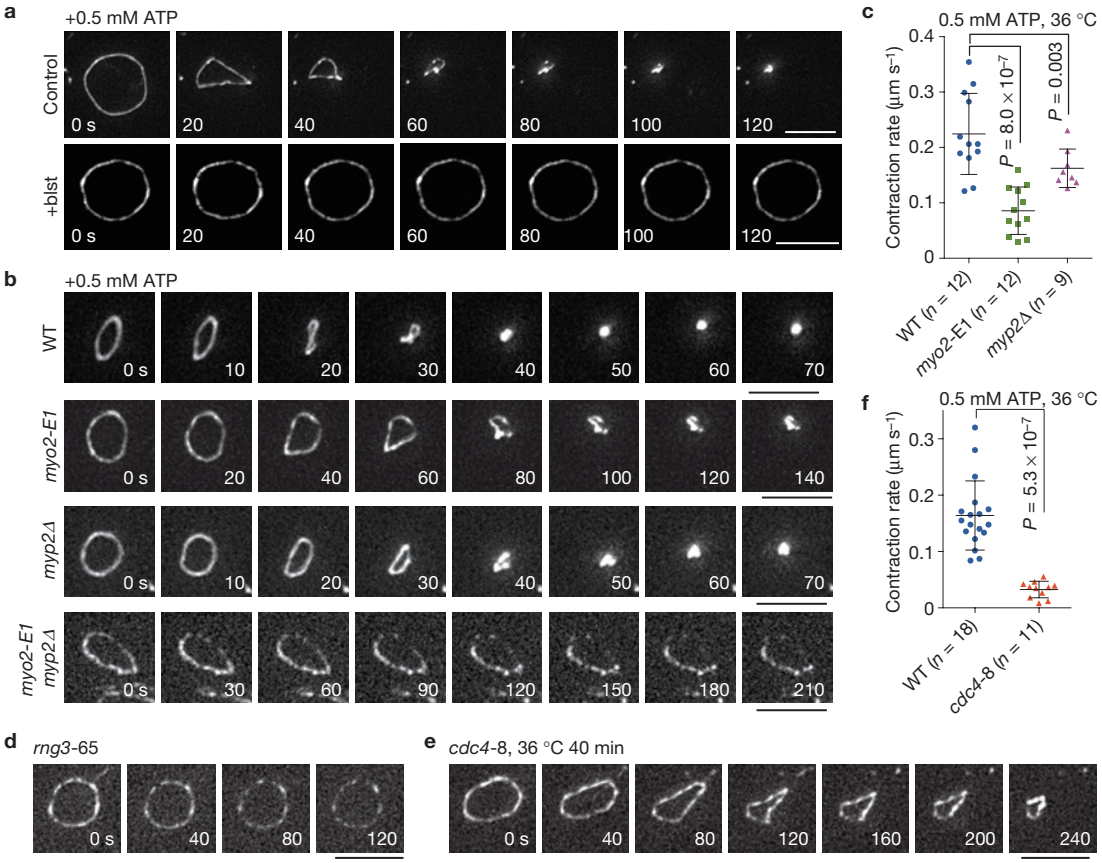

Figure 3 Myosin-II drives ring contraction *in vitro*. ATP concentration in each experiment was 0.5 mM. Fluorescence micrographs of Rlc1–3xGFP are shown as maximum projections of *Z*-stacks. (**a**) Effect of blebbistatin on ring contraction *in vitro*. Rings were pre-incubated in 0.1 mM blebbistatin for 3 min before perfusion with ATP (time 0 s) at 25 °C. (**b**) Rings in wild-type or myosin-II mutant cell ghosts. Ring contraction after ATP addition was monitored at the permissive temperature, 25 °C. (**c**) Contraction rate ($\mu m\,s^{-1}$) of contractile rings in myosin-II mutant cell ghosts at the permissive temperature. Each spot represents the rate of contraction of an individual ring. Medial horizontal lines and error bars represent mean values and s.d., respectively. Two-tailed *t*-test was used for statistical analysis. (**d**) Ring behaviour in *rng3*-65 mutant cell ghosts after ATP addition at the permissive temperature of 25 °C. (**e**) Ring contraction in *cdc4*-8 mutant cell ghosts 40 min after the temperature shift to 36 °C. (**f**) Contraction rate ($\mu m\,s^{-1}$) of rings in *cdc4*-8 mutant cell ghosts at the restrictive temperature. The graph is represented as in **c**. All scale bars, 5 μm. See Supplementary Videos S6–S8.

There are two genes that encode myosin-II heavy chain in fission yeast, essential *myo2*$^{+}$ (ref. 19) and non-essential *myp2*$^{+}$ (also known as *myo3*$^{+}$; refs 20,21). Spheroplasts were prepared from the temperature-sensitive (ts) mutant *myo2*-E1 (ref. 22), the *myp2*-null mutant (*myp2*Δ) and the *myo2*-E1 *myp2*Δ double-mutant grown at the permissive temperature of 25 °C. Mutant Myo2-E1p has been shown to have a reduced ATPase activity and an associated reduction in its motor activity even at the permissive temperature[23]. Rings in *myo2*-E1 or *myp2*Δ cell ghosts showed slower contraction even at 25 °C (Fig. 3b,c and Supplementary Videos S6 and S7). Most of the rings in *myo2*-E1 *myp2*Δ cell ghosts were either fragmented or deformed and these rings did not show any ATP-dependent contraction (Fig. 3b and Supplementary Video S8), suggesting that the contractile ring was not in a proper organization. Taken together, these experiments established that ATP hydrolysis by myosin-II powers the fission yeast ring contraction *in vitro*. Contractile rings in cell ghosts isolated from *rng3*-65^{ts} (defective in the UCS-domain-containing myosin-II activator and chaperone Rng3p; refs 23,24) were also unstable and did not undergo perceptible contraction even at 25 °C (17 out of 20 rings, Fig. 3d) even though they did retain all of the essential contractile ring proteins tested (Supplementary Table S4). Rings prepared from the myosin-II essential light chain mutant (*cdc4*-8^{ts}) underwent complex behaviour, ranging from very slow contraction to ring disintegration, possibly owing to the multiple roles performed by Cdc4p in cytokinesis[25] (Fig. 3e,f).

Previous studies in yeasts and animal cells have proposed the requirement for actin depolymerization and/or severing in ring contraction[3,26]. We first established that F-actin fluorescence was almost completely lost during ring contraction in cell ghosts (Fig. 4a,b). Using biochemical assays we found that on ATP addition to cell ghosts, actin was released from the ghosts (Fig. 4c,d). Myosin-II behaved differently, as most of it remained in the cell ghosts after ATP addition (Fig. 4e). This is consistent with the presence of myosin in a large spot following ring contraction on ATP addition (Figs 2a,f and 4a,b).

We next investigated whether this loss of F-actin was essential for ring contraction *in vitro*. To this end we first treated the cell ghosts with an F-actin-stabilizing drug jasplakinolide (Jasp). We found that on ATP addition ring contraction in cell ghosts occurred at normal

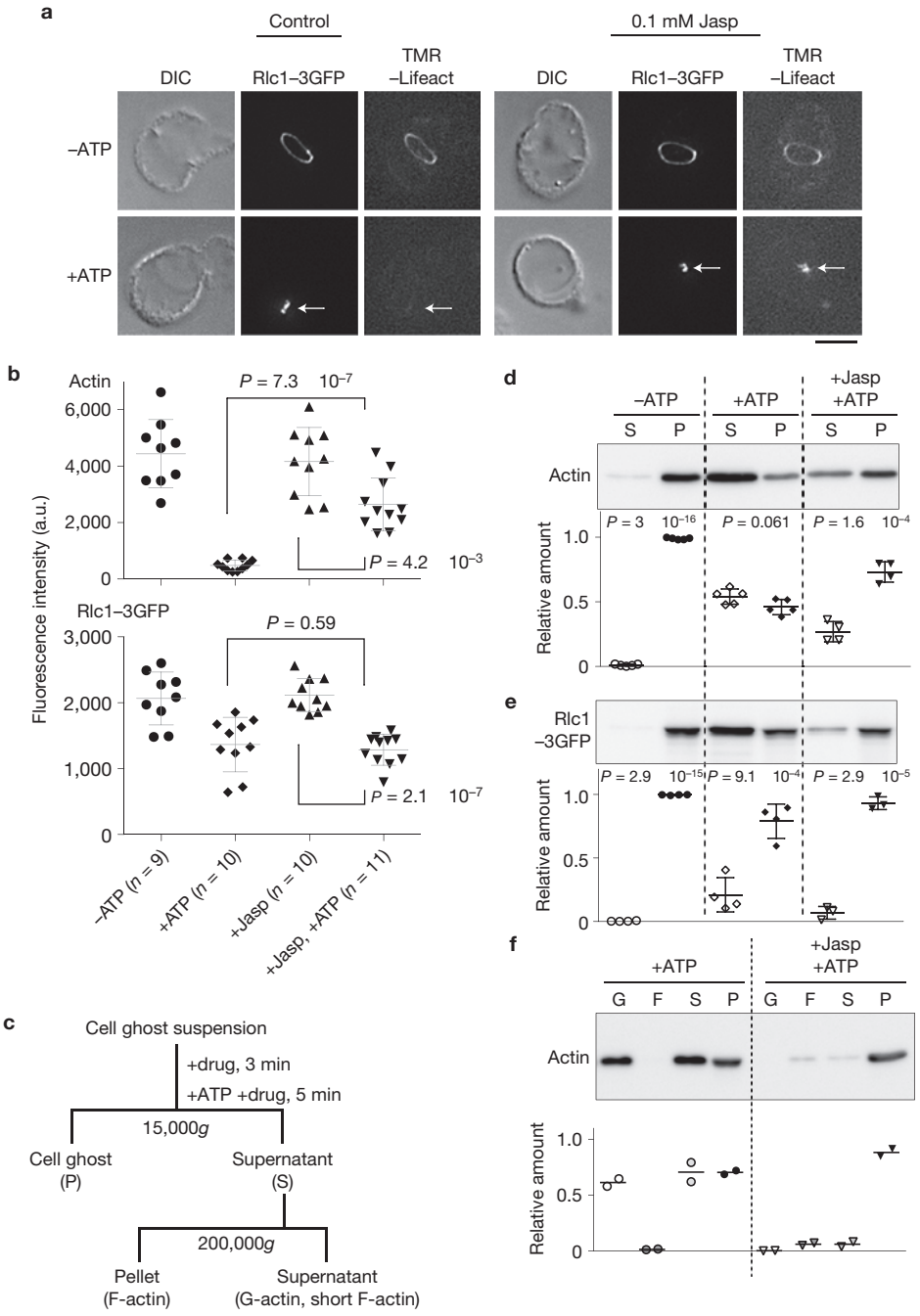

Figure 4 Contribution of actin dynamics to ring contraction *in vitro*. (**a**) Actin stabilization by Jasp does not block ring contraction. Actin was stained with 10 μg ml^{-1} TMR–Lifeact before or after contraction. White arrows indicate the positions of contracted rings. Scale bar, 5 μm. (**b**) Fluorescence intensity of TMR–Lifeact or Rlc1–3xGFP in contractile rings before and after ATP addition. Each spot represents the integrated intensity of actin or Rlc1–GFP in each contractile ring. Medial horizontal lines and error bars represent mean values and s.d., respectively. (**c**) Schematic flow chart of actin disassembly assay (Methods). (**d**,**e**) Western blot analysis of actin or Rlc1 disassembly on ATP addition in the absence or presence of Jasp. S, supernatant; P, pellet. Amount of pellet loaded is threefold lower than that of the corresponding supernatant. Each relative amount was calculated from the total intensity (S + P × 3). Statistics source data for **d**,**e** can be found in Supplementary Table S6. (**f**) Sedimentation assay of released actin on ATP addition in the absence or presence of Jasp. G, G-actin and short F-actin; F, F-actin. Amount of pellet loaded is one-and-a-half times lower than that of its supernatant. Each relative amount was calculated from the amount of actin in the pellet without ATP. Two-tailed *t*-test was used for all statistical analyses. Statistics source data for **f** can be found in Supplementary Table S6. All error bars represent s.d.

kinetics in the presence of 0.1 mM Jasp (Supplementary Fig. S4a and Video S9). Other F-actin stabilizers, phalloidin or phallacidin at 0.1 mM, also did not affect the rate of ring contraction (data not shown). Unlike in the contractile rings of untreated cells, actin filaments were readily visible in rings treated with Jasp, phalloidin or phallacidin (Fig. 4a,b and Supplementary Fig. S4c).

We reconfirmed the effect of Jasp, phalloidin or phallacidin treatment on actin stabilization by sedimentation assays. When ghosts

were treated with ATP and Jasp, most actin was still retained in the cell-ghost pellet, and a small fraction was released in the supernatant (Fig. 4c,d). By performing further sedimentation assays, we found that actin released into the supernatant in the presence of Jasp was largely composed of F-actin (Fig. 4c,f). This contrasts with ghosts treated with ATP alone, in which most actin detected in the supernatant might be monomeric (Fig. 4f). Similar results were obtained when phalloidin- or phallacidin-treated cell ghosts were biochemically characterized (Supplementary Fig. S4d). These results suggest that actin filament depolymerization is not required for ring contraction *in vitro*.

The small amount of actin filaments released during ring contraction *in vitro* suggested that, although actin filament depolymerization and monomer release were not required for this process, actin severing might be important. We therefore examined whether the F-actin-severing protein ADF/cofilin Adf1p, which is known to function in actin turnover and contractile ring formation[27], plays an essential role in ring contraction. Rings in *adf1*-1^{ts} cell ghosts contracted at rates comparable to those in the wild type at 36 °C (Supplementary Fig. S4b and Video S10). These results implied that actin severing by ADF/cofilin was not required for ring contraction *in vitro*. The experiments with Jasp and the *adf1*-1^{ts} mutant collectively established that neither actin severing nor depolymerization was essential for ring contraction *in vitro*.

It has been proposed that actin polymerization itself might generate the force required for ring contraction[12]. We directly examined whether actin polymerization was required for contractile ring contraction by pre-incubation of cell ghosts with the actin polymerization inhibitor latrunculin A (LatA) or cytochalasin A (CytA) before ATP addition. These rings contracted at a rate comparable to that of the control (Supplementary Fig. S4a and Video S11). The formin Cdc12p is an actin nucleator essential for cytokinesis[28,29]. The F-BAR domain protein Cdc15p recruits Cdc12p to the division site[30]. Contractile rings in cell ghosts of both *cdc12*-112^{ts} mutants and *cdc15*-140^{ts} mutants incubated at the restrictive temperature underwent normal contraction (Supplementary Fig. S4b and Videos S12 and S13). Contractile ring in cell ghosts of *cdc3*-124^{ts} cells (defective in the formin-binding protein profilin)[7] also contracted at wild-type rates (Supplementary Fig. S4b). Taken together these experiments demonstrated that actin polymerization was not essential for ring contraction.

We then tested investigated whether yeast tropomyosin Cdc8p is required for ring contraction. Cdc8p is essential for cytokinesis and is known to regulate actin stability and modulate actomyosin interaction, possibly by competing with fimbrin Fim1p and/or Adf1p for binding to actin filaments[27,31,32]. Contractile rings in *cdc8*-110^{ts} cell ghosts were capable of undergoing ATP-dependent contraction at the permissive temperature ($n = 5$, data not shown). Although these rings retained most essential contractile ring components at the restrictive temperature (Supplementary Table S4) they became discontinuous and did not contract to completion at the restrictive temperature (8 out of 9 rings, Fig. 5a and Supplementary Video S14). Thus, we concluded that Cdc8p is required for ring integrity during contraction.

The contractile ring contains F-actin-crosslinking proteins α-actinin Ain1p, the IQGAP Rng2p and Fim1p (refs 33–35), which are essential for proper organization of the actin bundles in the ring. We investigated whether an excess of actin crosslinker(s) impeded ring contraction by addition of these actin-crosslinking proteins to the cell ghosts

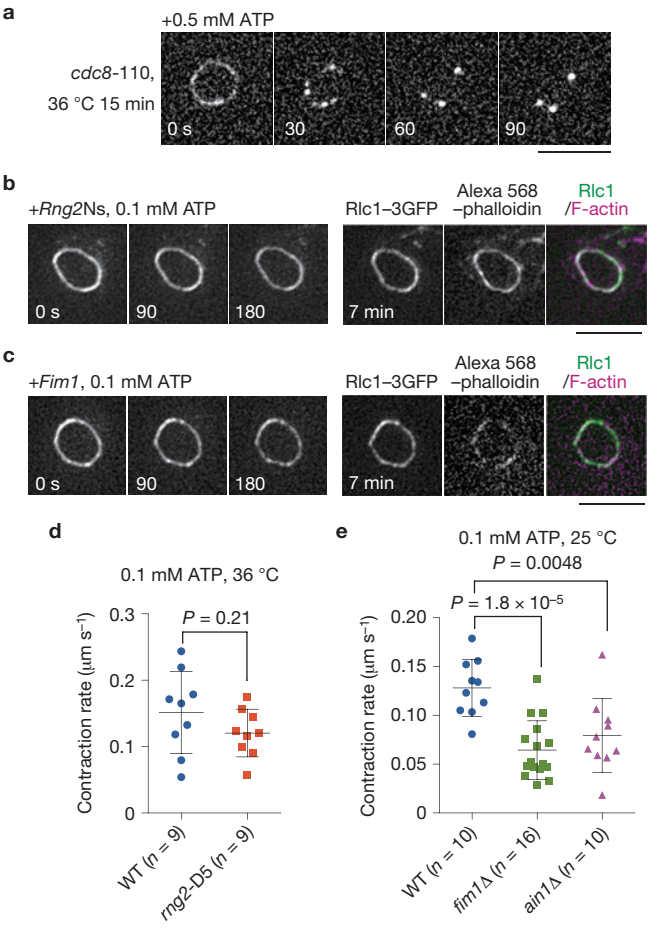

Figure 5 Effect of tropomyosin and actin-crosslinking proteins on ring contraction *in vitro*. (**a**) Ring behaviour in *cdc8*-110 mutant cell ghosts 15 min after the temperature shift to 36 °C. Fluorescence micrographs of Rlc1–3xGFP are shown as maximum projections of *Z*-stacks. ATP concentration was 0.5 mM. (**b**,**c**) Addition of purified amino-terminal region of IQGAP (Rng2Ns, 1 μM) or fimbrin (Fim1, 0.9 μM) blocks ring contraction *in vitro*. ATP concentrations were 0.1 mM. F-actin was stained with Alexa 568–phalloidin 7 min after ATP addition. (**d**) Contraction rate of rings in *rng2*-D5 mutant cell ghosts 40 min after the temperature shift to 36 °C. (**e**) Contraction rates of rings in *fim1*Δ and *ain1*Δ cell ghosts at 25 °C. All scale bars, 5 μm. Each spot represents the rate of contraction of an individual ring. Medial horizontal lines and error bars represent mean values and s.d., respectively. Two-tailed *t*-test was used for statistical analysis. See Supplementary Videos S9–S16.

before ATP addition. When cell ghosts were pre-incubated with purified Rng2Ns possessing the actin-bundling activity[35], contraction was blocked in a dose-dependent manner with a complete block at 1 μM ($n = 4$, Fig. 5b and Supplementary Fig. S5a and Video S15), a concentration that promoted robust actin filament bundling *in vitro* (Supplementary Fig. S5c). Phalloidin staining of these rings showed that actin filaments remained in the ring (Fig. 5b). Fim1p showed a similar dose-dependent inhibition of ring contraction *in vitro* with 0.9 μM Fim1p completely blocking ring contraction ($n = 3$, Fig. 5c and Supplementary Fig. S5b and Video S16). To determine whether a defect or absence of each crosslinker caused an increase in ring contraction rate, we prepared ghosts from *rng2*-D5^{ts} mutant cells or cells deleted for *fim1*$^{+}$ or *ain1*$^{+}$. Curiously, rings from *rng2*-D5^{ts}

spheroplasts contracted at a normal rate at 36 °C, and in the absence of Fim1p or Ain1p rings showed a slower rate of contraction (Fig. 5d,e). These experiments suggested that a balance of activity of crosslinking proteins was essential for proper ring contraction.

We have established an *in vitro* contractile ring activation system in which we have shown that fully formed contractile rings, but not partially formed arcs, undergo ATP-dependent contraction. The fact that the rings in cell ghosts undergo rapid contraction establishes that neither a constant supply of cytoplasmic material nor the concomitant ingression of septum is required for the mechanics of ring contraction in fission yeast. Our analysis, using this *in vitro* approach, therefore leaves us with the minimal requirements for ring contraction; namely, F-actin, myosin-II ATPase and the appropriate actin-crosslinking. □

METHODS

Methods and any associated references are available in the online version of the paper.

Note: Supplementary Information is available in the online version of the paper

ACKNOWLEDGEMENTS

We thank D. McCollum (University of Massachusetts Medical School, USA), K. Gould (Vanderbilt University, USA), J-Q. Wu (Ohio State University, USA), V. Simanis (ISREC, Switzerland), J. Bähler (University College London, UK), T. D. Pollard (Yale University, USA), T. Toda (Cancer Research, UK), I. Hagan (Paterson Institute, UK), F. Chang (Columbia University, USA), D. Mulvihill (University of Kent, UK), P. Perez (CSIC, Spain), Y. Hiraoka (Osaka University, Japan), K. Nakano (University of Tsukuba, Japan), S. Oliferenko (TLL, Singapore), and M. Sato (Waseda University, Japan) and the Yeast Genetic Resource Center Japan for providing plasmids and strains, Y. Oba and M. Ojika (Nagoya University, Japan) for their kind gift of DXQ, Y. Toyoshima (University of Tokyo, Japan) for her kind gift of kinesin, R. Amikura for help in electron microscopy, and S. Oliferenko, S. Bulchand and D. Subramanian for critical reading of this manuscript. We thank K. Gull (Oxford University, UK) for antibodies. We thank M. Sevugan for technical assistance. This work was supported by a Japan Society for Promotion of Science (JSPS) grant-in-aid for scientific research (I.M., #22247031); JSPS research fellowships for young scientists (J.K.); NUS JSPS collaborative grant (I.M. and M.B.), Temasek Life Sciences Laboratory and Singapore Millennium Foundation (M.B. and M.M.); visiting scientist fellowship from the Gakushuin University (M.M.) and Mechanobiology Institute (M.B., R.S. and Y.H.).

AUTHOR CONTRIBUTIONS

I.M. (*in vitro* activation and biochemistry) and M.K.B. (establishment of ring assembly in protoplasts and mutant studies) conceived the study, I.M., M.M., M.K.B. and J.K. designed the experiments. I.M., J.K., M.M., T.T., R.S. and Y.H. conducted the experiments. J.K., I.M. and M.M. analysed the data. M.K.B., M.M., J.K. and I.M. wrote the manuscript.

COMPETING FINANCIAL INTERESTS

The authors declare no competing financial interests.

Published online at www.nature.com/doifinder/10.1038/ncb2781
Reprints and permissions information is available online at www.nature.com/reprints

1. Glotzer, M. The molecular requirements for cytokinesis. *Science* **307,** 1735–1739 (2005).
2. Pollard, T. D. Mechanics of cytokinesis in eukaryotes. *Curr. Opin. Cell Biol.* **22,** 50–56 (2010).
3. Mabuchi, I. Biochemical aspects of cytokinesis. *Int. Rev. Cytol.* **101,** 175–213 (1986).
4. Schroeder, T. E. in *Molecules and Cell Movements* (eds Inoué, S. & Stephens, R. E.) 305–334 (Raven, 1975).
5. Mabuchi, I., Tsukita, S., Tsukita, S. & Sawai, T. Cleavage furrow isolated from newt eggs: contraction, organization of the actin filaments, and protein components of the furrow. *Proc. Natl Acad. Sci. USA* **85,** 5966–5970 (1988).
6. Robinson, D. N. & Spudich, J. A. Mechanics and regulation of cytokinesis. *Curr. Opin. Cell Biol.* **16,** 182–188 (2004).
7. Pollard, T. D. & Wu, J. Q. Understanding cytokinesis: lessons from fission yeast. *Nat. Rev. Mol. Cell Biol.* **11,** 149–155 (2010).
8. Wolfe, B. A. & Gould, K. L. Split decisions: Coordinating cytokinesis in yeast. *Trends Cell Biol.* **15,** 10–18 (2005).
9. Mishra, M. *et al.* Cylindrical cellular geometry ensures fidelity of division site placement in fission yeast. *J. Cell Sci.* **125,** 3850–3857 (2012).
10. Young, B. A., Buser, C. & Drubin, D. G. Isolation and partial purification of the Saccharomyces cerevisiae cytokinetic apparatus. *Cytoskeleton* **67,** 13–22 (2010).
11. Motegi, F., Arai, R. & Mabuchi, I. Identification of two type V myosins in fission yeast, one of which functions in polarized cell growth and moves rapidly in the cell. *Mol. Biol. Cell* **12,** 1367–1380 (2001).
12. Pelham, R. J. & Chang, F. Actin dynamics in the contractile ring during cytokinesis in fission yeast. *Nature* **419,** 82–86 (2002).
13. Wu, J. Q., Kuhn, J. R., Kovar, D. R. & Pollard, T. D. Spatial and temporal pathway for assembly and constriction of the contractile ring in fission yeast cytokinesis. *Dev. Cell* **5,** 723–734 (2003).
14. Arai, R. & Mabuchi, I. F-actin ring formation and the role of F-actin cables in the fission yeast Schizosaccharomyces pombe. *J. Cell Sci.* **115,** 887–898 (2002).
15. Kamasaki, T., Osumi, M. & Mabuchi, I. Three-dimensional arrangement of F-actin in the contractile ring of fission yeast. *J. Cell Biol.* **178,** 765–771 (2007).
16. Mabuchi, I. & Okuno, M. The effect of myosin antibody on the division of starfish blastomeres. *J. Cell Biol.* **74,** 251–263 (1977).
17. Straight, A. F. *et al.* Dissecting temporal and spatial control of cytokinesis with a myosin II Inhibitor. *Science* **299,** 1743–1747 (2003).
18. Nakamura, M., Kakuda, T., Oba, Y., Ojika, M. & Nakamura, H. Synthesis of biotinylated xestoquinone that retains inhibitory activity against Ca^{2+} ATPase of skeletal muscle myosin. *Bioorg. Med. Chem.* **11,** 3077–3082 (2003).
19. Kitayama, C., Sugimoto, A. & Yamamoto, M. Type II myosin heavy chain encoded by the myo2 gene composes the contractile ring during cytokinesis in Schizosaccharomyces pombe. *J. Cell Biol.* **137,** 1309–1319 (1997).
20. Motegi, F., Nakano, K., Kitayama, C., Yamamoto, M. & Mabuchi, I. Identification of Myo3, a second type-II myosin heavy chain in the fission yeast Schizosaccharomyces pombe. *FEBS Lett.* **420,** 161–166 (1997).
21. Bezanilla, M., Forsburg, S. L. & Pollard, T. D. Identification of a second myosin-II in Schizosaccharomyces pombe: Myp2p is conditionally required for cytokinesis. *Mol. Biol. Cell* **8,** 2693–2705 (1997).
22. Balasubramanian, M. *et al.* Isolation and characterization of new fission yeast cytokinesis mutants. *Genetics* **149,** 1265–1275 (1998).
23. Lord, M. & Pollard, T. D. UCS protein Rng3p activates actin filament gliding by fission yeast myosin-II. *J. Cell Biol.* **167,** 315–325 (2004).
24. Wong, K. C., Naqvi, N. I., Iino, Y., Yamamoto, M. & Balasubramanian, M. K. Fission yeast Rng3p: An UCS-domain protein that mediates myosin II assembly during cytokinesis. *J. Cell Sci.* **113,** 2421–2432 (2000).
25. McCollum, D., Balasubramanian, M. K., Pelcher, L. E., Hemmingsen, S. M. & Gould, K. L. Schizosaccharomyces pombe $cdc4^{+}$ gene encodes a novel EF-hand protein essential for cytokinesis. *J. Cell Biol.* **130,** 651–660 (1995).
26. Mendes Pinto, I., Rubinstein, B., Kucharavy, A., Unruh, J. R. & Li, R. Actin depolymerization drives actomyosin ring contraction during budding yeast cytokinesis. *Dev. Cell* **22,** 1247–1260 (2012).
27. Nakano, K. & Mabuchi, I. Actin-depolymerizing protein Adf1 is required for formation and maintenance of the contractile ring during cytokinesis in fission yeast. *Mol. Biol. Cell* **17,** 1933–1945 (2006).
28. Kovar, D. R., Kuhn, J. R., Tichy, A. L. & Pollard, T. D. The fission yeast cytokinesis formin Cdc12p is a barbed end actin filament capping protein gated by profilin. *J. Cell Biol.* **161,** 875–887 (2003).
29. Chang, F., Drubin, D. & Nurse, P. cdc12p, a protein required for cytokinesis in fission yeast, is a component of the cell division ring and interacts with profilin. *J. Cell Biol.* **137,** 169–182 (1997).
30. Roberts-Galbraith, R. H. *et al.* Dephosphorylation of F-BAR protein Cdc15 modulates its conformation and stimulates its scaffolding activity at the cell division site. *Mol. Cell* **39,** 86–99 (2010).
31. Balasubramanian, M. K., Helfman, D. M. & Hemmingsen, S. M. A new tropomyosin essential for cytokinesis in the fission yeast S. pombe. *Nature* **360,** 84–87 (1992).
32. Stark, B. C., Sladewski, T. E., Pollard, L. W. & Lord, M. Tropomyosin and myosin-II cellular levels promote actomyosin ring assembly in fission yeast. *Mol. Biol. Cell* **21,** 989–1000 (2010).
33. Eng, K., Naqvi, N. I., Wong, K. C. & Balasubramanian, M. K. Rng2p, a protein required for cytokinesis in fission yeast, is a component of the actomyosin ring and the spindle pole body. *Curr. Biol.* **8,** 611–621 (1998).
34. Nakano, K., Satoh, K., Morimatsu, A., Ohnuma, M. & Mabuchi, I. Interactions among a fimbrin, a capping protein, and an actin-depolymerizing factor in organization of the fission yeast actin cytoskeleton. *Mol. Biol. Cell* **12,** 3515–3526 (2001).
35. Takaine, M., Numata, O. & Nakano, K. Fission yeast IQGAP arranges actin filaments into the cytokinetic contractile ring. *EMBO J.* **28,** 3117–3131 (2009).

DOI: 10.1038/ncb2781

METHODS

Strains, genetic techniques, chemicals and spheroplasting. *S. pombe* strains used in this study are listed in Supplementary Table S5. Standard procedures for *S. pombe* genetics were used[36]. Blebbistatin and Jasp were purchased from Calbiochem and CytA, MBC and TBZ were purchased from Sigma. Strains expressing epitope-tagged proteins were constructed using a PCR-based approach[37]. Spheroplasts were obtained as described previously[9,38]. The use of a synchronous cell culture of *cdc25*-22 cells carrying Rlc1–3xGFP enhanced the proportion of spheroplasts and cell ghosts with a contractile ring. Cells were first grown at the permissive temperature of 25 °C to early log phase in minimal medium containing 0.5% glucose. These cells were then shifted to the restrictive temperature of 36 °C for 4 h before spheroplasting. The time for cell wall digestion was different among various strains and varied from 20 min to a 1 h. Typically more than 90% of the cells were spheroplasted in all experiments. These spheroplasts were then grown in minimal medium with 0.8% sorbitol at 25 °C with slow shaking (80 r.p.m.). Contractile ring formation was monitored by fluorescence microscopy. For a typical experiment, at the point of spheroplasting Rlc1–3xGFP signal was detected in a single bright dot-like structure in 100% of the spheroplasts and actomyosin arcs or contractile rings were not seen. After 5 h of incubation at 24 °C, actomyosin arcs could be detected (in 3–7% of cells) and 25–35% of the spheroplasts had a fully formed contractile ring. At this point spheroplasts were collected for permeabilization and the analysis of the contraction competence of arcs and rings is described in the manuscript. For preparation of cell ghosts from various cytokinesis mutants, mutant cells expressing Rlc1–3GFP or Rlc1–GFP were grown at the permissive temperature of 25 °C overnight in minimal medium containing 0.5% glucose and spheroplasted at 25 °C. To determine the time taken for inactivation of various ts mutant proteins, intact mutant cells were shifted to the restrictive temperature of 36 °C and their inability to compact the contractile ring was monitored.

Permeabilization of spheroplasts and preparation of cell ghosts. Spheroplasts were washed twice with wash buffer (0.8 M sorbitol, 2 mM EGTA, 5 mM $MgCl_2$ and 20 mM PIPES–NaOH, at pH 7.0) and incubated for 5 min in isolation buffer (0.16 M sucrose, 50 mM EGTA, 5 mM $MgCl_2$, 50 mM potassium acetate, 50 mM PIPES–NaOH, at pH 7.0, 0.5% NP-40, 10 μg ml^{-1} leupeptin, 10 μg ml^{-1} aprotinin, 10 μg ml^{-1} pepstatin, 0.5 mM phenylmethylsulphonyl fluoride and 1 mM dithiothreitol) on ice. Spheroplasts were homogenized with a Teflon/glass homogenizer. Cell ghosts were washed twice with reactivation buffer (0.16 M sucrose, 5 mM $MgCl_2$, 50 mM potassium acetate, 20 mM MOPS–NaOH, at pH 7.0, 10 μg ml^{-1} leupeptin, 10 μg ml^{-1} aprotinin, 10 μg ml^{-1} pepstatin, 0.5 mM phenylmethylsulphonyl fluoride and 1 mM dithiothreitol). About 30% of the resultant cell ghosts retained intact contractile rings and another 5–10% had actomyosin arcs or discontinuous or fragmented contractile rings. Most intact fully formed contractile rings were competent for *in vitro* contraction on ATP addition.

Protein localization in cell ghosts and immunofluorescence microscopy. Cell ghosts were prepared from strains carrying the protein of interest fused to fluorescent proteins as described above. Indirect immunofluorescence was used to label Cdc4p and Adf1p. F-actin was stained with BODIPY-FL–phallacidin, Alexa 568–phalloidin (Molecular Probes-Invitrogen) or synthesized tetramethylrhodamine-labelled Lifeact peptide (Operon Biotechnologies). For immunofluorescence microscopy, cell ghosts were fixed with 3.8% paraformaldehyde in PEM buffer (1 mM EGTA, 1 mM $MgCl_2$ and 0.1 M PIPES–NaOH, at pH 6.9) for 30 min. After washing with PEM buffer, cell ghosts were blocked in PEM buffer containing 1% BSA, 0.1% NaN_3 and 10 mM L-lysine-HCl for 1 h at room temperature. Rabbit anti-Cdc4 polyclonal antibody[25] (1:100) and rabbit anti-Adf1 (ref. 27) polyclonal antibody (1:500) were used as a primary antibody for Cdc4p and Adf1p detection, respectively. Tetramethylrhodamine-conjugated anti-rabbit IgG was used as a secondary antibody at 1:1,000.

Electron microscopy. Cell ghosts for electron microscopy were prepared as described previously[39]. Actin filaments were decorated with skeletal heavy meromyosin for easy visualization. Sections were examined with a JEM1400 electron microscope (JEOL) at 80–100 kV.

Reactivation of contractile ring and microscopy. The reactivation of the contractile ring in the cell ghost was assessed with a hand-made perfusion chamber. The base of the chamber was constructed with a large coverslip (Matsunami Glass, 24 × 36 mm, No.1) coated with 0.01% poly-L-Lysine (Sigma, P1524) and double-sided tape (Nichiban; NW-5S, 60 μm wall thickness). Cell ghosts in suspension were adhered to the base of the chamber and then covered with a small coverslip (Matsunami, 18 × 18 mm, No. 1). The volume in the chamber was around 10 μl. Cell ghosts were washed with reactivation buffer by perfusion. Reactivation was performed by perfusion with reactivation buffer containing an appropriate concentration of ATP. Most intact contractile rings in wild-type cell ghosts underwent ATP-mediated contraction.

Conventional fluorescence microscopy, three-dimensional reconstruction and time-lapse observations were made using a DeltaVision system (Applied Precision) attached to an Olympus IX-70 wide-field inverted fluorescence microscope equipped with an Olympus UplanSApo ×100 oil-immersion objective lens (NA 1.4, Olympus), and a Photometrics CoolSNAP HQ camera (Roper Scientific). Temperature was controlled by both the thermo-plate and a lens heater (MATS-55RAF20, MATS-LH; TOKAI HIT). More than 14 optical sections (0.5 μm spaces) were acquired every 10 s. Images were captured and processed by iterative constrained deconvolution using SoftWoRx (Applied Precision), and analysed by SoftWoRx and ImageJ (W. S. Rasband, National Institutes of Health, Bethesda, MD) incorporated with the McMaster Biophotonics Facility ImageJ for Microscopy collection of plugins (T. Collins, McMaster Biophotonics Facility, Hamilton, Ontario, Canada). For measurement of the contraction rate, stacks of optical sections were reconstructed in a horizontal direction using the three-dimensional rotation tool of SoftWoRx and the perimeter of each ring was measured. Each contraction rate was determined by using values of the most linear phase of contraction. For measurement of fluorescence intensity in Fig. 4b, sum projections of six deconvolved sections were used. Integrated intensity was calculated from mean value and area, after subtracting the background mean value of the same area. Graphical images were established using Prism-5 (Graphpad Software).

Actin disassembly assay and western blotting. Cell ghosts suspended in reactivation buffer were split into three. A half-volume of reactivation buffer containing 15% dimethylsulphoxide or 0.3 mM Jasp was added and gently mixed. After three minutes, a one-quarter volume of reactivation buffer containing 5% dimethylsulphoxide, 5% dimethylsulphoxide and 2 mM ATP, or 0.1 mM Jasp and 2 mM ATP was added and gently mixed to induce ring contraction. After five minutes incubation at 25 °C, suspensions were centrifuged at 16,000*g* for 5 min at 4 °C. The pellet was frozen at −80 °C. Supernatant with 0.02% deoxycholate added was left for 30 min on ice followed by 10% trichloroacetic acid addition and overnight incubation on ice. Precipitates were washed with cold acetone and dried. The pellet and supernatant were analysed by SDS–PAGE and western blotting. The volume of pellet loaded was one-third that of the supernatant. For the sedimentation assay, half of the supernatant was centrifuged at 200,000*g* for 15 min at 4 °C. As primary antibody, mouse anti-actin monoclonal antibody MAB1501 (1:1,000, Millipore), rabbit anti-GFP polyclonal antibody 598 (1:2,000, MBL), rabbit anti-Cdc8 polyclonal antibody (1:250; ref. 40) or mouse anti-α-tubulin monoclonal antibody TAT-1 (1:1,000, gift from K. Gull) was used. Appropriate HRP-conjugated secondary antibody was used at 1:5,000. Western blots were developed using SuperSignal West Pico Chemiluminescent Substrate (Thermo Fisher Scientific, Waltham) and luminoimage analyser LAS3000 (Fujifilm). Each integrated intensity was calculated from the mean value and the area measured using ImageJ.

Measurement of ATPase activity. Motor proteins used were a mixture of rabbit skeletal muscle myosin chymotryptic S1 (0.18 mg ml^{-1}) and rabbit skeletal muscle F-actin (0.89 mg ml^{-1}), sea urchin sperm axonemal dynein (Tris–EDTA extract, 0.21 mg ml^{-1}), and recombinant rat brain kinesin-1 motor domain (relative molecular mass 430,000, 0.17 mg ml^{-1}, gift from Y. Toyoshima). These were incubated in 0.1 M KCl, 2.8 mM $MgCl_2$, 10 mM TES (pH 7.0) and 2.6 mM ATP at 25 °C. EDTA (0.55 mM) was also included for dynein and kinesin. Inorganic phosphates released were measured by the method of ref. 41 after removing proteins as trichloroacetic-acid-induced precipitates.

Statistical analysis. Statistical comparisons of mean values were made using the unpaired two-tailed *t*-test for two data sets and one-way analysis of variance for multiple data sets. The actual *P* values for each test are represented in each figure.

36. Moreno, S., Klar, A. & Nurse, P. Molecular genetic analysis of fission yeast Schizosaccharomyces pombe. *Methods Enzymol.* **194,** 795–823 (1991).
37. Bähler, J. *et al.* Heterologous modules for efficient and versatile PCR-based gene targeting in Schizosaccharomyces pombe. *Yeast* **14,** 943–951 (1998).
38. Kobori, H., Yamada, N., Taki, A. & Osumi, M. Actin is associated with the formation of the cell wall in reverting protoplasts of the fission yeast Schizosaccharomyces pombe. *J. Cell Sci.* **94,** 635–646 (1989).
39. Kamasaki, T., Arai, R., Osumi, M. & Mabuchi, I. Directionality of F-actin cables changes during the fission yeast cell cycle. *Nat. Cell Biol.* **7,** 916–917 (2005).
40. Arai, R., Nakano, K. & Mabuchi, I. Subcellular localization and possible function of actin, tropomyosin and actin-related protein 3 (Arp3) in the fission yeast Schizosaccharomyces pombe. *Eur. J. Cell Biol.* **76,** 288–295 (1998).
41. Fiske, C. H. & Subbarow, Y. The Colorimetric determination of phosphorus. *J. Biol. Chem.* **66,** 375–400 (1925).

DOI: 10.1038/ncb2781

nature cell biology

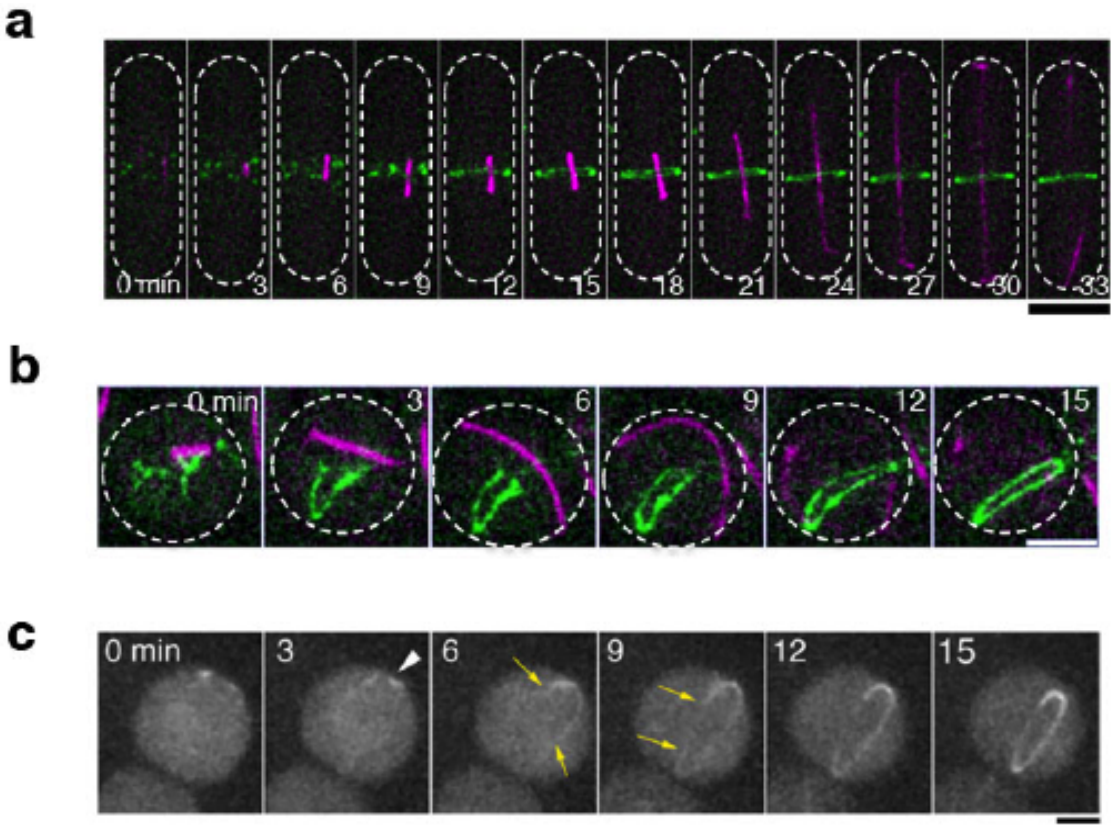

Figure S1 Examples of contractile ring formation in intact wild type cell, spheroplast and spherical mutant. (**a**) Maximum projections of deconvolved sections of Rlc1-3xGFP and mCherry-Atb2 images in an intact fission yeast cell. White doted lines indicate the cell outline. (**b**) Maximum projections of deconvolved sections of Rlc1-3xGFP and mCherry-Atb2 images in an intact spheroplast. White dotted line represents the outline of the spheroplast. (**c**) Maximum projections of contractile ring formation in *orb3/nak1* null cell (*orb3*Δ) expressing Rlc1-3xGFP at 25˚C. Contractile ring initiates from one predominant location on the surface of the spheroplast (shown by arrowhead at time 0 min) and grows in a bidirectional manner (shown by yellow arrows) to form a mature ring. Scale bars, 5 μm.

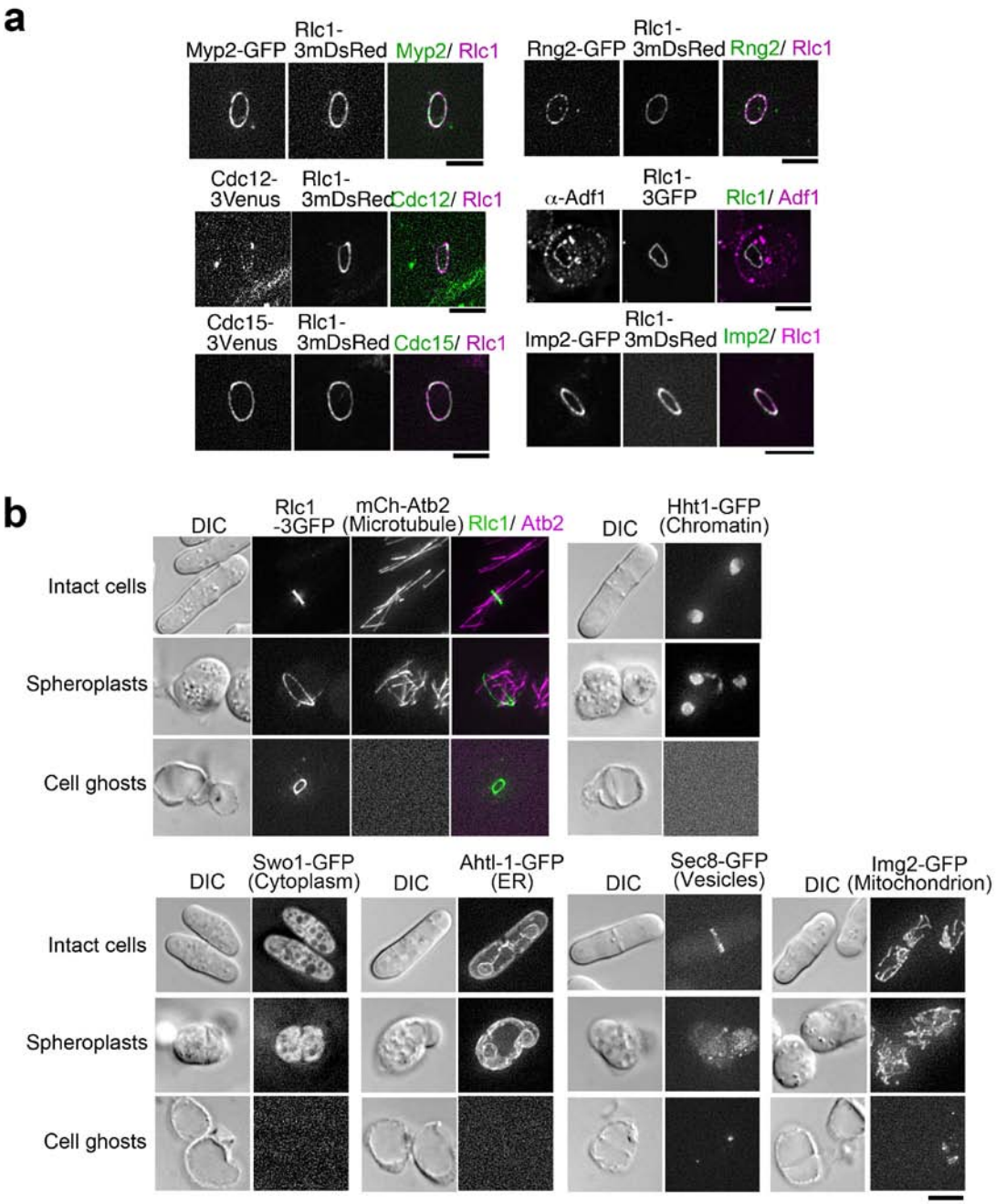

Figure S2 Cell-ghosts contain essential contractile ring proteins but lack other cytoplasmic components. (**a**) Essential components of the contractile ring are retained in cell-ghosts. Images are shown as maximum projections of Z-stacks. Spheroplasts expressing fluorescent-tagged proteins as indicated on each image were permeabilised before imaging. Adf1 was stained with anti-Adf1 antibody and anti-rabbit IgG labeled with tetramethylrhodamine after permeabilisation of spheroplasts expressing Rlc1-3xGFP. (**b**) Most cytoplasmic components are not retained in cell-ghosts. Fluorescence images are shown as maximum projections of deconvolved sections. Spheroplasts expressing fluorescent-tagged proteins as indicated were imaged before and after permeabilisation. Scale bars, 5 μm.

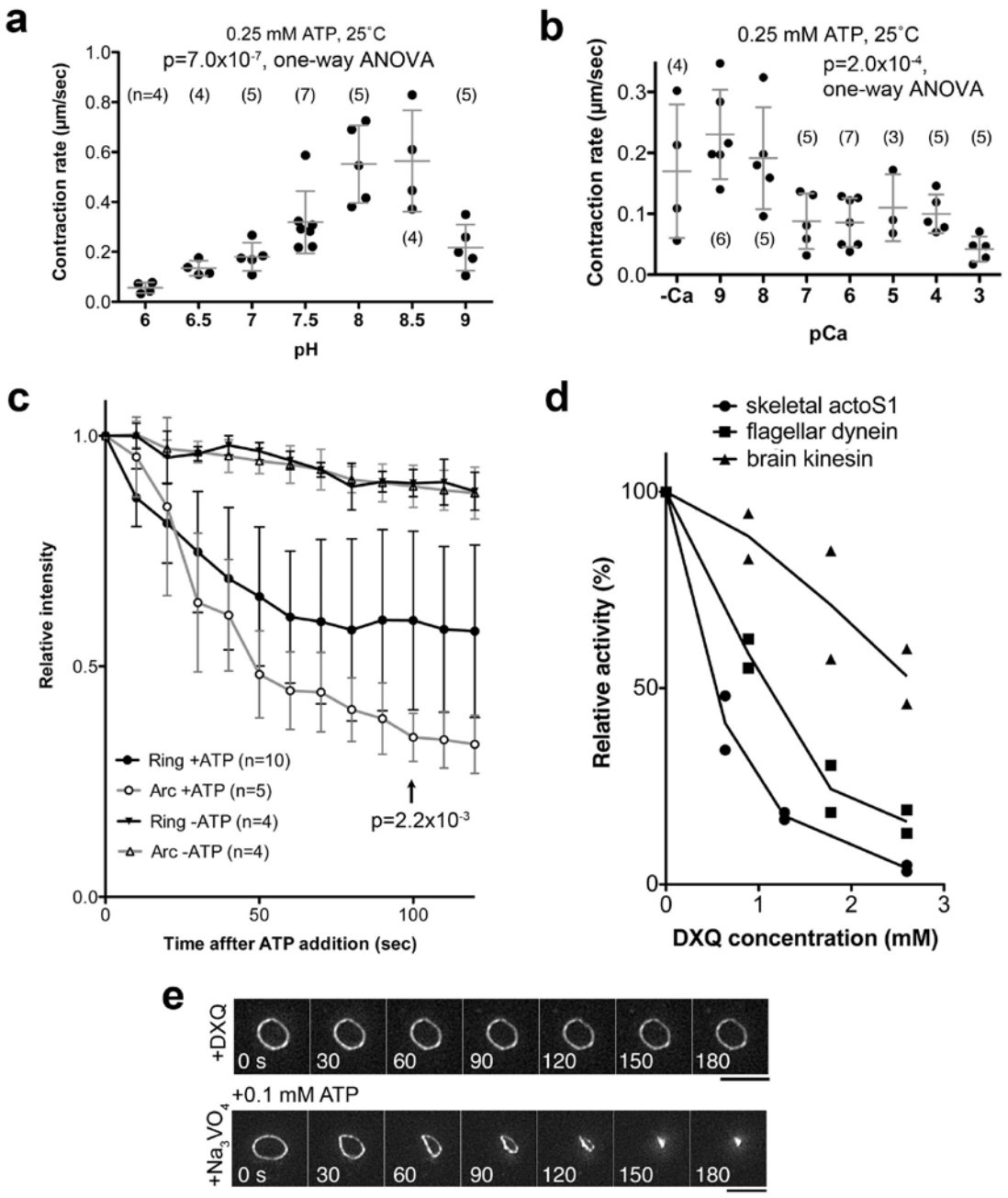

Figure S3 General features and myosin ATPase dependency of ring contraction *in vitro.* Experiments were done at 25˚C. (**a**) pH sensitivity of ring contraction *in vitro.* ATP concentration was 0.25 mM. Each spot represents the rate of contraction of an individual ring. Medial horizontal lines and error bars represent mean values and standard deviations, respectively. One-way analysis of variance (ANOVA) was used for statistical analysis. See Table S6 for statistics source data. (**b**) Ca^{++} sensitivity of ring contraction *in vitro.* ATP concentration was 0.25 mM. Statistical analysis in panel b was done as in panel a. See Table S6 for statistics source data. (**c**) Reduction of relative fluorescence intensity after 0.5 mM ATP addition. Integrated fluorescence was calculated from mean values of area of region of interest and were normalised to the value at time 0. It is apparent that the photobleaching and/or spontaneous loss of RIc1-3GFP from contractile ring or from the arc in the absence of ATP are relatively minor. (**d**) Effect of dehydroxestoquinone (DXQ) on ATPase activity of motor proteins. DXQ has been reported to be an ATPase inhibitor that inhibits ATPase activity of muscle myosin II. Since DXQ had not been tested on other ATPase-motors, we tested its effects on kinesin (from brain), dynein (flagella), and myosin II S1 fragment (skeletal muscle) as a control. DXQ showed strong inhibition of ATPase activity of myosin II and dynein and a weaker inhibition of kinesin. Mean values of two measurements are plotted. See Table S6 for statistics source data. (**e**) Ring contraction was inhibited by the addition of 2.5 mM DXQ. Vanadate, which at 100 µM inhibits kinesin and dynein ATPases, did not affect ring contraction. Fluorescent images of RIc1-3xGFP are shown as maximum projections of Z-stacks (0.5 µm spaces). ATP concentration was 0.5 mM for DXQ or 0.1 mM for vanadate. Scale bar, 5 µm.

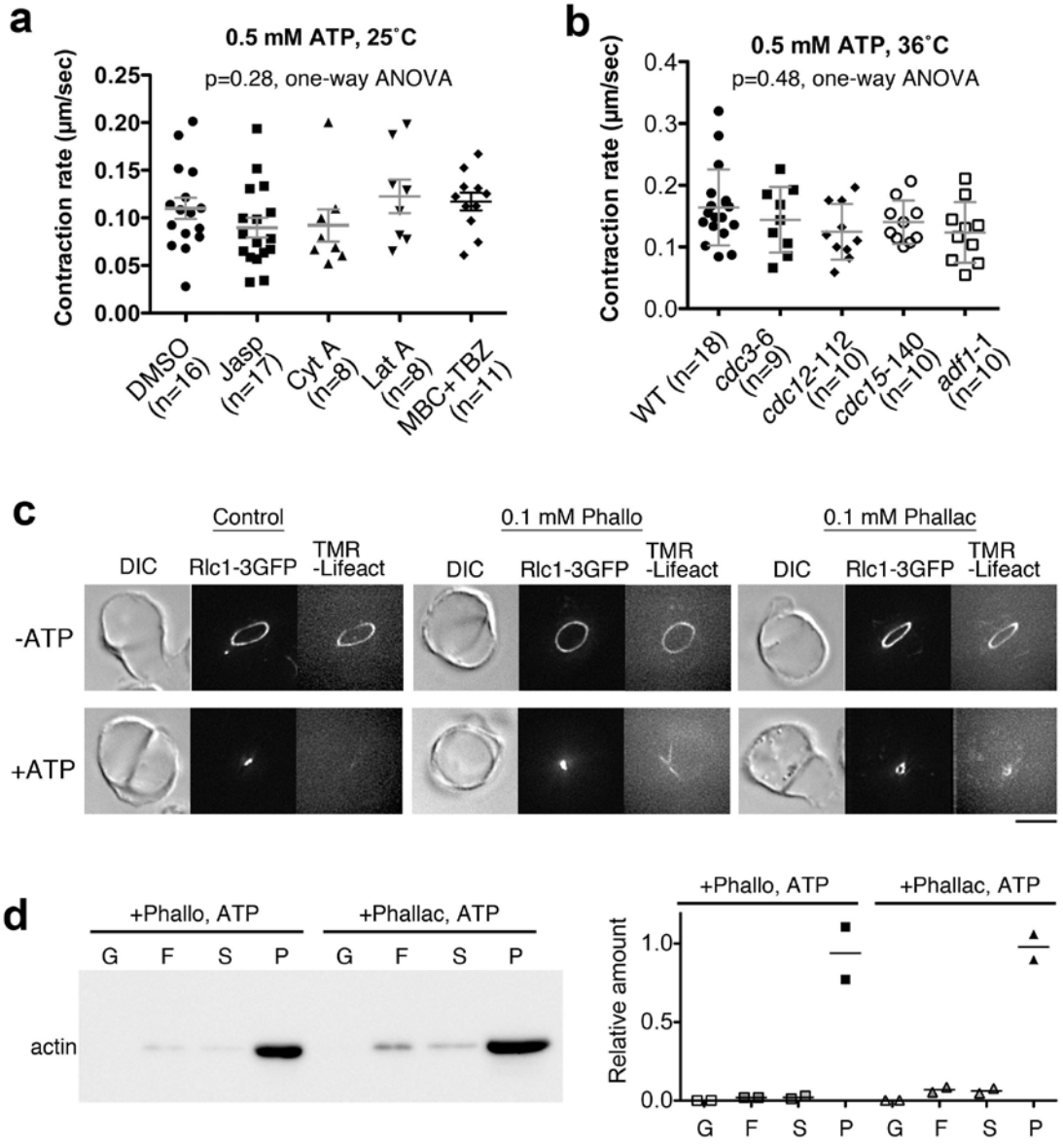

Figure S4 Neither actin polymerization nor depolymerization are required for ring contraction *in vitro*. (**a**) The effects of drugs (Jasp, 0.1 mM jasplakinolide; Cyt A, 0.1 mM cytochalasin A; Lat A, 10 μM latrunculin A; MBC+TBZ, 50 μg/ml MBC and 50 μg/ml TBZ) on ring contraction *in vitro*. 5% dimethyl sulfoxide (DMSO) was used for control experiment. Each spot represents the rate of contraction of an individual ring. Medial horizontal lines and error bars represent mean values and standard deviations, respectively. (**b**) 0.5 mM ATP was added after appropriate incubation at 36˚C (*cdc3*-6^{ts}, 20 min.; *cdc12*-112^{ts} *cdc15*-140^{ts} and *adf1*-1^{ts}, 15 min). Wild-type cell-ghosts were incubated at 36˚C for 30-40 minutes before ATP addition. A graphical representation of the data is shown. (**c**) Phalloidin and phallacidin prevent release of actin from contractile ring after ATP addition. Actin was stained with 10 μg/ml TMR-Lifeact before or after contraction. Fluorescent images of Rlc1-3xGFP and TMR-Lifeact are shown as maximum projections of Z-stacks (0.5 μm steps). Scale bar, 5 μm. (**d**) Western blot analysis of actin disassembly upon ATP addition in the presence of phalloidin or phallacidin. S, supernatant; P, pellet; G, G-actin and short F-actin; F, F-actin. Each relative amount was calculated from the amount of actin in the pellet without ATP. Each spot represents relative amount in individual experiment. See Table S6 for statistics source data. See also Fig. 4c, f.

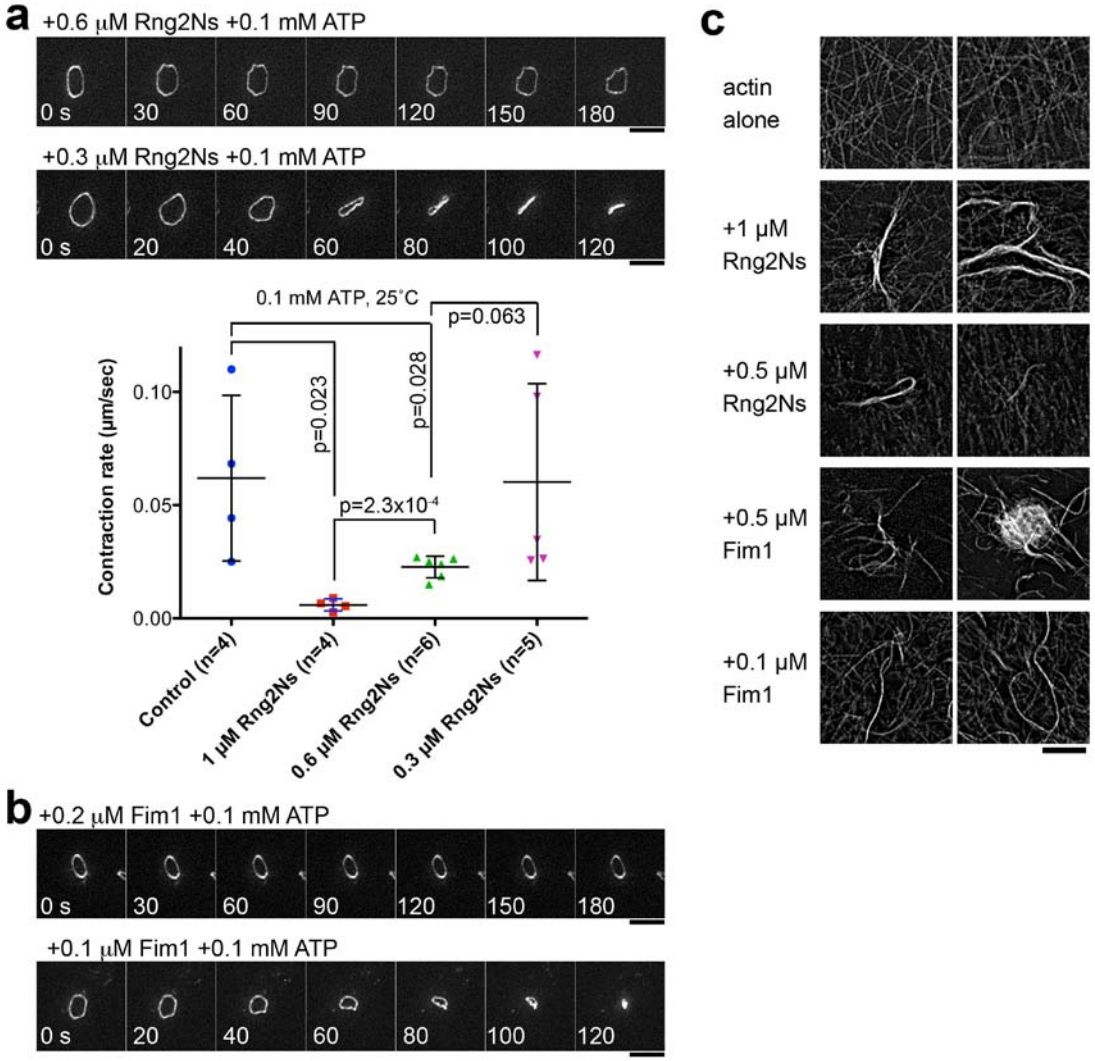

Figure S5 Dose dependent inhibition of ring contraction by purified actin-bundling proteins *in vitro*. (**a**-**b**) Cell-ghosts were incubated in the presence of purified proteins at the indicated concentrations for 3 minutes before addition of 0.1 mM ATP. Experiments were done at 25˚C. Fluorescent images of Rlc1-3xGFP are shown as maximum projections of Z-stacks (0.5 μm steps). Each spot represents the rate of contraction of an individual ring. Medial horizontal lines and error bars represent mean values and standard deviations, respectively. See Table S6 for statistics source data. (**c**) Actin-cross-linking activities of purified actin- bundling proteins. Skeletal actin (3 μM) was polymerised in the reactivation buffer including purified proteins for 30 minutes at room temperature. F-actin was stained with BODIPY-FL-phallacidin. Both, 1 μM Rng2Ns and 0.5 μM Fim1 show robust actin-bundling activity. Images are deconvolved from single focal planes. Scale bars, 5 μm.

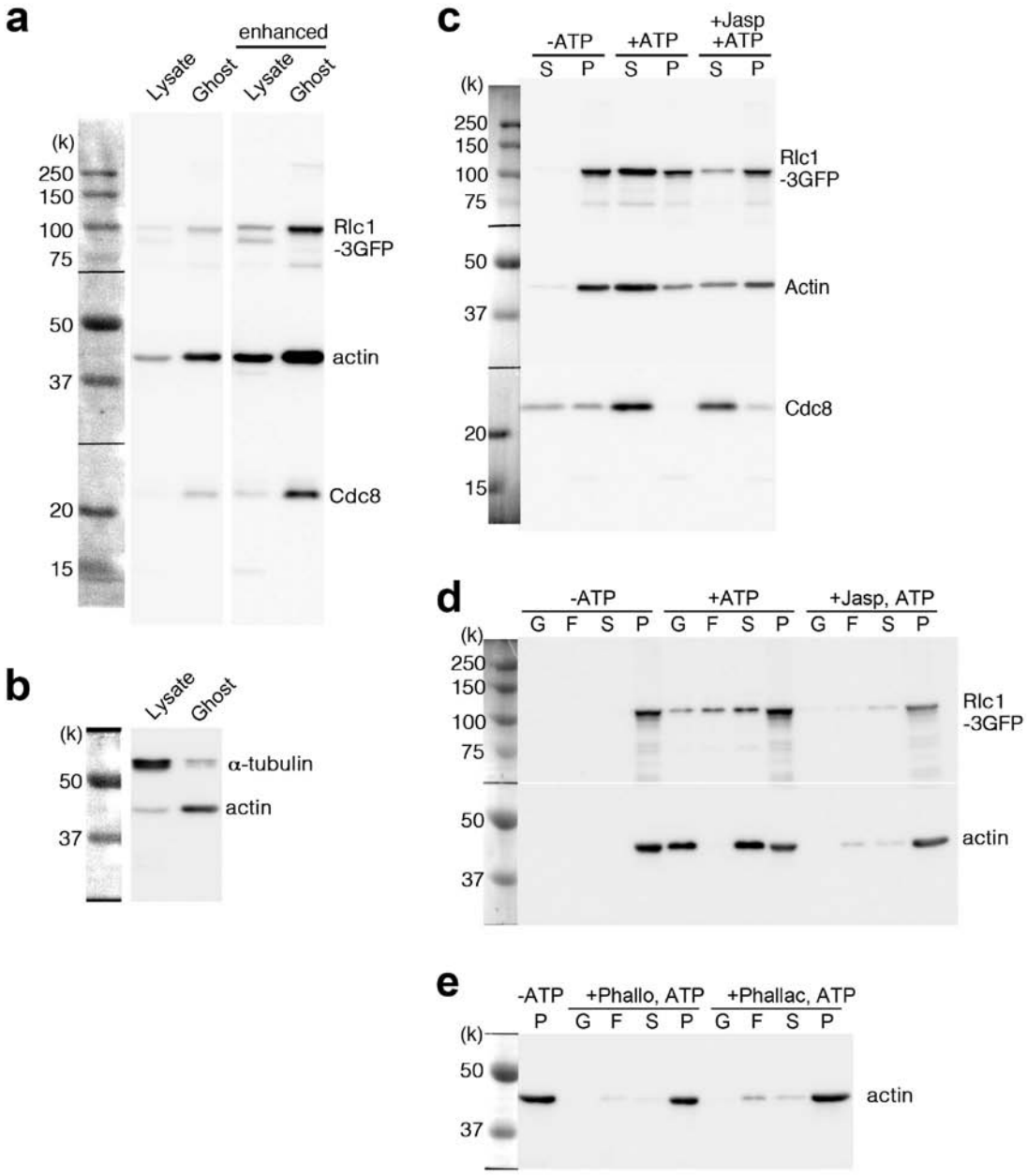

Figure S6 Full scans of original blots. (**a-b**) Full scan of blot shown in Fig. 1 h. (**c**) Full scan of blot shown in Fig. 4 d-e. (**d**) Full scan of blot shown in Fig. 4 f. (**e**) Full scan of blot shown in Fig. S4d.

Supplementary Table Legends:

Table S1. Proteins in the contractile rings. Intact cells and cell-ghosts expressing fluorescent-tagged proteins as indicated were imaged. Indirect immunoflurosence was used to label Cdc4p and Adf1p. Actin was detected by Alexa 568- phalloidin.

Table S2. *P* values for comparison of relative intensities of contractile ring components in Fig. 2f. Values at 100 seconds were compared. Unpaired two-tailed t-test was used for this analysis. *P* values less than 0.05, are represented in bold.

Table S3. Contraction rates in various nucleotide concentrations. Mean±SD was indicated. These datasets were used for the graph shown in Fig. 2h and calculation of K_m and V_m in Fig. 2i.

Table S4. Contractile ring components in the mutant rings. Cell-ghosts were prepared from the mutant cells expressing the indicated fluorescent-tagged proteins. Cell-ghosts were incubated at restrictive temperature to inactivate the mutant protein before imaging. Indirect immunofluorescence was used to label Cdc4p

Table S5. List of strains used in this study. *YGRC, Yeast Genetic Resource Center Japan. (http://yeast.lab.nig.ac.jp/nig/index_en.html).

Supplementary Video Legends:

Video S1. ATP drives ring contraction *in vitro*. The video of a contracting ring in the presence of 0.5 mM ATP at 25˚C corresponds to the frames shown in Fig. 2**a**. X-Y and Y-Z images were shown as non-tilted and 90˚-tilted maximum projections of Z-stacks, respectively.

Video S2. ATP drives ring contraction. The video of a contracting ring in the presence of 0.01 mM ATP at 25˚C corresponds to the frames shown in Fig. 2**c**. X-Y and Y-Z images were shown as non-tilted and 90˚-tilted maximum projections of Z-stacks, respectively.

Video S3. AMP-PNP does not induce ring contraction *in vitro*. Experiment was done at 25˚C. The video corresponds to the frames shown in Fig. 2**d**. X-Y and Y-Z images were shown as non-tilted and 90˚-tilted maximum projections of Z-stacks, respectively.

Video S4. The plasma membrane of Rlc1-3xGFP expressing cell-ghosts stained with FM4-64 during contraction *in vitro*. Experiment was done at 25˚C. The membrane did not ingress as the ring contracts. The video corresponds to the frames shown in Fig. 2**g**.

Video S5. Incomplete actomyosin arcs do not show ATP-dependent contraction *in vitro*. The GFP fluorescence decays the presence of 0.5 mM ATP but the actomyosin arc do not show any contraction at 25˚C. The video corresponds to the frames shown in Fig. 2**j**. X-Y and Y-Z images were shown as non-tilted and 90˚-tilted maximum projections of Z-stacks, respectively

Video S6. Contractile ring of *myo2*-E1^{ts} undergoes slow *in vitro* contraction even at the permissive temperature of 25˚C. The video corresponds to the frames shown in Fig. 3**b**.

Video S7. Contractile ring of *myp2* null mutant (*myp2*Δ) *in vitro*. Experiment was done at 25˚C. The video corresponds to the frames shown in Fig. 3**b**.

Video S8. Contractile ring contraction of the double mutant of *myo2* and *myp2* (*myo2*-E1^{ts} *myp2*Δ) *in vitro*. These rings did not show any contraction and instead fragmented and disassembled in presence of ATP at 25˚C. The video corresponds to the frames shown in Fig. 3**b**.

Video S9. Addition of Jasplakinolide does not affect ring contraction *in vitro*. Experiment was done at 25˚C.

Video S10. ADF/cofilin (Adf1p) is not required for ring contraction *in vitro*. Cell-ghosts from *adf1*-1^{ts} were held at 36˚C for 15 minutes before ATP addition.

Video S11. LatA has minimal effect on ring contraction *in vitro*. Experiment was done at 25˚C.

Video S12. Formin (Cdc12p) is not required for ring contraction *in vitro*. Experiment was done at 36˚C. Cell-ghosts from *cdc12*-112^{ts} were held at 36˚C for 15 minutes before ATP addition.

Video S13. F-BAR protein (Cdc15p) is not required for ring contraction *in vitro*. Experiment was done at 36˚C. Cell-ghosts from *cdc15*-140^{ts} were held at 36˚C for 15 minutes before ATP addition.

Video S14. Tropomyosin (Cdc8p) is required for integrity and contraction of ring *in vitro*. Cell-ghosts from *cdc8*-110^{ts} were held at 36˚C for 15 minutes before ATP addition. The video corresponds to the frames shown in Fig. 5**a**.

Video S15. Addition of 1 μM purified N-terminal region of IQGAP (Rng2Ns) completely blocks ring contraction *in vitro*. Experiment was done at 25˚C. The video corresponds to the frames shown in Fig. 5**b**.

Video S16. Addition of 0.9 μM purified fimbrin (Fim1p) completely blocks ring contraction *in vitro*. Experiment was done at 25˚C. The video corresponds to the frames shown in Fig. 5**c**.

C0233 In vitro reactivation of the cytokinetic contractile ring of fission yeast cells

I. Mabuchi*,[1], J. Kashiwazaki*, M. Mishra[§]
*Gakushuin University, Tokyo, Japan
[§]Tata Institute of Fundamental Science, Mumbai, India
[1]Corrresponding author: E-mail: issei.mabuchi@gakushuin.ac.jp

CHAPTER OUTLINE

Abstract

Cytokinesis is a process by which a mother cell is divided into two daughter cells after chromosome segregation. In both animal and fungal cells, cytokinesis is carried out by the constriction of the contractile ring made up of actin, myosin-II, and other conserved proteins. Detailed genetic and cell biological analysis of cytokinesis has led to the identification of various genes involved in the process of cytokinesis including the cytological description of the process. However, detailed biochemical analysis of the process is lacking. Critical questions that aim to understand aspects, such as the organization of actin and myosin in the contractile ring, the architecture of the ring, and the molecular process of ring contraction, remain unanswered. We have developed a method to address these aspects of cytokinesis. Using the fission yeast *Schizosaccharomyces pombe*, we present a method

Methods in Cell Biology, Volume 137, ISSN 0091-679X, http://dx.doi.org/10.1016/bs.mcb.2016.03.037

10233-MCB-9780128096734

whereby cell-ghosts containing functional contractile rings can be isolated and used to perform various biochemical analysis as well as detailed electron microscopy studies.

s0010 INTRODUCTION

p0010 Cell division is an essential event for proliferation, development, and maintenance of multicellular organisms. It is composed of mitosis and cytokinesis. In mitosis chromatids are segregated on a mitotic spindle leading to the formation of daughter nuclei. On the other hand, cytokinesis is a distinct process in which a force to divide the cell into two is generated at the division cortex of the cell. The machinery which exerts the force for cleavage at the division site was found by electron microscopy (EM) in the late 1960s to 1970s to be a bundle of actin filaments forming a ring structure in the division cortex of various animal cells (reviewed by Mabuchi, 1986), and the ring was called **the contractile ring**.

p0015 It has been established that the contractile ring contracts via interaction of actin filaments and myosin-II ATPase activity (Mabuchi & Okuno, 1977; Straight et al., 2003). However, there are many unsolved questions about cytokinesis: How are actin and myosin recruited to the division site? How are these proteins organized into the contractile ring structure? What is the detailed architecture of the contractile ring? What is the molecular process of ring contraction? How are actin and myosin disassembled during and after contraction?

p0020 To solve these important questions, it is desirable to have an in vitro system to study the mechanism of cytokinesis. Pioneering work was done using "glycerinated fibroblasts" (Hoffman-Berling, 1954). The telophase fibroblasts were permeabilized by glycerol at a low temperature. Upon addition of ATP the cleavage furrow advanced in these cells. This method was improved later using a detergent solution (Cande, 1980), but never used or developed further probably because of the difficulty to obtain a high proportion of dividing cells and to visualize the contractile ring during its contraction.

p0025 In 1988 we isolated the cleavage furrow from dividing newt eggs by a surgical technique (Mabuchi, Tsukita, Tsukita, & Sawai, 1988) and confirmed that the contractile ring was composed of actin filaments of opposite directionalities. These filaments were attached to the plasma membrane at their plus ends and were cross-linked with each other by cross-linking proteins. We also demonstrated that the isolated furrow contracted upon addition of ATP, which confirmed that the isolated furrow retained the original structure. These were novel findings but the mechanism of contraction was still unclear. Furthermore, this method did not become popular because it was difficult to collect many furrows in a short period, which was required for biochemical analyses or EM.

p0030 Next we isolated the cleavage furrow possessing the contractile ring, on a large scale from sea urchin eggs (Fujimoto & Mabuchi, 1997; Yonemura, Mabuchi, & Tsukita, 1991). Using this system we showed that elongation factors were concentrated in the isolated furrow preparation, and EF1α was necessary in progression of the cleavage (Fujimoto & Mabuchi, 2010). However, these furrows did not contract

upon addition of ATP suggesting that the structure was damaged during isolation. In spite of this unsatisfactory result, the isolation medium was successfully applied in the following experiments.

p0035 More than 10 years after the discovery of the contractile ring in animal cells, a similar ring, which was called the F-actin ring, was found at the division site of the fission yeast *Schizosaccharomyces pombe* (Kanbe, Kobayashi, & Tanaka, 1989; Marks & Hyams, 1985). Since *S. pombe* is genetically tractable and many useful cell division mutants have been isolated in the past, we chose this organism for studying the mechanism of cytokinesis. We have recently developed an in vitro system by which we can study contraction of the contractile ring using *S. pombe* cells (Mishra et al., 2013). We used a cell cycle mutant *cdc25* to synchronize the cells in G2 phase of the cell cycle. These cells were engineered to express myosin-II-GFP to visualize the contractile ring. The cell walls of synchronized cells were removed by [Q1] enzymic digestion to obtain spheroplasts. When these spheroplasts formed contractile rings, they were permeabilized by a detergent solution. The permeabilized cells thus obtained had some plasma membrane remnants but did not have visible cytoplasms, and they were called cell-ghosts. The myosin ring was retained in the cell-ghosts as seen by fluorescence microscopy (Fig. 1). Proteins which were reported to be essential for cytokinesis were largely localized in the contractile ring.

p0040 Upon addition of ATP, the contractile ring in the cell-ghost contracted to completion. The attachment of the ring to the perforated cell membrane seemed to be weak because the ring contracted leaving the membrane behind. The speed of contraction was more than 20 times faster than that in live cells, and it was similar to contraction rates observed in animal cells. Rings contracted slowly in the presence of other nucleotides, but did not show any contraction in the presence of nonhydrolyzable form of ATP, AMP-PNP. The C-shaped immature ring was also present in the ghost preparation but this structure did not contract at all upon ATP addition. The myosin-II ATPase inhibitor Blebbistatin interfered with contraction, and the ring in the ghost obtained from *myo2·myp2/myo3* double myosin-II mutant cells did not show contraction, indicating that myosin-II ATPase activity is required for ring contraction. Rings obtained from *cdc8* (tropomyosin) mutant cells also did not contract at a restrictive temperature but disassembled, suggesting that tropomyosin is required in maintaining the integrity of the ring. Addition of actin filament–cross-linking proteins IQGAP or fimbrin interfered with contraction in a dose-dependent manner, suggesting that excess cross-linking of actin filaments interferes with filament sliding during ring contraction.

s0015 1. METHODS

s0020 1.1 PREPARATION OF CELL-GHOSTS

s0025 *1.1.1 Genetic techniques and chemicals*

p0045 *Schizosaccharomyces pombe* strain used in this study was MBY 5763, *cdc25*-22 *rlc1*::*3xGFP-kan*^{r} *leu1*-32 h^{-} (Mishra et al., 2013). *cdc25* gene encodes a

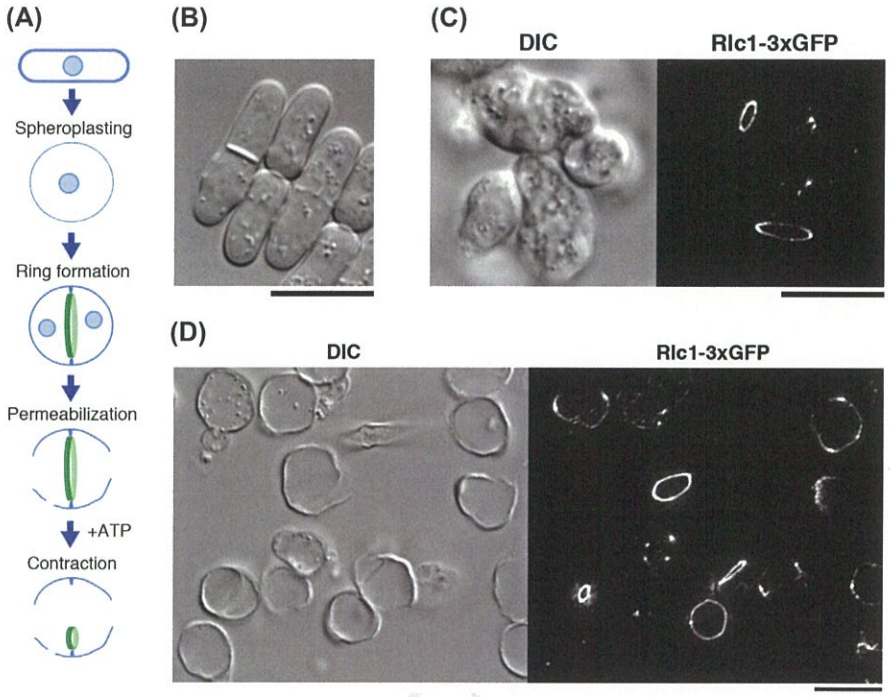

f0010 **FIGURE 1**

Fission yeast cells and cell-ghosts with contractile rings. (A) Schematic illustration of procedure to obtain cell-ghosts. (B) Live fission yeast *Schizosaccharomyces pombe* cells. (C) Live spheroplasts expressing Rlc1-3xGFP. Contractile rings are clearly seen under a fluorescence microscope. (D) Cell-ghosts prepared from spheroplasts expressing Rlc1-3xGFP. Scale bars, 10 μm.

phosphatase which activates cyclin-dependent kinases. Standard procedures for *S. pombe* genetics are described elsewhere (Moreno, Klar, & Nurse, 1991). It is recommended to use the temperature-sensitive cell division mutant *cdc25-22* cells to obtain a synchronous cell culture to enhance the proportion of spheroplasts and cell-ghosts with contractile rings.

p0050 Strains expressing epitope-tagged proteins are constructed using a PCR-based approach (Bähler et al., 1998). It is necessary to transform the strain with GFP-tagged contractile ring–specific protein to visualize the contractile ring under a fluorescence microscope before preparation of the cell-ghosts, and during reactivation of the contractile ring. The most convenient protein to be tagged with GFP is myosin regulatory light chain Rlc1 as these strains do not show any defects in cytokinesis.

p0055 Actin or myosin in *S. pombe* cells can be perturbed either in live cells or in isolated ghosts. Myosin ATPase inhibitor Blebbistatin (B0560, Sigma) can be used for the in vitro system (the ghosts) at a concentration around 0.1 mM. F-actin stabilizer Jasplakinolide (ALX-350-275, Alexis Corporation) can also be used for both live

cells and the in vitro system at a concentration around 0.1 mM. The other F-actin stabilizer phalloidin (P2141, Sigma) and phallacidin (P8157, Sigma) can only be used in vitro experiments at a concentration around 0.1 mM because these cyclic peptides cannot enter the cell membrane. Actin polymerization inhibitor Cytochalasin A (C6637, Sigma) and microtubule polymerization inhibitors methyl benzimidazole-2-yl-carbamate (381586, Sigma) and thiabendazole (T-8904, Sigma) can be used both for live cells and in vitro system at concentrations of 25 and 50 μg/mL, respectively.

s0030 *1.1.2 Spheroplasting*

p0060 Spheroplasts are obtained as described previously (Mishra et al., 2012). Cells are first grown at the permissive temperature of 25°C to early log phase in minimal medium (MM) containing 0.5% glucose (Fig. 1). These cells are then shifted to the restrictive temperature of 36°C for 4 h before spheroplasting. Cells (30 mL culture of OD 0.4–0.6) are harvested at 3000 rpm for 3 min, using either a fixed angle or a swing out rotor and washed once with 20 mL 1X E-buffer (50 mM sodium citrate, 0.1 M sodium phosphate pH 6.0) once and resuspended in 1X E-buffer with 1.2 M sorbitol. The cell suspension is adjusted to 5×10^7 cells/mL and incubated with 6 mg/mL lysing enzyme (L-1412; Sigma) at 36°C for 20–50 min. Cells are monitored for spheroplasting using a phase contrast microscope. Cells are then washed with E-buffer containing 1.2 M sorbitol once 90% of cells were spheroplasted, followed by a wash with E-buffer containing 0.6 M sorbitol. Cells were then suspended in MM with 0.8 M sorbitol and grown with gentle shaking (80 rpm) at 25°C (Fig. 1).

s0035 *1.1.3 Permeabilisation of spheroplasts and preparation of cell-ghosts*

p0065 Contractile ring formation in these spheroplasts is monitored by fluorescence microscopy. For a typical experiment, at the point of spheroplasting, Rlc1-3xGFP signal is detected in a single bright dotlike structure in 100% of the spheroplasts and actomyosin arcs or contractile rings are not seen. After 5 h of incubation at 25°C actomyosin arcs can be detected (in 3–7% of cells) while 25–35% of spheroplasts have fully formed contractile rings (Fig. 1).

p0070 Spheroplasts are washed twice with wash buffer (0.8 M sorbitol, 2 mM EGTA, 5 mM $MgCl_2$, 20 mM PIPES-NaOH, pH 7.0) and incubated for 5 min in isolation buffer (0.16 M sucrose, 50 mM EGTA, 5 mM $MgCl_2$, 50 mM potassium acetate, 50 mM PIPES-NaOH, pH 7.0, 0.5% NP-40, 10 μg/mL leupeptin, 10 μg/mL aprotinin, 10 μg/mL pepstatin, 0.5 mM PMSF, 1 mM DTT) on ice. Spheroplasts are homogenized with a Teflon/glass homogenizer. Cell-ghosts thus obtained are washed twice with reactivation buffer (0.16 M sucrose, 5 mM $MgCl_2$, 50 mM potassium acetate, 20 mM MOPS-NaOH, pH 7.0, 10 μg/mL leupeptin, 10 μg/mL aprotinin, 10 μg/mL pepstatin, 0.5 mM PMSF, 1 mM DTT). About 30% of the resultant cell-ghosts retain intact contractile rings (Fig. 1) while another 5–10% have actomyosin arcs or discontinuous or fragmented contractile rings. Majority of intact fully formed contractile rings are competent for in vitro contraction upon ATP addition.

s0040 1.2 IN VITRO CONTRACTION ASSAY

s0045 *1.2.1 Chamber assembly, sample application, and reactivation of contractile ring*

p0075 The reactivation of contractile ring in the cell-ghost is assessed with the handmade perfusion chamber shown in Fig. 2. The base of the chamber is constructed with a large coverslip (Matsunami Glass Ind., Ltd., Tokyo, Japan; 24 × 36 mm, No. 1) coated with 0.01% poly-L-lysine (Sigma, P1524) and double-sided tape (Nichiban, Tokyo, Japan; NW-5S, 60-μm wall thickness). The coverslip should be used within 2–3 h after adhering poly-L-lysine. Suspension of cell-ghosts are adhered to the base of chamber and then covered by a small coverslip (Matsunami, 18 × 18 mm, No. 1). Volume in the chamber is around 8 μL. Cell-ghosts are washed with reactivation buffer by perfusion to wash away cell-ghosts, which did not attach to the glass surface. Reactivation is performed by perfusion with reactivation buffer containing appropriate concentration of ATP. A majority of intact contractile rings in wild-type cell-ghosts undergo ATP-mediated contraction. If 0.5 mM ATP is perfused, contraction is usually accomplished in 30–60 s at 25°C.

s0050 *1.2.2 Microscopy*

p0080 Myosin-II is visualized by Rlc1-3xGFP as described previously. F-actin can be stained with BODIPY-FL-phallacidin, Alexa 568-phalloidin (Molecular Probes-Invitrogen, Eugene, OR) or synthesized tetramethylrhodamine-labeled Lifeact peptide (Operon Biotechnologies, Tokyo, Japan). Conventional fluorescence microscopy, three-dimensional reconstruction, and time-lapse observations are performed using a DeltaVision system (Applied Precision, Issaquah, WA) attached to an Olympus IX-70 widefield inverted fluorescence microscope equipped with Olympus UplanSApo ×100 oil immersion objective lens (NA 1.4, Olympus, Tokyo, Japan), and a Photometrics CoolSNAP HQ camera (Roper Scientific, San Diego, CA).

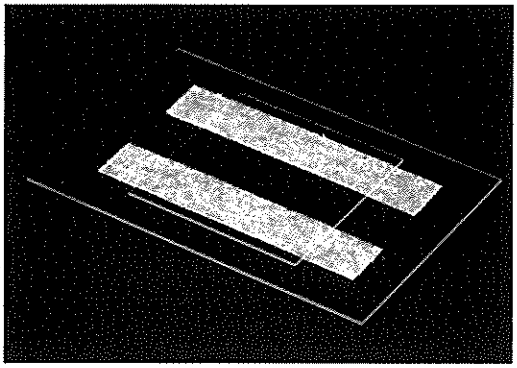

f0015 **FIGURE 2**

Assembly of flow chamber for reactivation analysis. Two strips of double-stick tape are attached on a coverslip (24 × 36 mm) to which poly-L-lysine had been applied. A smaller coverslip (18 × 18 mm) is mounted on the double-stick tapes.

10233-MCB-9780128096734

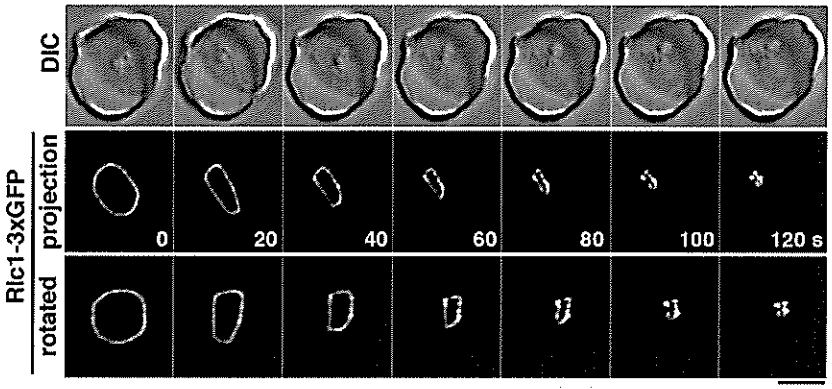

f0020 **FIGURE 3**

Reactivation of a contractile ring with an ATP-containing reactivation medium. (*Pictures are taken by DeltaVision system.*) Numbers indicate time in seconds after addition of 0.5 mM ATP. The lowest images are obtained from the middle images by rotation so that the ring plane is perpendicular to our view axis. Scale bar, 5 μm.

Temperature is controlled by both, the heated stage and a lens heater (for example, MATS-55RAF20, MATS-LH; TOKAI HIT, Shizuoka, Japan). More than 14 optical sections (0.5 μm spaces) can be acquired every 10 s. Images are captured and processed by iterative constrained deconvolution using SoftWoRx (Applied Precision), and analyzed by SoftWoRx and ImageJ (W.S. Rasband, National Institutes of Health, Bethesda, MD) incorporated with the McMaster Biophotonics Facility "ImageJ for Microscopy" collection of plugins (T. Collins, McMaster Biophotonics Facility, Hamilton, ON, Canada).

p0085 For measurement of contraction rate, stacks of optical sections are reconstructed in a horizontal direction using the three-dimensional rotation tool of SoftWoRx and the perimeter of each ring is measured (Fig. 3). Each contraction rate is determined by using values of the most linear phase of contraction. For measurement of fluorescence intensity sum projections of six deconvolved sections were used. Integrated intensity is calculated from mean value and area, after subtracting the background mean value of the same area. Graphical images are established using Prism-5 (Graphpad Software, La Jolla, CA, USA).

s0055 CONCLUSION

p0090 We presented a method to isolate a cell-ghost from a fission yeast cell and reactivate the contractile ring retained in the cell-ghost. This method enables in vitro manipulation of the contraction of the contractile ring so that the conditions which are required for the contraction of the ring can be studied. This will also enable ultrastructural studies of the contractile ring because the potency of contraction is proof

that the contractile ring possesses its normal ultrastructure, and loss of cytoplasm would benefit EM observation of the ring.

ACKNOWLEDGMENTS

We are grateful to Dr. Sarada Bulchand for her critical reading of the manuscript.

REFERENCES

Bähler, J., Wu, J. Q., Longtine, M. S., Shah, N. G., McKenzie, A., 3rd, Steever, A. B., ... Pringle, J. R. (1998). Heterologous modules for efficient and versatile PCR-based gene targeting in *Schizosaccharomyces pombe*. *Yeast, 14*, 943–951.

Cande, W. Z. (1980). A permeabilized cell model for studying cytokinesis using mammalian tissue culture cell. *Journal of Cell Biology, 87*, 326–335.

Fujimoto, H., & Mabuchi, I. (1997). Isolation of cleavage furrows from regular sea urchin eggs and identification of furrow-specific proteins. *Journal of Biochemistry, 122*, 518–524.

Fujimoto, H., & Mabuchi, I. (2010). Elongation factors are involved in cytokinesis of sea urchin eggs. *Genes to Cells, 15*, 123–135.

Hoffman-Berling, H. (1954). Die Glycerin-wasserextrahierte Telophasenzelle als Modell der Zytokinese. *Biochimica et Biophysica Acta, 15*, 332–339.

Kanbe, T., Kobayashi, I., & Tanaka, K. (1989). Dynamics of cytoplasmic organelles in the cell cycle of the fission yeast *Schizosaccharomyces pombe*: three dimensional reconstruction from serial sections. *Journal of Cell Science, 94*, 647–656.

Mabuchi, I. (1986). Biochemical aspects of cytokinesis. *International Review of Cytology, 101*, 175–213.

Mabuchi, I., & Okuno, M. (1977). The effect of myosin antibody on the division of starfish blastomeres. *Journal of Cell Biology, 74*, 251–263.

Mabuchi, I., Tsukita, S., Tsukita, S., & Sawai, T. (1988). Cleavage furrow isolated from newt eggs: contraction, organization of actin filaments, and protein components of the furrow. *Proceedings of the National Academy of Science of the United States of America, 85*, 5966–5970.

Marks, J., & Hyams, J. S. (1985). Localization of F-actin through the cell division cycle of *Schizosaccharomyces pombe*. *European Journal of Cell Biology, 39*, 27–32.

Mishra, M., Huang, Y., Srivastava, P., Srinivasan, R., Sevugan, M., Shlomovitz, R., ... Balasubramanian, M. K. (2012). Cylindrical cellular geometry ensures fidelity of division site placement in fission yeast. *Journal of Cell Science, 125*, 3850–3857.

Mishra, M., Kashiwazaki, J., Takagi, T., Srinivasan, R., Huang, Y., Balasubramanian, M. K., & Mabuchi, I. (2013). *In vitro* contraction of cytokinetic ring depends on myosin II but not on actin dynamics. *Nature Cell Biology, 15*, 853–859. http://dx.doi.org/10.1038/ncb2781.

Moreno, S., Klar, A., & Nurse, P. (1991). Molecular genetic analysis of fission yeast *Schizosaccharomyces pombe*. *Methods in Enzymology, 194*, 795–823.

Straight, A. F., Cheung, A., Limouze, J., Chen, I., Westwood, N. J., & Mitchison, T. J. (2003). Dissecting temporal and spatial control of cytokinesis with a myosin II Inhibitor. *Science, 299*, 1743–1747.

Yonemura, S., Mabuchi, I., & Tsukita, S. (1991). Mass isolation of cleavage furrows from dividing sea urchin eggs. *Journal of Cell Science, 100*, 73–84. [Q2]

光学顕微鏡技術を駆使した生体分子の動態の可視化

教授　西坂　崇之

[目的]

ほぼすべての微生物は運動する機能を持ち、生存のため適した環境に移動する手段として、その機能を巧みに用いている。バクテリア（真正細菌、bacteria）とアーキア（古細菌あるいは始原菌、archaea）は、真核生物で知られている従来の分子モーターとは異なった多様な運動装置を有しており、生物学のみならず、それらの未知の動作原理は物理の視点からも注目すべき研究対象となっている。

我々のグループでは、広く知られているべん毛回転モーターとは異なり、ユニークな運動装置を持つ幾つもの種を培養して研究を進めている。独自に開発した先進的な光学顕微鏡を駆使し、モーターという観点から装置の動作メカニズムについて明らかにすることを目的としている。本課題では、分子レベルから集団レベルまでのマルチスケールにおいて多面的な研究を展開し、微生物の様々な新しい運動様式を発見し、詳細に解析した。ステップ状の運動から集団運動に至るまで、これまでの成果の概要について以下に記す。

[*Mycoplasma mobile* のゴーストモデルによるステップ状運動]

Mycoplasma mobile（以下 *M. mobile*）は遊泳能を持たず、基板の上を一方向に滑走運動を行う。その滑走速度はバクテリアの中で最大であり、運動に関与するタンパク質は同定されているものの、基本的な動作原理は仮説の域を出ていない。

膜を部分的に透過性にしたゴーストモデルに、高精度の位置検出顕微鏡を応用することで、*M. mobile* の滑走装置は 70 nm の変位を行いながら運動を実現していることを明らかにした（参考文献１）。バクテリアの運動装置におけるステップ状運動を観察したのは、べん毛回転モーターの報告に引き続き２例目である。

観測されたステップの大きさ自体は、「巨大な脚状タンパク質の屈曲による運動」に矛盾はしないものの、既に報告のあるタンパク質の柔軟性を考えると、繰り返し正確なステップを行う機構がまったく説明できないことになる。新しいモデルとして、膜内にある回転モーターが別のタンパク質の回転を誘起し、その運動が未知の機構により直線運動へと変換される「回転⇔並進 変換モデル」を提案している。

[超解像顕微鏡による *M. mobile* の詳細な運動の定量化]

基板表面に可視光の波長より小さい金属のパターンを蒸着し、そこに全反射照明を行うこ

とで、表面近傍に「異常光学透過（EOT)」という特徴的な電磁波の分布を作ることができる。EOT の分布は、AFM や電子顕微鏡で決定したパターンの構造と、詳細なシミュレーションを組み合わせることにより推定できる。この分布を参照パターン（kernel）とし、一定速度で運動する蛍光バクテリアからのシグナルを kernel で再構成することによって、滑走中のバクテリア（*M. mobile*）の位置を３次元的に高精度で決定する新しい実験方法を提案した（参考文献２)。

[*Flavobacterium johnsoniae* の集団運動]

桿菌である *Flavobacterium johnsoniae*（以下 *F. johnsoniae*）も *M. mobile* 同様、基板の上で滑走運動を行うが、その運動機構はまったく異なる仮説が提唱されている。細胞表面から突き出た接着タンパク質がらせん状に配置したレールの上を動き、この流れが細胞全体の一方向の運動を生み出すと考えている。我々は *F. johnsoniae* が飢餓状態において、特徴的な渦運動を生み出すことを見出し、研究機関の初年度に基本的なデータの収集を終えた。次年度ではこの機構を解明するため、渦の形成過程を長時間にわたり安定して記録するシステムの構築に成功した。

[アーキア回転モーターのステップ状回転]

アーキアの遊泳運動の研究は、試料調製の難しさからバクテリアと比べ未踏の領域であると言える。我々は *Hanobacterium salinarum* を対象として、再現性良く運動を観察する実験系の構築に成功した。さらに ATP 駆動によるモーターのステップ状運動の計測にも成功した。この結果については生物物理学会のシンポジウム、および Pachifichem 2015 において招待講演として発表し、まだ原著論文は発表されていないものの（参考文献３）既に高い評価を得ている。

[参考文献]

1. Kinosita, Y., Nakane, D., Sugawa, M., Masaike, T., Mizutani, K., Miyata, M., and Nishizaka, T. (2014). Unitary step of gliding machinery in Mycoplasma mobile. Proc Natl Acad Sci USA *111*, 8601-8606.

2. Lee, W., Kinosita, Y., Oh, Y., Mikami, N., Yang, H., Miyata, M., Nishizaka, T., and Kim, D. (2015). Three-Dimensional Superlocalization Imaging of Gliding Mycoplasma mobile by Extraordinary Light Transmission through Arrayed Nanoholes. ACS Nano *9*, 10896-10908.

3. Kinosita, Y., Uchida, N., Nakane, D., and Nishizaka, T. (2016). Direct observation of rotation and steps of the archaellum of swimming halophilic archaea. (submitted)

［原著論文］

1. Kinosita, Y., Nakane, D., Sugawa, M., Masaike, T., Mizutani, K., Miyata, M., and Nishizaka, T. (2014). Unitary step of gliding machinery in Mycoplasma mobile. Proc Natl Acad Sci USA *111*, 8601-8606.
2. Kurushima, J., Nakane, D., Nishizaka, T., and Tomita, H. (2015). Bacteriocin protein BacL1 of Enterococcus faecalis targets cell division loci and specifically recognizes L-Ala2-cross-bridged peptidoglycan. Journal of bacteriology *197*, 286-295.
3. Lee, W., Kinosita, Y., Oh, Y., Mikami, N., Yang, H., Miyata, M., Nishizaka, T., and Kim, D. (2015). Three-Dimensional Superlocalization Imaging of Gliding Mycoplasma mobile by Extraordinary Light Transmission through Arrayed Nanoholes. ACS Nano *9*, 10896-10908.
4. Yamaguchi, S., Saito, K., Sutoh, M., Nishizaka, T., Toyoshima, Y.Y., and Yajima, J. (2015). Torque generation by axonemal outer-arm dynein. Biophys J *108*, 872-879.
5. Sugawa, M., Okazaki, K., Kobayashi, M., Matsui, T., Hummer, G., Masaike, T., and Nishizaka, T. (2016). F1-ATPase conformational cycle from simultaneous single-molecule FRET and rotation measurements. Proc Natl Acad Sci USA (in press).

[総説等]

1. Katoh, T.A., Fujimura, S., and Nishizaka, T. (2015). 3-D Single Particle Tracking Using Dual Images Divided by Prism: Method and Application to Optical Trapping. In Handbook of Photonics for Biomedical Engineering.

［口頭発表］

1. Itou, T., Y. Kinosita, D. Nakane, H. Wada, W. Wang, T. Nishizaka (2015). Spiroplasma eriocheiris において観察されたキンクの伝搬によって生じるらせん型スクリューの向きと回転速度の変化　Change in handedness and rotational speed of helical screw of Spiroplasma eriocheiris driven by kink propagation. 第53回日本生物物理学会年会, 金沢大学 角間キャンパス 自然科学本館, September 13-15, 2015.
2. Iwase, T., M. Suegara, R. Nakayama, T. A. Katoh, M. Setou, T. Nishizaka, K. Ikegami, T. Masaike (2015). 三次元で見た ATP 依存的な繊毛運動の Ca2+ による制御　Regulation of ATP-dependent ciliary motility by Ca2+ observed in three dimensions. 第53回日本生物物理学会年会, 金沢大学 角間キャンパス 自然科学本館, September 13-15, 2015.
3. Mizutani, M., Y. Kinosita, T. Nishizaka, M. Miyata (2015). Mycoplasma mobile が捕捉状態で発生する力　Force generation of Mycoplasma mobile at trapped state. 日本マイコプラズマ学会第42回学術集会, 慶應義塾大学薬学部 芝共立キャンパス, May 22-23.
4. Mizutani, M., Y. Kinosita, T. Nishizaka, M. Miyata (2015). Mycoplasma mobile のストール力　Stall force of Mycoplasma mobile. 第53回日本生物物理学会年会, 金沢大学 角間キャンパス 自然科学本館, September 13-15, 2015.

5. Mizutani, M., Y. Kinosita, T. Nishizaka, M. Miyata (2015). Mycoplasma mobile のストール力　Stall force of Mycoplasma mobile. 第88回日本細菌学会総会, 長良川国際会議場, March 26-28.
6. 下澤東吾, 橋本優, 井合健太郎, 宗行英朗, 政池知子, 西坂崇之 (2013). 回転軸をねじったF1-ATPase変異体の回転特性解析. 日本生体エネルギー研究会　第39回討論会, 静岡県コンベンションアーツセンター　グランシップ, December 18, 2013.
7. 加藤孝信, 岩瀬寿仁, 瀬藤光利, 池上浩司, 西坂崇之, 政池知子 (2013). マウス気管繊毛の３次元運動解析と力測定. 新学術研究領域「シリア・中心体による生体情報フローの制御」第2回領域会議プログラム, ルブラ王山（名古屋）, November 28, 2013.
8. 加藤孝信, 岩瀬寿仁, 政池知子, 池上浩司, 瀬藤光利, 西坂崇之 (2013). Three-dimensional motion of an isolated murine tracheal cilium under load　負荷をかけた状態での単離マウス気管上皮シリアの三次元運動. 第51回日本生物物理学会年会, 国立京都国際会館, October 28, 2013.
9. 加藤孝信, 岩瀬寿仁, 政池知子, 池上浩司, 瀬藤光利, 西坂崇之 (2014). 負荷をかけた状態での単離マウス気管上皮シリアの三次元運動. 生体運動研究合同班・2014年班会議, 千葉大学西千葉キャンパス, January 10, 2014.
10. 加藤孝信, 池上浩司, 岩瀬寿仁, 政池知子, 瀬藤光利, 西坂崇之 (2014). 単離マウス気管上皮繊毛が生み出す力の三次元顕微計測　Force measurement of individual isolated mouse tracheal cilia using three-dimensional optical trapping. 第52回日本生物物理学会年会, 札幌コンベンションセンター, September 25-27, 2014.
11. 加藤孝信, 池上浩司, 岩瀬寿仁, 政池知子, 瀬藤光利, 西坂崇之 (2014). 単離繊毛非対称運動における発生張力の三次元顕微計測. 第5回繊毛研究会, 浜松市研修交流センター, May 24-25, 2014.
12. 加藤孝信, 池上浩司, 岩瀬寿仁, 政池知子, 瀬藤光利, 西坂崇之 (2015). マウス気管繊毛の非対称運動メカニズム -軸糸の変形の視点から-. 生体運動研究合同班・2015年班会議, 学習院大学, January 7-9, 2015.
13. 加藤孝信, 池上浩司, 岩瀬寿仁, 政池知子, 瀬藤光利, 西坂崇之 (2015). マウス気管繊毛の非対称運動メカニズム -軸糸の変形の視点から-. 第67回日本細胞生物学会大会, 東京都 タワーホール船堀, June 30-July 2, 2015.
14. 加藤孝信, 池上浩司, 内田就也, 岩瀬寿仁, 政池知子, 瀬藤光利, 西坂崇之 (2015). マウス気管繊毛の非対称運動メカニズム ー軸糸の変形の視点からー　Mechanism of asymmetric beating of mouse tracheal cilia - from the perspective of the axoneme bending -. 第53回日本生物物理学会年会, 金沢大学 角間キャンパス 自然科学本館, September 13-15, 2015.
15. 岩瀬寿仁, 加藤孝信, 瀬藤光利, 西坂崇之, 池上浩司, 政池知子 (2014). Ca2+依存的な運動性を持つ気管繊毛の三次元解析. 第5回繊毛研究会, 浜松市研修交流センター, May 24-25, 2014.
16. 久留島潤, 林幾江, 中根大介, 西坂崇之, 菅井基行, 富田治芳 (2014). 腸球菌バクテリオシンBac41による殺菌メカニズムの解析　Functional analysis of bacteriocin Bac41

produced by Enterococcus faecalis. 第87回日本細菌学会総会, 東京都江戸川区船堀・タワーホール船堀, March 26-28,2014.

17. 三上渚, 政池知子, 須川光弘, 西坂崇之 (2013). "Advanced TIRF microscopy to detect single-molecule conformational changes in both azimuth and axial axis using polarization switching　方位と倒れの構造変化を１分子レベルで検出する偏光スイッチングを用いた新しいTIRFM." 第51回日本生物物理学会年会 October 28, 2013.
18. 三上渚, 政池知子, 西坂崇之 (2014). 全反射型蛍光顕微鏡における受像偏向と偏光変調 －F1-ATPase の構造変化検出への応用－　Emitter modulation and polarization switching under TIRF illumination: Application for detection of conformational change in F1-ATPase. 第52回日本生物物理学会年会, 札幌コンベンションセンター, September 25-27, 2014.
19. 三上渚, 西坂崇之 (2015). １分子の複数状態モニタリングにより明らかとなった F1-ATPase におけるヌクレオチド周辺の局所環境と化学状態の相関　Correlation between local environment around nucleotide and chemical state in F1-ATPase revealed by single-molecule modes monitoring. 第53回日本生物物理学会年会, 金沢大学 角間キャンパス 自然科学本館, September 13-15, 2015.
20. 三上渚, 中根大介, 西坂崇之 (2014). Polarization- and emitter- Modulation TIRF Microscopy to Detect 3-D Oriental of Single Protein. International Symposium on Mechanobiology 2014, 岡山大学鹿田キャンパス, May 20-23, 2014.
21. 三上渚, 内藤達也, 下澤東吾, 政池知子, 宗行英朗, 西坂崇之 (2014). Detection of Conformational Change of the Cylinder in Single F1-ATPase and its Interaction with the Shaft under Advanced Optical Microscopes. Tokyo ATPase Workshop, 東京大学本郷キャンパス, June 2-3, 2014.
22. 山口真, K. Saito, M. Sutoh, 西坂崇之, 豊島陽子, 矢島潤一郎 (2014). 軸糸外腕ダイニンによるトルク発生　Torque generation by axonemal outer-arm dynein. 第52回日本生物物理学会年会, 札幌コンベンションセンター, September 25-27, 2014.
23. 山口真, 西坂崇之, 豊島陽子, 矢島潤一郎 (2015). 微小管コークスクリュー運動の三次元計測による軸糸外腕ダイニン及びそのサブユニットの運動特性の定量. 生体運動研究合同班・2015年班会議, 学習院大学, January 7-9, 2015.
24. 小高祥子, 中根大介, 西坂崇之 (2013). "Three-dimensional tracking of tank-like motility apparatus of the gliding bacterium　滑走するバクテリアの戦車のような運動装置を三次元で追跡する." 第51回日本生物物理学会年会 October 28, 2013.
25. 小高祥子, 中根大介, 西坂崇之 (2014). バクテリアの集団運動による巨大渦パターン形成　Large-scale vortex pattern emerging from bacteria collective motion. 第52回日本生物物理学会年会, 札幌コンベンションセンター, September 25-27, 2014.
26. 小高祥子, 中根大介, 西坂崇之 (2014). バクテリアの集団運動による巨大渦パターン形成　Large-scale vortex pattern emerging from bacterium collective motion. 第87回日本細菌学会総会, 東京都江戸川区船堀・タワーホール船堀, March 26-28, 2014.
27. 小高祥子, 中根大介, 西坂崇之 (2014). 滑走するバクテリアがつくる巨大渦パターン. 生体運動研究合同班・2014年班会議, 千葉大学西千葉キャンパス, January 10, 2014.

28. 小高祥子, 中根大介, 西坂崇之 (2015). 滑走するバクテリアの自己集合により形成される巨大渦の一方向性回転　Directional rotation of large-scale vortex made of self-assembly of gliding bacteria. 第53回日本生物物理学会年会, 金沢大学 角間キャンパス 自然科学本館, September 13-15, 2015.
29. 須河光弘, 山口真, 柴田桂太郎, 藤. 政池知子, 豊島陽子, 矢島潤一郎, 神隆, 西坂崇之 (2013). "受像偏向蛍光イメージングによる分子モーターの運動計測　生体運動研究合同班・2013年班会議: January 13, 2013.
30. 須河光弘, 小林大, 松井貴志, 政池知子 (2013). "Analysis of the ATP-waiting form of F1-ATPase by single-pair FRET measurement　1分子FRET計測によるF1-ATPaseのATP結合待ち構造の解析." 第51回日本生物物理学会年会: October 28, 2013.
31. 須河光弘, 小林大, 松井貴志, 政池知子, 西坂崇之 (2014). CONFORMATIONAL CHANGES IN THE β SUBUNITS OF F1-ATPase REVEALED BY FRET MEASUREMENTS DURING ROTATION OF THE γ SUBUNIT. Biophysical Society Annual Meeting 2014, San Francisco, California, February 15-19, 2014.
32. 須河光弘, 政池知子, 山口真, 柴田桂太郎, 豊島陽子, 矢島潤一郎, 神隆, 西坂崇之 (2013). "受像偏向蛍光顕微鏡による分子モーターの運動計測　Development of circular orientation fluorescenceemitter imaging（COFEI）." 日本顕微鏡学会第69回学術講演: May 21, 2013.
33. 政池知子 (2013). "タンパク質の動きを解き明かす 1 分子計測の最前線." 日本物理学会 第68回年次大会 領域12, 11合同シンポジウム　March 26, 2013.
34. 政池知子, 西坂崇之 (2013). "蛋白質の動きとはたらきを直接見て調べる." 第22回 日本バイオイメージング学会学術集会・公開講座: september 14-16,2013.
35. 政池知子, 池上浩司, 瀬藤光利, 鈴木裕, 西坂崇之 (2013). "1個から数個の分子が引き起こす運動と酵素反応のイメージング." 第51回日本生物物理学会年会・シンポジウム: Octorber 28-30,2013.
36. 政池知子, 池上浩司, 瀬藤光利, 鈴木裕, 西坂崇之 (2013). "蛋白質1分子の構造変化と化学反応を可視化する." 2013年度 若手イメージング研究会: september 7-8,2013.
37. 政池知子, 鈴木裕, 西坂崇之 (2013). "プローブの向きと位置から蛋白質の局所構造変化を検出する." 日本顕微鏡学会第57回シンポジウム: November 15-16,2013.
38. 西坂崇之 (2015). Mechanics of Motor Proteins and Supermolecular Motility Machinery Revealed under Advanced Optical Microscopes. WPI-next international workshop ~~High resolution cell biology~~, E & S building, Nagoya Univ., 1st Oct. 2015.
39. 西坂崇之 (2015). シンポジウム「べん毛・繊毛が織りなす多様な生命現象に挑む　～分子から個体まで～ Diverse functions of flagella and cilia; -From molecules to mammalian development-」
40. 先進光学顕微鏡により明らかになる繊毛とアーキアべん毛の力学機能　Mechanical function of cilia and archaeal flagella resolved by advanced optical microscopes. 第53回日本生物物理学会年会, 金沢大学 角間キャンパス 自然科学本館, September 13-15, 2015.

41. 西坂崇之, D. Kim, 須河光弘, 政池知子 (2013). "Imaging of Function and Orientation of Single Motor Proteins Under Advanced Optical Microscopy." The 8th Asian Biophysical Association (ABA) Symposium: May 27, 2013.
42. 西坂崇之, 加藤孝信, 木下佳昭 (2014). Analysis of three-dimensional motion of motor proteins and supermolecular motility machinery. The 6th International Symposium on Aero Aqua Bio-Mechanics, Hawaii Tokai International College, Honolulu, Hawawii, USA, November 13-16, 2014 (Nov 14).
43. 西坂崇之, 須河光弘, 木下佳昭, 政池知子 (2013). "1 細胞や1 分子の動態を直感的かつ定量的に検出する　Intuitive but quantitative approach to image singlecells and molecules." 日本顕微鏡学会第69回学術講演会: May 22, 2013.
44. 西坂崇之, 中根大介 (2013). "Single-Molecule Imaging of Protein Conformations under Advanced Optical Microscopes." Protein Dynamics: August 5, 2013.
45. 西坂崇之, 中根大介 (2014). Mechanics of novel motors revealed under advanced optical microscopes. The 45th NIPS International symposium “Cutting-edge approaches towards the functioning mechanisms of membrane proteins”, 岡崎コンファレンスセンター, November 25-28, 2014 (26 Nov).
46. 西坂崇之, 中根大介 (2014). Single-molecule imaging of protein conformations under advanced optical microscopes. 1st International Conference on Nano-Bio-Medicine Convergence (NBMC-2014), Pusan Nat’l University, 24-25 February 2014 (25 Feb).
47. 池上浩司, 政池知子, 西坂崇之, 瀬藤光利 (2014). 繊毛と鞭毛におけるチューブリンポリグリシン化の異なる寄与度. 第5回繊毛研究会, 浜松市研修交流センター, May 24-25, 2014.
48. 池上浩司, 政池知子, 西坂崇之, 瀬藤光利 (2015). 軸糸チューブリンポリグリシン化消失による鞭毛繊毛運動の亢進. 生体運動研究合同班・2015年班会議, 学習院大学, January 7-9, 2015.
49. 中根大介, 佐藤啓子, M. J. McBride, 中山浩次, 西坂崇之 (2013). "戦車のような仕組みで動くバクテリア." 第7回細菌学若手コロッセウム: August 7, 2013.
50. 中根大介, 佐藤啓子, 中山浩次, 西坂崇之 (2014). 戦車のような仕組みで動くバクテリア　Bacterium moves likes a tank. 第87回日本細菌学会総会, 東京都江戸川区船堀・タワーホール船堀, March 26-28, 2014.
51. 中根大介, 佐藤啓子, 和田浩史, M. Mark, 中山浩次, 西坂崇之 (2013). "Bacterium moves like a tank　戦車のような仕組みで動くバクテリア." 第51回日本生物物理学会年会 October, 28, 2013.
52. 中根大介, 小高祥子, 佐藤啓子, 和田浩史, M. Mark, 中山浩次, 西坂崇之 (2014). 戦車のような仕組みで動くバクテリア　Bacterium moves likes a tank. 日本農芸化学会2014年度大会, 明治大学生田キャンパス March 27-30, 2014.
53. 中根大介, 小高祥子, 西坂崇之 (2014). Large-scale vortex lattice emerging from gliding bacteria　滑走するバクテリアがつくる巨大渦パターン. 第19回べん毛研究交流会, 広島県民文化センター(鯉城会館), March 1-3, 2014.

54. 中根大介, 西坂崇之 (2013). "戦車のような仕組みで動くバクテリア." 第29回日本微生物生態学会大会: November 23, 2013.
55. 中根大介, 西坂崇之 (2014). 1 細胞レベルにおけるバクテリア走化性のメカニズム Mechanism of phototaxis of bacteria at single cell level. 第52回日本生物物理学会年会, 札幌コンベンションセンター, September 25-27, 2014.
56. 中根大介, 西坂崇之 (2015). 局所的な照明により制御される IV 型線毛の収縮 Retraction of Type IV pili controlled by local light gradient. 第53回日本生物物理学会年会, 金沢大学 角間キャンパス 自然科学本館, September 13-15, 2015.
57. 田中晃弘, 中根大介, 西坂崇之 (2013). "“あし”の結合の方向性で説明される Mycoplasma mobileの滑走運動." 第86回日本細菌学会総会: March 18, 2013.
58. 田中晃弘, 中根大介, 西坂崇之, 宮田真人 (2013). "Gliding of Mycoplasma mobile can be explained by directed binding." Blast XII: January 20, 2013.
59. 田中晃弘, 中根大介, 西坂崇之, 宮田真人 (2013). "Mycoplasma mobile“あし”結合の方向性." 生体運動研究合同班・2013年班会議: January 12, 2013.
60. 田中晃弘, 中根大介, 西坂崇之, 宮田真人 (2014). 滑走細菌Mycoplasma mobile の"あし"の結合の方向性 Directed binding of gliding bacterium, Mycoplasma mobile. 第87回日本細菌学会総会, 東京都江戸川区船堀・タワーホール船堀, March 26-28, 2014.
61. 藤村章子, 伊藤祐子, 足立健吾, 池口満徳, 西坂崇之 (2015). 等方型 TRIFM とデフォーカスイメージングによる単一蛍光色素の角度と回転方向の検出 Detection of 3-D orientation and rotation handedness of single fluorophore by isotropic TIRFM and defocused imaging. 第53回日本生物物理学会年会, 金沢大学 角間キャンパス 自然科学本館, September 13-15, 2015.
62. 藤村章子, 三上渚, 伊藤竜朗, 西坂崇之 (2014). 偏光変調 TRIFM とデフォーカスイメージングによる単一蛍光色素の角度と回転方向の検出 Detection of 3-D orientation and rotation of single fluorophores by combination of polarization-modulation TIRFM and defocused imaging. 第52回日本生物物理学会年会, 札幌コンベンションセンター, September 25-27, 2014.
63. 藤村章子, 足立健吾, 西坂崇之 (2015). 微小管のコークスクリュー運動を利用した三次元角度検出技術の確立. 生体運動研究合同班・2015年班会議, 学習院大学, January 7-9, 2015.
64. 藤村章子, 大和田伸介, 西坂崇之, 矢島潤一郎 (2013). "Three-dimensional corkscrewing motion of a microtubule driven by single-headed kinesins with mutations in the N terminal region." The 8th Asian Biophysical Association (ABA) Symposium: May 26, 2013.
65. 藤村章子, 大和田慎介, 西坂崇之, 矢島潤一郎 (2013). "N末端領域変異単頭キネシンによる微小管の3次元コークスクリュー運動." 生体運動研究合同班・2013年班会議: January 13, 2013.
66. 藤村章子, 大和田慎介, 西坂崇之, 矢島潤一郎 (2013). "Three-dimensional corkscrewing motion of a microtubule driven by single-headed kinesins with

mutations in the N-terminal region　N末端領域変異単頭キネシンによる微小管の3次元コークスクリュー運動." 第51回日本生物物理学会年会: October 28, 2013.

67. 内藤達也, 岡田薫, 政池知子, 西坂崇之 (2013). "F1-ATPaseの軸とシリンダーの結合寿命の測定." 日本生体エネルギー研究会　第39回討論会 December 18, 2013.
68. 内藤達也, 岡田薫, 政池知子, 西坂崇之 (2013). "Measurement of lifetime of the bond between the shaft and the cylinder in single F1-ATPase　F1-ATPaseの軸とシリンダーの結合寿命の測定." 第51回日本生物物理学会年会: October 28, 2013.
69. 内藤達也, 岡田薫, 政池知子, 西坂崇之 (2013). "Measurement of lifetime of the bond between the shaft and the cylinder in single F1-ATPase." The 8th Asian Biophysical Association (ABA) Symposium: May 26, 2013.
70. 内藤達也, 岡田薫, 中山莉奈子, 政池知子, 西坂崇之 (2013). "F1-ATPaseの軸とシリンダーの結合寿命の測定." 生体運動研究合同班・2013年班会議: January 12, 2013
71. 木下佳昭, 中根大介, 宮田真人, 西坂崇之 (2013). "Nucleotide-dependent interaction between legs of Mycoplasma mobile and sialyllactose　マイコプラズマモービレのあしとシアル酸の結合はヌクレオチドに依存する." 第51回日本生物物理学会年会: October 28, 2013.
72. 木下佳昭, 中根大介, 宮田真人, 西坂崇之 (2013). "マイコプラズマモービレのあしとシアル酸の結合様式はヌクレオチド状態によって変化する." 新学術領域研究「運動超分子マシナリーが織りなす調和と多様性」第一回全体会議: June 28, 2013.
73. 木下佳昭, 中根大介, 宮田真人, 西坂崇之 (2014). Unitary step and nucleotide-dependent binding change of gliding machinery in Mycoplasma mobile. Tokyo ATPase Workshop, 東京大学本郷キャンパス, June 2-3, 2015.
74. 木下佳昭, 中根大介, 宮田真人, 西坂崇之 (2014). Unitary step and nucleotide-dependent binding change of gliding machinery in Mycoplasma　mobile. 第19回べん毛研究交流会, 広島県民文化センター(鯉城会館), March 1-3, 2014.
75. 木下佳昭, 中根大介, 宮田真人, 西坂崇之 (2014). 光ピンセットで明らかになったマイコプラズマモービレ滑走運動の化学力学共役. 生体運動研究合同班・2014年班会議, 千葉大学西千葉キャンパス, January 10, 2014.
76. 木下佳昭, 中根大介, 宮田真人, 西坂崇之 (2014). 最先端の光学顕微鏡技術で明らかになるマイコプラズマモービレの滑走メカニズム　Gliding mechanism of Mycoplasma mobile revealed by advanced optical microscopy. 第87回日本細菌学会総会, 東京都江戸川区船堀・タワーホール船堀, March 26-28, 2014.
77. 木下佳昭, 中根大介, 宮田真人, 西坂崇之 (2014). 微生物の運動超分子マシナリーの単位ステップの直接観察：滑走バクテリアと遊泳古細菌について　Direct observation of unitary steps of supermolecular motility machineries of microorganisms: gliding bacterium and swimming archaeon. 第52回日本生物物理学会年会, 札幌コンベンションセンター, September 25-27, 2014.
78. 木下佳昭, 中根大介, 政池知子, 水谷加奈, 宮田真人, 西坂崇之 (2013)."Direct observation of unitary step of gliding machinery in Micoplasma mobile." Blast XII: January 20, 2013.

79. 木下佳昭, 中根大介, 政池知子, 水谷加奈, 宮田真人, 西坂崇之 (2013). "Mycoplasma mobileの単一滑走装置の動きの直接観察　Unitary Step of Gliding Machinery in Mycoplasma mobile." 日本マイコプラズマ学会第40回学術集会: May 23, 2013.
80. 木下佳昭, 中根大介, 政池知子, 水谷加奈, 宮田真人, 西坂崇之 (2013). "マイコプラズマモービレの単一滑走装置におけるステップの直接観察." 第86回日本細菌学会総会: March 18, 2013.
81. 木下佳昭, 中根大介, 西坂崇之 (2015). アーキアのべん毛は回転する. 生体運動研究合同班・2015年班会議, 学習院大学, January 7-9, 2015.
82. 木下佳昭, 中根大介, 西坂崇之 (2015). アーキアべん毛の回転計測. 第20回べん毛研究交流会, 三重県 合歓の郷ホテル&リゾート, March 1-3, 2015.
83. 木下佳昭, 内田就也, 中根大介, 西坂崇之 (2015). 高度高塩菌ハロバクテリウムサリナラムの遊泳運動特性の解析　Characterization of the swimming motility of halophilic archaea, Halobacterium salinarum. 第53回日本生物物理学会年会, 金沢大学 角間キャンパス 自然科学本館, September 13-15, 2015.

Unitary step of gliding machinery in *Mycoplasma mobile*

Yoshiaki Kinosita[a,1], Daisuke Nakane[b,1,2], Mitsuhiro Sugawa[a], Tomoko Masaike[a,c,3], Kana Mizutani[a], Makoto Miyata[b,4], and Takayuki Nishizaka[a,4]

[a]Department of Physics, Faculty of Science, Gakushuin University, Toshima-ku, Tokyo 171-8588, Japan; [b]Department of Biology, Graduate School of Science, Osaka City University, Sumiyoshi-ku, Osaka 558-8585, Japan; and [c]Precursory Research for Embryonic Science and Technology, Japan Science and Technology Agency, Kawaguchi, Saitama 332-0012, Japan

Edited* by Howard C. Berg, Harvard University, Cambridge, MA, and approved April 28, 2014 (received for review June 22, 2013)

Among the bacteria that glide on substrate surfaces, *Mycoplasma mobile* is one of the fastest, exhibiting smooth movement with a speed of 2.0–4.5 μm·s^{-1} with a cycle of attachment to and detachment from sialylated oligosaccharides. To study the gliding mechanism at the molecular level, we applied an assay with a fluorescently labeled and membrane-permeabilized ghost model, and investigated the motility by high precision colocalization microscopy. Under conditions designed to reduce the number of motor interactions on a randomly oriented substrate, ghosts took unitary 70-nm steps in the direction of gliding. Although it remains possible that the stepping behavior is produced by multiple interactions, our data suggest that these steps are produced by a unitary gliding machine that need not move between sites arranged on a cytoskeletal lattice.

bacteria tracking | gliding ghost | leg protein | pairwise distance function | F_1-ATPase

The fastest of the *Mycoplasma* species is *Mycoplasma mobile* (*M. mobile*); they glide with a speed of 2.0–4.5 μm·s^{-1} (1, 2). Under an optimal-growth condition, cultivated single *M. mobile* cells are flask-shaped (Fig. 1*A*) and glide smoothly across a substrate covered with surface-immobilized sialylated oligosaccharides (3) in the direction of protrusion at a constant speed (Movie S1). Genomic sequencing and analysis have revealed that the mechanism must differ from other forms of motor protein systems and bacterial motility, because *M. mobile* lacks genes encoding conventional motor proteins in eukaryotes, such as myosin, kinesin, and dynein, in addition to lacking other motility structures in bacteria, such as flagella and pili (4). So far, three proteins have been identified as a part of the gliding machinery (Fig. 1*B*, *Bottom*): Gli123 (5), Gli521 (6), and Gli349 (7). The machinery units localize around the cell neck, and their number has been estimated to be ∼450 (2, 5, 8). Gli349 extends out from the cell membrane and shows a rod structure, ∼100 nm in total, with two flexible hinges when isolated (9). Notably, the machinery is driven by hydrolysis of ATP to ADP and inorganic phosphate, caused by an unknown ATPase (10). Because of the large size and characteristic structure of Gli349, and a series of studies with mutants and inhibitory antibodies (2, 11), it has been hypothesized that Gli349 works as a "leg" by binding to and releasing from a substrate covered with randomly arranged sialylated oligosaccharides (2) consuming the chemical energy of ATP. In addition, the pivoting movement of an elongated cell suggests that there are units working not simultaneously but rather independently to propel the cell forward (12). To test this hypothesis and identify conformational changes of a key part of the gliding machinery, we here designed an assay to detect the movement of *M. mobile* by high precision colocalization microscopy. In the presence of an excess number of binding targets in the solution, which decreased the number of active legs, stepwise displacement was shown for the first time, to our knowledge, to occur in gliding bacteria.

Results

Construction of an Assay for Tracking a Ghost with High Accuracy. To track *M. mobile* with nanometer-scale precision, its cell surface was stained with a fluorescent probe, Cy3, and its position was localized by an EMCCD camera with a time resolution of 2 ms. Note that the shape of the cell is mostly symmetric and its size is less than 1 μm, which is close to the wavelength of visible light (Fig. 1 *C* and *D*). These two features made it possible to track the movements of the bacteria with nanometer-scale precision by fitting the intensity profile of a fluorescent cell with a 2D Gaussian function (Fig. 1*E* and Fig. S1), a technique (13) that has been successfully applied to submicron-scale plastic probes to detect the rotation of a single F_1-ATPase, the smallest rotary molecular motor made of a single molecule (14, 15). Because motility at the cellular scale likely involves a large number of motors, isolating unitary conformational changes is essential for a complete understanding of the gliding mechanism. To dissect the movement, we used a permeabilized ghost model (10), in which the cell membrane was damaged with Triton X-100 and, thus, we could regulate the activity of ATPase by changing [ATP] (Fig. 1 *B* and *F* and Fig. S2). Finally, to reduce the number of functional gliding machinery units, sialylated oligosaccharides, which have been identified as the binding target of

Significance

The mechanism of movement of bacteria shows extensive diversity, and some bacteria glide on the substrate surface via an unknown process. *Mycoplasma mobile* is one of the fastest, exhibiting smooth gliding movement with a speed of 2.0–4.5 μm/s. By applying the modified in vitro ghost model of *Mycoplasma mobile* to high precision colocalization microscopy, steps of the regular size, ∼70 nm, were detected for the first time in bacteria, to our knowledge. The binding target of the gliding machinery, sialylated oligosaccharides, was expected to be randomly oriented on the surface and, thus, our results suggest that the machinery can drive the steps with a cycle of attachment and detachment even if there is no periodic structure on the substrate.

Author contributions: Y.K., D.N., M.M., and T.N. designed research; Y.K. and D.N. performed research; M.S. and T.M. contributed new reagents/analytic tools; Y.K. and D.N. analyzed data; Y.K., D.N., M.M., and T.N. wrote the paper; M.S. developed a framework of step fitting algorithm and applied it to data; T.M. verified the observation system; K.M. initially designed the assay to observe gliding through a fluorescently labeled *M. mobile*; and T.N. constructed the optical setup, microscope, and analysis software.

The authors declare no conflict of interest.

*This Direct Submission article had a prearranged editor.

[1]Y.K. and D.N. contributed equally to this work.

[2]Present address: Department of Physics, Gakushuin University, Toshima-ku, Tokyo 171-8588, Japan.

[3]Present address: Department of Applied Biological Science, Faculty of Science and Technology, Tokyo University of Science, 2641 Yamazaki, Noda City, Chiba 278-8510, Japan.

[4]To whom correspondence may be addressed. E-mail: takayuki.nishizaka@gakushuin.ac.jp or miyata@sci.osaka-cu.ac.jp.

This article contains supporting information online at www.pnas.org/lookup/suppl/doi:10.1073/pnas.1310355111/-/DCSupplemental.

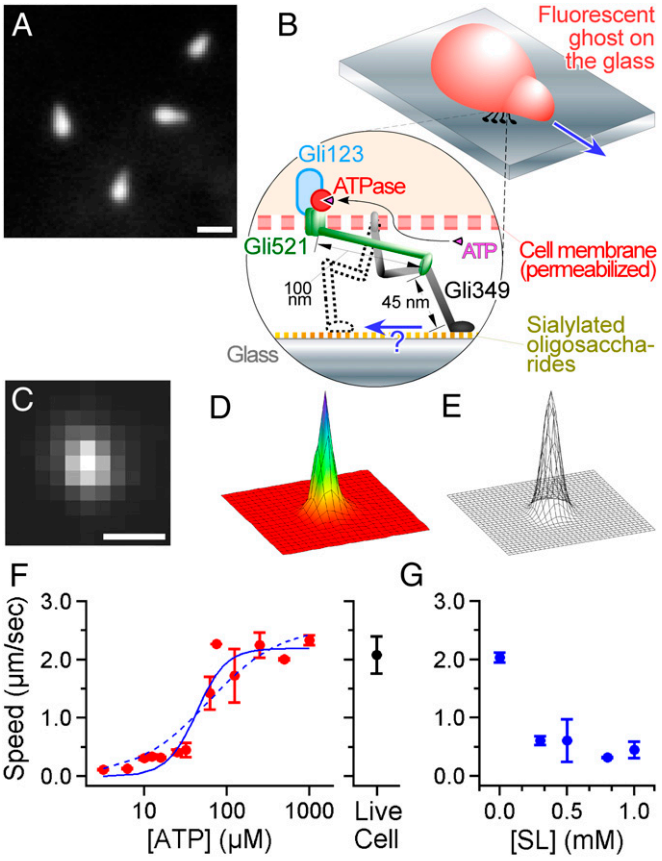

Fig. 1. Nanometer-scale tracking of *Mycoplasma* gliding. (*A*) A dark-field image of *M. mobile*. The image was captured with center-stop optics to maintain the high numerical aperture of the objective, which enabled a high spatial resolution (35). (Scale bar: 1 μm.) (*B*, *Upper*) Illustration of the fluorescent ghost. The gliding machinery was distributed around the neck portion, but only the active machinery bound to the glass is shown for simplicity. (*Bottom*) A construction model of the gliding machinery comprising three proteins: Gli123, Gli521, and Gli349. See the review by Miyata (2) for more detail. (*C*) A fluorescent image of the labeled ghost was acquired with a time resolution of 2 ms. (Scale bar: 1 μm; pixel size: 240 nm.) (*D*) The intensity profile of *C*. The *XY* area is 5 × 5 μm. (*E*) Gaussian fitting to *D*. Nanometer-scale tracking is achieved by positioning the peak of the 2D Gaussian function fitting to the intensity profile of the ghost. (*F*, *Left*) The speed of gliding ghosts at different [ATP]s in the solution (n = 129). The cyan curve shows a fit with Michaelis–Menten kinetics; V_{max}^{speed} and K_m are 2.6 μm·s^{-1} and 61 μM, respectively. The dotted cyan curve shows a fit with the kinetics including the Hill coefficient; V_{max}^{speed}, [ATP$_{50}$] and n are 2.2 μm·s^{-1}, 43 μM, and 2.4, respectively. (*Right*) The speed of living cells with no ATP in the solution (2.1 ± 0.1 μm·s^{-1}; n = 22). (*G*) Effect of SL on the gliding velocity of the ghost at saturated [ATP]s, 0.3–1.0 mM (n = 50).

Gli349 (3, 16) and serve as a scaffold for *M. mobile* gliding, were added to the solution in the form of *N*-acetylneuraminyllactose (sialyllactose, SL). Notably, the gliding speed became slower with higher concentrations of SL (Fig. 1*G*), and the ghosts finally became unbound from the glass when [SL] was higher than 1.0 mM, presumably because the number of legs acting on the sialylated oligosaccharides on the glass was decreased as free SL was added to the solution. To optimize the conditions of the motility assay, 0.1% methylcellulose was also added to the solution to suppress the detachment of ghosts. Because the gliding speed did not alter much with or without methylcellulose (Fig. S3), we judged that the viscous drag against the gliding movement caused by a 0.1% concentration of methylcellulose was negligible.

Detection of Steps. We recorded sequences of the gliding of ghosts under various [ATP]s at [SL] = 1.0 mM, and carefully observed their traces. Typically, the ghost glided with repetition of pauses and sudden displacements as shown in dense dots in Fig. 2*A*. This tendency was also confirmed at the high concentration of ATP (Fig. 2*B*), suggesting that the ghosts move not smoothly but rather intermittently under the condition where the number of acting legs was expected to be decreased. To check whether the displacements included a regular dispersion, we analyzed 937 ghosts at various ATP concentrations in the range of 6–1,330 μM. The period in which the ghost moved in a nearly straight line (e.g., the black portion in Fig. 2*A*) was further extracted. Although most runs showed creeping displacement and few intermittent pauses in the irregular manner, 196 ghosts showed more than two stepwise displacements. Among them, 134 records in 105 ghosts at [ATP] = 8–500 μM showed more than four clean steps. We also extracted 70 time courses in 60 ghosts that showed instantaneous stepping motion and could successfully be fitted with a step function by the step-finding algorithm as described in a later section.

An example of multiple steps is shown in Fig. 2*C, Left*. The unfiltered trajectory along the displacement direction showed clean steps with regular intervals, indicating that the movement driven by the gliding machinery of *M. mobile* may involve unitary steps. The existence of a step becomes apparent when the pairwise distance function (PDF) is applied to each run. As exemplified in Fig. 2*C, Right*, the intervals between pauses appeared as peaks of the PDF. The position of the peaks was precisely correlated with multiples of the size of a single step, suggesting that the gliding machinery repeats the stroke cycle for movement with high precision. The tendency was barely shown even in the absence of SL (Fig. S4); however, stepping was not instantaneous but gradual, possibly because the number of functional legs was still too large under this condition (*Discussion*). Displacements with regular steps were observed under a variety of [ATP]s (Fig. 2*D*), and particularly at a high [ATP], under which condition the dwells awaiting ATP binding were expected to be negligible from the estimation based on Fig. 1*F*. Fig. 2*E* shows a histogram of the step value determined from the PDF. The size of the step under these conditions was 72 ± 14 nm, assuming that the histogram comprises a single peak.

Characteristics of Dwell Time. As reported for other molecular motors, the dwell time allows us to better understand the mechanism of motors at the molecular level in terms of chemomechanical coupling, i.e., the relationship between a chemical reaction (nucleotide binding and subsequent hydrolysis) and mechanical event (conformational change(s) of a motor). We applied a "step-finding algorithm" that was originally developed to analyze the position of tips of microtubules growing in a regular manner (17) to quantify the frequency and position of pauses. The fitting was performed to minimize the variation based on the algorithm (for details of the analysis, see *Materials and Methods*). As shown by the rectangles in Fig. 2 *C* and *D*, moments when stepping occurred were roughly estimated from the raw trajectory in each run. Histograms of the dwell time at various [ATP]s, 8–500 μM, were thus constructed from the fitting (Fig. 3*A*).

Note that, in our assay at this point, we were not able to determine the exact number of legs interacting with the surface, although steps of the regular size were successfully detected in each run. It may be possible that dwells with several or multiple motor units are incorporated in the histograms, which makes the interpretation of results quite complicated, as considered below in *Discussion*. The average of the dwell times at various [ATP]s is summarized in Fig. 3*B*. The maximum rate was estimated to be 24 s^{-1} at [ATP] = 500 μM, at which concentration the binding rate was expected to be almost saturated (Fig. 1*F*). A small increase in the dwell time was observed at the low [ATP]s of 8 and 16 μM, compared with that at 500 μM (arrows in Fig. 3*A*;

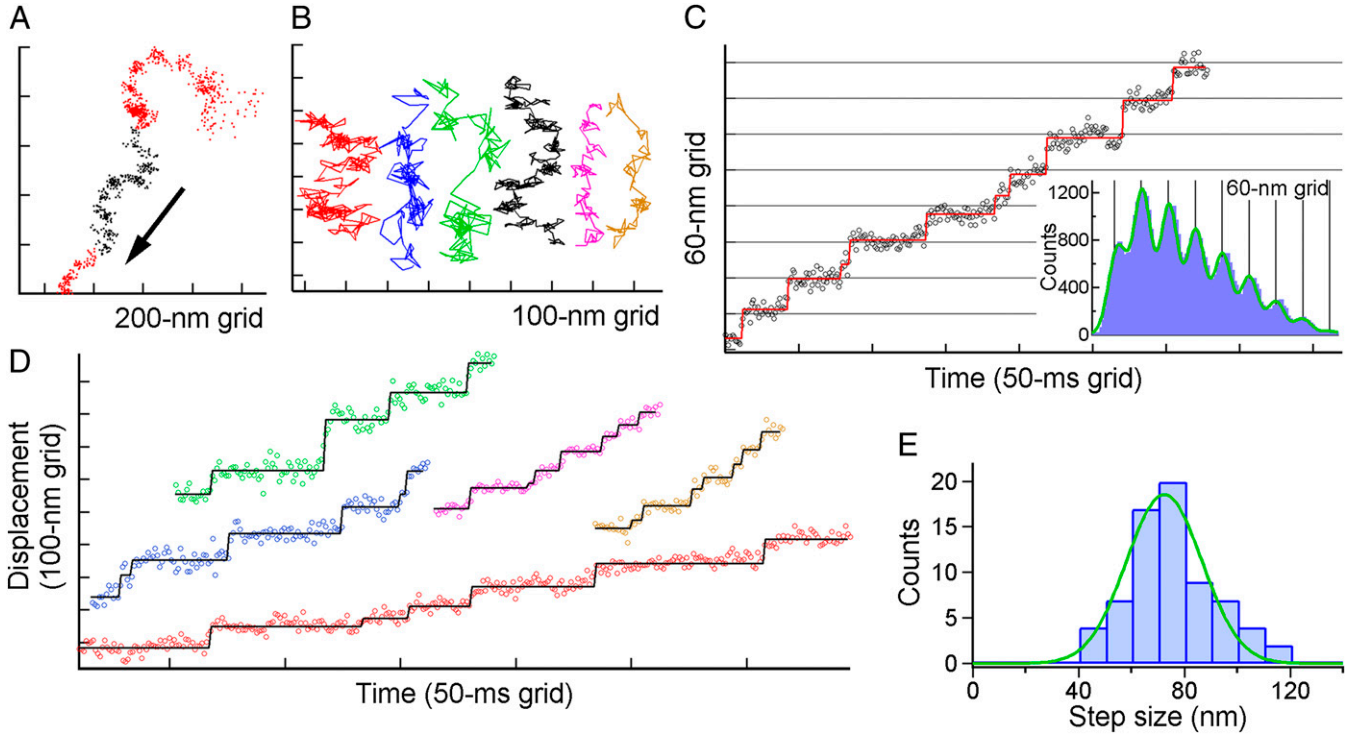

Fig. 2. Steps of single ghosts of *M. mobile* driven by ATP. (*A*) A typical example of the *XY* trace of the single gliding ghost. Black points in the trace show the range in which we judge that the ghost moved in a nearly straight line and were subsequently analyzed with the pairwise distance function in *C*. (*B*) Examples of the trace at various concentrations of ATP. Red, blue, green, black, magenta, and orange represent [ATP] = 8, 16, 55, 90, 285, and 500 μM, respectively, and their colors coincide with those of the time course of the displacement in *C* and *D*. (*C*, *Left*) A typical example of the displacement along the gliding direction. Open circles are unfiltered data points, and rectangles in the displacement time course were the lines fitted with the step-finding algorithm. (*Right*) Histograms of the pairwise distance function (PDF) of the run. The green solid line is fitted to the sum of eight Gaussians. (*D*) Other examples of the displacement time course at various [ATP]s. (*E*) Histogram showing the distribution of step sizes estimated from the PDF analysis (n =70 runs in 60 ghosts; each run contains 4–9 steps) separated by 10-nm bins for clarity. The green solid curve shows the Gaussian distribution with 72 ± 14 nm.

$P = 8.4 \times 10^{-6}$ and 1.0×10^{-4}, respectively, < 0.05 by Welch's t test). Notably, the dwell time was merely doubled in the presence of SL at [ATP] ~10 μM (Fig. 3*B*), whereas, in the absence of SL, the average gliding speed was ~10 times lower compared with that at saturated [ATP] (Fig. 1*F*). This discrepancy may suggest that legs in the holding state could increase drag and, thus, reduce the speed of the movement driven by the leg in the power-stroke state only in the case that the number of legs was huge, while they immediately detached from the surface when they were fewer in number. This interpretation coincides with the observation of stepping without SL, in which the creeping displacement between steps was observed as shown in Fig. S4*B*, *Inset*.

Steps of Intact *M. mobile*. To check whether the properties of steps in the ghost, especially their average size, were specific to the intact gliding machinery, we also analyzed the movement of *M. mobile* that was not treated with the detergent. Note that in this assay, we were not able to control the concentration of ATP inside the cell, and so we only reduced the number of legs by adding SL to the solution. As expected from the results of the ghost assay (Fig. 1*G*), the fraction of cells binding to the glass also depended on the concentration of SL in the solution (Fig. 4*A*). Gelatin was added to increase the solution viscosity, to make the fraction higher, and to maintain a sufficient number of cells on the surface for recording. The gliding speed decreased as SL was added to the solution (Fig. 4*B*), suggesting that the number of legs was successfully minimized. A single fluorescent particle was nonspecifically attached to the surface of the cell and was tracked with a nanometer-scale precision based on a technique for individual fluorescent probes (13) that has also been successfully applied to submicrometer-scale plastic probes to detect the rotation of a single F_1-ATPase (15). As the speed decreased, the gliding showed intermittent pauses and, finally, stepwise movement appeared when 4–8 mM SL was added (Fig. 4*C*), although creeping was not eliminated during stepping. PDF analysis showed clear peaks being precisely correlated with multiples of the size of a single step (e.g., Fig. 4*D*). The size of step was estimated as 69 ± 11 nm (Fig. 4*E*; n = 35 runs in 23 cells), which was similar to the case of the ghost assay ($P = 0.377 > 0.05$ by Welch's t test). We conclude that the gliding machinery moves in unitary steps even when it operates under an intact condition where it is buried in the nontreated cell membrane, and the size of the step is ~70 nm for both the ghosts and intact cells.

Discussion

In this study, we established an assay in which the gliding motion of *M. mobile* was localized with nanometer-scale precision under an optical microscope. Cells were stained with a fluorescent probe and subsequently permeabilized on the glass to prepare the ghost model. Although the ghost showed frequent pauses and the histogram of PDF barely showed peaks of multiple numbers (Fig. S4), the steps were not clear because the stepping between pauses was not instantaneous but rather gradual (Fig. S4*B*, *Inset*). We further modified the motility assay system. The addition of free SL to the solution hindered the attachment of each leg to the sialylated oligosaccharides on the glass. Inversely, a high concentration of methylcellulose in the solution suppressed the detachment of *M. mobile*. By balancing these two conditions, stepwise displacement was finally achieved for the first time in gliding bacteria. Note that the concentration of SL approached that at which the ghost fully detaches from the surface. In fact, with the addition of SL, the average speed of

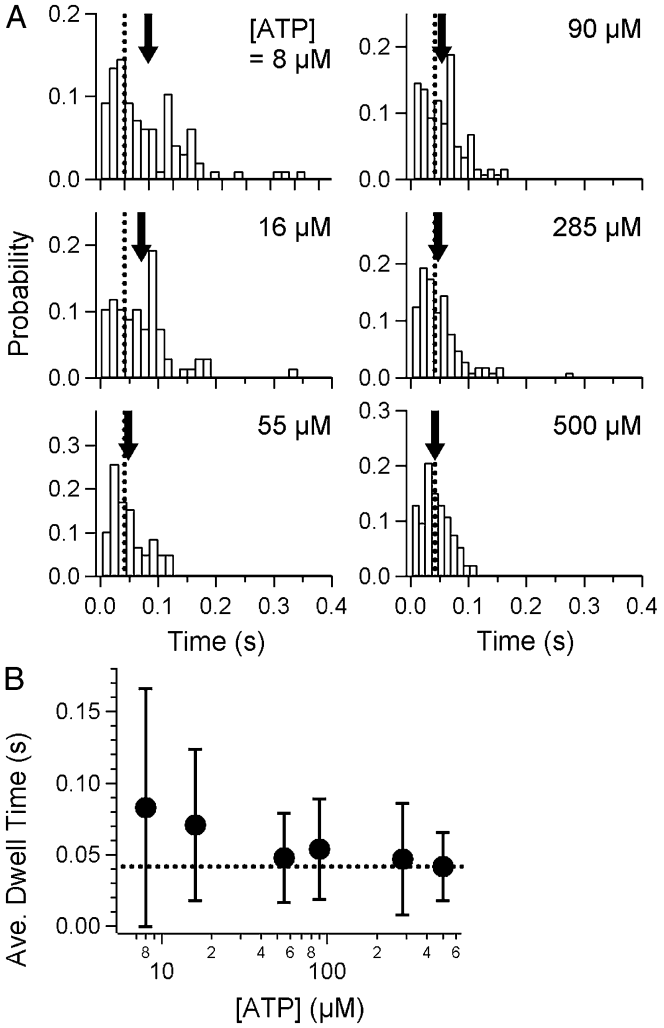

Fig. 3. Dwell-time analysis of displacements. (*A*) Histograms of dwell times under various concentrations of ATP. Arrows indicate the average in each graph, and dashed lines indicate the average at 500 μM ATP. There was a slight, barely detectable increase at 8 and 16 μM, relative to that at 500 μM ATP, as shown by the gaps between the arrows and dashed lines. (*B*) Average of the dwell times (filled circles). The dashed line is the value at 500 μM ATP.

ghosts decreased by about one-fourth (Fig. 1*G*). In the case that the duty ratio–the fraction of binding time over the single ATPase turnover–of the motor is low, it is generally considered that the average speed should decrease as the density of the motor decreases (18, 19). This model coincides with our observations.

Although the number of gliding machines involved in forward movement during the unitary step was not conclusively determined in our assay, we can infer a possible mechanism of the gliding machinery from the fact that the ghost showed clean and repetitive steps, as depicted in Fig. 2 *C* and *D*. One simple interpretation is that each 70-nm stepwise displacement corresponds to a single turnover in a single motor unit. In conventional linear motors such as myosin V, the size of a step is determined by the conformational change and additional Brownian search to land the next binding site on its track (20). However, the scenario including the track with a periodic structure is not the case for the gliding machinery of *M. mobile*, because its binding target is randomly oriented on the substrate surface. There might be unique and inherent characteristics that realize the huge but precise size of the steps. Probably, the specific conformational change in one of three (or more) machinery proteins directly determines the forward 70-nm movement of the ghost. Such conformational change itself could fluctuate largely and, thus, an additional mechanism would be needed to explain the occurrence of precise repetitive steps like those in Fig. 2. For example, it may be that the tip of the leg can bind to the target only when it makes a certain angle to the surface, as proposed for the mechanism of myosin (21, 22).

If the gliding machinery of *M. mobile* is a processive motor in the manner of kinesin-1 and myosin V, each of which has two functional domains in a single molecule and walks in a hand-over-hand manner by alternately using them (23, 24), then the dwell time between steps would be equal to the inverse of the rate of a rate-limiting chemical step of the single motor unit. In contrast, in the case that multiple active motors independently interact with the surface-immobilized sialylated oligosaccharides to move the ghost forward, the apparent dwell time would be expected to be shorter, because, in this case, one motor would stochastically induce the displacement before the rate-limiting chemical step in the other motor completed. With the above arguments in mind, we cannot evaluate the histograms in Fig. 3 without an assumption.

The increase in the dwell time was barely observed at low [ATP] (compare 8 and 16 μM), suggesting that the histograms

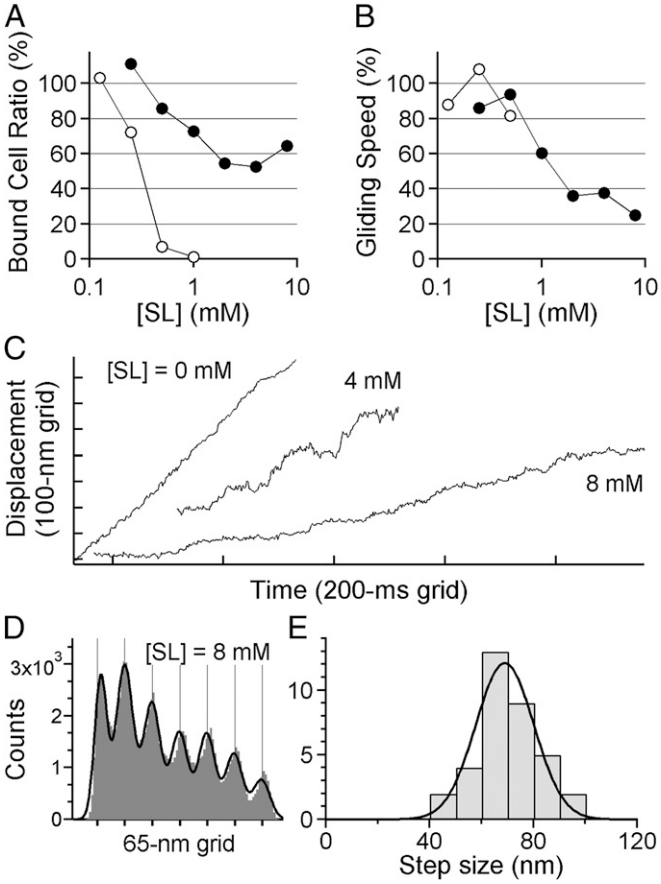

Fig. 4. Steps of intact *M. mobile* without the detergent treatment. (*A*) Binding activity of intact *M. mobile* at various [SL]s. (*B*) Gliding speed. In *A* and *B*, filled and open circles show the data with or without, respectively, gelatin in the solution ($n = 40$); 100% means the number of cells bound to the glass surface at [SL] = 0 mM. (*C*) Gliding of intact *M. mobile* at various [SL]s. The displacement appeared smooth at 0 mM, whereas it became rather stepwise at 8 mM. (*D*) An example of histograms of the PDF analysis. The black line is fitted to the sum of seven Gaussians. (*E*) Histogram showing the distribution of step sizes of intact *M. mobile* from PDF analysis separated by 10 nm bins ($n = 35$ runs in 23 cells). The black curve shows the Gaussian distribution with 69 ± 11 nm.

may include a component that depends on [ATP]. Additionally, at high [ATP], the dwell time reached 42 ms, indicating the existence of a rate-limiting step, apart from ATP binding, on the order of 20 s^{-1} at most. The estimation of the average speed, (step size) × (rate) = (~70 nm) × (~20 s^{-1}) = 1.4 μm·s^{-1}, roughly coincides with the maximum speed of *M. mobile*. Additionally, if we assume that the number of legs is single, then k_{on} of ATP and k_{cat} of ATPase are estimated to be 15 × 10^{-6} s^{-1}·M^{-1} and 15 s^{-1}, respectively (Fig. S5, red curves), by the global fitting through histograms. Two chemical steps may be included at saturated [ATP] (Fig. S5, blue curve at 500 μM).

To address whether these estimations are proper, a reconstructed in vitro motile system, in which the number of gliding machineries is known to be one, is inevitable, as in cases of conventional motors such as myosin, kinesin, and dynein. The assay has not been established yet for the gliding machinery of *M. mobile*, because at least four proteins are needed and the legs are assumed to protrude from the membrane. In the future, some additional techniques, which incorporate protein arrangements in nanodiscs or liposomes, will be needed to reconstruct the unit as a whole active motor.

Because we cannot be certain about the number of active units when clean steps were detected in our present assay, one could argue that 70 nm is not the step size driven by the single assembly of the gliding machinery, but the sum of smaller steps driven by multiple motors. One possible scenario is that the clean 70-nm displacement is comprised of cooperative and sequential displacements of smaller steps. For example, repetitive small steps without an intermission longer than the time resolution of the observation system may appear as a large step, although strong cooperativity would be needed to explain the clear peaks in the histogram of PDF (Fig. 2*C*). Alternatively, the unbinding process of legs holding the ghost may directly determine the apparent size of each step. If the leg(s) that has just finished the conformational change still attaches to the ghost, it is probable that the leg subsequently works as a load when the other leg strokes and induces pauses at the halfway point of each step. This scenario would be similar to that reported for kinesin, in which the step sizes half those of a single motor were found as the result of force balance between two motors (25). To examine the above possibilities, again, a reconstructed in vitro motile system will be needed in the near future; in addition, it should be checked whether the motor in *M. mobile* can function as a processive motor.

From the structural point of view, what possible mechanisms can explain the regular step size of ~70 nm? For the 8-nm step of kinesin and 36-nm step of myosin V, the sizes are determined by the repetitive structure of their substrate filaments, i.e., the microtubule and actin filaments, respectively. In contrast, *M. mobile* glides on a surface on which the binding target (16) is distributed randomly rather than being arranged in a regular manner. Additionally, because the leg protein, Gli349, is expected to be flexible rather than rigid (9), a simple stroke model like that of skeletal myosin (26), in which the lever part executes a stroke at a regular angle, is unlikely to explain the clear peaks of the PDF observed in Figs. 2*C* and 4*D*. Here, we propose a model in which stepwise movement is induced not by the tilting of the leg protein, but by the movement of the protein that connects the leg to ATPase. Gli521, which is assumed to work as a crank, is a rod-like structure with a size of 120 nm (27). The unidirectional movement and the large size of Gli521, in either the lateral, tilted, or rotating direction, could explain the step we observed. Because a protein similar to the catalytic subunit of F_1-ATPase is located at the cytoskeleton-like structure that may arrange Gli123, Gli521, and Gli349 (28, 29), we hypothesize a model in which Gli521 converts a rotational motion of ATPase to a directed linear motion, much like a connecting rod between the wheels of a steam train. The movement of Gli521 may be effectively transmitted to Gli349 to make Gli349 pull against sialylated oligosaccharides on the glass. The broad distribution shown in Fig. 2*E* might be attributable to the variation of the binding configuration of Gli349 to the glass. In addition, to consistently maintain the regular steps, the detachment process of a leg is also important and could be regulated in terms of load dependence and directionality. This point, which is essential for elucidating the gliding mechanism in greater detail, will be addressed by measuring the unbinding force of a single leg of a ghost as in the case of myosin (30, 31), by using an optical trapping of the bead applied to the cell surface (32).

Materials and Methods

Preparation of the Fluorescent *M. mobile*. A mutant strain of *M. mobile*, the P476R *gli521* mutant, which binds to sialylated oligosaccharides more tightly than the wild-type strain (10, 11), was used in this study. Cells were cultured in Aluotto medium [2.1% (wt/vol) heart infusion broth, 0.56% yeast extract, 10% (vol/vol) horse serum, 0.025% thallium acetate, and 0.005% ampicillin] at 25 °C (33) until the absorbance at 600 nm reached 0.06–0.10. Cells in a culture with 1 mL of volume were collected by centrifugation at 12,000 × *g* for 4 min at 25 °C, resuspended in Aluotto medium, and subsequently incubated for 30 min before labeling. Cells were incubated in buffer A (75 mM sodium phosphate at pH 7.4 and 68.4 mM NaCl) containing 50 mM glucose and Cy3-NHS ester (GE Healthcare) for 2 h at room temperature and subsequently cleaned by two rounds of centrifugation after suspending with 500 and 200 μL of buffer A containing glucose.

Assay for Tracking the Gliding of Ghosts. The flow chamber was comprised of two coverslips (No. 1, 0.12–0.17 mm thickness; Matsunami Glass) with different sizes (24 × 24 and 24 × 36 mm). Two pieces of double-sided tape, which were cut approximately 5 mm wide and 30 mm in length, were used as the spacers between coverslips (7). The resulting flow chamber had an internal volume of ~7 μl. Aluotto medium was infused to the chamber and, thus, sialylated oligosaccharides included in the serum in the medium was nonspecifically bound to the glass surface. Fluorescent cells were infused into the chamber from one side and kept for 30 min. Unbound cells were removed with 20 μL of buffer B (buffer A containing 2 mM $MgCl_2$, 1 mM DTT, and 1 mM EGTA). The solution in the chamber was replaced with 10 μL of buffer B containing 0.01% Triton X-100 (MP Biomedicals). Gliding cells were permeabilized with the surfactant and their movement was stopped and, thus, ghosts were prepared (10), typically within 1 min. The membrane permeabilization was judged by eye as the cytosol was ejected from the body and, thus, the density of the cells was reduced. At the moment when their density was reduced in the observation field, the solution was immediately replaced with 10 μL of buffer C [10 mM Tris·HCl at pH 7.5, 50 mM NaCl, 1 mM DTT, 1 mM EGTA, 2 mM $MgCl_2$, and 0.5 mg/mL bovine-serum albumin (Sigma-Aldrich)] containing 1 mg·ml^{-1} DNase (Sigma-Aldrich). The chamber was subsequently washed with 10 μL of buffer C containing 0.1% methylcellulose (M0512, 4,000 cps at 2% solution; Sigma-Aldrich). Note that the drag force on the ghost from the viscosity of the surrounding fluid was calculated to be $F_d = 2\pi\eta b/(\ln(2b/a) - 0.5) \times v_{glid}$ = 0.008–0.07 pN and, thus, negligible (34), where the viscosity η is 1–5 cps for 0.1% methylcellulose solution; the half length of the ghost *b* is 0.5 μm; half of the size of the waist of the ghost *a* is 0.3 μm; and the gliding velocity v_{glid} is 2–3 μm·s^{-1}. The value of 5 cps was estimated from an extrapolation of the product information, and was used as the maximum viscosity of 0.1% methylcellulose solution, whereas 1 cps, equivalent to water, was used as the minimum viscosity in the case that *M. mobile* was too small to apply the macroscopic viscosity. Finally, to activate ghosts and observe their gliding, the solution was replaced with 30 μL of buffer C containing a desired amount of ATP (Sigma-Aldrich), 0.2 mg·mL^{-1} creatine kinase (Roche), 0.8 mg·mL^{-1} creatine phosphate (Roche), 1 mM *N*-acetylneuraminyllactose (SL; Sigma-Aldrich), and 0.1% methylcellulose. After the fluorescent image of the moving ghosts was captured, their phase-contrast image was also recorded to check whether each cell was successfully permeabilized and converted into a ghost; the density of ghosts was clearly lower than that of the living cells.

Gliding Assay of *M. mobile* with Fluorescent Beads. After the infusion of unlabeled cells into the flow chamber, fluorescent beads of 100-nm diameter (Invitrogen) were infused. An individual bead could be nonspecifically attached to the cell membrane by chance, and the bead could be easily detected during its continuous movement on the glass surface when the flow chamber was observed under a fluorescence microscope.

Microscopy. Fluorescent *M. mobile* was visualized under an inverted fluorescence microscope (Ti-E; Nikon Instruments) equipped with a 100× objective (Fluor 100 with Ph and 1.3 N.A.; Nikon Instruments), a filter set (TxRed-

4040B; Semrock), an EMCCD camera (iXon$^+$ DU860; Andor), a highly-stable customized stage (Chukousha), and an optical table (RS-2000; Newport). Projection of the image to the camera was made at 240 nm per pixel. Phase-contrast images of ghosts were also taken with another CCD camera (CS8420i; Toshiba TELI) to determine whether the cells were permeabilized by a surfactant. To acquire the image in Fig. 1*A*, a custom-made dark-field microscope (35) was used with a 100× objective (Plan Apo TIRF 1.4 N.A.; Olympus) and a CCD camera (CCD-300-RCX; Dage-MTI) under an inverted microscope (IX71; Olympus). In the gliding assay of *M. mobile* with a fluorescent bead, images were recorded by using a high-speed CCD camera system (HDR1600; Digimo).

Data Analyses. Sequential images of the gliding of fluorescent ghosts were captured as 14-bit images with an EMCCD camera under 2-ms resolution and converted into a sequential TIF file without any compression. The position of single ghosts, (x_c, y_c), was determined by fitting each image with a 2D Gaussian including the cross-correlation term, *cor*, as $I_0 + A\exp[-((x-x_c)^2/2\sigma_x^2 + (y-y_c)^2/2\sigma_y^2 - 2cor(x-x_c)(y-y_c)/\sigma_x\sigma_y)/2(1-cor^2)]$, where I_0 is the background intensity; A is a peak of the intensity of the ghost; and σ_x and σ_y are intensity variances along the x and y axis, respectively. For tracking of *M. mobile*, the parameters σ_x, σ_y, and *cor* were required to achieve a proper fitting, because single ghosts often appeared not as spherical but as ellipsoidal shapes. A was typically 800–2,000 under our capture conditions. In Fig. 1*F*, $V = V_{max}^{speed}[ATP]/(K_m + [ATP])$ and $V = V_{max}^{speed}[ATP]^n/([ATP_{50}]^n + [ATP]^n)$ were used as formulae for Michaelis–Menten kinetics and the kinetics including the Hill coefficient, respectively. To estimate the size of the unitary step, a PDF was independently adopted for each run showing stepwise displacement. A histogram with 5-nm bin width is shown in Fig. 2*B* and was fitted with the sum of the Gaussians with periodic intervals, Δ, as $\sum_i A_i \exp[-(x-i\Delta)^2/(2\sigma_i^2)] + A_0\exp[-(x-x_0)^2/(2\sigma_0^2)]$. Note that, in the case that stepwise displacements are always clean and pauses are stable, x_0 should be 0 as indicated in the processive motor dynein (36). In contrast, creeping motions were observed to some extent in our measurement and, thus, we set the parameter x_0 in the fitting. Back steps, $i = -1$ or less, were not included in the fitting, because they were not observed in our measurement.

Step-Finding Algorithm. The step-finding algorithm was initially developed for quantitative detection of the growth and shrinkage of microtubule ends (17). The algorithm consists of three processes: (*i*) finding steps, (*ii*) evaluating the quality of the step fits, and (*iii*) finding the step distribution. (*i*) This process is the same as in the original method (17). Briefly, by fitting a single large step to the data based on a calculation of the χ^2 statistics, the first step is determined. Next, the subsequent steps are found by fitting new steps to the dwells of the previous fitting, in the same way as for the first step. (*ii*) The second process was modified as follows: The quality of the fitting was based on evaluation of the variance of the displacement in each dwell, which was defined as $Q = 1/\sum_i^{N+1}(\sigma_i^2 - \langle\sigma^2\rangle)^2$. N is the number of steps. σ_i^2 is a variance of the displacement in the i-th dwell. $\langle\sigma^2\rangle$ is a mean of the variances in each dwell. In addition, Q weighed by $w = 1/\langle\sigma^2\rangle$ ($\hat{Q} = wQ$) was used for the third process. In the case of under-fitting, the large values of $(\sigma_i^2 - \langle\sigma^2\rangle)^2$ and the weight (w) contribute to the low value of $\hat{Q}$. In the case of overfitting, the values of $(\sigma_i^2 - \langle\sigma^2\rangle)^2$ are small but N is large, so that the summation of $(\sigma_i^2 - \langle\sigma^2\rangle)^2$ allows the value of $\hat{Q}$ to be low. (*iii*) The highest $\hat{Q}$ value basically represents the best fitting. In practical terms, a value of $\hat{Q}$ that was not the highest value (usually the second highest value) toward the overfitting, was often adopted as the best fitting, especially when some data had nonuniformity of fluctuation of the displacement.

ACKNOWLEDGMENTS. We thank A. Upadhyaya for critical comments, M. P. Sheetz for comments on an earlier draft, and M. Kaya and A. Tatsuguchi for their technical advice and critical discussion. This study was supported in part by the Funding Program for Next Generation World-Leading Researchers Grant LR033 (to T.N.) from the Japan Society for the Promotion of Science, by Grant-in-Aid for Scientific Research on Innovative Areas "Harmonized Supramolecular Motility Machinery and Its Diversity (M.M. and T.N.) and "Fluctuation & Structure" (Grant 26103527 to T.N.), by Grant-in-Aid for Young Scientists (Grant 25893230 to D.N.) from the Ministry of Education, Culture, Sports, Science, and Technology of Japan, by the Asahi Glass Foundation (D.N.), by the Institute for Fermentation (D.N.), and by the Naito Foundation Natural Science Scholarship (D.N.).

1. Rosengarten R, Kirchhoff H (1987) Gliding motility of *Mycoplasma* sp. nov. strain 163K. *J Bacteriol* 169(5):1891–1898.
2. Miyata M (2010) Unique centipede mechanism of *Mycoplasma* gliding. *Annu Rev Microbiol* 64:519–537.
3. Nagai R, Miyata M (2006) Gliding motility of *Mycoplasma mobile* can occur by repeated binding to *N*-acetylneuraminyllactose (sialyllactose) fixed on solid surfaces. *J Bacteriol* 188(18):6469–6475.
4. Jaffe JD, et al. (2004) The complete genome and proteome of *Mycoplasma mobile*. *Genome Res* 14(8):1447–1461.
5. Uenoyama A, Miyata M (2005) Identification of a 123-kilodalton protein (Gli123) involved in machinery for gliding motility of *Mycoplasma mobile*. *J Bacteriol* 187(16):5578–5584.
6. Seto S, Uenoyama A, Miyata M (2005) Identification of a 521-kilodalton protein (Gli521) involved in force generation or force transmission for *Mycoplasma mobile* gliding. *J Bacteriol* 187(10):3502–3510.
7. Uenoyama A, Kusumoto A, Miyata M (2004) Identification of a 349-kilodalton protein (Gli349) responsible for cytadherence and glass binding during gliding of *Mycoplasma mobile*. *J Bacteriol* 186(5):1537–1545.
8. Miyata M (2007) *Cell Motility "Molecular Mechanism of Mycoplasma Gliding -A Novel Cell Motility System"* (Springer, New York), pp 6, 137–175.
9. Adan-Kubo J, Uenoyama A, Arata T, Miyata M (2006) Morphology of isolated Gli349, a leg protein responsible for *Mycoplasma mobile* gliding via glass binding, revealed by rotary shadowing electron microscopy. *J Bacteriol* 188(8):2821–2828.
10. Uenoyama A, Miyata M (2005) Gliding ghosts of *Mycoplasma mobile*. *Proc Natl Acad Sci USA* 102(36):12754–12758.
11. Uenoyama A, Seto S, Nakane D, Miyata M (2009) Regions on Gli349 and Gli521 protein molecules directly involved in movements of *Mycoplasma mobile* gliding machinery, suggested by use of inhibitory antibodies and mutants. *J Bacteriol* 191(6):1982–1985.
12. Nakane D, Miyata M (2012) *Mycoplasma mobile* cells elongated by detergent and their pivoting movements in gliding. *J Bacteriol* 194(1):122–130.
13. Thompson RE, Larson DR, Webb WW (2002) Precise nanometer localization analysis for individual fluorescent probes. *Biophys J* 82(5):2775–2783.
14. Nishizaka T, et al. (2004) Chemomechanical coupling in F_1-ATPase revealed by simultaneous observation of nucleotide kinetics and rotation. *Nat Struct Mol Biol* 11(2):142–148.
15. Sugawa M, Okada KA, Masaike T, Nishizaka T (2011) A change in the radius of rotation of F_1-ATPase indicates a tilting motion of the central shaft. *Biophys J* 101(9):2201–2206.
16. Kasai T, et al. (2013) Role of binding in *Mycoplasma mobile* and *Mycoplasma pneumoniae* gliding analyzed through inhibition by synthesized sialylated compounds. *J Bacteriol* 195(3):429–435.
17. Kerssemakers JW, et al. (2006) Assembly dynamics of microtubules at molecular resolution. *Nature* 442(7103):709–712.
18. Sakakibara H, Kojima H, Sakai Y, Katayama E, Oiwa K (1999) Inner-arm dynein c of Chlamydomonas flagella is a single-headed processive motor. *Nature* 400(6744):586–590.
19. Uyeda TQP, Warrick HM, Kron SJ, Spudich JA (1991) Quantized velocities at low myosin densities in an in vitro motility assay. *Nature* 352(6333):307–311.
20. Shiroguchi K, Kinosita K, Jr. (2007) Myosin V walks by lever action and Brownian motion. *Science* 316(5828):1208–1212.
21. Ali MY, et al. (2004) Unconstrained steps of myosin VI appear longest among known molecular motors. *Biophys J* 86(6):3804–3810.
22. Shiroguchi K, et al. (2011) Direct observation of the myosin Va recovery stroke that contributes to unidirectional stepping along actin. *PLoS Biol* 9(4):e1001031.
23. Yildiz A, Tomishige M, Vale RD, Selvin PR (2004) Kinesin walks hand-over-hand. *Science* 303(5658):676–678.
24. Yildiz A, et al. (2003) Myosin V walks hand-over-hand: Single fluorophore imaging with 1.5-nm localization. *Science* 300(5628):2061–2065.
25. Leduc C, Ruhnow F, Howard J, Diez S (2007) Detection of fractional steps in cargo movement by the collective operation of kinesin-1 motors. *Proc Natl Acad Sci USA* 104(26):10847–10852.
26. Ruff C, Furch M, Brenner B, Manstein DJ, Meyhöfer E (2001) Single-molecule tracking of myosins with genetically engineered amplifier domains. *Nat Struct Biol* 8(3):226–229.
27. Nonaka T, Adan-Kubo J, Miyata M (2010) Triskelion structure of the Gli521 protein, involved in the gliding mechanism of *Mycoplasma mobile*. *J Bacteriol* 192(3):636–642.
28. Nakane D, Miyata M (2007) Cytoskeletal "jellyfish" structure of *Mycoplasma mobile*. *Proc Natl Acad Sci USA* 104(49):19518–19523.
29. Tulum I, Yabe M, Uenoyama A, Miyata M (2014) Localization of P42 and an F_1-ATPase α-subunit homolog of the gliding machinery in *Mycoplasma mobile* revealed by newly developed gene manipulation and fluorescent protein tagging. *J Bacteriol* 196(10):1815–1824.
30. Nishizaka T, Miyata H, Yoshikawa H, Ishiwata S, Kinosita K, Jr. (1995) Unbinding force of a single motor molecule of muscle measured using optical tweezers. *Nature* 377(6546): 251–254.
31. Nishizaka T, Seo R, Tadakuma H, Kinosita K, Jr., Ishiwata S (2000) Characterization of single actomyosin rigor bonds: Load dependence of lifetime and mechanical properties. *Biophys J* 79(2):962–974.
32. Nishizaka T, Shi Q, Sheetz MP (2000) Position-dependent linkages of fibronectin-integrin-cytoskeleton. *Proc Natl Acad Sci USA* 97(2):692–697.
33. Miyata M, et al. (2000) Gliding mutants of *Mycoplasma mobile*: Relationships between motility and cell morphology, cell adhesion and microcolony formation. *Microbiology* 146(Pt 6):1311–1320.
34. Miyata M, Ryu WS, Berg HC (2002) Force and velocity of *Mycoplasma mobile* gliding. *J Bacteriol* 184(7):1827–1831.
35. Masaike T, Koyama-Horibe F, Oiwa K, Yoshida M, Nishizaka T (2008) Cooperative three-step motions in catalytic subunits of F_1-ATPase correlate with 80° and 40° substep rotations. *Nat Struct Mol Biol* 15(12):1326–1333.
36. Mallik R, Carter BC, Lex SA, King SJ, Gross SP (2004) Cytoplasmic dynein functions as a gear in response to load. *Nature* 427(6975):649–652.

JB Journals.ASM.org

Bacteriocin Protein $BacL_1$ of *Enterococcus faecalis* Targets Cell Division Loci and Specifically Recognizes L-Ala_2-Cross-Bridged Peptidoglycan

Jun Kurushima,[a] Daisuke Nakane,[b] Takayuki Nishizaka,[b] Haruyoshi Tomita[a,c]

Department of Bacteriology, Gunma University Graduate School of Medicine, Maebashi, Gunma, Japan[a]; Department of Physics, Faculty of Science, Gakushuin University, Tokyo, Japan[b]; Laboratory of Bacterial Drug Resistance, Gunma University Graduate School of Medicine, Maebashi, Gunma, Japan[c]

Bacteriocin 41 (Bac41) is produced from clinical isolates of *Enterococcus faecalis* and consists of two extracellular proteins, $BacL_1$ and BacA. We previously reported that $BacL_1$ protein (595 amino acids, 64.5 kDa) is a bacteriolytic peptidoglycan D-isoglutamyl-L-lysine endopeptidase that induces cell lysis of *E. faecalis* when an accessory factor, BacA, is copresent. However, the target of $BacL_1$ remains unknown. In this study, we investigated the targeting specificity of $BacL_1$. Fluorescence microscopy analysis using fluorescent dye-conjugated recombinant protein demonstrated that $BacL_1$ specifically localized at the cell division-associated site, including the equatorial ring, division septum, and nascent cell wall, on the cell surface of target *E. faecalis* cells. This specific targeting was dependent on the triple repeat of the SH3 domain located in the region from amino acid 329 to 590 of $BacL_1$. Repression of cell growth due to the stationary state of the growth phase or to treatment with bacteriostatic antibiotics rescued bacteria from the bacteriolytic activity of $BacL_1$ and BacA. The static growth state also abolished the binding and targeting of $BacL_1$ to the cell division-associated site. Furthermore, the targeting of $BacL_1$ was detectable among Gram-positive bacteria with an L-Ala-L-Ala-cross-bridging peptidoglycan, including *E. faecalis*, *Streptococcus pyogenes*, or *Streptococcus pneumoniae*, but not among bacteria with alternate peptidoglycan structures, such as *Enterococcus faecium*, *Enterococcus hirae*, *Staphylococcus aureus*, or *Listeria monocytogenes*. These data suggest that $BacL_1$ specifically targets the L-Ala-L-Ala-cross-bridged peptidoglycan and potentially lyses the *E. faecalis* cells during cell division.

Enterococcus faecalis is a commensal Gram-positive bacterium in the intestinal tract of healthy humans or animals and is also known to be an opportunistic pathogen causing various infectious diseases, including urinary infectious disease, bacteremia, infective endocarditis, and others (1–3). The infection-derived *E. faecalis* strains often produce various plasmid-encoded bacteriocins (4, 5).

Bacteriocins are bacterial peptides or proteins with antimicrobial activities (6). Heat- and acid-stable bacteriocin peptides produced by Gram-positive bacteria are divided into class I and class II according to posttranslational modifications (7, 8). Class I bacteriocins are lantibiotics that contain nonproteinogenic amino acids generated by posttranslational modification (9). Only two class I bacteriocins have been identified in enterococci: β-hemolysin/bacteriocin (cytolysin) and enterocin W (10–14). In contrast, most enterococcal bacteriocins belong to class II and are nonmodified antimicrobial peptides, such as AS-48, enterocin A, and others (7, 15, 16). We have found the enterococcal class II bacteriocins, including Bac21, Bac31, Bac32, Bac43, and Bac51, in clinical strains of *E. faecalis* or *Enterococcus faecium* (17–21). Unlike the low-molecular-weight peptide-type class I and II bacteriocins, heat-labile antimicrobial proteins are referred to as bacteriolysins, previously named class III bacteriocins, and show enzymatic bactericidal activity (22, 23). In enterococci, the bacteriolysins enterolysin A and bacteriocin 41 (Bac41) have been identified (24–26).

Bac41 was originally found expressed from the pheromone-responsive plasmid pYI14 carried by the clinical strain *E. faecalis* YI14 (26, 27). The Bac41-type bacteriocins were also found in the *E. faecalis* VanB-type vancomycin-resistant *E. faecalis* (VRE) outbreak strains (27). Bac41 is specifically active only against *E. faecalis* (26, 28). The determinant region of Bac41 contains six open reading frames (ORFs), including $bacL_1$, $bacL_2$, *bacA*, and *bacI* (Fig. 1A). The bactericidal activity of Bac41 is actually expressed by the two extracellular components, the $bacL_1$- and *bacA*-encoded proteins $BacL_1$ and BacA (26). $BacL_1$ and BacA are secreted proteins that coordinately exert bactericidal activity against *E. faecalis* (26, 28). $BacL_2$ positively regulates the transcripts of $bacL_1$ and $bacL_2$ itself (unpublished data). BacI is the specific immunity factor protecting a Bac41 producer from Bac41 activity (26).

We previously demonstrated that $BacL_1$ is a peptidoglycan D-isoglutamyl-L-lysine endopeptidase (28). $BacL_1$ has 595 amino acids with a molecular mass of 64.5 kDa and consists of two distinct peptidoglycan hydrolase homology domains and three repeats of the SH3 domain (Fig. 1B). The two peptidoglycan hydrolase domains located in the regions from amino acid 3 to 140 and amino acid 163 to 315 show homology to the bacteriophage-type pepti-

Received 11 August 2014 **Accepted** 27 October 2014

Accepted manuscript posted online 3 November 2014

Citation Kurushima J, Nakane D, Nishizaka T, Tomita H. 2015. Bacteriocin protein $BacL_1$ of *Enterococcus faecalis* targets cell division loci and specifically recognizes L-Ala_2-cross-bridged peptidoglycan. J Bacteriol 197:286–295. doi:10.1128/JB.02203-14.

Editor: P. J. Christie

Address correspondence to Haruyoshi Tomita, tomitaha@gunma-u.ac.jp.

Supplemental material for this article may be found at http://dx.doi.org/10.1128/JB.02203-14.

doi:10.1128/JB.02203-14

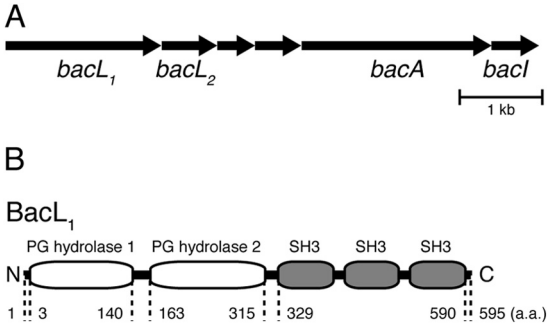

FIG 1 Schematics of Bac41 gene organization and $BacL_1$ structure. (A) Organization of Bac41-related genes (GI 169635857). (B) Molecular structure of $BacL_1$ (GI 169635864). Two domains with homology to distinct peptidoglycan hydrolases, bacteriophage-type hydrolase and NlpC/P60 family hydrolase, are present in the regions from amino acid (a.a.) 3 to 140 and amino acid 163 to 315, respectively. Three repeats of the bacterial SH3 domain are present in the region from amino acid 329 to 590.

doglycan hydrolase and the NlpC/P60 family peptidoglycan hydrolase, respectively (26, 29, 30). The second peptidoglycan hydrolase homologue, with similarity to NlpC/P60, has D-isoglutamyl-L-lysine endopeptidase activity against the purified peptidoglycan component from *E. faecalis* (28). On the other hand, the molecular function of the first peptidoglycan hydrolase domain, with similarity to bacteriophage-type peptidoglycan hydrolase, remains to be elucidated but is still required for the bactericidal activity against viable *E. faecalis* cells (28). The SH3 repeat domain is located in the region from amino acid 329 to 590 and functions as the binding domain to the peptidoglycan (28). However, $BacL_1$ is not sufficient for bactericidal activity. BacA appears to be essential for bactericidal activity, together with $BacL_1$, although its function also remains to be determined (26, 28).

On the basis of cell morphology, enterococci are grouped in the ovococci, whose cell shapes are elongated ellipsoids (31–33). In ovococci, the model of the dividing cell wall assembly process is distinct from that of other shaped bacteria, such as spherical cocci. The cell division of ovococci is achieved by two distinct cell wall-synthesizing machineries that manage peripheral and septal cell wall growth. The peripheral cell wall growth is responsible for the longitudinal cell elongation. On the other hand, the septal cell wall growth occurs to allow splitting into separated daughter cells. In this study, by using fluorescent dye-conjugated recombinant proteins, we demonstrated that $BacL_1$ localized to the cell division-related cell surface of target *E. faecalis* cells and that cell division was required for susceptibility to the bactericidal activity expressed by $BacL_1$ and BacA.

MATERIALS AND METHODS

Bacterial strains, plasmids, oligonucleotides, media, and antimicrobial reagents. The bacterial strains and plasmids used in this study are shown in Table 1. A standard plasmid DNA methodology was used (34). Enterococcal strains were routinely grown in Todd-Hewitt broth (THB; Difco, Detroit, MI) at 37°C (35), unless otherwise noted. *Escherichia coli* strains were grown in Luria-Bertani medium (LB; Difco) at 37°C. Gram-positive bacterial species (other than *Enterococcus*) were grown in brain heart infusion (BHI) medium (Difco) at 37°C. The antibiotic concentrations for the selection of *E. coli* were 100 mg liter^{-1} ampicillin and 30 mg liter^{-1} chloramphenicol. The concentration of chloramphenicol for the routine selection of *E. faecalis* carrying plasmid pAM401 or its derivatives was 20 mg liter^{-1}, unless otherwise noted. All antibiotics were obtained from Sigma Co. (St. Louis, MO).

Recombinant proteins and antibodies. The histidine-tagged recombinant proteins of full-length $BacL_1$, its truncated derivatives, and BacA

TABLE 1 Bacterial strains and plasmids used in this study

Strain or plasmid	Description	Source or reference
Strains		
E. faecalis OG1S	*str*, derivative of OG1	35
E. faecalis OG1X	*str*, protease-negative derivative of OG1	35
E. faecalis OG1RF	*rif fus*, derivative of OG1	35
E. faecalis FA2-2	*rif fus*, derivative of JH2	60
E. faecium BM4105RF	*rif fus*, derivative of BM4105	61
E. hirae 9790	Type strain	ATCC 9790
S. aureus F-182	Clinical isolate, resistant to methicillin and oxacillin	ATCC 43300
S. pyogenes MGAS315	Clinical isolate, serotype M3	ATCC BAA-595
S. pneumoniae 262	Quality control strain, serotype 19F	ATCC 49619
L. monocytogenes EGD	Serovar 1/2a	ATCC BAA-679
E. coli DH5α	*endA1 recA1 gyrA96 thi-1 hsdR17 supE44 relA1* Δ(*argE-lacZYA*)*U169*, host for DNA cloning	Bethesda Research Laboratories
E. coli BL21	*ompT hsdSB*(r_B^- m_B^-) *gal*(λcI 857 *ind1 Sam7 nin5 lacUV5-T7gene1*) *dcm*(DE3), host for protein expression	Novagen
Plasmids		
pAM401	*E. coli-E. faecalis* shuttle plasmid; *cat tet*	62
pHT1100	pAM401 derivative containing wild-type Bac41 genes	26
pET22b(+)	Expression plasmid for His-tagged protein in *E. coli*	Novagen
pET::*bacL*$_1$	pET22b(+) derivative expressing $BacL_1$	28
pET::*bacL*$_1$ Δ1	pET22b(+) derivative expressing $BacL_1$Δ1	28
pET::*bacL*$_1$ Δ2	pET22b(+) derivative expressing $BacL_1$Δ2	28
pET::*bacL*$_1$ Δ1Δ2	pET22b(+) derivative expressing $BacL_1$Δ1Δ2	28
pET::*bacL*$_1$ Δ3	pET22b(+) derivative expressing $BacL_1$Δ3	28
pET::*bacA*	pET22b(+) derivative expressing BacA	28

were prepared by the Ni-nitrilotriacetic acid (NTA) system as previously described (28). The green or red fluorescent dye-labeled recombinant proteins were prepared with NH_2-reactive fluorescein or NH_2-reactive HiLyte Fluor 555 (Dojindo, Kumamoto, Japan), respectively. By performing a soft-agar bacteriocin assay, we confirmed that fluorescent dye-conjugated $BacL_1$ remains active (see Fig. S1 in the supplemental material). Anti-$BacL_1$ antibody was prepared by immunization of rabbits with recombinant $BacL_1$-His protein as previously described (Operon Technologies, Alameda, CA) (28).

Fluorescence microscopy. Bacteria diluted with fresh medium were mixed with fluorescent recombinant protein as indicated and incubated at 37°C for 1 h. The bacteria were collected by centrifugation at 5,800 × *g* for 3 min and then fixed with 4% paraformaldehyde at room temperature (RT) for 15 min. The bacteria were rinsed and resuspended with distilled water and mounted with Prolong gold antifade reagent with 4′,6-diamidino-2-phenylindole (DAPI; Invitrogen, Carlsbad, CA) on a glass slide. The sample was analyzed by fluorescence microscopy (Axiovert 200; Carl Zeiss, Oberkochen, Germany), and images were obtained with a DP71 camera (Olympus, Tokyo, Japan).

Immunogold TEM. Bacteria in early exponential phase were treated with recombinant $BacL_1$ and BacA as indicated and incubated at 37°C for 1 h. The bacteria were fixed with 3% paraformaldehyde–0.1% glutaraldehyde for 10 min at RT and mounted on an electron microscopy (EM) grid. After fixation, the sample grid was treated with 10-fold-diluted anti-$BacL_1$ antibodies in phosphate-buffered saline (PBS) containing 2% bovine serum albumin (BSA) at 37°C for 1 h, followed by a wash with PBS. Then, the grid was treated with 10-fold diluted colloidal gold (15 nm)-conjugated anti-rabbit IgG in PBS containing 2% BSA for 30 min at RT, washed with PBS, and then negatively stained with 2% ammonium molybdate for 1 min at RT. The resulting samples were analyzed by transmission electron microscopy (TEM) (JEM-1010; JEOL Ltd., Tokyo, Japan).

Bacteriolytic assay. The soft-agar assay or liquid-phase assay for bacteriocin activity was performed as described previously (36). Briefly, the test bacterial strain or 1 μl of the recombinant protein solution was inoculated onto THB soft agar (0.75%) containing the indicator strain and was then incubated at 37°C for 24 h. The formation of an inhibitory zone was evaluated as susceptibility to the bacteriocin. For the agar-based bacteriolytic assays using *Streptococcus pyogenes* and *Streptococcus pneumoniae*, the indicator bacteria were spread on agar plates by swab instead of using the soft agar. In this swab method, *E. faecalis* OG1S and *E. faecium* BM4105 RF were used for the positive control and the negative control, respectively. For the liquid-phase bactericidal assay, an overnight culture of the indicator strain was diluted with fresh medium, and then the recombinant proteins were added and the sample was incubated at 37°C. Changes in turbidity were monitored by using a spectrometer (DU730; Beckman Coulter, Fullerton, CA) or microplate reader (Thermo Scientific, Waltham, MA).

Cell wall degradation assay. For the cell wall degradation assay, a cell wall fraction was prepared as described previously, with slight modifications (28, 37). The bacterial culture was collected by centrifugation and rinsed with 1 M NaCl. The bacterial pellet was suspended in 4% SDS and heated at 95°C for 30 min. After rinsing with distilled water four times, the bacterial pellet was resuspended with distilled water and mechanically disrupted with 0.1-mm glass beads (As One, Osaka, Japan) using a FastPrep FP100A (Thermo Scientific, Waltham, MA). After unbroken cells were removed by centrifugation at 1,000 rpm for 1 min, the cell wall fraction in the supernatant was collected by centrifugation at 15,000 rpm for 10 min and was then treated with 0.5 mg ml^{-1} trypsin (0.1 M Tris-HCl [pH 6.8], 20 mM $CaCl_2$) at 37°C for 16 h. The sample was further washed with distilled water four times and was resuspended in 10% trichloroacetic acid (TCA), followed by incubation at 4°C for 5 h, and then given additional washes with distilled water four times (38). Finally, the cell wall fraction was resuspended in PBS and quantified by measuring the turbidity for the cell wall degradation assay. Mutanolysin (Sigma) was used as a positive control for the cell wall degradation enzyme.

RESULTS

$BacL_1$ targets the cell division-associated region on the *E. faecalis* surface via its cell wall binding domain. To investigate the localization of $BacL_1$ on target *E. faecalis* cells, we coincubated *E. faecalis* cells and the recombinant $BacL_1$ labeled with red fluorescent dye in the absence or presence of BacA, followed by analysis using fluorescence microscopy (Fig. 2A and B). A specific localization signal of $BacL_1$ in the midcell was observed independently of BacA (Fig. 2A). Furthermore, the four characteristic localization patterns closely correlated with cell growth division were detected (31, 33, 39). First, the most typical localization signal of $BacL_1$ was detected in the midcell, which corresponds to the equatorial ring (Fig. 2B). The equatorial ring structure of the $BacL_1$ localization in the midcell was clearly recognized by the reconstructed image of fluorescence microscopy analysis (see Movie S1 in the supplemental material). Second, the duplicated equatorial ring structure was detected as the source of the localization signal of $BacL_1$ in the cells initiating elongation prior to cell division. Third, in the cells where the cell division process had progressed further, to formation of the division septum, the localization signal of $BacL_1$ was distributed in the area from the equatorial ring to the division septum, where the cell wall is newly synthesized (nascent cell wall) (32). Furthermore, when cell division was completed, localization at the division septum between separated daughter cells, as well as at the equatorial ring, was detected. In addition, immunogold TEM analysis using anti-$BacL_1$ antibodies in *E. faecalis* cultures treated with $BacL_1$ and BacA also showed the equatorial ring localization of $BacL_1$ (Fig. 2C).

We previously reported that $BacL_1$ binds to peptidoglycan of *E. faecalis* via a C-terminal SH3 triple repeat domain localized in the region from amino acid 329 to 590 (28). To investigate the domain required for the specific targeting, domain deletion derivatives of $BacL_1$ were labeled with green fluorescent dye (Fig. 3A) and mixed with *E. faecalis* cells, followed by analysis of their location signal by fluorescence microscopy (Fig. 3B). $BacL_1\Delta3$, the derivative with deletion of the C-terminal SH3 repeat, failed to localize to the equatorial ring and did not show any detectable signal. In contrast, $BacL_1\Delta1$, $BacL_1\Delta2$, and $BacL_1\Delta1\Delta2$, derivatives with deletion of the phage-type peptidoglycan hydrolase homology domain, NlpC/P60 family peptidoglycan hydrolase homology domain, or both domains, respectively, were targeted to the equatorial ring similarly to wild-type $BacL_1$. These results indicate that the SH3 repeat was sufficient for the targeting to the equatorial ring on the cell surface of *E. faecalis*. Collectively, $BacL_1$ appeared to target the cell division-related cell surface, including the equatorial ring, the division septum, and the nascent cell wall, via its C-terminal SH3 repeat domains.

Cell division is required for the septum targeting of $BacL_1$ and for the cell lysis triggered by $BacL_1$ and BacA. To analyze the involvement of cell division in Bac41 activity, we investigated the relationship of growth phase and susceptibility to Bac41-induced lysis. *E. faecalis* was grown in fresh THB broth, and a mixture of recombinant $BacL_1$ and BacA was added at different points in the growth phases (Fig. 4A). Adding $BacL_1$ and BacA at the start of incubation (time zero) completely inhibited the increase of the bacterial suspension's turbidity (cell growth). When $BacL_1$ and BacA were added at early or mid-exponential phase, bacterial turbidity was also dramatically decreased, indicating that cells were lysed. In contrast, treatment with $BacL_1$ and BacA at the stationary

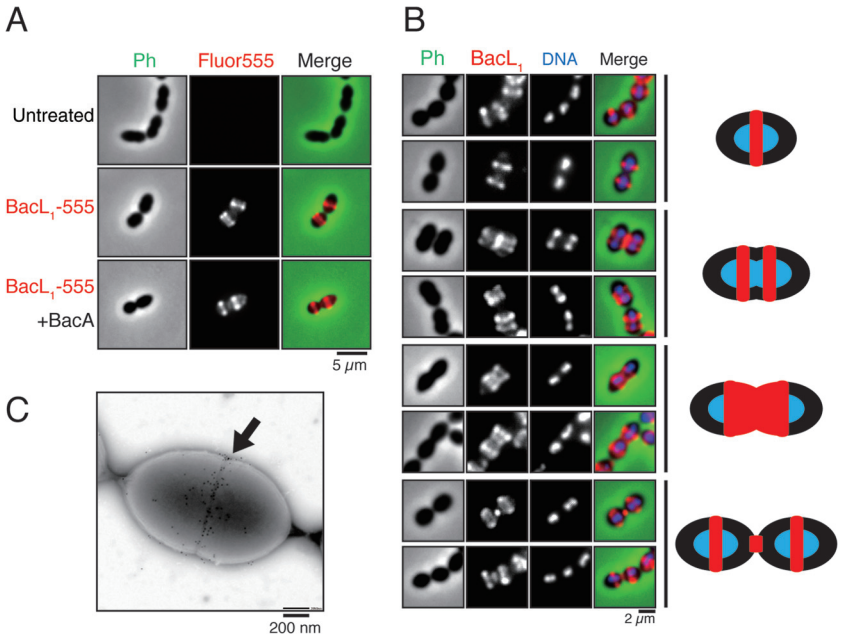

FIG 2 Localization of $BacL_1$ on the *E. faecalis* cell surface. (A) An overnight culture of *E. faecalis* OG1S diluted 5-fold with fresh THB broth was incubated with HiLyte Fluor 555 fluorescent dye-labeled (red) $BacL_1$ (5 μg/ml) in the presence (bottom) or absence (middle) of BacA, followed by analysis using fluorescence microscopy. Bacteria grown without red fluorescent conjugate are also shown as a negative control (top). Phase contrast (Ph) is pseudocolored (green) in the merged image. (B) Extensive representation of the localization pattern of red fluorescent dye-labeled $BacL_1$. The sample preparation was performed exactly as described for panel A. DNA was visualized with DAPI (blue). The schematic on the right illustrates the four characteristic patterns of $BacL_1$ localization and cell division states. (C) *E. faecalis* treated with $BacL_1$ and BacA (5 μg/ml each) was subjected to immunogold transmission electron microscopy using anti-$BacL_1$ antibodies. The arrow indicates the septum localization of gold particles.

phase did not affect the bacterial turbidity, similar to the results for the untreated culture. The bacterial viability test by colony formation assay also indicated that the bactericidal activity of $BacL_1$ and BacA was effective only in early or exponential phase but not stationary phase (Fig. 4B). In contrast, egg white lysozyme was able to decrease the viability of bacteria even in stationary phase (Fig. 4B). These observations indicated that *E. faecalis* in stationary phase was not susceptible to the cell lysis induced by $BacL_1$ and BacA. Then, to test the growth phase dependence of the septum targeting of $BacL_1$, the red fluorescence-labeled $BacL_1$ was incubated with *E. faecalis* cells in early exponential or stationary phase, and the $BacL_1$ localization was analyzed by fluorescence microscopy (Fig. 4C). In the case of the bacteria in early exponential phase, $BacL_1$ localized at the division septum. In contrast, the septum localization of $BacL_1$ was not observed in bacteria in stationary phase. $BacL_1$ also failed to even bind to the cell surface in stationary-phase bacteria (Fig. 4C). These results suggested that $BacL_1$ recognized the dividing cell surface. Furthermore, we investigated the susceptibility to bactericidal activity of $BacL_1$ and BacA when bacterial cell growth was artificially restricted with various antibiotic reagents (Fig. 5). Treatment with bacteriostatic antibiotics, such as chloramphenicol and tetracycline, almost completely rescued the cells from the bacteriolytic activity of $BacL_1$ and BacA (Fig. 5A and B). The localization of $BacL_1$ to the equatorial ring was also abolished in the chloramphenicol- or tetracycline-treated bacteria (Fig. 5C). Treatment with vancomycin, a bactericidal drug blocking cell wall synthesis, resulted in relief of the sensitivity of *E. faecalis* to lysis by $BacL_1$ and BacA and abolished $BacL_1$ targeting to the cell surface (Fig. 5A, B, and C). Interestingly, the bacteria treated with ampicillin, which has an elongating effect on bacterial cells by inhibiting the penicillin binding protein (PBP) functions, appeared to be more susceptible to the bactericidal activity of $BacL_1$ and BacA (Fig. 5A and B) and to the septum targeting of $BacL_1$ (Fig. 5C).

Specific recognition by $BacL_1$ of L-Ala_2-type peptidoglycan cross-bridging structure. The composition and length of the cross-bridge peptide-linking stem peptides bound to *N*-acetylmuramic acid are diverse among bacterial species (Fig. 6A) (40, 41). Lu et al. reported that the SH3 domain of ALE-1, a bacteriolytic peptidoglycan hydrolase of *Staphylococcus aureus*, specifically recognizes the pentaglycine cross bridge, which is a specific structure in the peptidoglycan of *S. aureus* (42). As shown by the results in Fig. 3, the SH3 domains appeared to be necessary for targeting the cell division-related region. To investigate whether the SH3 domain of $BacL_1$ also specifically recognizes the cross-bridging structure in the peptidoglycan of *E. faecalis*, we analyzed the cell division-associated targeting of $BacL_1$ in various Gram-positive bacterial species, including *E. faecalis* OG1S, *E. faecalis* OG1X, *E. faecalis* OG1RF, *E. faecalis* FA2-2, *E. faecium* BM4105RF, *Enterococcus hirae* 9790, *S. pyogenes* MGAS315, *S. pneumoniae* 262, *S. aureus* F-182, and *Listeria monocytogenes* EGD (Fig. 6B and Table 2). In bacteria with L-Ala-L-Ala-cross-bridging peptidoglycans, including *E. faecalis* strains OG1S, OG1X, OG1RF, and FA2-2 and *S. pyogenes*, $BacL_1$ clearly localized in the equatorial ring (38, 43–45). In contrast, the $BacL_1$ signal was not detected on *E. faecium*, *E. hirae*, or *S. aureus*, which have L-Asp-, D-Asn-, or penta-Gly-cross-bridging peptidoglycan, respectively (37, 46, 47). *L. monocytogenes*, which has direct bridging between stem peptides, was also not bound with $BacL_1$ (48, 49). In the case of *S. pneumoniae*, which has a hetero-cross-bridging structure consisting of L-Ala-L-Ala

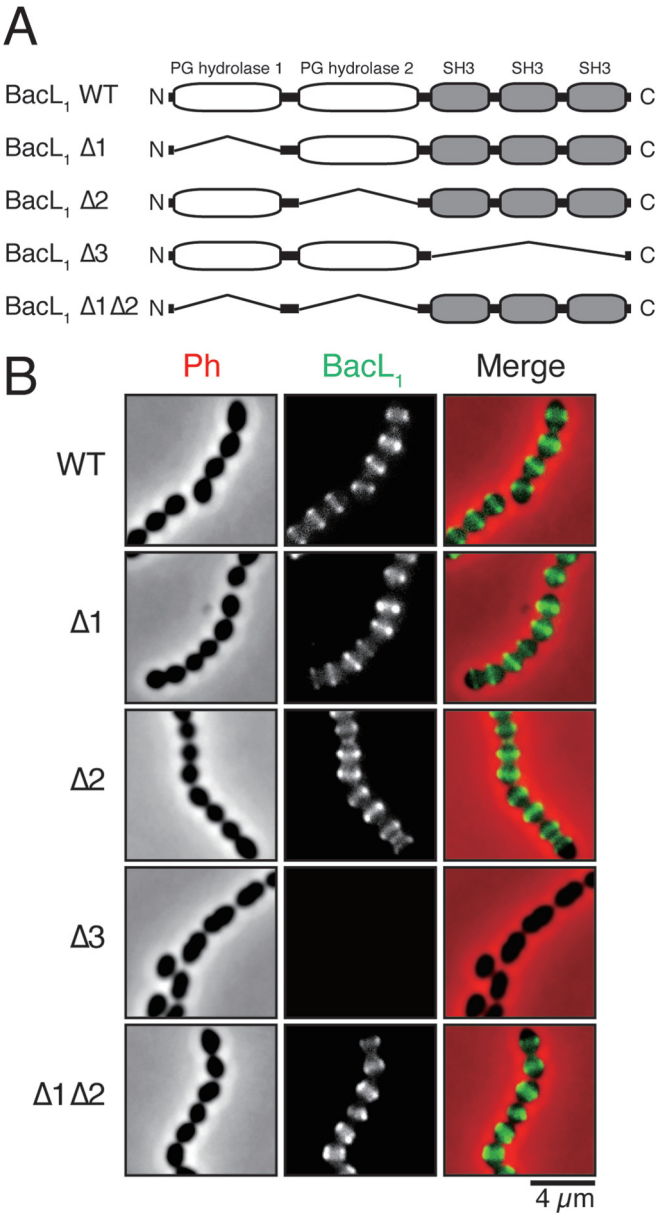

FIG 3 Domain of $BacL_1$ that is responsible for septum targeting. (A) Schematics of truncated $BacL_1$ constructs. (B) Overnight culture of *E. faecalis* OG1S diluted 5-fold with fresh THB broth was incubated with the fluorescein dye-labeled (green) truncated $BacL_1$ proteins (5 μg/ml) depicted in panel A, followed by analysis using fluorescence microscopy. Phase contrast (Ph) is pseudocolored (red) in merged images.

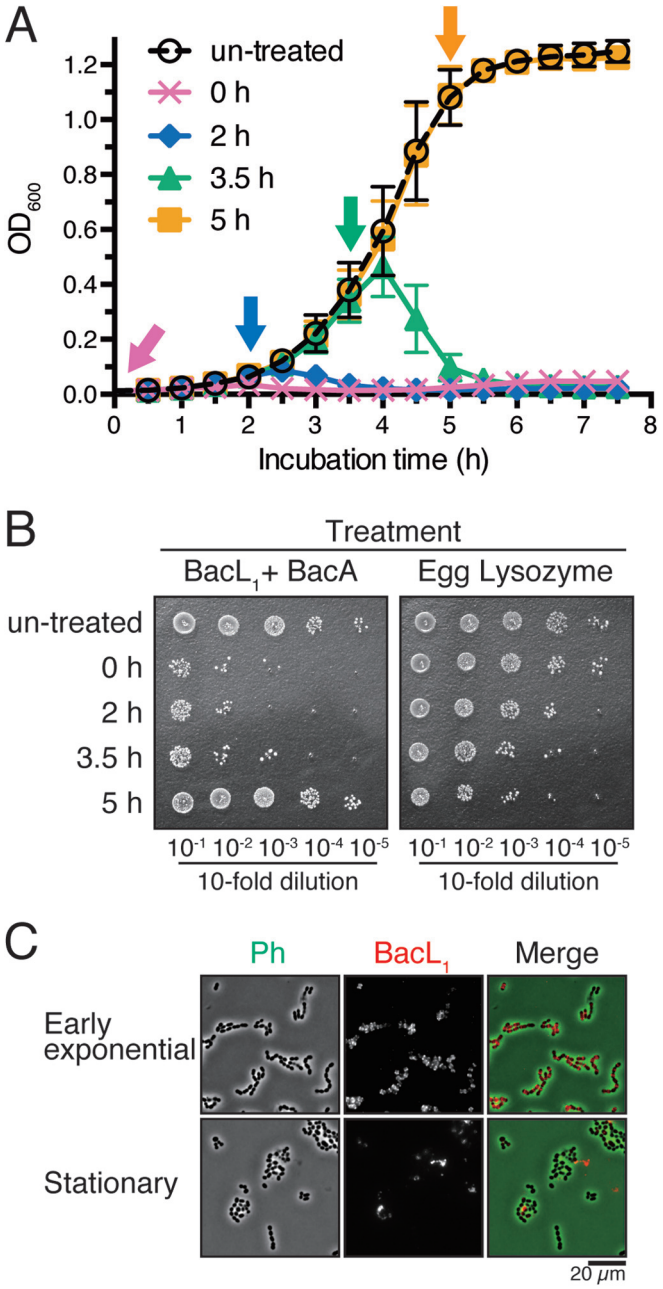

FIG 4 Growth phase dependence of the susceptibility to Bac41. (A) An overnight culture of *E. faecalis* OG1S diluted 100-fold with fresh THB broth was incubated at 37°C. A mixture of recombinant $BacL_1$ and BacA (5 μg/ml each) was added at different growth phases corresponding to 0 h, 2 h, 3.5 h, or 5 h, as indicated with arrows. An untreated culture served as the negative control. The turbidity (optical density at 600 nm [OD_{600}]) was monitored in each culture. The data are presented as the mean results ± standard deviations (SD) of three independent experiments. (B) *E. faecalis* was treated with $BacL_1$ and BacA at different growth phases as described for panel A. After further incubation for 1 h from each time point of addition, the bacterial suspensions were serially diluted 10-fold with fresh THB broth and then spotted onto a THB agar plate, followed by incubation overnight. Colony formation was evaluated as a measure of bacterial viability. Lysozyme was used as a control. (C) *E. faecalis* was treated with HiLyte Fluor 555-labeled (red) $BacL_1$ (5 μg/ml) in the early-exponential (2 h) or stationary (5 h) phase of growth. After further incubation for 1 h from each time point of addition, the cells were fixed and analyzed by fluorescence microscopy. Phase contrast (Ph) is pseudocolored (green) in the merged images.

and L-Ala-L-Ser, the equatorial localization was not observed; however, localization in the division septum was detected (50). Collectively, these observations suggest that $BacL_1$ specifically binds to the L-Ala-L-Ala-cross-bridged peptidoglycan. On the other hand, the bactericidal phenotype of $BacL_1$ and BacA was observed only in *E. faecalis* strains and not in the other bacterial species in soft-agar bacteriocin assays (Table 2). It is notable that *S. pyogenes* and *S. pneumoniae* were not susceptible to $BacL_1$ and BacA despite the targeting of $BacL_1$ to their cell surface (Table 2).

Immunity factor does not alter the $BacL_1$ equatorial targeting. The $BacL_1$- and BacA-producing *E. faecalis* has a self-resis-

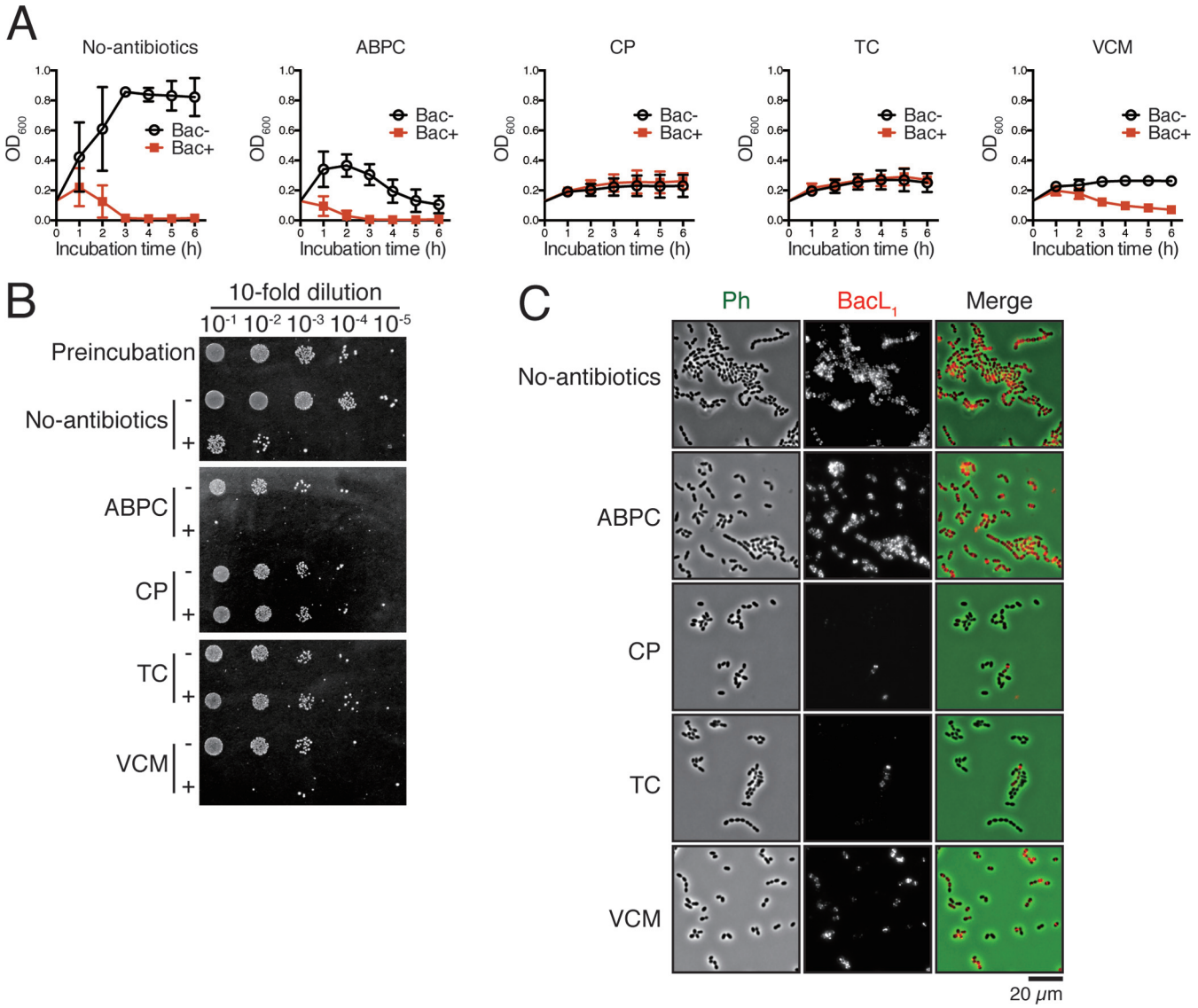

FIG 5 Effects of antibiotics on the susceptibility to Bac41. (A) An overnight culture of *E. faecalis* OG1S diluted 5-fold with fresh THB broth was incubated with (Bac+) or without (Bac−) a mixture of recombinant $BacL_1$ and BacA (5 μg/ml each) in the presence or absence of ampicillin (ABPC; 20 μg/ml), chloramphenicol (CP; 100 μg/ml), tetracycline (TC; 12.5 μg/ml), or vancomycin (VCM; 10 μg/ml). The turbidity at 600 nm was measured with a microplate reader during the incubation period. The data are presented as the mean results ± SD of three independent experiments. (B) *E. faecalis* was treated with (+) or without (−) a mixture of $BacL_1$ and BacA in the presence of antibiotics as described for panel A. After incubation for 6 h, the bacterial suspensions were serially diluted 10-fold with fresh THB broth and then spotted onto a THB agar plate, followed by incubation overnight. Colony formation was evaluated as a measure of bacterial viability. (C) An overnight culture of *E. faecalis* diluted 5-fold with fresh THB broth was treated with HiLyte Fluor 555-labeled (red) $BacL_1$ (5 μg/ml) in the presence of antibiotics as shown. After incubation for 1 h, the cells were fixed and analyzed by fluorescence microscopy. Phase contrast (Ph) is pseudocolored (green) in merged images.

tance factor, BacI, encoded in the vicinity of the *bacA* gene (Fig. 1A) (26). *E. faecalis* carrying the *bacI* gene is completely resistant to the bacteriolytic effect of $BacL_1$ and BacA (26, 28). Therefore, by fluorescence microscopy, we investigated whether the immunity factor *bacI* affects the $BacL_1$ targeting. The equatorial localization of $BacL_1$ was observed in *E. faecalis* carrying pHT1100 (a plasmid containing all Bac41 genes, including immunity factor *bacI*), as well as in *E. faecalis* carrying pAM401 (a vector control without the *bacI* gene) (Fig. 7A). Furthermore, the peptidoglycan purified from *E. faecalis* carrying pHT1100 was still degraded by $BacL_1$ (Fig. 7B). These results suggest that the specific immunity factor, BacI, has no effect on the $BacL_1$ activities of binding, targeting, and degrading peptidoglycan.

DISCUSSION

In this study, we report that $BacL_1$ targets the cell division-associated site, including the equatorial ring, division septum, and nascent synthesized cell wall (Fig. 2), to exert potential bactericidal activity against *E. faecalis* cells in the dividing state (Fig. 4 and 5). We also demonstrate that $BacL_1$ specifically recognizes peptidoglycan structures cross-linked by L-Ala-L-Ala but not by other peptide linkers (Fig. 6). Although the entire cell wall in *E. faecalis* is

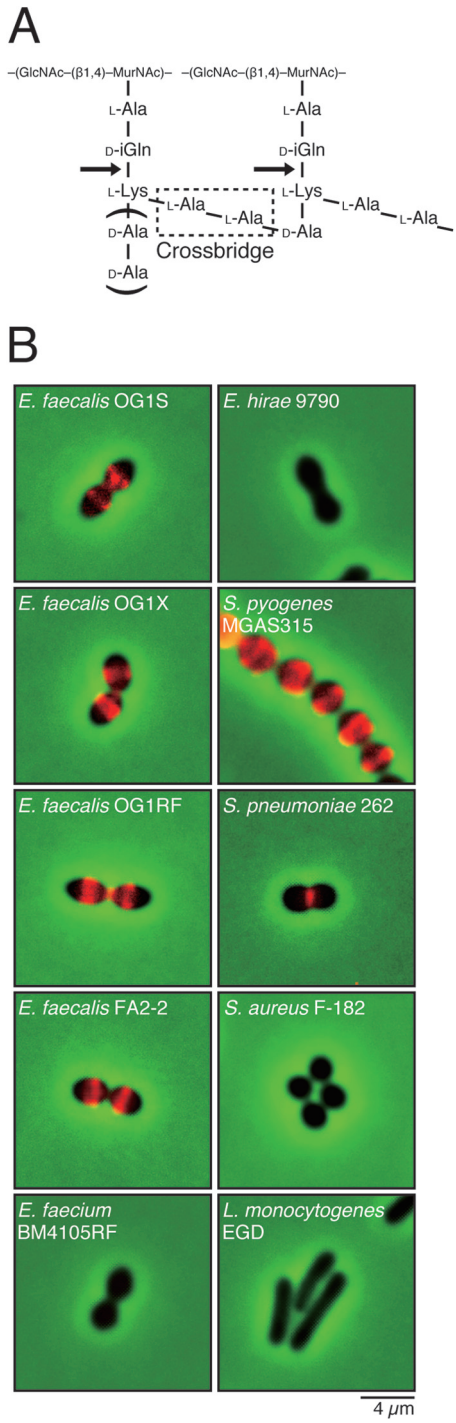

FIG 6 $BacL_1$ localization in various Gram-positive bacterial species. (A) Peptidoglycan structure of *E. faecalis*, representing an example of the organization of peptide chain-cross-linking by a dipeptide. The dotted-line frame indicates the cross-bridging peptide between stem peptides bound to *N*-acetylmuramic acids. Arrows indicate the sites of cleavage by the endopeptidase activity of $BacL_1$. (B) Overnight cultures of Gram-positive bacteria, diluted 5-fold with fresh THB broth, were treated with HiLyte Fluor 555-labeled (red) $BacL_1$ (5 μg/ml). After incubation for 1 h, the cells were fixed and analyzed by fluorescence microscopy. Phase contrast is pseudocolored (green) in the merged images.

composed of L-Ala-LAla-cross-bridged peptidoglycan that is likely to be recognized by $BacL_1$, there must be an additional determinant(s) for the localized targeting of $BacL_1$ to the cell division-associated sites. The equatorial ring is a characteristic structure observed at the middle of ovococcus cells (32, 51, 52). This ring structure marks the initiation site for the peripheral cell wall-synthesizing machinery to construct the new peptidoglycan during cell elongation. Therefore, $BacL_1$ might recognize the cell wall-synthesizing machinery complex that is formed at the equatorial ring or division septum during cell division. Alternatively, the relatively extended distribution of $BacL_1$, from equatorial ring to division septum, raises the possibility that $BacL_1$ preferentially binds to newly synthesized nascent cell wall. Martínez et al. demonstrated that a bacteriocin of *Lactococcus lactis*, lactococcin 972, inhibits the septum formation to cause abnormal cell morphology in sensitive target cells. Although they have not shown this, lactococcin 972 itself might be associated with the cell-dividing structure, like $BacL_1$ (53). Understanding the determinant(s) restricting the targeting site of $BacL_1$ to cell division-related areas requires further analysis.

As shown by the results in Fig. 3, the SH3 repeat moiety of $BacL_1$ was required and sufficient for its localized targeting. These repeats are present in the region from amino acid 329 to 590 of $BacL_1$ (see Fig. S2A in the supplemental material). These individual SH3 repeats are nearly identical to each other (see Fig. S2B). The SH3 domain sequences of $BacL_1$ also show significant homology to SH3 domains from other bactericidal proteins (see Fig. S2C), such as ALE-1 from *S. aureus* (54). Crystal structure analysis of the SH3 domain in ALE-1 revealed that the N-terminal conserved motif YXXNKYGTXYXXESA is a recognition groove that specifically binds to penta-Gly-cross-bridging peptides in *S. aureus* peptidoglycan (42). The YXXNKYGTXYXXESA motif (see Fig. S2C, blue frames) is not present in the SH3 domain of $BacL_1$. Instead, extra conserved residues (see Fig. S2C, red frames) are present among the SH3 domains targeting bacteria with an L-Ala-L-Ala-cross-bridged cell wall, including *E. faecalis*, *Streptococcus agalactiae*, and *S. pneumoniae*. Furthermore, amino acids 15 and 14 in the N terminus and C terminus, respectively, are highly conserved motifs (see Fig. S2C, magenta highlighting) among the three SH3 domains of $BacL_1$, suggesting that these conserved motifs in $BacL_1$ may play a role in the specific recognition of the L-Ala-L-Ala-cross-bridged peptidoglycan structure.

Lysostaphin, with activity specific against *S. aureus*, is able to distinguish the penta-Gly-cross-bridging structure in the peptidoglycan of *S. aureus* from the cross-bridging structures of other peptidoglycans (55). The lysostaphin-specific immunity factor Lif, a FemABX-like protein, incorporates serine into the cross-bridging peptides in peptidoglycan of *S. aureus* and converts it from the penta-Gly-type cross bridge (56). This conversion of the cross-bridging peptide in peptidoglycan results in resistance to lysostaphin. Zoocin A is a bacteriolytic endopeptidase against the cell wall of sensitive bacteria produced by *Streptococcus equi* subsp. *zooepidemicus* strain 4881 (57). The cross bridge in peptidoglycan of *S. equi* is an L-Ala-L-Ala peptide and is susceptible to the peptidoglycan hydrolase activity of zoocin A (57). Zif, an immunity factor of zoocin A, belongs to the FemABX-like protein family (58). It additively increases L-Ala residues in the cross bridges of peptidoglycans and converts L-Ala-L-Ala into L-Ala-L-Ala-L-Ala, resulting in resistance to zoocin A activity. Meanwhile, BacI,

TABLE 2 Summary of cross-bridge structure and phenotypes against Bac41 in various bacterial species

Species	Strain	Cross-bridging peptide	Presence of phenotype[a]	
			Targeting of $BacL_1$[b]	Susceptibility to Bac41[c]
Enterococcus faecalis	OG1S	L-Ala-L-Ala	+	+
Enterococcus faecalis	OG1X	L-Ala-L-Ala	+	+
Enterococcus faecalis	OG1RF	L-Ala-L-Ala	+	+
Enterococcus faecalis	FA2-2	L-Ala-L-Ala	+	±
Enterococcus faecium	BM4105RF	L-Asp	−	−
Enterococcus hirae	9790	D-Asn	−	−
Streptococcus pyogenes	MGAS315	L-Ala-L-Ala	+	−
Streptococcus pneumoniae	262	L-Ala-L-Ala/L-Ser	±	−
Staphylococcus aureus	F-182	Gly_5	−	−
Listeria monocytogenes	EGD	NA[d]	−	−

[a] +, clear/positive; ±, obscure/weak; −, negative.
[b] Targeting of $BacL_1$ was determined from the results shown in Fig. 6B.
[c] Susceptibility to Bac41 ($BacL_1$ and BacA mixture) was determined by a soft-agar-based bacteriocin assay.
[d] NA, not applicable; *L. monocytogenes* has direct bridging between stem peptides.

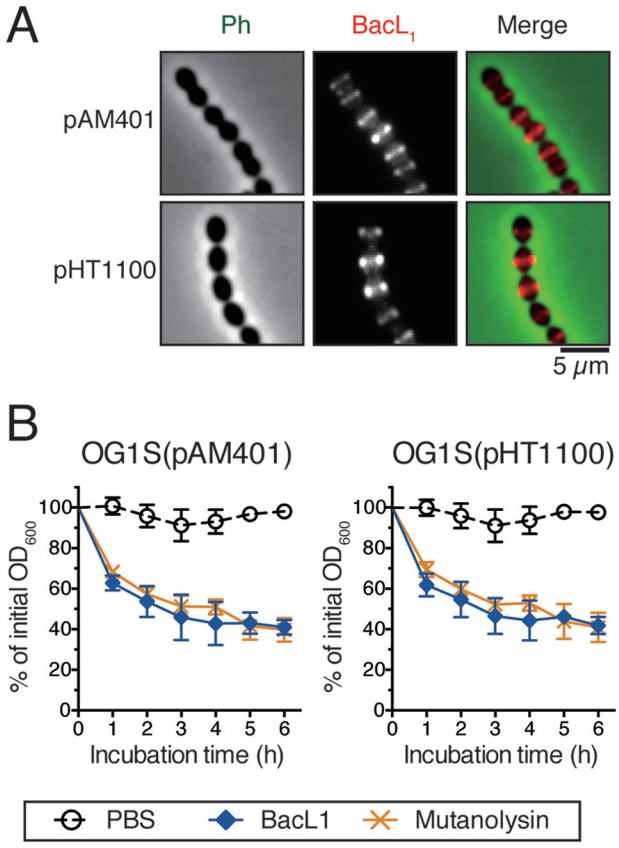

FIG 7 Involvement of Bac41 specific immunity factor BacI in the susceptibility of cell wall to $BacL_1$. (A) An overnight culture of *E. faecalis* carrying pAM401 (a vector control without the *bacI* gene) or pHT1100 (a pAM401 derivative containing all Bac41 genes, including immunity factor *bacI*) diluted 5-fold with fresh THB broth was treated with HiLyte Fluor 555-labeled (red) $BacL_1$ (5 μg/ml). After incubation for 1 h, the cells were fixed and analyzed by fluorescence microscopy. Phase contrast (Ph) is pseudocolored (green) in merged images. (B) A cell wall fraction prepared from *E. faecalis* carrying pAM401 or pHT1100 in exponential phase was diluted with PBS. Recombinant $BacL_1$ (5 μg/ml) or mutanolysin (1 μg/ml) was added to the cell wall suspension, and the mixture incubated at 37°C. The turbidity at 600 nm was quantified at the indicated times during incubation. The values presented are the percentages of the initial turbidity of the respective samples. The PBS-treated sample is presented in each graph as a negative control. The data are presented as the mean results ± SD of three independent experiments.

which is the cognate immunity factor against Bac41, did not affect the $BacL_1$ targeting (Fig. 7A). In addition, the cell wall fraction prepared from *E. faecalis* that is resistant to Bac41 due to the presence of *bacI* was still susceptible to the peptidoglycan-degrading activity of $BacL_1$ (Fig. 7B), suggesting that BacI is not involved in the activity of $BacL_1$. This result suggests the possibility that BacI confers immunity by acting on the function of BacA rather than that of $BacL_1$ or that another factor(s) of target cells, such as molecules or receptors that are only present in the growing cells, is involved in the BacI-mediated resistance.

The bactericidal activity of Bac41 ($BacL_1$ and BacA) is strictly specific against *E. faecalis*, and Bac41 does not show any activity against the other bacterial species tested (Table 2). The specificity could be partially explained by the diversity of cross-bridging peptides of peptidoglycan among bacterial species. As demonstrated by the results in Fig. 6B, $BacL_1$ appears to discriminate target bacterial species from nontarget species by specific recognition of L-Ala-L-Ala-cross-bridged peptidoglycan. Indeed, $BacL_1$ is able to target bacteria with L-Ala-L-Ala-cross-bridged peptidoglycan, such as *S. pyogenes* and *S. pneumoniae*, regardless of the bacterial genus. In contrast, *E. faecium* and *E. hirae*, with peptidoglycans cross bridged by L-Asp and D-Asn, respectively, were not recognized by $BacL_1$ although they are phylogenetically classified in the same genus as *E. faecalis*. These observations demonstrated that the activity of $BacL_1$ is specific against bacteria with L-Ala-L-Ala-cross-bridged peptidoglycans. However, the bacteriolytic phenotype in the copresence of $BacL_1$ and BacA appears to be more complex (Table 2). The bactericidal effect of $BacL_1$ and BacA (Bac41) was observed only against *E. faecalis* even though other bacteria are of the L-Ala-L-Ala-cross-bridge type. Interestingly, *S. pyogenes* and *S. pneumoniae* were not susceptible to $BacL_1$ and BacA although they were targeted with $BacL_1$. One possibility is that BacA is not able to access *S. pyogenes* and *S. pneumoniae*. Furthermore, the susceptibility of *E. faecalis* FA2-2 to $BacL_1$ and BacA was lower than that of *E. faecalis* OG1-derived strains, such as OG1S, OG1X, and OG1RF. Thurlow et al. reported that enterococcal capsular polysaccharide is present in FA2-2 but not in OG1 strains (59). Thus, probably the capsule on the cell surface of strain FA2-2 cells limits the access of BacA, resulting in the decreased susceptibility to Bac41-induced lysis. To reveal the detailed mo-

lecular mechanism of the Bac41 module, further functional analysis of BacA is needed.

The Bac41-mediated fratricide module excludes *E. faecalis* strains without the Bac41-encoding plasmid. Therefore, this module is inferred to play a role in the effective expansion of the Bac41-carrying plasmid. Our conclusion that cell growth is required for cell lysis by $BacL_1$ and BacA (Fig. 4 and 5) is consistent with the hypothesis because selection is involved in possible plasmid loss during distribution to daughter cells. Hence, it is reasonable that the Bac41 system works only when bacteria are allowed to grow, replicate DNA, and distribute plasmid to daughter cells. Our results in this study suggest a novel player involved in the plasmid maintenance system.

ACKNOWLEDGMENTS

This work was supported by grants from the Japanese Ministry of Education, Culture, Sport, Science and Technology [Grant-in-Aid for Young Scientists (B) 25870116, Gunma University Operation grants] and the Japanese Ministry of Health, Labor and Welfare (H24-Shinkou-Ippan-010 and H24-Shokuhin-Ippan-008).

REFERENCES

1. **Jett BD, Huycke MM, Gilmore MS.** 1994. Virulence of enterococci. Clin Microbiol Rev **7:**462–478.
2. **Murray BE.** 1990. The life and times of the *Enterococcus*. Clin Microbiol Rev **3:**46–65.
3. **Arias CA, Murray BE.** 2012. The rise of the *Enterococcus*: beyond vancomycin resistance. Nat Rev Microbiol **10:**266–278. http://dx.doi.org/10.1038/nrmicro2761.
4. **Clewell DB.** 1981. Plasmids, drug resistance, and gene transfer in the genus *Streptococcus*. Microbiol Rev **45:**409–436.
5. **Ike Y, Hashimoto H, Clewell DB.** 1987. High incidence of hemolysin production by *Enterococcus* (*Streptococcus*) *faecalis* strains associated with human parenteral infections. J Clin Microbiol **25:**1524–1528.
6. **Jack RW, Tagg JR, Ray B.** 1995. Bacteriocins of gram-positive bacteria. Microbiol Rev **59:**171–200.
7. **Nes IF, Diep DB, Ike Y.** 2014. Enterococcal bacteriocins and antimicrobial proteins that contribute to niche control. *In* Gilmore MS, Clewell DB, Ike Y, Shankar N (ed), Enterococci: from commensals to leading causes of drug resistant infection. Massachusetts Eye and Ear Infirmary, Boston, MA.
8. **Nes IF, Diep DB, Holo H.** 2007. Bacteriocin diversity in *Streptococcus* and *Enterococcus*. J Bacteriol **189:**1189–1198. http://dx.doi.org/10.1128/JB.01254-06.
9. **Field D, Hill C, Cotter PD, Ross RP.** 2010. The dawning of a "Golden era" in lantibiotic bioengineering. Mol Microbiol **78:**1077–1087. http://dx.doi.org/10.1111/j.1365-2958.2010.07406.x.
10. **Ike Y, Hashimoto H, Clewell DB.** 1984. Hemolysin of *Streptococcus faecalis* subspecies zymogenes contributes to virulence in mice. Infect Immun **45:**528–530.
11. **Chow JW, Thal LA, Perri MB, Vazquez JA, Donabedian SM, Clewell DB, Zervos MJ.** 1993. Plasmid-associated hemolysin and aggregation substance production contribute to virulence in experimental enterococcal endocarditis. Antimicrob Agents Chemother **37:**2474–2477. http://dx.doi.org/10.1128/AAC.37.11.2474.
12. **Van Tyne D, Martin MJ, Gilmore MS.** 2013. Structure, function, and biology of the *Enterococcus faecalis* cytolysin. Toxins (Basel) **5:**895–911. http://dx.doi.org/10.3390/toxins5050895.
13. **Jett BD, Jensen HG, Nordquist RE, Gilmore MS.** 1992. Contribution of the pAD1-encoded cytolysin to the severity of experimental Enterococcus faecalis endophthalmitis. Infect Immun **60:**2445–2452.
14. **Sawa N, Wilaipun P, Kinoshita S, Zendo T, Leelawatcharamas V, Nakayama J, Sonomoto K.** 2012. Isolation and characterization of enterocin W, a novel two-peptide lantibiotic produced by *Enterococcus faecalis* NKR-4-1. Appl Environ Microbiol **78:**900–903. http://dx.doi.org/10.1128/AEM.06497-11.
15. **Aymerich T, Holo H, Håvarstein LS, Hugas M, Garriga M, Nes IF.** 1996. Biochemical and genetic characterization of enterocin A from *Enterococcus faecium*, a new antilisterial bacteriocin in the pediocin family of bacteriocins. Appl Environ Microbiol **62:**1676–1682.
16. **Martínez-Bueno M, Maqueda M, Galvez A, Samyn B, Van Beeumen J, Coyette J, Valdivia E.** 1994. Determination of the gene sequence and the molecular structure of the enterococcal peptide antibiotic AS-48. J Bacteriol **176:**6334–6339.
17. **Tomita H, Fujimoto S, Tanimoto K, Ike Y.** 1997. Cloning and genetic and sequence analyses of the bacteriocin 21 determinant encoded on the *Enterococcus faecalis* pheromone-responsive conjugative plasmid pPD1. J Bacteriol **179:**7843–7855.
18. **Tomita H, Fujimoto S, Tanimoto K, Ike Y.** 1996. Cloning and genetic organization of the bacteriocin 31 determinant encoded on the *Enterococcus faecalis* pheromone-responsive conjugative plasmid pYI17. J Bacteriol **178:**3585–3593.
19. **Inoue T, Tomita H, Ike Y.** 2006. Bac 32, a novel bacteriocin widely disseminated among clinical isolates of *Enterococcus faecium*. Antimicrob Agents Chemother **50:**1202–1212. http://dx.doi.org/10.1128/AAC.50.4.1202-1212.2006.
20. **Todokoro D, Tomita H, Inoue T, Ike Y.** 2006. Genetic analysis of bacteriocin 43 of vancomycin-resistant *Enterococcus faecium*. Appl Environ Microbiol **72:**6955–6964. http://dx.doi.org/10.1128/AEM.00934-06.
21. **Yamashita H, Tomita H, Inoue T, Ike Y.** 2011. Genetic organization and mode of action of a novel bacteriocin, bacteriocin 51: determinant of VanA-Type vancomycin-resistant *Enterococcus faecium*. Antimicrob Agents Chemother **55:**4352–4360. http://dx.doi.org/10.1128/AAC.01274-10.
22. **Klaenhammer TR.** 1993. Genetics of bacteriocins produced by lactic acid bacteria. FEMS Microbiol Rev **12:**39–85. http://dx.doi.org/10.1111/j.1574-6976.1993.tb00012.x.
23. **Cotter PD, Hill C, Ross RP.** 2005. Bacteriocins: developing innate immunity for food. Nat Rev Microbiol **3:**777–788. http://dx.doi.org/10.1038/nrmicro1273.
24. **Nilsen T, Nes IF, Holo H.** 2003. Enterolysin A, a cell wall-degrading bacteriocin from *Enterococcus faecalis* LMG 2333. Appl Environ Microbiol **69:**2975–2984. http://dx.doi.org/10.1128/AEM.69.5.2975-2984.2003.
25. **Hickey RM, Twomey DP, Ross RP, Hill C.** 2003. Production of enterolysin A by a raw milk enterococcal isolate exhibiting multiple virulence factors. Microbiology **149**(Pt 3):655–664. http://dx.doi.org/10.1099/mic.0.25949-0.
26. **Tomita H, Kamei E, Ike Y.** 2008. Cloning and genetic analyses of the bacteriocin 41 determinant encoded on the *Enterococcus faecalis* pheromone-responsive conjugative plasmid pYI14: a novel bacteriocin complemented by two extracellular components (lysin and activator). J Bacteriol **190:**2075–2085. http://dx.doi.org/10.1128/JB.01056-07.
27. **Zheng B, Tomita H, Inoue T, Ike Y.** 2009. Isolation of VanB-type *Enterococcus faecalis* strains from nosocomial infections: first report of the isolation and identification of the pheromone-responsive plasmids pMG2200, encoding VanB-type vancomycin resistance and a Bac41-type bacteriocin, and pMG2201, encoding erythromycin resistance and cytolysin (Hly/Bac). Antimicrob Agents Chemother **53:**735–747. http://dx.doi.org/10.1128/AAC.00754-08.
28. **Kurushima J, Hayashi I, Sugai M, Tomita H.** 2013. Bacteriocin protein $BacL_1$ of *Enterococcus faecalis* is a peptidoglycan D-isoglutamyl-L-lysine endopeptidase. J Biol Chem **288:**36915–36925. http://dx.doi.org/10.1074/jbc.M113.506618.
29. **Sheehan MM, García JL, López R, García P.** 1997. The lytic enzyme of the pneumococcal phage Dp-1: a chimeric lysin of intergeneric origin. Mol Microbiol **25:**717–725. http://dx.doi.org/10.1046/j.1365-2958.1997.5101880.x.
30. **Pecenková T, Benes V, Paces J, Vlcek C, Paces V.** 1997. Bacteriophage B103: complete DNA sequence of its genome and relationship to other *Bacillus* phages. Gene **199:**157–163. http://dx.doi.org/10.1016/S0378-1119(97)00363-6.
31. **Pinho MG, Kjos M, Veening J-W.** 2013. How to get (a)round: mechanisms controlling growth and division of coccoid bacteria. Nat Rev Microbiol **11:**601–614. http://dx.doi.org/10.1038/nrmicro3088.
32. **Zapun A, Vernet T, Pinho MG.** 2008. The different shapes of cocci. FEMS Microbiol Rev **32:**345–360. http://dx.doi.org/10.1111/j.1574-6976.2007.00098.x.
33. **Monahan LG, Liew ATF, Bottomley AL, Harry EJ.** 2014. Division site positioning in bacteria: one size does not fit all. Front Microbiol **5:**19. http://dx.doi.org/10.3389/fmicb.2014.00019.
34. **Sambrook JJ, Russell DW.** 2001. Molecular cloning: a laboratory manual, 3rd ed. Cold Spring Harbor Laboratory Press, Cold Spring Harbor, NY.
35. **Dunny GM, Craig RA, Carron RL, Clewell DB.** 1979. Plasmid transfer in *Streptococcus faecalis*: production of multiple sex pheromones by

recipients. Plasmid **2:**454–465. http://dx.doi.org/10.1016/0147-619X(79)90029-5.
36. **Ike Y, Clewell DB, Segarra RA, Gilmore MS.** 1990. Genetic analysis of the pAD1 hemolysin/bacteriocin determinant in *Enterococcus faecalis*: Tn*917* insertional mutagenesis and cloning. J Bacteriol **172:**155–163.
37. **Kajimura J, Fujiwara T, Yamada S, Suzawa Y, Nishida T, Oyamada Y, Hayashi I, Yamagishi J-I, Komatsuzawa H, Sugai M.** 2005. Identification and molecular characterization of an *N*-acetylmuramyl-L-alanine amidase Sle1 involved in cell separation of *Staphylococcus aureus*. Mol Microbiol **58:**1087–1101. http://dx.doi.org/10.1111/j.1365-2958.2005.04881.x.
38. **Eckert C, Lecerf M, Dubost L, Arthur M, Mesnage S.** 2006. Functional analysis of AtlA, the major *N*-acetylglucosaminidase of *Enterococcus faecalis*. J Bacteriol **188:**8513–8519. http://dx.doi.org/10.1128/JB.01145-06.
39. **Mellroth P, Daniels R, Eberhardt A, Ronnlund D, Blom H, Widengren J, Normark S, Henriques-Normark B.** 2012. LytA, major autolysin of *Streptococcus pneumoniae*, requires access to nascent peptidoglycan. J Biol Chem **287:**11018–11029. http://dx.doi.org/10.1074/jbc.M111.318584.
40. **Schleifer KH, Kandler O.** 1972. Peptidoglycan types of bacterial cell walls and their taxonomic implications. Bacteriol Rev **36:**407–477.
41. **Magnet S, Arbeloa A, Mainardi J-L, Hugonnet J-E, Fourgeaud M, Dubost L, Marie A, Delfosse V, Mayer C, Rice LB, Arthur M.** 2007. Specificity of L,D-transpeptidases from gram-positive bacteria producing different peptidoglycan chemotypes. J Biol Chem **282:**13151–13159. http://dx.doi.org/10.1074/jbc.M610911200.
42. **Lu JZ, Fujiwara T, Komatsuzawa H, Sugai M, Sakon J.** 2006. Cell wall-targeting domain of glycylglycine endopeptidase distinguishes among peptidoglycan cross-bridges. J Biol Chem **281:**549–558. http://dx.doi.org/10.1074/jbc.M509691200.
43. **Arbeloa A, Segal H, Hugonnet J-E, Josseaume N, Dubost L, Brouard J-P, Gutmann L, Mengin-Lecreulx D, Arthur M.** 2004. Role of class A penicillin-binding proteins in PBP5-mediated beta-lactam resistance in *Enterococcus faecalis*. J Bacteriol **186:**1221–1228. http://dx.doi.org/10.1128/JB.186.5.1221-1228.2004.
44. **Uchiyama J, Takemura I, Hayashi I, Matsuzaki S, Satoh M, Ujihara T, Murakami M, Imajoh M, Sugai M, Daibata M.** 2011. Characterization of lytic enzyme open reading frame 9 (ORF9) derived from *Enterococcus faecalis* bacteriophage phiEF24C. Appl Environ Microbiol **77:**580–585. http://dx.doi.org/10.1128/AEM.01540-10.
45. **Lood R, Raz A, Molina H, Euler CW, Fischetti VA.** 2014. A highly active and negatively charged *Streptococcus pyogenes* lysin with a rare D-alanyl-L-alanine endopeptidase activity protects mice against streptococcal bacteremia. Antimicrob Agents Chemother **58:**3073–3084. http://dx.doi.org/10.1128/AAC.00115-14.
46. **Mainardi J-L, Fourgeaud M, Hugonnet J-E, Dubost L, Brouard J-P, Ouazzani J, Rice LB, Gutmann L, Arthur M.** 2005. A novel peptidoglycan cross-linking enzyme for a beta-lactam-resistant transpeptidation pathway. J Biol Chem **280:**38146–38152. http://dx.doi.org/10.1074/jbc.M507384200.
47. **Barrett JF, Shockman GD.** 1984. Isolation and characterization of soluble peptidoglycan from several strains of *Streptococcus faecium*. J Bacteriol **159:**511–519.
48. **Kamisango K, Saiki I, Tanio Y, Okumura H, Araki Y, Sekikawa I, Azuma I, Yamamura Y.** 1982. Structures and biological activities of peptidoglycans of *Listeria monocytogenes* and *Propionibacterium acnes*. J Biochem **92:**23–33.
49. **Ronholm J, Wang L, Hayashi I, Sugai M, Zhang Z, Cao X, Lin M.** 2012. The *Listeria monocytogenes* serotype 4b autolysin IspC has N-acetylglucosaminidase activity. Glycobiology **22:**1311–1320. http://dx.doi.org/10.1093/glycob/cws100.
50. **Severin A, Tomasz A.** 1996. Naturally occurring peptidoglycan variants of *Streptococcus pneumoniae*. J Bacteriol **178:**168–174.
51. **Le Gouëllec A, Roux L, Fadda D, Massidda O, Vernet T, Zapun A.** 2008. Roles of pneumococcal DivIB in cell division. J Bacteriol **190:**4501–4511. http://dx.doi.org/10.1128/JB.00376-08.
52. **Sham L-T, Barendt SM, Kopecky KE, Winkler ME.** 2011. Essential PcsB putative peptidoglycan hydrolase interacts with the essential FtsXSpn cell division protein in *Streptococcus pneumoniae* D39. Proc Natl Acad Sci U S A **108:**E1061–E1069. http://dx.doi.org/10.1073/pnas.1108323108.
53. **Martínez B, Rodríguez A, Suárez JE.** 2000. Lactococcin 972, a bacteriocin that inhibits septum formation in lactococci. Microbiology **146**(Pt 4)**:** 949–955.
54. **Sugai M, Yamada S, Nakashima S, Komatsuzawa H, Matsumoto A, Oshida T, Suginaka H.** 1997. Localized perforation of the cell wall by a major autolysin: *atl* gene products and the onset of penicillin-induced lysis of *Staphylococcus aureus*. J Bacteriol **179:**2958–2962.
55. **Gründling A, Schneewind O.** 2006. Cross-linked peptidoglycan mediates lysostaphin binding to the cell wall envelope of *Staphylococcus aureus*. J Bacteriol **188:**2463–2472. http://dx.doi.org/10.1128/JB.188.7.2463-2472.2006.
56. **DeHart HP, Heath HE, Heath LS, LeBlanc PA, Sloan GL.** 1995. The lysostaphin endopeptidase resistance gene (*epr*) specifies modification of peptidoglycan cross bridges in *Staphylococcus simulans* and *Staphylococcus aureus*. Appl Environ Microbiol **61:**1475–1479.
57. **Gargis SR, Heath HE, Heath LS, Leblanc PA, Simmonds RS, Abbott BD, Timkovich R, Sloan GL.** 2009. Use of 4-sulfophenyl isothiocyanate labeling and mass spectrometry to determine the site of action of the streptococcolytic peptidoglycan hydrolase zoocin A. Appl Environ Microbiol **75:**72–77. http://dx.doi.org/10.1128/AEM.01647-08.
58. **Gargis SR, Gargis AS, Heath HE, Heath LS, LeBlanc PA, Senn MM, Berger-Bachi B, Simmonds RS, Sloan GL.** 2009. Zif, the zoocin A immunity factor, is a FemABX-like immunity protein with a novel mode of action. Appl Environ Microbiol **75:**6205–6210. http://dx.doi.org/10.1128/AEM.01011-09.
59. **Thurlow LR, Thomas VC, Hancock LE.** 2009. Capsular polysaccharide production in *Enterococcus faecalis* and contribution of CpsF to capsule serospecificity. J Bacteriol **191:**6203–6210. http://dx.doi.org/10.1128/JB.00592-09.
60. **Clewell DB, Tomich PK, Gawron-Burke MC, Franke AE, Yagi Y, An FY.** 1982. Mapping of *Streptococcus faecalis* plasmids pAD1 and pAD2 and studies relating to transposition of Tn917. J Bacteriol **152:**1220–1230.
61. **Tomita H, Pierson C, Lim SK, Clewell DB, Ike Y.** 2002. Possible connection between a widely disseminated conjugative gentamicin resistance (pMG1-like) plasmid and the emergence of vancomycin resistance in Enterococcus faecium. J Clin Microbiol **40:**3326–3333. http://dx.doi.org/10.1128/JCM.40.9.3326-3333.2002.
62. **Wirth R, An FY, Clewell DB.** 1986. Highly efficient protoplast transformation system for *Streptococcus faecalis* and a new *Escherichia coli-S. faecalis* shuttle vector. J Bacteriol **165:**831–836.